

WRIGHT RESEARCH AND DEVELOPMENT CENTER



AD-A210 201

WRDC-TR-89-4044  
Volume II

CONFERENCE ON AEROSPACE TRANSPARENT MATERIALS AND ENCLOSURES  
VOLUME II - SESSIONS VI-IX

S. A. Marolo  
Materials Engineering Branch  
Systems Support Division

April 1989

Conference Report for Period 16-20 January 1989

Approved for Public Release; Distribution Unlimited

SDTICD  
ELECTE  
JUL 10 1989

CH

MATERIALS LABORATORY  
WRIGHT RESEARCH AND DEVELOPMENT CENTER  
AIR FORCE SYSTEMS COMMAND  
WRIGHT-PATTERSON AIR FORCE BASE, OHIO 45433-6533


89 7 10 017


NOTICE

When Government drawings, specifications, or other data are used for any purpose other than in connection with a definitely related Government procurement operation, the United States Government thereby incurs no responsibility nor any obligation whatsoever; and the fact that the government may have formulated, furnished, or in any way supplied the said drawings, specifications, or other data, is not to be regarded by implication or otherwise as in any manner licensing the holder or any other person or corporation, or conveying any rights or permission to manufacture, use, or sell any patented invention that may in any way be related thereto.


This report has been reviewed by the Office of Public Affairs (ASD/PA) and is releasable to the National Technical Information Service (NTIS). At NTIS, it will be available to the general public, including foreign nations.

This technical report has been reviewed and is approved for publication.

  
THEODORE J. REINHART, Chief  
Materials Engineering Branch  
Systems Support Division  
Materials Laboratory

  
RALPH J. SPEELMAN, Chief  
Aircrew Protection Branch  
Vehicle Subsystems Division  
Flight Dynamics Laboratory

FOR THE COMMANDER

  
WARREN JOHNSON, Chief  
Systems Support Division  
Materials Laboratory

If your address has changed, if you wish to be removed from our mailing list, or if the addressee is no longer employed by your organization please notify WRDC/FIVR, W-PAFB, OH 45433-6533 to help us maintain a current mailing list.

Copies of this report should not be returned unless return is required by security considerations, contractual obligations, or notice on a specific document.

UNCLASSIFIED

SECURITY CLASSIFICATION OF THIS PAGE

## REPORT DOCUMENTATION PAGE

Form Approved  
OMB No. 0704-0188

1a. REPORT SECURITY CLASSIFICATION <b>UNCLASSIFIED</b>		1b. RESTRICTIVE MARKINGS	
2a. SECURITY CLASSIFICATION AUTHORITY		3. DISTRIBUTION / AVAILABILITY OF REPORT Approved for public release; distribution unlimited.	
2b. DECLASSIFICATION / DOWNGRADING SCHEDULE			
4. PERFORMING ORGANIZATION REPORT NUMBER(S) WRDC-TR-89-4044, Vol II		5. MONITORING ORGANIZATION REPORT NUMBER(S) <i>London Ohio</i>	
6a. NAME OF PERFORMING ORGANIZATION Materials Laboratory	6b. OFFICE SYMBOL (if applicable) (WRDC/MLSE)	7a. NAME OF MONITORING ORGANIZATION <i>Wright-Patterson AFB</i>	
6c. ADDRESS (City, State, and ZIP Code) Materials Laboratory (WRDC/MLSE) Wright Research and Development Center, AFSC Wright-Patterson AFB, OH 45433		7b. ADDRESS (City, State, and ZIP Code)	
8a. NAME OF FUNDING / SPONSORING ORGANIZATION Flight Dynamics Laboratory	8b. OFFICE SYMBOL (if applicable) WRDC/FIVR	9. PROCUREMENT INSTRUMENT IDENTIFICATION NUMBER F33615-84-C-3404	
8c. ADDRESS (City, State, and ZIP Code) Flight Dynamics Laboratory (WRDC/FIVR) Wright Research and Development Center, AFSC Wright-Patterson AFB OH 45433		10. SOURCE OF FUNDING NUMBERS	
		PROGRAM ELEMENT NO. 64212F/62102F	PROJECT NO. 1926
		TASK NO. 01	WORK UNIT ACCESSION NO. 12
11. TITLE (Include Security Classification) CONFERENCE ON AEROSPACE TRANSPARENT MATERIALS AND ENCLOSURES Volume II - Sessions VI-IX			
12. PERSONAL AUTHOR(S) Compiled by Samuel A. Marolo			
13a. TYPE OF REPORT Final	13b. TIME COVERED FROM 16JAN89 TO 20JAN89	14. DATE OF REPORT (Year, Month, Day) April 1989	15. PAGE COUNT 732
16. SUPPLEMENTARY NOTATION			
17. COSATI CODES		18. SUBJECT TERMS (Continue on reverse if necessary and identify by block number)	
FIELD	GROUP	SUB-GROUP	polycarbonate, Acrylic, Interlayers, Windshields, Canopies, Coatings, Transparent Materials, Environmental Resistance, Optical Requirements, Computed Design, Design Criteria, Cost of Ownership Reduction, Transparency Refurbishment, Frameless
			Transparency, New Transparent Materials
19. ABSTRACT (Continue on reverse if necessary and identify by block number) The purpose of this report is to make available the technical papers presented at the Fifteenth Conference on Aerospace Transparent Materials and Enclosures. Seventy-two technical papers are presented in nine sessions that address transparent material for enclosures, coatings for transparencies, transparency design; bird impact resistance; human factor and optics; operational problems; design criteria on transparent plastics, glasses and elastomers; aircraft-structural integration of windshields and canopies; computed design; testing techniques; and cost of ownership reduction. The papers contained herein have been reproduced directly from the original manuscripts. <i>h-1</i>			
20. DISTRIBUTION / AVAILABILITY OF ABSTRACT <input checked="" type="checkbox"/> UNCLASSIFIED/UNLIMITED <input type="checkbox"/> SAME AS RPT <input type="checkbox"/> DTIC USERS		21. ABSTRACT SECURITY CLASSIFICATION Unclassified	
22a. NAME OF RESPONSIBLE INDIVIDUAL Theodore J. Reinhart		22b. TELEPHONE (Include Area Code) 513-255-3691	22c. OFFICE SYMBOL WRDC/MLSE

DD Form 1473, JUN 86

Previous editions are obsolete

SECURITY CLASSIFICATION OF THIS PAGE

Unclassified

SESSION VI

BIRDSTRIKE HAZARD (PART A)

Chairman: Maj. R. L. Merritt  
Bird Aircraft Strike Hazard  
Team  
Washington, D.C.

Co-Chairman: J. Thorpe  
UK Civil Aviation Authority  
West Sussex, England

Coordinator: Capt. R. L. Dogan  
Bird Aircraft Strike Hazard  
Team  
Washington, D.C.



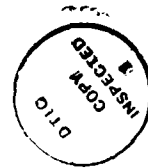
DEVELOPMENT OF A BIRD PROOF WINDSHIELD  
FOR THE B-2 BOMBER

J. B. Hoffman  
Northrop Corporation

PAPER WAS WITHDRAWN

ESTIMATING THE BIRDSTRIKE RISK TO THE SPACE SHUTTLE ORBITER

Maj. Jeffrey J. Short  
AFWAL/FDER



Accession For	
NTIS GRA&I	<input checked="" type="checkbox"/>
DTIC TAB	<input type="checkbox"/>
Unannounced	<input type="checkbox"/>
Justification	
By _____	
Distribution/	
Availability Codes	
Dist	Avail and/or Special
A-1	

## ESTIMATING THE BIRDSTRIKE RISK TO THE SPACE SHUTTLE ORBITER

Jeffrey J. Short, Major, USAFR  
AFWAL/FDER  
Wright-Patterson AFB OH 45433

### ABSTRACT

The Bird Avoidance Model (BAM), developed for the United States Air Force by the University of Dayton Research Institute, is used to predict bird hazards for high-speed, low-level flight routes in the continental United States. The BAM calculates the birdstrike risk on a route by estimating the number of birds occupying the route airspace at a particular time. The BAM was used to calculate the probability of local bird impacts to the Space Shuttle Orbiter while landing at the Kennedy Space Center (KSC), Florida. The relative birdstrike risk was examined at KSC, Edwards AFB, California and Vandenberg AFB, California.

The BAM estimates for KSC were multiplied by the proportion of the local bird population in discrete weight categories. This yielded the probability of a birdstrike involving a bird of a particular weight. This analysis indicated that the chance of the Shuttle hitting a 2-pound bird is close to 4 per 100 approaches during the late fall each year. One out of every 100 landings could involve a 3-pound bird during the fall and early winter. The predominant risk at KSC comes from waterfowl with the chance of encountering larger (over 4-pound) raptors highest during the summer. The relative birdstrike risks are roughly the same at both KSC and Edwards AFB.

### BACKGROUND

The National Aeronautics and Space Administration requested an evaluation of the Space Shuttle Orbiter windshield system. To support this damage assessment analysis, the Air Force Wright Aeronautical Laboratories' Aircraft Windshield System Programs Office directed a characterization of the bird populations which would present a hazard to the Shuttle at its primary landing sites: Kennedy Space Center, Florida; Edwards AFB and Vandenberg AFB, California [1]. The potential for failure of the windshield system is directly related to the potential for hitting a bird of a certain weight. The research objective was to determine the expected birdstrike risk to the Shuttle during approaches. This information can be used to validate design criteria for the windshield system or can be used to schedule missions to avoid the peak periods of birdstrike risk.

One method of determining the birdstrike hazard to the Shuttle is to document the birdstrikes to aircraft landing at KSC. One birdstrike (species unknown) is known to have occurred during Shuttle mission 1042A, 11 Feb 85 at 1215 hours GMT (Karen Edelstein, personal communication). Birdstrike records for aircraft (T-38; Gulfstream II) used to practice Shuttle approaches at the SLF are also available. Approximately 38 birdstrikes on the Gulfstream II were recorded at KSC over a five year period. Almost 40 percent of these birdstrikes were attributed to Tree Swallows (*Iridoprocne bicolor*); however, the involved bird species were not identified in 50 percent of the incidents.

## DATA COLLECTION AND ANALYSIS

### Bird Populations

The KSC Shuttle Landing Facility (SLF) is adjacent to the Merritt Island National Wildlife Refuge (MI NWR). Extensive bird population data is available for the SLF owing to its proximity to MI NWR and by special studies conducted by NASA [2]. MI NWR attracts hundreds of thousands of waterfowl (mostly ducks and coots), waders, shorebirds, and songbirds. Additionally, large numbers of raptors, especially vultures, roost in the immediate area of KSC. The movements of these birds to and from MI NWR frequently cross the flight paths into the SLF. These flights constitute a significant flight hazard to the Shuttle (or other aircraft) landing there.

Monthly waterfowl censuses (1978-84), performed by U.S. Fish and Wildlife Service (USFWS) and quarterly surveys of raptors, waders and shorebirds were analyzed to characterize the bird population at MI NWR. Bird censuses show that most waterfowl leave the MI NWR by May of each year and return in October. Large raptors are present year-round but are most numerous near KSC from April through September.

Determining the weight distribution of birds requires identification of the predominant bird species in a population. Bird weight varies with species (and subspecies) sex, age, and season. Body weights were assigned to each species according to the highest, published mean weight [3]. All weights were converted to pounds.

The bird population data was separated into three groups to compare the weight distribution of the waterfowl, raptor and wader/shorebird populations (Table 1). The cumulative distribution frequency (CDF) of the weights of the bird populations at MI NWR were calculated from the annual proportion of each weight class for a bird group. Weights for the population samples involved in birdstrikes characteristically fit a Weibull curve [4;5]. The CDF (Figure 1) for the MI NWR waterfowl population approximates a Weibull distribution but the raptor and wader/shorebird

curves are flattened, indicating a higher percentage of heavy birds in the population; e.g., Black Vulture (4.7 pounds) and Wood Stork (6.0 pounds).

Table 1. Quarterly proportion of birds at MI NWR in a particular weight class.

WATERFOWL POPULATION					Total 311,900
Weight (lbs)	Jan-Mar	Apr-Jun	Jul-Sep	Oct-Dec	Annual
< 1	0.0836	0.1277	0.5547	0.0621	0.0810
1 - 2	0.7408	0.6915	0.1434	0.7481	0.7349
2 - 3	0.1753	0.1808	0.3015	0.1896	0.1838
3 - 4	0.0003	0.0000	0.0004	0.0000	0.0000
4 - 6	0.0000	0.0000	0.0000	0.0000	0.0000
> 6	0.0000	0.0000	0.0000	0.0001	0.0000

RAPTOR POPULATION					Total 3,387
Weight (lbs)	Jan-Mar	Apr-Jun	Jul-Sep	Oct-Dec	Annual
< 1	0.4741	0.1842	0.0710	0.4060	0.3493
1 - 2	0.1034	0.0614	0.0772	0.0855	0.0856
2 - 3	0.0233	0.1023	0.1235	0.0744	0.0676
3 - 4	0.2888	0.5048	0.4537	0.3248	0.3637
4 - 6	0.1034	0.1364	0.2469	0.1026	0.1240
> 6	0.0069	0.0109	0.0278	0.0068	0.0097

WADER/SHOREBIRD POPULATION					Total 96,285
Weight (lbs)	Jan-Mar	Apr-Jun	Jul-Sep	Oct-Dec	Annual
< 1	0.6405	0.6804	0.0710	0.4060	0.3493
1 - 2	0.0636	0.0274	0.0313	0.0587	0.0465
2 - 3	0.1529	0.1279	0.1341	0.1528	0.1428
3 - 4	0.0794	0.0365	0.0670	0.0745	0.0654
4 - 6	0.0199	0.0434	0.0257	0.0205	0.0267
> 6	0.0437	0.0845	0.0293	0.0634	0.0551

Bird Avoidance Model

Previous studies [6; 7] show that risk of a damaging birdstrike is predicted by the bird density along the flight path (D), the forward projected area of the aircraft or component (A), average velocity (V) and the total time spent in the bird airspace (T):

$$E(n) = D \times A \times V \times T \quad (1)$$

Combining records on the behavioral, chronological, geographical and vertical distribution of birds provides the density input into the BAM. The frontal area is specific to the type of aircraft or component. Mission details concerning the time spent in the birds' airspace are highly variable.

## MERRITT ISLAND NWR FLORIDA YRLY BIRD WT DISTRIBUTION

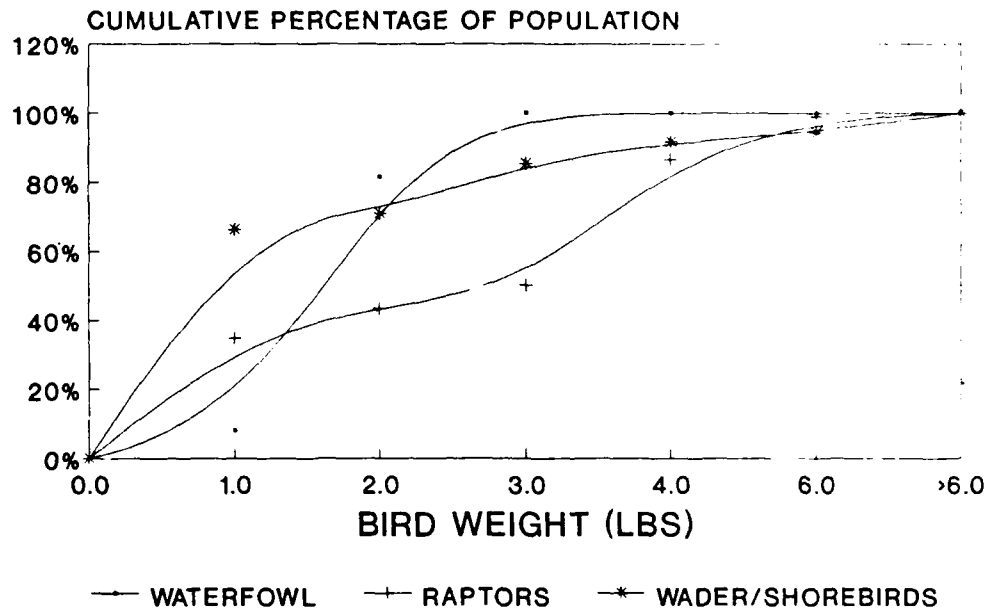


Figure 1. Cumulative distribution frequency plot of bird weights at the Merritt Island National Wildlife Refuge.

In 1981, the University of Dayton Research Institute (UDRI), under contract from the BASH Team, developed and implemented the Bird Avoidance Model (BAM). BAM quantifies birdstrike risk as a function of mission profile, route-of-flight, date, time of day, and aircraft frontal area [6;7]. The original purpose of the BAM was to annotate birdstrike risks on low-altitude flight routes to allow mission scheduling to avoid the worst hazards. It also enabled route planners to redesign flight segments to minimize the risk of birdstrikes. This study is the first application of the model to characterize bird weight distributions for birdstrikes.

The BAM assumes a uniform distribution of birds within a standard radius of known congregation points such as breeding grounds or wildlife refuges. The BAM originally is based on generalized waterfowl distributional data obtained from refuges, feeding areas, migration routes, and hunting records in the contiguous 48 states. Originally, BAM was based solely on waterfowl populations and their migrations. Quantifiable data on raptor populations and movements and breeding populations of waterfowl were included in 1985 to enhance the BAM. Additional data is sought for other bird groups to upgrade the capabilities of the BAM.

Birdstrike risk is defined by BAM as the number of birds that will be encountered along a flight route during a particular mission. BAM uses latitude, longitude, and segment altitude to calculate birdstrike risk on each segment. The risks are summed over all segments to give the total birdstrike risk for the entire route. BAM allows the user to compare routes/route segments based on an expected number of birdstrikes for each mission. To assess the risk expected during a Shuttle approach, it was necessary to identify the individual flight segments that comprise a typical approach at its three landing sites.

### Shuttle Operations

The Shuttle uses basically the same approach window (airspeeds and procedures) for each landing. The estimate of birdstrike risk is a function of the number of birds within a volume defined by the frontal area swept along the length of the flight route. The frontal area is the square footage of a component/aircraft as it approaches head-on. For the Shuttle, the total frontal area varies from 768.7 to 944.1 square feet corresponding to 3-8 degrees nose-high landing attitude. For this analysis, the nominal 5 degrees (818 square feet) was used.

Since this BAM analysis is based on the total frontal area of 818 square feet, an evaluation of the birdstrike risks to any component of the Shuttle, such as the windscreen, can be made. For example, if the windscreen area is 40 square feet, the birdstrike risk would be about 5 percent those depicted in the figures.

The BAM calculates the number of birds expected for any segment -as defined by geographic coordinates and base altitude-of a standard or user-defined flight route. In this analysis, a typical Shuttle approach was constructed for the SLF with information provided by NASA personnel (Karen Edelstein, personal communication). The Shuttle intercepts a 19-degree glide angle at 12,600 feet AGL approximately 6 miles from the runway and flies to a point 1700 feet AGL and 8,000 feet from the runway where it intercepts a 1.5-degree glide slope until touchdown. For input to the BAM, the final approach was broken into a series of segments based on the lowest altitudes of each segment (Table 2).

Table 2. Segment altitude and geographic coordinates for the SLF.

Segment	START		END		Altitude (ft AGL)
	Lat	Long	Lat	Long	
A:	28 44'N	80 47'W	28 43'N	80 46'W	10,000
B:	28 43'N	80 46'W	28 42'N	80 45'W	5,000
C:	28 42'N	80 45'W	28 40'N	80 44'W	2,100
D:	28 40'N	80 44'W	28 39'N	80 43'W	1,700
E:	28 39'N	80 43'W	28 38'N	80 42'W	100

## BIRDSTRIKE RISK

The total birdstrike risks calculated for the SLF by BAM for each period include the effects of both waterfowl and raptors but not wader/shorebird populations. The latter group has not been included in the BAM due to a lack of reliable data on the altitude of their daily/seasonal movements.

Separate BAM estimates were obtained for waterfowl and raptors to show the size distribution effects on risk attributable to each population. Waterfowl risks at KSC were multiplied by two to correspond with the increased waterfowl populations reported in the MI NWR censuses. Each weekly risk was multiplied by the proportion of the local (MI NWR) bird population of a particular weight class.

Figures 2 and 3 depict the individual risks from waterfowl and raptors, respectively. When the figures are combined, the higher risks from waterfowl obscure the raptor risks. The comparison shows that the annual effects of raptors on the total birdstrike risk at KSC is negligible. These figures also indicate that the waterfowl hazard is more predictable than the raptor hazard. Two- and 3-pound waterfowl present the most risk to Shuttle operations for the cooler months at KSC. However, during the summer months at KSC 1-pound raptors are replaced by 4-pound ones.

The highest level of risk from waterfowl occurs in the first and last quarter of each calendar year. When plotted (Figure 2), the resultant risk estimates show levels of bird activity and the size relationships of expected birdstrikes. This graph indicates that the most serious birdstrike hazards at KSC occur in the last quarter of the year when almost 4 of every 100 shuttle flights will impact a bird weighing 1 to 2 pounds and 1 of every 100 will weigh 2 to 3 pounds.

Risk from raptors at KSC (Figure 3) is about 4 orders of magnitude smaller than the waterfowl risks. However, there are much larger birds in the population. There is a significant increase in the risk of hitting a 3-4 pound raptor from April to September. Migrational "pulses" are quite evident for raptors at KSC.

### Relative Birdstrike Risk

Since specific bird censuses were not available for the Edwards AFB and Vandenberg AFB, California, their bird weight distributions could not be determined. However, a comparison between the three sites was possible using the original BAM calculations. The estimated risks were plotted to show temporal birdstrike relationships for each landing site.



# KSC WATERFOWL RISK ADJUSTED FOR WEEKLY DAYLIGHT

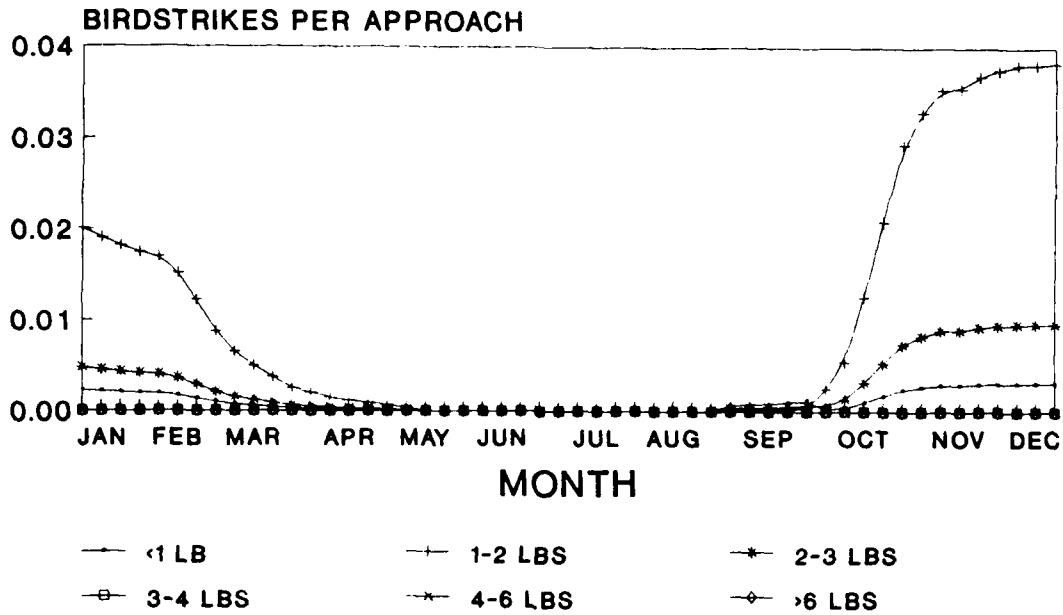


Figure 2. Total waterfowl risk by weight category.

# KSC RAPTOR RISK ADJUSTED FOR WEEKLY DAYLIGHT

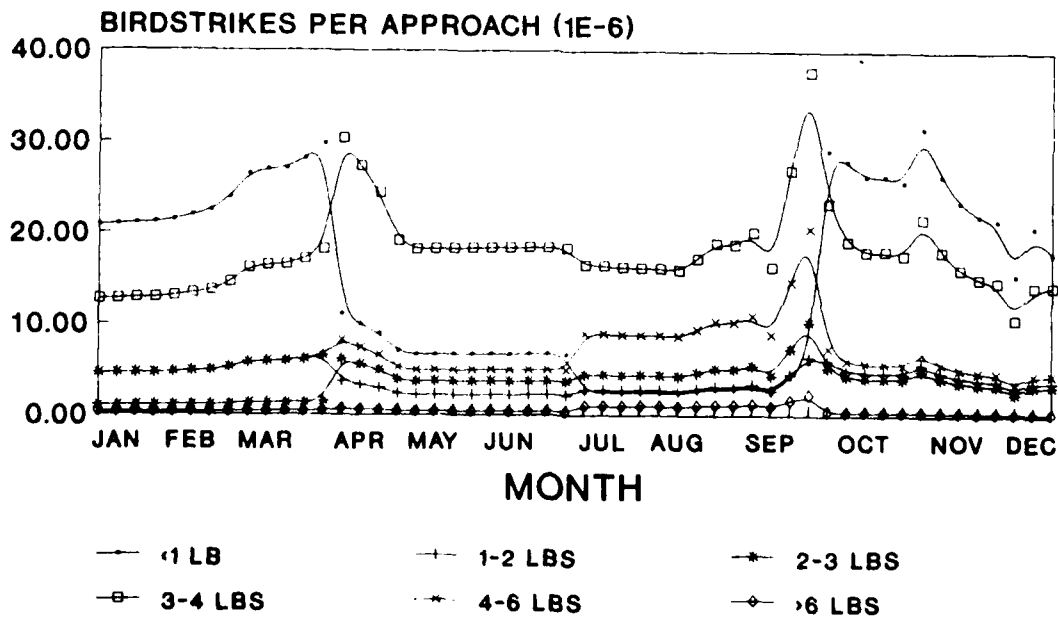
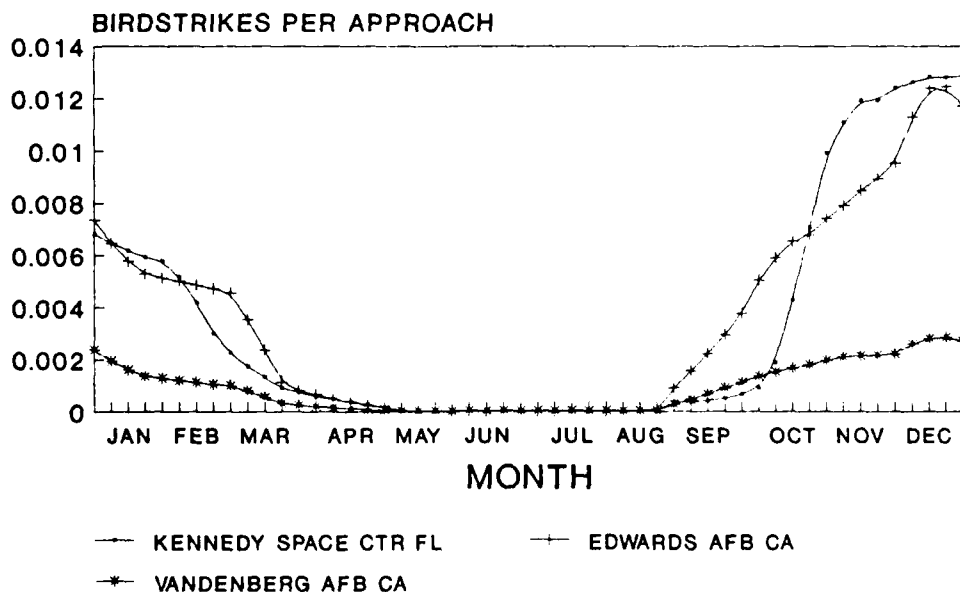


Figure 3. Total raptor risk by weight category.

The relative birdstrike risk between the landing sites is not the simple sum of the risks from the daily periods (a.m./p.m., midday, night) used by the BAM to model the different periods of bird activity. (Mid-day corresponds to the hours between 1000 to 1500 each day; a.m./p.m. refers to the hours between dawn and 1000 and after 1500 until dusk; night covers the period between dusk and dawn.) The timing of bird behavior is closely tied to the amount of daylight at different locations each week. Birds respond to the actual illumination of their surroundings for feeding, migration and other behaviors. Since the BAM does not consider this aspect in its calculations of bird movements, the risk estimates were standardized to the proportion of daylight at each location. The combined weekly birdstrike risks for the landing sites were calculated by multiplying waterfowl and raptor risks (from the BAM) for each daily period at each site by the proportional number of hours of weekly daylight at that location. The average weekly daylight estimates were obtained from the civil twilight tables which are published for each airfield by the U.S. Naval Observatory.

After adjustment for site variation for daylight, Figure 4 shows that all three sites display a similar seasonal distribution of birdstrike risk. Though usually lower than KSC, the birdstrike risk at Edwards AFB are highest in early spring and early fall.

### RELATIVE BIRDSTRIKE RISK FOR SHUTTLE LANDING SITES



ADJUSTED WATERFOWL & RAPTOR ESTIMATES  
 Figure 4. Total birdstrike risk for primary landing sites.

## DISCUSSION

BAM results for KSC show that as many as 4 percent of the shuttle approaches in the early winter months would encounter a 2-pound bird while about 1 percent would involve a 3-pound bird. About three Shuttle approaches in every 100,000 during the summer months at KSC would involve a 4-pound raptor. At KSC, the chance of hitting a 2- to 3-pound duck close to touchdown ranges between 1 and 4 per 100 flights except during summer when it is essentially zero. While the probability of hitting a 4-pound bird may be numerically remote in the fall and winter each year, the warmer months offer a good chance of encountering a soaring, large (heavier than 4-pound) bird, such as a vulture, at higher approach altitudes and consequently, higher airspeeds. This level of birdstrike hazard is due to the relatively large proportion of waterfowl in the nearby bird populations and is the most intense during the fall migration and subsequent overwintering each year.

Waterfowl typically migrate at altitudes below 5,000 feet AGL and are most likely encountered at altitudes below 500 feet AGL during local movements; e.g., when engaged in feeding activities around refuges. They tend to travel in flocks and fly directly between resting areas and feeding sites. Waterfowl are frequently involved in multiple birdstrikes (more than one bird at a time) with USAF aircraft. Approach birdstrike hazards are created by waterfowl at low altitudes and, to a lesser extent, by raptors at high altitudes.

Raptor populations comprise a relatively small part of the birdstrike risk at all landing sites but the hazard may be greater to the Shuttle because of their large size and soaring behavior. Their flight paths are erratic and may reach thousands of feet in the air creating problems at the higher Shuttle approach altitudes and speeds.

Wader/shorebird populations are not included in the BAM --as well as some really major players in birdstrikes such as gulls-- so their influence on birdstrike risk cannot be considered in this analysis. This means that the calculated birdstrike risk estimates presented here are somewhat less than the actual risks expected, especially during the summer months when waders/shorebirds are concentrated in large nesting colonies. These two groups constitute a substantial part of the birdstrike hazard at KSC in the summer months [2]. Some soaring waders could create a hazard similar to raptors.

At the peak of bird activity, the Shuttle can expect to hit thirteen birds in every 1000 approaches at either KSC or Edwards and two birds in every 1000 approaches at Vandenberg. Birdstrike risk to the Shuttle is highest in the early winter at all landing sites.

The BAM mathematically depicts patterns of bird movement according to basic assumptions about similarities of flight habits; i.e., what a certain bird population is doing at a certain moment and at what altitude they are doing it. Since the BAM makes no distinction other than numbers of birds found at certain altitudes during certain periods, it is possible to include taxonomically diverse groups of birds in the analysis. For instance, the soaring behavior exhibited by certain waders, especially the Wood Stork, at MI NWR would create a hazard to flight similar to soaring raptors. However, including Wood Storks as a part of the raptor analysis --with the assumption that the Wood Stork flights occur in similar ways-- would only increase the estimated birdstrike risks at the SLF by approximately one birdstrike per 1000 flights for those birds 6 pounds and over. The estimated birdstrike risk for hitting any wader or shorebird at KSC is estimated at 3 per 1000 approaches.

Operational constraints on where and when an approach may be conducted could reduce the prospect of a birdstrike; however, this could adversely affect mission accomplishment. Scheduled landings should be avoided at night during the spring and fall migrations. The raptor hazard could be avoided by scheduling daytime landings in the winter months or by early morning landings in the summer. Other bird control techniques (harrassment) could be used in conjunction with bird avoidance procedures to reduce the probability of birdstrike to the Shuttle.

This was the first application of the BAM on other than military aircraft. Though the BAM is certainly an imperfect model, it provides a method of quickly estimating the relative birdstrike risk from waterfowl and raptor populations in the continental United States. More bird population data is needed for other bird species (gulls, blackbirds) known to present hazards to flight to improve the BAM's predictive ability.

#### CONCLUSION

Reliable bird population data from the region around the landing site, combined with the BAM estimates, can provide design engineers with a good idea of the bird hazards that the Shuttle will encounter during particular time periods. If some aspect of the design is inadequate to provide an acceptable level of birdstrike resistance, the flight hazards can be minimized by scheduling Shuttle landings at a particular site to a time when the birdstrike risk is lowest. If rescheduling is not feasible, then measures to reduce the birds along the Shuttle approach could be implemented.

## REFERENCES

1. McCarty, R.E. and R.A. Smith. 1988. Assessment of Bird Impact Protection Provided by the Space Shuttle Orbiter Windshield System Using the MAGNA Computer Program. Proceedings of the AIAA 4th Flight Test Conference; San Diego CA: 288-298.
2. Skole, D. 1978. A Preliminary Report on the Species Specific Avian Populations at KSC in Relation to Bird-Strike Hazard. Unpublished report to KSC/MD-B: 115 pp.
3. Dunning, J.B. 1984. Body Weights of 686 Species of North American Birds. Western Bird Banding Association, Monograph No.1. Eldon Publishing; Cave Creek, AZ: 38 pp.
4. Berens, A.P., B.S. West and M.A. Turella. 1978. On a Probabilistic Model for Evaluating the Birdstrike Threat to Aircraft Crew Enclosures. University of Dayton Research Institute, Dayton OH Report No. UDR-TR-78-124: 45 pp.
5. Kolodziejczyk, P. 1984. Evaluation of the Birdstrike Threat to the F-15 Present Fleet, Rapid Deployment Force, and Dual Role Fighter Transparencies. Aeronautical Systems Division, Wright-Patterson AFB OH Report No. ASD-TR-84-5026: 147 pp.
6. Skinn, D., D.L. Applegate and A.P. Berens. 1981. The Bird Avoidance Model (BAM) Phase II/III Report: Programmer's guide. University of Dayton Research Institute, Dayton OH Report No. UDR-TR-81-10. 137 pp.
7. Skinn, D. and A.P. Berens. 1980. Bird Avoidance Model (BAM) Phase I Report: Feasibility Demonstration. University of Dayton Research Institute, Dayton OH Report No. UDR-TR-80-122. 100 pp.

BIRDSTRIKES TO UK CIVIL AIRCRAFT WINDSHIELDS

John Thorpe  
UK Civil Aviation Authority

**BIRDSTRIKES TO UK CIVIL AIRCRAFT WINDSHIELDS**

**John Thorpe - UK Civil Aviation Authority**

**ABSTRACT**

The paper presents data on windshield birdstrikes to UK registered civil aircraft during the period 1976 to 1986.

The paper shows the strike rate and percentage of damaging cases to individual aircraft types. The weights of the bird species involved as well as the airspeed are examined.

The paper is divided into three sections

- Transport aircraft
- Helicopters
- General Aviation aircraft of 5700 kg and below

An Attachment presents recent world-wide reports on windshield birdstrike damage.

The paper concludes that as a result of the penetration of helicopter and general aviation aeroplane windshields by small birds and at comparatively modest airspeeds by small and medium bird, that there may be justification for more stringent design requirements.

## 1. INTRODUCTION

During the five years since the previous meeting in Arizona, there have been two particularly tragic accidents due to birdstrikes. The first was the loss of an Ethiopian Airlines Boeing 737 in September 1988. During take off the engines ingested Speckled pigeons (*Columba guinea* weight 320 gms). The aircraft crashed killing 34 people during an attempt to land back at Bahar Dar Airport in Ethiopia. The other major accident was the loss of a B1B bomber on a low level training mission in Colorado in September 1987. While flying at 560 knots at 600 ft large birds (American White Pelicans, *Pelecanus erythrorhynchos* weight 3.5 kg and Sandhill Cranes, *Grus canadensis* weight 4.2 kg) penetrated the wing/nacelle structure rupturing hydraulic and fuel lines and starting a massive fire. Three of the crew were killed. A massive modification programme is under way. Neither of these accidents was anything to do with windshield. However, the recent incident where a Boeing 747 at cruise speed was reputed to have collided with a goose at 33,000 ft damaging the radome, resulted in much media comment and speculation on what would have happened if it had hit the windshield. Thanks to the requirement (see Table 1) that a transport aircraft windshield must be able to withstand a 41b bird at speeds used up to 8,000 ft, which has been applicable for several decades, no cases are known to this author of jet transport aircraft windshields having been penetrated by birds. The same cannot be said for helicopters and general aviation aircraft.

This paper examines data from worldwide birdstrikes to UK registered civil aircraft for the 12 years from 1975 to 1986, involving around 10 million aircraft movements, to see whether any factors become evident. The data has been divided into three categories, transport aeroplanes, general aviation aeroplanes below 5700 kg (12,500lb) and helicopters. Attachment 1 present recent reports from worldwide operators etc of windshield damage due to birds (Ref 6 & 7).

Note: The bird weights used in this paper are from "Average Weight of Birds" by T Brough of the Aviation Bird Unit, Worplesdon Laboratory, (Ref 1). The paper contains the average weight, weight range and data source for weights of 2,256 bird species.

## 2. DISCUSSION OF DATA

### 2.1 Transport Aircraft

#### a. Likelihood of large birds striking windshield.

Of the 5000 birdstrikes to UK registered aircraft, 15.5% strike the windshield. Using the very large data sample (Ref 2 and 3) available from Bird Strike Committee Europe sources it can be seen from Figure 1 that the windshield was struck in 16% of birdstrikes reported by European airlines during the period 1981 to 1985. The sample size is some 7500 birdstrikes. The European and UK data is in line with ICAO data for the year 1986 from the IBIS system (Ref 4). This shows 15.3% of strikes involve the windshield. From Figure 2 it can be seen that the percentage of birds struck which are over 41bs in weight is around 1%. Thus it is not surprising that in Figure 3 there have only been 25 cases of windshield damage during this period. However, the 486 engine damage cases, is noteworthy.



b. Detailed examination of windshield strikes. (see Table 2)

From the UK data used throughout the rest of this paper the number of strikes to the windshield have been compared with those to any part of the aircraft, to see if any aircraft types are more likely to suffer windshield strikes. From Table 2 it can be seen that certain aircraft have an above average proportion of strikes to the windshield (Boeing 727, B737, B757, DC9) whilst others have a lower proportion (A310, B747, CL44, BAE748). Local airflow could be a factor. The aircraft movements and number of strikes vary from aircraft to aircraft so the samples are not of equal size. When aircraft movements are taken into account so that a windshield strike rate is produced it can be seen that the B737, BAE146, DC10, Short SD330/360, and Vickers Viscount have above average strike rate to the windscreen. The B727, B747 and Herald have lower than average strike rate to the windshield.

c. Damage (see Table 3).

There are only 19 cases of damage to transport aircraft windshields of which 7 were to the Viscount and 2 on the F27. There was one each on the Boeing 707/720, 727, B737, B747, BAC111, HS125, DC3, Herald, Short SD360, Trident and Viscount. These damage cases were irrespective of bird size or aircraft speed. Only one of the above incidents was at a speed of greater than 180 knots (see Table 5). From Table 3 it can be seen that those aircraft types which have an above average percentage of damage are mainly from the earlier generation of aircraft whilst some of the later aircraft designs are conspicuous by their absence having had no damaging strikes at all.

d. Flight Phase.

The flight phases during windscreen strikes were 9 on take off, 2 each in the climb and en route, with 3 each during approach landing.

e. Bird species causing damage (see Table 4).

So what sort of birds cause the windshield damage? Unfortunately in 9 of the 19 cases the bird species is not known. In the 10 known cases the birds were Herring gulls, unknown Gull species, Lapwing, Pigeon and Passeriformes. None of these were over 4lb in weight.

f. Speed (see Table 5)

No cases of damage occurred at speeds below 90 knots. Most occurred between 91 and 180 knots. Only one case was above 250 knots. Although at first glance it may appear that these cases of damage were at surprisingly low speeds it should be borne in mind that only one layer was damaged, air and pressurisation loads can be sustained by the remaining layer.

g. Cabin Windows of B747

The data does not include cabin window damage. In Dec 1984 a UK B747 was climbing at 260 kts through 4000ft at night over North London when it struck a flock of lapwings (*vanellus vanellus* weight 215gm). The top corner of the left front cabin window in the first class area, was struck forcing the outer pane against the inner pane which cracked and broke against the retaining clips. A passenger was badly splattered with blood and remains. Fuel was jettisoned and the aircraft returned. A similar event had occurred to a US registered B747. Even though the angle is very acute, consideration should perhaps be given to some action to prevent any further cases.

## 2.2 Helicopters

- a. As helicopters mostly operate at low level (especially the smaller types) it might be expected that birdstrikes are more frequent, indeed hours are used in the statistics rather than movements which are used for transport aircraft data. There were only 26 windshield strikes reported to helicopters. It may be that the relatively low speed and high forward noise gives birds adequate warning enabling them to avoid being struck. The windshield is also partly protected by the downwash and by the rotor arc. The Sikorsky S61 not surprisingly, had the greatest number of strikes due to its very intense use on North Sea oil rigs. Some strikes were while the helicopter was parked on the rig with rotors turning, birds attempted to land on the rotor disc which appeared solid to them with dire results - for the birds. The very active North Sea Bird Club (Ref 5) produces comprehensive data on bird species which are seen from oil rigs. From Table 7 it can be seen that large birds are present in the North Sea in very significant numbers, thus demonstrating the potential for a hazardous event. Fortunately much of the helicopter traffic to the oil rigs cruises at around 6000ft, where less birds are likely to be present.
- b. There have only been five cases of damage to helicopter windshields, most on light helicopters. In one case a Swift (*Apus apus* weight 14gm) holed the canopy and another Swift flying in line astern with the first came through the hole and was flying around inside the helicopter. The pilot had to deal with alarmed passengers, the wind and noise, fly the helicopter and despatch the Swift in the cockpit. In view of the fact that significant number of passengers can be carried in light helicopters, with only one pilot, the adequacy of the design requirements on helicopter windshield may need to be reviewed. For other reasons, e.g. noise reduction, some helicopters may have in-built resistance to birdstrikes.
- c. In 11 of the windshield strike incidents the helicopter was en route, 3 occurred while parked, one while on the approach, one while landing and 2 while taking off.

- d. From Table 5 it can be seen that the helicopter speed when damage occurred was somewhat lower than for transport aircraft, thus highlighting the lack of windshield requirements. Furthermore, with rising helicopter speeds, and reducing noise levels birds will have less opportunity to get out of the way, although the downwash may provide some protection.
- e. Bird species. Unfortunately in only 3 cases were the bird species known, one was a Herring Gull, one a Swift and one a Teal.

### 2.3 General Aviation Aeroplanes of 2730 kg (6000lbs) and less

- a. Table 6 shows the number of windshield strikes reported on each type. Unfortunately the hours are not available but those with high numbers of strikes are generally the busiest, so the figures reflect this utilisation.
- b. A paper presented at the previous meeting (Ref 8) detailed 5 fatal accidents of which 3 were the result of windshield penetrations on Mitsubishi MU2J, Lear 23 and Cessna 402. In addition, there were 6 cases of injury following windshield penetration. In several of these incidents the birds were heavier than 1.8 kg (4lb) and in all of them they were heavier (possibly much heavier) than 300g.
- c. Aircraft in this class spend more of their time at lower altitudes where birds are prevalent (92% of strikes are below 2500 ft - ref 4). The increased risk is offset by the lower flying speed which allows birds a better opportunity to avoid the aircraft particularly during take off and landing. However, there is increasing use of turbo prop commuter aircraft which are permitted to carry more and more passengers, sometimes flown by a single pilot.
- d. From Table 6 it can be seen that certain aircraft types have a considerable percentage of damage to the windscreen. However, because of generally poorer standard of reporting on general aviation aircraft these figures should be treated with some caution. The damage rate is around 2.3 per million hours, however it must be recognised that this is a minimum since much of the reporting on this class of aircraft is voluntary. From Table 4 it can be seen that many of the general aviation aircraft windshield damage cases are due to small birds. (11 of the cases were birds less than 450 gm, 1lb). In the majority of impacts on the general aviation aircraft the bird ends up inside the cockpit because the windscreens are penetrated. Although not required to be capable of meeting birds except in the UK, it is known that for noise and other reasons some aircraft have considerable windscreen impact capability.
- e. As to the speeds where windshield damage occurred, 11 of them were between 51 and 90 knots. The latest generation of custom-built aircraft are designed for high speed, the Glasair III is capable of 300 mph and is unpressurised and likely to be flown at low altitude. Fortunately, the designer of this aircraft has specified a thicker windshield to improve the resistance to bird strikes.

- f. In the UK a General Aviation Safety Sense Leaflet 'Bird Avoidance' has been widely distributed (Ref 9). This is intended to minimise the risk of collision for general aviation pilots. It provides specific advice on detecting and avoiding birds, and on what to do after a collision. The effect of a smashed windshield during the first solo of a student pilot can be imagined.

### 3. CONCLUSIONS

- a. The damage rate due to birdstrikes to UK transport aircraft windshields is around 2 per million movements, a very low rate indeed. This damage rate is irrespective of bird weight and aircraft speed, and only affects one layer.
- b. The more recent transport aircraft types appear to suffer less windshield damage than the earlier types.
- c. Although helicopter windshield damage is not common (a rate of 6.4 per million hours on transport type helicopters) the number of penetrations of the canopy by small birds at modest speeds is an area for concern. In view of rising helicopter speeds and increased emphasis on noise prevention it may be that further consideration could be given to design requirement action on helicopters.
- d. The number of windshield penetrations to general aviation aircraft demonstrates that in view of the low speed and at times light weight of the birds, design requirement action may be desirable on this class of aircraft. Although the reported damage rate at 2.3 per million hours is comparatively modest the effect of penetration of a single crew aircraft windshield, should be borne in mind.
- e. Any design requirement action may not necessarily result in any great costs since a number of aeroplane and helicopters windshields would already have considerable capability as a result of noise or pressurisation design factors.

Figure 1

**PART STRUCK -  
1981 to 1985 European Airlines**

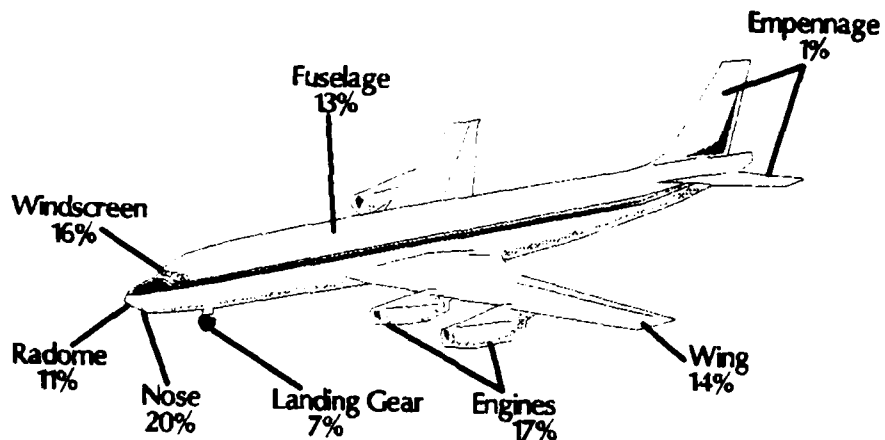


Figure 2

**WEIGHT DISTRIBUTION  
OF IDENTIFIED BIRDS  
1981 to 1985 - European Airlines**

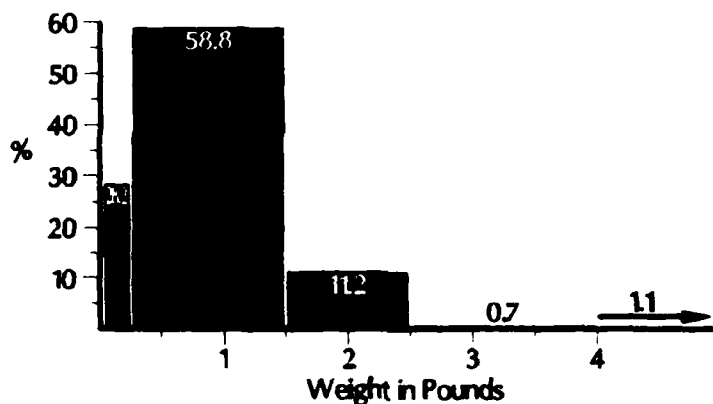
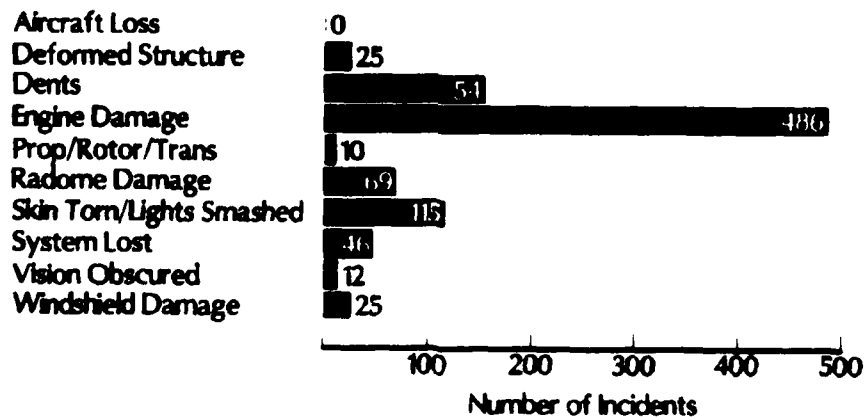


Figure 3

**EFFECT OF STRIKE -  
1980 to 1985**



**Table 1 - BIRDSTRIKE DESIGN REQUIREMENTS FOR AIRCRAFT WINDSHIELDS**

Aircraft		European (JAR)	UK (BCAR)	US (FAR)
Aeroplanes	Maximum weight greater than 5700 Kg (12,500lb)	1.8 Kg (4lb) VC at sea level or 0.85 VC at 8000 ft whichever is the more critical	as European	1.8 Kg (4lb) VC at sea level
	Maximum weight 2730 Kg (6000lb) to 5700 Kg (12,500lb)	To be discussed	0.91 Kg (2lb) speeds appropriate to climb after T/O and during approach	Nil
	Below 2730 Kg (6000lb)	Nil	Nil	Nil
Rotorcraft	Maximum weight greater than 5700 Kg (12,500lb)	Nil	1.8 Kg (4lb) at maximum TAS used up to 8000 ft	Nil
	Maximum weight greater than 2730 Kg (6000lb) and less than 5700 Kg (12,500lb)	Nil	0.91 Kg (2lb) at maximum TAS used up to 8000 ft	Nil
	Below 2730 Kg (6000lb)	Nil	Nil	Nil
Agricultural	Any weight	Nil	0.91 Kg (2lb) speeds used in agricultural operation	

**Table 2 - TRANSPORT AIRCRAFT BIRDSTRIKES**

	Strikes to ALL Parts	Strikes to Windshield	%	Movements (10,000)	Windshield Strike Rate
<b><u>JET</u></b>					
A300 Airbus	4	-	-	0.7	-
A310 Airbus	27	1	3.7	0.8	-
B707/720	254	31	12.2	39.9	0.77
B727	55	10	18.2	17.9	0.56
B737	928	169	18.2	168.7	1.00
B747	211	20	9.5	45.2	0.44
B757	100	21	21.0	24.0	0.87
B767	22	2	9.1	2.5	0.80
BAC 1-11	868	143	16.5	226.7	0.63
BAe 146	35	5	14.4	4.9	1.02
Concorde	7	-	-	3.5	-
DC8	15	2	13.3	2.1	0.95
DC9	99	18	18.0	19.4	0.92
DC10	99	15	15.0	15.4	0.97
L1011 Tristar	119	18	15.1	27.6	0.65
Total/Mean	2947	470	15.9	599.3	0.78
<b><u>TURBOPROP</u></b>					
BAe 748	267	26	9.7	55.7	0.47
Canadair CL44	18	1	5.5	3.2	-
DHC 7	9	-	-	5.8	-
Fokker F27	199	28	14.0	56.8	0.49
HP7 Herald	115	16	13.9	54.3	0.29
Short SD330/360	188	28	14.9	45.4	0.62
Short Belfast	5	-	-	-	-
Vickers Viscount	440	62	14.1	98.7	0.62
Total/Mean	1241	161	13.0	319.9	0.50
<b><u>PISTON</u></b>					
DC3	7	3	42.8	8.0	0.37

	Strikes to ALL Parts	Strikes to Windshield	%	Movements (10,000)	Windshield Strike Rate
<b>HELICOPTERS</b>				10,000 (hours)	
AS 330/332 Puma	N/A	1	N/A	16.1	0.6
AS 350 Ecuriel	N/A	1	N/A	N/A	-
Bell 47	N/A	1	N/A	N/A	-
Bell 206	N/A	4	N/A	N/A	-
Bell 212/214	N/A	2	N/A	2.1	0.95
Boeing 243 Chinook	N/A	-	N/A	3.5	-
SA 341 Gazelle	N/A	1	N/A	N/A	-
SA 365 Dauphin	N/A	1	N/A	N/A	-
S 61N	N/A	9	N/A	55.2	0.16
S 76 Spirit	N/A	1	N/A	3.5	-
Westland WG30	N/A	1	N/A	1.0	1.0
<b>TOTAL/Mean</b>	-	23	-	77.9*	0.17*

Notes: \*Transport sized helicopters only

Aircraft types not in current use have been excluded.



**Table 3 - WINDSHIELD DAMAGE, TRANSPORT AIRCRAFT**

<b>Aircraft</b>	<b>Windshield Strikes</b>	<b>Damage Cases</b>	<b>% with Damage</b>	<b>Comparison with Mean</b>
Boeing 707/720	31	1	3.2	-
Boeing 727	10	1	10.0	High
Boeing 737	169	1	0.6	Low
Boeing 747	20	1	5.0	High
BAC 1-11	143	1	0.7	Low
BAC 125	15	1	6.7	High
DC3	3	1	33.3	High
F27	28	2	7.1	High
HP7 Herald	16	1	6.2	High
HS Trident	121	1	0.8	Low
Short SD 360	28	1	3.6	-
Viscount	62	7	11.3	High
<b>Total/Mean</b>	<b>646</b>	<b>19</b>	<b>2.9</b>	

**Table 4 - BIRD SPECIES CAUSING WINDSHIELD DAMAGE**

Name	Scientific Name	Weight	Transport Aeroplane	General Aviation	Helicopter
Fulmar	Fulmaris glacialis	750 gm	-	1	-
Gannet	Sula basana	2.9 Kg	-	1	-
Duck	Anas sp	250 gm to 1.3 Kg	-	1	-
Teal	Anas creeca	325 gm	-	-	1
Lapwing	Vanellas vanellus	215 gm	3	4	-
Gull	Larus spp.	280 gm to 1.8 Kgm	4	3	-
Black-headed gull	Larus ridibundas	275 gm	-	1	-
Herring gull	Larus argentatus	1.0 Kg (2.21b)	1	1	1
Pigeon	Columbiformes	up to 465 gm	1	2	-
Swift	Apus apus	40 gm	-	1	1
Swallow	Hirundo rustica	19 gm	-	1	-
Perching bird	Passeriformes	15 gm to 1.1 Kg	1	1	-
Unknown			9	3	2
<b>TOTAL</b>			<b>19</b>	<b>20</b>	<b>5</b>

**Table 5 - WINDSHIELD DAMAGE SPEED**

Speed Band	Transport Aircraft	Helicopters	General Aviation
51-60	-	-	2
61-70	-	-	3
71-80	-	-	1
81-90	-	-	5
91-100	2	1	-
101-110	4	2	2
111-120	4	-	1
121-130	1	-	1
131-140	-	1	-
141-150	1	-	-
151-160	1	-	1
161-170	2	-	2
171-180	2	-	1
above 250	1	-	-
Unknown	1	1	3
<b>TOTAL</b>	<b>19</b>	<b>5</b>	<b>20</b>
Movements/Hours	9,272,000	* 779,000 hrs	8,500,000 hrs
Rate per Million	2.05	6.4	2.3

\* Transport sized helicopter hours only

**Table 6 - WINDSHIELD DAMAGE, GENERAL AVIATION AIRCRAFT**

<b>Aircraft</b>	<b>Windshield Strikes</b>	<b>Damage to Windshield</b>	<b>% with Damage</b>
Beech 55 Baron	6	-	-
Beech 90 King Air	6	2	33
BN2 Islander	3	1	33
Cessna 150/152	21	4	19
Cessna 172	5	-	-
Cessna 421 Golden Eagle	7	-	-
DHC 6 Twin Otter	5	-	-
Embraer Bandeirante	12	-	-
Gulfstream American AA5	4	1	25
Piper PA23 Apache/Aztec	6	1	17
Piper PA28 Cherokee	30	3	10
Piper PA31 Navajo	9	1	11
Piper PA34/39 Twin Comanche	6	-	-
Piper PA38 Tomahawk	5	-	-

Note:- Aircraft types with two or less strikes have been excluded.

**Table 7 - BIRDS WITH MORE THAN 1000 OF SPECIES SEEN FROM NORTH SEA OIL RIGS IN 1984**

<b>Name</b>	<b>Scientific Name</b>	<b>Birds Seen</b>	<b>Weight</b>
Fulmar	Fulmarus glacialis	7,882	750 gm
Common gull	Larus canus	4,030	420 gm
Herring gull	Larus argentatus	5,152	1.02 Kg
Great blackbacked gull	Larus marinus	4,431	1.69 Kg
Kittiwake	Rissa tridactyla	19,089	390 gm
Field Fare	Turdus pilaris	3,781	98 gm
Redwing	Turdus iliacus	9,296	67 gm
Blackbird	Turdus merula	2,831	106 gm
Starling	Sturnus vulgaris	71,171	80 gm

ATTACHMENT 1 - WINDSHIELD DAMAGE DUE TO BIRDSTRIKES, WORLD-WIDE OPERATORS

TRANSPORT AEROPLANES

<u>Date</u>	<u>Aircraft</u>	<u>Regn</u>	<u>Operator</u>	<u>Location</u>	<u>Injury</u>
6.11.83	Convair 580	N-	Republic Airlines	Sioux Falls, USA	1 Serious

The aircraft had just levelled off at night, 7 miles from Sioux Falls, 2900 ft and reduced speed to 185 kts, when a migrating 2.5 lb goose struck the windshield. The windshield was holed seriously, injuring the captain. The first officer took control, noise causing communications difficulty. The gear locked lights did not indicate, as the bird tripped the DC and other circuit breakers on the panel behind the captain. After a go-around and re-setting of the breakers, a safe landing was made during which the captain, who was unable to see, operated the nose-wheel steering under the first officer's direction. The captain had lost 3 pints of blood and the permanent sight of one eye.

16.04.85	DC3	G-AMCA	Air Atlantique	Nr Luton, UK	-
----------	-----	--------	----------------	--------------	---

At about 1000 ft and 120 kts during the approach, birds struck the windshield causing a crack in both the inner and outer panes.

06.07.85	BAE 146	N-	-	Nr Los Angeles, USA	-
----------	---------	----	---	---------------------	---

Whilst climbing through 7000 ft at 250 kts, a flock of gulls broke the right A windshield.

30.04.86	Boeing 737 (JT8D)	VT-EAG	-	Delhi, India	-
----------	-------------------	--------	---	--------------	---

At 800 ft and 150 kts, on the approach the windshield on the captain's side was shattered after striking a bird of unknown species.

21.12.86	DHC-8	N-	-	Nr Philadelphia, USA	
----------	-------	----	---	----------------------	--

While en-route at 9500 ft and 210 kts, a bird of unknown species struck the windshield causing a crack and complete electrical failure. Engine 1 was lost.

AEROPLANES OF 5700 Kg (12,500 lb) AND BELOW

18.07.81 C152 G-BIOM - Nr Lerwick, UK 1 Minor

While descending through 1000 ft at about 90 kts, the aircraft struck a gull, breaking the windshield. The pilot suffered a cut nose.

26.07.82 Piper PA23 VH- - En-route Australia Minor

An eagle penetrated the windshield causing a deep cut to the pilot's head and cuts to his hand. The aircraft was landed satisfactorily.

09.09.82 Wasmser Guepard F-BXCA - Limoge, France 1 Serious

While descending through 1800 ft at 140 kts; the aircraft struck an Osprey (Pandion Haliaetus - weight 1.5 kg). The windscreen was shattered and the pilot's head and face badly cut.



31.10.82 Piper PA24 - - Bensbach, Papua - New Guinea

The right-hand windshield was broken by a cockatoo (weight up to 900 gm).

17.09.85 MS890 Rallye SE-GFA - Nr Vasterlik, Sweden

While cruising at 105 kts at 1000 ft, a 20 cm hole was made in the windshield after the aircraft struck a bird of unknown species.

- 18.09.85 Cessna 310 - - Carrasco, Uruguay  
 At 3500 ft and 140 kts, on the approach the wind shield was broken on the left side with inward separation fragments and frame denting after a bird struck the aircraft.
- 02.04.86 Piper PA28 N- - Nr Madison, Minor  
 Wisc, USA  
 While en-route at 3300 feet, a flock of ducks penetrated the windshield causing facial cuts to the pilot.
- 25.05.86 SF260 I-LELC - Nr Alghero, -  
 Italy
- At 4500 ft and 120 kts, a bird of unknown species struck the windshield causing penetration and a hole of about 51 cm diameter. A precautionary landing was made.
- 24.07.86 Cessna 152 G-BHDR - Dundee, UK -  
 While at 100 ft and 80 kts, on the approach a pigeon (Columba sp. weight up to 465 gm) broke the windshield causing a large section to almost separate from the aircraft.

#### HELICOPTERS

- 24.02.82 SA341 Gazelle F-GAMK - Marseilles, Minor  
 France
- While flying at 200 ft and 100 kts, the aircraft struck a gull, smashing the window in the door causing minor injury to the passengers.
- 16.07.82 SA319 Allouette F- - France Minor  
 While flying at 1500 ft and 200 kts, a Martin (Riparia, weight 14 gm) penetrated the windshield, injuring the pilot.
- 21.07.82 SA318 Allouette F- - Lyon Satolas, -  
 France
- While approaching to land at 500 ft and 6 kts, the windshield was penetrated by a Starling (Sturnus vulgaris, weight 80 gm).
- .---.82 Bell 206 N- - - Detroit, USA Minor  
 A Mallard Duck weighing 5 lb broke the windscreen, knocking the pilot unconscious and breaking his nose. The helicopter was on autopilot (fitted at pilot's request) and the pilot came to at 700 ft and 110 kts over Detroit.



01.09.83 SA316 Alouette F-BYCS - Montpellier, 1 Minor  
France

Approaching the airfield at 150 ft and 85 kts, the helicopter collided with a gull weighing 1.2 kg and 4 ft wingspan. The windscreen was shattered, the remains striking the pilot, who retained control and landed safely in spite of cuts on his hands.

--.11.83 Bell 206 - - Sandakan, Minor  
Borneo

Large bird of prey attacked the helicopter, the pilot managed to dodge the bird's first attempt but when the pilot looked up, the eagle was again diving with wings folded. At the last second the bird must have realised there was something odd about its "prey", as it spread its wings and attempted to turn away. The wing smashed the nose bubble and the body holed the honeycombe belly structure. Bird was Brahminy Kite (*Haliastur indus*, weight 570 gm).

22.08.85 Bell 206 N- - Nr Venice, -  
Luisianna, USA

While on route at 110 kts and 800 ft, a flock of gulls penetrated the pilot's wind shield, he was not injured.

08.10.85 Bell 206 N- - Arancus City, USA

Whilst climbing out at 74 kts, a gull broke the left lower pilot's windshield.

31.03.86 Hughes 500 N- - Lunken, USA -

Fifty feet in a climb, the helicopter struck a flock of Starlings causing damage to the oil cooler resulting in the engine overheating, cracking the lower windshield and causing numerous dents.

13.06.86 Agusta 206 G-BCWM - St Bede, Minor  
Cumbria, UK

Whilst on route at 600 feet and 110 kts, a Herring gull (*Larus argentatus*, weight 1.0 kg) holed the windscreen, bounced off the pilot's head and struck the roof window which broke. The pilot suffered slight cuts to the nose and head. A precautionary landing was made.

13.07.86 Hughes 500 G-GASC - Nr Biggin Hill, UK

Whilst en-route at 500 ft and 90 kts, the helicopter hit a flock of Swifts (*Apus apus*, weight 40 gm) causing a hole in the windshield. Live Swift was flying around inside the cockpit and the pilot had to contend with alarmed passengers and the bird flying around inside, together with coping with the wind blast and noise from the hole. A precautionary landing was made.

24.09.86 Gazelle F- - Marignane, France

At 500 ft and 125 kts, the helicopter struck a flock of Nightjars (*Caprimulgus europaeus*, weight 70 gm) resulting in the windshield being penetrated. The carcass struck the rear bulkhead.

07.11.86 Bell 206 N83086 - Nr JFK, Serious  
New York

Gulls penetrated the windshield resulting in a precautionary landing. Serious injury resulted.

30.07.87 Bell 212 G-BFER - Nr Unst, UK Minor

While on long final approach at 300 ft and 105 kts at dusk, a Gannet (*Sula Basana*, weight 2.9 kg) was seen approximately 100 yards ahead. The Gannet hit the top right hand corner of the captain's windshield, penetrating the glass and splattering into the cockpit. The pilot's windshield was totally shattered, so the co-pilot took over and landed the helicopter. A crewman in the rear suffered small glass particles in his eye, requiring medical attention.



## REFERENCES

1. 'Average Weights of Birds' by T Brough, Aviation Bird Unit, Worplesdon Laboratory, Tangley Place, Guildford, Surrey, England, GU3 3LQ.
2. 'Analysis of Birdstrikes reported by European Airlines 1976-1980' by J Thorpe, CAA Paper 84019.
3. 'Analysis of Birdstrikes reported by European Airlines 1981 to 1985' by J Thorpe - in preparation.
4. '1986 Bird Strike Analysis' - ICAO IBIS Report AN 4/9.1.1 - 88/1, ICAO, 1000 Sherbrooke Street West, Montreal, Quebec, Canada, H3A 2R2.
5. 'Report for 1984 by North Sea Bird Club' - Editor A Anderson, University of Aberdeen, UK.
6. 'Serious Birdstrikes to Civil Aircraft 1981 to 1985' by J Thorpe. Proceeding of 18th Meeting of Birdstrikes Committee Europe, Copenhagen, May 1986.
7. 'Serious Birdstrikes to Civil Aircraft 1985 to 1987' by J Thorpe. Proceeding of 19th Meeting of Birdstrikes Committee Europe, Madrid May 1988.
8. 'Civil Aircraft Windshield Damage due to Birdstrikes', J Thorpe, Civil Aviation Authority. Proceedings of Conference on Aerospace Transparent Materials and Enclosures, Scottsdale Arizona July 1983.
9. 'Bird Avoidance'. General Aviation Safety Sense Leaflet No 10. CAA Safety Promotion, Aviation House, Gatwick Airport, W Sussex, RH6 OYR, England.

DEVELOPMENT OF A CALCULATION MODEL FOR  
WINDSHIELD BIRDSTRIKE DESIGN

Rolph Wegmann  
Lars Sjöström  
Saab Aircraft Division

## **DEVELOPMENT OF A CALCULATION MODEL FOR WINDSHIELD BIRDSTRIKE DESIGN**

**Authors**                      Rolph Wegmann and Lars Sjöström  
                                         Saab Aircraft Division  
                                         Linköping, Sweden

### **Introduction**

This paper, first presented at the Conference on Aerospace Transparent Materials and Enclosures in Monterey, 16 - 20 January 1989, deals with the development of a FE (Finite Element) calculation model for predicting the deflection of a windshield (Phase I).

It is divided into two parts. Part I, Testing deals with static and dynamic testing performed to generate the necessary input for the FE-model.

Part II, Analysis deals with the development of the calculation model using DYNA3D as a basis.

Phase II in the project will cover the development of a failure criteria for implementation into the model.

## **Background**

The design for good birdstrike qualities of particularly the windshield of a fighter aircraft has been largely a trial and error process in the past as well as the present. Various formulae of predicting failure speeds for laminated glass windshields were evolved during the 50's, but no true candidate design tool was available until the nonlinear Finite element applications on computers came along.

At Saab some existing programmes have been evaluated such as ABAQUS and MAGNA.

The need of a closed-loop design tool has been present for a very long time at Saab Aircraft Division (Saab) and a project for the development of one was started in 1986 supported by the Swedish Defence Materiel Administration (FMV). Basically it satisfies the need of tying together analysis, testing, service experience, material characteristics and requirements.

The overall ambitions in the project are:

- Predicting deflections (Phase I)
- Predicting bird-speed for failure (Phase II)
- Ability to perform sensitivity analysis
- Create a suitable design tool

The strategy to achieve this is:

- Performing material tests at high strain rates
- Implementation of a general material model
- Implementation of a general bird model
- Integration into a CAE environment
- Verification through idealized geometries
- Final verifications on fullscale windshields

Two of the most important problem areas are the contact conditions between bird and windshield, and the characteristics of the material at high strain rates, typically 50 to 200 per second. Both areas were addressed in the project and gave their share of practical problems. Currently, in phase

II of the project, the aim is to establish a failure criteria for prestretched acrylics (PMMA), which is the material concerned.

The need to know more about the material stretched acrylic also presented itself soon enough.

### **Design driven development**

Saab has been using prestretched acrylic in the windshields of the 35 Dragon, 37 Viggen and now in the JAS 39 Griffin. The use of wrap-around windshields came in response to requirements of better visibility for the pilot, but took away the load carrying supports and the laminated glass.

Requirements on the windshield as a structural component has increased considerably over the years and added to the list are better quality optics over a larger area. From an ordinary window the windshield has transformed into a sophisticated piece of equipment.

The designer is therefore in need of an aid to help him to implement as many of the requirements as possible.

In the design of the windshield for the JAS 39, prestretched acrylics was chosen in favour of, for instance, polycarbonate due to its greater stiffness. One of the requirements from particularly the flight safety point of view has been the aspect of not sending a shower of glass in the face of the pilot after a birdstrike on the windshield. The aim being to avoid contact between the windshield and the HUD-glass. The development of the calculation models and its associated material model is therefore done with material data of prestretched acrylics, but the material model is not limited by this and can be used for many types of materials provided the specific material data is known. The work of obtaining material data has been the major part of the work and has involved testing at the extremes of the known equipment envelopes.

## **PART I, TESTING**

The material testing has been performed on coupons. The verification of the model is done on flat circular specimens and full scale windshields. The

material properties in tension and compression were investigated. The size of the coupons was largely determined by the machines, but they were always taken out of the windshield or canopy thickness. In order to investigate the material properties further, tests of water content, anisotropy, prestretch factors and the influence of adhesives were performed on material from two suppliers. The use of strain gauges in the circular specimen testing and the full scale test has always been in question as to the influence of the adhesives.

### **Anisotropy**

These tests were carried out as an ordinary tension test of the coupons.

The coupons were taken out from the undamaged areas of a canopy used for MDC (Micro Detonating Cord) tests. In all, 18 coupons were tested, which is not a very large number, but giving enough information. The results showed very little variation in ultimate tension between coupons taken out surface- or thickness-wise. It was concluded for the material tested that no significant anisotropy was present.

### **Water content**

In parallel to the anisotropy tests a check on the influence of water content was done. The coupon size and material was the same as in the anisotropy tests.

Again 18 coupons were used and they were divided into three groups. The tests were also performed in tension.

The first group of six was dried in 70°C (158°F) for four days, while the second group of six was immersed in distilled water at 40°C (104°F) for the same period of time.

The remaining group was conditioned together with the anisotropy coupons for eleven days in 23°C (73°F) and 50°C (122°F) room temperature.



The subsequent tests in tension showed significant dependency of the water content in failure values. The variation being some 20 % based on the values of the ultimate tensile strength for normally conditioned coupons. The variations in failure strain was some 85 %.

The highest tensile strength was in the group with the smallest water content. The group having the largest water content showed the highest ultimate strain. This gives the conclusion that the water content in the specimens has to be controlled for minimizing the variation in test results.

### **Influence of adhesives**

This investigation was made as an addendum to the tests planned as it was queried if the presence of strain gauges did compromise the test. It was concluded from these tests that the presence of initial defects such as scratches had a larger influence than adhesives and paint. No absolute value could be gained with any significance even though 50 coupons were tested. The test method was both tensile- and charpy-test.

### **Dynamic testing**

The static tests mentioned previously were in preparation for the dynamic tests, which were conducted at the University of Dayton Research Institute (UDRI). For the first phase of the project tests in tension and compression were done. The object of these tests was to generate stress-strain curves at high rates of strain. In order to understand the test results, some parallel tests using a different type of test method were performed in Sweden. The curves were implemented into the calculation model.

The data for tension and compression were generated by utilizing a high rate MTS machine. The test specimens were not fitted with strain gauges, but in calibrating the set up some specimens with strain gauges were used.

The generation of data was a pretty straight forward affair. Most of the difficult part was the evaluation of data for transformation into usable curves for the calculation model. The data comprised of piston-position vs

time and load vs time, which were transformed into stress vs strain diagrammes.

## **PART II, ANALYSIS**

### **Methods Development**

The analysis methodology development consists of three parts:

1. Finding a suitable description of the material properties of the windshield.
2. Finding a suitable description of the bird.
3. Integrate the analysis code into the Computer Aided Analysis (CAE) system at Saab Aircraft Division to form a tool for production use.

### **Analysis Code**

The bird impact problem includes highly nonlinear effects, such as large deformations and plasticity. To get a general analysis tool, independent of windshield geometry, it was decided to model both the bird and the windshield and solve the contact/sliding problem.

The finite element (FE) code DYNA3D by J O Hallquist (ref. 1) was selected. DYNA3D has capabilities to model contact/impact between two deformable bodies with arbitrary large sliding motions. The code uses a Lagrangian formulation and explicit time integration. Several material models exist that can serve as basis for further development.

DYNA3D is developed for maximum performance on CRAY, which is the computer we have used for these analyses.

## **Description of the windshield material**

The material data we had when we started this project consisted of static stress-strain relationship of the acrylic from the material supplier. This showed an elasto-plastic behaviour with a fairly large plastic strain at the ultimate stress.

To get a more accurate material model strain rate effects had to be considered. As mentioned above, tension and compression coupon tests were done at strain rates of 50, 100 and 200/s. This would cover the anticipated range of strain rates in the windshield at impact.

The test results show some vibrations caused by the test equipment, figure 1. The most extreme results at each strain rate were discarded and the remaining stress-strain curves averaged.

A material model was implemented in DYNA3D which consists of a bilinear elastic-plastic behaviour. Young's modulus, yield stress and hardening modulus can all be functions of the strain rate.

## **Description of the bird**

The bird was idealized as a sphere with radius 75 mm. In the actual tests the bird is contained in a fabric bag, so a spheric or ellipsoid shape is a good approximation.

We assume that the bird behaves as a fluid at high velocity impact. A constitutive equation similar to water is used.

To determine contact conditions, DYNA3D uses contact segments that cover the potential contact surfaces of the two bodies.

## **Comparison with circular plate tests**

An analysis was done of the circular plate problem, using the above mentioned descriptions of the acrylic and the bird (velocity ~ 75 m/s).

Figures 2 - 4 show the deformation shape at 0, 1, 2 ms after impact respectively.

The agreement between measured and calculated center plate deflections is good up to about 2 ms, when the bird elements become too distorted, figure 5.

### **Integration into CAE-system**

To use DYNA3D efficiently it needed to be integrated into the CAE system at Saab Aircraft Division. This means that interfaces were written to connect DYNA3D to our normal FE pre- and postprocessor, SDRC I-DEAS.

The complete chain is illustrated by figure 6 showing the outer surfaces at the windshield of the 39 Griffin in CATIA (a general 3D geometry system by Dassault Systemes). Figure 7 shows the CATIA geometry transformed into a wireframe model, which can be transferred to I-DEAS where the FE-mesh is created, figure 8.

For results evaluation, we primarily use DYNA3D's postprocessor TAURUS. We have also modified TAURUS to transfer displacements back to I-DEAS.

### **Calculation of bird impact on windshield**

As a final verification of the methodology, a calculation was done of a bird impact on the 39 Griffin windshield using the model shown in figure 8.

Figure 9, 10, 11, and 12 show the behaviour at 0, 1, 2, and 3 ms after impact respectively.

The agreement between calculated and measured deformations is illustrated by figure 13, showing measured deflections at points corresponding to the initial impact at the windshield centerline (it is very difficult to establish the exact impact point in a test). For comparison the calculated response is shown.

The behaviour differs between test and analysis after approximately 2 ms after impact. This is probably due to cracks that were developed in the windshield near the aft arch in the test (no failure model was included in the analysis).

### **Conclusions and plans for further work**

The described analysis method seems to be able to predict the deformations of the windshield at bird impact with fairly good accuracy.

Phase II of this project aims at implementing a failure model for the acrylic, thus making it possible to predict both deformations and failure of the windshield.

The work in Phase II has been started by initiating further coupon tests (in shear) of the acrylic material, and planning tests of idealized geometries at biaxial stress states and high strain rates.

\* \* \*

### **References**

- (1) DYNA3D User's Manual, John O Hallquist, Lawrence Livermore National Laboratory, UCID-19592, 1988.

SAAB Compression Test  
Specimen #18 @100/S  
9 June 1986

U D R I  
Structural Test Lab

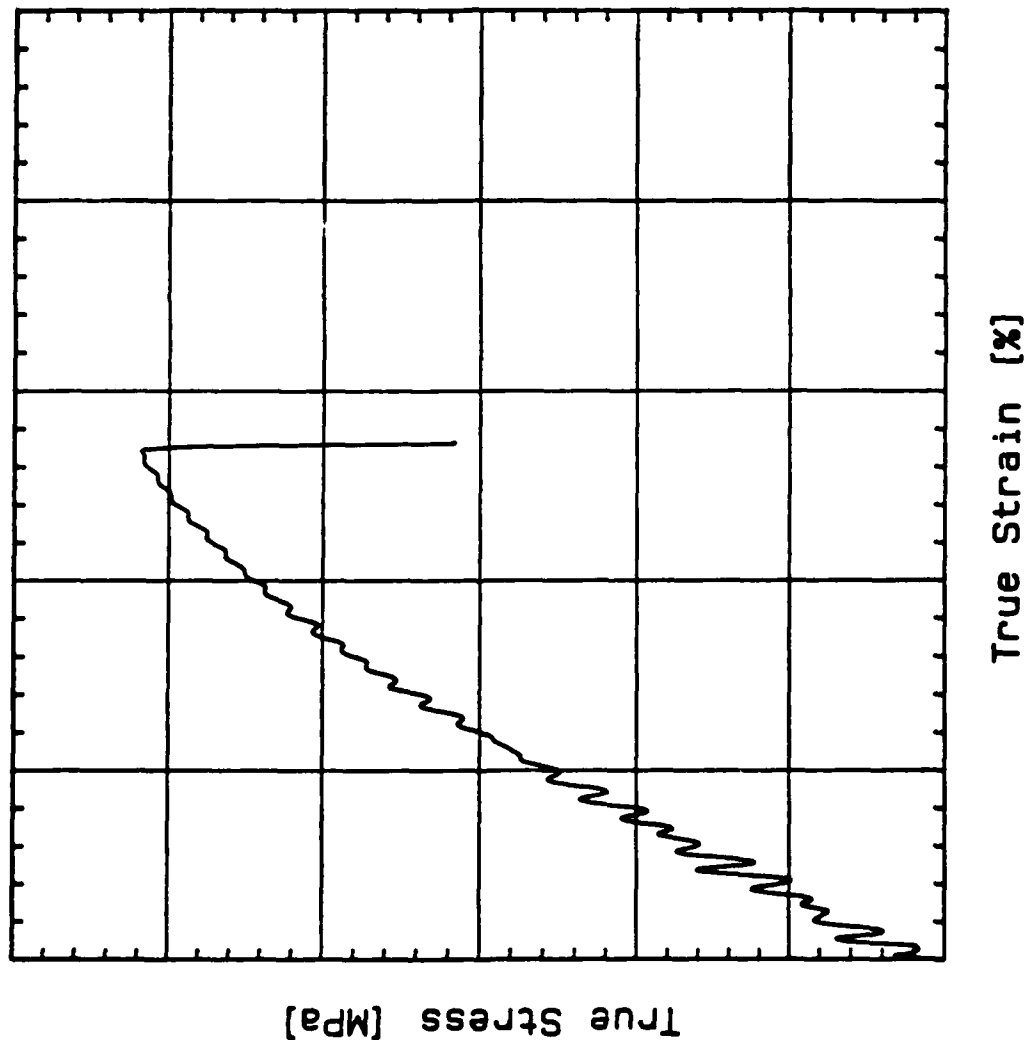


Figure 1

TIME = 0.00000E+00

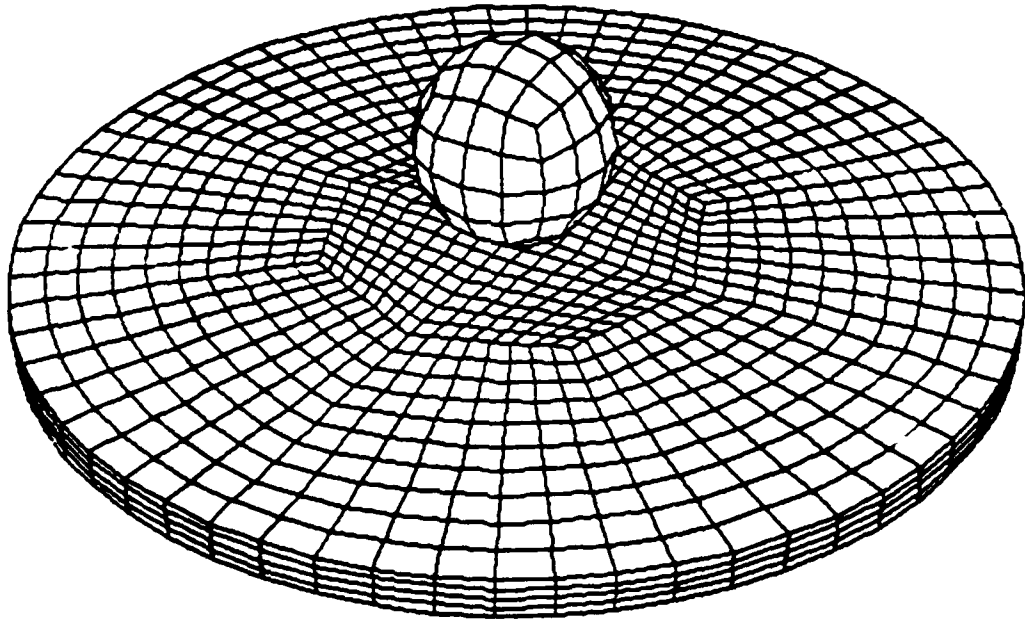


Figure 2

TIME = 0.10000E-02

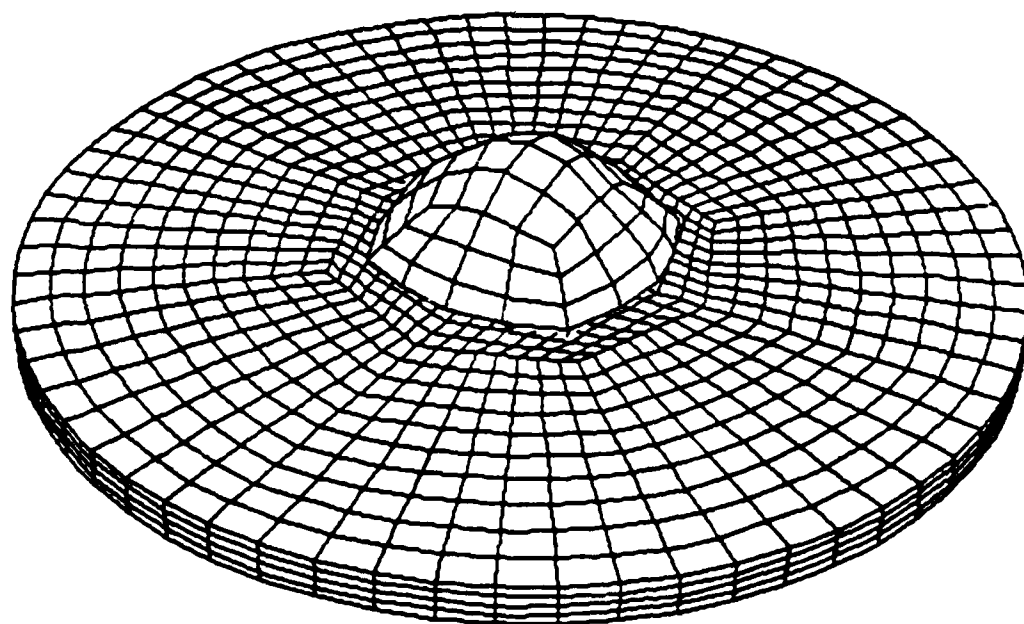


Figure 3



TIME = 0.20000E-02

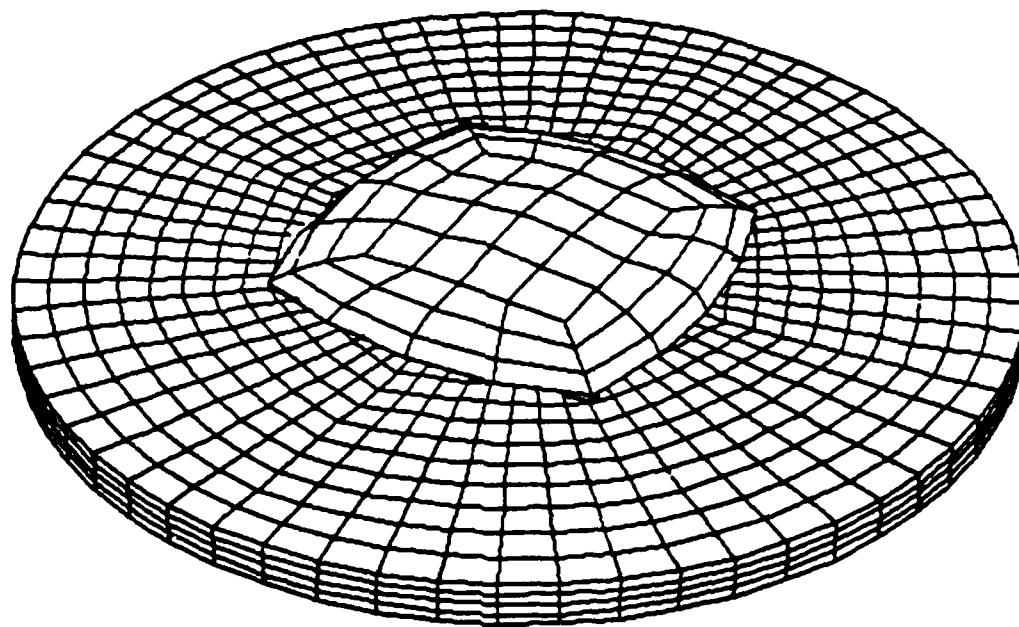


Figure 4

Z DISPLACEMENT

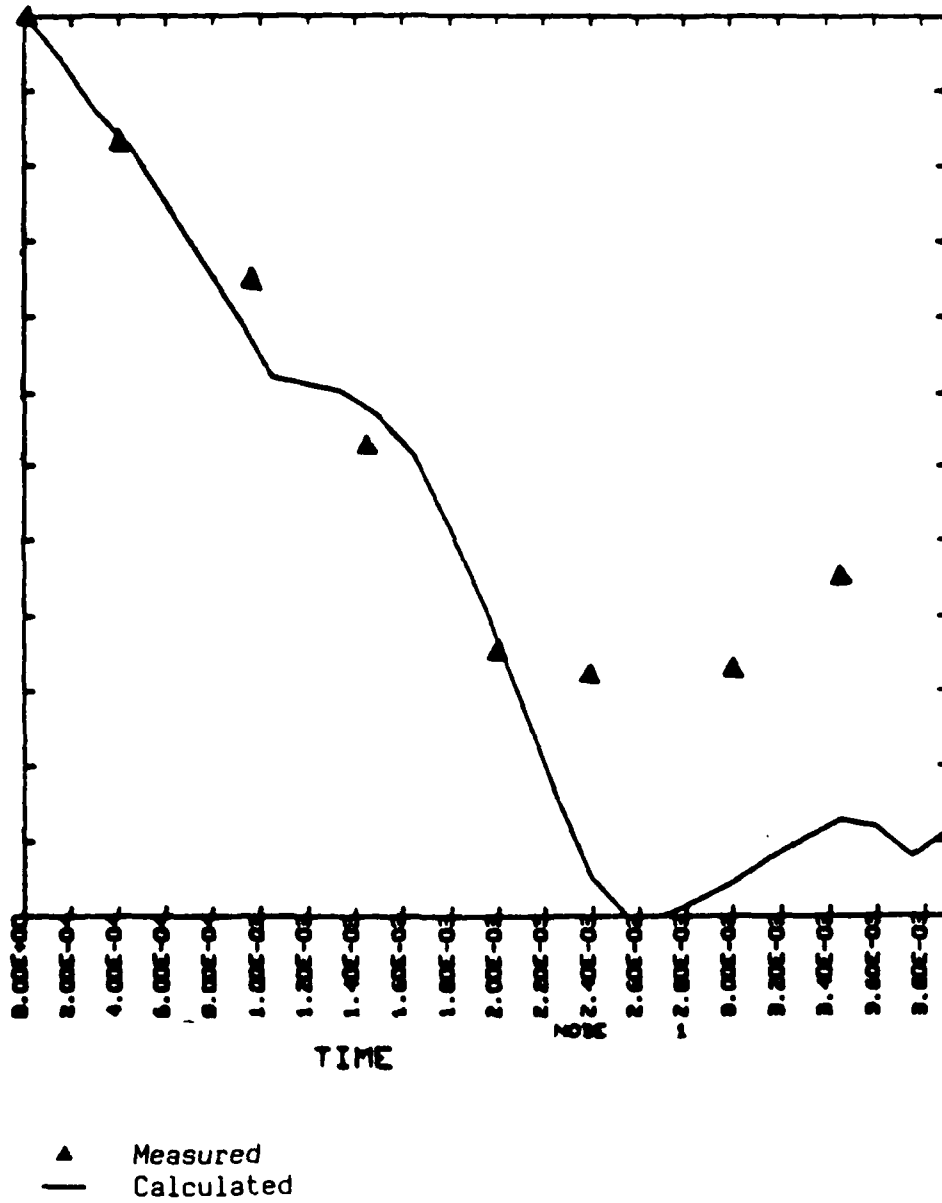


Figure 5

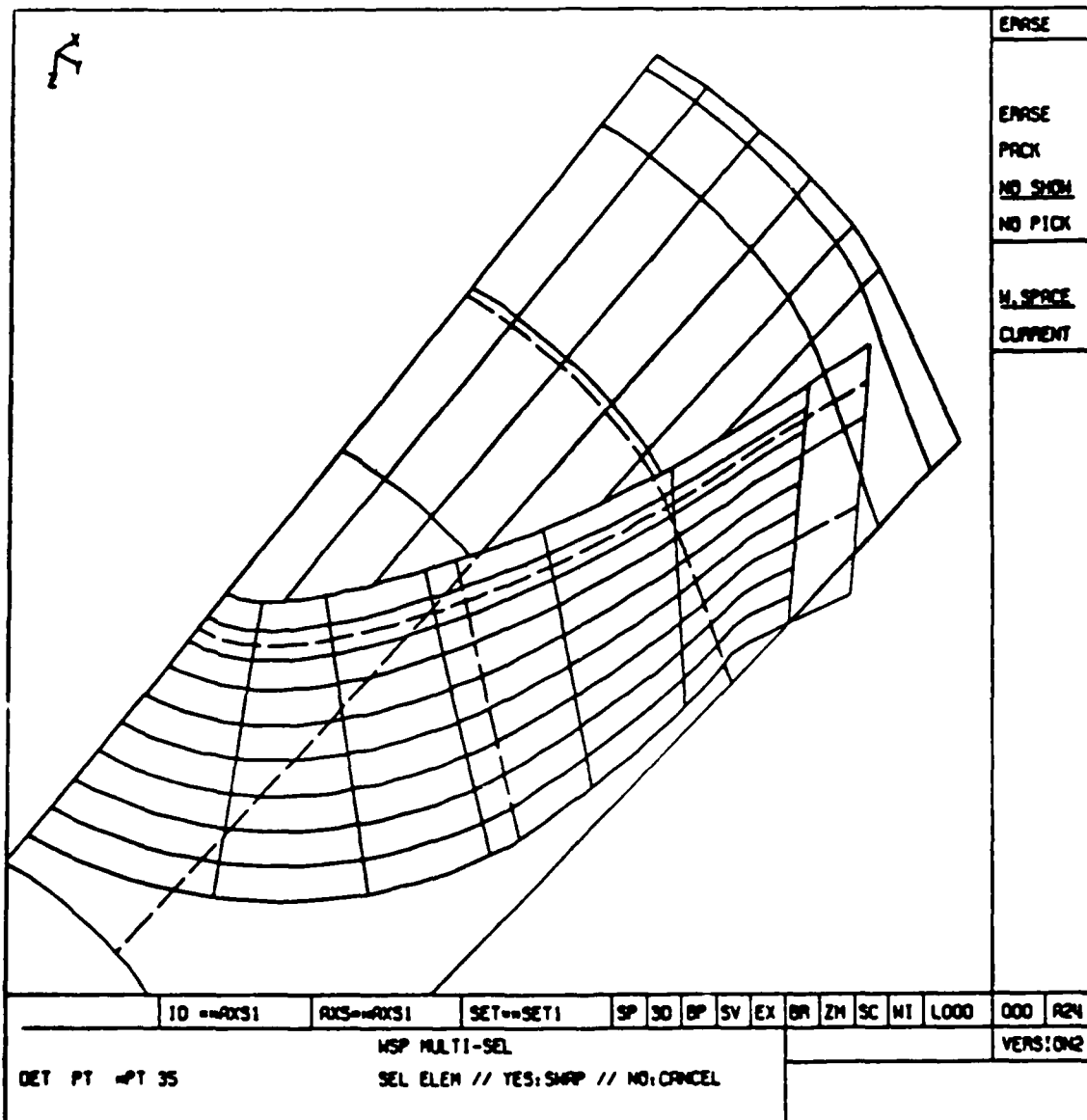


Figure 6

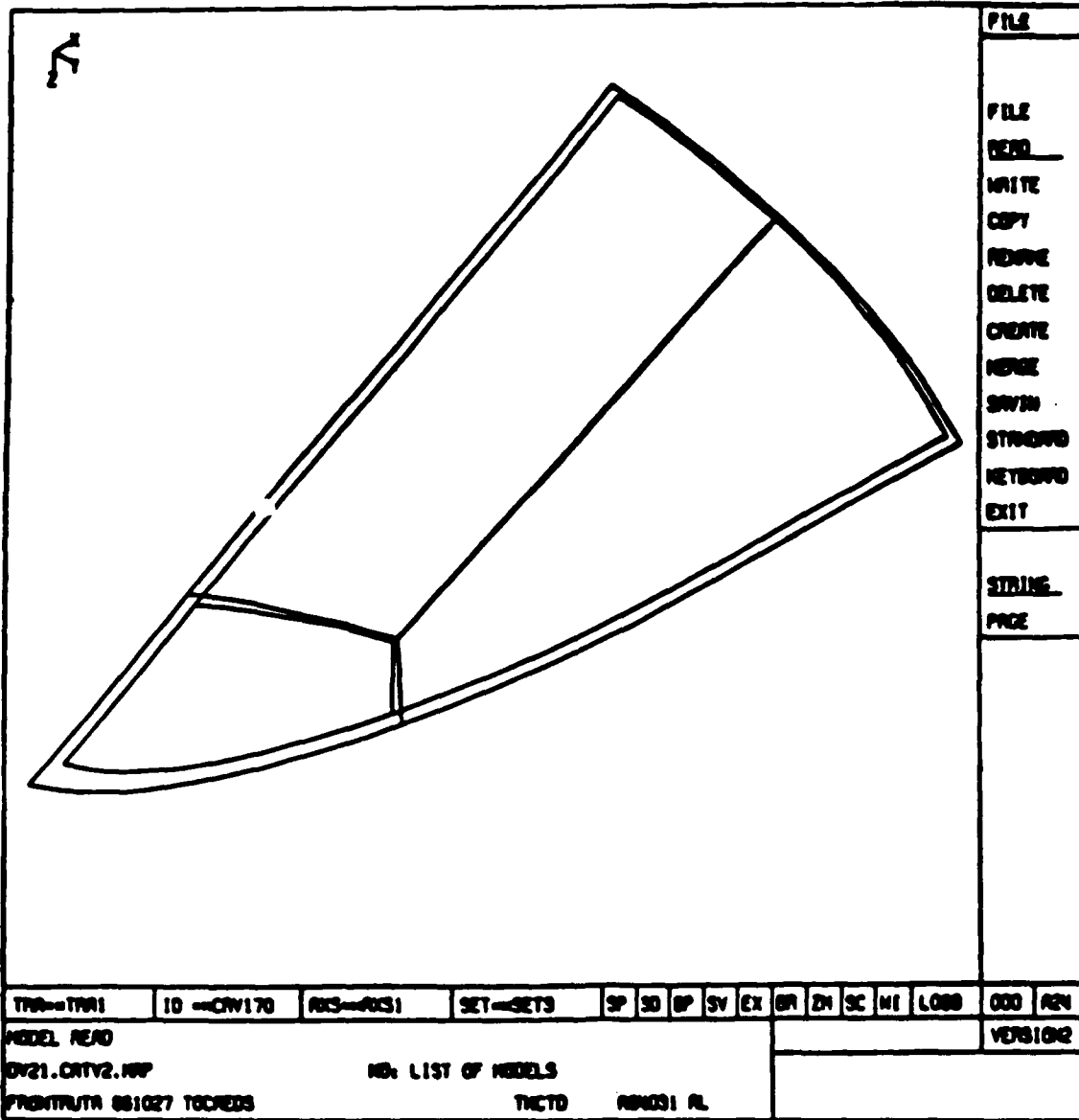


Figure 7

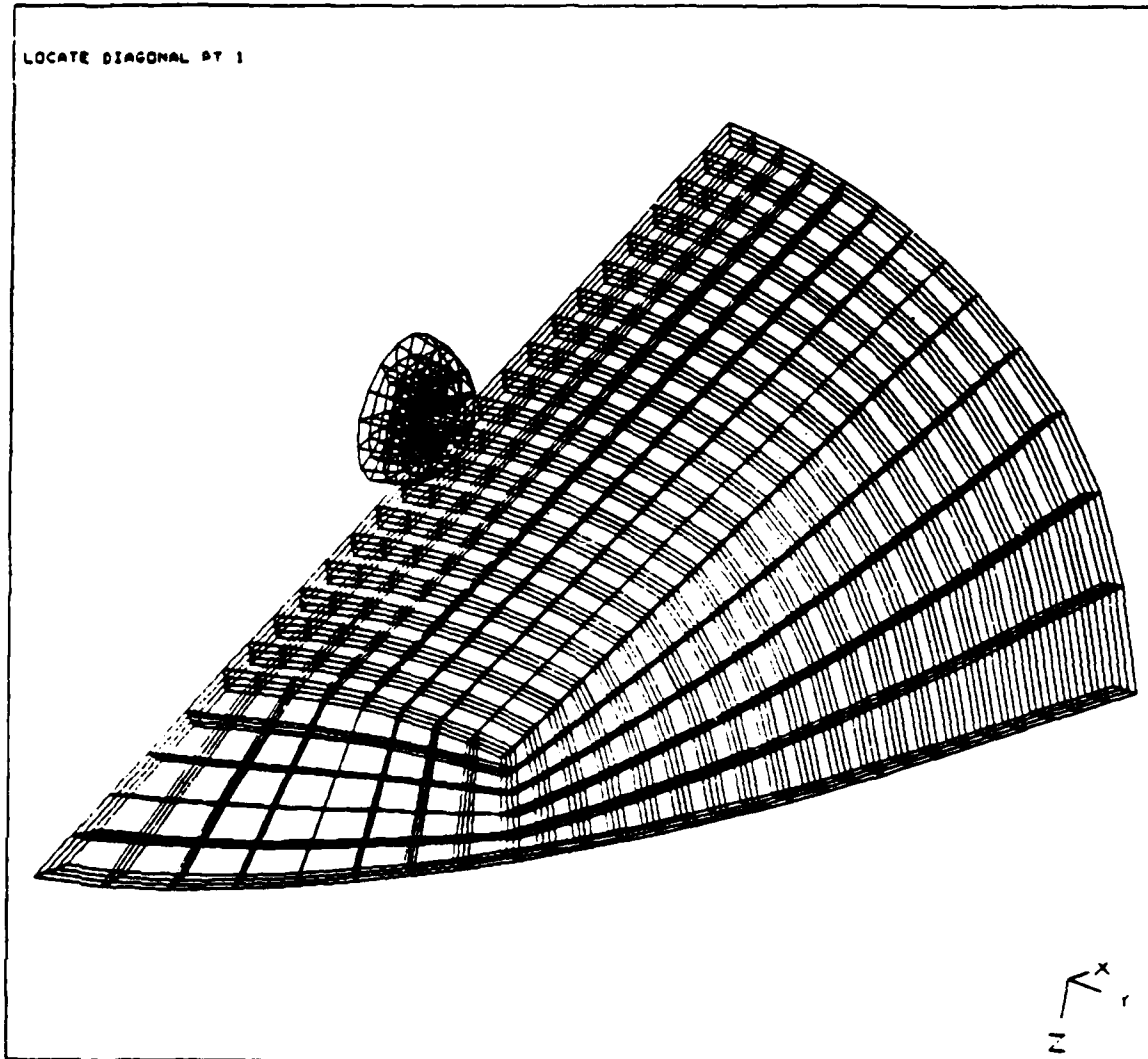


Figure 8

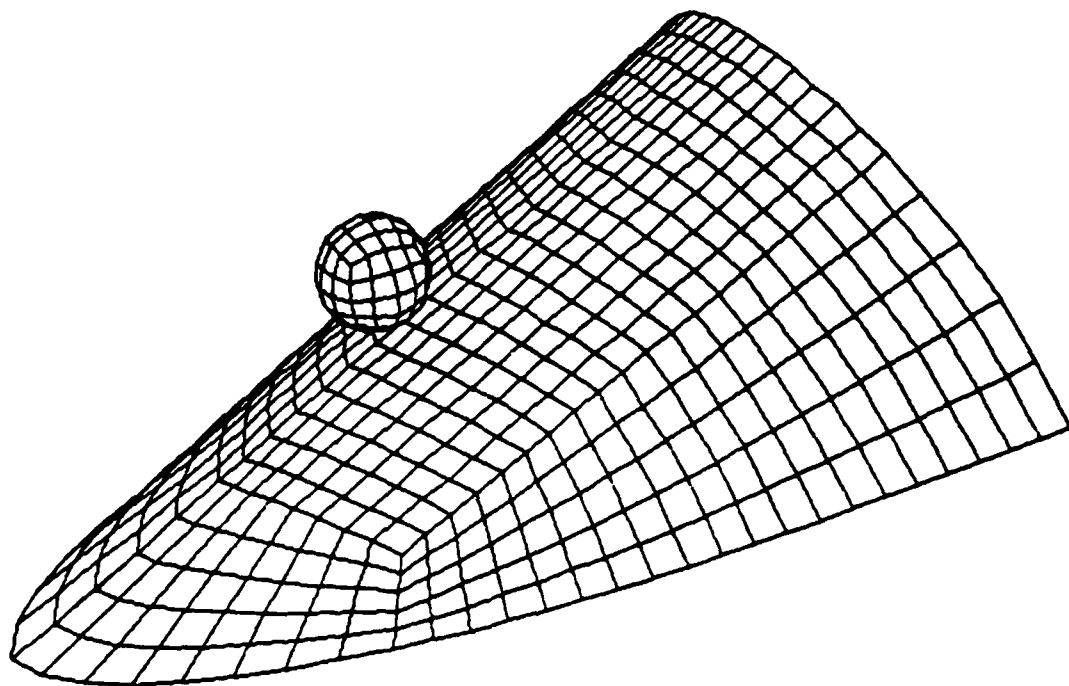


Figure 9

TIME = 0.10000E-02

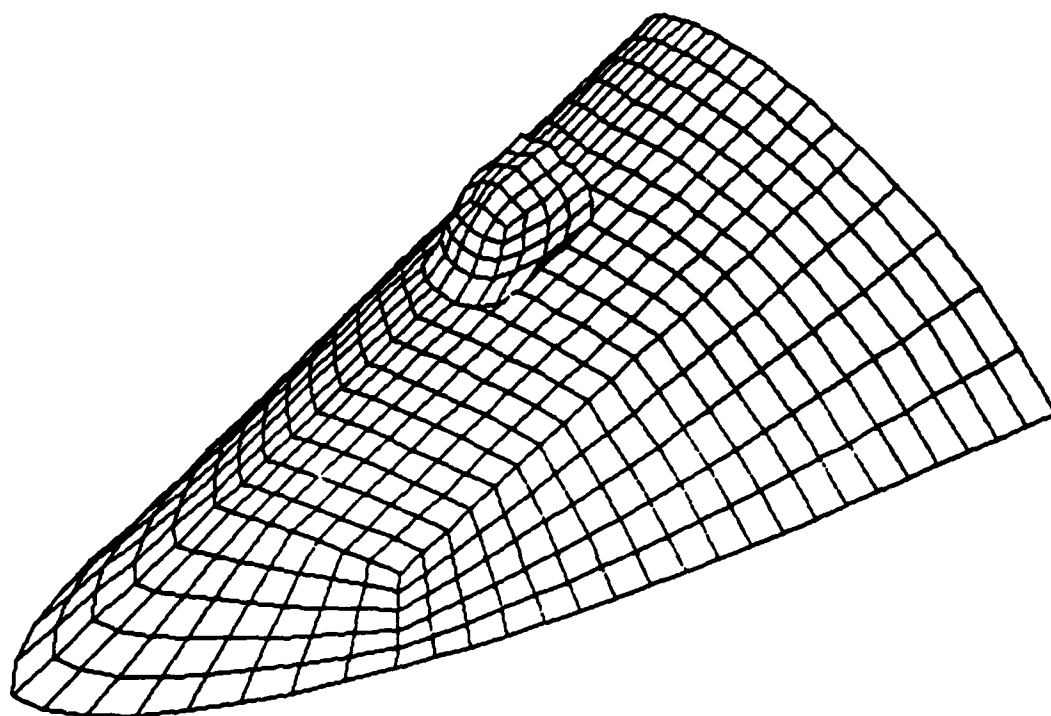


Figure 10

TIME = 0.20000E-02

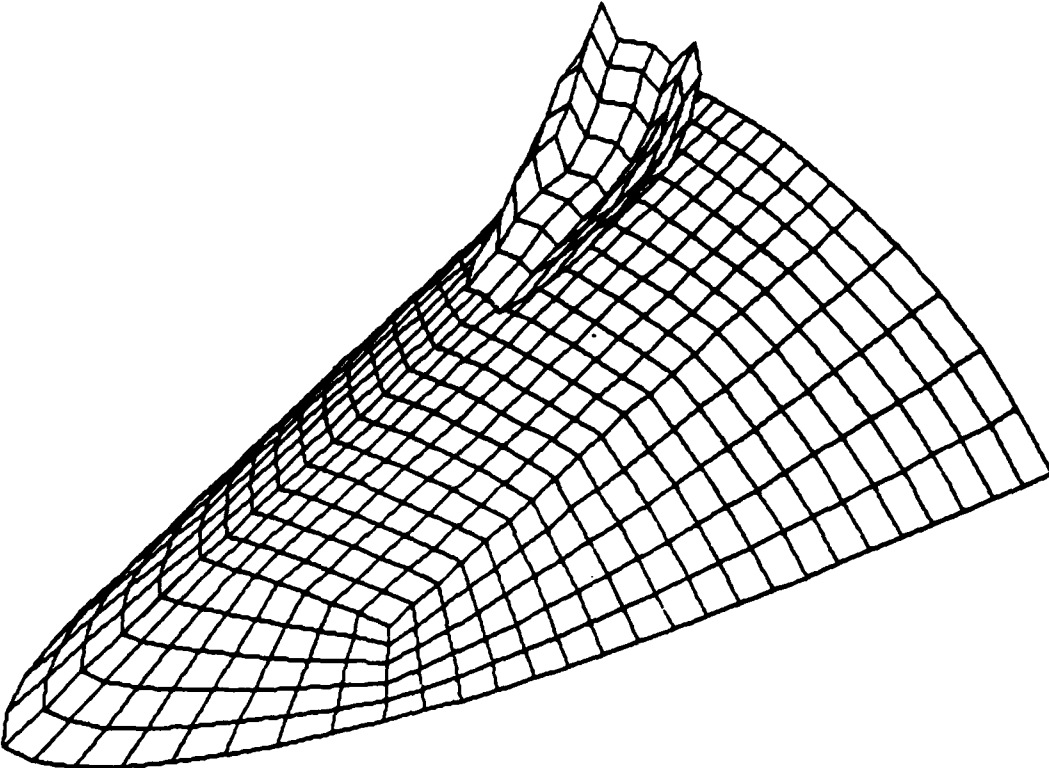


Figure 11



TIME = 0.30000E-02

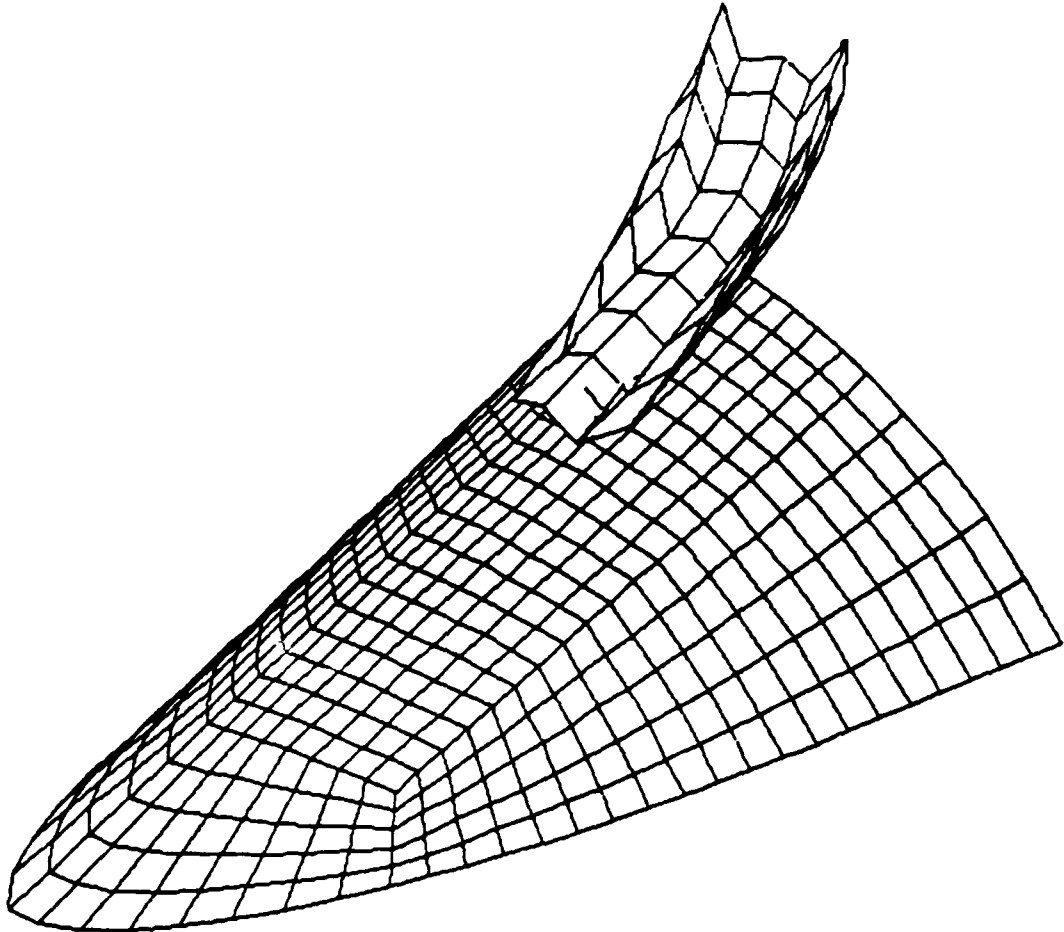


Figure 12

Z DISPLACEMENT

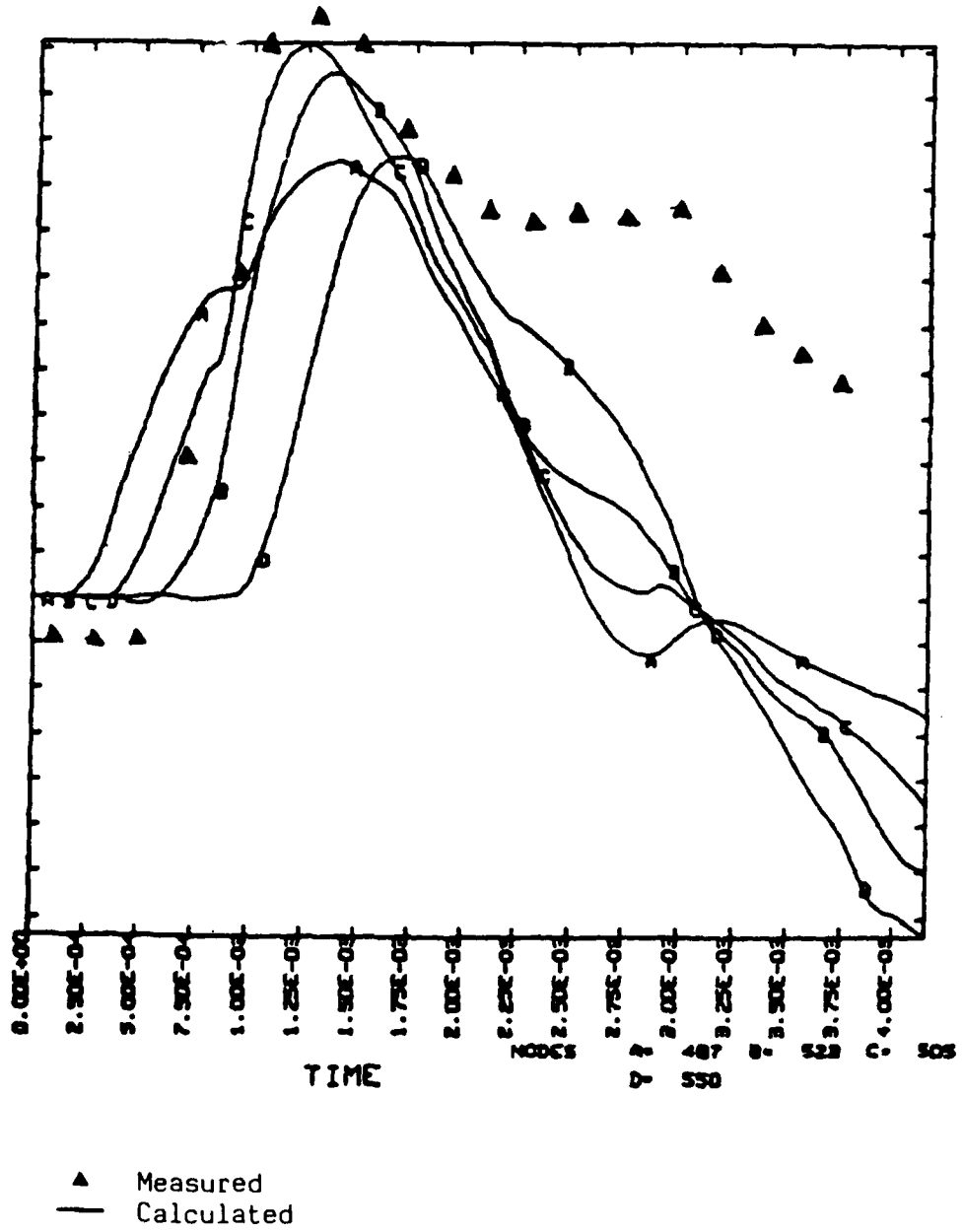


Figure 13

SESSION VI

BIRDSTRIKE HAZARD (PART B)

Chairman: J. Thorpe  
UK Civil Aviation Authority  
West Sussex, England

Co-Chairman: Maj. R. L. Merritt  
Bird Aircraft Strike Hazard  
Team  
Washington, D.C.

Coordinator: Capt. R. L. Dogan  
Bird Aircraft Strike Hazard  
Team  
Washington, D.C.

A-7 IMPROVED TRANSPARENCY DEVELOPMENT PROGRAM

D. Dversdall  
AFWAL/FDER

Gregory J. Stenger  
University of Dayton

S. Hargis  
AFWAL/FDER

A-7 IMPROVED TRANSPARENCY DEVELOPMENT PROGRAM  
D. Dversdall, AFWAL/FDER, Gregory J. Stenger,  
University of Dayton Research Institute, and  
S. Hargis, AFWAL/FDER

Birdstrikes on the USAF A-7D transparency system have continued to rise, resulting in a flight safety risk to the aircraft and aircrew. The Air Force Wright Aeronautical Laboratory, Improved Windshield Protection Program Office, initiated a program to develop an improved windshield system for the A-7 aircraft which has four pound, 480 knot bird impact resistance capability. The program consisted of three phases: system assessment studies, design choice development, and fleet implementation.

The OC-ALC, NGB, and FDER worked together to select a transparency system. Alternate transparency systems were evaluated in ten key areas, which included: initial cost, life cycle cost, weight, producibility, durability, interchangeability, maintainability, optics, visibility, and birdstrike resistance. A single piece windshield system with a composite aft arch was selected for development.

UDRI worked with LTV Aerospace and Defense Company to develop the windshield-to-fuselage interface hardware. Existing structure was used wherever possible. UDRI recommended a windshield system (both transparency and aft arch) from which the three participating companies developed windshield systems. These windshield systems were first tested on a "hard stand" at AEDC in order to, first, screen each design, providing each vendor with valuable design information for further tests; and second, develop design loads (using strain gages on the hard stand) which were used to verify the predicted loads. Each company had at least one windshield pass these tests.

Six months after the hard stand tests, birdstrike tests were conducted on a modified forward fuselage section. These tests were used to qualify each company's design as well as evaluate the fuselage modification. UDRI worked closely with the Arizona Air National Guard and LTV to install a prototype windshield on an operational ANG A-7D aircraft for flight testing.

## A-7 IMPROVED TRANSPARENCY DEVELOPMENT PROGRAM

Lt D. Dversdall  
Flight Dynamics Laboratory

G. J. Stenger  
University of Dayton

Birdstrikes on the Air Force and Air National Guard (ANG) A-7D/K transparency systems have been occurring with increasing frequency, resulting in a flight safety risk to the aircraft and aircrew. The A-7D/K fleet experienced ten transparency system penetrations between 1976 and 1984. Many of these strikes occurred while the aircraft were flying their routine low altitude attack and navigation training missions. In order to reduce the risk to their aircraft and crews, the Air National Guard Bureau (NGB) prohibited all low altitude training missions at several bases for 4.5 to 5 months a year, during the peak migratory seasons along the central migratory routes.

This was an incomplete solution to the problem. Even with the flight restrictions, birdstrikes continued to occur, and being unable to practice low level flying, the pilots found it difficult to maintain their required proficiency. The NGB decided that in order to permanently solve the birdstrike problem they would have to increase the birdstrike resistance of the plane's transparency system. To this end they initiated a transparency improvement program with the Windshield Systems Program Office, AFWAL/FDER, and Oklahoma City Air Logistics Center, the maintenance depot for the A-7 fleet.

The program was conducted in a three phased approach, directed by FDER. Before the program began, the commitment of the aircraft owners and operators was secured, and as the program progressed AFLC/NGB/AFSC jointly chose which one of the alternative windshield designs that would be fully developed. In Phase I the capabilities of, and the threat to the existing windshield were determined. Then based upon that information several alternate designs were developed, and from those, the best one was chosen for prototype development in Phase II. Phase II consisted of the prototype development and qualification of the design. Extensive birdstrike testing was conducted, both to evaluate different prototype configurations and then to qualify the final designs. Phase III will be the fleet implementation stage of the program. AFLC/NGB plan to retrofit the entire A-7D/K fleet with the improved windshield system.

The first step in the development process was to evaluate the recent birdstrike history of the A-7. The information on the number of birdstrikes against the windshield and canopy was acquired from the Norton Flight Safety Center, for the period April 1976 to December 1984, the time of the request for information. Table 1 presents that data

received for the A-7 birdstrike history. Both the number of impacts and penetrations would have been higher if the NGB had not implemented their flight restrictions. Of the ten transparency penetrations two resulted in minor injuries; fortunately none resulted in the loss of life or aircraft.

TABLE 1  
A-7D/K BIRDSTRIKE HISTORY  
APRIL 1976 TO DECEMBER 1984

COMPONENT	NO. OF IMPACTS	NO. OF PENETRATIONS	PERCENTAGE OF COMPONENT PENETRATIONS	PERCENTAGE OF TOTAL TRANS. PENETRATIONS
Windshield Center Panel	2	0	0	0
Right Side Panel	3	2	66.7	20
Left Side Panel	8	7	87.5	70
Total Windshield	13	9	69.2	90
Canopy	3	1	33.3	10
TOTAL SYSTEM	16	10	62.5	100

The next step was conducting a Birdstrike Risk Assessment for the baseline A-7 transparency configuration, and for each potential configuration. This effort provided statistical data concerning the most effective alternative. A probabilistical model was developed utilizing as inputs, the velocity distribution for the aircraft mission profiles, total annual flight time, total birdstrikes, bird weight distribution, the transparency frontal area, and the transparency system strength.

The baseline birdstrike capabilities were determined by estimation, projecting the A-7 capabilities based upon those of the F-4 transparency systems. A high level of confidence was placed in these estimated protection levels because of the similarity between the two transparency systems and the full-scale baseline birdstrike testing that had been conducted on the F-4. These capabilities were estimated in order to save both the time and the money it would have cost to conduct a full-scale set of baseline tests.

Table 2 presents the results of the Birdstrike Risk Assessment Studies. These studies projected the number of birdstrike penetrations for the A-7 fleet over a period of ten years, with an average of 79,000

flight hours per year. Several alternatives were considered, three of which were determined to be feasible. Each entailed a different level of complexity and aircraft modification.

The simplest was installing bird resistant side panels while retaining the existing frame and center panel. This would have increased the birdstrike protection from the baseline 155 knots to 220 knots. This approach was limited to the amount of birdstrike resistance it could provide, because regardless of how much the windshield panels were improved the existing frame could only withstand impact forces up to 220 knots.

The second option was to install a reinforced frame and birdproof sidepanels, while still retaining the original center panel. This raised the protection level to 350 knots, constrained by the impact resistance of the center panel.

The third option was to replace the existing windshield, sidepanels, and frame with an improved single piece windshield, and a new aft arch. This would increase the birdstrike protection level to 480 knots while also increasing the pilots forward viewing area.

Designs that would have included an improved canopy system were considered, however they were decided against because of the relatively small exposed frontal area of the canopy and the high cost of requalifying the ejection system. The A-7 has a through the canopy ejection requirement, and any new design would have to prove it could meet that requirement.

TABLE 2  
PREDICTED NUMBER OF DAMAGING BIRDSTRIKES

ALTERNATIVES	PENETRATIONS	% OF NON-PENETRATING STRIKES
Existing Windshield	13	59
Existing Center Panel with Bird Resistant Side Panels	7.4	77
Existing Center Panel with Bird Proof Side Panels and Reinforced Frame	3.0	90
Single Piece Windshield	1.2	96



In order to evaluate the designs developed in Phase I of the program, a method of rating the various transparency design cross-sections was devised to systematically evaluate the variables involved in determining the best transparency configurations for further consideration. Ten categories, which included initial cost, life cycle cost, weight, producibility, durability, interchangeability, maintainability, optics, visibility, and bird impact resistance were evaluated using a matrix evaluation technique. Note that an in-depth evaluation was not performed in each of the above categories; all ratings were relative to each other and not absolute. Eight transparency cross-sections, shown in Figure 1, were evaluated. These candidate cross-sections resulted from transparency configurations that have been used in the past on similar aircraft or that have been suggested as alternate designs by industry.

The transparency evaluation represents the combined rating of UDRI, Goodyear Aerospace, and AFWAL/FDER and were based on their experience gained in past programs. The rating or weighting factors were assigned in each category after considering the explanations listed below.

- The "design requirement weighting factors" are a rating of the categories relative to each other based on the projected Air National Guard requirements. For example, bird impact was rated higher than weight or cost. The most important category was assigned a "10"; other categories are rated according to the relative importance.

- The "transparency rating" prioritizes each transparency cross-section in a given category. The best material is given 10 points. All other cross-sections are to be rated relative to the best, on a scale of 0 to 10. Listed below is an explanation of each category.

- Initial Cost - initial cost of making the retrofit (cost of all hardware and the work required for installation, reflecting any development cost).

- Life Cycle Cost - cost of replacing transparency on an annualized basis.

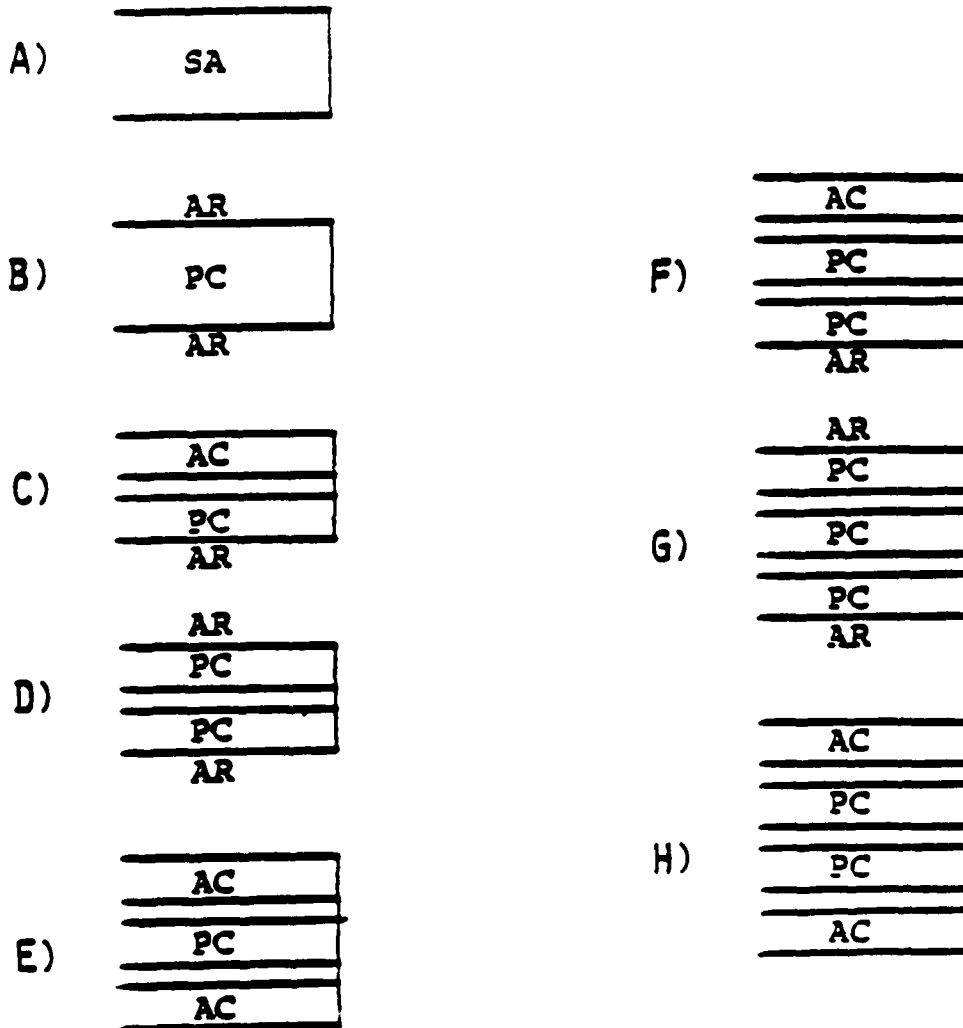
- Weight - relative weight of the windshield assembly.

- Producibility - reflects the development time required and potential production difficulties (proven vs. new technology).

- Durability - based on the actual service life of similar transparencies if possible.

- Interchangeability (Installability) - the expected difficulties of installing a given cross-section. Edge design considerations were included here.

FIGURE 1  
 CANDIDATE TRANSPARENCY CROSS-SECTION IDENTIFICATION



**KEY**

- AC As-Cast Acrylic
- AR Abrasion Resistant Coating
- PC Polycarbonate
- SA Stretched Acrylic
- SI Silicone Interlayer
- UI Urethane Interlayer

-- Maintainability - any maintenance required on the windshield system.

-- Optics - reflects expected optics which could be achieved and maintained during production and service.

-- Visibility - the relative visibility between designs.

-- Birdstrike Resistance - the relative birdstrike resistance of each design.

- The "Overall Windshield Rating" is the summation of the products for each category of the "Design Requirement Weighting Factor" times the "Transparency Rating."

All transparency designs are a compromise of many different and sometimes conflicting design requirements and goals. This evaluation is an attempt to quantify these requirements and goals in order to objectively select the best alternative. AFWAL/FDER, Goodyear Aerospace, and UDRI conducted this evaluation as objectively as possible based on their combined experience in aircraft transparencies. The evaluation results have been summarized in Table 3.

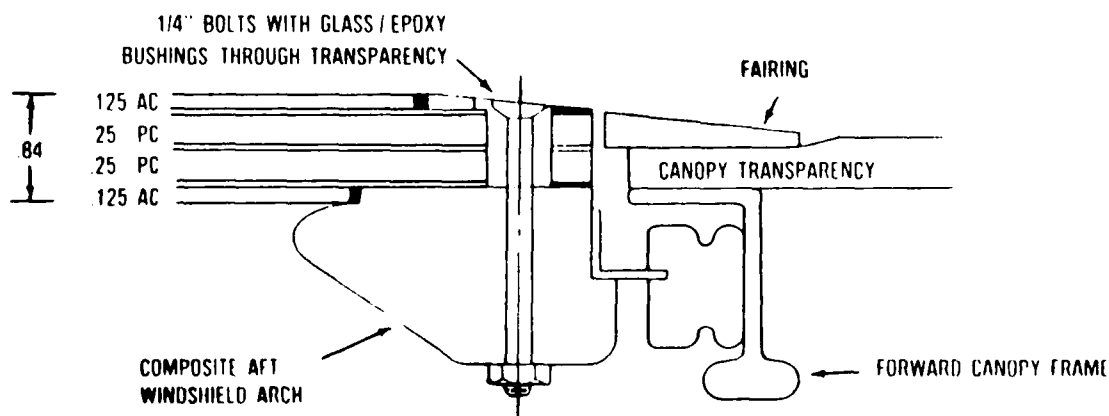
TABLE 3  
MATRIX OF OVERALL RATINGS

MATERIAL CROSS-SECTION DESIGNATION	3-PIECE WINDSHIELD WITH PRODUCTION FRAME	3-PIECE WINDSHIELD WITH REINFORCED PRODUCTION FRAME	1-PIECE WINDSHIELD USING EXISTING FRAME WHERE POSSIBLE
A	5498.	5448.	5154.
B	4634.	4606.	4880.
C	5844.	5865.	6064.
D	4680.	4643.	4948.
E	6448.	6498.	6644.
F	5718.	5756.	6064.
G	4458.	4505.	4962.
H	6448.	6498.	6644.

A single piece of windshield and composite aft arch having four pound-480 knot birdstrike protection, and using the existing frame where possible, was selected in conjunction with transparency cross-section H. This windshield design was selected because it reduces the number of penetrating birdstrikes by a factor of over 10. This transparency represents a low technical risk as similar systems have been proven in service. Cost of modifying the aircraft is minimized because existing fuselage structure is used wherever possible. A composite aft arch was selected because it rebounds after a birdstrike, minimizing air blast into the cockpit. This system is also compatible with night vision and HUD requirements.

The objective of the Phase II program was to develop the system selected in Phase I. This was accomplished by LTV Aerospace & Defense Co., working in cooperation with UDRI. A detailed transparency/aft arch system was designed by UDRI and recommended to the transparency companies participating in the program. Each company was then free to design and develop their own systems. The recommended transparency cross-section shown in Figure 2 was selected because it represented a low technical risk. This transparency mounts to the existing side rails, resulting in the additional thickness of the transparency being outside the moldline by 3/8 inch.

FIGURE 2  
PREFERRED A-7 WINDSHIELDS CROSS-SECTION



The composite aft arch was designed using a Kevlar -49/S-2 glass/expoxy hybrid material. This material was configured to maximize energy absorption. The versatility of the composite allows it to be tailored for strength and stiffness with a controlled failure mode. Birdstrike loads in the transparency can be minimized by using this feature. The forward edge of the arch was angled to maximize visibility. The striker (part of the canopy seal system) was not changed from the current production system. A new canopy fairing had to be incorporated to blend the new windshield moldline back into the canopy.

Several design features make this transparency system unique. This system was the first flying prototype birdproof windshield system to use an all-composite aft arch. The aft arch-to-fuselage connection is also unique in that it was designed to minimize the applied moment on the sill. This has been done by using a clevis fitting. During a birdstrike, the base of the arch can rotate over 10°, and by pinning this connection virtually no moment is applied to the fuselage, minimizing the possibility of major fuselage damage. To further reduce the possibility of damage, the clevis fitting was designed as the fuse in the system, that is, it will fail prior to damage to the fuselage.

Basic design changes to the aft arch were studied using a nonlinear static finite element analysis. Table 4 shows the results of six finite element analyses. Note that simply changing the connection at the base of the arch significantly changes the loads applied to the fuselage. This analysis was also used to define design details of the arch itself. Primary design considerations (which are many times conflicting) were as follows: (1) failure load of the arch must be below the capability of the transparency to apply the load; (2) loads applied to the fuselage should be minimized; (3) deflection should be minimized; and (4) energy absorbed prior to failure should be maximized.

TABLE 4

SUMMARIZED RESULTS OF NONLINEAR STATIC FINITE ELEMENT ANALYSIS

MODEL	ARCH GEOMETRY	END CONDITION	FAILURE LOAD LBS	SIDE LOAD LBS	MOMENT FT-LBS	DEFLECTION IN	ENERGY IN LBS
	$C_L$	END					
1	1.4" Tapering to 3/4"	Pinned	18,600	3280	0	1.9	35,400
2	1.4" Tapering to 3/4"	Fixed through Link	23,100	6410	2450	1.5	35,200
3	1.4" Tapering to 1"	Pinned	21,900	4490	0	1.6	34,600
4	1.4" Tapering to 1"	Pinned with Link/Torsional Spring	22,600	5040	520	1.5	34,700
5	1.4" Tapering to 1"	Fixed through Link	26,700	8000	3340	1.3	34,400
6	1.4" Tapering to 1"	Fixed	25,700	7420	1570	1.4	34,800

Initial testing of the prototype windshield systems was conducted on a rigid test fixture. This fixture was instrumented to measure the load which could be applied to the fuselage. These loads were, in turn, used to ensure the fuselage modifications would withstand the loads. Typical peak loads are summarized in Table 5.

TABLE 5  
TYPICAL PEAK IMPACT LOADS

---

Side Load	9001b per in of sill
Compression Load	20001b per in of sill

---

From the beginning of the program the optical quality of the improved one piece windshield was an important design consideration. The A-7D/K aircraft has a very good record of accuracy in weapons delivery, and the optics of the windshield play a large factor in that record. In order to maintain the overall quality of the system, the optical specifications developed for the one piece windshield were some of the most stringent in the industry. There were five major performance characteristics that each windshield must possess in order to be acceptable, they are luminous transmittance, haze, optical defects, angular deviation, and optical distortion.

The minimum acceptable luminous transmittance is 79 percent and the maximum acceptable haze is 3.5 percent. This is when measured a zero angle of incidence and in accordance with ASTM Method D1003-61, Standard Test Method for Haze and Luminous Transmittance of Transparent Plastics.

Optical defects come in many different forms such as scratches, orange peel, embedded particles, flaws, inclusions, or bubbles. They will be considered a problem when they cause vision through the windshield to be distracted and focus on the defect. Scratches shall be measured and compared to the ASTM-F548B, Scratch Standard for allowable limits. Orange peel will be visually evaluated from the pilot's eye position, and if it is found objectionable then it will be considered a defect. Embedded particles, flaws, inclusions, and other minor optical defects are compared against a maximum size. Inside the Critical Optical Area they shall have a maximum diameter of 0.035 in, outside that area they can exist up to 0.09 in. The Critical Optical Area extends 14° below the design eye line of sight and 8° left and right of the centerline.

The angular deviation can be a maximum of +/-2 millirad (6.88 minutes of arc) throughout the critical optical area. The azimuthal deviation is allowed to deviate a maximum of +/-3 MRD (10.32 minutes of arc) over the full Critical Optical Area, however inside the azimuth

viewing angles of  $\pm 2^\circ$  the deviation is limited to  $\pm 2$  MRD (6.88 minutes of arc). The method of measurement was defined to be in accordance with ASTM F-801-83, the Standard Method for Measuring Optical Angular Deviation of Transparent Parts.

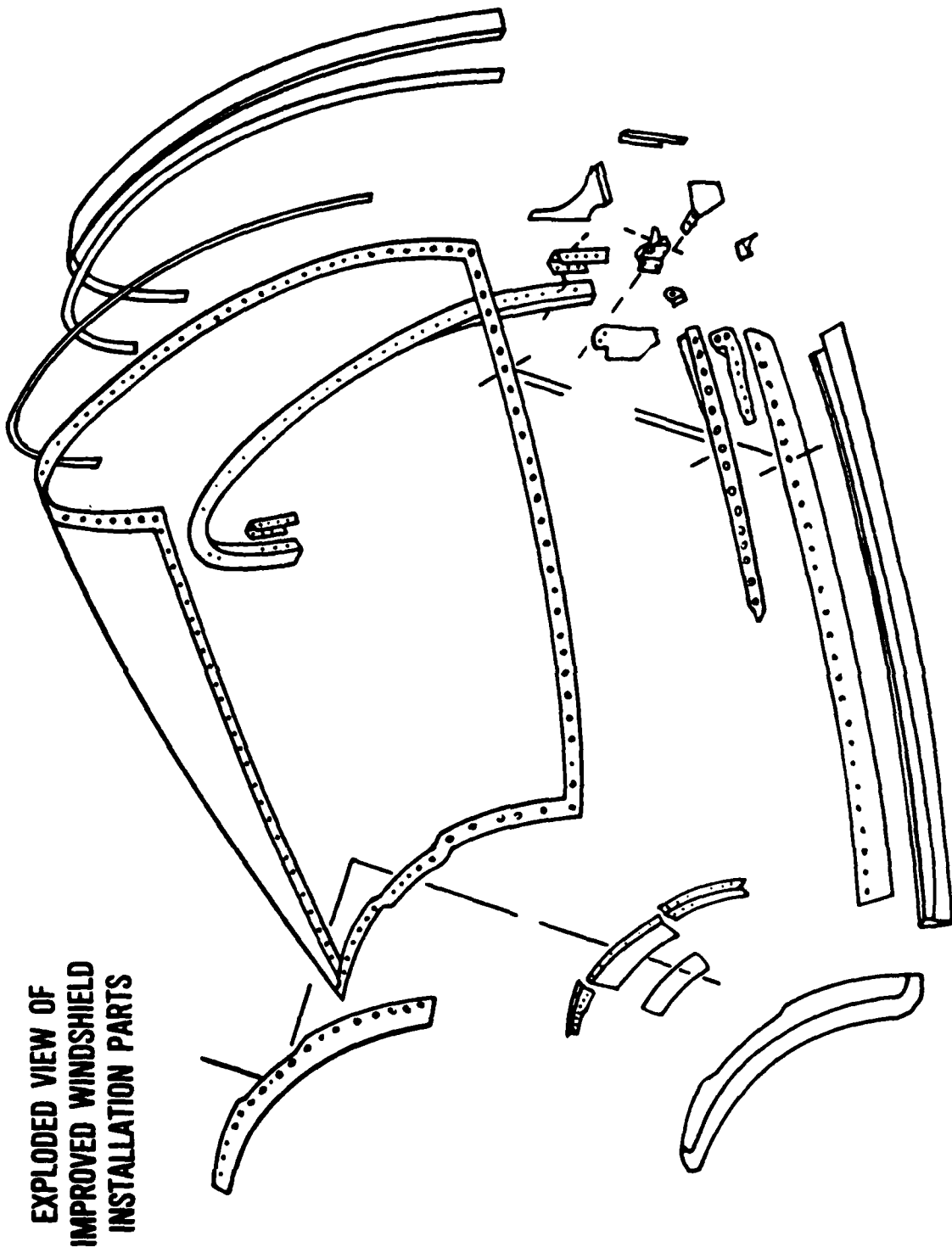
Optical distortion will be visually evaluated against a grid board background, and the transparency shall indicate no apparent bending, blurring, divergence, convergence, or jumping of grid lines. Photos of the windshield were then to be taken from the pilot's eye position and the photos then evaluated using the procedures in ASTM-F733-81 to assure the windshield has distortion no greater than that which would cause a grid line slope of one to ten in the optical area of the windshield.

The new one piece windshield replaces the existing transparency and its arches, while making use of the existing sills. To begin the installation, the old windshield and side panels are removed, and the existing aft arch and center panel frame are cut off. The aft arch is cut at the sill and the center panel frame is cut at the forward pressure bulkhead. Then the four pieces of the new forward arch and the aft arch attachment saddles are installed. A reinforcing piece is installed along the sill to ensure that in the event of a birdstrike the sill doesn't fail. Once these parts are in place, the windshield and aft arch are installed. Because the new windshield slightly exceeds the existing mold lines, glass epoxy fairings are used to smooth the transition and reestablish the mold lines. Figure 3 shows the exploded view diagram, displaying all of the major parts involved in the installation. Field modification of the aircraft will take a three man team ten days to install the system on an aircraft.

Currently one of the prototype improved windshields is undergoing flight evaluation of the Tucson Air National Guard Base. There it has demonstrated compatibility with the weapons delivery system, night time mid air refueling, and night vision goggle systems. The pilots have also benefitted from the 20 percent increase in field of view and the overall high optical quality of the system.

The production contract is to be issued in the Spring of 1989. Currently the NGB and AFLC are planning to refit the entire Air Force A-7D/K inventory with the improved transparency system.

Figure 3





BIRD STRIKES TO U.S. AIR FORCE AIRCRAFT 1987

Capt Russell P. DeFusco  
Capt Robert L. Dogan  
Maj Ronald L. Merritt

Bird Aircraft Strike Hazard  
(BASH) Team

**Bird Strikes to U.S. Air Force Aircraft  
1987**

**Capt Russell P. DeFusco  
Capt Robert L. Dogan  
Maj Ronald L. Merritt  
Bird Aircraft Strike Hazard (BASH) Team  
HQ USAF/LEEV, Bolling AFB DC**

The U.S. Air Force suffered it's most disasterous year in loss of life and aircraft damage due to bird strikes in 1987. 2,559 bird strikes costing \$250,000,000 and five fatalities were reported to the Bird Aircraft Strike Hazard (BASH) Team. Included in these figures were three Class A mishaps.

-- In May, an F-4E on deployment from Spangdahlem AB Germany struck a 16 pound Griffon Vulture on the Bardenas Range in Spain. The bird penetrated the windscreen and canopy of the aircraft striking the pilot, killing him instantly. Bird remains and pieces of canopy ripped through the cockpit impacting the weapons systems officer. His injuries and visual impairment caused by the strike prevented escape from the aircraft and he was killed upon ground impact.

-- In September, a B-1B on a low-level training mission from Dyess AFB, Tx struck a 16 pound American White Pelican near LaJunta, Colorado. Aircraft control was lost and the crew initiated ejection. Three crewmembers ejected successfully. The remaining crewmembers were killed upon ground impact.

-- In December, an E-4 struck approximately 40 Snow Geese shortly after takeoff from Offutt AFB, Ne. The crew jettisoned fuel and managed to land safely despite of extensive damage to the airframe and engines. Both wings, the radome, and two engines sustained significant damage costing over \$1,650,000.

These examples are but a few of the devastating effects birds had on our aircraft in 1987. The severity of many of these strikes is due to encounters on high-speed, low-level missions. The Air Force's increased emphasis on realistic low-level mission profiles places our aircrews in prime avian habitat. High airspeed and high bird densities often result in significant damage or destruction of aircraft. Mission planning and airspace development to avoid birds requires more emphasis as our low-level activity increases. Several major commands have initiated aggressive bird strike reduction programs to combat these problems. Despite the staggering losses during 1987, many units reported significant reductions in their bird strike rates. The overall Air Force bird strike rate was 69.9 per 100,000 flying hours in 1987. This rate is

over 10% lower than 1986 and may reflect an improvement in base-level BASH programs and a heightened awareness of BASH reduction strategies. Bird strike damages can be further reduced through a variety of operational and environmental modifications adapted to the unique mission requirements of each unit.

The following summary of bird strike data reported throughout the Air Force during 1987 is offered to illustrate the impact birds had on our aircraft. While thorough statistical analysis is not yet available on these data, general trends can be used to concentrate BASH reduction efforts for each mission profile.

#### **Aircraft Involved in Bird Strikes**

Virtually every aircraft in the USAF inventory reported bird strikes during 1987. Figure 1 shows the percentage of strikes by aircraft type. Cargo and fighter/attack aircraft reported the most strikes. Bird strikes to cargo aircraft are increasing each year as their low-level missions increase.

Bird strike rates per 100,000 flying hours ranked by rate are reported by aircraft type in Table 1. Table 2 shows these data ranked by number of reported strikes.

**TABLE 1**  
**Bird Strike Rate By Aircraft**  
**(RANKED BY STRIKE RATE)**  
**1987**

ACFT	STRIKES	RATE
E-4	12	655.0
C-18	3	320.2
B-1	27	217.8
KC-10	70	179.3
B-52	155	150.6
F-111	115	134.6
C-9	34	117.5
KC-135	288	111.7
H-60	3	107.8
A-10	217	98.6
T-38	305	87.8
F-106	10	86.5
C-130	274	76.9
T-43	12	76.2
C-5	44	73.8
C-20	4	71.8

# BIRD STRIKES BY TYPE OF AIRCRAFT 1987

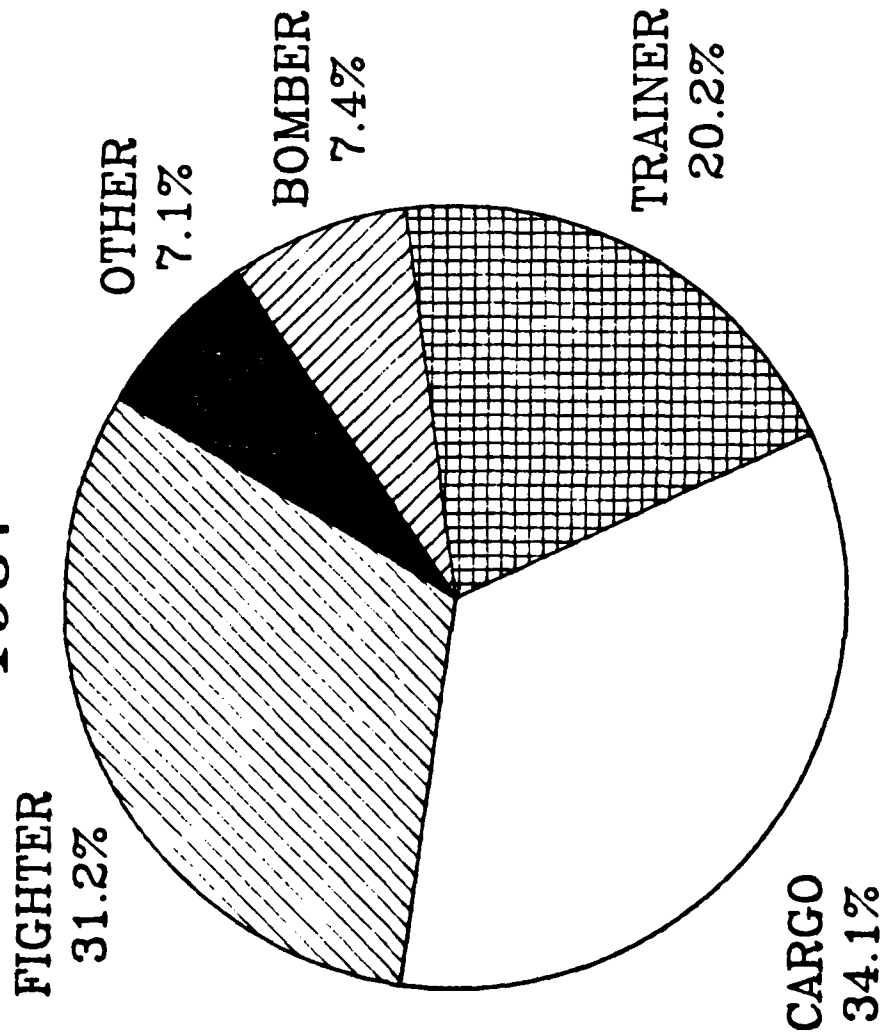


FIGURE 1

**TABLE 2**  
**Bird Strike Rate By Aircraft**  
**(RANKED BY NUMBER OF STRIKES)**  
**1987**

ACFT	STRIKES	RATE
T-38	305	87.8
KC-135	288	111.7
C-130	274	76.9
A-10	217	98.6
T-37	207	66.1
F-16	183	58.5
B-52	155	150.6
F-111	115	134.6
F-4	87	40.7
C-141	85	30.1
F-15	76	37.2
KC-10	70	179.3
RF-4	50	69.0
C-5	44	73.8
A-7	44	52.9
C-9	34	117.5
B-1	27	217.8
C-21	27	46.9
E-4	12	655.0

**IMPACT LOCATIONS**

Distribution of bird strikes to various aircraft components is basically random and related to the frontal surface area. Table 3 shows the percentage of total bird strikes by impact location.

**TABLE 3**  
**Bird Strikes By Impact Location**  
**1987**

Impact Location	Percent of Total
Windshield/Canopy	21.4
Engine/Cowling	18.0
Radome/Nose	16.8
Wings	16.3
Fuselage	8.8
External Tanks/Pods/Gear	6.4
Multiple Locations	10.0
Other	2.3

Windshield and canopy strikes topped the list again in 1987. Two fatalities and several injuries due to canopy penetrations resulted from these strikes. We also anticipate further problems with canopy strikes and penetrations as the Air Force's low-level role increases. For example, the current F-15 canopy is only capable of withstanding a 4 pound bird at 180 knots. With the deployment of Strike Eagle, the F-15 will encounter birds more frequently than in its current role.

#### **BIRD STRIKES BY ALTITUDE**

Birds can be encountered at nearly all flight levels. The highest strike ever recorded was to a vulture at 37,000 feet. However, most birds fly much closer to ground level and over 95 percent of all strikes are reported below 3,000 feet AGL. Figure 2 shows 1987 bird strikes by altitude. Strike rates rise significantly as altitude decreases. This is partly due to where we fly, but mostly because birds are commonly active close to the ground. Any gain in altitude represents a substantially reduced threat of a bird strike. Pilots should consider higher altitudes whenever crossing known bird concentration areas, particularly during migratory periods.

#### **TIMES WHEN BIRD STRIKES OCCUR**

Bird strikes occur around the clock and throughout the year, but are most likely during certain periods. Figure 3 shows distribution of bird strikes by time of day. Most strikes are reported during daylight hours when we do most of our flying. Despite the low numbers, dawn and dusk are particularly hazardous times since many birds are most active at these times. Several bases have limited operations during these periods and have reduced their strike rate as a result. Most nighttime strikes are reported during migratory movements of birds during the spring and fall.

Figure 4 indicates bird strikes by month. Strike rates peak during the spring and fall migratory periods. These rates are perennially highest during September and October as birds move south. Bird populations are highest at this time following the summer breeding cycle.

#### **Bird Strike By Phase Of Flight**

Birds can be, and have been, struck in all phases of flight. Approximately half of the reported strikes occurred in the airfield environment during 1987 (Figure 5). Fortunately, most of these strikes were not as severe as in previous years. A substantial improvement in airfield grounds maintenance

# BIRD STRIKES BY ALTITUDE 1987

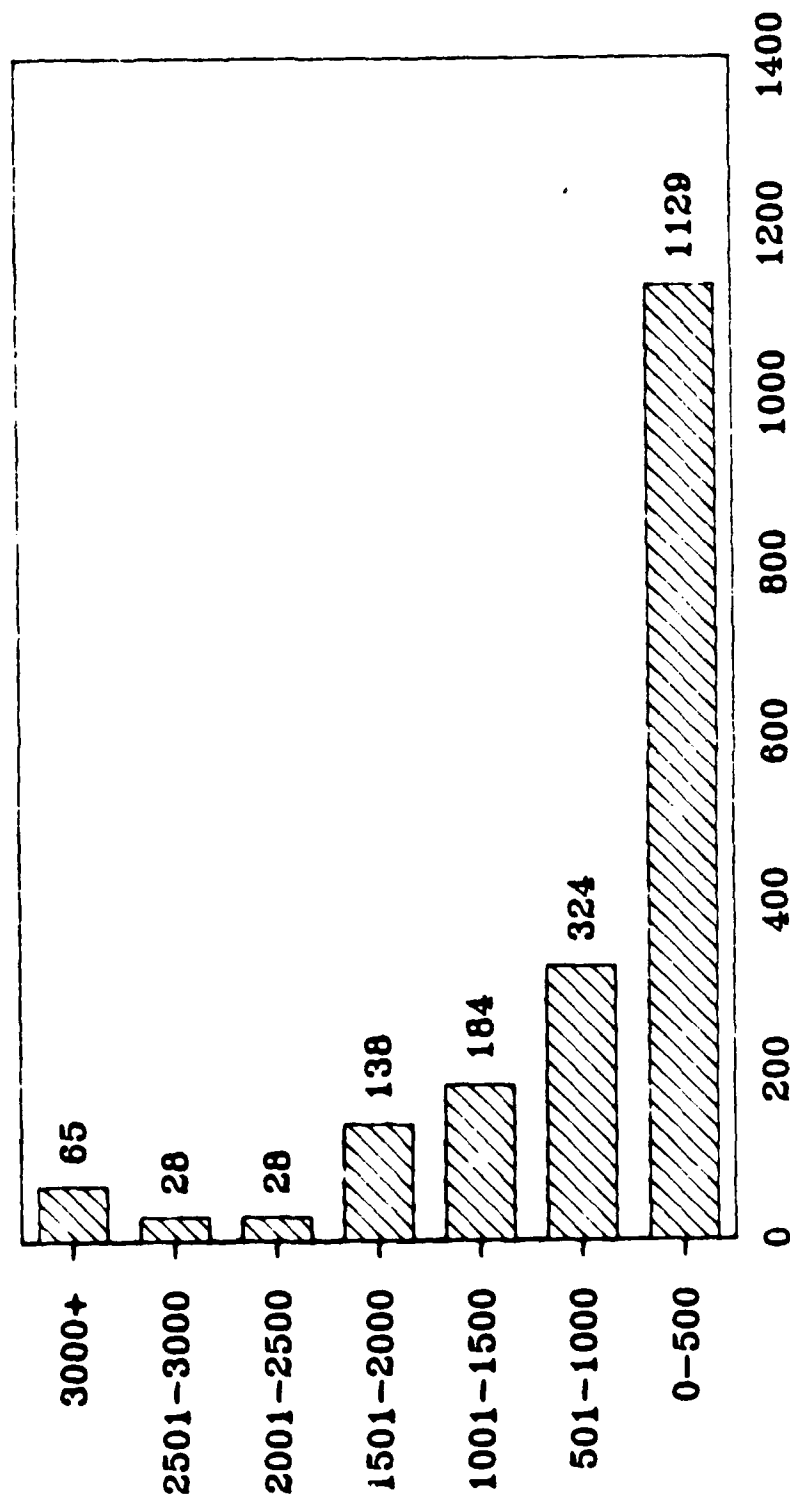


FIGURE 2

# BIRD STRIKES BY TIME OF DAY 1987

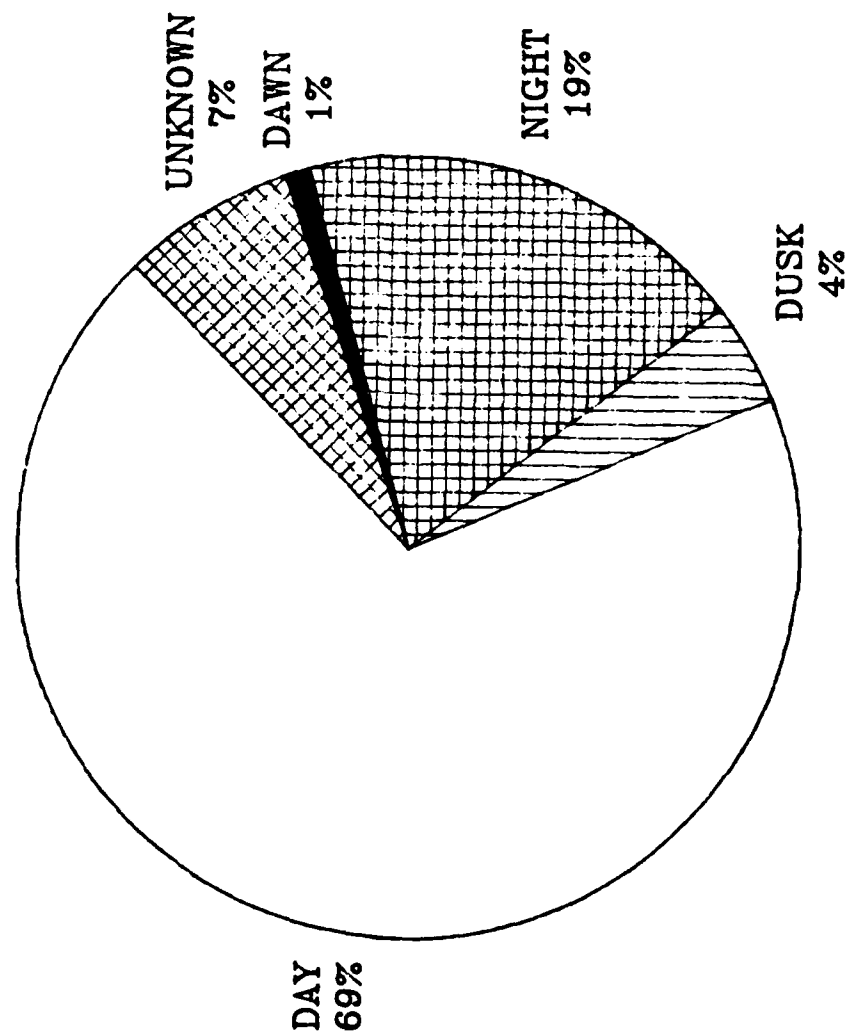


FIGURE 3



# BIRD STRIKES BY MONTH 1987

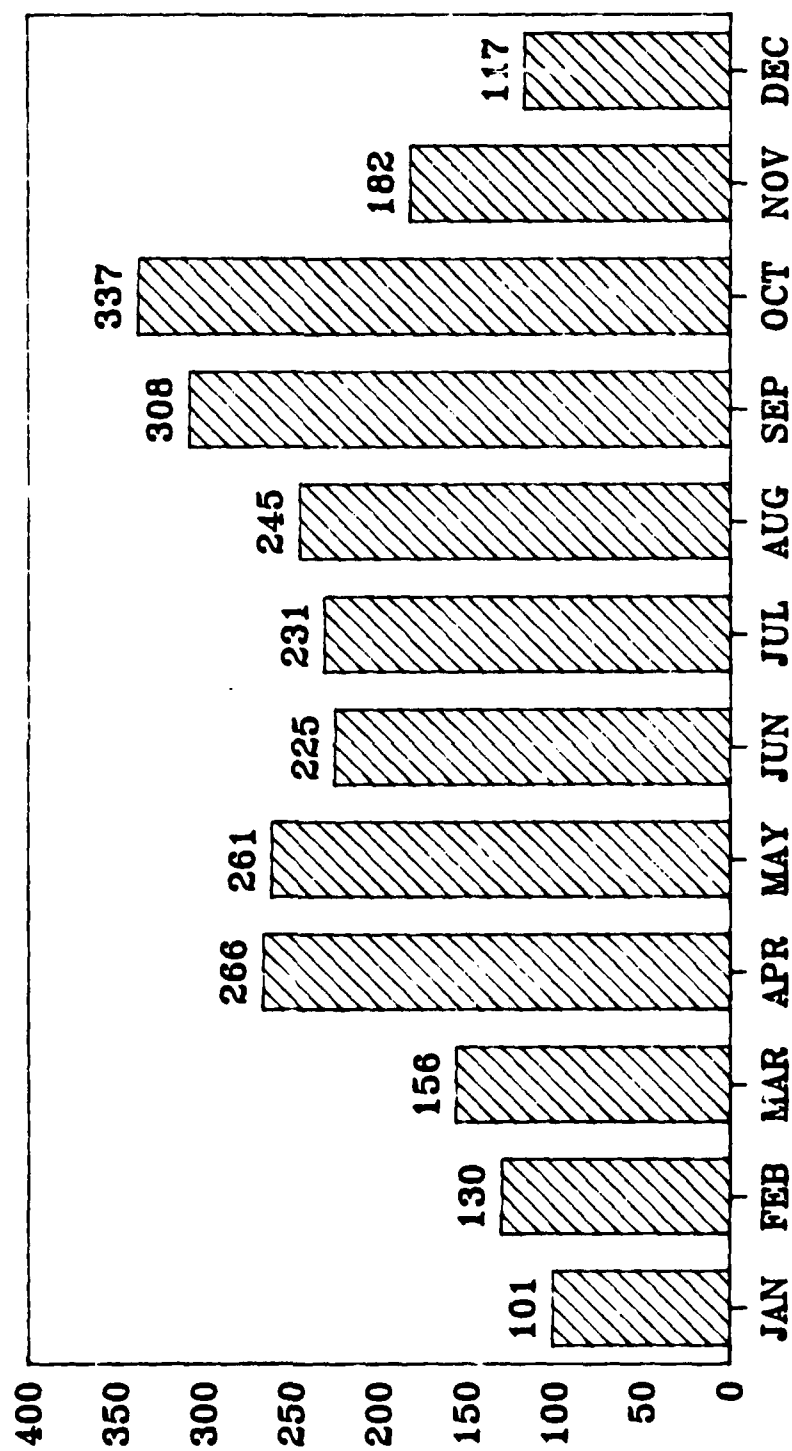


FIGURE 4

# BIRD STRIKES BY PHASE OF FLIGHT

1987

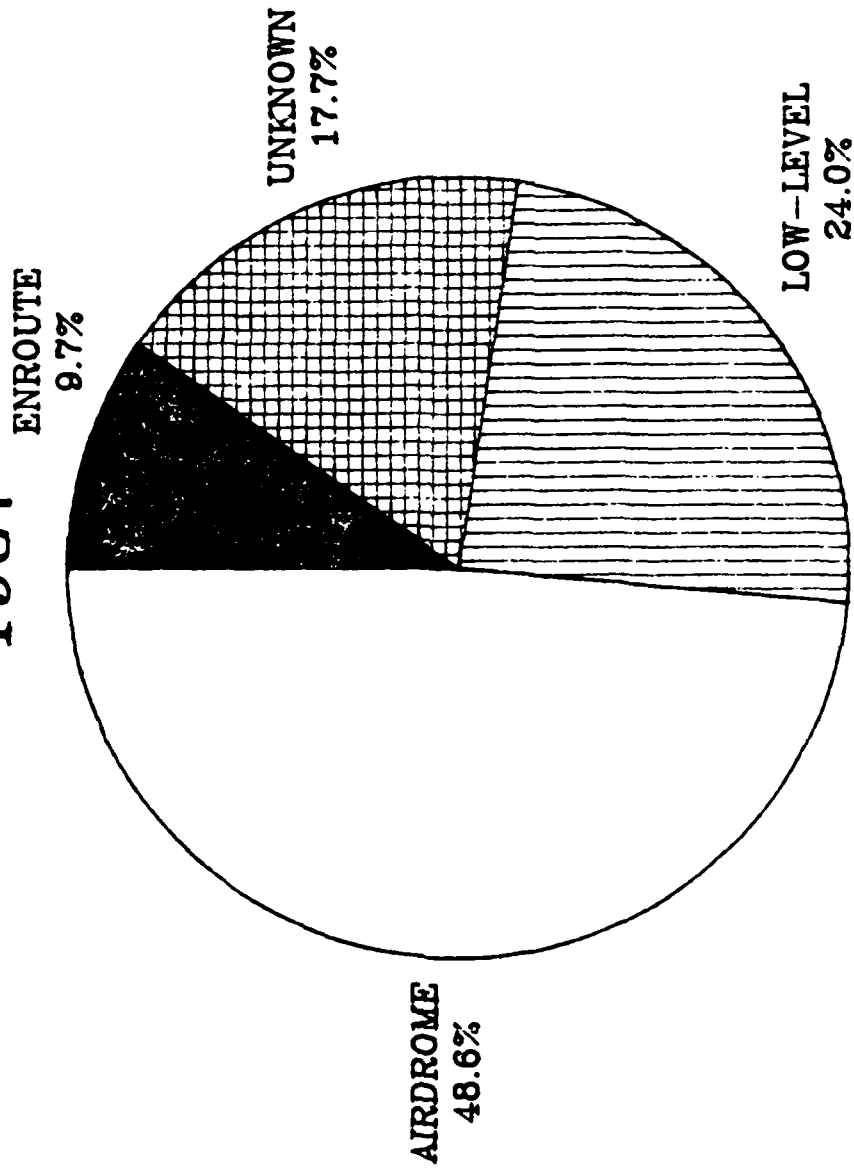


FIGURE 5

procedures and bird dispersal techniques in the past several years have resulted in improved flight safety in the airfield vicinity.

While only one quarter of reported strikes occurred in the low-level and range environments, the vast majority of damage and all five fatalities resulted here. Reduction of bird strikes in this environment can only be accomplished by careful airspace planning, development, and scheduling to avoid potential bird hazards. The Air Force is focusing efforts on reducing the low-level bird hazard in the future. The BASH Team is currently working on several major projects to address these hazards. Expansion of the Bird Avoidance Model (BAM) to include all high-risk bird species and all theaters of operation is being researched. The current model includes populations and movement data for waterfowl and some species of raptors (birds of prey) for the continental United States. Units using the current model reported up to 70 percent reductions in strikes to these birds.

Another area currently under research is the use of radars, particularly the Next Generation Weather Radar (NEXRAD), to help observe birds. Preliminary results indicate that this doppler weather radar network can detect bird movements and provide altitude data. This information may provide aircrews with bird hazard warnings for mission planning and possibly enroute avoidance. The BASH Team is sponsoring the development of a bird recognition algorithm for possible inclusion in this system. We are continuing to explore new radar technology that may provide real-time bird detection in the airfield environment.

With these systems operating, we anticipate a future reduction of the severe bird strike hazard in the low altitude flight environment.

#### **SUMMARY**

The Air Force continues to suffer tremendous losses to bird strikes each year. 1987 was the most disasterous year in terms of aircraft damage and lost lives. Recent incidents have created an increase in interest in BASH reduction efforts. Much needs to be done to reduce the hazards in all operating environments, but especially away from the airfield. The BASH Team considers development of complete bird population and movement data, and issuance of bird hazard advisories in our low-level and operating areas among its top priorities for future reductions of bird strike hazards. Armed with this information, we anticipate safer flying conditions and a substantial savings of resources throughout the Air Force.

DEFINITION AND REDUCTION OF THE F-18 WINDSHIELD  
BIRDSTRIKE HAZARD

G. J. Stenger  
University of Dayton

J. L. Terry  
Flight Dynamics Laboratory

# DEFINITION AND REDUCTION OF THE F-18 WINDSHIELD BIRDSTRIKE HAZARD

G. J. Stenger  
University of Dayton Research Institute  
J. L. Terry  
Flight Dynamics Laboratory

## INTRODUCTION

Since 1983 there have been nine reported bird impacts on the F-18 windshield, see Figure 1, resulting in one penetration. Associated with this penetration was an injury to the pilot. The number of penetrations can be expected to increase as the F-18 fleet size increases. There are approximately 270 aircraft in the fleet (mid-1986), with 84 aircraft being added per year to achieve a total fleet size of 1300 aircraft.

The Improved Windshield Protection Program Office (AFWAL/FIEA) of the Air Force Wright Aeronautical Laboratory was contacted by NAVAIR to evaluate the F-18 windshield system and recommended an improved system having a birdstrike resistance capability consistent with the current and expected future mission requirements. FIEA contracted with the University of Dayton Research Institute (UDRI) to conduct a seven-part study (see Figure 2) to develop and evaluate alternate transparency system concepts and to recommend a system which would provide the most cost effective approach meeting the design requirements and goals.

## OBJECTIVE

The primary purpose of this study was to evaluate transparency systems for the F-18 with increased bird impact resistance capability. Because of the limited frontal area of the canopy, the threat of bird impacts on the canopy was not considered critical to aircraft survivability. As a result, this effort was limited to evaluating windshield systems; the canopy was not considered for redesign.

## DESIGN GUIDELINES, REQUIREMENTS AND CONSTRAINTS

The UDRI, in conjunction with the AFWAL Project Engineer, defined the guidelines and constraints that governed the design of the alternate windshield systems, as well as the evaluation of each of the design concepts. Similar programs have been conducted on the T-38, F-4, and A-7 aircraft, and the experience and knowledge gained in these programs were used to make critical decisions relating to optics, fabrication, maintainability, and life cycle costs.



Figure 1. F-18 Aircraft.

# UDRI PROGRAM SUMMARY

## SYSTEMS APPROACH

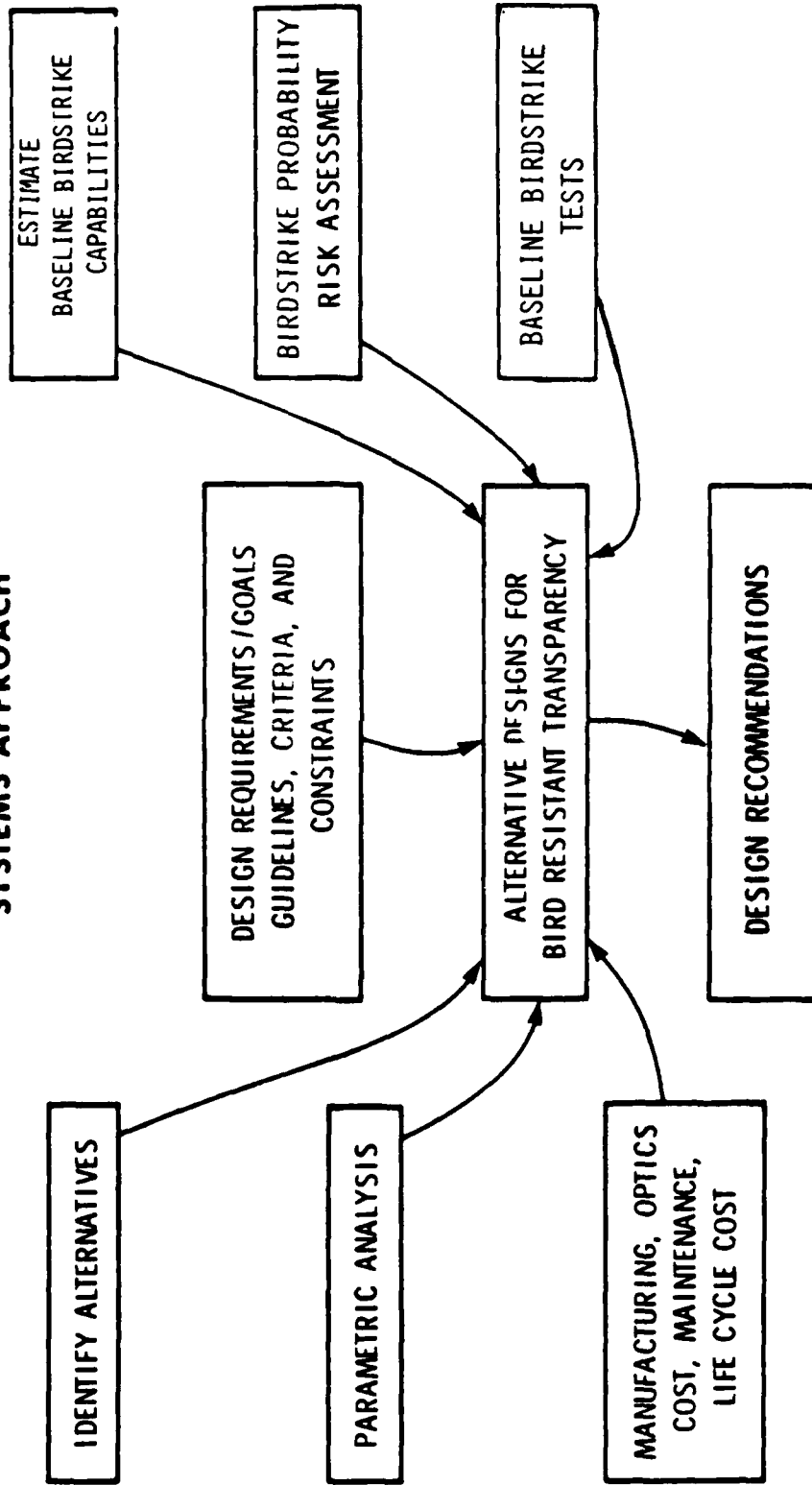


Figure 2. Tasks Considered in the F-18 Improved Transparencies Program.

Key design considerations were:

- o Birdstrike protection must be consistent with current and expected future mission requirements.
- o System must be producible using existing technology.
- o Optics must meet current and expected future mission requirements including compatibility with night vision and HUD requirement.
- o Weight, cost, and changes to exterior moldline must be minimized.
- o Visibility and durability must be maximized.

#### ESTIMATED BASELINE BIRDSTRIKE CAPABILITY

The F-18 windshield system consists of a 0.6 inch thick monolithic stretched acrylic panel mounted to an assembled aluminum frame, fastened to the aircraft at six locations (see Figure 3), and is hinged forward. Baseline birdstrike test results were not available during the initial phase of this program, so the baseline birdstrike capability was estimated from parametric equations and test results on similar systems. These estimated capabilities were experimentally verified later in the program.

The estimated current F-18 birdstrike resistance capability is summarized in Figure 4. The critical impact location is just forward of the aft arch along the aircraft centerline. The capability at this location was estimated to be 265 knots with a four pound bird (all capabilities are quoted for using a four-pound bird).

The estimated capabilities for the stretched acrylic transparency were based on test data for similar systems and parametric equations, see Figure 5. Note that test results on the T-38 student windshield showed that the 0.6 inch thick windshield has a capability of approximately 210 knots just forward of the aft arch, and 320 knots at the center-center impact point. It was estimated that the F-18 would have a higher capability than the T-38 primarily because it has a lower bird impact angle (24° versus 27.5°).

The current F-18 production aft arch is fabricated from 7075-T73 aluminum. The birdstrike resistance capability of this arch was estimated by comparing it to the T-38 and F-4 test results (References 2 and 3). Figure 6 shows a plot of stress (measured using strain gages at the failure location) versus velocity for various tests conducted on the F-4 aircraft. AEDC test numbers have been shown for each F-4 data point. A curve, based on the structural and geometric properties, was fit to the test data points.



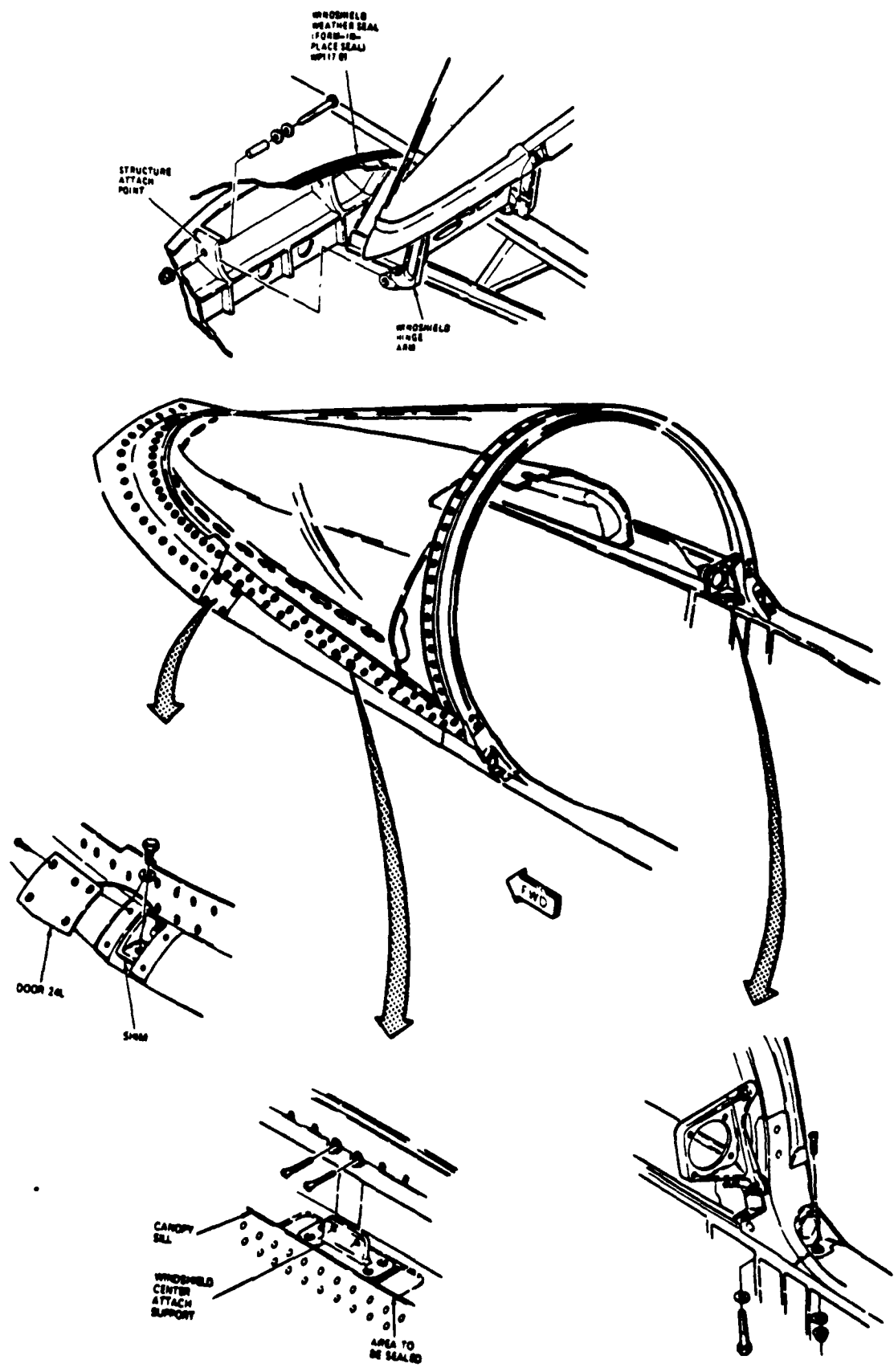
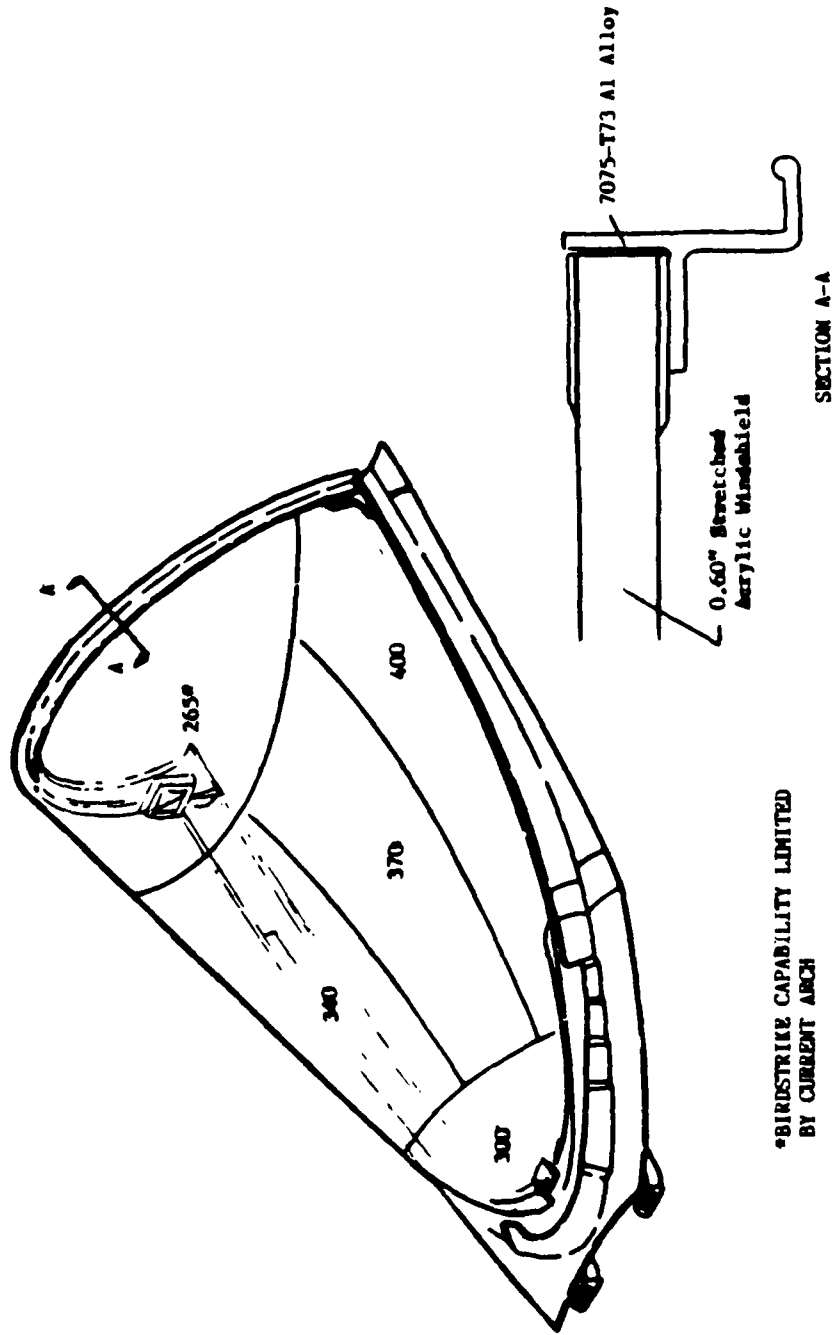


Figure 3. Windshield to Fuselage Interface (Ref. T.O. A1-F18AC-120-300).

CURRENT F-18 WINDSHIELD CAPABILITY (ESTIMATED)



\*BIRDSTRIKE CAPABILITY LIMITED BY CURRENT ARCH

Figure 4. Estimated F-18 Birdstrike Resistance Capability.

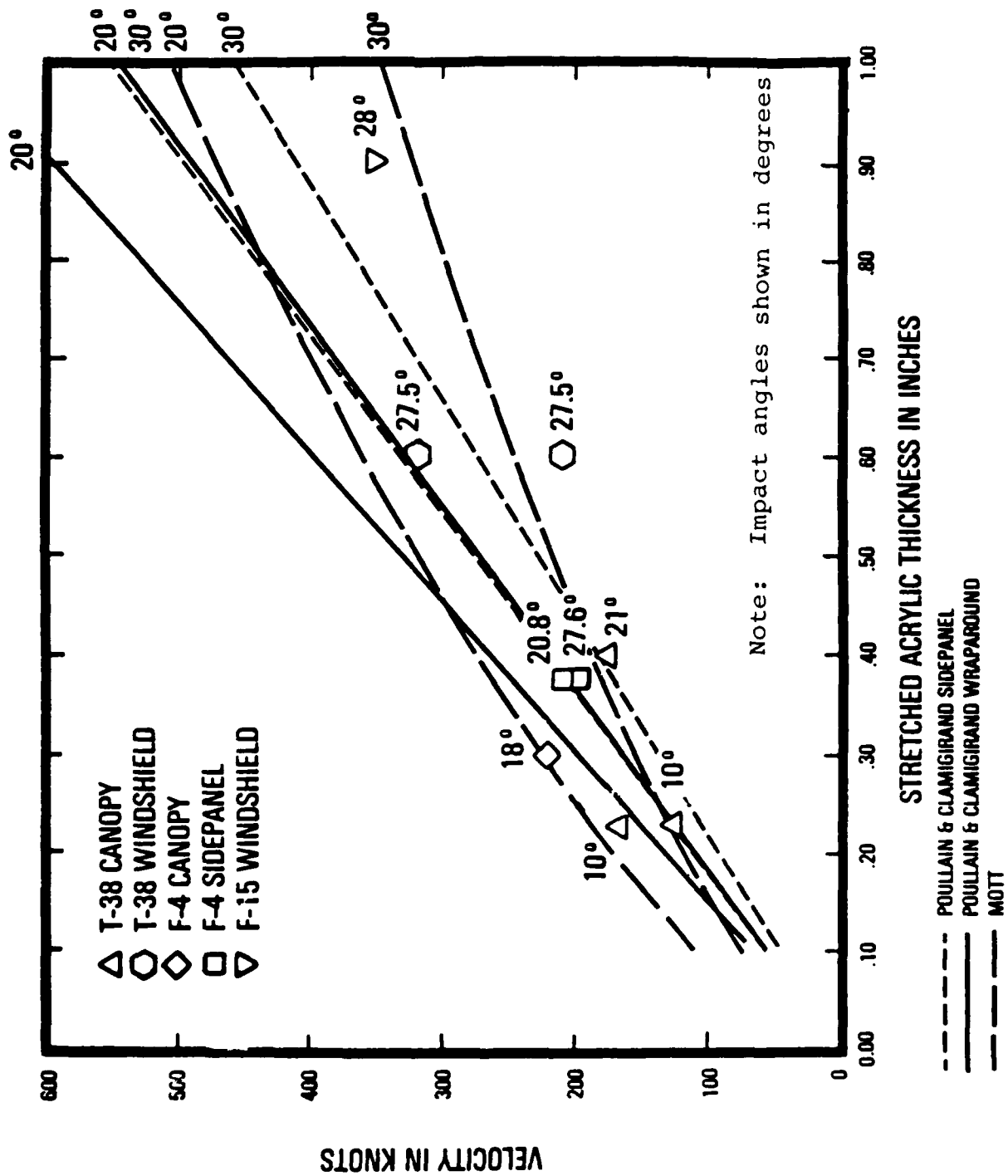


Figure 5. Summary of Parametric Equations and Test Data Points for Stretched Acrylic. Ref. 1,2,3.

# CURRENT ARCH FAILURE ANALYSIS

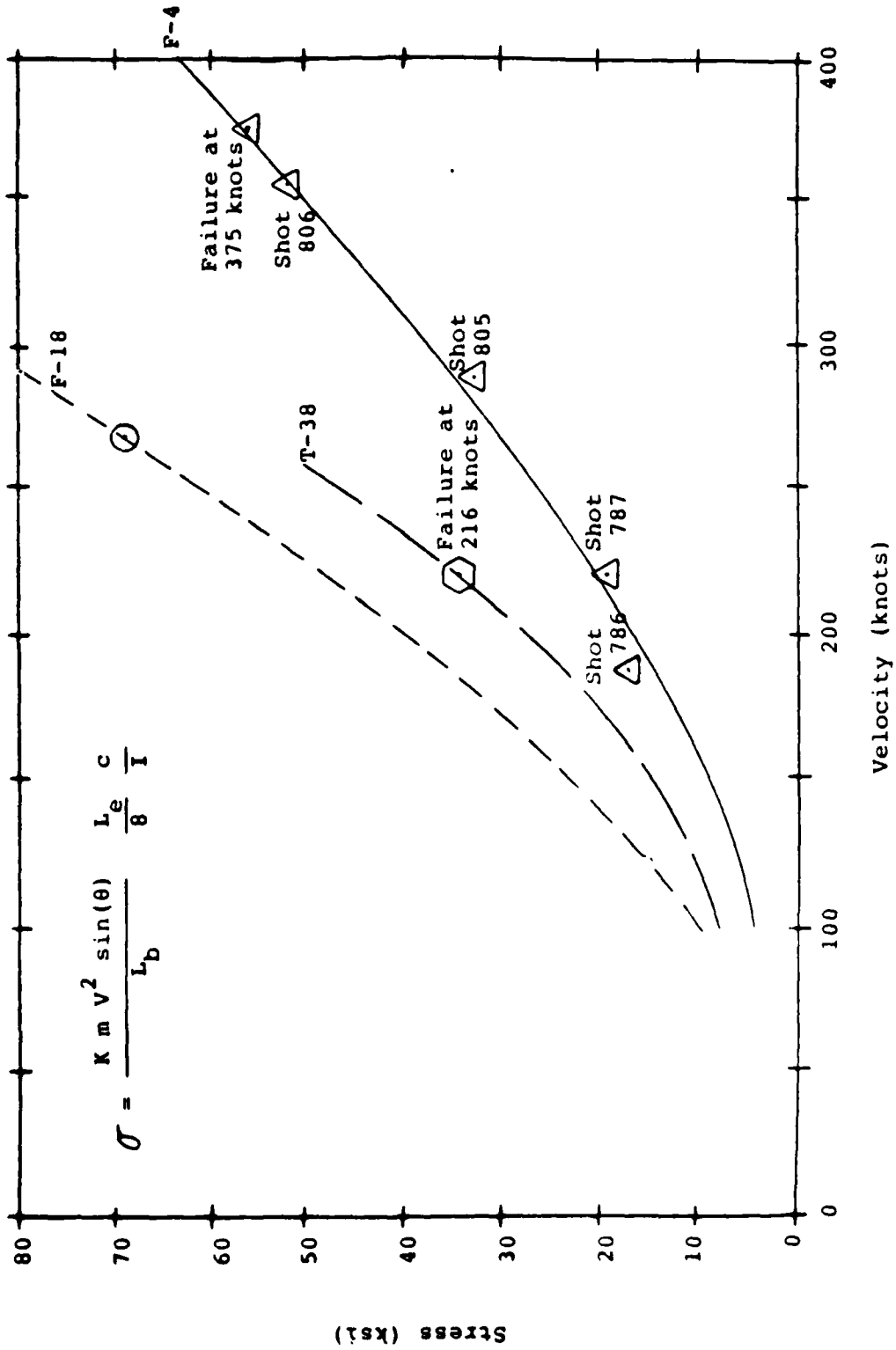


Figure 6. Plot of Aft Arch Outer Fiber Bending Stress vs. Velocity (Ref. 3).

An F-18 curve, based on its structural and geometric properties, was plotted as shown in on Figure 6. At approximately 265 knots, the stress in the arch was estimated to be equal to the ultimate strength of the material and is, therefore, the predicted capability.

#### IDENTIFICATION OF ALTERNATE WINDSHIELD SYSTEMS

Alternate systems were based on the combined experience of AFWAL and UDRI, and on the guidelines and constraints which governed this study. The current monolithic stretched acrylic transparency provides good serviceability and life; however, increased bird impact resistance results in an increase in the acrylic thickness.

The McDonnell Aircraft Company proposed a 0.94-inch thick stretched acrylic windshield with a redesigned frame which was included as an alternative in this study.

Seven transparency alternatives and four frame alternatives were identified; each representing a major trade-off between birdstrike protection, weight, cost, visibility and durability. Below are listed each of the transparency and frame alternatives.

#### Transparency Alternatives

- o Coated monolithic polycarbonate - total thickness 0.6 inches.
- o Two plies of laminated polycarbonate separated by a low modulus interlayer and coated on the interior and exterior surfaces - total thickness 0.6 inches.
- o Two plies of laminated polycarbonate with an exterior ply of acrylic and an interior coating; plies to be separated by a low modulus interlayer - total thickness 0.6 inches.
- o Monolithic stretched acrylic - total thickness 0.94 inches (Reference 4).
- o Two plies of laminated polycarbonate with an exterior ply of acrylic and an interior coating; plies to be separated by a low modulus interlayer - total thickness 0.66 inches.
- o Two plies of laminated polycarbonate with an exterior ply of acrylic and an interior coating. Plies to be separated by a low modulus interlayer - total thickness 0.73 inches.
- o Two plies of laminated polycarbonate with both an exterior and interior ply of acrylic; plies to be separated by a low modulus interlayer - total thickness 0.84 inches.

### Frame Alternatives

- o Current aluminum frame with new composite aft arch.
- o Current aluminum frame with new titanium aft arch.
- o Current aluminum frame with reinforced aft arch.
- o New redesigned aluminum frame for the .94 inch thick acrylic transparency (Reference 4).

### ESTIMATED BIRDSTRIKE CAPABILITIES OF ALTERNATE WINDSHIELD SYSTEMS

The bird impact capability of each alternate transparency was estimated using parametric equations (assuming that the transparency support structure would be designed to optimize the transparency performance) in conjunction with the results of bird impact tests conducted on similar transparency systems. As part of this effort, the strength of the fuselage structure which supports the transparency was also evaluated.

The fuselage analysis evaluated the fuselage structure which reacts the loads resulting from a birdstrike on the windshield. The analysis included the following structure: upper longeron, ribs at station 233.7 and 240.2, effective skin, and critical fasteners. The most critical component was found to be the rib at station 240.2. The three possible failure modes and corresponding loads are shown in Figure 7.

In order to determine the velocity at which fuselage failure could occur, a family of vertical sill load versus birdstrike impact velocity curves was generated for various fighter aircraft (reference Figure 8). The failure points for the F-4 and T-38 aircraft were based on experimental test results and were used as input in generating the curves.

The F-18 curve predicts a 7,000 lb. sill load at about 475 knots. A transparency system for the F-18 having a birdstrike capability higher than 475 knots may result in damage to the fuselage or require some fuselage modification to prevent failure of the fuselage.

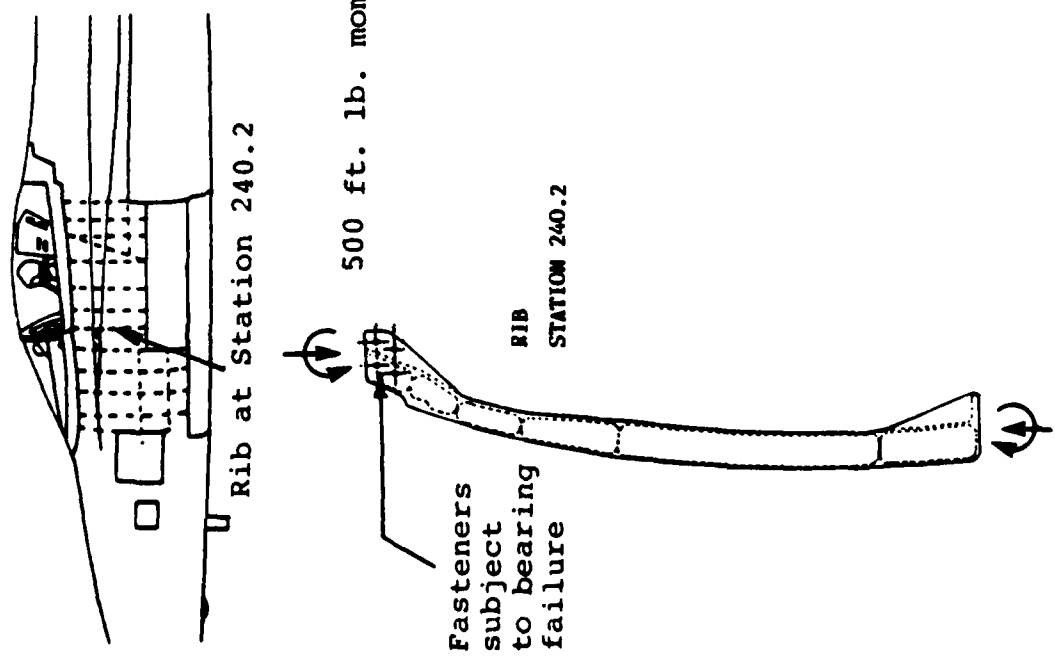
The transparency capability for each alternate transparency system was estimated using parametric equations and experimental test results from aircraft with similar transparency systems, both are summarized on Figures 9 and 10.

The estimated capabilities for the F-18 alternate transparency systems have been summarized on Figure 11, 12 and 13.

### BIRDSTRIKE RISK ASSESSMENT

The birdstrike probability risk assessment was conducted to provide statistical data concerning the effect of alternate levels of bird impact resistance on the number of penetrating

# FUSELAGE CRITICAL STRUCTURE



## Critical Fuselage Structure

Maximum Allowable Birdstrike Load	
Crippling Failure:	5690 lbs.
Buckling Failure:	9752 lbs.
Bearing Load Failure:	7020 lbs.

Figure 7. Critical Fuselage Structure.

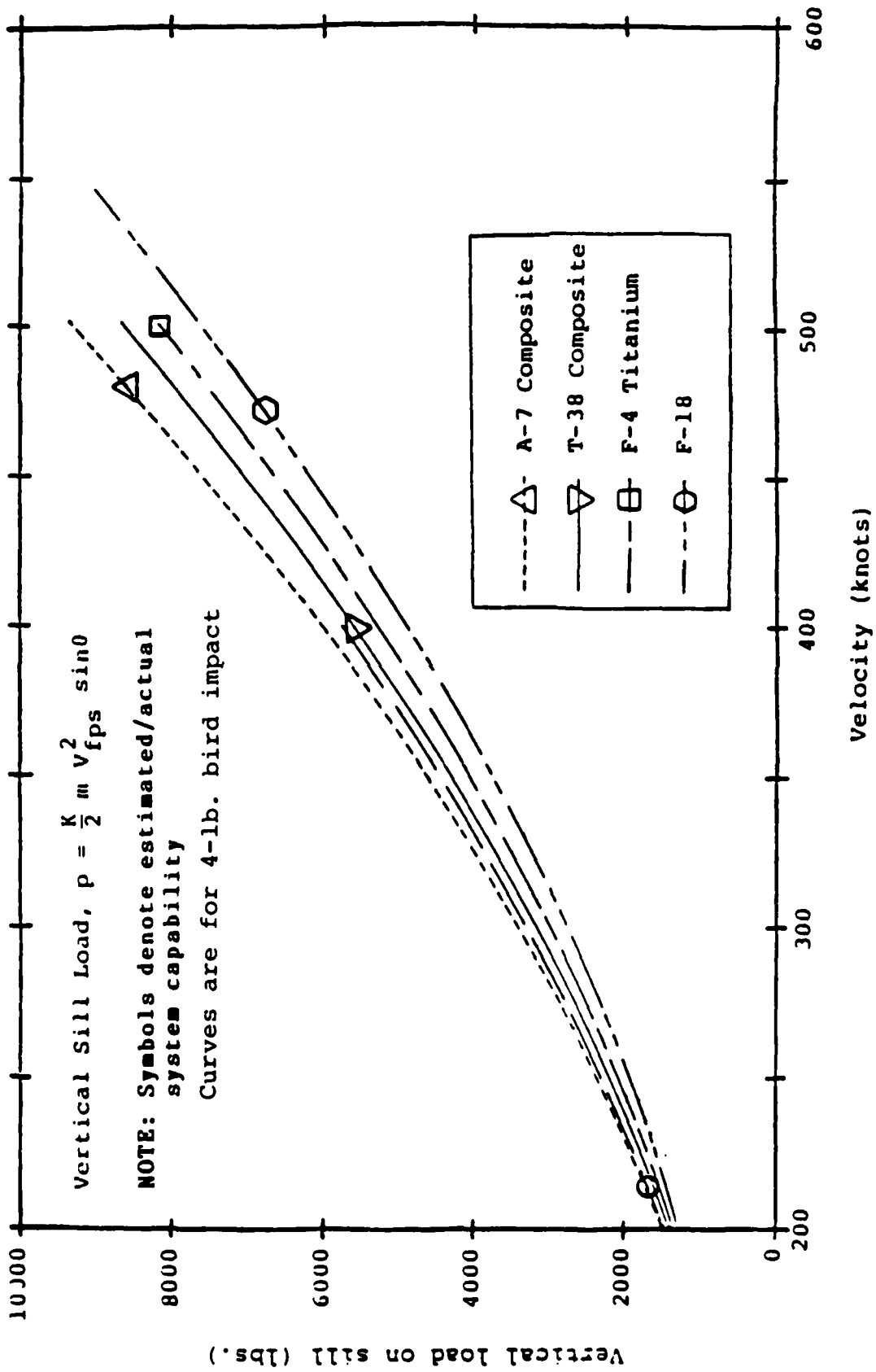


Figure 8. Vertical Sill Load vs. Impact Velocity.



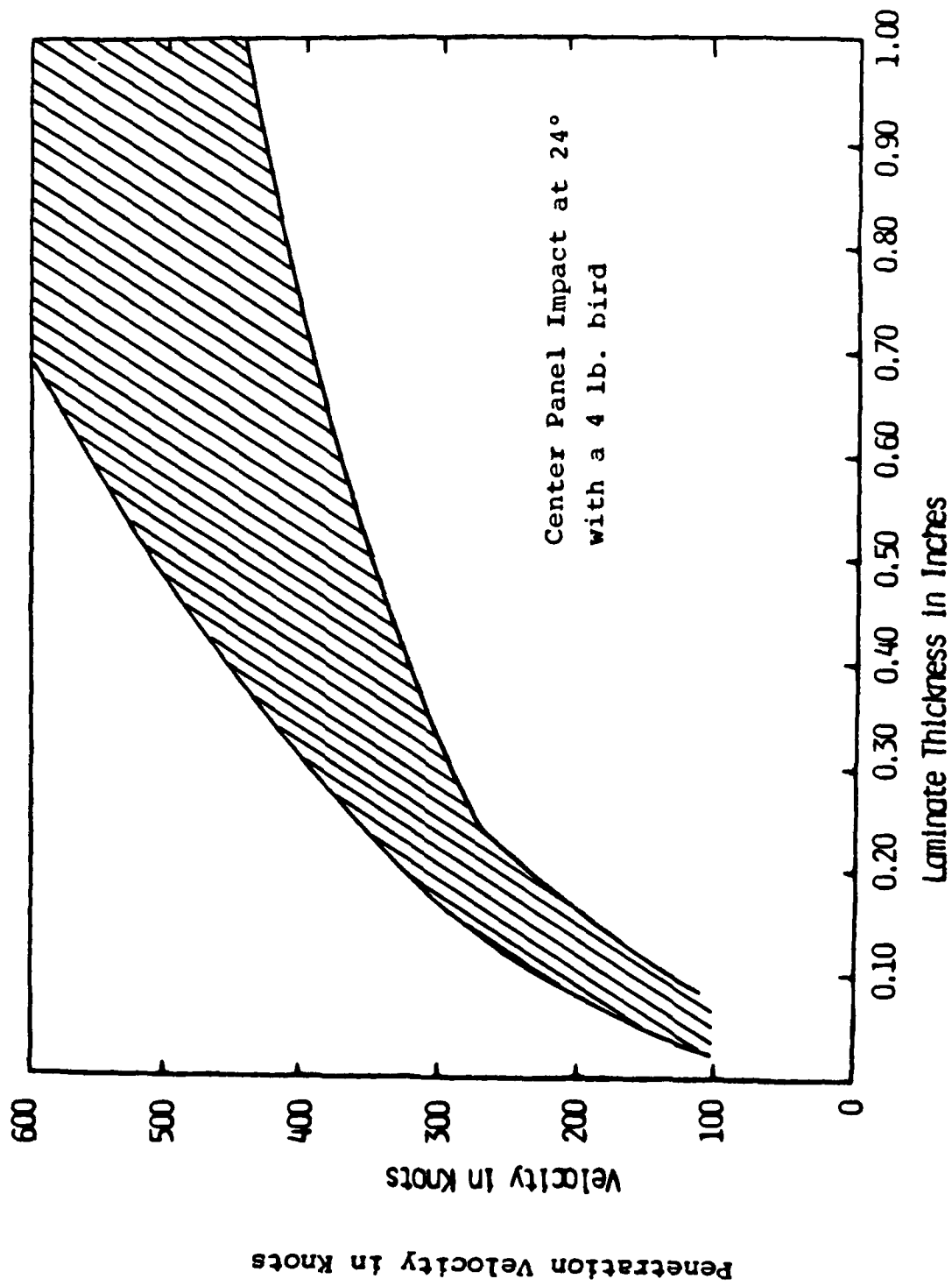


Figure 9. Theoretical Thickness versus Velocity Curves for Laminated Polycarbonate. (Reference 1)

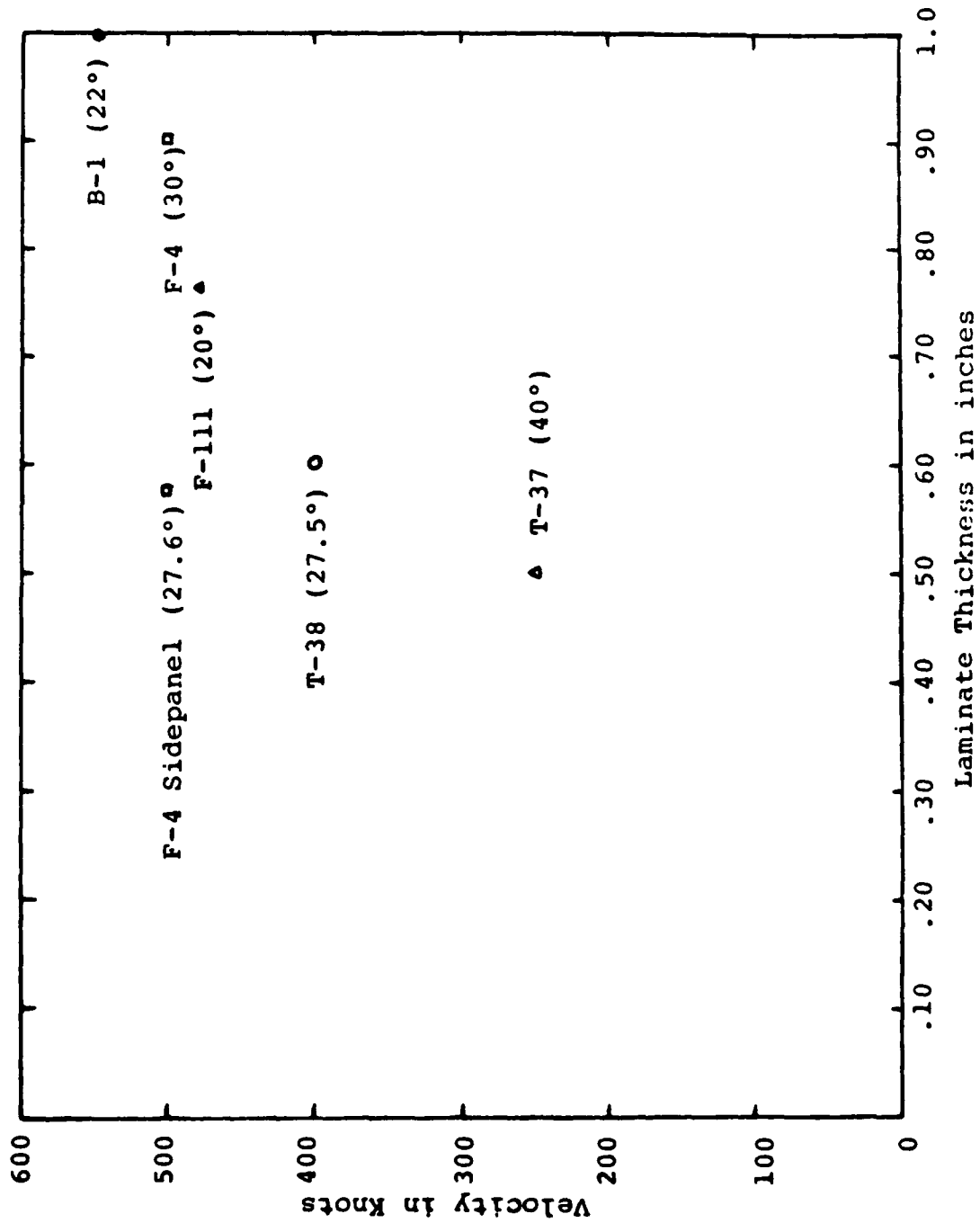


Figure 10. Summary of Capabilities Based on Birdstrike Tests.  
(Reference 1)

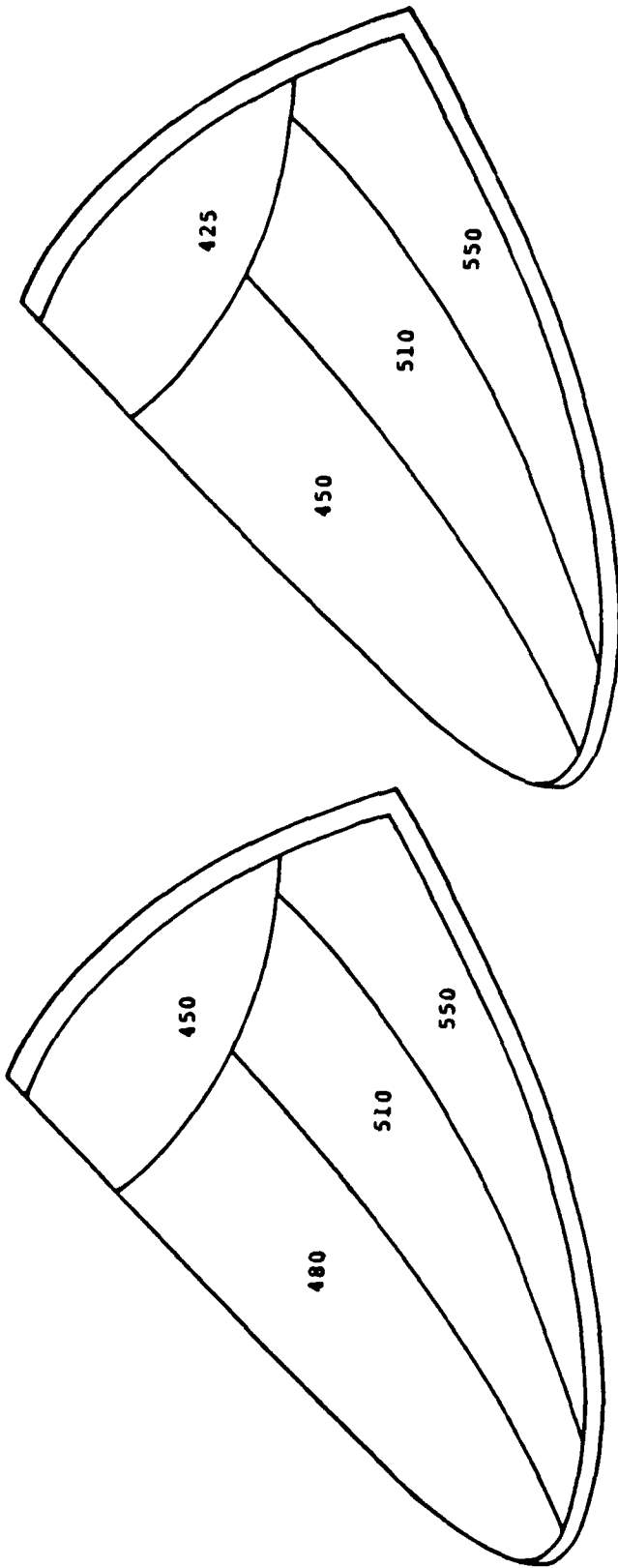


Figure 11. Alternate Transparencies Having a Coated Polycarbonate Exterior Surface.

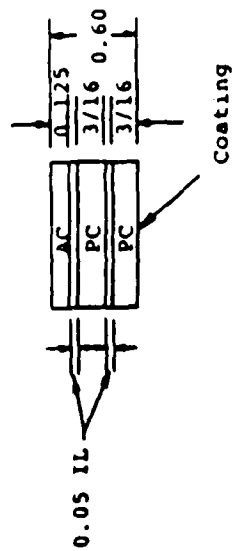
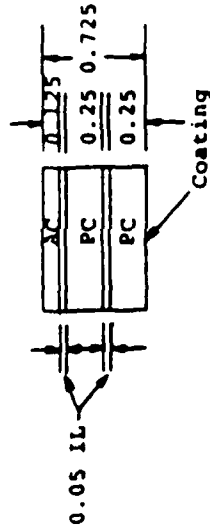
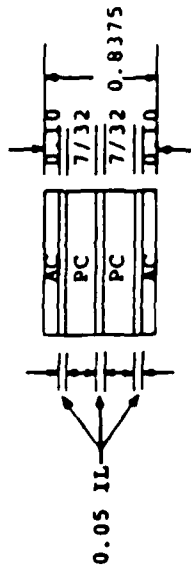
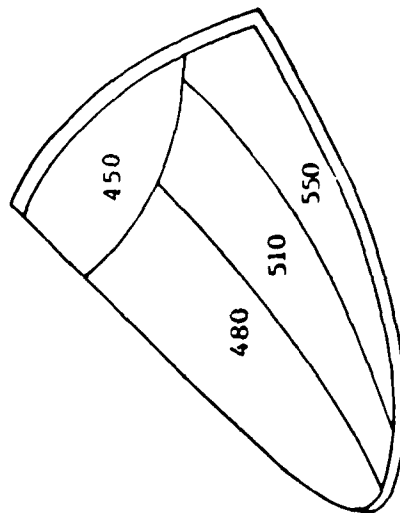
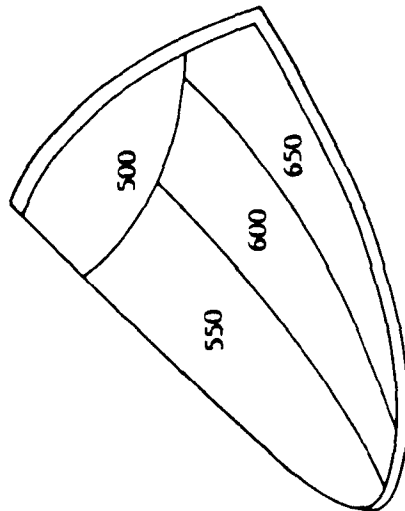
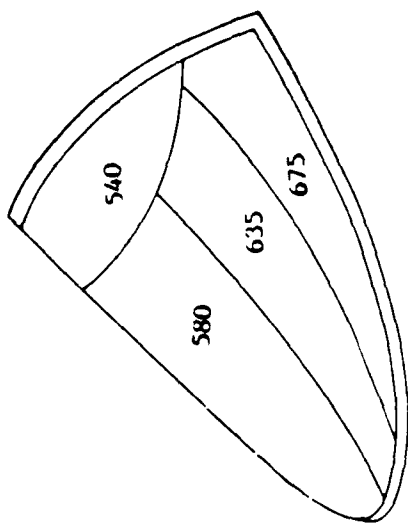
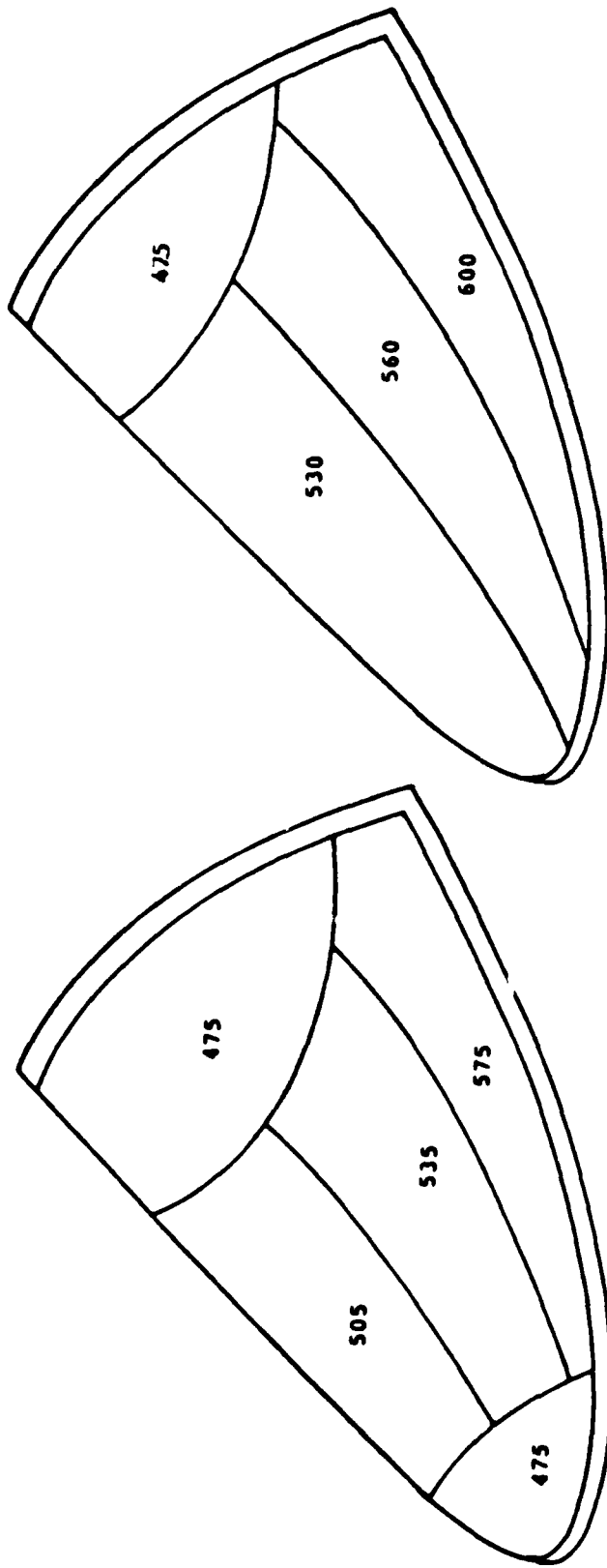


Figure 12. Alternate Transparencies Which are a Laminated Acrylic/Polycarbonate.



Requires Research and Development

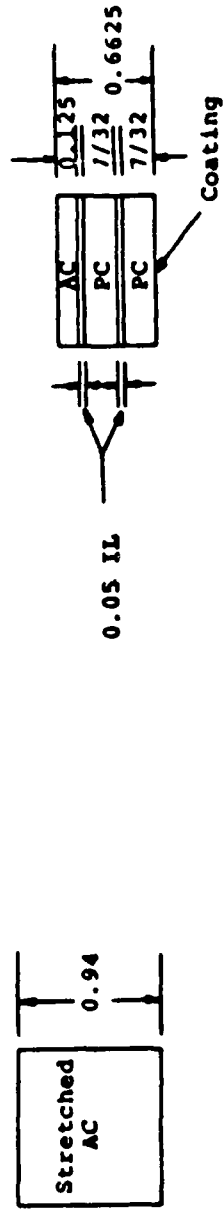


Figure 13. Alternate Transparencies Having a 475 Knot Birdstrike Resistance Capability.

birdstrikes (References 5 and 6). Seven models, representing the seven alternate transparency capabilities (see Figures 11, 12, and 13) were constructed and analyzed. The aircraft history, summarized in Table 1, is used to validate this analysis. The analysis predicts the number of penetrating birdstrikes over a ten-year period. Because of unknown future changes in the number of in-service aircraft and mission profiles, the analysis may not accurately represent the total number of penetrating birdstrikes. However, the predicted percent reduction in the number of future penetrating birdstrikes per low level flight hour for an alternate windshield system will be representative of the actual reduction.

The results of the birdstrike risk assessment are summarized in Table 2. With the current monolithic acrylic system, 15.8 penetrations were predicted in 10 years. The 0.6 inch thick bird proof polycarbonate transparencies increase the birdstrike resistance capability, lowering the expected penetration by over 60 percent without significantly increasing the weight. The 0.94 inch thick stretched acrylic transparency has the same minimum capability (475 knots) as the 0.66 inch thick laminated acrylic/polycarbonate transparency; and results in a total of about three penetrating birdstrikes in a ten year period, an 80% reduction.

#### PRELIMINARY TRANSPARENCY DESIGN/CROSS-SECTION EVALUATION

A method of rating the various transparency design cross-sections was devised to systematically evaluate the variables involved in determining the best transparency configurations for further consideration. Nine categories, which included initial cost, life cycle cost, weight, producibility, durability, maintainability, optics, visibility, and birdstrike resistance were evaluated by UDRI and AFWAL/FIEA using a matrix evaluation technique. Note that an in-depth evaluation was not performed in each of the above categories; all ratings were relative to each other and not absolute. Seven transparency cross-sections were evaluated.

The rating or weighting factors were assigned in each category after considering the explanations summarized below.

- o The "design requirement weighting factors" are a rating of the categories relative to each other based on the projected Navy requirements. For example, bird impact was rated higher than weight or cost. The most important category was assigned a "10"; other categories are rated according to the relative importance.
- o The "transparency rating" prioritizes each transparency cross section in a given category. The best material is given 10 points. All other cross-sections are to be rated relative to the best, on a scale of 0 to 10. Listed below is an explanation of each category.

TABLE 1  
SUMMARY OF F-18 BIRDSTRIKES

YEAR	NUMBER REPORTED	CREW INJURIES	FLIGHT MODE/ ALTITUDE	COMMENTS
1983	3	--	LOW LEVEL/500'	
		--	TAKE OFF/200'	STARLING
		--	LANDING/0'	SMALL BIRD
1984	3	--	LANDING/50'	SMALL BIRD
		--	DESCENT/3000'	MEDIUM BIRD
		MINOR	LOW LEVEL/600'	420 kts., 4.5 lb. TURKEY BUZZARD
1985	3	--	TAKE OFF/200'	SMALL BIRD
		--	CRUISE/3000'	185 kts., 2 lb. BIRD
		--	CRUISE/3000'	DAMAGED WINDSCREEN EDGING STRIP

TABLE 2  
SUMMARY OF BIRDSTRIKE RISK ASSESSMENT

Definition of Models	System Capability	Predicted Number of Penetrations in 10 Years	Percent Reduction in Penetrations
Current Windshield System	265	15.8	0
0.6 Coated Polycarbonate	425	5.0	68
0.6 Laminated	450	4.2	73
0.94 Stretched Acrylic	475	3.4	78
0.66 Laminated	475	2.7	83
0.73 Laminated	500	2.3	85
0.84 Laminated	540	1.6	90



- Initial Cost - initial cost of making the retrofit (cost of all hardware and the work required for installation, reflecting any development cost).
  - Life Cycle Cost - cost of replacing transparency on an annualized basis.
  - Weight - relative weight of the windshield system.
  - Producibility - rating should reflect the development time required and potential production difficulties (proven vs. new technology).
  - Durability - if possible, should be based on the actual service life of similar transparencies.
  - Maintainability - any maintenance required on the windshield system.
  - Optics - rating reflects expected optics which could be achieved and maintained during production and service.
  - Visibility - rates the relative visibility between designs.
  - Birdstrike Resistance - rates the relative birdstrike resistance of each design.
- o The "Overall Windshield Rating" is the summation of the products for each category of the "Design Requirement Weighting Factor" times the "Transparency Rating."

The evaluation has been summarized on Table 3. The design requirements weighting factors are summarized in the first line of the table. The transparency rating factors are summarized next, followed by a summary of the overall ratings.

The results of this evaluation are as follows: The 0.6 through 0.73 inch thick acrylic faced polycarbonate transparencies had the highest overall rating. The 0.94 inch thick stretched acrylic transparency followed. The transparency designs with an outer surface coating had the lowest rating.

#### BASELINE BIRDSTRIKE TEST RESULTS

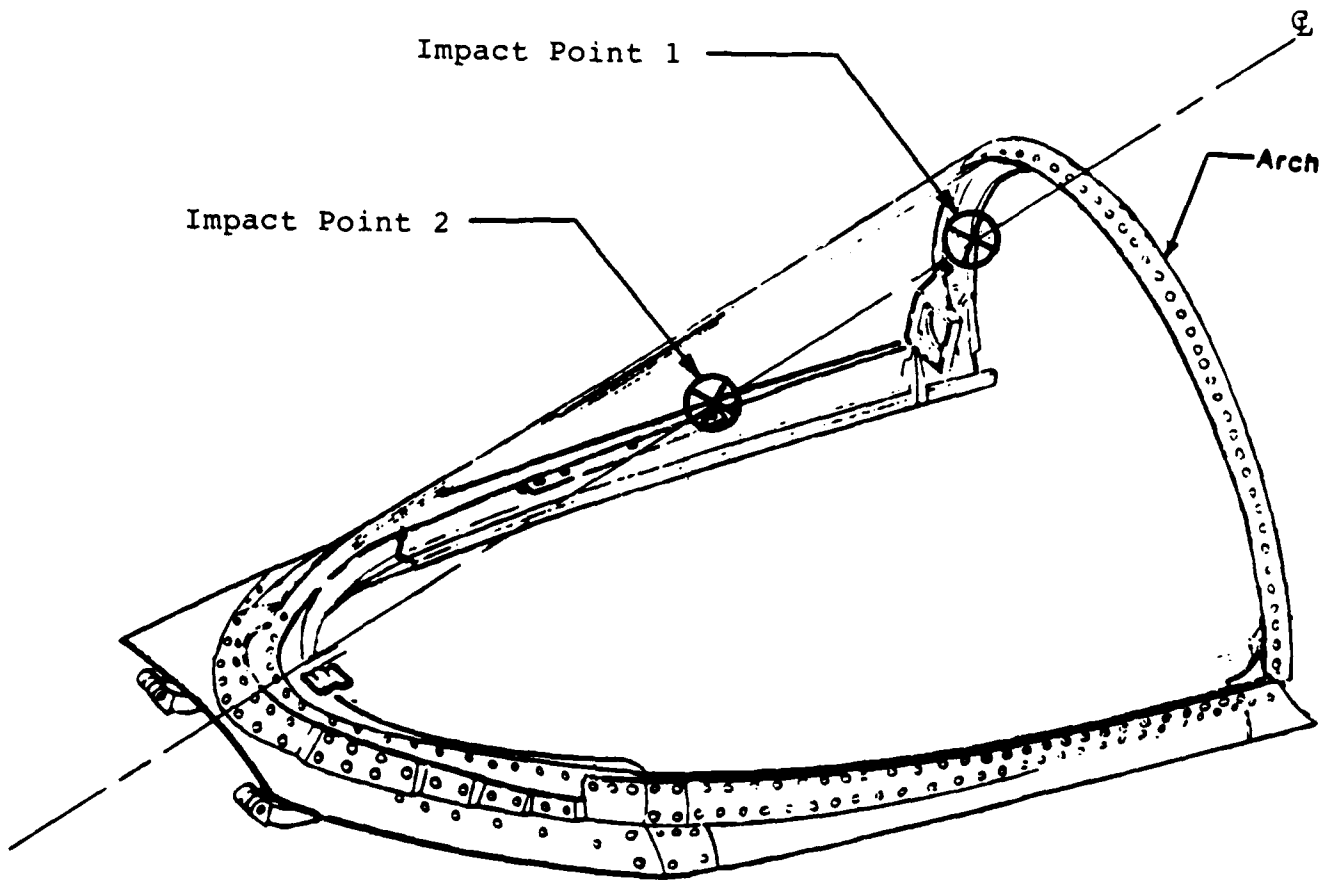
Baseline birdstrike tests were conducted at Arnold Engineering Development Center (AEDC), Arnold Air Force Station, Tullahoma, TN, during August 1987 (Reference 7). The results of these tests are contained in Reference 7. Figure 14 shows the two impact points on the transparency. Table 4 presents a summary of the birdstrike test results. Two impacts were made at the critical location (along the aircraft centerline just forward of the aft arch), a 225 knot pass and a 269 knot failure. Four

TABLE 3  
OVERALL DESIGN BASED WEIGHTING FACTORS OF WINDSHIELD AND CANOPY

	INITIAL COST	LIFE CYCLE COST	WEIGHT	PRODUCIBILITY	DURABILITY	MAINTAINABILITY	OPTICS	VISIBILITY	BIRDSTRIKE RESISTANCE	TOTAL
Design Requirement Weighting Factors	6	8	9	7	7	7	9	9	10.0	
.6 Coat	10	6	10	7	6	7	9	10	5	
.6 Coat Laminata	10	6	10	10	6	7	8	10	6	
.6 Acrylic Laminata	10	8	10	10	8	10	8	10	6	
.94 SA	9	10	4	6	10	10	10	8	7	
.66 Acrylic Laminata	10	8	9	10	8	10	8	10	7	
.73 Acrylic Laminata	8	8	8	10	8	10	8	9	8	
.84 Acrylic Laminata	4	7	6	10	8	10	7	8	10	
.6 Coat	60	48	90	49	42	49	81	90	50	559
.6 Coat Laminata	60	48	90	70	42	49	72	90	60	581
.6 Acrylic Laminata	60	64	90	70	56	70	72	90	60	632
.94 SA	54	80	36	42	70	70	90	72	70	584
.66 Acrylic Laminata	60	64	81	70	56	70	72	90	70	633
.73 Acrylic Laminata	48	64	72	70	56	70	72	81	80	613
.84 Acrylic Laminata	24	56	54	70	56	70	63	72	100	565

TRANSPARENCY RATING

Overall Windshield Rating Factor = Transparency Rating x Design Requirement Rating Factor



NOTE: All tests with four pound bird.

Figure 14. Bird Impact Test Points.

TABLE 4  
SUMMARY OF BIRDSTRIKE TEST RESULTS

Transparency No.	Shot No.	Date	Transparency Temp (°F)	Velocity (knots)		Bird Weight (lb)	Impact Point	Results
				Desired	Actual			
1	975	8-10-87	85	225	225	4	1	Passed
1	976	8-11-87	82	245	250	4	2	Passed
1	977	8-11-87	88	340	346	4	2	Failed
2	978	8-13-87	81	265	269	4	1	Failed
4	980	8-17-87	89	305	309	4	2	Passed
5	981 <sup>⊙</sup>	8-20-87	91	330	330	4	2	Failed

⊙ Strain gages were not included in the instrumentation.

birdstrike tests were conducted on the center of the windshield resulting in a pass at 309 knots and a failure at 330 knots.

The average peak load on the rib at station Y240.2 was 1170 lbs. downward force with an outward moment of 380 ft. lbs. This resulted in an applied down force from the arch to the sill, of 1680 lbs. The compares favorably with the estimated load (1590 lbs.) predicted from Figure 8.

As a result of these birdstrike tests and structural analysis, it was estimated that some fuselage damage could occur in the 450 to 470 knot velocity range. However, damage to the fuselage in this area as a result of birdstrike would not be expected to prevent the aircraft from returning home, based on discussions with NAVAIR concerning the location of critical flight controls.

### CONCLUSIONS

The windshield system alternatives have been summarized in Table 5 along with information in eight key areas. These areas include birdstrike capability, predicted number of penetrations, weight change, optics, peak deflection at design capability, technical risk, durability and life cycle cost.

The four alternate aft arches (See Figure 15) were designed to support a transparency having a four pound, 475 knot birdstrike resistance capability. The composite, titanium, and reinforced aluminum arch designs can be used with all of the transparency alternatives except the 0.94 inch thick monolithic acrylic, which would use an aluminum design.

### RECOMMENDATIONS

The existing 0.6 inch thick monolithic stretched acrylic windshield should be replaced to reduce the risk of a penetrating birdstrike. A 0.66 inch thick laminated acrylic/polycarbonate transparency is recommended because it significantly reduces the birdstrike hazard (by over 80%).

This would provide a level of protection that would minimize the possibility of damage to the fuselage while significantly reducing the birdstrike hazard. The initial cost and development time would be minimized by using the existing windshield frame (except for the aft arch), and the weight increase over the current system would be minimized (about a 10% increase).

TABLE 5

## SUMMARY

DESCRIPTION	MINIMUM CAPABILITY (KNOTS)	PENETRATIONS IN 10 YEARS	WEIGHT CHANGE (POUNDS)	OPTICS (MINUTES OF ARC)	PEAK DEFLECTION AT DESIGN CAPABILITY (INCHES)	TECHNICAL RISK	DURABILITY (YEARS)	LIFE CYCLE COST (\$K/10 YEARS)	OVERALL RATING
0.6" COATED MONOLITHIC POLY	425	5.0	N.C.	2	4.5	HIGH	2-5	12-14	7
0.6" COATED LAMINATED PC/PC	450	4.2	N.C.	5	5.0	HIGH	2-5	14-16	5
0.6" LAMINATED AC/PC/PC	450	4.2	N.C.	5	4.25	LOW	3-6	11-13	2
0.94" STRETCHED ACRYLIC	475**	3.4	+26.4	1**	1.0	MED	4-7	8-10	4
0.66" LAMINATED AC/PC/PC	475	2.7	+5.0	5	4.25	LOW	3-6	11-13	1
0.73" LAMINATED AC/PC/PC	500*	2.3	+12.0	5	4.0	LOW	3-6	11-13	3
0.84" LAMINATED AC/PC/PC/AC	540*	1.6	+19.0	5	3.75	LOW	3-6	11-13	6
COMPOSITE ARCH	475		+6.5		2.5	MED	LIFE OF AC	4-6	
TITANIUM ARCH	475		+3.9		2.5	LOW	LIFE OF AC	4-6	
REINFORCED ALUM. ARCH	475		+5.5		2.5	MED	LIFE OF AC	4-6	
ALUMINUM ARCH FOR .94 ACRYLIC	475		+3.5		0.8	LOW	LIFE OF AC	1-2	

NOTE: 15.8 PENETRATIONS IN 10 YEARS WITH THE CURRENT SYSTEM  
 CURRENT WINDSHIELD WEIGHT: 46.61 LBS  
 CURRENT ARCH WEIGHT: 1.82 LBS

\* REQUIRES FUSelage MODIFICATIONS  
 \*\*REQUIRES RAD

ALUMINUM ARCH FOR 0.94 ACRYLIC $+\Delta W = +3.5$ LBS. FIELD OF VIEW = $-2.25^\circ$	REINFORCED ALUMINUM ARCH $+\Delta W = 5.5$ LBS. FIELD OF VIEW = $-2.1^\circ$	COMPOSITE ARCH $+\Delta W = 6.5$ LBS. FIELD OF VIEW = $-2.4^\circ$	TITANIUM ARCH $+\Delta W = 3.9$ LBS. FIELD OF VIEW = $-1.25^\circ$
-----------------------------------------------------------------------------------------------	------------------------------------------------------------------------------------	--------------------------------------------------------------------------	--------------------------------------------------------------------------

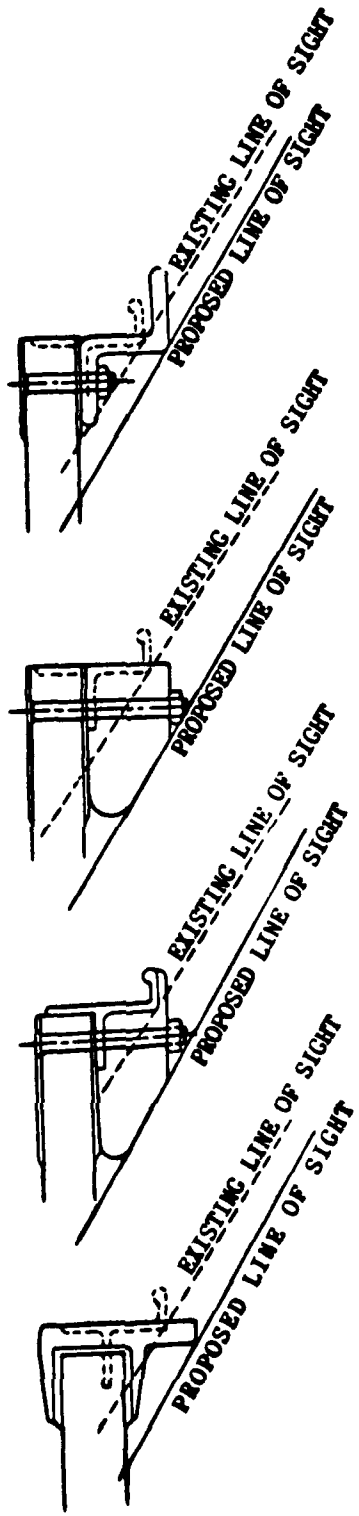


Figure 15. Proposed Arch Designs.

## REFERENCES

1. J. H. Lawrence, Jr., Guidelines for the Design of Aircraft Windshield/Canopy Systems, AFWAL-TR-80-3003, February 1980.
2. Blaine S. West, Alternate T-38 Transparency Development - Part II: Baseline Birdstrike Testing, AFWAL-TR-80-3132, Part II, December 1980.
3. Gregory J. Stenger, Blaine S. West, Richard A. Nash, and J. Patrick Ryan, Definition and Reduction of the F/RF-4 Windshield Birdstrike Hazard, AFWAL-TR-84-3033, May 1984.
4. "F/TF-18 Windshield Birdstrike Consideration", briefing presented by McDonnell Aircraft at the McDonnell Aircraft Company, St. Louis, 5 December 1985.
5. A. P. Berens, B. S. West, and M. A. Turella, "On a Probabilistic Model for Evaluating the Birdstrike Threat to Aircraft Crew Enclosures," UDR-TR-78-124, November 1978.
6. Daniel R. Bowman, "Birdstrike Probability Program User's Manual," UDR-TM-88-15, April 1988.
7. K. D. Mead, F-18 Windshield Test, Arnold Engineering Development Center AEDC-TSR-87-V30, August 1987.



SESSION VII

UNDERSTANDING CURRENT SYSTEMS (PART A)

Chairman: A. Gibbs  
British Aerospace  
Surrey, England

Co-Chairman: S. Wortman  
Sacramento Air Logistics Center  
McClellan AFB, California

Coordinator: D. Wamba  
Rockwell International  
Los Angeles, California

MANAGEMENT OF TRANSPARENCY RELATED COSTS IN  
AIR FORCE AIRCRAFT: A PARETO APPROACH

Paul S. Lee  
Japheth Nkonge  
North Carolina A & T  
University

Nisar Shaikh  
University of Nebraska

Arnold H. Mayer  
Michael Gran  
Air Force Wright Aero-  
nautical Laboratories

MANAGEMENT OF TRANSPARENCY RELATED COSTS IN AIR FORCE AIRCRAFT:  
A PARETO APPROACH

Paul S. Lee and Japheth Nkonge, North Carolina A & T University Nisar  
Shaikh, University of Nebraska - Lincoln  
Arnold H. Mayer and Michael Gran, Air Force Wright Aeronautical Laboratories

ABSTRACT

The study to be reported was conducted in the spirit of the now-famous English economist, Wilfredo Pareto, who was reputed to have observed that "80% of the problems could be solved with 20% of the effort." The effort in the present case is directed at minimizing the durability related problems and their cost consequences that currently plague the transparent crew enclosures, alias windshields and canopies, or just plain transparencies of Air Force fighter aircraft. It is reported, for example, that the cost of maintaining serviceable transparencies on the fleet of F-16 aircraft is currently running at a figure of \$100,000 per day which is equal to the cost of an average single family home. The premise underlying this work was that something could be done about this situation if one knew the variety of different durability problems that afflict aircraft transparencies and could rank these with respect to frequency of occurrence or some other criterion which captures the magnitude of the cost impact. Then one could attack these problems starting from the top of the list, knowing that one was making at any given moment the largest possible impact on life cycle cost reduction. It was decided also that one should bring to bear on the solution of these problems the positive forces inherent in the free enterprise system, namely the motivating power of potential sales and profit. This led to the desirability of developing as an objective a battery of full scale and coupon level accelerated durability tests which could reproduce in the laboratory the principal failure modes accounting for the preponderance of durability related transparency costs. These laboratory durability tests ideally would reproduce field failure modes at times that bore a known quantitative relationship to the times of occurrence of the same types of failure in service. The tests could be applied to transparencies offered for sale to the Air Force and used to control durability and costs by limiting purchases to sources that offered the lowest cost per year of predicted service life, in much the same way as is currently the practice in the acquisition of aircraft tires.

The first objective was approached by inspecting and collecting failure data on F-111 and F-16 transparencies located in various Air Force warehouses and analyzing the collected data to determine the salient prioritized failure modes. The results of this analysis are presented and used to justify the immediate development and validation of an accelerated temperature-pressure fatigue durability test for full scale transparencies and an accelerated chemical crazing test to be performed on acrylic laminated transparency coupons. The full scale test is described in a companion paper of this conference, while the coupon chemical crazing test is described in this paper. The description is followed by a detailed discussion of the status of development and validation of the accelerated chemical crazing test.

MANAGEMENT OF TRANSPARENCY RELATED COSTS IN AIR FORCE AIRCRAFT:  
A PARETO APPROACH

Paul S. Lee and Japheth Nkonge, North Carolina A & T University Nisar  
Shaikh, University of Nebraska - Lincoln  
Arnold H. Mayer and Michael Gran, Air Force Wright Aeronautical Laboratories

The study to be reported was conducted in the spirit of the now-famous English economist, Wilfredo Pareto, who was reputed to have observed that "80% of the problems could be solved with 20% of the effort." The effort in the present case is directed at minimizing the durability related problems and their cost consequences that currently plague the transparent crew enclosures, alias windshields and canopies, or just plain transparencies of Air Force fighter aircraft. It is reported, for example, that the cost of maintaining serviceable transparencies on the fleet of F-16 aircraft is currently running at a figure of \$100,000 per day (1), which is equal to the cost of an average single family home. The premise underlying this work was that something could be done about this situation if one knew the variety of different durability problems that afflict aircraft transparencies and could rank these with respect to frequency of occurrence or some other criterion which captures the magnitude of the cost impact. Then one could attack these problems starting from the top of the list, knowing that one was making at any given moment the largest possible impact on life cycle cost reduction. It was decided also that one should bring to bear on the solution of these problems the positive forces inherent in the free enterprise system, namely the motivating power of potential sales and profit. This led to the desirability of developing as an objective a battery of full scale and coupon level accelerated durability tests which could reproduce in the laboratory the principal failure modes accounting for the preponderance of durability related transparency costs. These laboratory durability tests ideally would reproduce field failure modes at times that bore a known quantitative relationship to the times of occurrence of the same types of failure in service. The tests could be applied to transparencies offered for sale to the Air Force and used to control durability and costs by limiting purchases to sources that offered the lowest cost per year of predicted service life, in much the same way as is currently the practice in the acquisition of aircraft tires.

The first objective was approached by inspecting and collecting failure data on F-111 and F-16 transparencies located in various Air Force warehouses and analyzing the collected data to determine the salient prioritized failure modes. The results of this analysis are presented and used to justify the immediate development and validation of an accelerated temperature-pressure fatigue durability test for full scale transparencies and an accelerated chemical crazing test to be performed on acrylic laminated transparency coupons. The full scale test is described in a companion paper of this conference, (2) while the coupon chemical crazing test is described in this paper. The description is followed by a detailed discussion of the status of development and validation of the accelerated chemical crazing test.

The composition of the data base reflects a statistical snapshot of the removed transparencies that occupied the warehouses at the time the visits were made. For example, the make-up of the F-16 data base by vendor and type of transparency is shown in Table I. The relative proportions of transparencies from the various vendors is not necessarily an indication of which sources are most problematic, but rather reflect the relative proportions of transparencies purchased from these various vendors. Histograms or relative frequencies of the various failure modes for F-111 and F-16 transparencies are shown in Figure 1 and Figure 2 respectively.

A breakdown of relative percentages of various failure modes associated with various Air Force Bases is shown in Table 2. It is evident that certain types of failures are predominantly associated with particular bases. For example, MacDill Air Force Base seems to be the main source of crazed canopies, while Luke AFB and Torrejon appear to major in acrylic cracking and delamination respectively. There is a suspicion that the proximity of a cement plant to MacDill AFB may have something to do with the heavy transparency crazing that occurs there. The haze may be due to the same cause, while scratching is now believed to be induced by maintenance actions, possibly by the contact of the metal belt buckles of maintenance personnel with the windshield during cleaning and wiping actions, or inadvertent tool contact with the transparency during other maintenance actions.(11)

A further reorganization of the data for failure modes by aircraft and type of failure is shown in Table 3. Here the failure modes are regrouped into three main categories: 1) surface degradation modes: 2) fatigue induced failure modes, and, 3) other, which consists predominantly of scatching.

It is believed that the "Other" category of failures may be almost entirely avoided by suitable attention and care during maintenance actions. This would eliminate about 20% of the total failures. It is recalled that there are basically two main types of transparency constructions in current use in fighter aircraft, apart from some earlier glass coated transparencies that may still be in service. These two types are monolithic coated polycarbonate and laminated polycarbonate with acrylic outer plies. The coated monolithic transparencies account in the case of the F-16 almost exclusively for the coating-loss type of failure and also for a portion of the chipped/pitted failures (possibly in the ratio of F-16 incidences of coating loss to incidences of crazing failures). Taking these considerations into account, it is seen that coating loss is the single most frequent failure mode for monolithic polycarbonate transparencies, while crazing is the failure mode of second highest frequency (almost equal in frequency to chipped/pitted) for laminated polycarbonate constructions with acrylic outer plies. The latter amounts to about 24% of the total failures after the correctible "Other" and Coating Loss categories has been subtracted out. Likewise, fatigue induced failures under the same conditions represent 43% of the total types of failures, although this category does include two types of failure mode, namely cracking and delamination/distortion, each of these being about equal in frequency.

These considerations point to the urgency of developing accelerated life prediction tests for crazing and fatigue failure modes. Once this has been achieved, the means will exist for controlling (or eliminating) over 70% of the failures which afflict laminated transparencies. A further means when developed for predicting the durability of monolithic transparencies due to coating loss would enable control over 75% of all transparency failures on fighter aircraft.

It turns out that tests have already been defined and test facilities created that will produce fatigue type failures in full scale transparencies. This test capability will be described in a companion paper of this conference.(2) The accelerated crazing test, a standard ASTM Test, F484, also exists but the technique for using it to predict service life remains to be validated. Its state of development and validation will be described in the balance of this paper along with some background facts about the nature of crazing in thermoplastics.

#### Concept Development and Validation of an Accelerated Life Prediction Test for Crazing Limited Service Life of Aircraft Transparent Enclosures - A Status Report

This section begins with a background discussion on the nature of crazing in thermoplastics.

#### The Nature of Crazing in Thermoplastics

Crazing refers to the appearance on the surface of a thermoplastic part of a cloud or collection of segments of tiny hairline cracks which become noticeable by the way they scatter light, very much like the way a dirty car windshield does. The nucleation of crazes is believed to be a cavitation or void formation phenomenon much akin to what occurs in liquids due to an inability to support dilatational (tensile) pressures in excess of some threshold value. The crazes nucleate and grow with their lengths oriented perpendicular to the local principal longitudinal strain direction on the surface. Their spatial distribution is random with a uniform average density. Unlike the cracks of fracture mechanics in metals, the region of the crazes between the parallel sides of the cracks are not occupied purely by voids, but by porous fibrillar polymer material oriented perpendicular to the craze lengths. (3) Several of the points made above are confirmed by the picture of crazes formed around a hole in a plastic plate subjected to a uniform state of tension at points far from the hole as shown in Figure 3.(4)

Crazes are believed to form at defects in the material such as dust specks which cause the local stress to become concentrated to the point of exceeding the cavitational threshold dilatational stress. The rates of nucleation and of growth of crazes increase with increasing temperature, stress and solubility properties of the liquid or gaseous environment contiguous to the surface of the plastic part. Crazes are important because they affect the optical properties of transparent plastics and represent the

initial stages of crack formation and growth. An equally important aspect of crazes is that their state of development is a measure of the aging and weathering to which a thermoplastic has been exposed. The prior history and dynamics of growth of crazes or cracks during dynamic loading govern whether a plastic part will fail in a ductile (shear yielding) or brittle (critical crack length controlled) manner.

This portion of the paper presents a status report on efforts to develop and validate an accelerated life prediction test for aircraft transparent enclosures when the life limiting phenomenon is crazing of acrylic outer plies of multiply laminated polycarbonate transparency constructions. The accelerated life test for crazing is based on the standard ASTM F484 cantilever beam test for chemical crazing. (5,6) This laboratory test generates a relationship between surface stress and time to initiate crazing. The proposed life prediction test concept would require that a chemical crazing test be performed on a sample coupon from each canopy, cut from the trim area or from a randomly selected representative canopy from each lot as it comes from the production line. At the same time a nondestructive measurement of surface stress would be made in the forward facing or other craze prone area with the canopy installed in a standard frame. The time-to-craze measured in the laboratory corresponding to this stress would be found from the curve generated by the chemical craze test. This laboratory time-to-craze in turn would be input into a previously established relationship between time-to-craze in service, and the measured time-to-craze in turn would be input into a previously established relationship between time-to-craze in service and the measured time-to-craze in the laboratory to obtain the prediction of service life. A capability such as described above would allow the Air Force to make durability a decision factor in the acquisition of transparencies. For example, one use would be to buy transparencies from that source that offered the lowest price for each year of predicted service life, given that all other criteria were also met or surpassed.

The rest of this paper will be devoted to a discussion regarding the detailed approach for providing a technically sound and consistent accelerated life prediction process. The most important aspects to be covered will address the development of the relationship between laboratory test time-to-craze and field service time-to-craze and the approach for relating times-to-craze for uniaxial and biaxial states of surface stress.

The time-to-craze under a uniaxial state of surface stress depends both on the temperature and the magnitude of the tensile stress. Results of chemical craze tests performed on as-cast acrylic at various temperatures by the McDonnell Douglas Aircraft Company are plotted in Figure 4. (7) These linear plots show a generally inverse relationship between stress level and time-to-craze. There is an apparent threshold tensile stress below which no crazing occurs. This will be shown later to be only apparent, but from a practical point of view, there will always be a level of stress corresponding to a given service life duration below which no crazing is initiated at a given tensile stress level.

Existing theory will now be presented which is in fairly good agreement with these sample test results. To begin, it is assumed that both the nucleation and the growth of crazes are random, time-dependent, thermally activated phenomena. The rate of nucleation is constant and given by the expression:

$$(8) \quad \frac{dN}{dt} = N_0 \exp(-\Delta E_N/RT) \cdot \sinh[(n-1)\sigma/\sigma^*] \quad (1)$$

The rate of linear growth of craze nuclei into a crack is also constant is expressed by: (8)

$$\frac{dG}{dt} = G_0 \exp(-\Delta E_G/RT) \cdot \sinh[\sigma/\sigma^*] \quad (2)$$

In these expressions the role of tensile stress, temperature, and nature of the material-environment combination, as reflected in the activation energy, and their formal resemblance to chemical reaction rate expressions may be noted. The total length of crazes per unit area is given by integrating the product of the number of nuclei, found by integrating the first expression, and of the second expression as follows: (8)

$$V_c = \beta_0 N_0 G_0 \exp[-(\Delta E_N + \Delta E_G)/RT] \sinh \frac{\sigma}{\sigma^*} \cdot \sinh \frac{(n-1)\sigma}{\sigma^*} \cdot \frac{t^2}{2} \quad (3)$$

Here beta is a porosity factor assumed to be constant. This expression says that the total length density of crazes is proportional to the square of time. We may then suppose that after a certain density of length of crazes per unit area has been reached the crazing becomes visible to the human eye. The time at this just visible level of crazing density will be called the time-to-craze. It is seen that this time is adversely proportional to an increasing function (hyperbolic sine) of stress. If the argument of this function is large, the function may be approximately by an exponential function of the stress. Therefore, the expression for the time-to-craze takes the form of an exponentially decaying function of stress which plots as a downward sloping straight line on semi-log graph paper.

$$\log t = A - B\sigma \quad (4)$$

The consistency of this result with the McDonnell Douglas chemical craze tests is shown in Figure 5, where the data of Figure 4 is replotted on semi-log graph paper. Especially convincing is the result that all the lines representing craze test data taken at different temperatures are parallel while only the y-axis intercept is a function of temperature, exactly as predicted by the theory.

The important result obtained thus far is a knowledge of the specific mathematical form of the time-to-craze versus surface stress relationship for a uniaxial stress state. Notice that this relationship was developed for a constant temperature and constant stress condition. The analysis could have been carried out equally well for any other known temperature and stress history and the same mathematical form, evaluated at a pair of reference temperature and stress peculiar to a given stress-temperature history would then have been used to predict the time-to-craze for a particular environmental life cycle. It is expected, in general, that for



similar environmental histories higher temperatures and stresses will be associated with shorter times-to-craze.

Attention is now focused on the issue of relating the time-to-craze for a certain level of uniaxial stress during a cantilever beam chemical craze test to the time-to-craze during an accelerated chemical craze test on a portion of the surface of an aircraft transparency which may be in general in a biaxial state of stress.

Investigators (3,4,9,10) have found that the time-to-craze under a multiaxial state of stress is related to the state of stress by the following relationship, in which  $Y$  and  $X$  are functions of temperature and time-to-craze and the 1-direction coincides with the direction of the maximum longitudinal strain:

$$\sigma_1 - \nu\sigma_2 - \nu\sigma_3 = Y + 3X / (\sigma_1 + \sigma_2 + \sigma_3) \quad (5)$$

This relationship appears to be universal for all thermo=plastics. Test data for acrylic was only available for one value of time-to-craze. Available test data for polystyrene is shown in Figure 6 for four different constant values of time-to-craze. A statistical regression analysis on these data was performed to determine the values of the two functions at the four values of time. It was found that the supposed function  $X$  was really essentially a constant, and that the strong variations with time were confined mainly to the  $Y$  function.

$$\sigma_1 - \nu\sigma_2 - \nu\sigma_3 = Y(t) + 3X / (\sigma_1 + \sigma_2 + \sigma_3) \quad (6)$$

Since this relationship applies to all states of stress, it certainly would apply to the uniaxial stress state. Solution of equation (6) for the uniaxial stress corresponding to each value of time-to-craze yields the expression:

$$\sigma = \frac{1}{2} Y(t) + \sqrt{[Y(t)/2]^2 + 3X} \quad (7)$$

This relationship is plotted versus the logarithm of time-to-craze on semi-logarithmic graph paper in Figure 7. This step results in the negatively sloping straight line form as should now be expected based on earlier discussions in this paper. What has been shown is that the form of the relation between time-to-craze and stress for a uniaxial state of stress may be derived from that for a multiaxial stress state.

It would be most convenient if the reverse process could be accomplished and the function  $Y(t)$  and the constant  $X$  appearing in the multiaxial stress state correlation also could be deduced from a uniaxial stress chemical craze test. As may be seen by solving for the function  $Y(t)$  from equation (6) for the case of a uniaxial stress condition, namely,

$$Y(t) = \sigma - 3X/\sigma \quad (8)$$

that the form of the functional dependence of  $Y(t)$  time-to-craze is thereby neatly determined, but the value of the constant  $X$  remains undetermined. We therefore have that

$$Y(t) = A/B - \ln(t)/B - 3X/(A/B - \ln(t)/B) \quad (9)$$

by recalling that the time-to-craze was related to the stress by the expression:

$$\ln(t) = A - B\sigma \quad (10)$$

The constant  $X$  would therefore have to be determined in general from a chemical craze test on new transparency coupons under biaxial states of stress. One suggestion for doing this would be to use a cross shaped double cantilever beam specimen in order to create the biaxial state of stress in the center plate intersection of the perpendicular beam elements.

It is clear, at any rate, that the determination of the multiaxial stress time-to-craze correlation for new transparency material is greatly facilitated by a knowledge of the explicit form of the dependence of the function  $Y(t)$  on the time-to-craze. This will also be true for full scale transparencies under constant stress, temperature, and chemical environments.

#### Development of the Time-To Craze Correlation for In-Service Transparencies

It has been shown that the time-to-craze dependence on constant values of stress and temperature has the same form regardless of the chemical environment, be it air or any of various chemical liquids. The degree of success with which in-service transparency life-times may be correlated by an expression of the same form will depend upon whether an individual, roughly constant, dominant state of stress can be determined which may be associated with each canopy and which is also basically a function of manufacturing, material and dimensional quality control.

It may be noted that the effect of temperature in the time-to-craze relationship appears as a function of absolute temperature. Thus temperature variations can be expected not to produce overwhelming variations in this expression.

Three possible sources of this dominant state of stress may be identified. These are

- 1) the initial residual stresses built into a transparency as a result of fabrication:
- 2) the installation stresses resulting from excessive dimensional tolerances in the fabricated product relative to those of the frame; and
- 3) the thermal or environmentally induced stresses resulting from climate and ground and flight operations.

It was initially suspected that residual stresses might represent the dominant stresses, and this hypothesis has not been ruled out completely as yet. Table 4 shows the results of representative residual stress measurements made on removed F-16 canopies stored in warehouses at Hill Air Force Base, Ogden, Utah, for which the installed service life was known and which exhibited a light state of crazing. No crazing should have occurred on these parts since the measured residual stresses varied basically from high compressive to low tensile stresses. It is now thought that these measurements using the hole drilling strain rosette technique (a destructive test) were not performed under controlled conditions. For example, significant compressive stresses such as those measured could have been induced merely by dragging these laterally compliant shells across the ground. For this reason it is planned to perform near future canopy surface stress measurements with the transparent articles installed in a standard frame.

Prior analyses have shown that static and dynamic flight pressure loads do not induce significant stresses. (12) Analyses are planned to be conducted to assess the magnitude of the thermal stresses induced by flight and ground operations. Operational time segments during which high temperatures and high stresses occur together need to be screened as possible sources of the dominant stress state relative to crazing.

In the process of testing the validity and degree of universality of a service life time-to-craze versus surface stress correlation, it is deemed necessary to obtain at least five lightly crazed, removed F-16 canopies for which the installed life is known from each of two vendors and for each of these vendors from each of two geographically and environmentally distinct bases at which the total service life was experienced. Thus a total of six correlations need to be established. This will involve determining the three constants, A, B, and X in the following expression experimentally and by statistical regression for new canopies from each of the two vendors and for removed canopies from each of the two vendors for each of two Air Force Bases at which their service life occurred. Each correlation, as mentioned previously will be based on five sample canopies. The total number of canopies required will be 30, of which 10 will be new canopies. Optical rejects will be acceptable as samples for the new canopies. The new canopies will be subjected to a chemical craze test under biaxial states of surface stress to generate the laboratory correlations. The correlations for the removed canopies will be based on installed service for canopies which exhibited a light degree of crazing when selected as a sample from the population of removed canopies stored in the warehouses at Hill Air Force Base. The expression to which the six correlations will be fitted is as follows:

$$\sigma_1 - \nu\sigma_2 - \nu\sigma_3 = A/B - \ln(t)/B - 3X/(A/B - \ln(t)) + \frac{3X}{\sigma_1 + \sigma_2 + \sigma_3} \quad (11)$$

The mathematics for determining the three constants from this exact form of the relation has not been worked out yet, although this does not appear to be an insurmountable task given the availability of digital computers.

The following mathematical simplification, however, which was found to be valid in the case of polystyrene, will facilitate the correlation of field life data for crazing under biaxial surface states of stress and may allow the laboratory correlation for multiaxial states of stress for acrylic to be derived from the usual uniaxial chemical craze test supplemented by information from the field life correlations.

It is based on the following considerations. The dependence of uniaxial stress on the functions  $Y(t)$ , and the constant  $X$  may be simplified when  $Y = 2(3X)^{0.5}$ , which was found to be the case for polystyrene data. In this case, approximately,

$$\sigma = Y(t)/2 + \sqrt{3X} \quad (12)$$

Comparing with

$$\sigma = A/B - \ln(t)/B \quad (13)$$

we see that approximately

$$Y(t) = 2(A/B - \sqrt{3X}) - 2 \ln(t)/B \quad (14)$$

so that

$$\sigma_1 - 2\sigma_2 - 2\sigma_3 = 2(A/B - \sqrt{3X}) - 2 \ln(t)/B + \frac{3X}{\sigma_1 + \sigma_2 + \sigma_3} \quad (15)$$

It is easy to correlate sets of field data for which  $\sigma_1, \sigma_2, \sigma_3$  and  $t$  are known. The maximum likelihood estimation process leads to three linear equations in the three unknowns, namely,

$$2(A/B - (3X)^{0.5}), 2/B, \text{ and } 3X \quad (16)$$

from which  $A, B,$  and  $X$  may be determined.

Let us set

$$r(f) = (B/A * (3X)^{0.5}) \quad (17)$$

where the subscript,  $f$ , denotes field and  $1$  denotes laboratory. If it turns out, as seems reasonable, that

$$r(f) = r(1), \quad (18)$$

then the laboratory multiaxial stress time-to-craze correlation can be generated from a simple cantilever beam uniaxial stress chemical craze test as follows:

$$\sigma_1 - 2\sigma_2 - 2\sigma_3 = 2(A/B)(1 - r_f) - 2 \ln(t)/B + (A/B)^{0.5} * 2 * r_f^{0.5} / (\sigma_1 + \sigma_2 + \sigma_3) \quad (19)$$

## REFERENCES

1. Communication, Ralph Speelman, AFWAL/FDER, WPAFB, OH
2. Urzi, R. E. and Capt. J. V. Anselmo, "Windshield System Life Cycle Durability Facility", 15TH Aerospace Transparent Materials and Enclosures Conference, 16-20 January 1989, Monterey, CA
3. Kinloch, A. J. and R. J. young, "Fracture Behaviour of Polymers", Applied Science Publishers, Ltd., London, 1983.
4. "Polymeric Materials", American Society for Metals, Metals Park, Ohio, 1975.
5. American Society of Testing and Materials Standards, "Plastics-Genera Methods of Testing-Nomenclature", Part 27, 1966, p. 568
6. Clayton, K. I., B. S. West and D. R. Bowman, Aircraft Transparency Test Methodology, AFWAL-TR-85-3125, March 1986
7. McDonnell Aircraft Company Report, MDC A3751, 1973
8. Nicolasis, L. and DiBenedetto, A. T., "Failure Criteria For Polymeric Solids", Journal of Applied Polymer Science, vol 15, pp. 1585-1598
9. Sternstein, S. S. and Ongchin, L., (1969) Polymer Preprints, American Chemical Society, vol 19, no. 2, p. 1117
10. Oxbouough, R. J. and Bowden, P. B., (1973) Phil. Mag., vol 28, p. 547, "A General Critical-Strain Criterion for Crazing in Amorphous Glassy Polymers"
11. Communication, Malcolm Kelley, AFWAL/FDER, WPAFB, OH
12. Communication, Robert McCarty, AFWAL/FDER, WPAFB, OH

**Table 1**  
**TYPE OF TRANSPARENCY BY VENDOR (F16)**

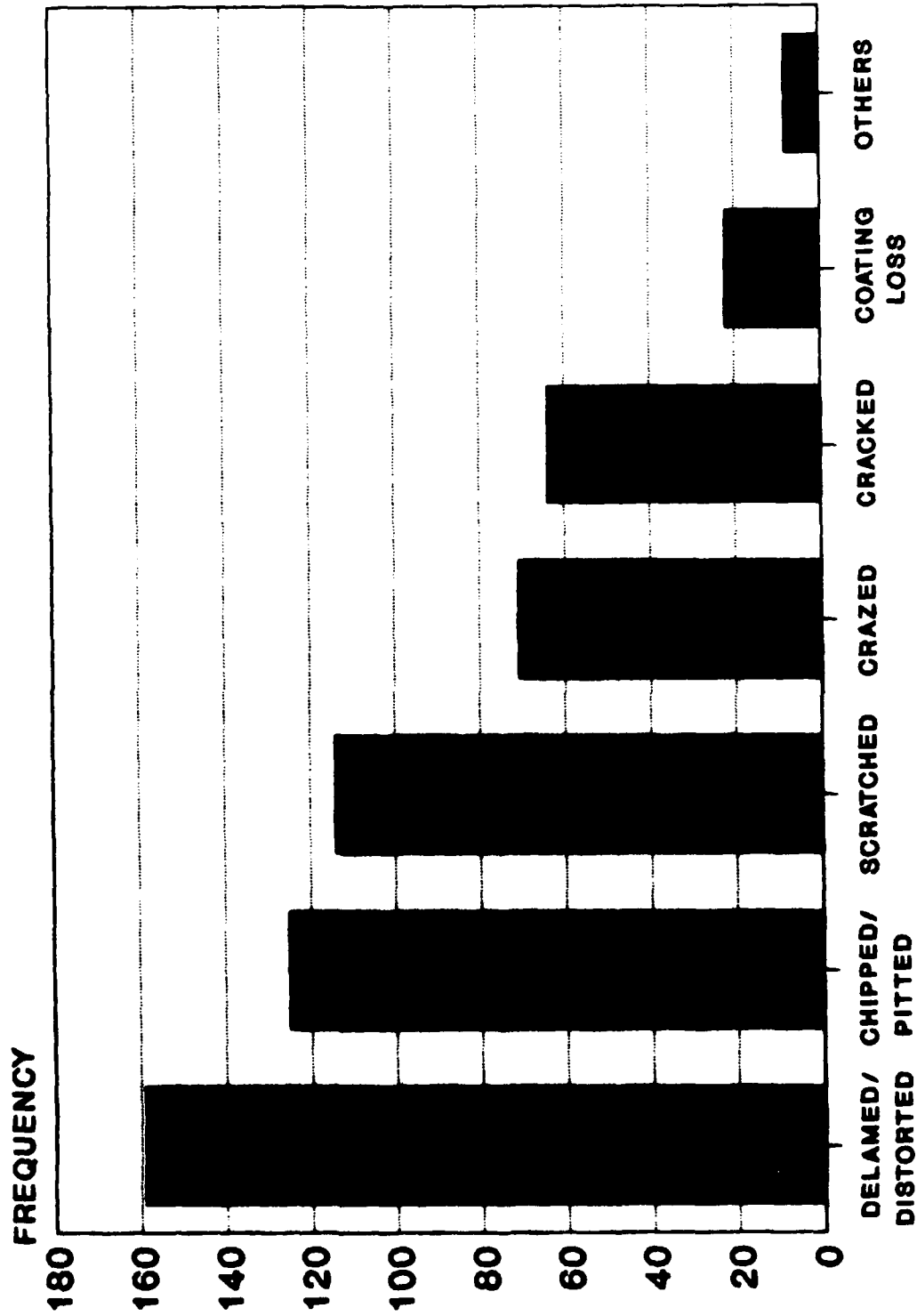
VENDOR	TOTAL		TYPE OF TRANSPARENCY					
	No.	Percent	FORWARD		AFT		N.A.*	
			No.	Percent	No.	Percent	No.	Percent
Goodyear	280	29.4	121	25.5	73	54.0	86	25.0
Sieracin	192	20.1	74	15.6	21	15.6	97	28.2
Texstar	433	45.4	237	50.0	39	28.9	157	45.6
N.A.*	48	5.1	42	8.9	2	1.5	4	1.2
<b>Total</b>	<b>953</b>	<b>100.0</b>	<b>474</b>	<b>100.0</b>	<b>135</b>	<b>100.0</b>	<b>344</b>	<b>100.0</b>

\*N.A. stands for information is "not available" or "not identifiable".

Source: Air Force D Base, 1987  
North Carolina A&T State University

FIGURE 1

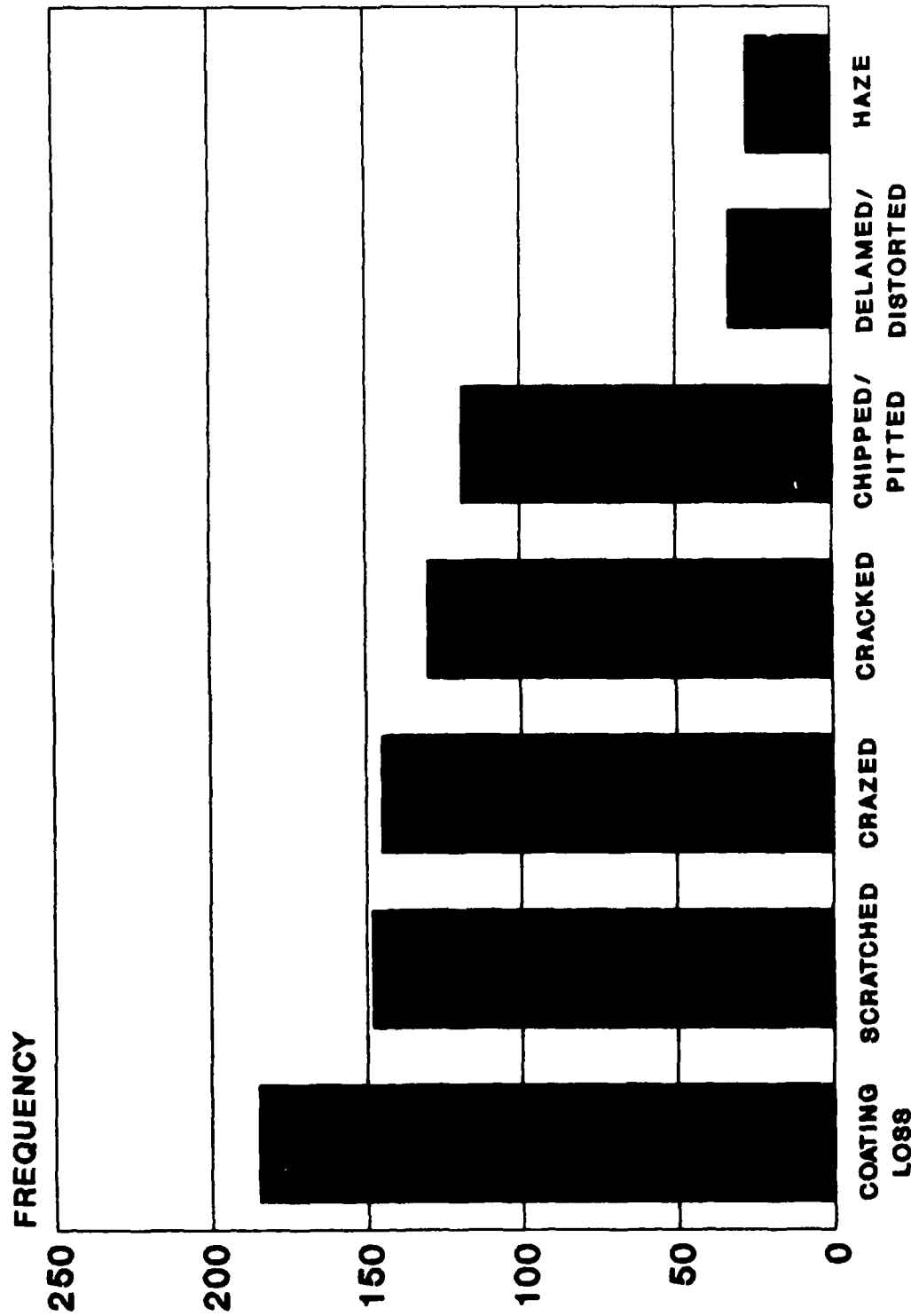
# HISTOGRAM OF TRANSPARENCY FAILURES F-111



AF D BASE 1987 N.C. A&T STATE UNIVERSITY

FIGURE 2

# HISTOGRAM OF TRANSPARENCY FAILURES F-16



AF D BASE 1987 N.C. A&T STATE UNIVERSITY



Table 2

F-16 TRANSPARENCY FAILURE MODES

Air Force Base	Acrylic crazing		Acrylic cracks		Delaminated		Scratched		Haze	
	No.	Percent	No.	Percent	No.	Percent	No.	Percent	No.	Percent
Elgin, FL	6	4.2	2	1.8	0	0.0	4	3.2	0	0.0
G.D., TX	2	1.4	13	11.4	0	0.0	6	4.8	0	0.0
Hahn, Germany	0	0.0	1	0.9	0	0.0	3	2.4	0	0.0
Hill, UT	5	3.5	20	17.5	0	0.0	16	12.7	3	18.8
Kunsan, Korea	1	0.7	2	1.8	0	0.0	1	0.8	1	6.3
Luke, AZ	5	3.5	41	36.0	2	10.0	26	20.6	1	6.3
Torrejon, Spain	0	0.0	8	7.0	10	50.0	11	8.7	0	0.0
MacDill, FL	110	76.9	17	14.9	0	0.0	31	24.6	7	43.8
Shaw, SC	1	0.7	3	2.6	1	5.0	6	4.8	1	6.3
Misawa, Japan	1	0.7	0	0.0	5	25.0	1	0.8	0	0.0
Nellis, NE	12	8.4	7	6.1	2	10.0	21	16.7	3	18.8
<b>Total</b>	<b>143</b>	<b>100.0</b>	<b>114</b>	<b>100.0</b>	<b>20</b>	<b>100.0</b>	<b>126</b>	<b>100.0</b>	<b>16</b>	<b>100.0</b>

$\chi^2 = 475.8^*$

Degree of freedom = 70

\*Very significant at 0.05 level of significance

Table 3

Failure Mode Analysis

	F-16	F-111	Total	%	% (Minus Other)	% (Minus Other, Minus F-16 Coating Loss)
Surface Degradation						
Coating Loss	185	22	207	51	64	57
Crazed	145	71	216	15	19	2
Chipped/Pitted	119	125	244	16	20	24
Haze	27	0	27	18	23	27
	<u>476</u>	<u>218</u>	<u>694</u>	2	2.5	3
Fatigue Failures						
Cracked	130	64	194	29	36	43
Delaminated/Distorted	33	159	192	14	18	22
	<u>163</u>	<u>223</u>	<u>386</u>	14	18	21
Other						
Scratched	148	114	262	20	0	0
Miscellaneous	0	8	8	19		
	<u>148</u>	<u>122</u>	<u>270</u>	1		

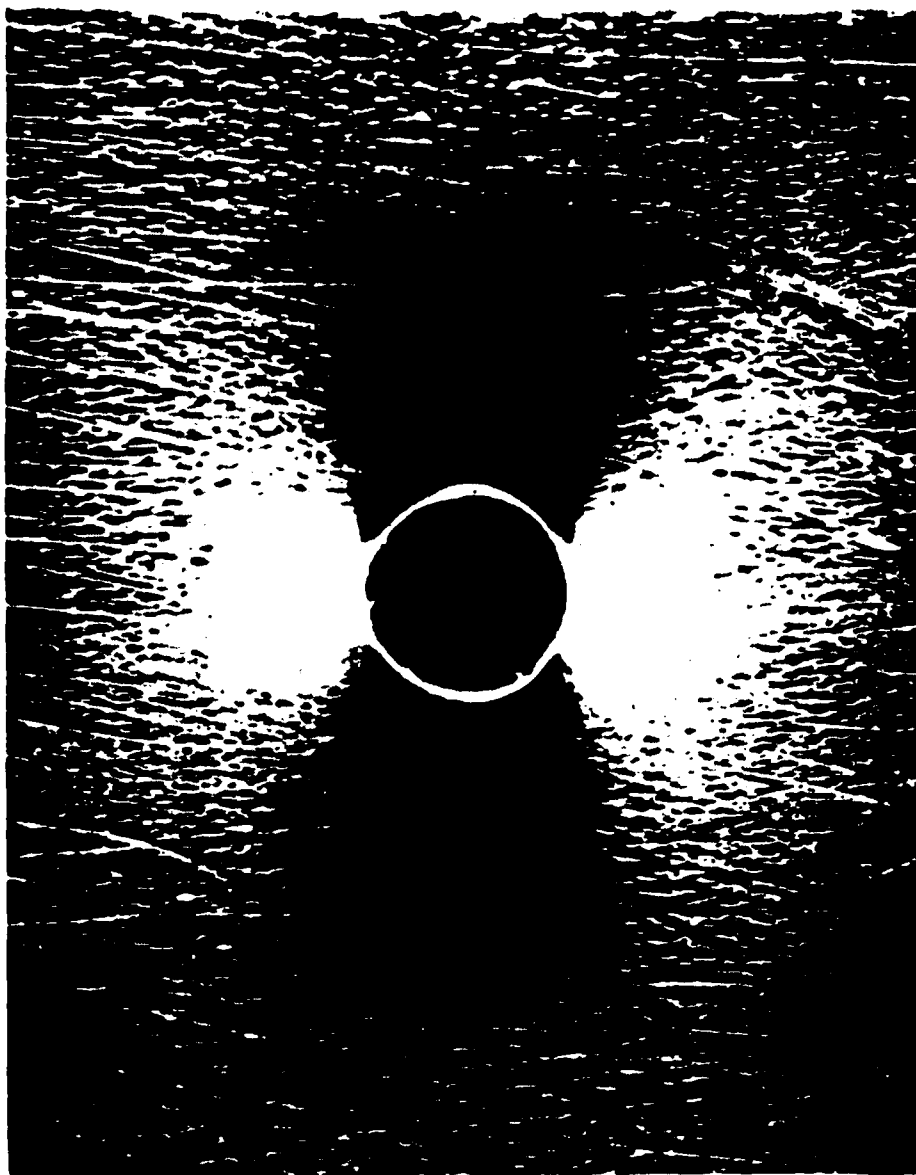
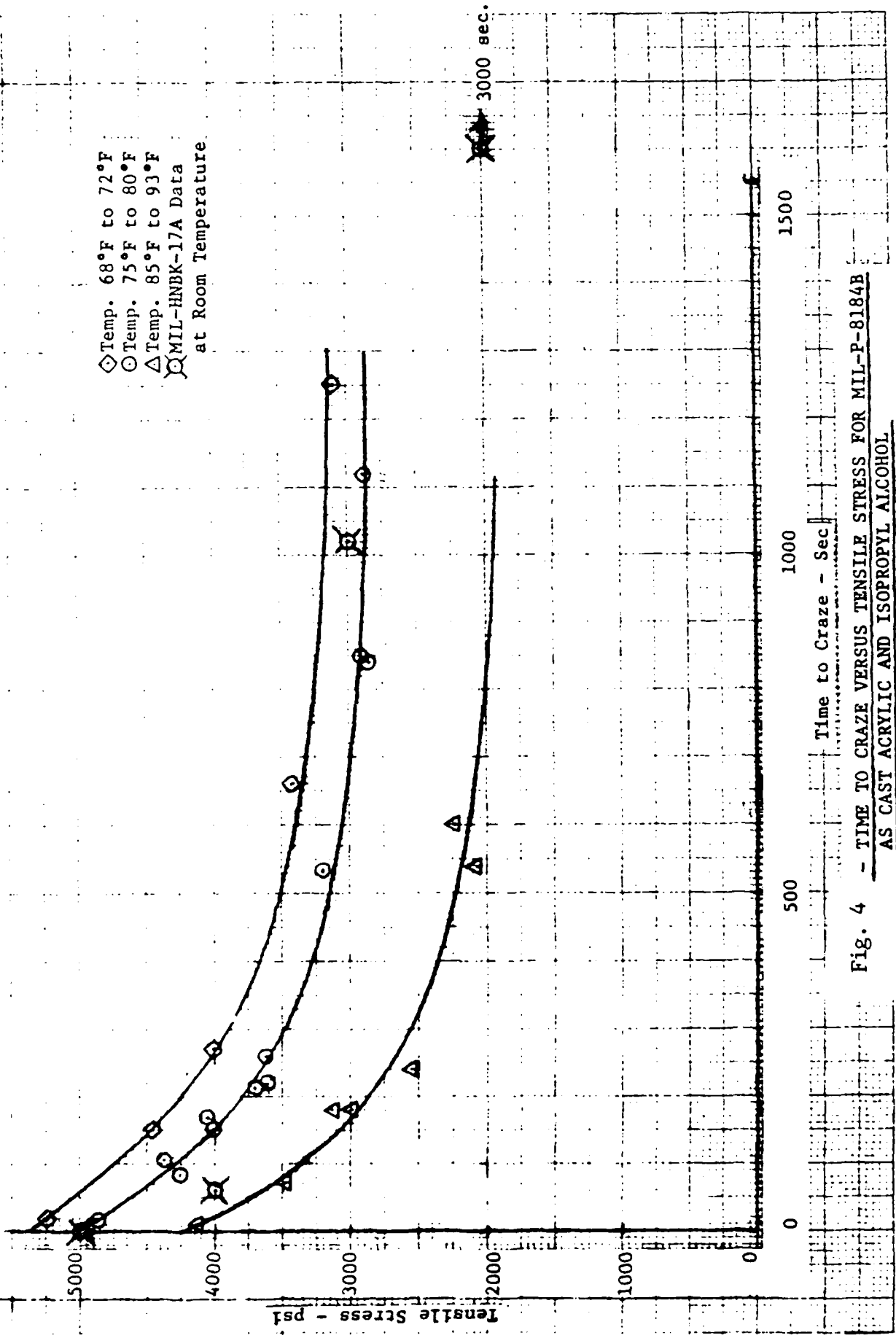


Fig. 3 Craze pattern (white lines) obtained in PMMA containing a drilled hole and subjected to uniaxial tension. The applied stress is horizontal. (From Ref 8)

◇ Temp. 68°F to 72°F  
 ○ Temp. 75°F to 80°F  
 △ Temp. 85°F to 93°F  
 ⊗ MIL-HNBK-17A Data  
 at Room Temperature

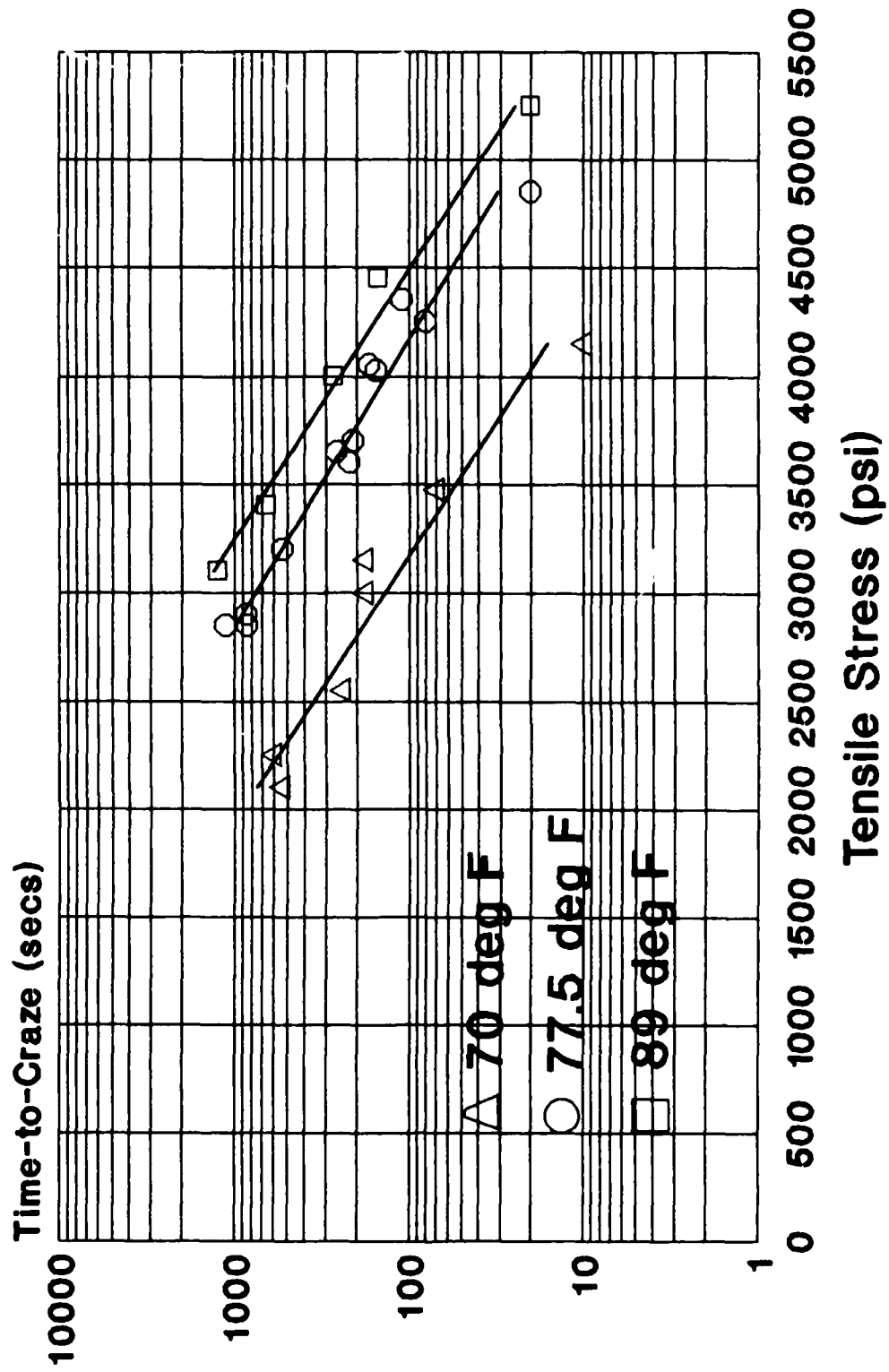


3000 sec.

Fig. 4 - TIME TO CRAZE VERSUS TENSILE STRESS FOR MIL-P-8184B  
 AS CAST ACRYLIC AND ISOPROPYL ALCOHOL

FIGURE 5

# TIME-TO-CRAZE VS TENSILE STRESS AS CAST ACRYLIC AND ISOPROPAL ALCOHOL



McDonnell Aircraft Data

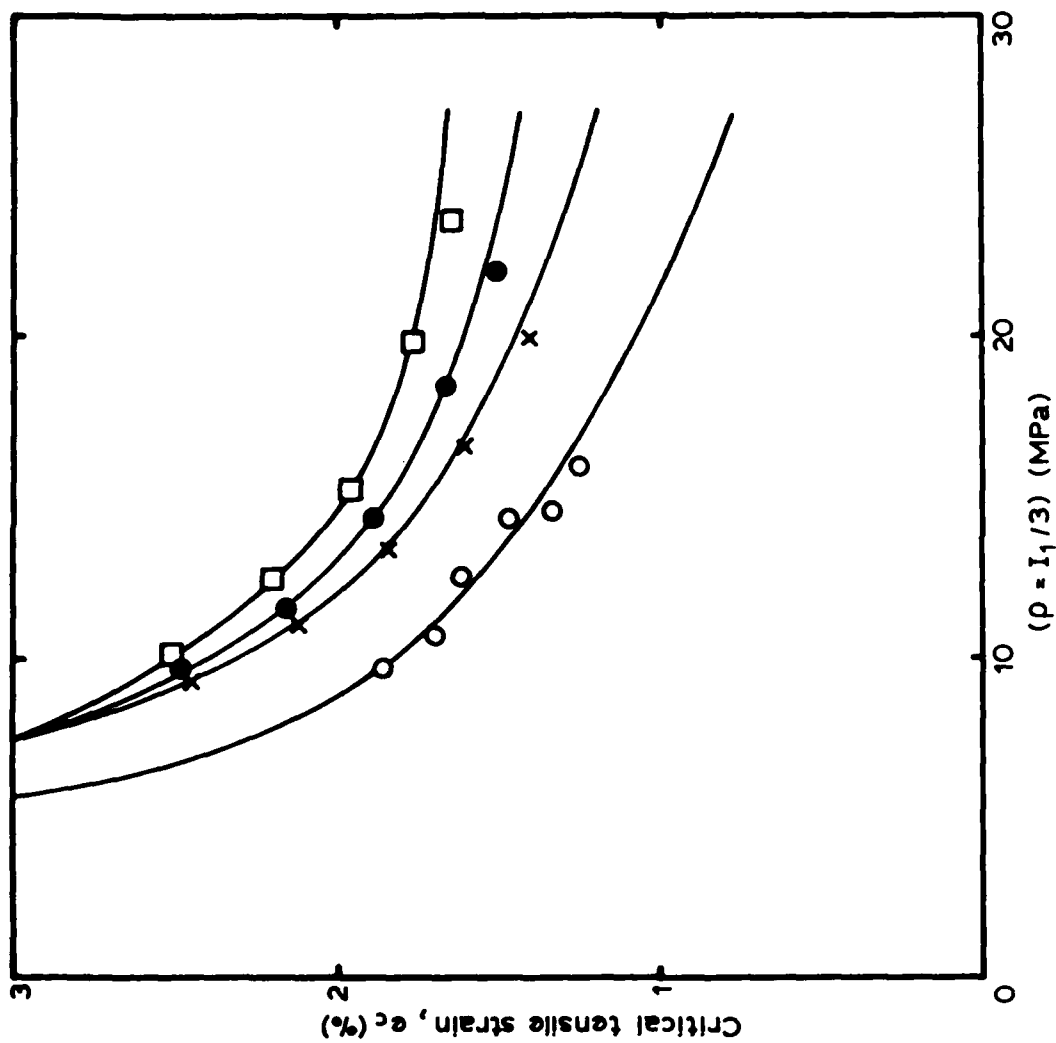


Fig. 6 Critical tensile strain,  $e_c$ , for craze initiation as a function of the hydrostatic tensile component of the applied stress tensor for polystyrene in air. Points are for different load hold times and represent experimental results; the solid curves represent eqn. (5.7). □, 1 s test,  $E = 3.22$  GPa; ●, 10 s test,  $E = 3.20$  GPa; ×, 100 s test,  $E = 3.07$  GPa; ○, 1000 s test,  $E = 2.92$  GPa (after Bowden & Oxborough<sup>65</sup>).

# TIME-TO-CRAZE VS UNIAXIAL TENSILE STRESS POLYSTYRENE IN AIR

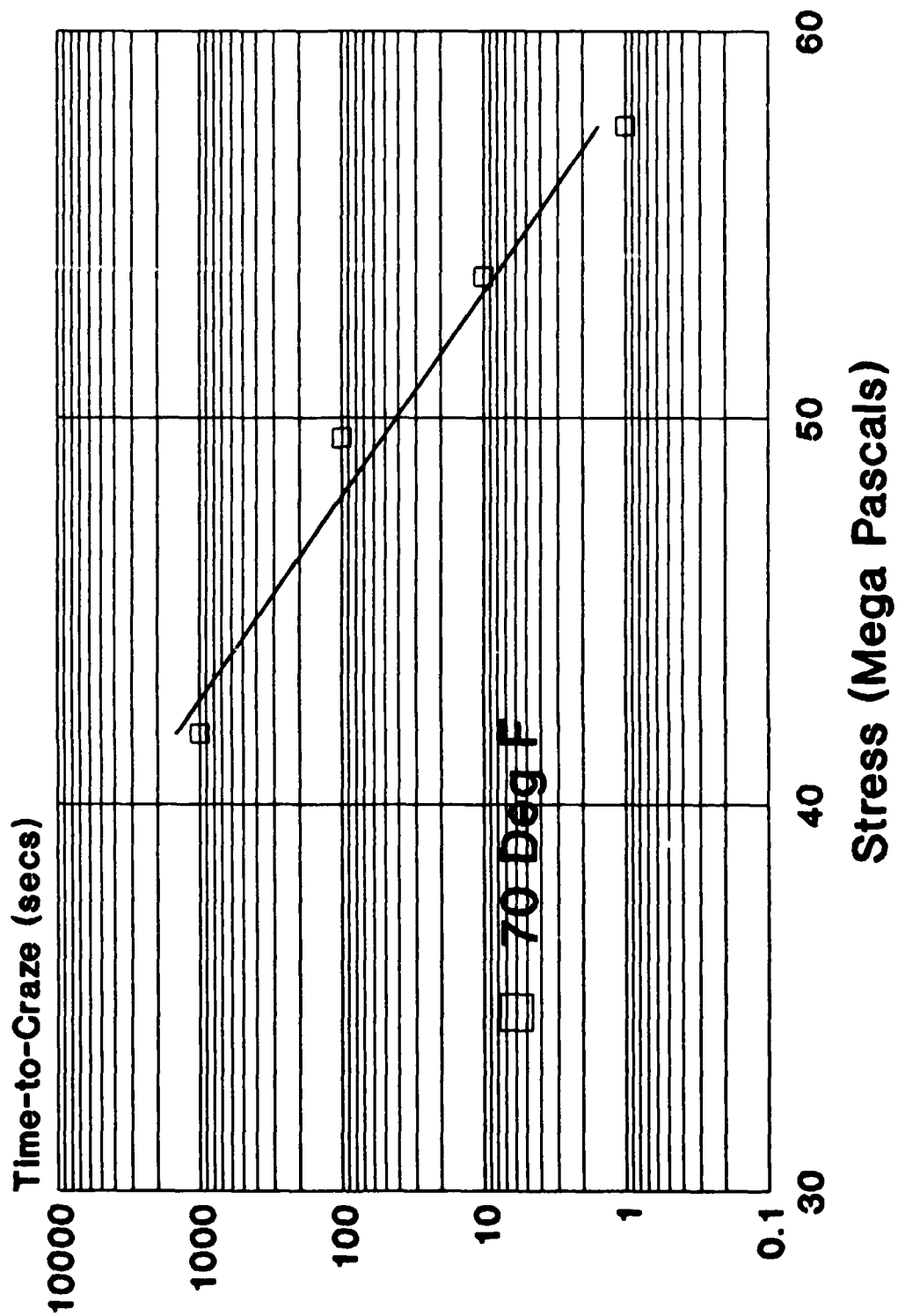


Table 4

## F-16 CANOPY RESIDUAL STRESS MEASUREMENT

Canopy No.	Gauge No.	Location	Principal No. 1	Principal Direction (Degrees)	Stresses (PSI) No. 2	Principal Direction (Degrees)
1	101	B	-2260.	-51.2	-1435.	-51.2
	102	A	266.	52.8	1031.	52.8
	103	C	-804.	47.3	-483.	47.3
	104	D	-1849.	-53.2	-548.	-53.2
2	201	B	-1522.	-48.4	-744.	-48.4
	202	A	-1528.	75.9	-874.	75.9
	203	D	-2111.	-57.6	58.	-57.6
	204	C	-2226.	61.4	-813.	61.4
3	301	A	-568.	30.0	101.	30.0
	302	B	-1440.	-57.0	-692.	-57.0
	303	C	-3792.	59.9	-1063.	59.9
	304	D	-457.	-38.9	2194.	-38.9
4	401	A	-2390.	-44.2	-663.	-44.2
	402	B	-7784.	35.3	2675.	35.3
	403	C	-2622.	41.9	2097.	41.9
	404	D	-2185.	-37.6	-112.	-37.6
5	501	A	-377.	-33.6	573.	-33.6
	502	B	-2598.	-50.5	1118.	-50.5
	503	C	1253.	-80.9	3114.	-80.9
	504	D	-3724.	-48.6	1163.	-48.6
6	601	A	-1136.	20.2	3313.	20.2
	602	B	-4853.	-31.9	1818.	-31.9
	603	C	4414.	-46.1	9154.	-46.1
	604	D	-7057.	-41.4	6741.	-41.4

LOCATIONS: A CENTERLINE FORWARD FACING  
 B RIGHT SIDE FORWARD FACING  
 C CENTERLINE REAR  
 D RIGHT SIDE REAR



MANAGEMENT OF TRANSPARENCY RELATED COSTS IN  
ELECTROSTATIC DISCHARGE DAMAGE TO F-16 CANOPY SOLAR COATINGS

B. G. Hinds  
H. DeCamp

Sierracin/Sylmar Corporation

ELECTROSTATIC DISCHARGE DAMAGE TO  
F-16 CANOPY SOLAR COATINGS

Authors:  
B. G. Hinds  
H. DeCamp

Sierracin/Sylmar Corporation

ABSTRACT

As reports of electrostatic discharge damage to F-16 canopies accumulated during the past year, Sierracin began studying how to improve solar coating systems. This damage, as observed in the field, consists of narrow, clear or blue-tinged arc tracks burned across the inside of canopies. Besides disrupting the continuity of the solar coating, the discharges can also be distracting to pilots.

Before a laboratory study could be made, Sierracin had to obtain a generator to produce static electricity in the accepted range of in-flight triboelectric charging. Since a commercial unit with sufficient current output could not be located, a large Van deGraaff generator was assembled. Subsequent tests of canopies and canopy sections produced streamer discharge phenomena which matched the appearance of arc tracks occurring in flight.

As a result of these electrostatic tests, a damage-resistant gold-based solar coating system has been developed. Even better, a new coating system, Sierracin's indium tin oxide on plastic, has proven by the same tests to be undamageable by what we believe to be the most severe arcing that triboelectric charging might produce.

## INTRODUCTION

The requirement for a solar coating on the interior surface of F-16 canopies (see Figure 1) was imposed by the USAF in 1984, well after canopy production had begun. As the quantity of solar-coated canopies in service increased, a growing number removed from service were found to be damaged by electrostatic discharge (ESD). During flight, triboelectric charging of the F-16 canopy exterior occurs and the accumulating electrical potential can escalate to hundreds of kilovolts. The electrically conductive solar coating should carry resulting induced charges, which develop on the interior of canopies, to the air frame. Instead, the metallic gold and organic coatings break down, leaving permanent arc tracks, and pilots can be distracted at night by arcs flashing across canopy interiors. This ESD damage reduces the solar-coated area into ever smaller sections which become electrically-isolated from grounding.

The obvious solution to this problem is to develop a more resistant coating system and/or a more effective grounding system to minimize charge accumulation. Fortunately, Sierracin was just introducing two new solar coating systems that might meet the first solution requirement. They are -- UV radiation-cured basecoat/topcoat system for gold coatings, and ITO-on-plastic. However, to determine the effectiveness of any solution developed, it was necessary to have a quick and cost-effective test method which, hopefully, avoids having to conduct flight tests. Since simulation of flight environment is difficult, Sierracin's approach was to test beyond the extreme limit; i.e., to use higher voltages than observed or predicted for real flight. How this was accomplished follows.

## DISCUSSION

A recent survey of 722 F-16 canopies removed from flight service and scrapped for various reasons has been conducted by the Air Force, General Dynamics and the transparency suppliers. During the period 1981 to 1988, loss from ESD damage was 4% or 29 units; however, all 722 of these canopies did not have solar coatings. A total of 418 from the three canopy manufacturers did. This meant that 7% of the solar-coated canopies had significant ESD damage.

A closer examination of typical ESD damage to solar coatings is shown in Figures 2 and 3 as viewed from the inside of an F-16 aircraft. Figure 4 is a closeup photo of ESD damage to a canopy edge. As electrostatic energy generated in flight by triboelectric charging accumulates on the outside of a canopy, induced charging occurs on the inside surfaces. Electrical discharges burn paths in the solar coating as the interior discharges to conductive structure at canopy edges. This results in transparent or purple-tinged streaks which are no longer conductive, and they continue to form with repeated exposure to high voltage.

General Dynamics previously encountered this type of coating damage in the course of its tests, reported in 1981 (ref. 1), simulating F-16 streamer mechanisms. The purpose of their work was, however, to find ways to prevent charge buildups and electric shocks to pilots. Streamer inside cockpits had been reported by pilots flying with uncoated canopies during penetration of heavy cirrus clouds. In the course of this project, they observed that "evaporation paths" formed on interiors of canopies experimentally coated with gold. The purpose of the work we are reporting on was to carry this type of testing further to prevent evaporation paths from forming in current solar coatings. To this end, a laboratory source of very high voltage was needed to produce negative static electricity in the accepted range for in-flight triboelectric charging: 100 KV to 500 KV with current sufficient for 10-50  $\mu\text{A}/\text{ft}^2$  of windshield frontal area.

There are two general methods for producing continuous high-voltage direct current: rectification of high-voltage AC, and electrostatic generators. The former involve great expense, substantial shock hazard, and other complications. The latter can be simple, safe and less-expensive to construct and operate. Although a power supply such as the Van deGraaff generator appears to be a good choice, commercially available units sold mainly for science demonstrations produce too little current. Reference books indicate that Van deGraaff generators operating in air are of only historical interest today and give no practical details for constructing one. Sierracin, therefore, had to design and assemble its own as General Dynamics did for the earlier F-16 canopy testing. Such generators have been employed by others at least as far back as 1956 (ref. 2) to simulate tribo-electric charging of aircraft structures. In the event it might help others who need to do similar testing, we will describe the design of our test equipment.

The Van deGraaff generator was invented and used in early 1930 to power linear accelerators for nuclear research. They are still made today for the same purpose, but in more sophisticated forms for multi-million dollar installations. Van deGraaff generators operate by depositing negative or positive charges on a non-conductive belt traveling rapidly over two pulleys. These charges are transferred to an isolated high-voltage terminal where they accumulate on its outside surface. Maximum potential developed is limited by the size of the HV terminal and ultimately by the breakdown voltage of air surrounding it. Voltage can be varied by belt travel speed and the potential at the generator's charging source. Current output, on the other hand, is limited by belt width (the wider the belt, the more charge it can carry) as well as belt speed. The upper limit of voltage can only be reached if the HV terminal surface is polished and clean, and the polarity of the charge can be reversed in a number of ways. Van deGraaff generators are either internally (frictionally) excited or externally excited (boosted with a separate power supply). The latter produces lethal power, but the former, the one employed for these tests, rarely exceeds 80  $\mu$ A output and can be sized to operate safely in a typical laboratory environment.

Details of the generator are shown in Figure 5. The 30-inch separation between the base and HV terminal is the minimum to prevent arcing between the base and top terminals; i.e., a gradient of more than one million volts would be required for arcing to occur. The HV terminal (28-inch major diameter) is constructed of spun aluminum in an oblate spheroidal shape (this develops higher potentials than a true sphere). Since surface burrs can reduce voltage as much as 40% or more, the surface must be polished. The belt entry hole causes the most voltage loss and should not be larger than half the diameter of the terminal. Also, from our experience, a belt width of 4" will have charge distribution problems and loss of efficiency.

For design sizing, the HV terminal develops a voltage gradient of:

$$E_{\text{max air}} = \frac{V}{r}$$

where  $V$  = volts  
 $r$  = terminal radius, cm

In dry air, the max. gradient is  $3 \times 10^4$  V/cm.

Since our generator has a radius of 14" (35.56 cm),

$$V = 3 \times 10^4 (35.56) = 106.7 \times 10^4 \text{ volts}$$

At the expected 85% max. efficiency, the generator should develop a maximum potential of  $\sim 900$  KV, which in fact, it did.

The charge-carrying belt was constructed of unfilled silicone rubber (Shore A 55 hardness) reinforced with Dacron fabric. Highly resistant to ozone produced in the generator, it is long-wearing and enhances frictional charging. Current output of such a generator is difficult to predict due to the many variables involved. To develop as much current as possible, the belt must run as fast as practical; however, speed is limited by pulley bearings to approx. 117 rps. In our device, pulley circumference was 10.98", belt width was 4" and belt contact area per rotation of the two pulleys was 44 sq. in. While there are a number of ways to calculate current output expected, a rule of thumb is that one needs 50 sq. in. of belt/second passing over the rollers for each microamp of current generated. Thus,

$$117 (44) = 5148 \text{ in}^2/\text{sec of belt travel}$$

$$\frac{5148}{50} = 103 \mu\text{A max. output}$$

Although literature predicts 50-60% efficiency, this generator regularly produced 80  $\mu\text{A}$ ; i.e., was 78% efficient.

The belt pulley (roller) surfaces for internally excited generators contributes both to frictional charging and to polarity developed at the HV terminal. Practical extremes of the triboelectric series were chosen; solid nylon (+) and Teflon (-). By comparison, some typical small commercial units are equipped with less-effective wood and polyethylene rollers. If the top roller is Teflon, this combination will give a negative charge to the HV terminal, which in turn deposits a negative charge on the outer surface of canopy specimens. Reversing the belt rollers reverses polarity.

To calibrate operation of the generator for ESD testing, current measurement is no problem using microammeters to determine current into the generator and out of the canopy solar coating. But, measuring electrostatic kilovolt potentials is more of a problem. Various devices, such as absolute or commercial electrostatic voltmeters are expensive and sometimes erratic. The simplest way is to measure flashover voltage between spherical electrodes of identical size and shape, in air. Although polarity, wave form and air temperature, pressure and humidity affect accuracy, they can be corrected for. Ambient air conditions affect accuracy to around  $\pm 10\%$ , but by using Paschen Curves (ref. 3) extrapolated to one-million volts, plus correction factors, reasonably accurate determinations of high voltage can be made. These curves are for an air temperature of 20°C and 1013 millibar pressure. For other conditions, the following correction can be used.

$$d = \frac{p}{1013} \times \frac{(273 + 20)}{(273 + t)}$$

where t = temperature (°C)  
 p = pressure in millibars  
 d = correction factor voltage is to be multiplied by.

The voltage curve reference does not include a correction for humidity but humidity is reported to change flashover voltage by only 3-4%.

Tests of solar coatings were conducted both on full-size F-16 canopies and on 2' x 2' specimens (size chosen for convenience) cut from canopies. The earliest types of coatings, vulnerable to ESD damage, were tested first and served for comparison to ESD damaged canopies removed from aircraft.

Before starting each ESD test, the output of the generator was calibrated since Van deGraaff generators tend to perform erratically. Full-size canopies were mounted upright and the Van deGraaff generator was positioned a few inches from the canopy OML. The setup is shown in Figure 6. The 2' x 2' specimens were set up similarly (see Figure 7), with the concave (canopy IML) surface facing away from the generator. A current collecting busbar was attached at the lower edge of the IML surface and was connected through an ammeter to ground. As the generator was turned on and belt speed increased, a negative charge was applied to the canopy specimen. This in turn, transferred to the conductive solar coatings. When power was high enough to cause coating damage in susceptible coatings, evaporation paths were formed (see Figure 8). The resulting paths had the same appearance as those produced in actual flight. Examples of these are shown in Figures 9 and 10. Generator voltage required to do this was in the range of 200 - 400 KV. Current out of the canopies and canopy sections was about 80% of generator input current.

Final tests of Sierracin's new solar coatings were conducted both on panels and full-size canopies. The improved coating, S-373, is now being delivered in F-16 canopies. When the generator potential was raised to 800 KV, far above potentials expected in flight, no ESD damage occurred to the new solar coating. Even more favorable results were noted when we tested Sierracin's indium tin oxide sputtered coating, S-404 PP, upscaled for the F-16 ITM Program. Unintentional arc strikes to the cut edges of the 2' x 2' specimens showed discoloration where the arc struck gold-based solar coatings, but no discoloration or burned effect whatsoever occurred to the ITO specimens.

## CONCLUSIONS

The test methods and equipment used appear to duplicate in-flight ESD damage to F-16 solar coatings. Gold film evaporation paths evident in damaged canopies returned from service appear comparable, if not identical, to those produced in the same solar coatings tested in the laboratory. Sierracin-manufactured canopies with the new S-373 solar coating will therefore be more resistant to ESD damage than those produced in the past. The even newer indium tin oxide-based solar coating would be, if accepted by the Air Force, the ultimate in long-life solar coating for aircraft canopies. This development from the ITM Program also offers the added advantage of greater light transmittance and lower reflectance than gold film solar coatings.



## REFERENCES

1. Zeitler, R. T., "F-16 Canopy Static Charge Test Report," G. D. 16PR1687, General Dynamics, Ft. Worth Div., Ft. Worth, TX (Jan, 1981).
2. Tanner, R. and J. Nanevicz, "Radio Noise Generated on Aircraft Surfaces," SRI/AF33 (616)-2761, Stanford Research Institute, Menlo Park, CA (1956).
3. Mardiquian, M., "Electrostatic Discharge," Interference Control Technologies, Inc., Gainsville, VA (1986).
4. Gallagher, T. and A. Pearmain, "High Voltage Measurement, Testing and Design," John Wiley & Sons, New York, NY (1983).



**FIGURE 1**

**SOLAR COATED F-16 CANOPY**



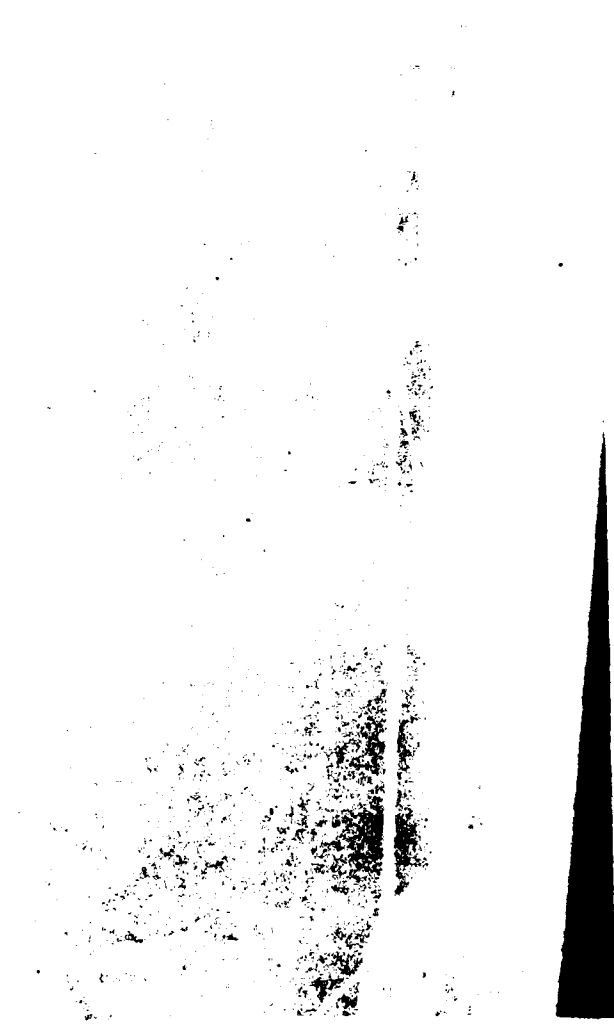
**FIGURE 2**  
**ESD DAMAGE TO SOLAR COATING**



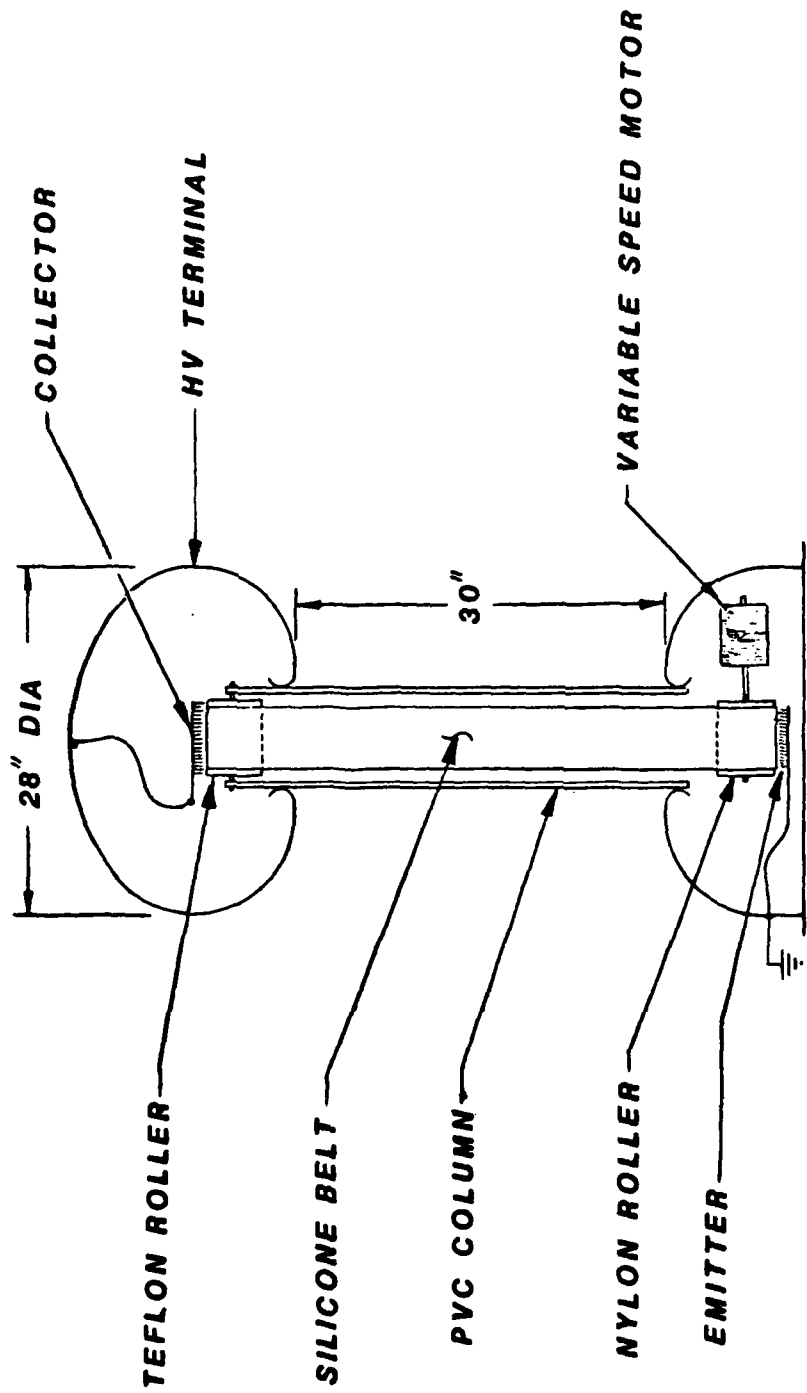
(FULL SIZE)

FIGURE 3

CLOSE UP VIEW OF COATING EVAPORATION PATHS



**FIGURE 4**  
**SOLAR COATING DAMAGE AT EDGE OF CANOPY**



**FIGURE 5**  
**CONSTRUCTION OF ELECTROSTATIC GENERATOR**

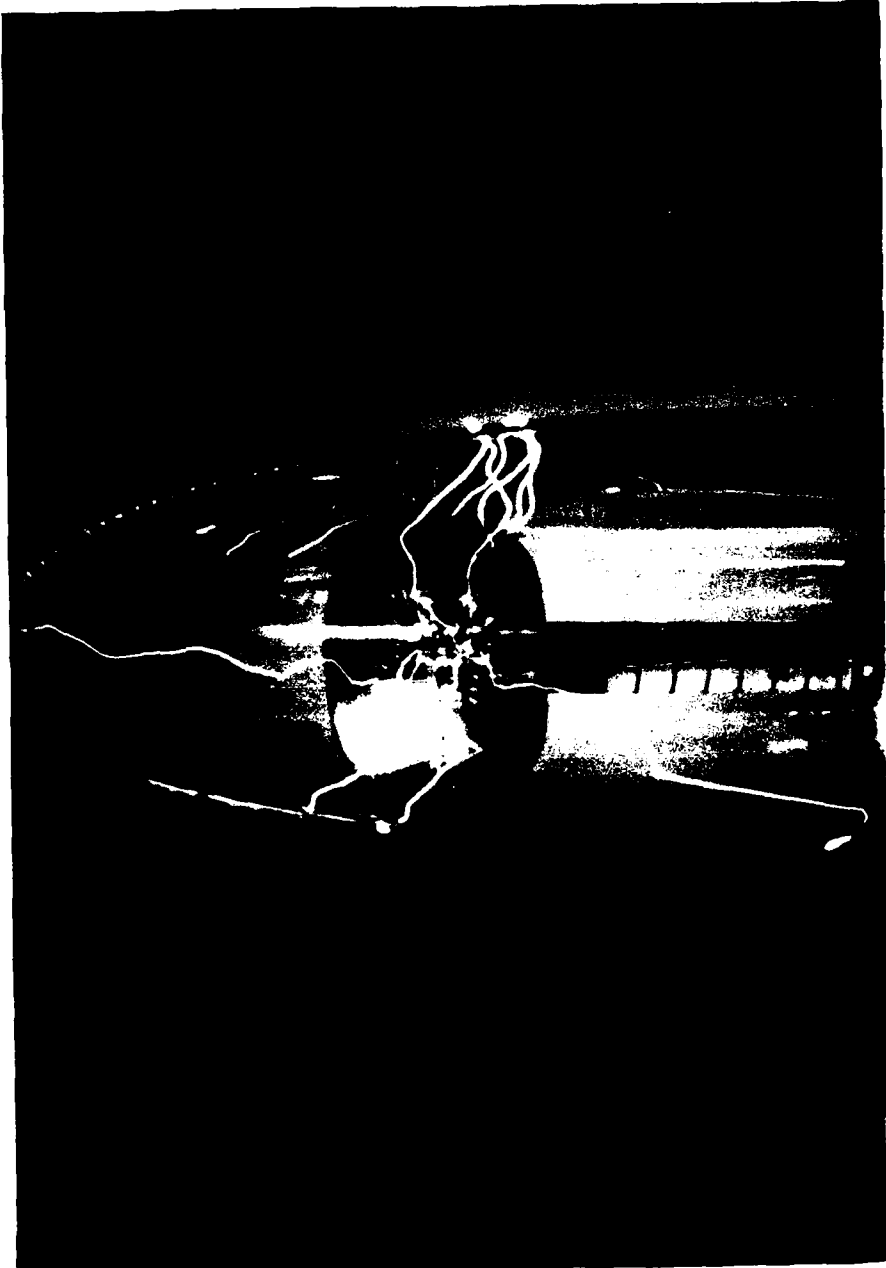


**FIGURE 6**  
**ELECTROSTATIC TESTING OF A SOLAR COATED F-16 CANOPY**

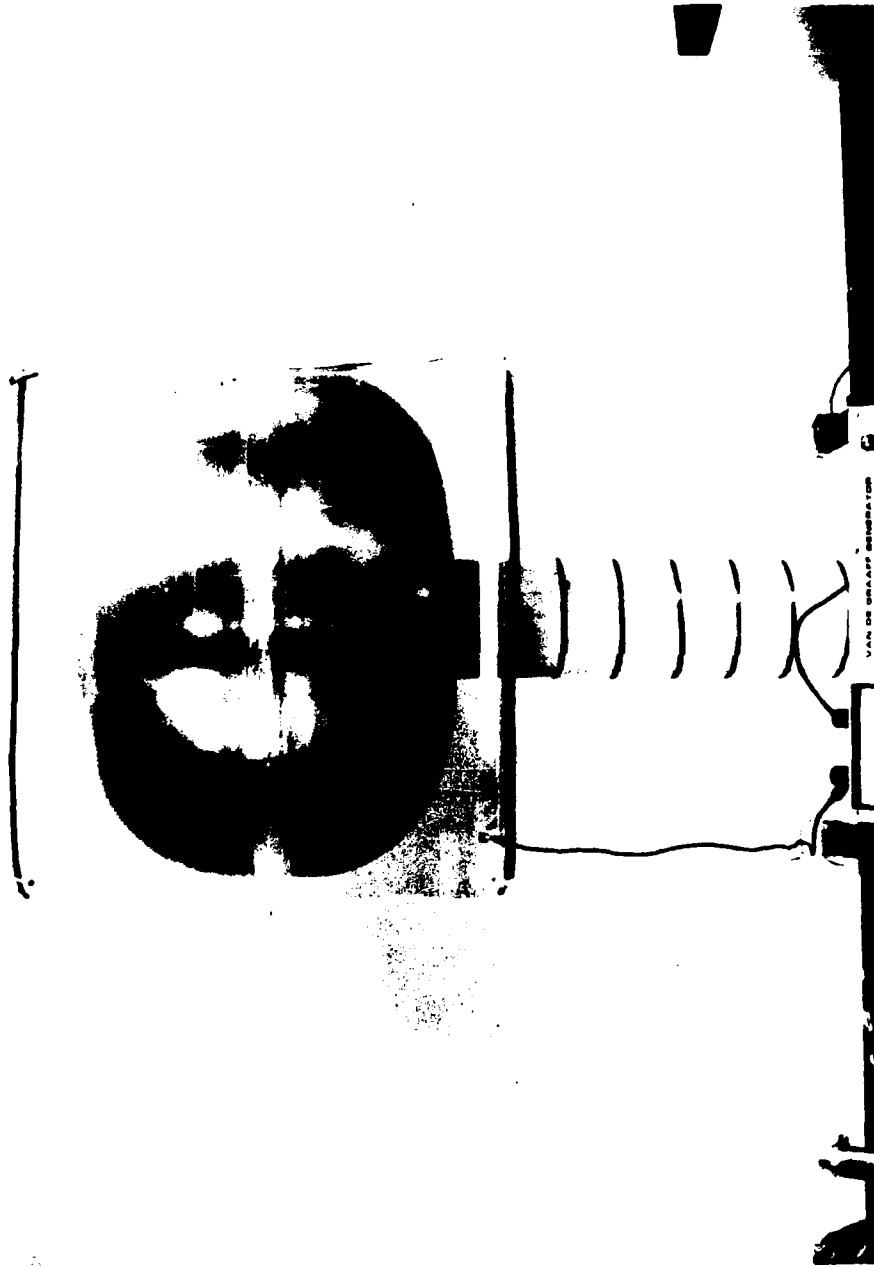


**FIGURE 7**

**TWO FT. SQUARE CANOPY SECTION ESD TEST**



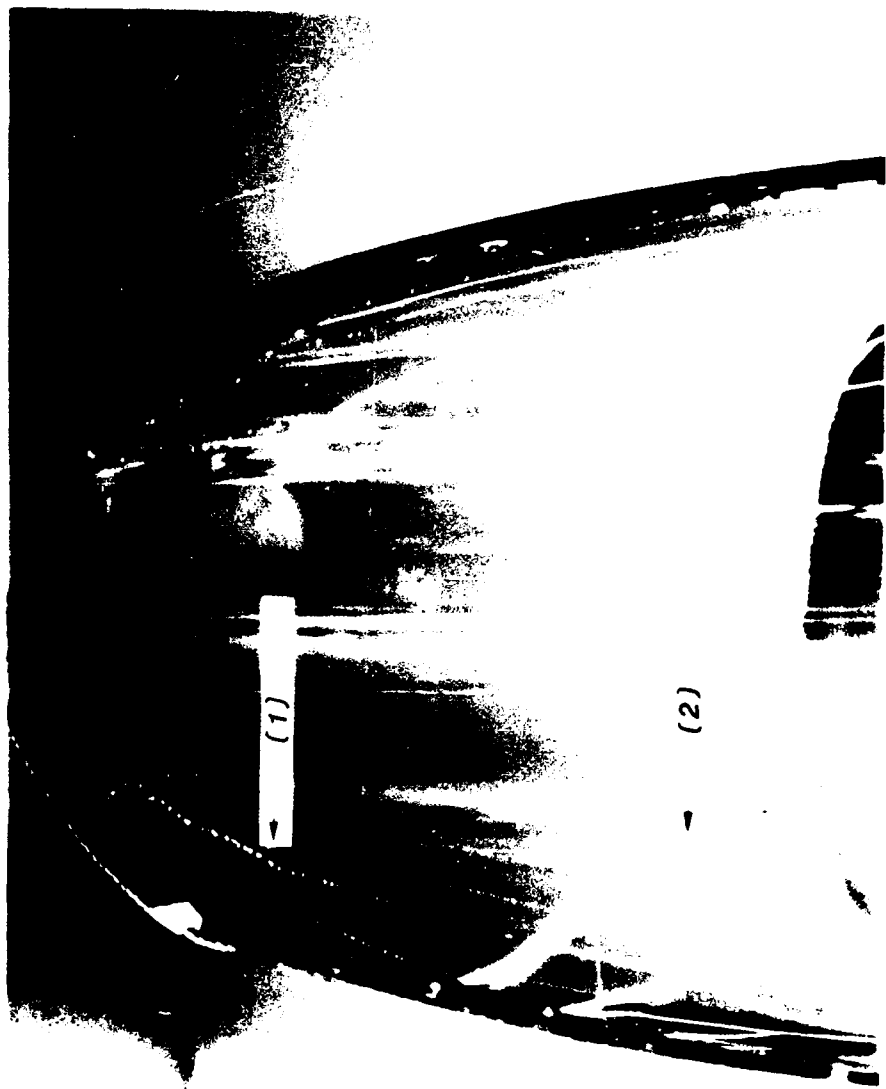
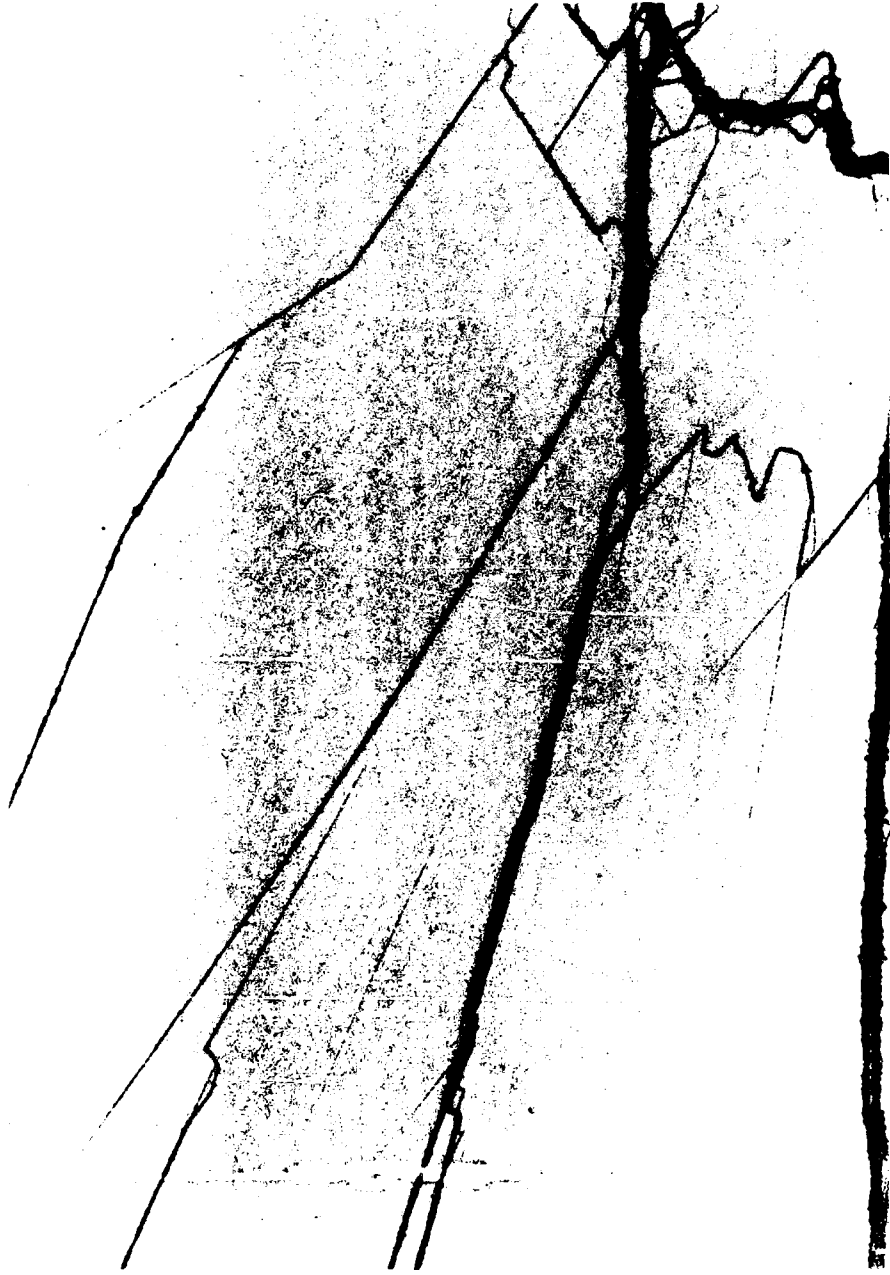


**FIGURE 8**

**FORMATION OF EVAPORATION PATHS DURING ESD TEST**

- (1) EVAP. PATH FORMING
- (2) ARCS ON CANOPY EXTERIOR



(FULL SIZE)

FIGURE 9

LABORATORY TEST INDUCED DAMAGE TO A FULL SIZE F-16 CANOPY



(FULL SIZE)

FIGURE 10

ESD DAMAGE TO SOLAR COATED 2 FT. SQ. CANOPY SPECIMEN

T-38 FLIGHT SERVICE AND LABORATORY TESTING  
OF PPG 5300 OUTBOARD LINER

James W. Myers  
PPG Industries, Inc.

## ABSTRACT

Prepared by: James W. Myers  
PPG Industries, Inc.  
Technology Development  
Huntsville, Alabama

Title: T-38 Flight Service and Laboratory Testing of PPG  
5300 Outboard Liner

PPG Industries, Inc. has developed an outboard liner material specifically formulated to provide complete isolation of the substrate to which it is applied. The thickness of the PPG 5300 liner is 30 mils and bonds directly to the substrate. Besides providing a much greater degree of substrate protection than thin coatings, PPG 5300 liner-faced transparencies offer superior abrasion-resistance, reduced weight, and are completely resistant to crazing. In addition, updated environmental-resistance testing has been performed which includes humidity exposure, ultraviolet radiation, chemical resistance, rain erosion resistance, accelerated and natural weathering, and abrasion resistance.

This paper covers the flight-testing of eight PPG 5300 liner-faced T-38 polycarbonate bird resistant student windshields, seven that have been in service since August 1986 at seven different Air Force Bases and one since July 1985 at NASA Langley. The fabrication and flight-testing of these units resulted from Contract F33615-81-C-3403 administered by Wright-Patterson Flight Dynamics Laboratory.

## INTRODUCTION

In 1983, PPG proposed a liner-faced polycarbonate T-38 Bird Resistant Student Windshield to Wright-Patterson Flight Dynamics Laboratory. This proposal was based on results that were seen during the laboratory testing of PPG's 5300 outboard liner. Laminated parasitic plies, such as commonly used acrylic, currently the most popular medium to protect polycarbonate from the environment in aircraft transparencies, add undesirable weight and are subject to stress crazing. Thin coatings also have drawbacks. They do not adequately protect the substrate from ultraviolet radiation nor do they protect the substrate from impingement type damage.

The use of polycarbonate as a substrate is in many ways an attractive alternative to glass in designing aircraft transparencies. The desirable characteristics of polycarbonate that make it useful as an engineering plastic are its outstanding impact strength, good oxidative stability, and lightweight. Undesirable characteristics include the tendency to craze or crack under stress, particularly when exposed to the environment or chemical solvents. Additionally, the susceptibility to surface degradation induced by ultraviolet light, and poor abrasion resistance are also undesirable. Therefore, the successful utilization of polycarbonate in aircraft transparency designs is dependent on the degree of the surface protection provided for the plastic.

This paper presents the results of extensive accelerated testing of the currently used formulation of PPG's 5300 outboard liner and the flight service testing of seven Air Force T-38's along with one NASA T-38 Student Windshield. PPG believes that PPG 5300 outboard liner is the best surface protective material to be developed for polycarbonate. Current outboard liner thickness is 30 mils and the liner is applied directly to the polycarbonate surface.

## ABRASION RESISTANCE

No single abrasion test is considered adequate to provide an accurate assessment of the abrasion resistance of transparent plastics used in aircraft transparencies because of the different types of abrasion actually encountered in service. For this reason three different types of abrasion tests were performed on the liner materials. Two of the tests are basically rubbing type abrasion tests and the third an impingement type test.

### BAYER ABRASION (ASTM F-735)

This test was developed by Bayer AG, West Germany and has been adopted by ASTM as a standard abrasion test method for abrasion resistance of transparent plastics used in aircraft transparencies. The test consists of quartz silica sand which is oscillated over the test specimen surface. The severity of abrasion is controlled by the number of oscillating cycles with 300 cycles being considered a relatively severe test for transparent plastics. Increase in haze is used as the criteria for measuring the severity of abrasion.

### SALT ABRADER (ASTM F-1128)

The salt abrader was developed by PPG several years ago as an impingement type test to simulate ice crystal erosion encountered on aircraft windshields when flying through certain types of clouds. The test consists of impacting the surface to be tested with salt crystals of specified size at a high velocity.

### TABER ABRASER (ASTM D-1044)

The Taber Abraser test is another well known ASTM abrasion test which has been in use for several years. This test consists of two abrasive wheels, to which a predetermined load is applied, which rest on the specimen surface. The specimen is fixed to a rotating table. As the specimen is rotated, the abrasive wheels abrade the surface of the specimen in a circular pattern.

### ABRASION TEST RESULTS

The results of the abrasion tests are given in Figures 1 and 2, and Table 1. The abrasion resistance of acrylic, stretched acrylic, and polycarbonate are also given for comparison purposes. This data shows that the abrasion resistance of the PPG 5300 is significantly superior to the acrylics and polycarbonate by all three abrasion tests used.

### HUMIDITY EXPOSURE

Cyclic humidity tests were performed on the liner materials on polycarbonate substrate in accordance with MIL-STD-810C, Method 507, Procedure I. This is a 10-day cyclic humidity test where the temperatures varies between ambient and 150°F and the humidity between 85% and 95%. After exposure, the specimens were inspected for any evidence of

degradation, adhesion loss, and change in light transmission or haze. The specimens were then tested for abrasion resistance using 300 cycles on the Bayer abrader to determine if the humidity exposure affected durability.

The results of the cyclic humidity tests are listed in Table 2. After exposure, there was no evidence of deterioration, loss of adhesion, and no significant change in optical properties. Abrasion resistance after exposure was not changed compared to unexposed material indicating durability was not degraded due to humidity.

#### ULTRAVIOLET RADIATION EXPOSURE

Accelerated weathering tests were performed on the liner materials using a carbon arc weather-ometer with intermittent water spray. The exposure was performed with the liner surface facing the light source and an exposure period of 1000 hours. After exposure, the specimens were subjected to 300 cycles on the Bayer abrader. The results of the ultraviolet radiation exposure are listed in Table 3. At the conclusion of the test, there was no evidence of liner degradation or adhesion loss and virtually no change in light transmission or haze. After abrasion, the haze increase was comparable to unexposed material indicating no change in abrasion resistance due to the ultraviolet exposure.

#### CHEMICAL AND STRESS CRAZE RESISTANCE

Stress craze resistance of PPG's 5300 liner on polycarbonate substrate was conducted in accordance with Federal Test Method Standard 406, Method 6053. This is the standard cantilever beam stress craze test used for transparent plastics. The tests were performed using a variety of fluids normally encountered by aircraft transparencies and are listed in Table 4. At the conclusion of the tests, there was no crazing, cracking, or other evidence of chemical attack.

#### SLED ABRASION TESTS

Since the PPG 5300 is relatively thick compared to coatings, the cantilever beam stress craze test is not considered entirely adequate for chemical resistance. For this reason, the PPG sled abrasion test was used to provide additional chemical resistance data. This test, illustrated in Figure 3, consists of a felt pad under a 1 1/2 psi load which is drawn back and forth over the specimen surface for



500 cycles using 400 mesh alundum abrasive. The test can be conducted dry with the abrasive only or wet with a variety of solvents.

The effect of the sled abrasion is determined by a subjective evaluation of the degree of scuffing of the substrate surface on a scale of 0 to 100 in which 0 indicates no effect and 100 indicates that the surface is virtually destroyed. This test is considered to be relatively severe. The PPG 5300 liner was tested using acetone, heptane, isopropyl alcohol, and a mixture of alcohol and water. The results of the sled abrasion tests are listed in Table 5 along with data for acrylic and polycarbonate. The data shows that the liner material significantly improves the chemical resistance of acrylic and polycarbonate.

#### WEIGHT SAVINGS

Substantial weight savings, approximately 1 lb/ft<sup>2</sup>, can be obtained using the PPG 5300 on transparencies that utilize laminated acrylic plies to isolate polycarbonate from the environment. For example, replacing the .125 outboard acrylic facing ply and the .060 interlayer used to bond the acrylic to the polycarbonate with .030 PPG 5300 liner results in a .95 lb/ft<sup>2</sup> weight savings. In a transparency having 10 sq. ft. of area using PPG 5300 liner would result in a weight savings of 9.5 lbs.

#### ULTRAVIOLET LIGHT PROTECTION

The surface of polycarbonate can be degraded by ultraviolet light and is particularly sensitive to wavelengths between 280-290 nanometers. Chain scission occurs at these wavelengths resulting in low molecular weight products which can cause surface embrittlement and loss of impact strength. PPG's 5300 liner will screen out virtually 100% of the UV light below 390 nanometers. The UV transmittance spectrum of 5300 liner is shown in Figure 4. A comparative spectrum of .100 poly 76 acrylic is shown in Figure 5.

#### FIELD TESTS

In July 1985, PPG supplied a prototype T-38 bird resistant student windshield with PPG 5300 liner to NASA Langley Research Center Figure 6. This windshield was requested to enable NASA to perform some specialized low level testing and to provide them with the qualified bird strike protection level of 4 lb. at 400 knots. Even though this windshield was an early prototype with barely acceptable

optics, NASA continued to fly the windshield after the special testing. NASA has accumulated 390 actual flying hours. One minor problem pertaining to the 5300 liner did develop during a flight to NASA Houston, a large hard shell bug was encountered in the right central area of the windshield. Some of the remains and a skid type mark was left on the surface of the 5300 liner. After a thorough cleaning to remove the remains, the skid mark was still visible, but after exposure to sunlight and several flights, the mark had disappeared. The reason for the disappearance is the "memory or self-healing characteristic" of the PPG 5300 liner. The self-healing characteristic is enhanced by warm sunshine or heat from a common hair dryer or heat gun. There has been no discoloration, delamination, peeling, crazing, loss of light transmission, or haze increase.

Under contract F33615-81-C-3403 with Wright-Patterson Flight Dynamics Laboratory, seven T-38's have been retrofitted with the bird resistant student windshield with PPG 5300 liner. These parts were installed at Randolph AFB, Texas, starting in July 1986 and completing in November 1986. After installation, the aircraft were assigned to seven different air training command bases shown in Figure 7. Upon release to the ATC bases, a tracking and evaluation process was started with the pilots completing a flight-log and evaluation form after each flight until September 1987. During this time, 1522 evaluations were completed and 1661 flight hours logged. Individual inspections were also performed by PPG in April and December 1987 along with maintenance and air-crew debriefings.

A conservative estimate would be in excess of 4,000 flight hours to date. During debriefing and inspection, no problems with the PPG 5300 liner have been discovered. In April 1987, the Sheppard AFB unit was severely abraded in an approximate 4 inch area by an unknown object, possibly a screwdriver or helmet rivet. This area was approximately 1/8 to 3/16 wide and .010 to .015 in depth. When this unit was re-examined in December 1987, the area was barely able to be seen and had seen no special treatment. Comments by pilots and maintenance personnel were completely positive with the one most positive comment being "The longer they fly and more exposure received, the better they look". Again, as in the NASA unit, there has been no discoloration, delamination, peeling, crazing, loss of light transmission, or haze increase on any of the units.

## CONCLUSIONS

PPG has developed a new material that has overcome the deficiencies of existing protective systems for polycarbonate aircraft transparencies. Extensive accelerated and field testing has shown PPG 5300 liner to be superior to thin coatings and laminated acrylic plies. The liner has been proposed on various existing transparencies and new designs. Although PPG-5300 liner has been used primarily on outboard surfaces, future development projects will investigate a variety of applications including the following:

- Thinner version for inboard protection
- A photochromic version
- Antistatic capabilities
- Laser defeat
- Flow coating
- High temperature protection

**TABLE 1**  
**TABER ABRASER TESTS RESULTS\***

<b>SUBSTRATE</b>	<b>HAZE INCREASE (%)</b>
<b>5300/POLYCARBONATE</b>	<b>3.8</b>
<b>PLEXIGLAS 55</b>	<b>19.8</b>
<b>STRETCHED ACRYLIC</b>	<b>29.5</b>
<b>POLYCARBONATE</b>	<b>36.4</b>

\* 100 CYCLES PER ASTM D-1044

**TABLE 2**  
**RESULTS OF CYCLIC HUMIDITY EXPOSURE**

MATERIAL	INITIAL OPTICAL		AFTER CYCLIC HUMIDITY		HAZE AFTER HUMIDITY AND ABRASION (%)
	L.T. (%)	HAZE (%)	L.T. (%)	HAZE (%)	
5300	88.9	1.86	88.9	2.66	3.76

**TABLE 3**  
**RESULTS OF WEATHEROMETER EXPOSURE (1000 HOURS)**

MATERIAL	ORIGINAL OPTICAL		AFTER U.V. EXPOSURE		HAZE AFTER U.V. AND ABRASION (%)
	L.T. (%)	HAZE (%)	L.T. (%)	HAZE (%)	
5300	88.9	1.86	89.6	3.23	3.87

## **TABLE 4**

### **SOLVENTS USED IN CRAZE RESISTANCE TESTS**

**JET FUEL (JP-4)**  
**ISOPROPYL ALCOHOL**  
**ETHYLENE GLYCOL**  
**LUBRICATION OIL (MIL-L-7808)**  
**GREASE (MIL-G-23827)**  
**HYDRAULIC FLUID (MIL-H-5606)**  
**AIRPLANE WASH (MIL-C-25769)**  
**BUG REMOVAL FLUID (P-6009)**  
**WINDSHIELD CLEANER (MIL-C-18767)**

**TABLE 5**  
**RESULTS OF SLED ABRADER TESTS**

MATERIAL	DRY	ABRASION RATINGS WITH CHEMICALS			ISOPROPYL ALCOHOL AND WATER (50/50)
		ACETONE	HEPTANE	ISOPROPYL ALCOHOL	
5300	70	4	50	30	30
ACRYLIC	70	80	70	70	60
POLYCARBONATE	80	100	70	70	60

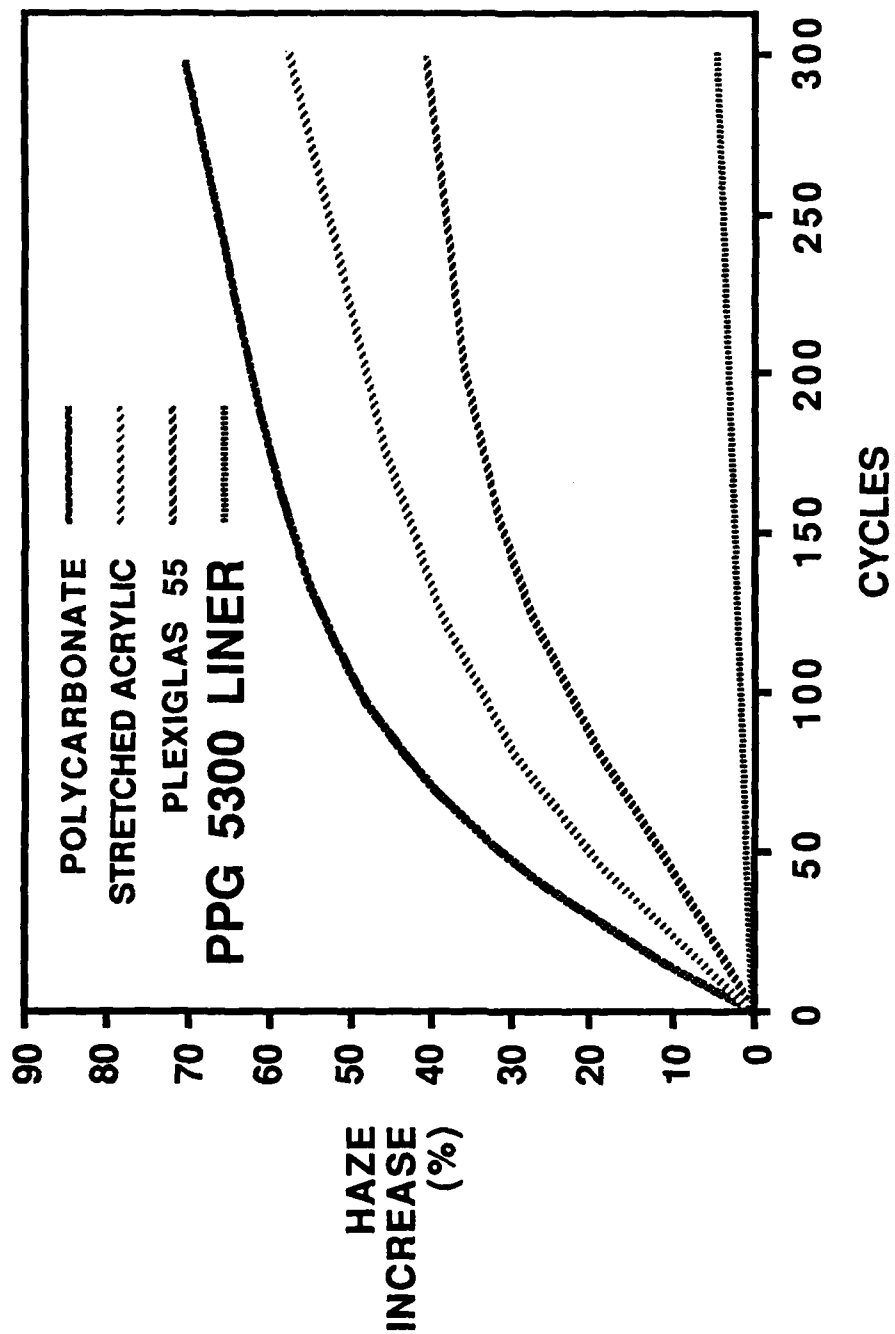


**FIGURE 1**  
**BAYER ABRADER TEST RESULTS**



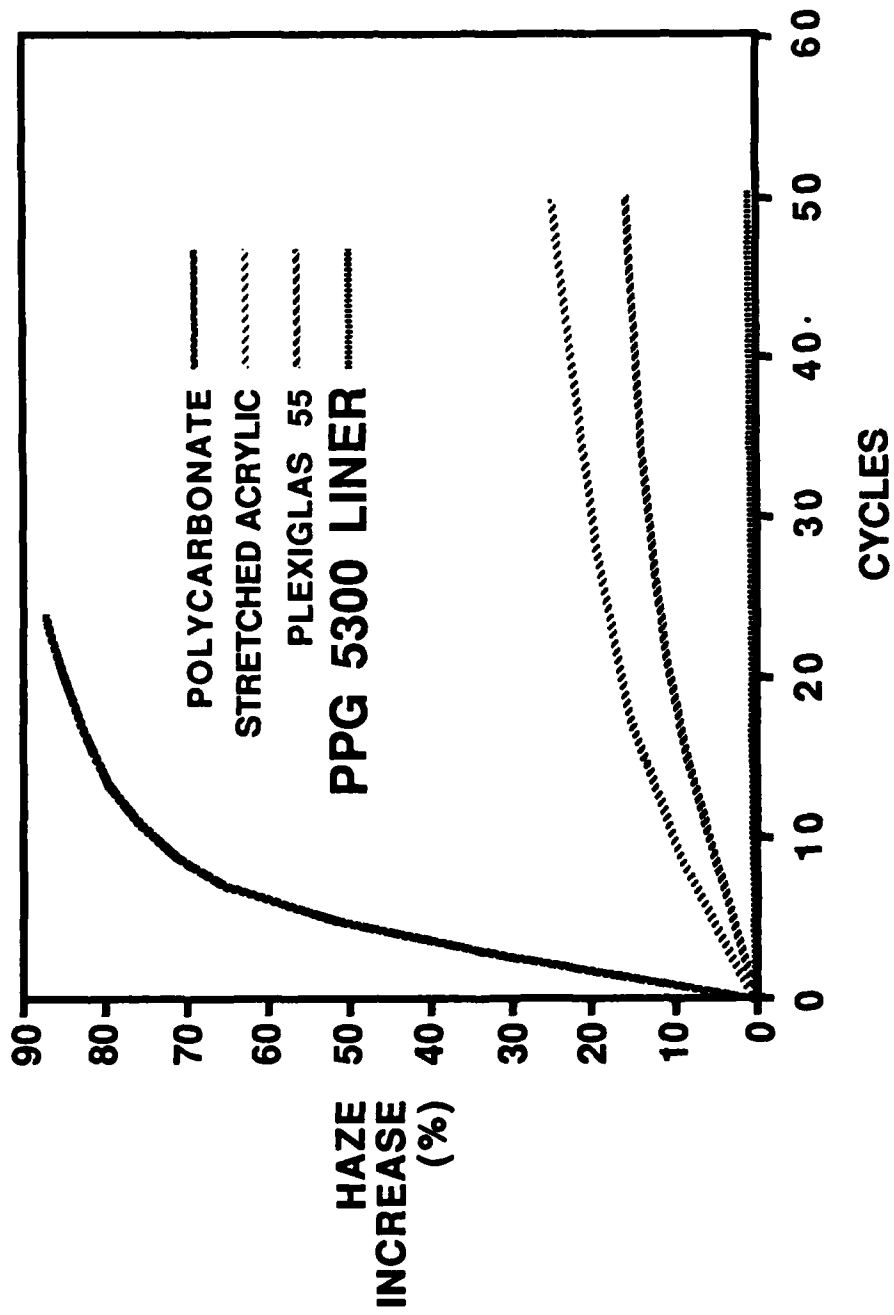


**FIGURE 2**  
**PPG SALT ABRADER TEST RESULTS**

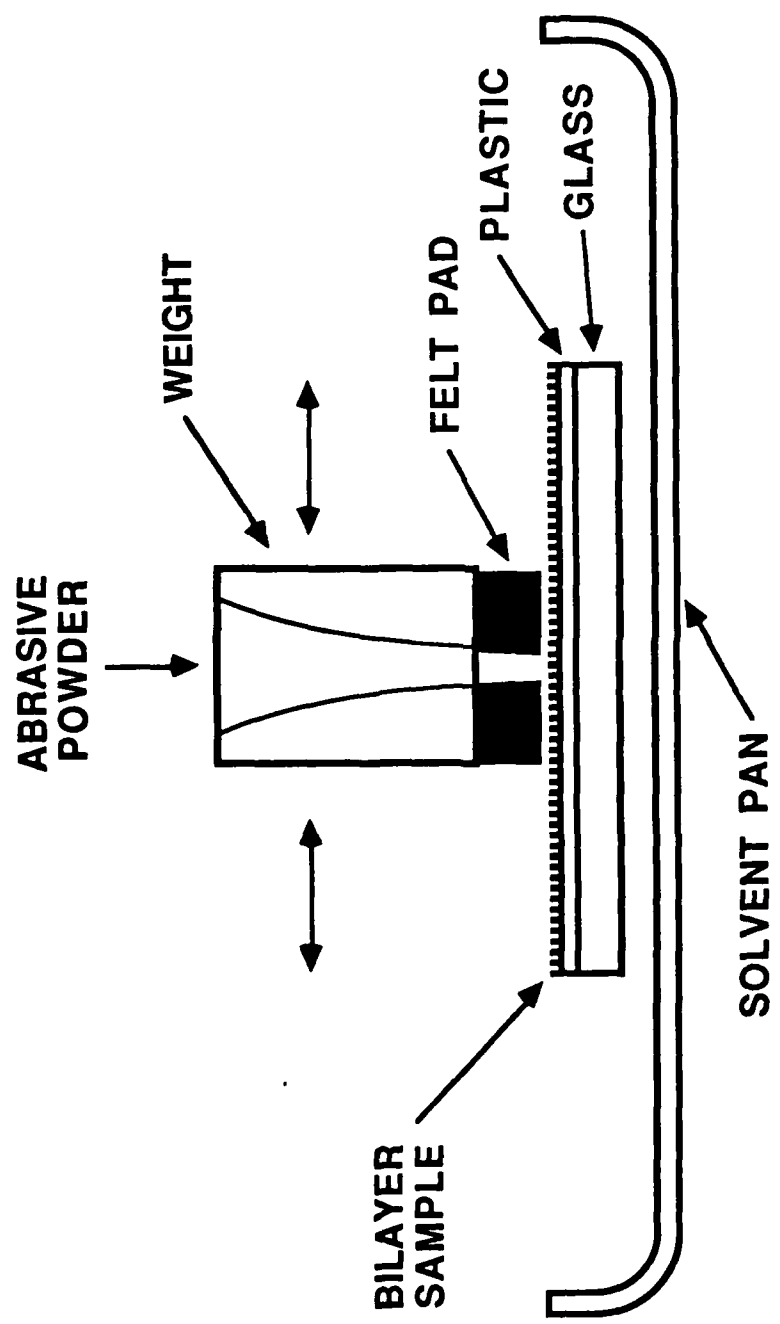


**FIGURE 3**  
**MODIFIED SLED ABRADER**

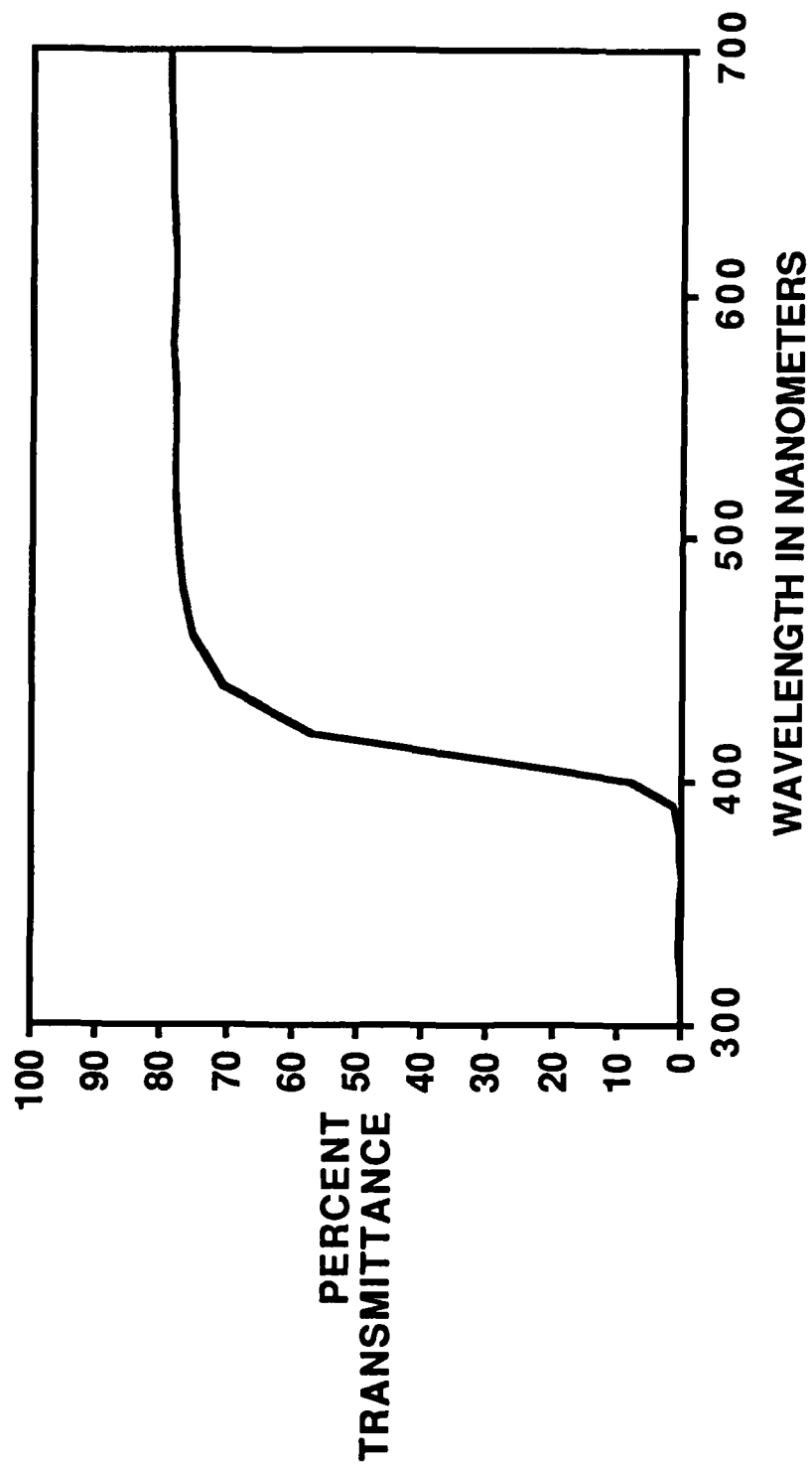


**FIGURE 4**  
**UV TRANSMITTANCE SPECTRUM**  
**5300 LINER**

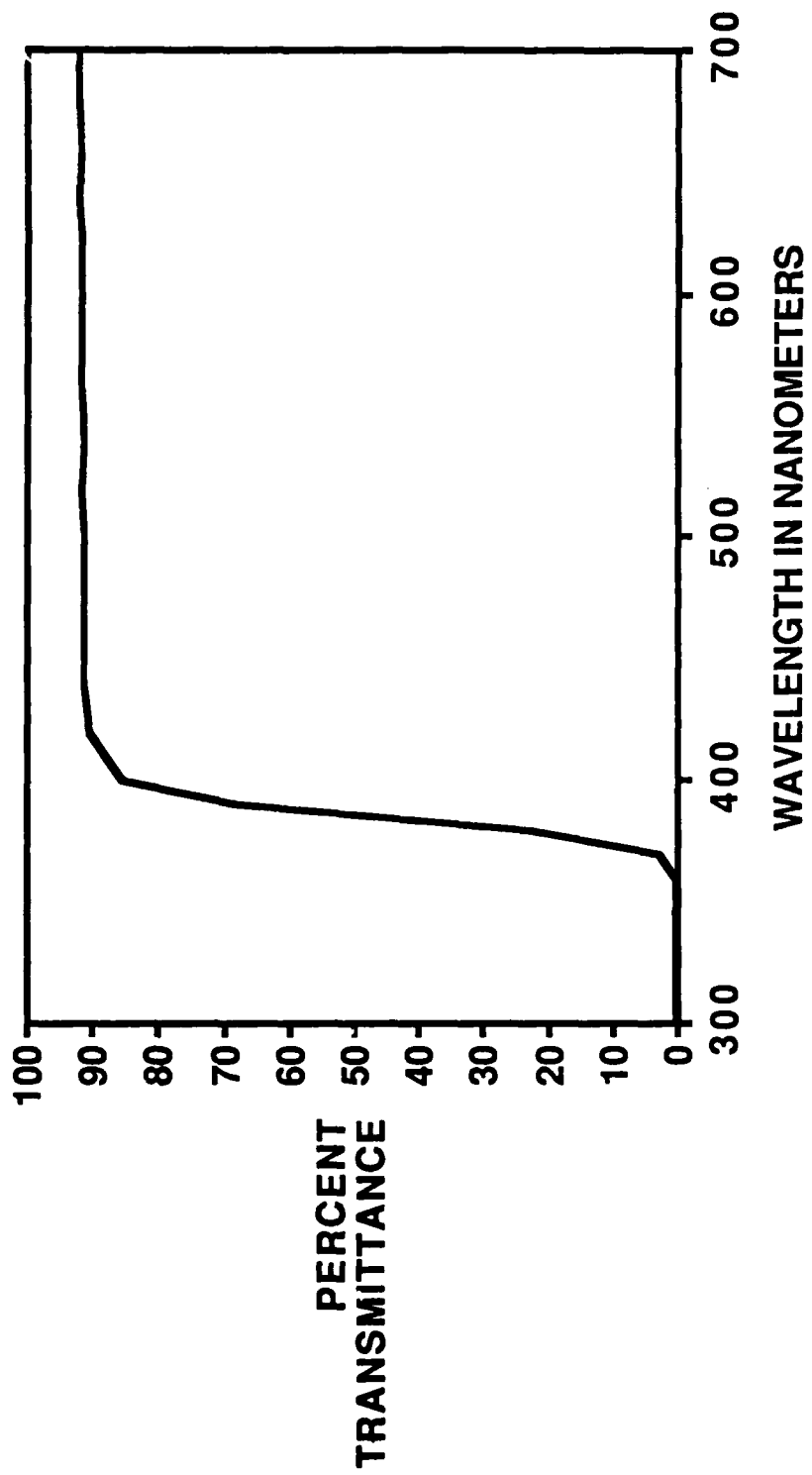


**FIGURE 5**  
**UV TRANSMITTANCE SPECTRUM**  
**.100 POLY 76 ACRYLIC**

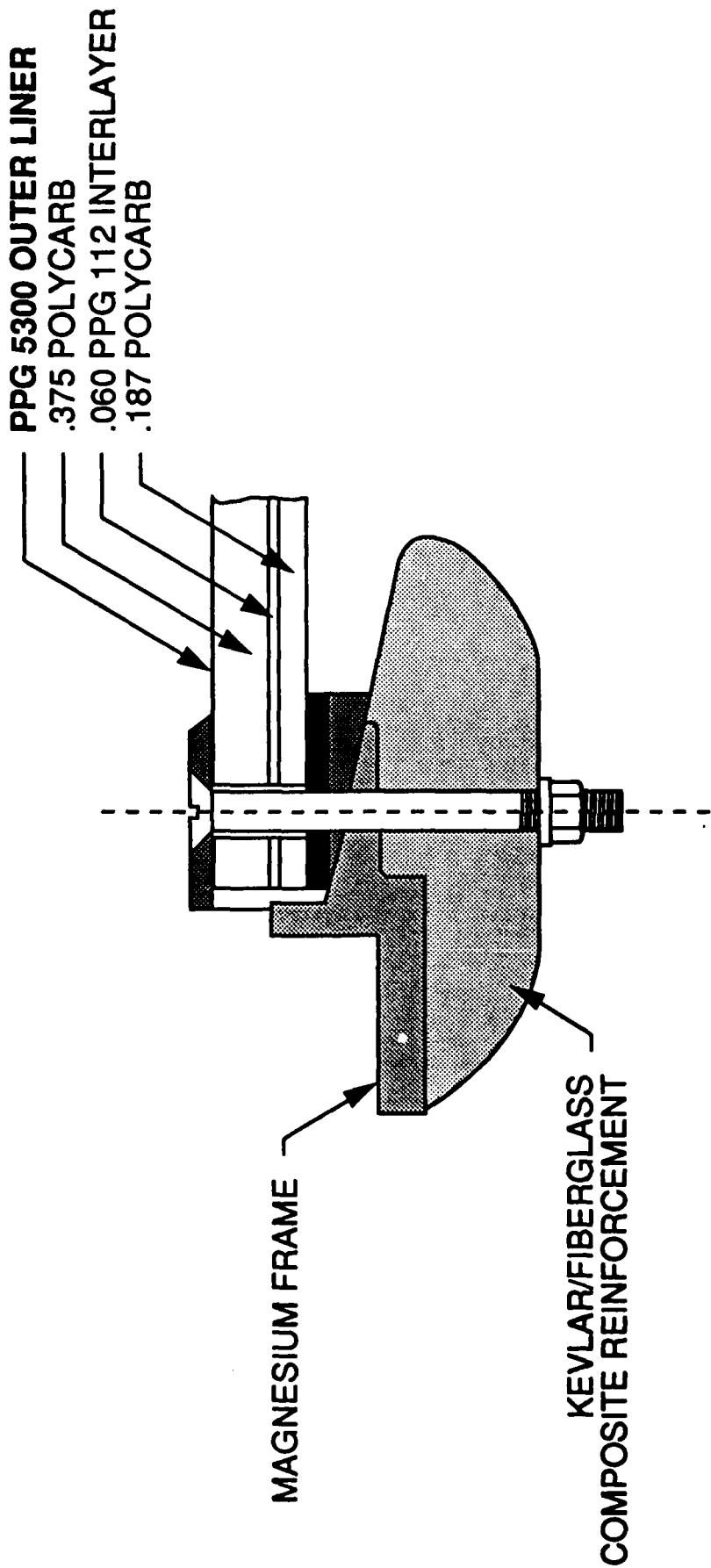


**FIGURE 6**  
**T-38 LAMINATED CROSS SECTION**

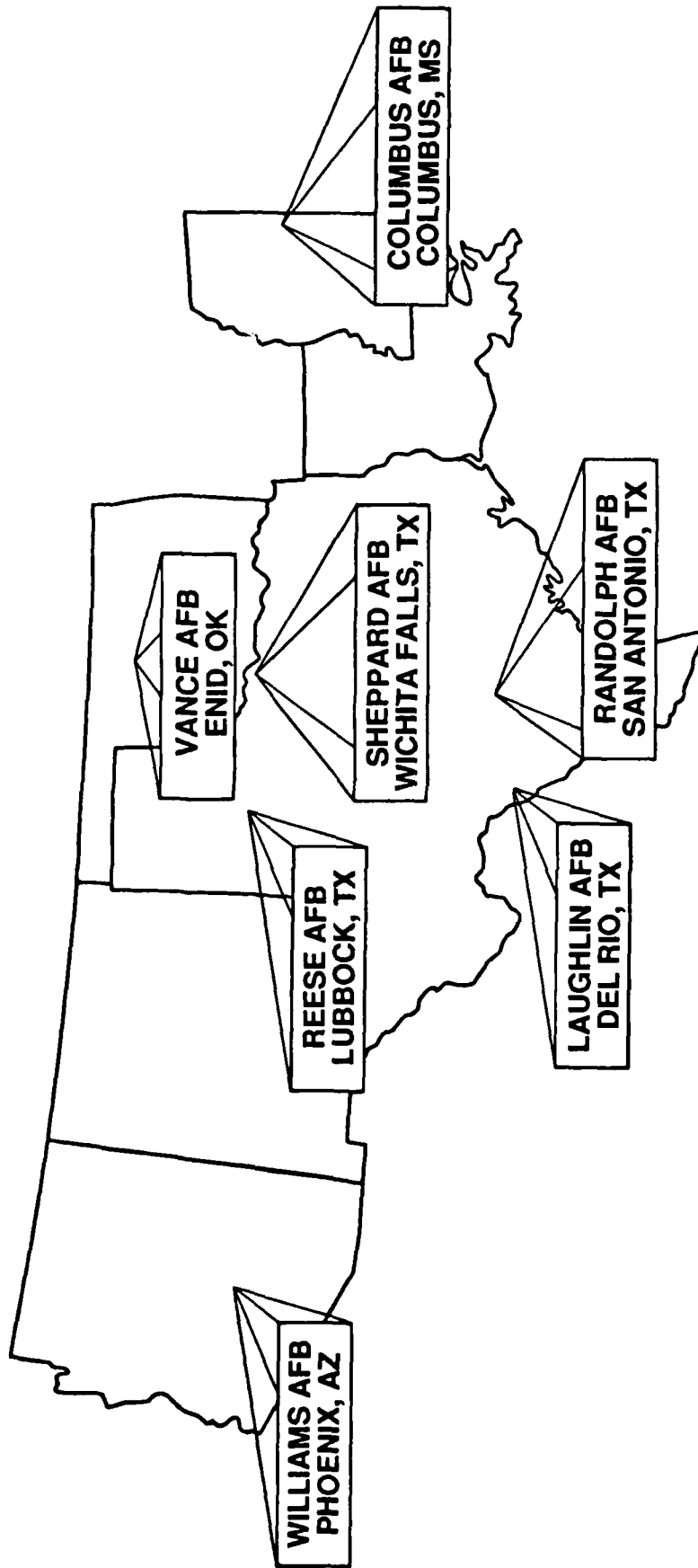


**FIGURE 7**  
**AIR FORCE AIR TRAINING COMMAND**  
**BASE LOCATIONS**

IMPROVED OPTICAL INTERLAYER ADHESIVES  
BOOST PERFORMANCE OF VISION SYSTEMS

Madhu "Dolly" Baile  
Kent R. Larson  
David G. Coble

Dow Corning Corporation

IMPROVED OPTICAL INTERLAYER ADHESIVES  
BOOST PERFORMANCE OF VISION SYSTEMS

Madhu "Dolly" Baile  
Kent R. Larson  
David G. Coble

Dow Corning Corporation  
Midland, Michigan

ABSTRACT

Liquid and sheet silicone laminating adhesives provide the clarity, adhesion, and performance characteristics required by aircraft windshield and canopy designs. Recent breakthroughs in primers, adhesives, and production technology ensure that these adhesive systems will continue to meet the evolving needs of aerospace applications.

Dow Corning has standardized primer spraying techniques to improve wet-out to plastics and bonding strength without affecting clarity. New statistical process control methods ensure consistent, high-quality production lots of both primers and adhesives.

The optical clarity of silicone laminating adhesives (less than 2.0% haze at 100 mil) is derived from the innovative wet-process hydrophobic (WPH) silica technology. The interlayers remain flexible, absorb differences in the rates of expansion and contraction of various substrates, and prevent delamination during extreme temperature cycling (from -54 to 204°C). Better understanding of the adhesion mechanism has enhanced performance dramatically. New release liners have improved the release of both 25- and 50-mil interlayers.

Liquid cast-in-place adhesives are particularly suited for users equipped to handle castable liquids. Recent composition changes have improved adhesion of the liquid systems, and the elimination of air entrapment has improved the quality of the laminates.

Silicone interlayer adhesives have low modulus, impact resistance, high dielectric properties and, unlike their nonsilicone thermoplastic counterparts, can withstand ultraviolet exposure and humidity without impairing adhesion or optics. These products are currently being used on the F-111A strategic bomber, V-22 Osprey prototype aircraft, and commercial aircraft. The adhesives are also being investigated in Europe for similar applications.



## INTRODUCTION

Optically clear, silicone laminating adhesives are designed for laminating lightweight, high-strength, high-performance aircraft windshields and canopies. These vision systems are laminates of glass, acrylic, or polycarbonate. The silicone interlayer adhesive bonds the layers of the laminate and reinforces its strength. Unlike nonsilicone sheet adhesives, silicone sheet adhesives retain adhesion and structural integrity, without yellowing, in temperatures cycling from  $-65^{\circ}\text{F}$  to  $+350^{\circ}\text{F}$ . Available in both sheet and liquid form, silicone interlayer adhesives have a range of properties which allow quality laminates from glass/plastic, plastic/plastic, or glass/glass substrates. Dow Corning offers each adhesive as a total system including adhesive, primer, application instructions, and technical service and support.

The technology behind these vision systems continues to evolve and both the processing and performance of the silicone interlayer adhesives are evolving with it. This paper will discuss the recent process and product improvements in sheet and liquid silicone interlayer adhesives and their primers.

## DISCUSSION

### Primer

The successful adhesion of any interlayer material depends on the quality of the prime coat used to prepare the substrate. The prime coat actually creates the bond between the interlayer and the substrate. The primers developed by Dow Corning penetrate the substrate, forming a physical association. The primer also forms a diffused interphase with the silicone elastomer. If the primer is a silicone primer, it forms a molecular association with the elastomer.

Two prime-coat materials are available; both use a silane coupling agent. The first has an organic nature with siloxane functionality. We recommend this primer for plastic substrates whether the sheet or liquid interlayer adhesive is used. The organic primer is also recommended for use with sheet interlayer adhesive and glass. The second primer has a siloxane nature which forms a chemically bonded interface between liquid interlayer adhesive and glass and so is recommended for that application. These primers have no significant effect on the optical clarity of the interlayer or the substrate.

The primers described here can be applied by wiping, spraying, or flow coating. Because contaminants can affect optical properties, applicators should carefully prepare the substrate by washing with generous amounts of solvent. Best adhesion is obtained by priming the substrate so that an even, wet layer is left on the surface. After priming, the substrate should be dried before the interlayer is applied.

We have made several improvements to the interlayer primers. A new solvent system improves wet-out to plastics. Spraying makes primer application easier, and we have further defined this technique to provide more uniform coverage. By improving wet-out and coverage, the strength of the laminate bond is improved.

## Sheet Silicone Interlayer Adhesives

The high-quality optics of the silicone interlayer sheets are derived from wet-process hydrophobic (WPH) silica technology. This process creates optical clarity by controlling the particle size of the silica rather than attempting to match the refractive indices of the polymer and fillers. By using particles smaller than the shortest wavelength of visible light, optical clarity is maintained over a broad temperature range.

The sheet adhesive is easy to handle, does not require complex tooling, and maintains its optics and parallelism in sharp contours and complex windshield shapes. Standard silicone interlayer sheet stock is available in rolls of platinum-catalyzed, unvulcanized sheets, 25 or 50 mils thick, 56 inches wide, and 110 feet long. Sheet interlayers are also available in rolls supplied to specified dimensions. All interlayers are supplied between two protective liners, designed for easy release when removed by the end user before fabrication.

After the interlayer is in place, it is cured by heat, which activates the platinum addition reaction. It is important to maintain pressure prior to heating and during heating and cooling. Rate of both heating and cooling should be slow.

Both high- and low-durometer silicone interlayer sheet adhesives offer low plasticity with a tack-free surface. They are high-tensile, high-tear materials with 100% modulus at 70 to 250 psi. Both cure in less than 4 hours at 100°C. But the most important properties of an interlayer are optics and adhesion. If these are not of the highest quality, the performance of the interlayer and of the entire laminate is inadequate. The silicone sheet interlayers have excellent optical clarity with less than 2% haze at 100 mil thickness.

TABLE 1

### NOMINAL PROPERTIES OF INTERLAYER SHEET ADHESIVES

	<u>X4-4643</u>	<u>X4-4647</u>
Durometer, Shore A	52	38
Haze, % at 100 mils	1.7	1.5
Tensile strength, psi (MPa)	1400 (9.65)	1200 (8.27)
Elongation, %	600	775
Modulus at 100% strain, psi (MPa)	250 (1.72)	70 (0.48)
Tear strength, Die B, psi (KN/m)	170 (29.7)	150 (26.2)
Specific gravity	1.12	1.12
Refractive index	1.413	1.413
Light transmittance, %	94	94
Plasticity, mils	130	130

Adhesion is also excellent, with lap shear adhesion at over 300 psi for most substrates. Average room-temperature peel adhesion for high-durometer sheet ranges from 43 pli for polycarbonate to 58 pli for Plex 2. Peak peel adhesion for high-durometer sheet is 96 pli for Plex 2; peak peel adhesion for low-durometer sheet is 110 pli for ITO-coated glass.

TABLE 2  
PEEL ADHESION OF SHEET ADHESIVES

<u>Substrate</u>	<u>X4-4643</u>	<u>X4-4647</u>
Lap shear adhesion at 50% RH, psi (polycarbonate, acrylic, glass)	>300	>300
Average peel adhesion, pli, RT		
Plex 55	46	64
Plex 2	58	--
Polycarbonate	43	50
Glass (ITO coated)	47	48

Mode of failure was cohesive for all samples.

Sheet interlayer adhesives can also be formulated to a customer's specific requirements. Dow Corning will work with laminate manufacturers on requests for custom sheet.

There have been several recent improvements to the sheet adhesives. The release liners now maintain Keil release strength for both 25- and 50-mil interlayers below 50 grams throughout the product shelf-life. Some inconsistencies in adhesion were found to be caused by a weak boundary layer within the silicone, not at the primer/substrate interface. A modified composition provides instant optimal adhesion and minimal standard deviation in peel, with physical and mechanical properties similar to the original interlayers.

An outer wrapping has improved the shelf-life of the interlayer roll. We recommend that, after opening and using the roll, the user rewrap the roll to maximize shelf-life. Another roll width will soon be available--we are optimizing a 72-inch-wide interlayer.

Statistical process control methods help ensure production lots of the highest quality. Dow Corning determines manufacturing capability and writes specifications based on continuous monitoring of the process and of properties such as haze.

## Liquid Silicone Interlayer Adhesives

Dow Corning can now supply optical-grade liquid silicone interlayer adhesives. Liquid silicone interlayer adhesives are particularly useful to those equipped to handle castable liquids. These resin-reinforced liquid systems are clear because the resin particles are so small that they do not scatter light. In addition, the resin is soluble in a polydimethylsiloxane polymer and does not introduce water into the system.

Liquid interlayer adhesives are supplied in two components, which begin the curing process when mixed. Two types of liquid are available: low and high viscosity.

The optical clarity, tensile strength, and modulus of the liquid systems are similar to those of the sheet systems. Adhesion is improved because of some recent composition changes. A new additive acts as a crosslinker and ensures consistently reliable adhesion when used with the appropriate silicone primer. This breakthrough is especially significant for acrylic and polycarbonate, which have traditionally been the most difficult to adhere to.

TABLE 3  
NOMINAL PROPERTIES OF LIQUID ADHESIVES

	<u>Low Viscosity</u>	<u>High Viscosity</u>
Viscosity, cps	7,000	50,000
Durometer, Shore A	50	30
Haze (300 mils thick), %	2	2
Tensile strength, psi (MPa)	1000 (6.9)	400 (2.8)
Elongation, %	100	200
Modulus at 100% strain, psi (MPa)	--	200 (1.4)
Tear strength, Die B, ppi (KN/m)	10 (1.75)	40 (5.25)
Light transmittance, %	92	95
Lap shear adhesion, psi (MPa)	200 (1.38)	--
Failure mode, % cohesive	90	90

Other improvements in liquid silicone interlayers include the elimination of air entrapment and the on-going development of a lower viscosity (200-7000 cps) liquid interlayer.

### Commercial Status

Sheet adhesives are qualified and being used on F-111A strategic bomber, V-22 Osprey prototype, and a commercial aircraft. They are being evaluated for

Eurofighter in Europe and advanced tactical fighter in the United States. Sheet adhesives are also being investigated for military tank unity vision systems.

M1-tank periscopes and vision blocks use a liquid adhesive. We are developing another liquid adhesive for some proprietary aircraft windshields.

#### SUMMARY

Dow Corning offers a full range of premium, optically clear, silicone interlayer materials and interlayer primers for both military and commercial aircraft. Recent improvements in the interlayer systems ensure that these products will continue to meet the evolving needs of modern aircraft.

TRANSPARENCY SYSTEM MISHAPS

Malcolm E. Kelley  
AFWAL/FDER

## TRANSPARENCY SYSTEM MISHAPS

Malcolm E. Kelley  
Air Force Wright Aeronautical Laboratories  
AFWAL/FDER  
Wright-Patterson Air Force Base, Ohio

### ABSTRACT

Aircraft incident reports that involved the transparency system and cockpit pressurization system were reviewed. Some interesting trends and lessons to be learned were noted. Both positive and negative lessons were learned, and some comments provided concerning what could be done with present and future aircraft to retain the positive and avoid the negative lessons learned. Specific areas include cockpit pressurization systems, canopy latching systems, and transparency heating systems (both hot air and electrical). Some ideas for canopy rigging and latching systems and cockpit pressurization systems are provided, along with suggested requirements for detection and warning systems for latching and pressurization problems. Some concepts for transparency heating system controls which would prevent overheating damage are also provided.

## TRANSPARENCY RELATED MISHAPS

1. Analysis was performed of mishap reports which were summarized and compiled in a document provided by the Air Force Inspection and Safety Center (AFISC/SERD). The 21 June 1988 document includes mishaps for a two year period (June 86 to June 88).

a. Some mishaps are known to not be reported in the AFISC document, so conclusions on particular failure modes should be recognized as being based on there being at LEAST that number of failures. For example, I was told of another F-16 birdstrike that blew out the rear portion of the canopy. Also noteworthy and absent is the F-111 windshield birdstrike that caused major cockpit damage when a bird punched through the windshield.

b. At one base a C-12F aircraft had two mishaps, both blamed on maintenance folks using abrasive and harmful chemicals for cleaning side windows. One aircraft had a side window outer face ply crack, another had a side window blow out of its frame. NOTE: For the window to blow out completely also suggests the sealant may not be too good. These windows (I believe) are two ply acrylic.

c. Some other acrylic designs broke out of their frames in flight. Fortunately, there were no serious injuries or aircraft losses. The "broke out of frame" failures occurred with an A-7 canopy, F-4 canopy, T-38 canopy, a C-130 side window (they knew it was cracked and flew it anyway), and two small sliding helicopter windows on the CH-3. Two polycarbonate parts made the report, the F-111 BIRT canopy that blew out in flight and an F-16A birdstrike that caused a 2 foot by 3 foot piece to blow out behind the pilot. A notable "almost" was a B-52 copilot's hatch. It had the inner structural ply crack, but after feeling the inner surface and NOT feeling the crack, they concluded it was the outer face ply and flew the whole mission, to include high altitude flight. It actually was the inner structural ply that was cracked and they incorrectly decided it was the outer ply. It held together until they landed, fortunately.

d. There were nine reported mishaps due to the hot air system melting the front of F-15 windshields. Since these reports would usually be optional, there may be a LOT more. The F-111s also have a problem, but the F-111 Wings have not sent in any reports on that area.

(1) One F-15 prototype windshield design being considered is an acrylic/polycarbonate laminate. We are



concerned that if a monolithic acrylic can't take the hot air, the chances of a laminate giving up the ghost after a much shorter exposure seems excellent.

(2) One way to prevent such problems would be a cockpit switch modification. This would be most effective as a feature on a new aircraft, since any retrofit actions are expensive with existing aircraft. As a retrofit, the switch modification would be applicable (at least conceptually) to many aircraft, to include F-15 and F-111. Windshield failures are caused by the aircrew or maintenance troop forgetting the hot air was on. I would replace the on/off switch with an on/off switch where the "on" position was a timer. After five minutes (for example) the switch would turn off automatically. A variation on that theme (for F-15 primarily) would have a switch cycling on and off - on for three minutes, off for 1 minute, etc. it could have a high and low setting (another variation) plus the off position. Low would be two minutes on, one off; high would be four on, one off.

e. Other aircraft with windshield heating mishaps reported included the A-19 (three center windshields cracked from electrical heating problems, C-12F (outer acrylic ply of pilot's (left) windshield shattered, device heat possible cause), C-20A (copilot windshield outer ply shattered due to arcing at buss bar - moisture related), and C-130 (three aircraft had smoke and flames from windshield heating, two of the three involved using fire extinguisher to put out the fire).

f. Apparently aircraft manufacturers are getting smarter with canopy latching mechanisms and warning systems, as the "canopy lost in flight" seems to primarily involve the older aircraft. Aircraft that had the canopy frame depart in flight were A-7D (1 event), A-10A (2), A-37B (1), F-106 (1), F-4 (3), F-5E (4), T-38 (4), T-33 (1), and F-15 (1). An F-15 with a pressure leak had the canopy out of adjustment, giving a false locked indication (lucky with that one). Also getting a mention was an F-4 that was unlatched along one side (gapped open in flight due to pressure), and an F-111 canopy hatch that opened in flight. The F-111 was the only aircraft that crashed, and the F-111 crew (both killed) were the only serious injuries.

g. Aircraft designers seem to have mixed success with cockpit pressurization and pressure seals.

(1) The T-38 has by far the most problems, with 37 pressure failures that prompted incident reports. The T-38 apparently has no warning system other than the breathing difficulties or physiological symptoms of the aircrew, who then

check the pressure gauge. the canopy and windshield seals are wearing out and when a failure occurs they often find multiple problems. Failed systems covered by the 37 total mishaps were canopy seals (27), windshield seals (10), seal hoses (3), and pressure regulators (2).

(2) The F-15 is in second place with 12 mishap reports due to pressurization problems. Five of the 12 were canopy seal failures, and one of the reports stated the seals were badly designed, with both rain and pressure seals becoming worn rapidly. I suspect the canopy latching system might not be optimum from a maintenance point of view also. One of the canopy seal failures was caused by the canopy rigging being out of adjustment causing both a seal hole and a false locked indication. Two pressure leaks were due to frame rigging (bellcrank adjustment for one, roller out of detent for the other), and three pressure leaks were attributed to gradual canopy warping. Warping? Sounds more like rigging problems plus frame and latching system design problems, perhaps aggravated by: (1) poor quality control for new canopies, new frames, and/or inadequate criteria for the assembled frame/transparency, and (2) poor analysis of failures and resulting non-wonderful mishap report messages. For example, how can "warping" cause major pressure leaks to occur simultaneously on the left side, right side, and at the front along the top?

(3) The F-4 and F-16 are tied for third with four mishap reports each. Seven of the eight pressure failures were due to canopy seals, the eighth being an F-4 pressure regulator failure. Other mishap reports were for the A-10 (3 seals), T-33 (2 seals), and F-5 (1 hose connection failure).

(4) Notable by its absence is the F-111. I know writeups by aircrews for suspected pressure leaks is not uncommon, and the cockpit often fails pressure leak checks. However, the aircrew writeups complain about the whistling noise from the leaks. I can't remember anytime I saw a problem reported where the cockpit pressure was not maintained in flight. Perhaps their pressurization system is so good it can easily overcome some leaks, and their seals are designed (intentionally or accidentally) so that all failures are small failures, with no large leaks from any failure.

2. Some design thoughts that come to mind for future transparency/cockpit systems (MITS among others) include the following:

a. Canopy latching systems should be made as idiot-proof (for both maintenance and aircrew personnel) as possible.

(1) Rigging/adjusting the canopy should be as easy as possible.

(2) the rigging tolerances involved for opening and closing the canopy should be much less forgiving than the tolerances for locking and unlocking the system. In other words, when a canopy is rigged out of adjustment (too far forward/back/sideways/cocked at an angle) it won't close. When it is rigged even farther out of tolerance in any direction and some clown manages to somehow get it closed (by trimming metal off the frame, etc.), the canopy will still securely lock and unlock. One F-15 canopy was misrigged, with the canopy giving a false locked indication. Misrigged canopy eventually wore a hole in a seal, which was how the problem was found.

(3) The unsafe canopy warning system must have a very obvious warning signal (light on master caution panel probably), it must be focused on the locking/latching system, and it must not be satisfied by either a closed but not locked condition or a hooks closed but not engaged condition. The detection/warning system must also be unaffected by the sequence of actions/activities, and reliably report the unlocked condition regardless of how that condition was obtained. For example, properly locking the canopy, shutting off all power, manually unlocking the canopy, and turning on the power should not fool it. these ideas are "lessons learned" (at least lessons I learned) from the reports. One warning system was defeated because with the canopy handle raised in the "closed but not locked" position, the handle blocked the pilot's view of the warning light announcing the canopy was not locked. Another warning system was defeated because it had to "see" a history of actions leading to the canopy locking event before it would activate. The pilot closed (but did not lock) the canopy with the power off. Power was then turned on, which "woke up" the warning system. However, since the warning system never "saw" step 1, closing the canopy) it never got to step 2 (noticing the canopy was not locked) and thus never announced the canopy unlocked condition. In another case (F-4) there was some binding/interference from a rivet. The hook was either prevented from closing on one side, or missed engaging on one side (the other side did close and lock). No warning system ever activated. The pilot noticed the canopy gapping open on that side in flight.

(4) Perhaps a way to help insure closed, not locked doesn't occur is to design the system so there is no closed/not locked position. Have switches/power designed so that if it's physically closed, whenever power is applied to the aircraft the canopy locks.

(5) Another way to insure that hooks did not just barely engage would be to have the hook grab a very strong "U" bolt shape (the top ends of the "U" attach to the sides of the fuselage, one end above the other, resulting hole being front to back). With a peg, a hook could move off the end of the peg under massive side loads due to some occurrence (birdstrike, hook broke on other side, etc.). With a "U" the hook would have to open to release the canopy. It couldn't slip off.

b. The cockpit seals, pressurization system, and pressure loss warning systems should be designed to prevent major leaks and pressure drops. Failures should be gradual, and the system should identify the condition of smaller leaks that the pressurization system could overcome rather than wait until the pressurization system's capacity was exceeded. Concepts to consider would include:

(1) Inner and outer seals, each capable of holding pressure, and each with separate inflation systems. Failure of either seal would not cause depressurization of cockpit, but would be identified as a minor defect (red diagonal in forms) to be repaired after the flight. No effect on that mission.

(2) Sensors would detect the consumption of air (i.e., leaks) from any of three different subsystems.

(a) Pressure regulator/air supply to inflate the outer seal.

(b) Pressure regulator/air supply to inflate the inner seal.

(c) Pressure regulator/air supply to maintain cockpit pressure.

(3) Air leak sensors would identify leaks at some reasonable sensitivity level, such as any seal inflation leak that indicated a hole in a seal, and cockpit leaks that equated to 50% of the pressurization system's capacity during the worst part of a mission (engine idle at high altitude perhaps). The indication would be a leak to be attended to after the mission as a minor defect (red diagonal in forms).

(4) There should be a primary and backup cockpit pressurization system so that pressure regulator failure would not cause cockpit depressurization and mission impairment or loss.

(5) Should a cockpit depressurization occur, despite the redundant design features, the warning system for the aircrew should be very obvious (flashing light and buzzer for example) and alert the aircrew as the pressure is falling rather than after the aircrew would experience symptoms from the pressure loss.

c. If electrical heating of a transparency is used, some consideration to keep in mind with the system would include:

(1) Insure that if a temperature controller failure occurred, any transparency failure would involve only the non-structural face ply (or plies of both sides are heated electrically).

(2) Wiring to electrically heated windows should have the appropriate electrical capacity, insulating materials, and routing so that overhead failures do not involve overheating the wire itself. The fires in the cockpit of C-130s from overheated wires (actually the connecting point to the transparency caught fire) should be avoided. Fires outside of the cockpit obviously should also be avoided.

SESSION VII

UNDERSTANDING CURRENT SYSTEMS (PART B)

Chairman: S. Wortman  
Sacramento Air Logistics Center  
McClellan AFB, California

Co-Chairman: A. Gibbs  
British Aerospace  
Surrey, England

Coordinator: D. Wamba  
Rockwell International  
Los Angeles, California

TRANSPARENCY SEALANTS

Malcolm E. Kelley  
AFWAL/FDER

## TRANSPARENCY SEALANTS

Malcolm E. Kelley  
Air Force Wright Aeronautical Laboratories  
AFWAL/FDER  
Wright-Patterson Air Force Base, Ohio

### ABSTRACT

There are numerous military specifications for sealants, and typically there are several different brands of sealant qualified for each of the MIL Specs. Two of these MIL Specs apply to the sealants which are used for installing F-16 and F-111 transparencies. However, both of these MIL Specs are for sealants intended for use with aircraft fuel tanks and none of the tests needed to qualify the sealants to the MIL Spec indicate what their effects would be on acrylic or polycarbonate. Concern about this situation prompted some investigations into what tests with these sealants on plastics might have been run, and a report was found that indicated they caused structural damage. Further investigations identified another military specification sealant used to install the polycarbonate transparency of another fighter aircraft, and test results found showed that sealants which met this MIL Spec also caused structural damage to polycarbonate. To define the extent of and seriousness of the transparency sealant problem a multi-faceted approach was initiated. All MAJCOMs were asked to have each of their Wings identify (by MIL Spec and brand name) the sealants used with transparencies. All sealants that were listed on the Qualified Products List (QPL) for each MIL Spec would be identified. Samples of those in use (priority 1) plus all other sealants on the applicable QPLs (priority 2) would then be obtained and tested. The latest results from these efforts will be presented and discussed, along with suggested future actions for both industry and DoD to take.



1. Last summer I had a spare moment, and during that moment I was struck by a passing thought. I asked myself if the military specifications for aircraft transparency sealants included all the tests that would be needed to insure the sealants would not harm acrylic or polycarbonate. I didn't know the answer, and my very mild curiosity provided barely enough motivation for me to order a couple mil specs. I had a couple tubes of sealant I'd picked up at an F-111 Wing a few years earlier, so all I had to do was read the mil spec numbers off the wrappers. If it had been more difficult than that I probably would have done nothing, since I really wasn't very interested in or concerned about sealants.

2. I received and skimmed through the two mil specs. I became somewhat discontented since the mil specs were both for fuel tank sealants and there were no tests of any kind that would indicate the effects the sealants would have on acrylic or polycarbonate.

3. My discontent provided the motivation to seek more information. I was confident that the information I needed to become reassured would be easily obtainable. One thing led to another, and I have acquired a lot of information on sealants. I have also been completely successful in eliminating any worries that I would run out of things to do to keep myself busy. I will let others judge for themselves whether or not my quest for reassurance that all is well has indeed been successfully concluded.

4. Here are the areas I looked into while seeking reassurance on the sealant topic. I'll discuss the results obtained (as of 2 Dec 88) from each area of inquiry.

a. Perhaps most or all sealants are inherently non-harmful to plastic transparencies due to the chemical composition for the sealants typically used throughout industry and DoD? After all, there are many other materials used with plastic transparencies that nobody worries about. For example, has anyone ever done a craze test to see if aluminum, titanium, or steel would chemically attack acrylic or polycarbonate? Probably not, and I certainly wouldn't advocate such tests be run. Perhaps sealants are as non-harmful to plastics as aluminum? This approach for becoming reassured that all was well didn't last long. Two test reports from industry (General Dynamics and University of Dayton Research Institute) were located that had sealants tested on polycarbonate coupons. Thirteen brand name sealants were tested by GD, UDRI, or both, and all but two caused damage to the polycarbonate coupons. With these odds, it would

not seem reasonable to assume all is well. My quest for reassurance was obviously not satisfied by these test reports.

b. The index of all military and federal specifications was obtained. I then ordered and read every spec whose title suggested there was any possibility that sealants used on aircraft transparencies could get into the supply system by being qualified under one of the specs. When the various operational Wings told me what sealants they were actually using, they identified a few specs I hadn't ordered, so I acquired and reviewed those also.

(1) The mil specs reviewed to date are summarized in Atch 1. I extracted from each spec the criteria I considered to be the most important for aircraft transparency sealants. The criteria I chose was whether or not an acrylic craze test was required, whether or not a pressure test was required, the percent solids (shows amount of volatiles in the sealant), the maximum temperature used in testing the sealant, and its intended use.

(2) There are many mil specs that include acrylic craze tests. There are ZERO specs that include tests with polycarbonate.

(3) There are many mil specs that include pressure tests. Most of these tests use fuel rather than air for the pressure tests, but I'm fairly comfortable with assuming that if a sealant will prevent pressurized fuel from passing, it should do a good job with preventing air leaks.

(4) There are a few mil specs that have both acrylic craze tests and pressure tests. One could theorize that most sealants in use for aircraft transparency pressure sealants would be qualified under these mil specs. The theory seems reasonable, but testing the theory requires knowing what sealants are actually in use.

(5) Let us consider just the mil specs for ten sealants for a moment. Eight of the ten were identified (as of 2 Dec 88) by one or more units as being a transparency sealant. It may be enlightening to scan the testing requirements and intended use for the mil spec sealants and rank order them by their apparent suitability for use with transparencies (see Atch 2).

(a) Two of the ten specs have both acrylic craze tests and pressure tests. Sealants qualified under those specs should logically be the first sealants considered when one is

selecting a sealant for use with a plastic transparency. These two sealants I rank ordered as Category I.

1. One of the sealants has the same working time as most other sealants between sealant mixing (adding catalyst) and the sealant starting to harden. The sealant has two applicable versions, one with a 30 minute working time, and one with a two hour working time. It would be at least as suitable in this regard as other sealants in use.

2. The other mil spec has a very short sealant working time, so is probably not suitable for installing large transparencies. However, for plugging pressure leaks and for providing aerodynamic smoothing and weather sealing at the outer edge of the transparency it seems excellent. On second thought, the mil spec sealants should be absolutely utopian! It's intended use is as a quick repair sealant, and the aircraft can be launched two to three hours after the sealant was first applied. The sealant would even hold 28 pound pressure loads after only four hours. Use of this sealant in place of sealants with long cure time would significantly increase operational availability of aircraft. For example, if this fast curing sealant were used (in combination with dry seals to hold pressurization loads) on only the F-111 and B-1, the payoff in aircraft availability would be equivalent to buying over \$500 million more aircraft. I was very curious to see how many flying units would identify sealants that met this mil spec as sealants they were using.

(b) Two of the mil specs have acrylic craze tests, but no pressure tests. These would seem to be prime candidates for exterior aerodynamic smoothing and weather sealing around the edges of transparencies, but their ability to hold pressure loads would need to be determined before they would be candidates for installing transparencies. I rank ordered these as Category II.

(c) Four of the mil specs have no craze tests but do have pressure tests. Three have the intended use as fuel tank sealants, and one is meant to be a firewall sealant. These might be candidates for installing transparencies, but it would not be known if they would chemically attack plastic transparencies. One of the three fuel tank sealants apparently deserves top billing in the category. It has an eight hour cure time, so would seem to be the preferred choice (of the three) at least for plugging pressure leaks and for sealing and smoothing the exterior surface. The firewall sealant deserves last place in the category. It has only 65% solids, so there are a lot of

volatiles that could attack the plastic transparencies. I rank ordered these four sealants as Category III.

(d) Two mil specs have neither acrylic craze tests nor pressure tests. In addition, each mil spec has sealant characteristics indicated which many people would probably say should eliminate those sealants from consideration as transparency sealants. I rank ordered these mil specs as Category IV.

1. One mil spec is for sealants that intentionally have very poor adhesion, with the intended use being for removable access panels into fuel tanks. They also have poor temperature resistance, being able to withstand only 180°F as a maximum service temperature.

2. One mil spec has an intended use as a protective coating on aluminum to prevent it from corroding. At 67°F the mil spec sealants have a cure time of 28 days. The 28 day cure would seem to be a veto condition and one would appear to be on fairly safe grounds if one predicted that this sealant would not be used for transparencies.

c. The simple, direct approach was used to identify the sealants actually in use. I asked every Air Force MAJCOM that flies aircraft to ask each of their units to identify what sealants they were using with their transparencies. Making sense of the replies and dealing with any questions that might come up seemed like a nice spare time project. Consider: There are less than 9500 Air Force aircraft, and perhaps not all the MAJCOMs will participate. Shouldn't a few minutes here and there be sufficient for this activity?

d. Every MAJCOM plus the Air National Guard tasked their units with responding. Even the Royal Australian Air Force participated, identifying the sealants used on their F111C aircraft. (I'm grateful that a copy of the sealant use letter didn't get to NATO. It's hard enough translating the responses from USAF units. If NATO had participated, some of their responses might have been Greek to me.)

(1) The responses began flowing in, and although the suspense dates imposed by some of the MAJCOMs are still several weeks away there were 60 units whose responses were received and logged in before 2 Dec, the cutoff point for data used in this paper. These 60 responses were enough to identify some interesting trends in sealant use. I had asked for information on sealants, and a lot of units provided information on not only

sealants, but other materials used as substitutes for sealants, or along with sealants (primers, release agents, etc.).

(2) As of 2 Dec 88, 48 different brand name products and 22 different aircraft are represented in the responses. Seventeen different mil specs for these materials are identified. Eight sealant mil specs are included, plus three adhesive specs, two adhesive tape specs, and one compound spec. (The compound seems to closely resemble a sealant in characteristics.) In addition, there are two specs for products whose purpose is to insure the sealant will NOT stick. One spec is a release agent, and one is a light lubricating oil. However, the mil spec number identified most frequently (over 1/3 of the total) is "NONE".

e. Attachment 2 rank ordered ten sealant mil specs by their apparent suitability for use with aircraft transparencies. Attachment 3 adds additional information to the Attachment 2 document. The mil spec number are added to identify the sealants. The number of uses, number of different brand name sealants, and the number of different aircraft types (indicated on the responses from flying units) are also indicated. You can judge for yourself if the mil spec sealants which are actually in use seem to be the logical sealants to use for transparencies.

(1) The "number of uses" and "number of different aircraft" need to be explained.

(a) When I compiled the information from each unit I considered a sealant identified as being used on or near the transparency as being one use. A sealant used only on the windshield was obviously one use. A sealant used on both the windshield and canopy was still one use. If a unit had two (or more) different types of aircraft (T-38 and T-37 for example) and indicated they used the same sealant on both aircraft, I considered that as two uses.

(b) For this paper I consider all model and variations of an aircraft as being one aircraft. For example, all seven versions of the F-111 are lumped together and counted as one type of aircraft.

f. For those who are interested (and all who are not interested have undoubtedly stopped reading before this), Attachment 4 provides a total listing of all the mil spec (including mil spec = none) which the units identified as being used on (or near) aircraft transparencies.

5. A lot of different analyses can be done with the sealant information that is being acquired. Since at the time this paper was written information was still being acquired at a rapid rate, it was premature to try and perform detailed analyses at that time. However, some interesting trends were noted that are worth mentioning.

a. The F-111 windshields are experiencing a 50% loss in birdstrike resistance after about two years service life. (see UDRI presentation.) As of 2 Dec every F-111 unit (except the 20TFW) had responded, and every unit identified PR1750 as the sealant they use for installing transparencies. The UDRI research indicates the F-111 windshield strength loss is apparently due to cracks at the bolt holes, and all (or almost all) cracks are in the inner ply. The previous sealant/polycarbonate tests by GD and UDRI (for F-16 application) included PR1750, and PR1750 caused polycarbonate cracking. Is there a cause and effect relationship between the PR1750 and the cracking of the inner polycarbonate ply? Perhaps. The PR1750 sealant is also indicated as being used on the B-1 and the F-15 windshields.

b. The F-16 technical orders specify two types of sealant for installing the transparency into the frame. A non-curing sealant (Tacky Tape) that comes in rolls (in various widths and thicknesses) is used between the transparency and the frame, in the location where the pressure sealing function should logically be performed. A wet sealant, brand name PR1425 is used on the exterior surface as a weather seal. A bead is also applied (after the transparency is bolted into the frame) on the inside along the frame edge (on the transparency inner surface). This would apparently have the intended function of blocking moisture or chemicals from flowing down the transparency inner surface and reaching the Tacky Tape. Both the Tacky Tape and the PR1425 wet sealant were thoroughly tested (by GD or someone following GD's instructions) and were non-harmful to polycarbonate. That is good news. The same sealant system (Tacky Tape plus PR1425) is also reported as being used by both of the F-4 units who indicated they have the new one-piece wrap-around bird resistant windshield. Unfortunately, the responding F-16 units do not all indicate they are using the Tacky Tape plus PR1425 sealants.

(1) Out of 15 replies from F-16 units, only nine identified one or more versions of the Tacky Tape as an item they use (it comes in various widths). I had occasion to discuss the Tacky Tape with two of the units. Each stated that their experiences indicated the Tacky Tape was not a reliable pressure

seal, and they locally required a 48 to 96 hour sealant cure time (for the PR1425) before a pressure test was performed. (Note: Their written responses to the sealant use survey had not complained about the Tacky Tape.)

(2) Thirteen of the 15 responses identified the PR1425 sealant. The same nine units who identified Tacky Tape also identified the PR1425 sealant, so the specified T.O. procedure could be followed by them. Two identified only the PR1425 sealant, so that had to be used between the transparency and frame as the pressure sealant. The only USAFE response and the only PACAF response each identified PR1425 as the sealant they wanted, but apparently couldn't obtain (at the time the reply was prepared). They didn't identify the Tacky Tape in their response, so if and when PR1425 was obtained it would be used as the pressure seal as well as the weather seal.

(3) Six units identified the GC 409 as sealant. Two of them (including the one PACAF unit responding by the date this paper was written) indicated that it was the only sealant they had. The one USAFE unit responding identified both GC 409 and PR1425 as applicable sealants. They gave complete information from the GC 409 wrapper, but the PR1425 they could only identify by brand name as a sealant they would use if they got any. Three of the GC 409 users indicated they used the Tacky Tape, PR1425 and GC 409. The GC 409 was provided by the supply system when the ordered PR1425 (according to the PACAF unit). So what, you ask? The GC 409 sealant was one of the sealants tested by UDRI (for GD), and polycarbonate damage was the test result.

(4) Why is GC 409 issued when PR1425 sealant is ordered? Initially I presumed the supply system provided GC 409 as a suitable substitute when the ordered sealant (PR1425) was not available. However, the situation is apparently worse than that. In my sealant survey form letter I neglected to ask for the national stock number (NSN), but many units provided that information anyway. Several different units provided the PR1425 NSN, and several others provided GC 409 NSN. The PACAF unit even sent the label off the sealant package. Two different NSNs are identified for PR1425, the difference being the way the PR1425 is packaged (tubes versus cans). Two different NSNs are also identified for GC 409. The bad news is the PR1425 and GC 409 NSNs are identical (8030-01-119-7885 and 8030-01-129-1141). As far as the supply system is concerned, PR1425 and GC 409 are not suitable substitutes. Instead, they are identical.

6. What will be done from here? Quite a few things. These include:

a. Continue to receive, compile, and try to make sense out of the responses from the flying units in the various MAJCOMs.

b. Identify sealants that should be tested to determine their effects on acrylic and polycarbonate. Prioritize testing efforts so that the sealants in widest use are tested first.

c. Keep applicable DoD and industry offices/individuals informed of results.

d. Seek additional information on sealants (product literature, etc.) from each of the sealant companies.

e. Take other actions as appropriate. Results from sealant efforts will help determine what actions should be taken.

f. The results from the sealant efforts will help define what should be included in a future mil spec for transparency sealants.

g. Those in the transparency industry can also do some things to improve the status quo. Everyone would be better off if those making decisions on transparency design details (such as how carefully to protect the transparency edges) were somewhat paranoid, being guided by the premise that aggressive DoD sealants and other chemicals would be striving to attack their parts. After all, the belief that "they are all out to get me" is a sign of mental illness only when it is not true.



POSSIBLY APPLICABLE MIL SPECS FOR ACFT TRANSPARENCIES

MIL SPEC#	TITLE	QUALIFICATION TESTS					% SOLIDS	MAXIMUM SERVICE TEMP °F	INTENDED USE/REMARKS
		ACRYLIC CRAZE TEST		PRESSURE TEST					
		YES	NO	YES	NO				
MIL-C-18255	Calking Compound, Synthetic rubber base, wooden deck seam application		X		X	---	158°F*	Intended for use on new or old wood decking, especially for sealing teak or fir decking. This mil spec replaces MIL-C-18969 (see below). *Max temp is lab testing temp, no service temp given.	
MIL-C-18969	Calking Compound, Metal seam and wood seam	-	-	-	-	---		The F-16 T.O.s specify brand names of non-curing sealants to use when installing the transparencies into the frames. The product literature for those brand name sealants state the sealants are qualified under this MIL-C-18969 spec and under federal spec TT-C-1796. This MIL-C-18969 spec was cancelled 6 Jul 71, replaced by MIL-C-18255 (see above).	
MIL-C-83982 (QPL has MIL-S-83982)	Compound, Sealing, Fluid Resistant		X		X	98% Class B	200°F	Sealant for aircraft exterior. Note: Class B items have the highest percent solids, are intended for use with an extrusion gun.	
MIL-S-4383	Sealing Compound, Topcoat, Fuel Tank, Buna-N-type					17% to 22%	180°F	Topcoat over other sealants-for fuel tanks.	

POSSIBLY APPLICABLE MIL SPECS FOR ACFT TRANSPARENCIES

MIL SPEC#	TITLE	QUALIFICATION TESTS					% SOLIDS	MAXIMUM SERVICE TEMP °F	INTENDED USE/REMARKS
		ACRYLIC CRAZE TEST		PRESSURE TEST					
		YES	NO	YES	NO				
MIL-S-7124	Sealing Compound, Polysulfide, Accelerator Required, for Aircraft Structures	X		X		97% Class B	180°F	For "sealing aircraft structure against the passage of air, liquids, and vapors." Pressure tested at 10 PSI. 72 hour acrylic craze test. Not intended for fuel tanks.	
MIL-S-8660	Silicone Compound, NATO Code, Number S-736		X		X	98%	400°F	For sealing out moisture from threads and electrical connections, and acting as a lubricant. Not a pressure sealant by itself, not applicable to transparencies.	
MIL-S-8784	Sealing Compound, Low Adhesion, for Removable Panels and Fuel Tank Inspection Plates		X		X	97%	180°F	For sealing access panels to fuel tanks, with low adhesion as a requirement. Not for use in repairing fuel tanks.	
MIL-S-8802	Sealing Compound, Temperature-Resistant, Integral Fuel Tanks and Fuel Cell Cavities, High Adhesion		X	X		92%	250°F	For sealing and repairing fuel tanks and fuel cell cavities. Six different brand name sealants on QPL as qualified sealants. 10 PSI pressure test at 250°F for one hour.	
MIL-S-11030	Sealing Compound, Non-curing, Polysulfide Base	X*			X	98.5%	180°F	Not to be used as fuel tank or cabin pressure sealant. Intended use is for sealant in telescope, binoculars, etc. with glass or plastic lenses, and for "general purpose as deemed necessary by the using service". Comes in cans, or as a 50 foot long roll of 1 1/2 inch wide tape on a suitable release paper. Does not cure. (*Craze test is with vapors from sealant)	

POSSIBLY APPLICABLE MIL SPECS FOR ACFT TRANSPARENCIES

MIL SPEC#	TITLE	QUALIFICATION TESTS					MAXIMUM SERVICE TEMP °F	INTENDED USE/REMARKS
		ACRYLIC CRAZE TEST		PRESSURE TEST		% SOLIDS		
		YES	NO	YES	NO			
MIL-S-11031	Sealing Compound, Adhesive: Curing (Polysulfide Base)	X*			X	97%	200°F For bonding metal to metal or glass to metal in optical instruments or fire control instruments. *Vapors not cause acrylic crazing (Sealant not in contact with acrylic.) Strong adhesive (200 PSI).	
MIL-S-12158	Sealing Compound, Non-Curing, Polybutene		X		X	97%	158°F* Soluble in kerosene and gasoline, but resistant to water. Low strength, low adhesion. Intended as waterproofing around hatches when crossing streams/rivers/lakes. *Max temp is laboratory temp used for curing testing sealant. No service temp given.	
MIL-S-14231	Sealing Compound, Joint, Two component, for Bolted Aluminum or Steel Petroleum-storage Tanks.		X	X		90%	158°F* Pressure test at 15 PSI using water and fuel. *Max temp is laboratory temperature used for curing/testing the sealant. No maximum service temp given. Intended for sealing bottom of metal storage tanks used for gasoline, jet fuel, and diesel fuel only.	
MIL-S-38228	Sealing Compound, Environmental, for Aircraft Surfaces	X			X	97%	250°F Type I; 500°F Type II Intended for filling gaps, slots, and depressions on exterior of aircraft and missiles to produce smooth contour	

POSSIBLY APPLICABLE MIL SPECS FOR ACFT TRANSPARENCIES

MIL SPEC#	TITLE	QUALIFICATION TESTS						MAXIMUM SERVICE TEMP °F	INTENDED USE/REMARKS
		ACRYLIC CRAZE TEST		PRESSURE TEST		% SOLIDS			
		YES	NO	YES	NO				
MIL-S-45180	Sealing Compound, Gaskets, Hydrocarbon Fluid and Water Resistant		X		X	76 to 87%	158°F*	Intended for sealing threads and gaskets where resistance to engine oils, fuel and water is required. *Max temp used during lab tests, no maximum service temp given.	
MIL-S-46874	Seal, RF and Pressure		X		X	- (100%)	No temps given	Seal is metal and rubber bonded together, intended for use as a compressible gasket where both RF and pressure sealing is required.	
MIL-S-47147	Seals, Rubber Extrusions, Non-Cellular		X		X	--	No temps given	From different shapes of rubber seal, for use as "seal or protective strips where resistance to weathering and certain fluids is required."	
MIL-S-48112	Sealing Compound, Butyl Rubber Sealant (for use in ammunition)		X		X	**	158°F*	Intended for filling cavities in ammunition items. *Max temp used during lab tests, no maximum service temp given. **Curing process involves evaporation of solvents, but % solids not given.	
DOD-S-82708	Sealing Compound, Preformed (Metric)		X		X	--	--	Two types of preformed sealing compound for filling voids in a guided missile rocket motor.	

POSSIBLY APPLICABLE MIL SPECS FOR ACFT TRANSPARENCIES

MIL SPEC#	TITLE	QUALIFICATION TESTS					MAXIMUM SERVICE TEMP °F	INTENDED USE/REMARKS
		ACRYLIC CRAZE TEST		PRESSURE TEST		% SOLIDS		
		YES	NO	YES	NO			
MIL-S-83315	Sealing Compound, Aluminum Structure Pressure and Weather Sealing, Low Density	X			X	97%	200°F	Intended use for "sealing pressure and weather cavity areas." Has many different sealant adhesion & strength tests after various exposures, but no pressure test. Not intended for faying surface sealing or for wet installing fasteners. Sealant may reduce structural fatigue strength when used to seal between metal surfaces. One sealant on QPL as qualified.
MIL-S-83318	Sealing Compound, Low temperature curing, quick repair, integral fuel tanks, and fuel cell cavities		X	X		87%	250°F	Intended as quick repair sealant for fuel tanks. Applies as a brush-on fluid (not a bead from an extrusion gun). "Quick" repair has 96 hour cure at 20°F. Pressure test has 10 PSI using jet fuel. Max Temp is lab testing temp. Service temp not given. Two sealants on QPL.
MIL-S-83430	Sealing Compound, Integral Fuel Tanks and Fuel cell cavities, intermittent use to 360°F		X	X		97%	250°F and 360°F (brief time)	Two sealants on QPL as qualified. For use on fuel tanks, mold lines, and fuel tank faying surfaces. Long term service temp exposure to 250°F, short term exposure to 360°F. Pressure test uses 10 PSI air after seven days immersion in heated jet fuel.

POSSIBLY APPLICABLE MIL SPECS FOR ACFT TRANSPARENCIES

MIL SPEC#	TITLE	QUALIFICATION TESTS						MAXIMUM SERVICE TEMP °F	INTENDED USE/REMARKS
		ACRYLIC CRAZE TEST		PRESSURE TEST		% SOLIDS			
		YES	NO	YES	NO				
MIL-S-83982 (on QPL sheet) MIL-C-83982 (on MIL SPEC)	Compound Sealing, Fluid resistant		X		X		180°F (Briefly to 200°F)	One sealant on QPL. (QPL incorrectly identified as MIL-S-83982; spec is MIL-C-83982.) Intended for sealing acft structures; NOT for fuel tanks.	
MIL-S-85312	Sealing Compound, Non-curing, Polysulfide, Groove Injection, for Integral Fuel Tanks.		X	X		98%	250°F	Sealant is a "permanently mastic polysulfide sealing compound for sealing or resealing integral fuel tanks." (In this context "Mastic" apparently means "pasty".) Pressure test: 5.9 PSI at 77°F, 1.7 PSI after lengthy immersion in heated (140°F) fuel, and 1.7 PSI in 250°F air.	
MIL-S-85334	Sealing Compound, Non-curing, Low Consistency, Silicone, Groove Injection, for Integral Fuel Tanks		X	X		98%	160°F	Sealant is a "permanently mastic fuel resistant polysiloxane polymer containing no solvents." Pressure test 5.9 PSI at 77°F, 1.7 PSI after fuel soaking, and 1.7 PSI in 160°F air.	
MIL-S-85420	Sealing Compounds, Quick Repair, Low Temperature curing Polysulfide, for aircraft structures	X		X		92%	None given	For two different types of sealant (Types I and II). Low temp cure is 77°F. Pressure tests: 29PSI after 4 hour cure 77°F (Types I and II) 10 PSI after 8 hour cure 45°F (Type I) 28 PSI after 6 hour cure 45°F (Type II) Intended use is as a "structural sealant which gives "flying-away" capability in 2 to 3 hours" (75°F cure), or 4 to 8 hour fly-away capability for 45°F cure. No QPL for this spec.	

POSSIBLY APPLICABLE MIL SPECS FOR ACFT TRANSPARENCIES

MIL SPEC#	TITLE	QUALIFICATION TESTS						INTENDED USE/REMARKS
		ACRYLIC CRAZE TEST		PRESSURE TEST		% SOLIDS	MAXIMUM SERVICE TEMP °F	
		YES	NO	YES	NO			
TT-C-1796	Calking Compounds, metal seam and wood seam		X		X	--	120°F*	Intended for use "as a calking material on metal and wood structures, and as a sealant for applications requiring the use of putty." A "Watertight seam is insured above and below the waterline." (*Max temp of 120°F is laboratory testing temp, no service temp given). The sealant specified in the F-16 technical orders (by brand name) for use when installing the transparency into the frame is qualified under this mil spec. Would other brand name sealants meet spec requirements also be suitable for use with the F-16? I wouldn't count on it. No QPL for this spec.
TT-S-222	Sealing Compound, Asbestos		X		X	--	225°F	Used to fill spark plug hole recesses of stored truck engines to keep water out. Made of soap (25%), mineral oil (51.5%) and asbestos fibers (19-21%). Soap and mineral oil would evaporate/burn if truck engines were run, leaving asbestos behind. Tests of sealant (for each procurement) include the sniff test for odor. (No, I'm not kidding). NOTE: Actions initiated seeking to cancel spec and safely dispose of sealing compound in supply.

POSSIBLY APPLICABLE MIL SPECS FOR ACFT TRANSPARENCIES

MIL SPEC#	TITLE	QUALIFICATION TESTS						INTENDED USE/REMARKS
		ACRYLIC CRAZE TEST		PRESSURE TEST		% SOLIDS	MAXIMUM SERVICE TEMP °F	
		YES	NO	YES	NO			
TT-S-227	Sealing Compound, Rubber Base, Two Component (for calking, sealing, and glazing in building construction)		X		X	90%	158°F	Max temp is lab testing temp, no service temp given. Cure time 14 days. Intended use is with building.
TT-S-1556	Sealing Compound, (Elastomeric joint sealants)		X		X	?	?	Commercial Item Description which can be used instead of the Federal Specifications TT-S-00227 and TT-S-00230. Sealant intended use is with Buildings
TT-S-230	Sealing Compound, Elastomeric type, single component (for calking, sealing, and glazing in Buildings and other structures)		X		X	90%	158°F	Intended for use with Buildings. Max temp is lab testing temp. Cure time 21 days.



POSSIBLY APPLICABLE MIL SPECS FOR ACFT TRANSPARENCIES

MIL SPEC#	TITLE	QUALIFICATION TESTS				% SOLIDS	MAXIMUM SERVICE TEMP °F	INTENDED USE/REMARKS
		ACRYLIC CRAZE TEST		PRESSURE TEST				
		YES	NO	YES	NO			
MIL-F-23142	Tape, Pressure-Sensitive Adhesive, for dissimilar metal separation		X		X	155°F (lab test temp)	Prevent galvanic attack between dissimilar metals.	
MIL-F-6841	Tape and sheet, Adhesive, rubber and cork composition	X			X	212°F (lab test temp)	For installing windshields, panels, and windows in cabins and cockpits, of aircraft. Consists of a tape which has a granulated cork and rubber mix on a cloth backing. The cloth has a pressure-sensitive adhesive on the reverse side. Comes up to 1/8 inch thick, 2 1/2 inches wide. Craze test at 110°F, 2000 PSI stress for 24 hours.	
VV-P-236	(Federal Specification) Petrolatum, Technical		X		X	Melts between 115°F and 140°F	Light lubricating grease. "Not to be used as a . . . . lubricant for the human body."	

SEALANT MILITARY SPECIFICATIONS

SEQ #	RANK CATEGORY	ACRYLIC CRAZE TEST	PRESSURE TEST	INTENDED/USE REMARKS	MJL-S-NUMBER	# OF USES	# OF DIFFERENT ACFT	# OF BRAND NAMES
1	I	Yes	Yes	Normal Cure Times				
2	I	Yes	Yes	Extremely fast cure. Fly ACFT in 3 hours, hold 28 PSI pressure in 4 hours.				
3	II	Yes	No	Cure time: 24 hrs (B-1), 48 hrs (B-2). 500°F temp. resistance.				
4	II	Yes	No (but probably OK)	Normal cure times. Intended as pressure holding sealant, has good strength & adhesion. 200°F temp resistance.				
5	III	No	Yes	8 hr cure. Intended for fuel tanks.				
6	III	No	Yes	Normal cure times. Intended for fuel tanks.				
7	III	No	Yes	Normal cure times. Intended for fuel tanks.				
8	III	No	Yes	Firewall sealant. Withstands 400°F sustained, 2000°F briefly. 65% solids (lots of volatiles).				
9	IV	No	No	Very low adhesion. For removable panels on fuel tanks. 180°F temp. resistance				
10	IV	No	No	Intended use to protect aluminum from corrosion. 28 day cure at 67°F.				

ATCH 2

SEALANT MILITARY SPECIFICATIONS

SEQ #	RANK CATEGORY	ACRYLIC CRAZE TEST	PRESSURE TEST	INTENDED/USE REMARKS	MIL-S-NUMBER	# OF USES	# OF DIFFERENT ACFT	# OF BRAND NAMES
1	I	Yes	Yes	Normal cure times.	7124	2	2	1
2	I	Yes	Yes	Extremely fast cure. Fly ACFT in 3 hours, hold 28 PSI pressure in 4 hours.	85420	0	0	0
3	II	Yes	No	Cure time: 24 hrs (B-1), 48 hrs (B-2). 500°F temp. resistance.	38228	2	2	1
4	II	Yes	No (but probably OK)	Normal cure times. Intended as pressure holding sealant, has good strength & adhesion. 200°F temp. resistance.	83315	0	0	0
5	III	No	Yes	3 hr cure. Intended for fuel tanks.	83318	4	4	1
6	III	No	Yes	Normal cure times. Intended for fuel tanks.	8802	34	10	4
7	III	No	Yes	Normal cure times. Intended for fuel tanks.	83430	18	4	3
8	III	No	Yes	Firewall sealant. Withstands 400°F sustained, 2000°F briefly. 65% solids (lots of volatile)	38249	2	2	1
9	IV	No	No	Very low adhesion. For removable panels on fuel tanks. 180°F temp. resistance.	8784	4	3	2
10	IV	No	No	Intended use to protect aluminum from corrosion 28 day cure at 67°F.	81733	23	10	5

ATCH 3

MILITARY SPECIFICATIONS  
Materials Used With Transparencies

MIL SPEC NUMBER	ACRYLIC CRAZF. TEST	PRESSURE TEST	INTENDED/USE REMARKS	# OF USES	# OF DIFFERENT ACFT	# OF BRAND NAMES
MIL-A-8576	Yes	Yes	Transparent glue, to glue acrylic plies together.	2	2	1
MIL-A-46106	No	No	RTV, 1 hour tack free time, 392°F temp resistance. Requires moisture from air to cure. 72 hr cure time (3 days)	4	3	3
MIL-A-46146	No	No	RTV, 5 hour tack free time, 392°F temp resistance. Requires moisture from air to cure. 168 hr cure time (7 days)	3	3	1
MIL-C-81733	No	No	Normal cure times. 180°F temp resistance (briefly to 200°F)	3	2	2
MIL-S-7124	Yes	Yes	Normal cure times.	2	2	1
MIL-S-85420	Yes	Yes	Extremely fast cure. Fly ACFT in 3 hours, hold 28 PSI pressure in 4 hours.	0	0	0
MIL-S-38228	Yes	No	Cure time: 24 hrs (B-1), 48 hrs (B-2). 500°F temp resistance.	2	2	1

**MILITARY SPECIFICATIONS**  
Materials Used With Transparencies

MIL SPEC NUMBER	ACRYLIC CRAZF. TEST	PRESSURE TEST	INTENDD/USE REMARKS	# OF USES	# OF DIFFERENT ACFT	# OF BRAND NAMES
MIL-S-83315	Yes	No (but probably OK)	Normal cure times. Intended as pressure holding sealant, has good strength & adhesion. 200°F temp resistance.	0	0	0
MIL-S-83318	No	Yes	8 hr cure. Intended for fuel tanks.	4	4	1
MIL-S-8602	No	Yes	Normal cure times. Intended for fuel tanks.	34	10	4
MIL-S-83430	No	Yes	Normal cure times. Intended for fuel tanks.	18	4	3
MIL-S-38249	No	Yes	Firewall sealant. Withstands 400°F sustained, 2000°F briefly. 65% solids (lots of volatiles)	2	2	1
MIL-S-8784	No	No	Very low adhesion. For removable panels on fuel tanks. 180°F temp resistance.	4	3	2
MIL-S-81733	No	No	Intended use to protect aluminum from corrosion. 28 day cure at 67°F.	23	10	5

MILITARY SPECIFICATIONS  
Materials Used With Transparencies

MIL SPEC NUMBER	ACRYLIC CRAZF. TEST	PRESSURE TEST	INTENDED/USE REMARKS	# OF USES	# OF DIFFERENT ACFT	# OF BRAND NAMES
MIL-T-6841	Yes	No	For installing windshields, panels, and windows in acft. 212°F temp resistance, craze test 24 hrs at 110°F. Sheets or rolls, up to 1/8 inch thick; rubber and cork composition on cloth, adhesive backing.	1	1	1
MIL-T-23142	No	No	Intended use: to separate dissimilar metals. Comes as rolls of adhesive tape, .004 inches thick. 155°F temp resistance (lab test temp). Spray-on release agent. (MIL SPEC on order)	1	1	1
MIL-L-60326	?	?		5	3	3
VV-P-236	No	No	Petrolatum, Technical. Light lubricating grease, melts between 115°F and 140°F. Intended use: helps prevent rust. "Not to be used as a remedy, medicine or lubricant for the Human Body." No mil spec for various items, mostly sealants.	1	1	1
None	--	--		52	12	17
			TOTALS (as of 2 Dec 88) for 16 MIL SPECS (Plus items not MIL SPEC qualified)	161 reported uses	22 different acft	48 different brand names

RESIDUAL STRESSES IN F-16 AIRCRAFT

M. G. Gran  
Flight Dynamics Laboratory

RESIDUAL STRESSES IN F-16  
AIRCRAFT

M. G. Gran  
Aircrew Protection Branch  
Flight Dynamics Laboratory  
Air Force Wright Aeronautical Laboratories  
Wright-Patterson Air Force Base, Ohio

Abstract

Residual stresses have always been a concern in the complex forming of aircraft transparencies. The question of how much residual stresses are present in these transparencies has never been answered. The manufacturers have an idea of the stresses involved, but no standard way of measuring these stresses has ever been accomplished. Knowing the amount of stress would help engineers understand the many different problems associated with these transparencies. If the stresses were known, it would shed some light on the severe problem of the acrylic face ply crazing. Measuring the residual stresses of certain transparencies has been accomplished. But this process must be validated so that the stress that is measured by this process is only the residual stress and not stress induced by the measuring technique. The technique for measuring the stresses uses hole drilling rosette strain gages. This technique is used quite frequently with metals, but little work has ever been done with plastics. Other testing will determine the distribution of the residual stresses over the entire F-16 transparency.



## Introduction

Knowing the residual stresses in any transparency design would help understand the different failure modes of these systems. These stresses must be measured to determine the history of stresses that an operational transparency system undergoes in the field. With this knowledge, the engineer can better understand what actual forces are the parts undergoing during their normal operation. From this knowledge, corrections can be made for different failure modes to give the Air Force better service life of the transparency systems. These corrections may be as simple as the way the transparency is cared for, to the complex problem of changing the manufacturing process. The transparency systems are a very large expense to the Air Force, because of the lack of service life for the advanced systems. The payoff for the testing will be tremendous when looking at the rate of replacement of the current systems.

The actual attempts at measuring the residual stresses in an operational system began in the June of 1988. The vendors have been asked on numerous occasions to what level of stress is introduced during the manufacturing process. The answers have always been a consistent range of values. These answers are helpful, but the exact values must be determined in order to fix the major problems with the current systems. The hole drilling rosette method was used for the first attempt at measuring residual stresses. This method was well defined for metals, but no work had ever been accomplished on themoplastics. The first attempts would be made on the most complex transparency system of today, the F-16 canopy.

## Residual Stress Information

The first question that is asked is, what will be done with this valuable information? The information will be used for a wide range of areas. But they will all have the same goal in mind and that is to improve the system in order to have an extended service life with better overall performance. Once the correct information from a verified testing procedure is produced, then the whole industry can use the information to try and understand why the transparency systems fail the way they currently do. There is basically three general areas where the information will be used. These are in the manufacturing process, in understanding and fixing the durability problems, and input for the computer codes.

The manufacturing process is very complicated for the transparency systems of today. The materials that are being used are not fully understood yet. There are many questions that are being asked about how the material properties change with age. Other problems exist when these parts are subjected to the manufacturing process. If the residual stresses could

be measured, then the part could be analyzed at different stages in the process. The process might be improved from this understanding of what stresses the part undergoes, during the different procedures. The transparency manufacturing process might be changed in order to improve a certain aspect of the design, if the transparency systems are failing do to a predominate failure mode. The whole manufacturing process will benefit if the residual stresses can be measured accurately.

The durability of the transparency systems is understood as a very important issue. But little is understood about why the transparency systems fail in the manner that they do, because the history of the part and what it undergoes during a normal service life are virtually unknowns. The parts leave the vendor's plants and little if any feedback is ever given back to the community. Better computerized tracking systems are being employed which hopefully will improve the way that information can filter back to the vendors. This information must be accurate in order to determine the problems of the systems. Up until now there has been very little feedback to industry and it is very difficult to draw conclusions on incomplete information. This is where the residual stress measurement will benefit everyone, because measurements can be made throughout the life of the transparency system. Knowing the stresses that the part undergoes, during the lifetime, will help in designing new parts that will be able to handle the forces and environment that these parts are subjected to.

The information can also be used for the advanced computer codes that currently exist and are being produced. These codes can help reduce the cost of development of a transparency system by analyzing the different designs before they are built. This will reduce the cost substantially and point out the problems of the design before the system is produced and a full scale test is performed. But the codes are only as good as the input to the problem. There are many gaps in the input properties for these materials that some of the codes need to give accurate results. One of these inputs is the residual stress that is introduced during manufacturing. This information must be obtained if the part is to be analyzed during a flight profile to determine the actual forces that the material is undergoing. Knowing these forces will help in understanding why a certain transparency design fails during specific conditions. This information can then be used to analyze a new design that will not fail under the same conditions.

### Residual Stress Measurements

There are basically two types of residual stress measurements that can be made. The first type is a destructive measurement. A destructive measurement can be used if a transparency can be destroyed. One method of destructive testing is the photoelastic stress analysis. Photo elasticity

is a full field technique. Initial observation of a photoelastic pattern provides quick qualitative analysis of the overall stress distribution. Then accurate quantitative data at any selected points is easily obtained using straightforward measurement techniques and modern optical instrumentation. For residual stress measurement a coating is applied to the transparency. The transparency is then cut at the point where the residual stress is to be measured. The relieved stress will make fringe patterns on the coating enabling the residual stresses in the sample to be determined. Another destructive method is the hole drilling rosette method. This method is basically a destructive method. It is used as a nondestructive method in the welding industry, but for the transparency systems the hole must be drilled through the thickness of the transparency. This method will hopefully give accurate measurements that will then be compared to another method that will be more advantageous to use. This method is a nondestructive technique. This technique will be portable and easy to use for repeated measurements of the parts. Measurements will be made throughout the life of the part using this technique. The results will be compared to the destructive measurements to make sure the technique is valid. The acoustic method promises to be the best technique to accomplish a nondestructive test.

#### Residual Stress Testing Methods

The different types of methods for obtaining residual stress information are:

1. Strain gage hole drilling technique
2. Strain gaged F-16 canopy
3. Photoelastic stress analysis
4. Surface wave ultrasonic technique

All of these methods will be very helpful in the beginning of the analysis to try and understand the overall picture of the stress distribution. Some of the methods will give a general qualitative measure of where the critical residual stress points are over the surface of the transparency. While others will answer the question of how localized are the stresses and how small of surface area must be analyzed before all of the stress is relieved. But the goal of all of this work is to obtain a nondestructive, quantitative method that can be employed in the field.

The hole drilling rosette method, for measuring the stress, has been attempted on several different transparencies.[1] This testing method is very well defined

for the metals industry. It is basically a destructive test, but can be used as a nondestructive test in metals and welds, because the hole for these materials only has to be drilled to a depth of 1.2 times the diameter of the hole. With the gage size diameters varying to under one-sixteenth of an inch, the holes can have little effect on the overall strength of the material. But this method has never been employed on thermoplastics. All the basic theory behind this method indicates that it should be possible to measure the residual stresses. Because of the laminated design of the transparencies involved in the testing, it was determined to drill the hole completely through the transparency. For the rosette gage to work the hole can be drilled either completely through or 1.2 times the diameter. The only difference between the two in calculating the stress is that the two methods have different constants involved. A rosette gage and the stress calculations are shown in Fig. 1.

The hole drilling strain gage method is a semidestructive method that is very straight forward in its use. The method involves attaching strain gages to the surface of the material. The adhesive must give a strong bond between the gage and the substrate. The leads of the gage are then soldered to wires that lead to the strain indicator. This soldering technique does require some experience, since the heat can destroy the gage as well as the substrate. A low temperature solder was used to try and avoid any damage to the substrate. A reading is then made on the three different gages on the rosette. The next step is to drill a hole through the gage and all the way through the transparency. This hole must be aligned exactly with the center of the gage or the readings from the gage will not be accurate. A drilling guide is needed in order to accomplish this task. The drill must also be exactly perpendicular to the surface of the transparency. There has to be additional testing on the effects of the drill feed, alignment and speed. All these are very important parameters in determining the stresses accurately. Another reading is then made from the strain indicator on the three gages that are aligned on different axes. The difference in the two readings is the strain relieved. This measurement is then used in a series of equations to determine the residual stress measurement. The measurements are of the principle stresses and the angle of rotation from the axis.

The measured surface strains can be calculated into stresses by certain equations. The surface strains relieved are related to the relieved principle stresses by the following relationship:

$$\epsilon_r = (A + B \cos 2\alpha) \sigma_x + (A - B \cos 2\alpha) \sigma_y \quad (1)$$

where:

$\epsilon_r$  = radial strain relieved at point P

$$A = - \frac{1 + \mu}{2E} \times \frac{1}{r^2} \quad (2)$$

$$B = - \frac{1 + \mu}{2E} \left( \frac{4}{1 + \mu} \times \frac{1}{r^2} - \frac{3}{r^4} \right) \quad (3)$$

$\sigma_x, \sigma_y$  = principle stresses present in the structure before drilling

$\alpha$  = angle between the directions of  $\epsilon_r$  and  $\sigma_x$

E = Young's modulus

$\mu$  = Poisson's ratio

$$r = \frac{D}{D_0}$$

D = diameter of gage circle

$D_0$  = diameter of drilled hole

Measuring the relieved radial strains  $\epsilon_1, \epsilon_2, \epsilon_3$  at points  $P_1, P_2,$  and  $P_3,$  respectively, provides sufficient information to calculate the principle stresses  $\sigma_x$  and  $\sigma_y$  and their orientation,  $\beta$ , with respect to an arbitrarily selected reference.

The residual stresses can be measured from the strain measurements, using the following equations. The directions (1) and (3) are perpendicular, while (2) direction coincides with one of the bisectors as shown in Fig. 2. The principle stresses  $\sigma_x$  and  $\sigma_y$  are located  $\beta^\circ$  clockwise from directions (1) and (3) when  $\beta$  is positive.

Compute the angle  $\beta$  from:

$$\tan 2\beta = \frac{\epsilon_3 - 2\epsilon_2 + \epsilon_1}{\epsilon_3 - \epsilon_1} \quad (4)$$

Compute the stresses  $\sigma_x$  and  $\sigma_y$  from:

$$\sigma_x, \sigma_y = \frac{\epsilon_1 + \epsilon_3}{4\bar{A}} \pm \frac{\sqrt{2}}{4\bar{B}} \sqrt{(\epsilon_1 - \epsilon_2)^2 + (\epsilon_2 - \epsilon_3)^2} \quad (5)$$

In the idealized case of a point sized strain gage and a through the thickness drilled hole, the constants  $\bar{A}$  and  $\bar{B}$  are identical to A and B. In order to account for the integrating

effect of a finite sized gage, and for a blind hole situation, these constants must be computed from the following equations:

$$\bar{A} = -((1 + \mu) / 2E) \bar{a} \quad (6)$$

$$\bar{B} = - (1 / 2E) \bar{b} \quad (7)$$

where  $\bar{a}$  and  $\bar{b}$  are dimensionless, material independent coefficients.

In the case of a through the thickness drilled hole,  $\bar{a}$  and  $\bar{b}$  are obtained by integrating the gage output over the gage area.

$$\bar{a} = \frac{2}{w(r_2 - r_1)} \times \frac{1}{r^2} (\theta_1 - \theta_2) \quad (8)$$

$$\bar{b} = \frac{2(1 + \mu)}{w(r_2 - r_1)} \times \frac{1}{r^2} \left[ \frac{2(1 - \mu)}{1 + \mu} (\theta_1 - \theta_2) + \right.$$

$$\left. (\sin 2\theta_1 - \sin 2\theta_2) - \frac{1}{r} \left( \frac{\sin 2\theta_1 \cos^2 \theta_1}{2r_1} - \frac{\sin 2\theta_2 \cos^2 \theta_2}{2r_2} \right) \right] \quad (9)$$

where:

$$w = (2GW/D)$$

$$r_1 = (2R_1/D)$$

$$r_2 = (2R_2/D)$$

GW, D, R<sub>1</sub>, R<sub>2</sub>, θ<sub>1</sub>, θ<sub>2</sub> are defined in Fig. 2.

The graph of coefficients  $\bar{a}$  and  $\bar{b}$  is shown in Fig 3.

The method was used on transparencies at Hill AFB that had seen service life. The goal of these measurements was to determine if the procedure would work and to try and get some qualitative readings on the residual stresses. Since this was the first attempt, all of the readings are not very accurate and it was decided that more work had to be accomplished on validating this measuring technique. This continued work will be accomplished by the University of Dayton Research Institute (UDRI) in the following six months. A total of eleven transparencies were measured. Some of the transparencies had

four gage locations, while others only had two. These locations were determined by the investigator and are shown in Fig 4. Two of the locations were on the centerline, one forward and one aft. While the others were on the left side closer to the sil, with one being forward and one aft. No points were chosen for the right side because symmetry was assumed. The readings were taken and the results are in Tables 1-4. The results are very scattered for even the same type of transparency built by the same vendor. But some of the numbers seem reasonable, so after further investigation the procedure will hopefully be repeatable and give consistent and accurate results.

The hole drilling method future work will be accomplished in the next few months. This work will include modifications to the hole drilling technique. The main thrust of this area is to come up with the test method that will not add stresses to the plastic during the hole drilling procedure. Different drilling parameters will be tested in order to come up with the correct speed and feed parameters. Also the differences in alignment of the drill and significance of the different angles will be investigated. A fixture for alignment must be designed to be used on the curved surfaces of the transparencies. This alignment tool must be able to align the hole and guide the drill perpendicularly to the surface. This was the hardest part of the previous measurements. The drill was usually on target, but the hole was not drilled perpendicular to the surface throughout the thickness of the transparency. The hole drilling method will be performed on specimens with a known state of stress to determine the accuracy of these measurements. Specimens will also be subjected to four point beam tests. These tests will be on laminated parts and the residual stress measurements will be compared to the other methods. Verification of the method is a long process that must be done in order to support the results that the technique gives.

Another destructive technique that UDRI will perform is using regular strain gages on a optically rejected F-16 transparency and cutting coupons from the transparency. A total of thirty-one gages will be mounted on one-half of the transparency. These locations will be determined by the investigator with an emphasis on the forward part of the transparency. The gages will be a special kind that do not have wires connecting them to the strain indicator. This will make it easier to cut around the gages. The gages will be monitored throughout the testing. The transparency will then be installed into a frame to better understand the stresses induced into the installation of a transparency. The transparency will then be cut into coupons to relieve the residual stresses involved. The strain gages will be monitored after each cut to understand the relieving of the stresses. Some of these coupons will be subjected to the hole drilling method to make sure that all of the stress has been relieved from the coupon. The results will finally give an indication

of the distribution of the residual stresses involved in the manufacturing of a F-16 transparency and also the stresses involved in the installation of the part. The mapping of the transparency will be used as a baseline for data gathered in the field on in-service transparencies. The goal of this test is to determine qualitatively the residual stress distribution over an entire F-16 transparency. This will also determine where the critical stress points lie on the surface.

Photoelastic analysis is an extremely versatile and easy to apply experimental stress analysis technique.[2] The technique combines the best features of strain gages and classical photoelasticity by providing a visible picture of the overall strain distribution of the coupon. An example of photoelastic stress analysis is shown in Fig 5. The strain distribution can also be measured at any point accurately in both magnitude and direction. For measuring the residual stress with this method, it must be done destructively. A special strain sensitive plastic coating is bonded to the transparency. The transparency is then cut in the area where the residual stresses are to be observed. The coating is then illuminated by polarized light from a reflection polariscope. When viewed through the polariscope, the coating displays the strains in a colorful, informative pattern which immediately reveals the overall strain distribution. This technique will also reveal the highly stressed areas because of the fringe patterns involved. The stress distribution can then be measured quantitatively through special instrumentation. This technique will be attempted in the next few months to try and see the overall distribution of the stresses. It will also be very interesting to compare these results with the other techniques.

The next method that will be investigated is the surface wave acoustic technique.[3] This technique is a nondestructive technique that can be made portable for easy access to field measurements. An acoustic transducer is shown in Fig. 6. This technique has been used extensively in metals and ceramics. It has never been successfully used on thermoplastics. The experimental technique is based on the measurement of changes in the velocity of acoustic surface waves due to internal stresses in the plastic material. The technique will use a pair of surface wave transducers mounted on a compliant fixture. The transducer consists of a material which contacts the sample surface by a thin element, producing a line of contact. The material is then driven by a short electrical pulse, which generates a displacement normal to the surface of the polymer. The pulse is detected by the other transducer at a known distance away.



## Conclusions

The measurement of residual stresses is needed immediately for many different applications. The different testing methods must be validated in order that the stress measured is the stress relieved and not the stress that was added during the testing procedure. The testing procedure must be accurate, repeatable and sensitive to give the industry qualitative analysis of their manufactured parts for the first time. From this initial testing, it is hoped that a nondestructive, portable technique will be able to give the same accurate results as the destructive methods. This nondestructive technique will then be used extensively in the field to understand the history of the stresses that an operational part undergoes during the normal life of the part. This will finally give answers to the questions of why some transparency systems fail in a predominant failure mode. Then the manufacturing process or the maintenance of the system can be addressed to give the additional service life that is needed for the advanced transparency systems. The information will also be very important for input data for the advanced computer codes. This will enable the engineers to predict the response of the systems for the established requirements, before a full scale part is built and tested. This will cut down the number of design iterations and save a large amount of money.

# RESIDUAL STRESS MEASUREMENTS

	S <sub>x</sub> (PSI)	S <sub>y</sub> (PSI)	B (DEG)
GOODYEAR			
003-101	390	966	-37.2
001-101	-2203	482	-43.7
001-101	-735	1682	17.8
001-101	-2425	2233	11.4
SIERRACIN			
163100-01	-1496	-1007	-14.1
163100-01	-256	460	-33.6
163100-01	-2033	-1732	25.4
TEXSTAR			
5003292-05	-496	0	30.0
5002935-03	-2247	-962	-44.2
5002236-09	-539	2812	20.0
5003292-09	-2499	-1711	38.4

Table 1 Residual Stresses at Location #1

# RESIDUAL STRESS MEASUREMENTS

	S <sub>x</sub> (PSI)	S <sub>y</sub> (PSI)	B (DEG)
GOODYEAR			
003-101	-2240	-1618	38.8
001-101	-1866	-1354	31.0
001-101	-2545	-1141	34.5
001-101	-2298	-818	43.0
SIERRACIN			
163100-01	-1476	-890	41.6
163100-01	-2172	627	39.5
163100-01	-1650	-1104	-26.6
TEXSTAR			
5003292-05	-1395	-832	33.0
5002236-09	-4096	4630	-31.9
5003292-09	-2908	-1840	-44.7

Table 2 Residual Stresses at Location #2

# RESIDUAL STRESS MEASUREMENTS

	S <sub>x</sub> (PSI)	S <sub>y</sub> (PSI)	B (DEG)
GOODYEAR 003-101	-790	551	-42.7
SIERRACIN 163100-01 163100-01	-2119 1580	-1055 2981	-20.6 9.1
TEXSTAR 5003292-05 5002935-03 5002236-09	-3569 -2051 5040	-1507 1502 0551	-30.1 41.9 43.9

Table 3 Residual Stresses at Location #3

# RESIDUAL STRESS MEASUREMENTS

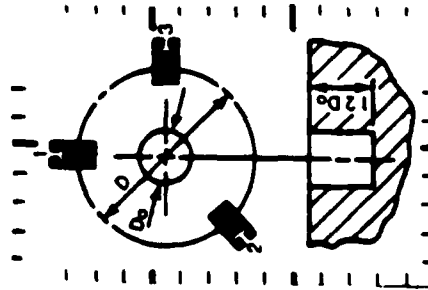
	S <sub>x</sub> (PSI)	S <sub>y</sub> (PSI)	B (DEG)
GOODYEAR			
003-101	-1741	-761	36.8
SIERRACIN			
163100-01	-1895	-257	32.3
163100-01	-3178	503	41.4
TEXSTAR			
5003292-05	-112	1852	-38.9
5002935-03	-1980	-419	-37.6
5002236-09	-5269	4952	-41.4

Table 4 Residual Stresses at Location #4

# HOLE DRILLING ROSETTE STRAIN GAGE

## DATA REDUCTION COEFFICIENTS FOR RESIDUAL STRESS CALCULATIONS

STRAIN GAGE



$$\sigma_{x,y} = \frac{(\epsilon_1 + \epsilon_3)}{4\bar{A}} \pm \frac{\sqrt{2}}{4\bar{B}} \sqrt{(\epsilon_1 - \epsilon_2)^2 + (\epsilon_2 - \epsilon_3)^2}$$

$$\bar{A} = -\frac{1 + \nu}{2E} \times \bar{a}$$

$$\bar{B} = -\frac{1}{2E} \times \bar{b}$$

Fig. 1

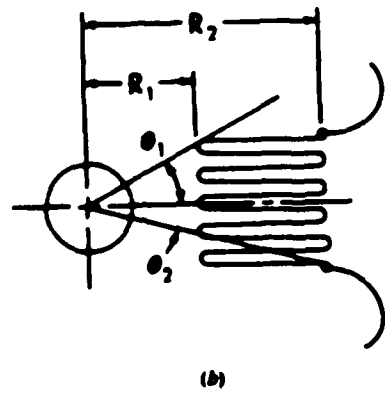
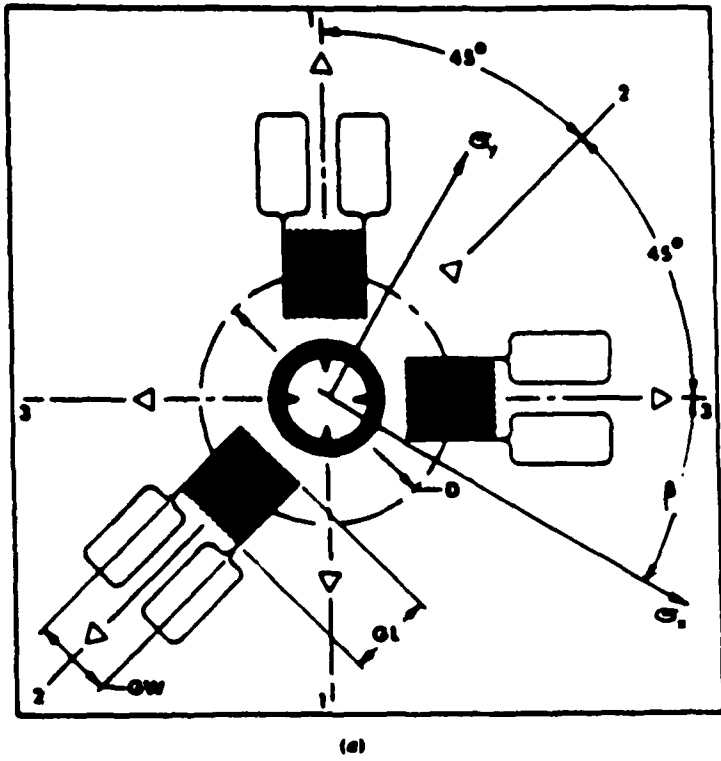
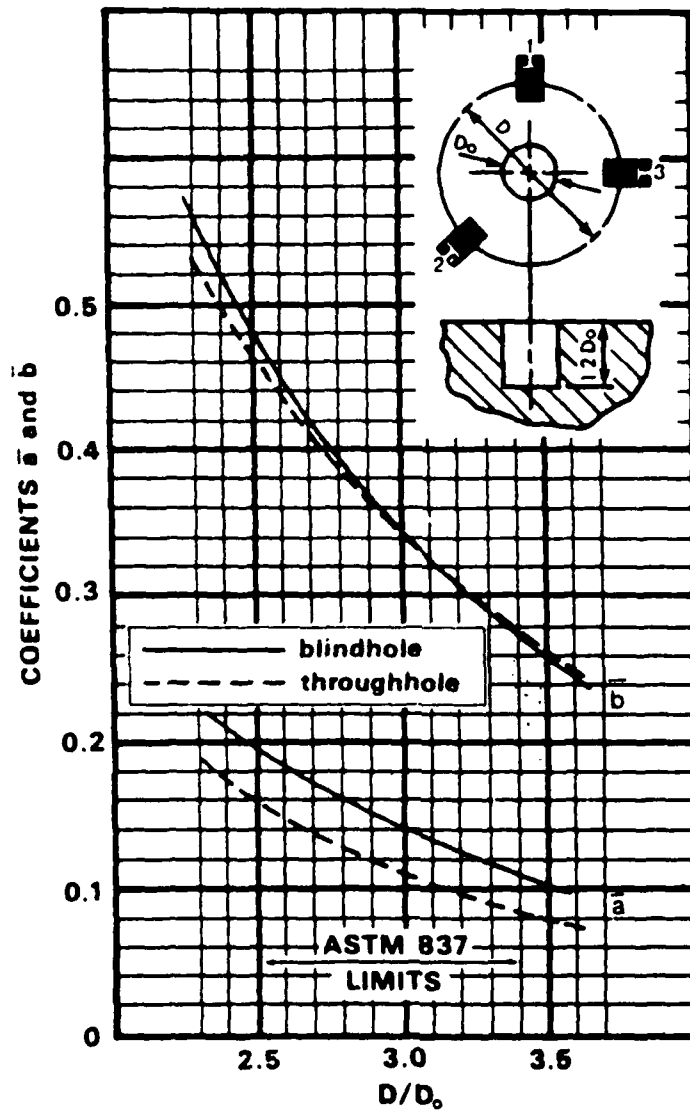


Fig. 2 Typical Three Element Strain Gage Rosette for the Hole Drilling Method

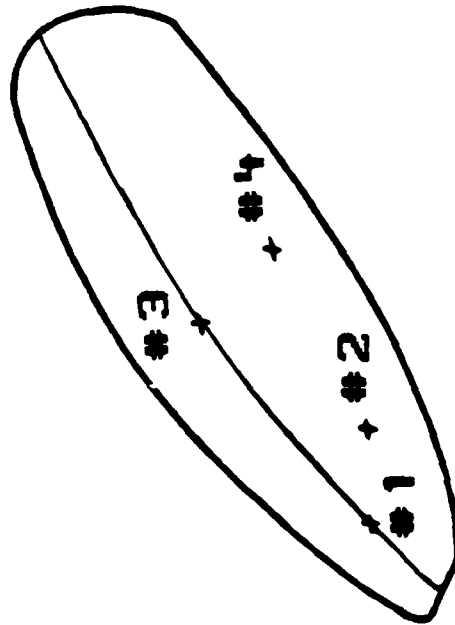


**FOR TEA-XX-062RK-120 &  
EA-XX-(031, 062, 125) RE-120  
ROSETTES**

Fig. 3 Plot of coefficients  $\bar{a}$  and  $\bar{b}$  versus diameter ratio



# F-16 RESIDUAL STRESS MEASUREMENT LOCATIONS



## COORDINATES

POINT	COORDINATES
1	8 inches AFT ON CENTERLINE
2	21.5 inches AFT 9 inches ABOVE SIL
3	51 inches AFT ON CENTERLINE
4	51 inches AFT 9 inches ABOVE SIL

Fig. 4

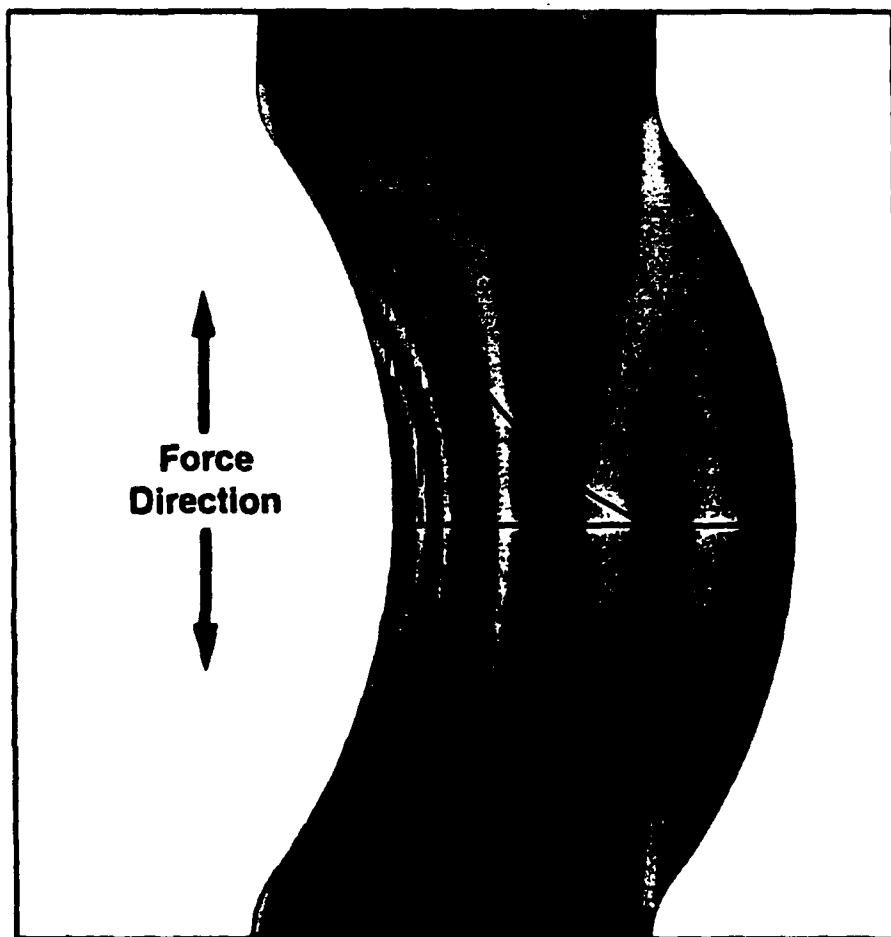
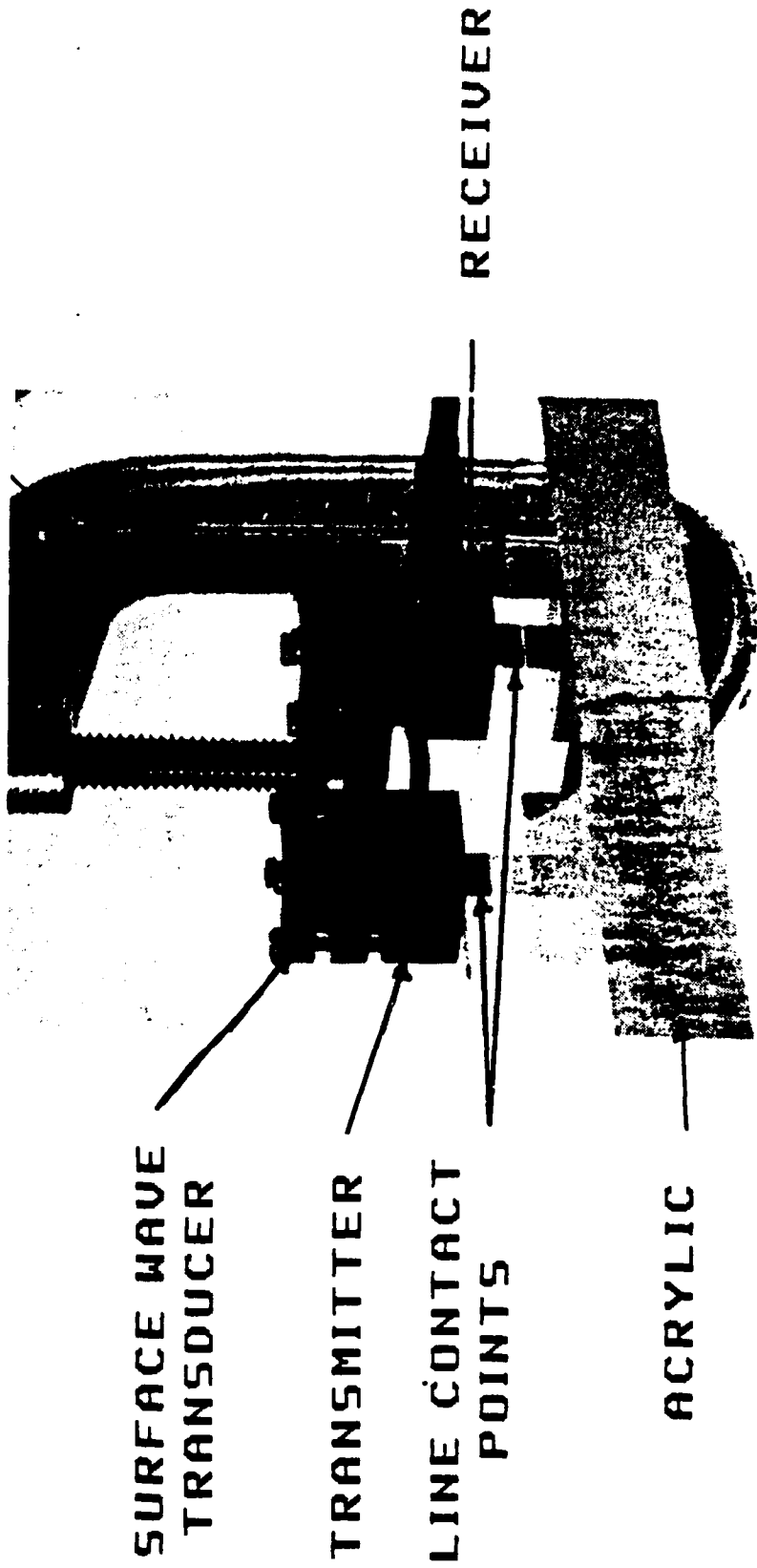


Fig. 5 Photoelastic Stress Analysis

# SURFACE WAVE TRANSDUCER



## References

- [1] ASTM Designation: E837-85, Standard Test Method for Determining Residual Stresses by The Hole-Drilling Strain Gage Method. American Society for Testing and Materials, 1916 Race St., Philadelphia, PA. 19103. Annual Book of ASTM Standards Vols 03.01 and 12.02, Pages C14 - D6.
- [2] Photoelastic Stress Analysis. Measurements Group, Photoelastic Division, P.O. Box 27777 Raleigh, NC 27611. Bulletin SFC-300 A, 1987.
- [3] Raju, B. Basava and West, Blaine S., Nondestructive Evaluation of Residual Stresses In Aircraft Transparencies, University of Dayton Research Institute, Dayton, Ohio 45469, UDR-TR-88-65, June 1988.

B-1B EXTENDED LIFE WINDSHIELD PROGRAM

Capt Steve Kolbow  
AFWAL/FDER

Capt Paul Berry  
OC-ALC/MMBRE

B-1B EXTENDED LIFE WINDSHIELD PROGRAM

Capt Steve Kolbow  
AFWAL/FDER, WPAFB, OH

Capt Paul Berry  
OC-ALC/MMBRE, Tinker AFB, OK

Title: B-1B Extended Life Windshield Program

Date: 12 December 1988

Authors: Capt Steve Kolbow AFWAL/FDER, WPAFB, OH  
Capt Paul Berry OC-ALC/MMBRE, Tinker AFB, OK

Presentation for: The AFWAL Transparent Materials Conference  
Monterey, California, 19 January 1989

Abstract: This presentation describes the Aeronautical Systems Division (ASD) and Air Force Logistics Command (AFLC) joint program to extend the service life of B-1B windshield replacement spares. The B-1B windshield has a service life of less than one year due to delaminations. Keeping the fleet supplied with windshields costs over \$10 million a year. The Windshield System Program Office (SPO) and Oklahoma City Air Logistics Center (OC-ALC) are conducting a joint program together with the B-1B SPO to evaluate windshield design changes aimed at doubling service life without requiring windshield birdstrike requalifications. Five longer life B-1B windshield designs will be evaluated in the full scale windshield durability facility and on B-1B aircraft. OC-ALC will use the results of these evaluations in future B-1B windshield spare procurements.

1. Introduction (Figure 1): The B-1B windshield has a proven four pound 560 knot birdstrike resistance which is one of the best flying. However its service life is less than one year due to delamination of the outer glass ply.
2. Background: In October 1985 a B-1B Windshield Tiger Team was formed to investigate problems with delamination, optical distortion, nighttime multiple imaging, and 4 day change out times. Based upon findings of the Tiger Team and the need for improved combat hazard protection for the 1990's the Windshield System Program Office and the B-1B SPO began a long term program to redesign the B-1B Windshield. In 1988 as a spinoff to the long term effort the Windshield SPO, the B-1B SPO, and OC-ALC formed a joint program to specifically address what could be done in the near term to extend the windshield's short service life which was costing the Air Force \$10M annually for windshield spares.
3. Problems:
  - a. Optical Distortion (Figure 2): The temperature difference along the electrical heater deletion line causes optical distortion when it is used (Figure 3). Presently only the hot air deice/defogger is used.
  - b. Night Time Multiple Imaging (Figure 4): Because the windshield is one and a half inches thick, is made up of multiple plies, and has an extreme viewing angle, there is a tendency for multiple imaging. This is most noticeable during night landing.

c. Change-out Time: The windshield takes four days to change-out. This is due primarily to sealant curing time. A complicated bolt torquing sequence also adds to change-out difficulty.

d. Delamination (Figure 5): The current windshield service life is less than one year due to delaminations of the outer glass ply (Figure 6). Probable causes are built in stresses caused by slight differences in contour between the glass ply and the main polycarbonate ply. Another probable cause is thermal stresses. Differences in thermal coefficients of expansion between the glass and polycarbonate, combined with the large windshield surface area create stress at the windshield edges during varying temperatures.

4. Approach: The B-1B Extended Life Windshield Program consists of the purchase and evaluation of prototype windshields designed to increase windshield service life. One windshield of each design will be evaluated in the full-scale windshield durability facility and the remaining flight evaluated on B-1B aircraft. Results of these evaluations will be used by OC-ALC in selecting the next design for windshield spare procurements beginning in FY90. Better than double the current service life is expected with the new windshield spare resulting in over \$5M savings annually.

#### 5. Discussion:

a. Windshield Design Criteria: The primary emphasis of the prototype windshield designs was to increase windshield durability while still meeting current windshield requirements. Other improvements in the areas of optics and supportability were also encouraged. The design changes made would not be requalified for birdstrikes; therefore, the main polycarbonate structural ply, the inner polycarbonate spall shield, and the interlayer between these two plies had to remain unchanged. There were to be no changes to the aircraft contour lines around the windshield. Changes to the outer ply, its interlayer, and the edge attachments were anticipated.

b. Purchase of Prototype Windshields: With funding from the B-1B SPO the Windshield Systems Program office purchased eight B-1B prototype windshields from each of the two firms qualified to produce them. Each firm is producing two designs. In addition OC-ALC purchased seven chemically tempered glass faced windshields through a value engineering proposal in their FY89 spares purchase (Figure 7).

#### c. Full-scale Durability Testing:

(1). The full-scale windshield durability facility at Wright Patterson AFB will be used to simulate the pressure thermal loads which the windshield encounters in flight (Figure 8). Three representative flight profiles were selected by the B-1B SPO for the simulation. By running the facility continuously, four years of flight time, 1400hrs,



can be simulated in about two months. Two current production windshields will be evaluated first to establish a baseline. Then the five prototypes windshields will be evaluated. Allowing time for change-outs and reinstrumentation the evaluations will be completed in ten to eleven months (Figure 9).

(2). A windshield test fixture was needed which accurately represented the stiffness and thermal characteristics of the B-1B windshield frame. After receiving bids to build the fixture, we found it would be more cost effective to ship a B-1 test sled from Holloman AFB to WPAFB, remove the cockpit module, and modify the windshield framing to match that of a B-1B (Figure 10). Hatches had to be obtained and installed so the module could be pressurized. A shroud to duct the airflow over the windshield was also contracted for fabrication.

d. Flight Evaluations: Deliveries of the prototype windshields will begin in March and continue through September of 1989. They will be optically evaluated and installed on aircraft at the four SAC B-1B bases, Grand Forks, Ellsworth, McConnell, and Dyess AFB. The windshields will be installed in place of the current production spares. OC-ALC is establishing a program to track the windshields. The number of flight hours on the windshields and reasons for their removal will be tracked. The tracking program will also follow all existing windshields so their service lives can be compared.

6. Results/Conclusions: Results of these full-scale durability evaluations and flight evaluations will be used by OC-ALC in their selection of windshields to fill the next spares order in early FY90. This timely identification of extended life windshields will result in savings of over \$5 million per year on future B-1B windshield spares.



Figure 1. B-1B



Figure 2. Distortion Along Heater Deletion Line

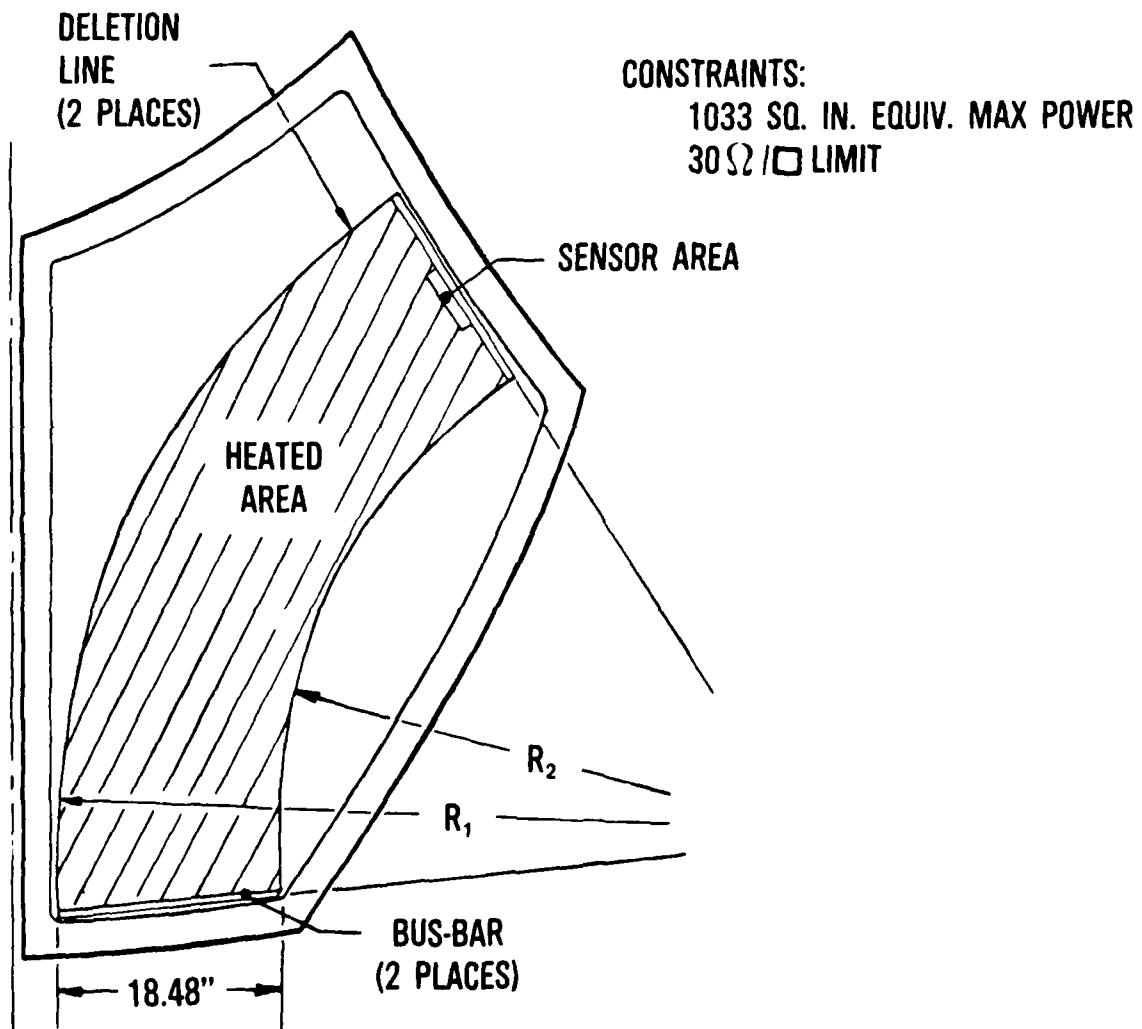


Figure 3. Swing Pattern Electrical Conductive Coating

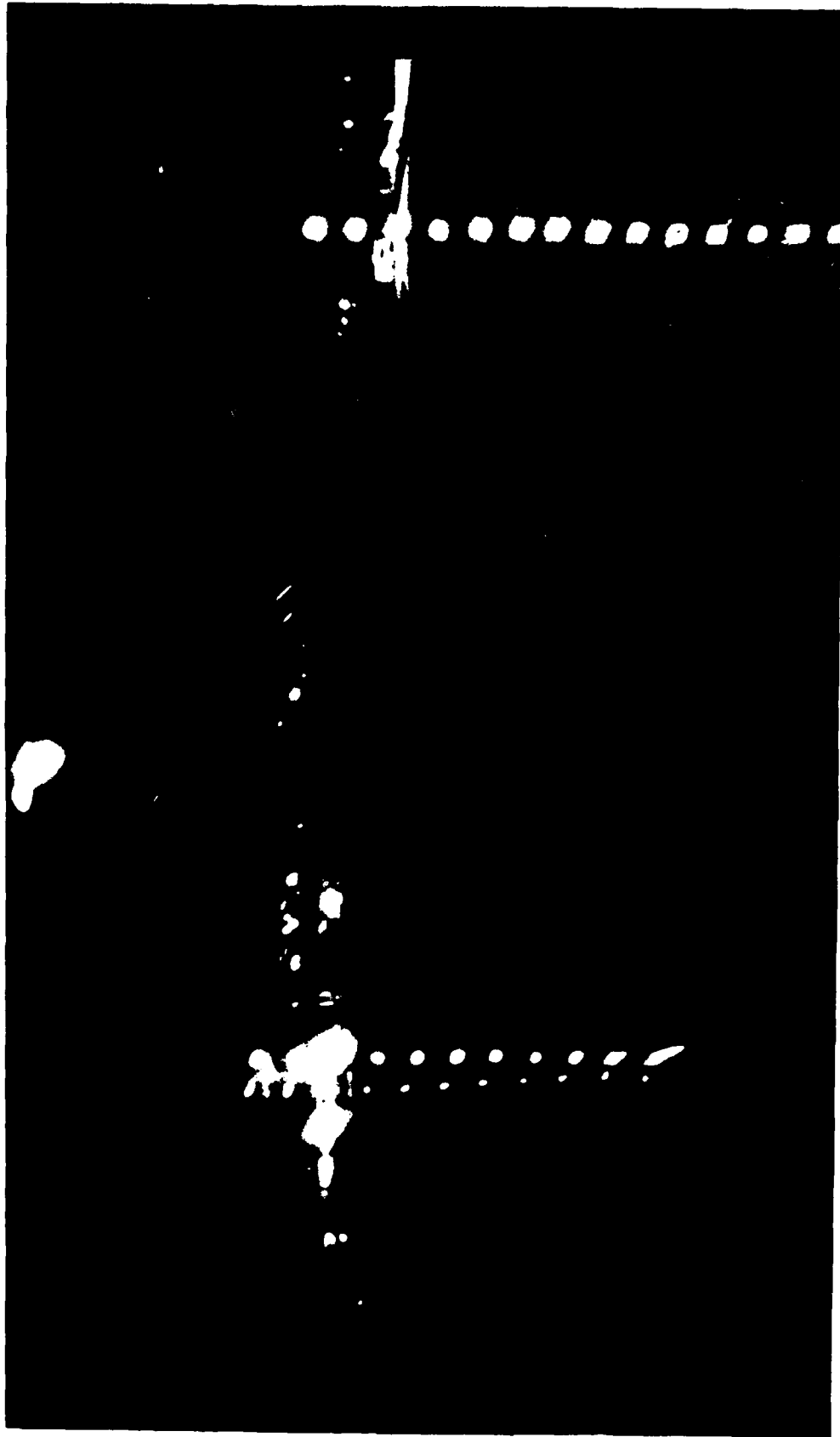


Figure 4. Night Time Multiple Imaging

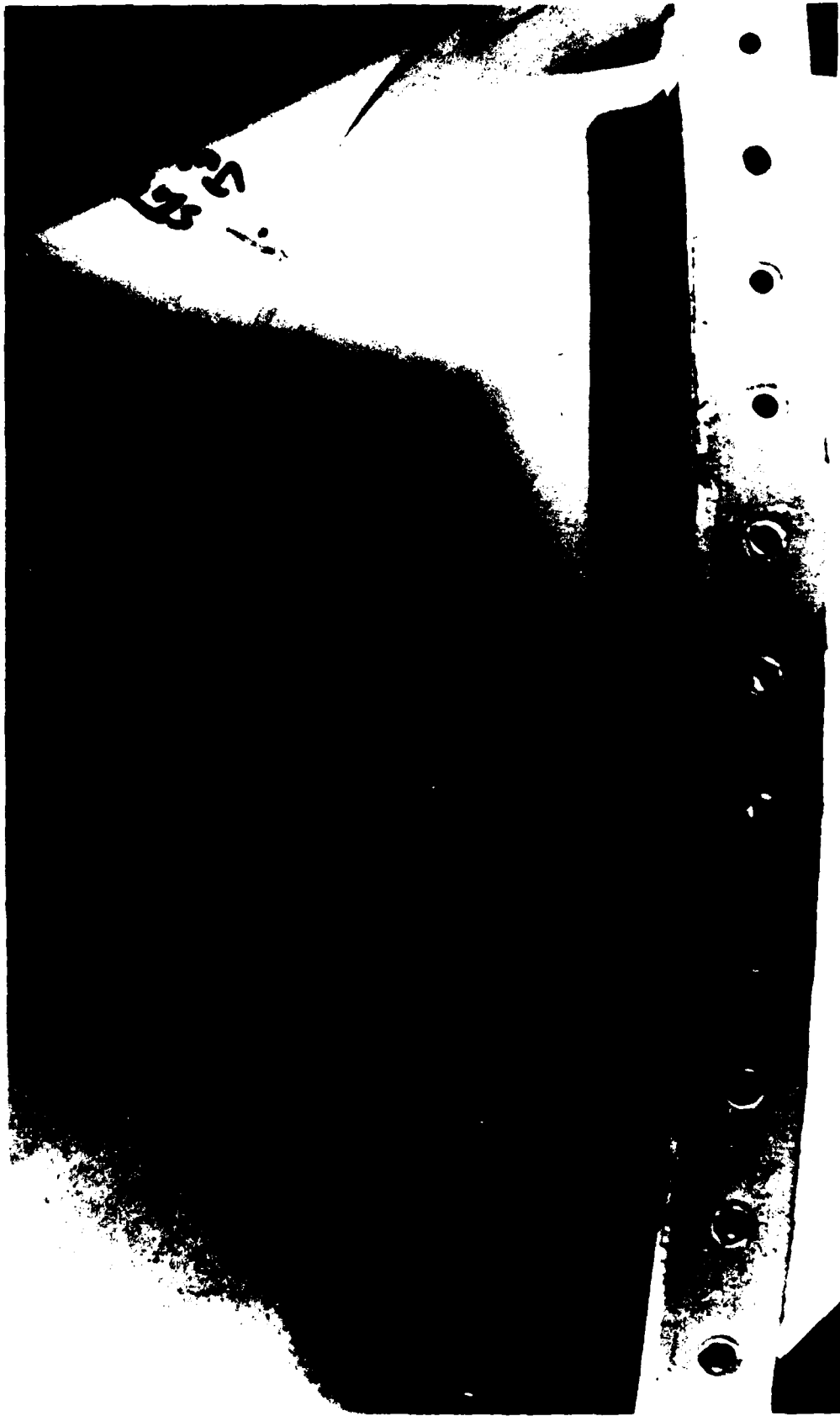


Figure 5. Outer Ply Delamination

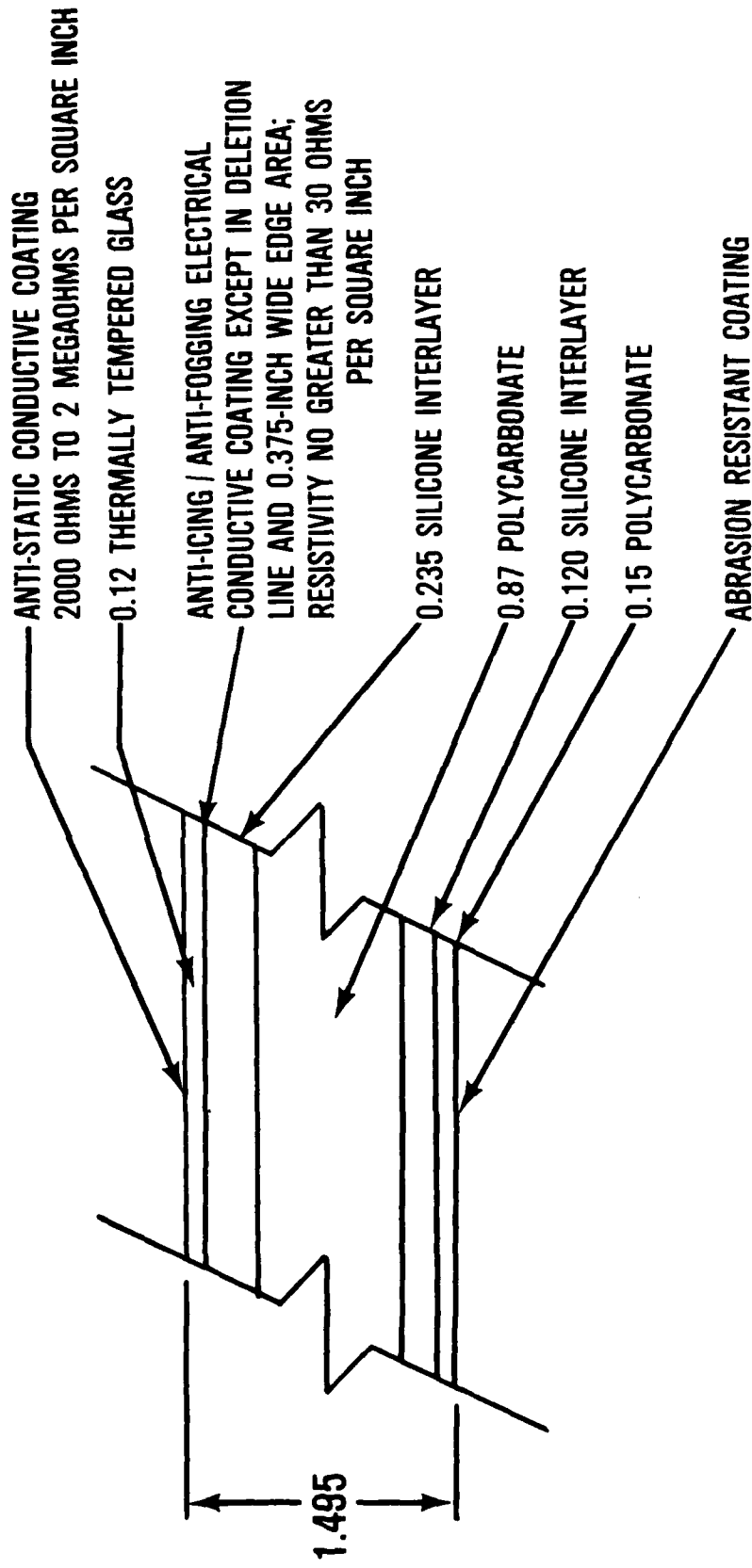
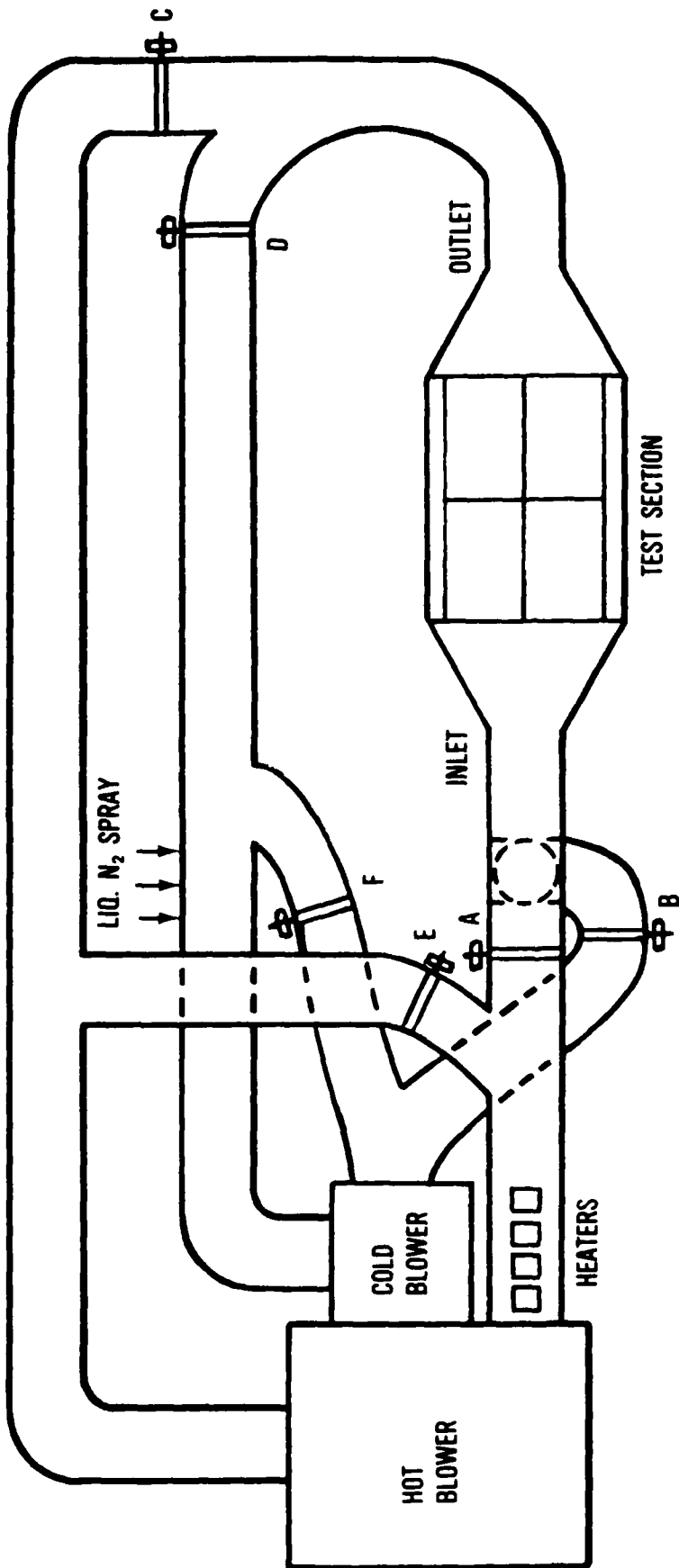


Figure 6. Existing B-1B Windshield Cross-Section

WINDSHIELD DESCRIPTION	PROCURED BY	QUANTITIES		
		TOTAL	DURABILITY EVALUATIONS	FLIGHT EVALUATIONS
SWEDLOW CURRENT PRODUCTION	AFWAL	1	1	--
SIERRACIN CURRENT PRODUCTION	AFWAL	1	1	--
SWEDLOW DESIGN I	AFWAL	4	1	3
SIERRACIN DESIGN I	AFWAL	4	1	3
SWEDLOW DESIGN II	AFWAL	4	1	3
SIERRACIN DESIGN II	AFWAL	4	1	3
SIERRACIN CHEM TEMP GLASS FACED	OC-ALC	7	1	6

Figure 7. Use of Prototype Windshields





- A - HOT LOOP    C - HOT LOOP STOP    E - HOT LOOP BYPASS
- B - COLD LOOP    D - COLD LOOP STOP    F - COLD LOOP BYPASS

Figure 8. Durability Facility

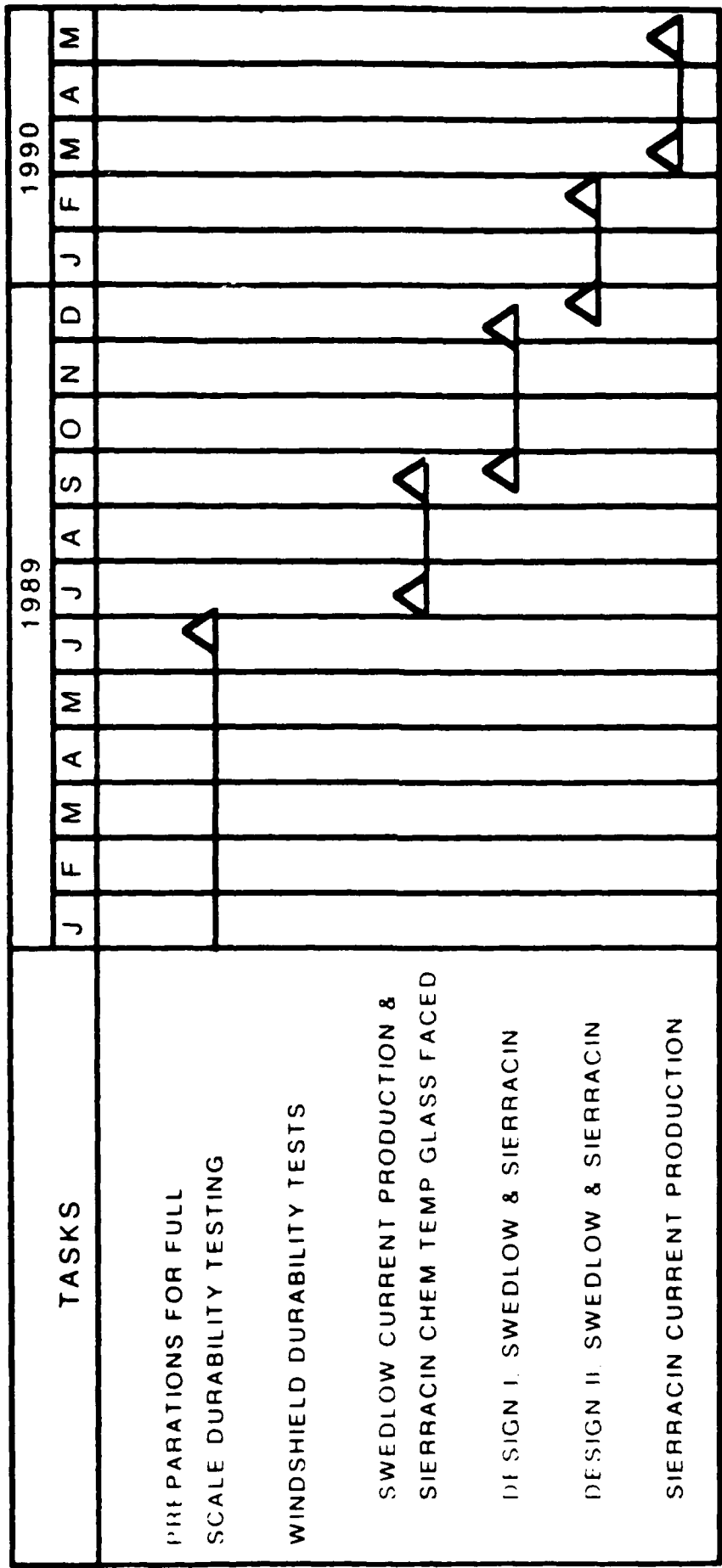


Figure 9. Full-Scale Durability Testing Schedule



Figure 10. Modification of B-1 Test Sled for Use as a Windshield Test Fixture

IN-SERVICE CRACKING OF F-16 WINDSHIELD/CANOPIES

B. G. Hinds  
J. A. Raffo

Sierracin/Sylmar Corporation

## IN-SERVICE CRACKING OF F-16 WINDSHIELD/CANOPIES

Authors:

B. G. Hinds  
J. A. Raffo

Sierracin/Sylmar Corporation

### ABSTRACT

In mid-1987, routine inspection of F-16 solar-coated transparencies at Shaw Air Force Base uncovered a serious problem with cracking of the polycarbonate structural ply along the bolt-hole line. Subsequent detailed inspection found the problem to be widespread and at several bases, but only on the solar-coated forward transparencies. The non-solar-coated forwards and both types of aft transparencies did not show any evidence of a similar problem.

Extensive laboratory analysis of cracked canopies and a thorough review of the maintenance procedures for the aircraft at the bases isolated the problem to the aircraft cleaning materials that are specified in Mil-C-87936A. A test methodology was developed that duplicated the in-service cracking in 15 minutes in the laboratory. Testing determined that the problem required the unique combination of solar coating, bus bars, holes, and aggressive cleaning compounds to cause the cracking to occur. The elimination of any one of these factors was enough to prevent or greatly increase the time to crack. A simple rework technique was subsequently developed and proved in lab testing.

Testing of the approved Mil-Spec cleaners revealed that only one of the more than 20 approved cleaners is truly safe to use around polycarbonate transparencies.

## BACKGROUND AND INTRODUCTION

Forward and aft canopies for the General Dynamics F-16 Fighter Aircraft have been manufactured since 1972. These transparency systems represent a producibility challenge for both qualified vendors due to their large size, extremely compound-curved shape and combination of materials in the laminated structure. In spite of the complex design and production challenges, the program has enjoyed relatively few field-service problems for such a high-usage aircraft.

Early canopy construction consisted of a monolithic ply of fusion-bonded polycarbonate. Interior and exterior surfaces are coated with hard coatings to enable the polycarbonate to withstand the environmental effects of humidity, heat and ultraviolet exposure, as well as cleaning and service abrasion, including rain erosion. An unacceptable incidence of erosion damage and an inability to field-polish the coated exterior were instrumental in the decision to replace the outer coating with a substantial thickness (0.125-0.187 inches) of cast acrylic. This design, demonstrated under an Air Force Manufacturing Technology Program, called for lamination of the acrylic faceply to the polycarbonate structural ply through the use of cast-in-place silicone, later urethane, adhesives. As requirements to reduce the solar heating loads on the cockpit became a necessity, the interior polycarbonate surface was coated with a combination of metal and organic films which were grounded to the frame of the aircraft via a conductive edge design. The solar coating has been in service since 1984, with only minor field-service incidents, until early 1987. At that time, concern was raised by USAF/WPAFB and General Dynamics regarding an increasing incidence of cracks occurring in the polycarbonate mainply. These cracks were almost always confined to the edge of the transparency and did not extend through to the interlayer or the acrylic faceply.

Most of the earliest reported incidents occurred at Shaw Air Force Base, South Carolina, with fewer reports from Luke Air Force Base, Phoenix, Arizona. Cracks occurred in both vendors' transparencies although the severity and number of cracks per canopy varied in each incident (see Figures 1 and 2). Many of the cracks reported in the Sierracin canopies extended radially out from the bolt-hole and bushing, with some reaching the visual area. Cracks in the Sierracin/Sylmar Corporation canopies did not usually extend from bolt-hole to bolt-hole as had been reported with the other vendors' hardware. Reported cracks were almost exclusively confined to solar-coated units of the single-place design. No cracks were reported in clear, non-solar forward, or any aft transparency units in spite of the fact that the clear units have the identical cross section except for the solar element and edge-grounding system.

An ad hoc Task Force was formed with the vendors, the airframe manufacturer, General Dynamics and USAF/F-16SPO/AFWAL participating to investigate the cause(s) of the problem and recommend possible solutions.

### DISCUSSION

Investigation of this problem at Sierracin has focused on the dissection and analysis of failed transparencies and the subsequent duplication of the phenomenon in the laboratory. This paper will describe the analysis of field-exposed transparencies with various sophisticated analytical instrumentation and the laboratory investigation using coupons cut from actual production hardware. Finally, we will review the recommended improvements which have been incorporated on recent production canopies.

### Shaw Air Force Base Field Investigation

Two forward solar canopies with reported cracks in the polycarbonate ply were isolated and carefully removed from their frames under close scrutiny. Upon removal, it was evident that the frame allows liquid to collect and contact the transparency where it attaches to the frame. This occurs in spite of the fact that ample sealing material is used to seal the canopy to the frame. Liquid found inside the frame on S/N 177 was collected, along with samples of liquids which may have contacted the outside of the canopy/frame while it was on the aircraft. Samples of aircraft cleaner detergent (Mil-C-87936), both concentrate and diluted, other cleaning/paint compounds and dilution water were collected. The liquid found inside the frame was analyzed and determined to be water; unfortunately, it had rained heavily the night before the investigation. Stress craze testing (per Mil-P-8184 and ASTM F-484) on the other fluids collected was performed in the laboratory using beams cut from polycarbonate sheet. All fluids were acceptable for polycarbonate except for the aircraft cleaner soap solutions which severely attacked polycarbonate at 300 psi in 30 minutes at elevated temperature (160F) or in less than 96 hours at room temperature and 500 psi outer fiber stress. It has been reported by General Dynamics that pressurization stresses can approach 1800 psi and that temperatures of 180-200F have been measured inside aircraft cockpits. Under less severe conditions, the Shaw soap was shown to attack polycarbonate. Clearly this material did not belong anywhere near the polycarbonate transparency.

### MIL-C-87936 Aircraft Cleaner Fluids Investigation

Given the above data and the fact that the Shaw soap was Mil-Spec-approved, an investigation into the other fluids approved for use in cleaning the aircraft was initiated. Samples of most materials on the Qualified Products List (QPL) were obtained and evaluated for critical stress craze level on polycarbonate and acrylic (Mil-P-5425) using the

specimen and techniques outlined in Mil-P-8184, Revision E. Initial stress levels of 2500 and 4000 psi were selected for elevated (160F) and room temperature testing respectively using an exposure time of 30 minutes. It should be noted that the Mil-C-87936 testing does not address the expectation that these materials could be used around polycarbonate components. No polycarbonate compatibility testing is required in the spec; therefore, it is not surprising that most of the materials approved under the specification crazed polycarbonate at or below the 1800 psi stress level. In fact, only one material did not craze either polycarbonate or acrylic at the test stress and temperatures (see Table 1). One other material was almost as severe on polycarbonate as was the Shaw soap. Other cleaner materials used around F-16 aircraft installations and near the transparencies were collected and screened in a similar manner. The data is presented in Table 2.

### Analysis of Field-Exposed Canopies

Cracked areas of canopies SN's 061, 073 and 177 from Shaw were cut up and an attempt made to analyze for the cause of the crazing. Based on the above observations with the Mil-Spec cleaners, the focus of the analysis was on extraneous chemicals or solvents which may have initiated crazing in the presence of elevated temperatures and/or stress. The techniques were Electron Spectroscopy for Chemical Analysis (ESCA), Mass Spectroscopy (MS) and Gas Chromatography (GC). All are specific for the detection of organic compounds in the presence of polycarbonate and acrylic, although each method has its own set of advantages, limitations and sample preparation requirements. ESCA, predominantly a surface technique, could not differentiate between polycarbonate samples with cracks and the control sample from areas without cracks. Initial MS results were also negative until refinements in sampling procedures were able to detect differences in the polycarbonate material in the cracked and uncracked areas.

Basically, it was determined that the polycarbonate in the cracks had been degraded, making it extractable in methanol. Lab stress craze samples treated with Shaw soap also indicated identical degradation spectra in MS analysis, unlike the control sample. Undegraded polycarbonate is not methanol-soluble. Although positive evidence of the presence of Shaw soap was not detected, circumstantial evidence implicated the soap as a possible cause of the problem; however, the analytical techniques used were not sensitive enough to confirm this. Another approach was taken.

Samples of the cracked area were cut in finely-divided pieces and extracted with boiling water for 96 hours. A Soxhlet extraction apparatus, commonly used in organic chemistry, was used to concentrate any traces of water-soluble material in the sample. The water extract was then analyzed in a GC for trace organic components. The cracked samples were compared to parts-per-million (ppm) concentration standards of Shaw soap in water and extracts of a control sample of F-16 edge



configuration made to duplicate all materials present in the field, including sealant, conductive pastes and coatings. The GC fingerprint of the cracked sample conformed identically to the Shaw Cleaner standard and was different from the control sample. Analytical evidence of the presence of soap in the cracks had finally been found, as suspected by appropriate modification of sampling techniques. The next sections detail evaluations performed to prove and confirm this finding using creative lab coupon testing.

#### Coupon Testing of Offcuts

The goal of this phase of the program was to duplicate the stress and temperature environment seen by field canopies, hoping to duplicate the cracking characteristics seen in the field as well. Emphasis was placed on a comparison of the clear and solar-coated units, since clear units had not reported cracking in the same period of time that solar transparencies showed problems.

#### Experimental Setup/Stress-Craze Testing

Beams of solar and clear canopies were cut from the edges of completed production windshields of the F-16 forward canopy configuration. The test beam dimensions are shown in Figure 3. In order to duplicate the real-world environment as closely as possible, each beam was torqued at each bolt-hole with appropriate attachment bolts to the specified installation torque of 80 inch/pounds using a square of aluminum, simulating the aluminum frame of the aircraft. In addition, a pan was devised and sealed to the inner surface of the transparency around the bushing, with the sealing material employed in actual aircraft installations (also depicted in Figure 3). This pan allowed the test fluids to contact the inner surface of the transparency throughout the testing period. The beams were loaded to various levels and the time-to-craze, or cracking noted at elevated temperature. A temperature of 160°F was selected as the upper exposure temperature.

#### F-16 Edge Configurations

Although the basic cross sections of the clear and solar transparencies are quite similar, significant differences exist at the edge of the transparency. As shown in Figure 4, the solar coating is comprised of a system of three coatings; i.e., an organic basecoat, a metal film, and another organic coating or topcoat to protect the metal. These coatings are covered with a silver-filled epoxy grounding material (busbar) and a protective, cosmetic sealant, identified as MAT-292. The clear system has the identical basecoat, S-233, as the MAT-292 sealant. The metal film, topcoat and silver-filled material are additional to solar units. The hole drilling, adhesive material and bushing attachment operations are identical for both systems with the exception of a few aluminum bushings placed around the transparency to facilitate grounding on the solar parts.

## Test Methodology and Results

Samples were set up using one of the Mil-C-87936 cleaners as the contact fluid. It was hoped to use the cleaner from Shaw as the test fluid, since it crazed polycarbonate most severely. However, all available samples were expended in the initial phases of the program and more was not obtainable. The fluid selected for all testing (EZE 206) was less severe than the Shaw material by a factor of at least two (see Tables 1 and 2). The first set of samples, with results shown in Table 3, were tested at two stress levels and compared the clear and solar canopies. An interesting observation was noted.

The solar configuration was attacked so severely that the coupon broke only about 15 minutes into the exposure period, while the clear version was unaffected after 90 minutes. This great difference in resistance to the effect of a cleaner was unexpected but consistent with field-service data. Subsequent testing was performed to investigate the phenomenon. Samples were prepared from sections of the canopy adjacent to the edge, without holes. This isolates the effect of the solar coating without holes or silver busbar material. No attack was noted on either coupon in the 90-minute test period, indicating that the basic solar-coating process was not causing the deterioration in performance (see Table 3). When the clear canopy edge sample was made more like the solar configuration by applying busbar material over the clear surface, it behaved like the initial solar configuration (results are shown in Table 4). When busbar material was applied on a clear coupon without holes, no craze occurred and it performed as a clear canopy. In similar coupons, when the test was performed without the application of soap, the coupons were not crazed. When a mild Mil-C-87936 soap (Fleetline), was used in place of the EZE 206, even solar-coated samples were unaffected in 90 minutes.

A distinct pattern was observed from this testing methodology. Three elements were needed to cause premature crazing:

- 1) the presence of an aggressive chemical agent -- a severe soap;
- 2) the presence of the busbar material with the soap;
- 3) an edge with holes.

In the absence of any one of the above three components, the coupons were craze-resistant. Without the severe soap, no attack occurred and the testing duplicated the effect seen in the field.

## Design/Material Improvements and Recommended Solutions

As a result of the directions indicated by all of the above testing, Sierracin/Sylmar Corporation has made and implemented a number of edge-design improvements to production F-16 transparencies in coordination with General Dynamics and USAF.

The old and new edge designs are compared in Figure 5. It is anticipated that these improvements are positive enough to act independently of any other corrective action which may prevent the transparency from being exposed to harsh cleaners. Laboratory coupons made with these modifications were unaffected and showed no sign of attack in over 240 minutes of exposure to the aggressive soap at high temperature (see Table 5).

The following modifications were made on the Sierracin/Sylmar-manufactured F-16 forward transparencies in order to reduce and eliminate any potential cleaner/solvent cracking of the polycarbonate mainly.

#### All Transparencies, Clear and Solar-Coated

- Bushings - Bushings were redesigned to transfer the compressive/radial stresses into more favorable compressive-only stresses.
- Bushing Holes - The bushing holes in the transparencies were modified to accept the redesigned bushings and enlarged to provide room for additional adhesive/sealant application for maximum sealing capability around each end of the bushing.
- Edge Sealant - The edge sealant was changed from Sierracin/Sylmar Material Specification MAT-292 to MAT-423, which is more durable and resistant to solvent/cleaner attack (see Table 5).

#### Solar-Coated Transparencies Only

- Busbar material was changed from Sierracin/Sylmar Material Specification FX-12/FX-176 to MAT-383. MAT-383 contains no solvents, unlike FX-12/-176, and is safe for polycarbonate up to 6000 psi. Although the testing did not isolate this component as the most significant factor, it did indicate room for improvement.
- Busbar Application - The application of busbar material MAT-383 is limited to the areas around the aluminum conductive grounding bushings only. This will limit any potential cleaner/solvent attack on polycarbonate to a minimum number of holes.

## CONCLUSIONS

1. The cause of the recent series of cracking and crazing on polycarbonate transparencies is due to the chemical attack caused by exposure to highly-aggressive cleaner materials, which were not properly evaluated for their effect on transparency materials prior to Mil-Spec qualification.
2. The problem was accentuated by the peripheral busbar -- which was thought to be essential for proper grounding in the original design -- and attachment holes, which need to be present.
3. Sierracin/Sylmar Corporation recommendations for bushing redesign, sealant/silver-filled material upgrades and busbar limitation produce a part which performs as well as, or better, in lab testing than clear transparencies, which do not fail in the field.

### ACKNOWLEDGMENTS

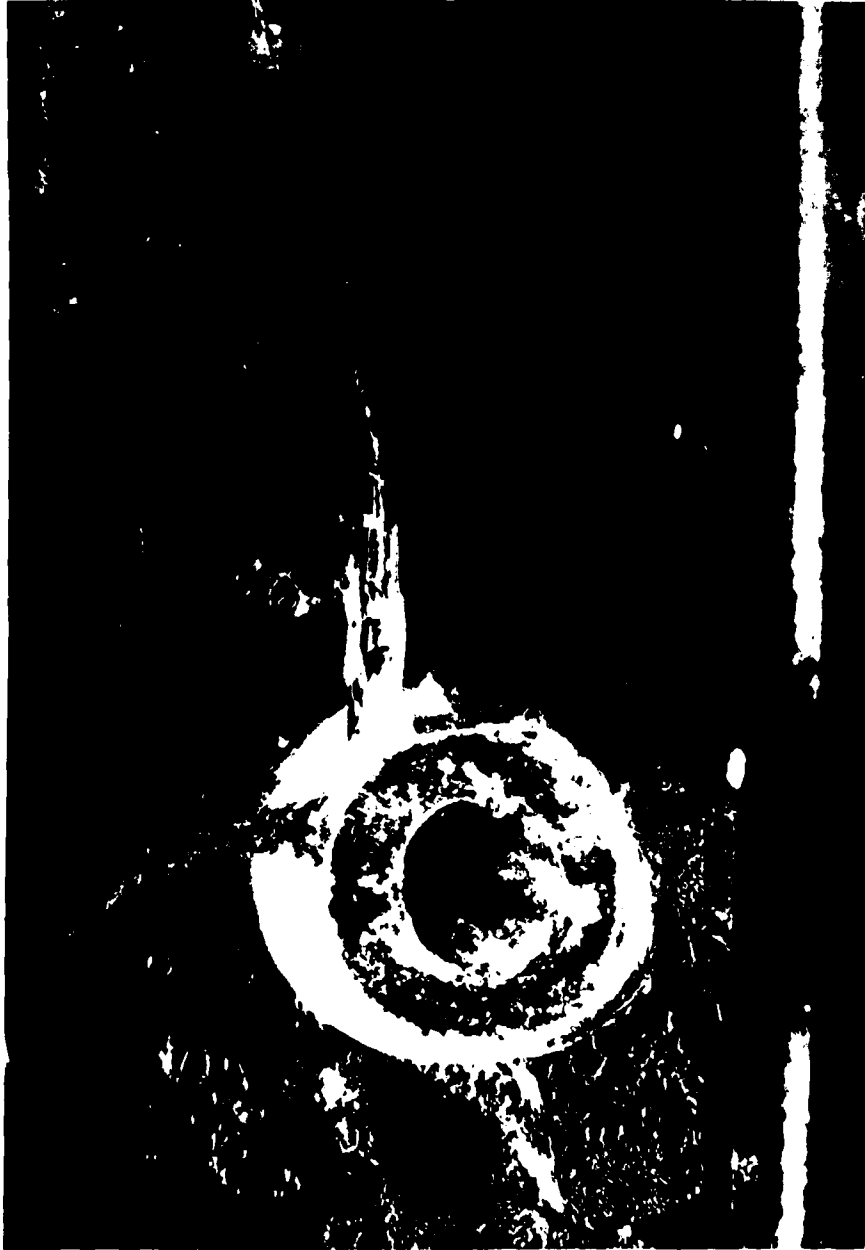
The authors wish to acknowledge the efforts of the following persons, all of whom contributed to the thinking on this program.

E. Iriana, who performed most of the testing; K. Lakdawala, who coordinated the analytical testing; C. Maglalang, who initiated the program direction and testing methodology.



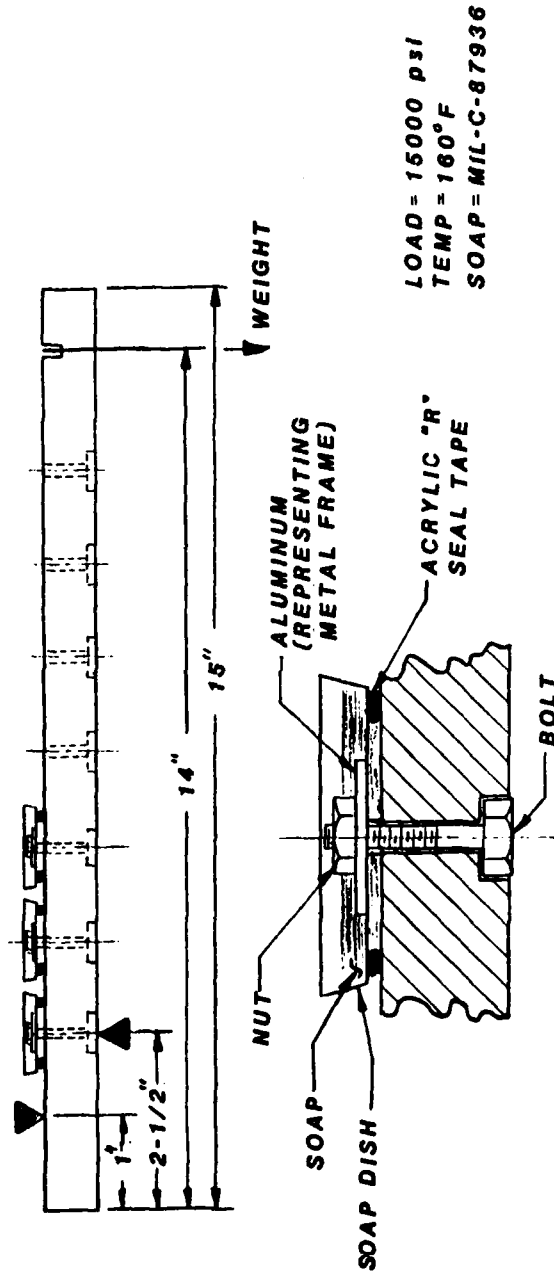
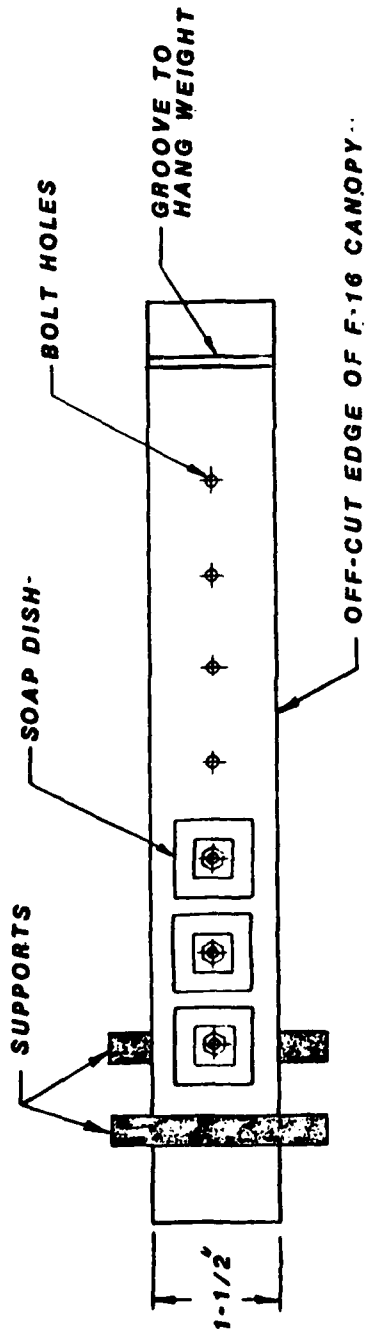
**POLYCARBONATE BOLT HOLE CRACK  
FROM F-16 W/S S/N 061**

**FIGURE 1**



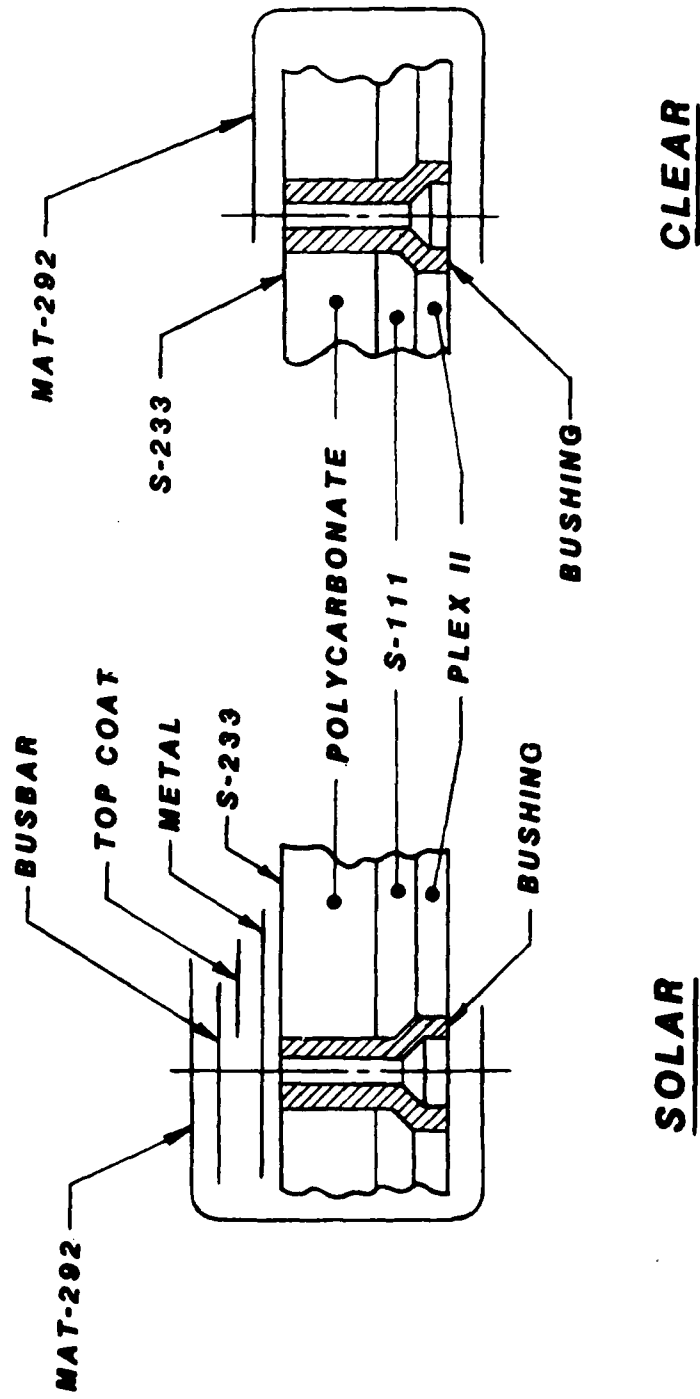
**EXAMPLE OF PC CRACK IN F-16  
TRANSPARENCY S/N 073**

**FIGURE 2**



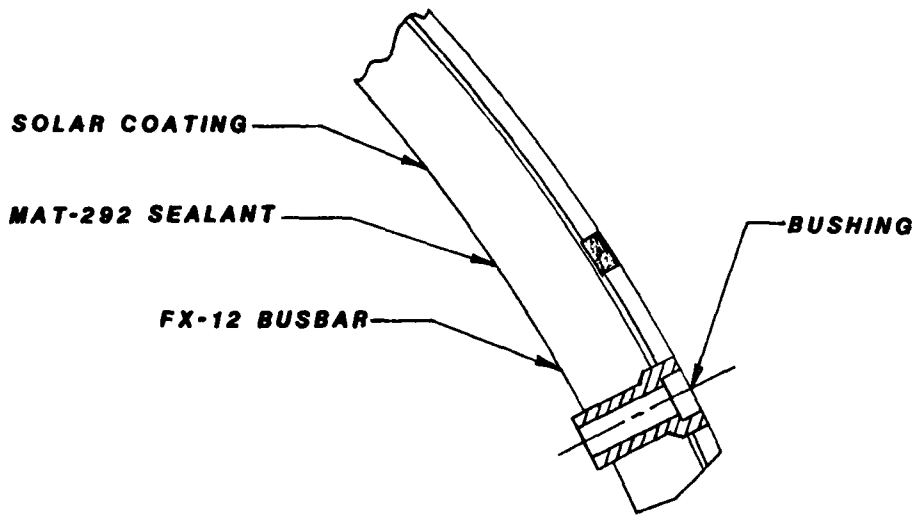
TEST COUPON CONFIGURATION CANOPY OFFCUTS  
FIGURE 3



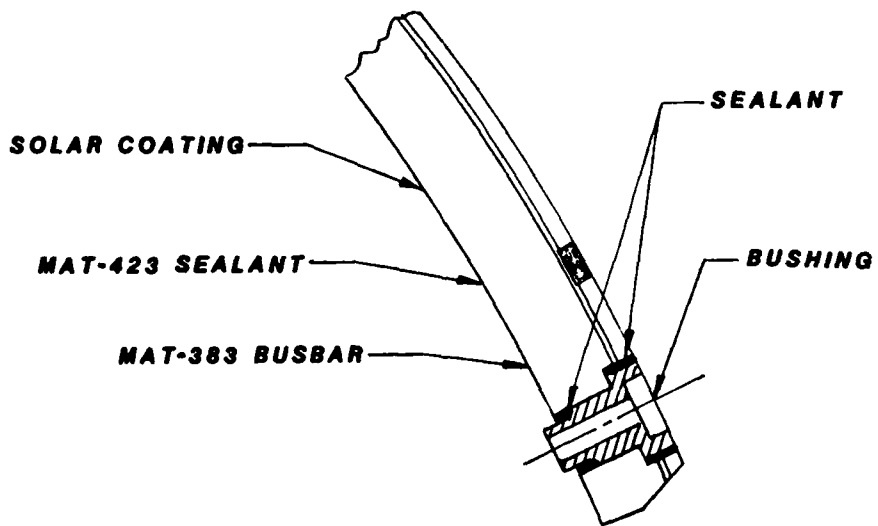


**F-16 EDGE CONFIGURATION**  
**FIGURE 4**

**BEFORE**



**AFTER**



**IMPROVED EDGE DESIGN  
FIGURE 5**

# AIRCRAFT CLEANER FLUIDS STRESS CRAZE EVALUATION (MIL-C-87936A)

TYPE OF CLEANER	POLYCARBONATE RT/4000 PSI	POLYCARBONATE 160F/2500 PSI	ACRYLIC II RT/4000 PSI	ACRYLIC II 160F/2500 PSI
SHAW SOAP CONCENTRATE	SEVERE	<300	NO CRAZE	N/A
EZE 206	NO CRAZE	666	NO CRAZE	1091
OAKITE FLEETLINE JC5	NO CRAZE	NO CRAZE	NO CRAZE	NO CRAZE
ELDORADO ASTROMAT HD	1565	1454	NO CRAZE	2017
TURCO AIR TEC 22	1848	1753	NO CRAZE	1472
BRULIN FORMULA 4183	1891	1196	NO CRAZE	1636
CALLA 800	NO CRAZE	2059	NO CRAZE	NO CRAZE
ELDORADO ALK-600	NO CRAZE	1726	NO CRAZE	2181
TURCO AIR TEC 23	NO CRAZE	1086	NO CRAZE	NO CRAZE
BRULIN 815 AF	NO CRAZE	1603	NO CRAZE	NO CRAZE
INTEX 8758	NO CRAZE	1726	NO CRAZE	1472
HOTSEY AERO ONE	NO CRAZE	1908	NO CRAZE	2154
B AND B 713 JET II	NO CRAZE	1467	NO CRAZE	NO CRAZE
B AND B 713 JET III	NO CRAZE	1145	NO CRAZE	1799

ALL AVAILABLE MATERIALS FROM MIL-C-87936A QPL WERE TESTED  
 RT = ROOM TEMPERATURE TEST CONDITION, ALL OTHERS AT 160 DEG. F  
 EXPOSURE TIME = 30 MINUTES  
 N/A = SAMPLE NOT TESTED

**TABLE 1**

# STRESS CRAZE EVALUATION OF CLEANER FLUIDS

TYPE OF FLUID/CLEANER	POLYCARBONATE RT/4000 PSI	POLYCARBONATE 160F/2500 PSI	ACRYLIC II RT/4000 PSI	ACRYLIC II 160F 2500 PSI
GENERAL DYNAMICS CLEANER	NO CRAZE	1712	NO CRAZE	NO CRAZE
AIR NAT GUARD (50% SOLUTION)	NO CRAZE	1086	NO CRAZE	NO CRAZE
LUKE AF RES (50 % SOLUTION)	NO CRAZE	1195	NO CRAZE	NO CRAZE
SHAW SOAP CONCENTRATE	SEVERE CRAZE	SEVERE CRAZE	NO CRAZE	N/A
SHAW SOAP (32 % SOLUTION)	<500	N/A	NO CRAZE	N/A
SHAW HI-TECH GLAZE	NO CRAZE	NO CRAZE	NO CRAZE	NO CRAZE
SHAW PAINT DRIER (CO. NAPHTHENATE)	NO CRAZE	N/A	N/A	N/A
SHAW WINDEX NON AEROSOL	NO CRAZE	NO CRAZE	NO CRAZE	NO CRAZE
GLASS PLUS	NO CRAZE	NO CRAZE	NO CRAZE	NO CRAZE
AMMONIUM HYDROXIDE (50% SOLUTION)	NO CRAZE	NO CRAZE	NO CRAZE	NO CRAZE
AMMONIUM HYDROXIDE CONCENTRATE	NO CRAZE	NO CRAZE	NO CRAZE	NO CRAZE
AMM. HYDR./WATER/ISOPROPYL ALCOHOL 1 / 1 / 1	NO CRAZE	NO CRAZE	N/A	N/A
SODIUM HYDROXIDE (10 % SOLUTION)	NO CRAZE	NO CRAZE	NO CRAZE	NO CRAZE
	SEVERE CRAZE	N/A	N/A	N/A

RT = ROOM TEMPERATURE TEST CONDITION  
 EXPOSURE TIME = 30 MINUTES  
 N/A = SAMPLE NOT TESTED

**TABLE 2**

# STRESS CRAZE TESTING OF EDGE COUPONS

CONFIGURATION	COATING SOLAR	CLEAR	HOLES	BUSBAR	APPLIED STRESS (PSI)	RESULTS TIME TO CRAZE
SOLAR	X	NO	X	X	2600	BROKE/12 MIN.
SOLAR	X	NO	X	X	1500	BROKE/12 MIN.
CLEAR	NO	X	X	NO	2600	NO CRAZE /90 MIN.
CLEAR	NO	X	X	NO	1242	NO CRAZE/90 MIN.
SOLAR	X	NO	NO	NO	3620	NO CRAZE/90 MIN.
CLEAR	NO	X	NO	NO	3620	NO CRAZE/90 MIN.

X = SAMPLE CONTAINS THAT CONFIGURATION  
TESTED AT 160 DEG. F WITH EZE 206 CLEANER

**TABLE 3**

# STRESS CRAZE INVESTIGATION OF CLEAR COUPONS

CONFIGURATION	CLEAR	HOLES	BUSBAR	SOAP	APPLIED STRESS (PSI)	RESULT TIME TO CRAZE
CLEAR/BUSBAR	X	X	X	X	1500	BROKE/15 MIN.
CLEAR/BUSBAR	X	NO	X	X	3620	NO CRAZE/90 MIN.
CLEAR/BUSBAR	X	X	X	NO	1500	NO CRAZE/90 MIN.
CLEAR/BUSBAR	X	X	X	X	1500	BROKE/15 MIN.
CLEAR/MAT-383	X	X	MAT-383	X	1500	BROKE/30 MIN.
CLEAR/BUSBAR	X	X	X-NOT ON HOLES	X	1500	NO CRAZE/90 MIN.
SOLAR/MILD SOAP	SOLAR	X	X	NON-CRAZING	1500	NO CRAZE/90 MIN.

X = COUPON CONTAINS THAT CHARACTERISTIC TESTED WITH EZE 206 SOAP AT 160 DEG. F

## TABLE 4

# STRESS CRAZE TESTING OF IMPROVED EDGE DESIGN COUPONS

CONFIGURATION	BUSBAR	SEAL	BUSHINGS	RESULT AT	EXPOSURE (MINUTES)	TIME
SOLAR/STANDARD	STD.	STD.	STD.	BROKE/15 MIN.	N/A	N/A
SOLAR	STD.	MAT-423	STD.	NO CRAZE	NO CRAZE	CRAZED
IMPROVED SOLAR	MAT-383	MAT-423 BLUE	HI SEAL	NO CRAZE	NO CRAZE	NO CRAZE
IMPROVED SOLAR	MAT-383	MAT-423 BLACK	HI SEAL	NO CRAZE	NO CRAZE	NO CRAZE

TEST CONDITIONS: 1500 PSI, 160 DEG. F, EZE 206 CLEANER

**TABLE 5**

AN ANALYSIS OF FLIGHT AND WINDSHIELD FAILURES  
IN F111 AIRCRAFT

P. J. Burchill  
R. H. Stacewicz

Materials Research Laboratory



AN ANALYSIS OF FLIGHT AND WINDSHIELD FAILURES IN F111 AIRCRAFT

by

P. J. Burchill and R. H. Stacewicz

Materials Research Laboratory  
Ascot Vale  
Victoria 3032  
Australia

ABSTRACT

Since the introduction of the laminated-plastic bird impact resistant transparencies in F111 Aircraft, there has been considerable concern over their failure in service. The main defects which occur, resulting in rejection of the windshield, are bad optical properties, cracking of the outer acrylic ply, and delamination. Identification of the cause of failure is a complex problem which has been studied both in the USA and Australia. Besides flight and the local environment in which the aircraft are stationed, abuse, manufacturing faults and bird strike are involved. This report of Australian work gives an analysis of flight and the distribution of all failures of windshields in flying hours. Failures show a bimodal distribution which has been interpreted in terms of the four causes above. Flight and abuse account for about 80% of all failures in approximately equal importance. An upper limit to the lifetime of a windshield with 95% probability of failure is about 700 flying hours or 3 years service under Australian conditions. The distribution of failures amongst the fleet has been investigated, and appears to show that supersonic flight may be a primary cause of cracking.

## Introduction

The Royal Australian Air Force (RAAF) fleet of 24 F111 aircraft has since 1978 been fitted with laminated plastic transparencies. The first such transparencies were known as 'Bird Impact Resistant Transparencies' (BIRT) which is a nine ply construction. These were later replaced by the Advanced Design BIRT (ADBIRT). Early experience with these parts showed that their optical properties were not as good as those of the glass laminates they replaced. Moreover, unless proper care is taken, the optical properties can worsen rapidly. The acrylic outer plies, though more crack resistant than glass, scratch easily and can also craze. The principle reasons for removal of a transparency from service are: crazing and cracking of the acrylic ply, delamination at the acrylic/rubber-interlayer interface, and optical distortion. These faults are caused by normal service conditions but their onset can be accelerated by abuse and manufacturing defects.

Since 1981 when the RAAF became concerned over the short service-life of their F111 transparencies the causes have been researched. The approach has been to understand the service environment and how the properties of the materials are altered by this environment. This report describes typical flight statistics of the aircraft, and gives a statistical analysis of failure of windshields over the period 1980-1986, and the effects of flying conditions. Since 1981, the actual part and/or a defect report for 83 windshields have been received for assessment. However, only 67 of the windshields can be clearly identified with a particular aircraft. Moreover, even though the fleet size is 24, there are 4 aircraft with which a failed part cannot be identified.

## Aircraft and Flight

About 11,000 flights have been analyzed to obtain a typical flight profile of the aircraft. The RAAF describe flight by speed and altitude and also in terms of activities undertaken by the pilot or navigator. There are 61 such descriptions, some of which are done rarely, and in order to reduce this number, they have been condensed into the 10 flying modes described in Table 1. The frequency with which an aircraft is flown in nine of the modes of flying, defined by height and speed, is shown in Figure 1. A typical flight lasts 2.5 hours, during which an average of 5 flying modes are carried out. As can be seen in the figure, high altitude flight (A & B), circuit training (F) and terrain following (L) activities account for about 70% of flying according to type. The distribution in terms of duration in which these activities

are undertaken is very similar, but with a greater amount of time spent at altitudes over 12,000'. Aircraft spend less than 1% of their time at supersonic speeds, and most of this is at high altitude.

In comparing the frequencies with which each aircraft is flown, in the ten modes, to the fleet average, only one aircraft was found to be flown differently: the test-bed aircraft. In terms of duration in which these activities were performed, the same aircraft was significantly different, while the four aircraft which are reserved for reconnaissance work are now distinguishable in the flight history analysis.

### Cracking of Windshields

Of the 67 windshields which have failed in service, and can be identified with a particular aircraft, 20 are cracked in the outer acrylic ply. The distribution of this mode of failure which occurs catastrophically would be expected to be a Poisson distribution of numbers of failures amongst the fleet if the process is random. The fleet size is 24, however there are 4 aircraft for which a failed part of any type cannot be identified. Since this is a most unlikely occurrence, the fleet size has been reduced to 20 to test if the number of failed by cracking parts is distributed randomly. Table 2 shows the expected and observed numbers of aircraft which would have none, 1, 2 or 3 windshields fail by cracking. The distribution of this failure in the fleet is random, no aircraft has suffered greater than the expected number of failures from cracking, and thus the type of flying is equally severe on all aircraft.

Despite this conclusion, one aircraft which is used as the test-bed for the fleet has had two windshields fail by cracking. This aircraft has flown only one quarter the number of hours that the most flown aircraft has been used which has also had two failures by cracking. The test-bed has carried out almost as many supersonic flights as the typical aircraft in the fleet, but very little terrain following flight. This suggests that supersonic flight is a primary cause of cracking. In addition, most incidents of cracking are reported as occurring when the aircraft decelerates to below Mach 1. However, a study of the fracture surface indicates that a cyclic process has occurred in the growth of the crack before failure [1]. The bands are very pronounced suggesting long periods of no crack growth, hence, supersonic flight alone is unlikely to be the main initiator of cracking since it is undertaken so rarely.

## Windshield Failures

The faults which cause windshields to be removed from service are: cracking, crazing, delamination, manufacturing faults, optical distortion and heat damage. The first three can arise from general service conditions not directly related to maintenance or air crew abuse. Heat damage is caused by overuse of the hot air rain removal system, and can be as slight as minor optical distortion to as severe as melting of the outer ply and consequent mechanical damage. Manufacturing faults are seen as cloudiness, as multiple imaging, and as optical distortion. Crazing may occur through incorrect cleaning procedures, and since 1982 the use of isopropanol to clean transparencies has been prohibited. Most failures since then have been cracking, delamination and manufacturing faults.

Of the 83 windshields or reports there are only 38 for which complete information is available. The reason for removal from service, the flying hours, and the aircraft are known. Fifteen have been identified as having failed by natural wear and tear, fifteen from abuse, seven from manufacturing defects, and one failure from bird impact. The average life over all failures was  $284 \pm 212$  flying hours. Figure 2 shows that the distribution of life times is bimodal. Short lives are due to manufacturing faults, and the use of isopropanol before 1982. Heat damage has also been found with parts having a short service life which may be due to inexperience.

In the analysis of failure due to natural wear and tear, windshield failures due to crazing or cracking before 1982 have been classed as due to ground crew abuse unless it was known that cracking occurred in flight. Of the 15 failures, 12 are from cracking and 3 from delamination of which one was also crazed. The average service life was  $510 \pm 98$  flying hours, and the distribution of life-times is skew (Figure 3) indicating an upper limit. An extreme value probability plot (Weibull), Figure 4 is linear and shows that there is a 95 percent probability that the service-life will be less than 700 flying hours. From the analysis of flight, an aircraft spends 200 hours per year in the air so a windshield would be expected to be replaced within 3 1/2 years. The chance that a windshield would fail due to natural processes within a year is less than 5%.

## Conclusion

With the elimination of malpractice, the service life of windshields can be almost doubled, as the analysis of failure histories has shown. The ultimate failure mode of the windshields appears to be cracking of the outer ply though the exact cause is not easy to pin-point. There are clues from

flying experience that cracking is associated with supersonic flight and deceleration. However, this flying mode is a rare occurrence in the life of a windshield and happens on average less than five times. Initiator cracks will be necessary for this catastrophic failure to occur, and these would be produced from chance impacts during the life of the windshield, and the slow growth of the crack.

TABLE 1

Aircraft Flying Modes

- A. Height above 12,000', speed less than 450 knots
- B. Height above 12,000', speed between 450 and 600 knots
- C. Any height, speeds greater than 600 knots
- D. Height between 5000' and 12,000', speed less than 600 knots
- F. Height between 1000' and 5000', speed less than 300 knots
- G. Height between 1000' and 5000', speed between 300 and 600 knots
- J. Height between 1000' and 5000', speed less than 450 knots
- K. Height less than 1000', speed between 450 and 600 knots
- L. Terrain following flight, speed less than 600 knots
- M. Performance test flights of aircraft or equipment, no description in height or speed

**TABLE 2**

**Distribution of Cracked Windshields**

		Number of Cracked Windshields per Aircraft			
		0	1	2	3
Number of Aircraft	Observed	7	8	3	2
	Expected	7	7	3	1

# ZONES OF ACTIVITY, HOW FREQUENTLY VISITED

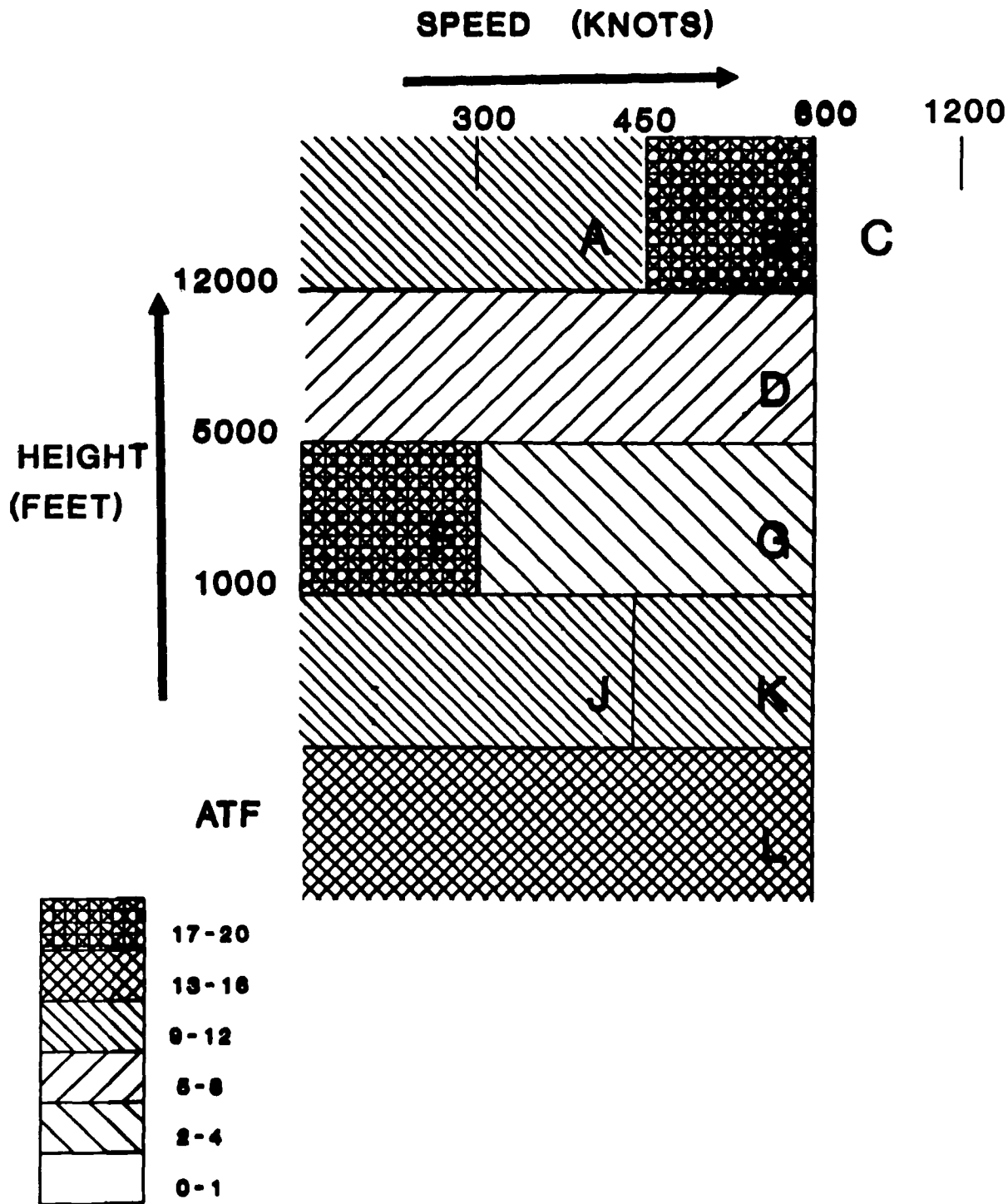


Figure 1. Frequency with which RAAF F111C aircraft are flown in ways defined in Table 1.



# WINDSHIELD FAILURES, ALL CAUSES

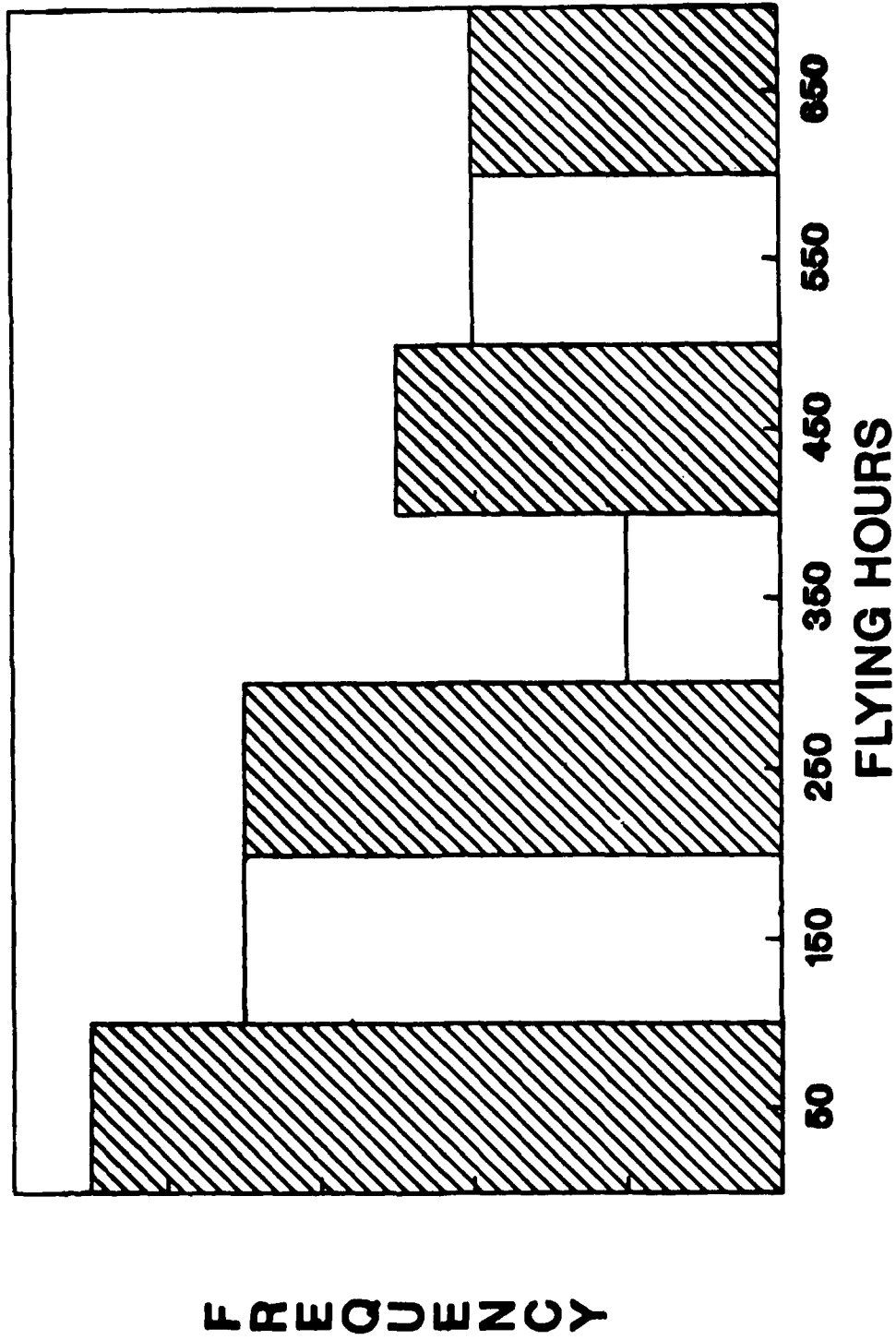


Figure 2. Distribution of windshield lifetimes for all documented failures.

# WINDSHIELD FAILURES DUE TO FLIGHT

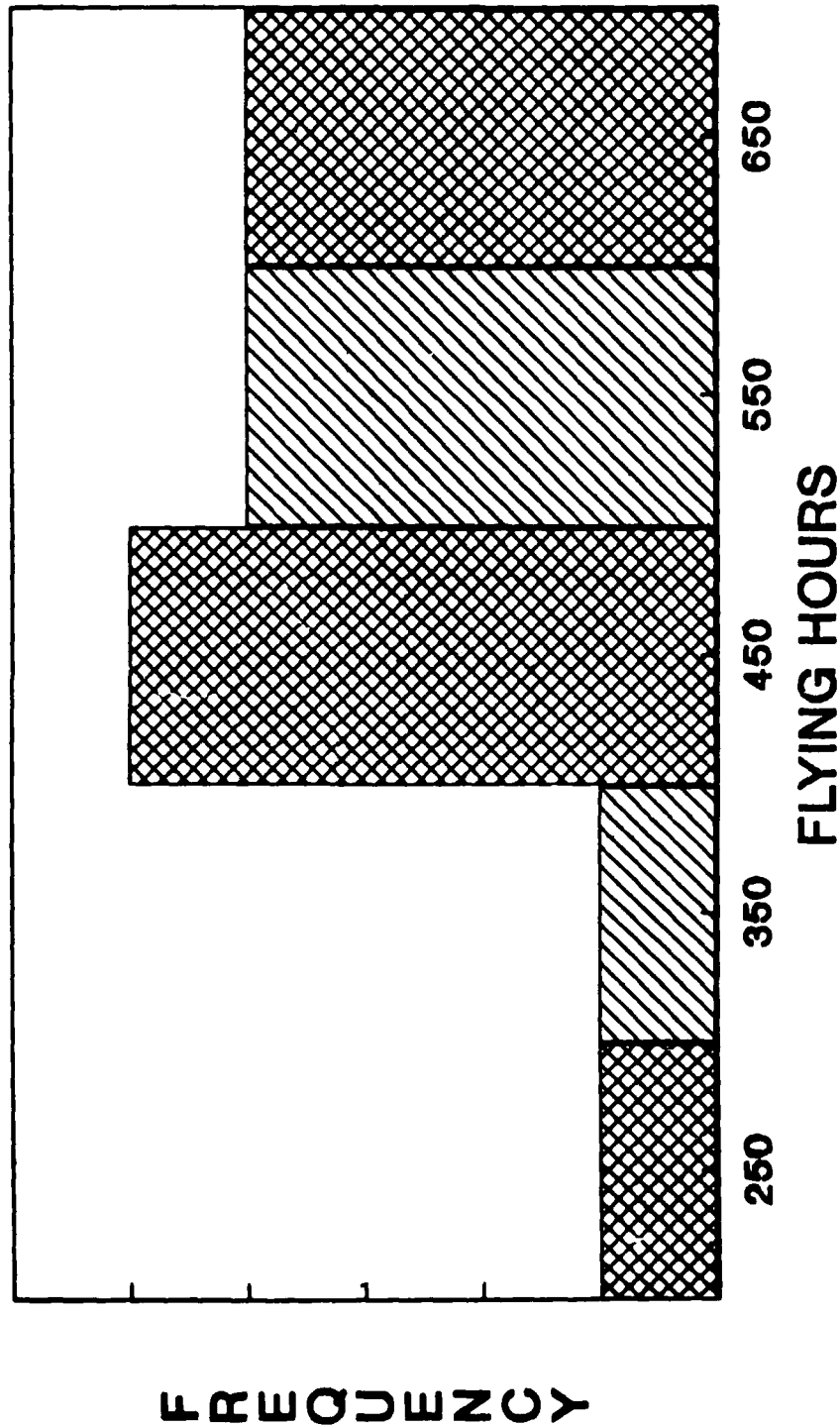


Figure 3. Distribution of windshield lifetimes for those that failed due to flight.

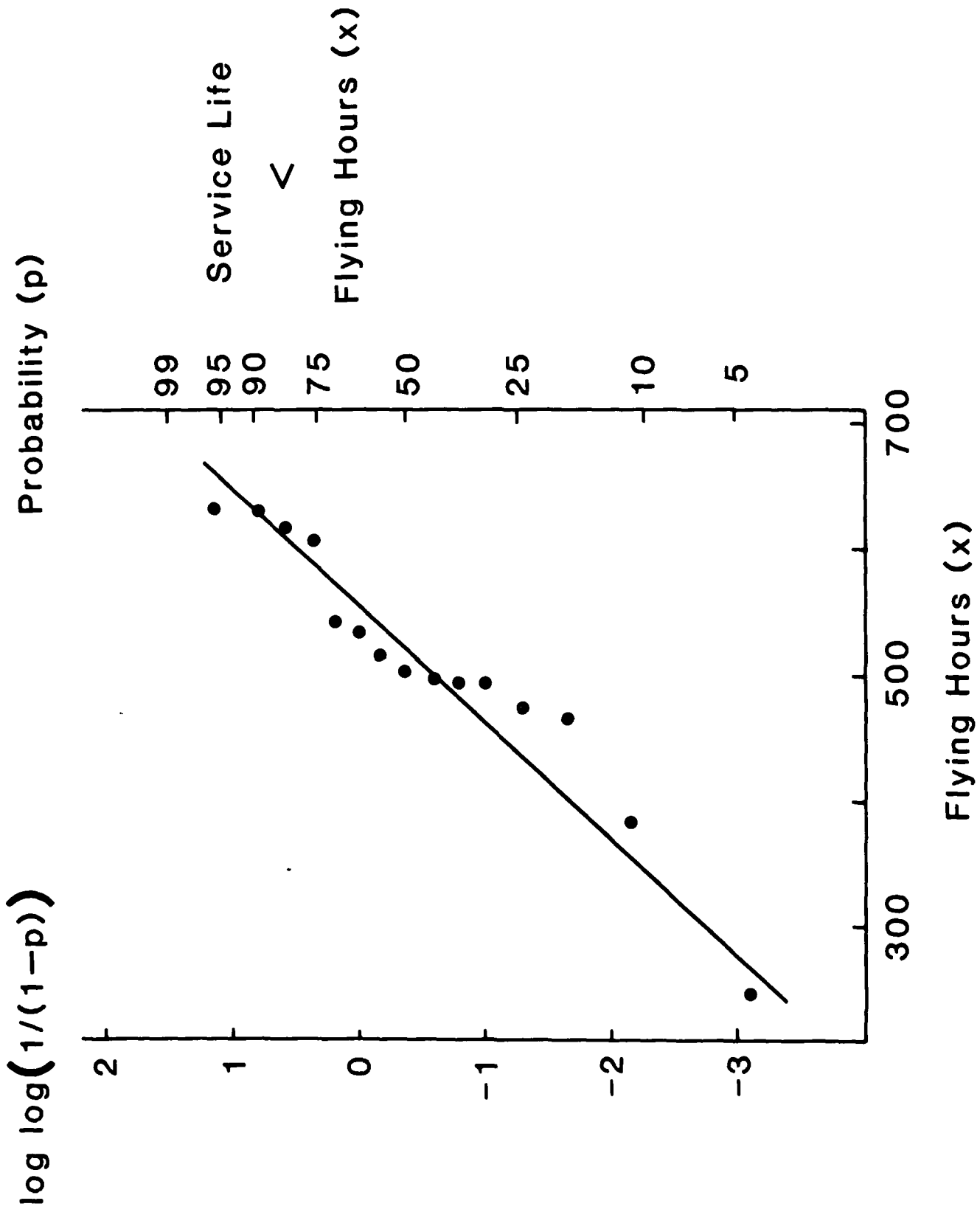


Figure 4. Extreme value probability plot of service lives of windshields from Fig. 3.

SESSION VIII

OPTICS (PART A)

Chairman: LTC L. V. Genco  
Armstrong Aerospace Medical  
Research Laboratory  
Brooks AFB, Texas

Co-Chairman: H. L. Task  
Armstrong Aerospace Medical  
Research Laboratory  
Wright-Patterson AFB, Ohio

Coordinator: W. N. Kama  
Armstrong Aerospace Medical  
Research Laboratory  
Wright-Patterson AFB, Ohio

VISION THROUGH AIRCRAFT TRANSPARENCIES

H. Lee Task, Ph.D.  
Human Engineering Division  
AAMRL

# VISION THROUGH AIRCRAFT TRANSPARENCIES

H. Lee Task, Ph.D.  
Human Engineering Division  
Armstrong Aerospace Medical Research Laboratory  
Wright-Patterson AFB, OH 45433-6573  
USA

## SUMMARY

The primary purpose of this paper is to discuss in detail the optical and visual effects of aircraft transparencies including windscreens, canopies, head-up display (HUD) combiners, and visors. The majority of the paper will treat aircraft windscreens and canopies with primary emphasis on high performance aircraft.

## INTRODUCTION

Aircraft windscreens have evolved from relatively small, flat pieces of glass to large, thick, curved, complex, multi-layered plastic structures. This evolution has resulted in windscreens that allow considerable out-of-the-cockpit visibility, provide significantly better birdstrike protection and improved aerodynamics. However, these advances have not come without a cost: the optical quality of the windscreens has suffered. New visual effects have arisen due to the thicker, curved, plastic structures. Each of these has required the development of measurement methods and standards to quantify the effects.

The first section of this paper will describe these optical effects in terms of physical cause, optical appearance, measurement method (both laboratory and field, if appropriate), typical values and possible effects on air crewmember vision. The latter part of the paper will treat helmet visors and HUD combiners and how they integrate with the windscreen. Table 1 lists the optical effects/parameters that are discussed in this paper.

=====  
Table 1. Optical parameters and effects of aircraft windscreens.  
-----

Angular Deviation	Minor Optical Defects
Binocular Disparity	Rainbowing/Birefringence
Distortion	Reflectivity
Haze/Diffraction	Transmissivity
Multiple Imaging	

=====

## AIRCRAFT WINDSCREEN OPTICAL PARAMETERS

### Angular Deviation

A ray of light passing through a section of transparent material, such as an aircraft windscreen, may be affected in two very separate and distinct ways. Figure 1 is a general example of a ray of light passing through a transparent medium. The light ray is refracted (bent) both as it enters the front surface of the material and as it exits the back surface of the material. The net change may be, as indicated in Figure 1, that the ray undergoes both lateral displacement and angular deviation. Lateral displacement means the ray has been shifted laterally but the exiting ray is parallel to the entering ray. Lateral displacement is usually of little interest in evaluating windscreens because it represents a relatively small (a few centimeters) and fixed effect. Angular deviation, on the other hand, is defined as the change in direction (angle) between the entering ray and the exiting ray. This is much more significant than lateral displacement when considering weapon systems aiming error. The impact of angular deviation on weapon system aiming error is discussed later.

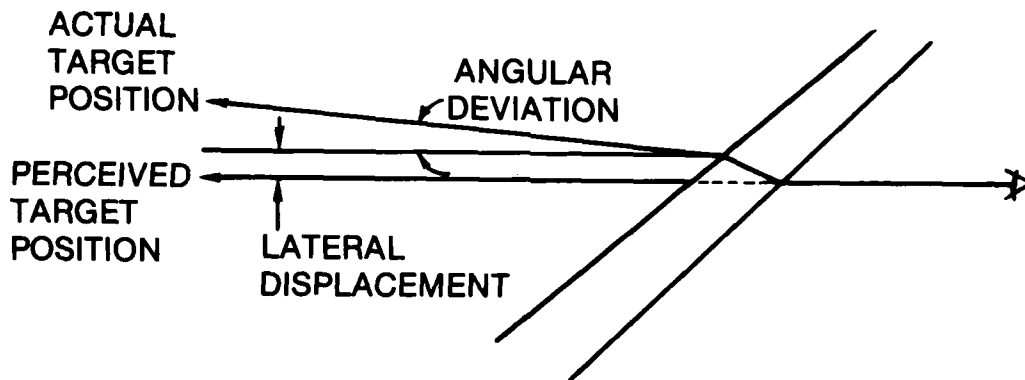


Figure 1. Lateral Displacement and Angular Deviation Effects of Aircraft Transparencies

Several methods have been used to measure angular deviation in windscreens for both laboratory research and manufacturing quality control. One of the original methods used for measuring the F-16 windscreen used a laser beam and a long, clear throw distance of 100 ft. The laser beam was positioned at about the design eye position of the windscreen and was imaged on a calibration pattern at the end of the 100 ft throw distance. With no windscreen in the path, the laser beam was imaged on the center of the calibration pattern. Then, the windscreen was inserted in the path. Any movement of the laser beam from the center of the calibration pattern was assumed to be due to angular deviation in the windscreen, although in fact at least some of the change in position was due to lateral displacement. The entire forward section of the windscreen was mapped by moving (rotating) the windscreen about the design eye position.

A second method was employed which eliminated the need for the long throw distance and eliminated the error due to lateral displacement contamination of the laser beam position change. This approach used a collimator and a telescope. The collimator was placed inside the canopy in line with the design eye position, the telescope was placed outside the canopy and aimed at the collimator. Inside the collimator was a calibrated test pattern that was viewed by the telescope. With no windscreen in the way, the crosshairs of the telescope were lined up with the center of the test pattern. Then, a windscreen was placed in the path between the telescope and the collimator. Any shift in the apparent location of the telescope crosshairs, with respect to the center of the collimated test pattern, was indicative of angular deviation in the windscreen. The amount of angular deviation was determined by the magnitude of the crosshair shift with respect to the center of the collimated test pattern. The forward section of the windscreen could then be mapped by rotating the windscreen about the design eye position as in the first method described. This method was superior to the first in that a smaller room was required for measurement and the measurements were not contaminated by lateral displacement. However, this method was somewhat time consuming.

The third method that has been employed to measure the angular deviation is described in detail in AAMRL-TR-81-21. Figure 2 is a sketch of the top view of the optical system that comprises the third method. Referring to Figure 2 (from left to right), light from an incandescent lamp is collected by a condensing lens to illuminate the target plane. The projection lens is located one focal length from the target plane such that it collimates the image of the target. This portion of the system is called the transmitter and is located such that the light exiting from it goes through the design eye position of the transparency.

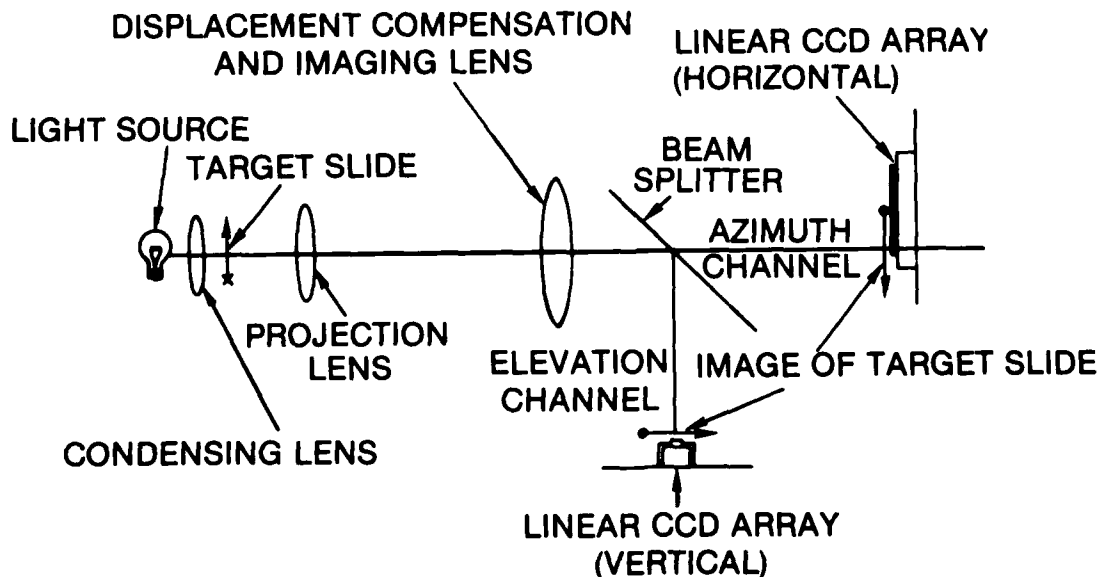


Figure 2. Pictorial Layout of Windscreen Angular Deviation Measurement Device (the windscreen to be measured is positioned between the projection lens and the displacement compensation lens)



The remainder of the system (the receiver) is located on the other side of the transparency. The receiving lens compensates for lateral displacement (thus eliminating that source of error) and images the target plane one focal length (of the receiver lens) away. A beam splitter divides the light into two approximately equal intensities: one channel to measure azimuth (horizontal) deviation and one to measure elevation (vertical) deviation. Except for a 90 degree rotation about the optical axis, both channels are identical. In each channel, a segment of the target image intersects a charge couple device (CCD) linear array. The positional change of this intersection between windscreen and no windscreen conditions is mathematically related to the angular deviation of the windscreen at the point measured.

The target used for this measurement is an "L" shaped pattern. It is important that the target "L" have uniform width on both the vertical and horizontal segments and that the segments be accurately perpendicular to each other. The "L" is projected by the transmitter system and imaged by the receiver lens onto the linear CCD array elements. The vertical segment of the "L" intersects a horizontally mounted linear CCD array which measures horizontal or azimuthal angular deviation. Similarly, the horizontal segment of the "L" falls on the vertically mounted CCD array to measure vertical or elevational angular deviation.

The elements in the CCD array are typically much smaller than the width of the image of the "L" segments and, therefore, several CCD elements are activated by the "L" image. The CCD array control electronics are designed to compensate for this problem. A counter is activated and counts each CCD element until the first element that is covered by the "L" segment is encountered. The counter then counts every other element until the next unactivated CCD element is encountered. Thus, the counter indicates distance from the end of the CCD array to the center of the "L" segment width in units of counts. By knowing the distance between the CCD array elements and the focal length of the receiver lens, it is possible to calculate the angle represented by the counts. In practice, a 10 inch focal length lens can be used in conjunction with a CCD array with 0.001 inch spacing which results in each count representing one-tenth of a milliradian.

This third method of measuring angular deviation is used by a majority of windscreen manufacturers in the USA for F-16 windscreens since it lends itself to direct computer interface, thus reducing the amount of time required to measure a windscreen.

The measurement of angular deviation came about primarily for the F-16 aircraft because of the curvature of the forward section of the windscreen. The visual effect of angular deviation is that the target viewed through the windscreen appears at a different location than it really is. This results in a weapon system aiming error when used in conjunction with a head-up display (HUD). The amount of the aiming error depends on the degree of angular deviation. To correct for this error, each F-16 windscreen is measured and the forward section of the windscreen is mapped. The angular deviation errors are recorded as a function of field angle

(look angles). A best fit curve is mathematically determined and the coefficients of the curve fit are affixed to the windscreen as name plate values. These name plate values are then entered into the F-16 fire control computer to correct the HUD aiming reticle for the angular deviation in the specific windscreen installed on the aircraft. Typical aiming errors may range from fractions of a milliradian to several milliradians without this correction procedure. Angular deviation is not easy to measure in windscreens already installed in aircraft and it therefore does not lend itself to field measurement.

### Binocular Disparity

There are two distinctly separate phenomena that occur that are commonly referred to as binocular disparity. One of these involves the combination of the windscreen and HUD interaction and is presented in a later section. The second effect is due only to angular deviation in the windscreen. As the pilot looks through a windscreen at a distant object, each eye sees the object through a different portion of the windscreen. If the angular deviation through these two different portions of the windscreen are different, then the image of the object will appear in a slightly different location for each eye. To compensate for this difference, the eye muscles must adjust the orientation of the eyes to cause the image of the object to fall on the appropriate corresponding points of each retina. If the difference in angular deviation between the two areas of the windscreen is too great, the eye muscles cannot shift the eyes sufficiently to compensate and a binocular rivalry condition occurs. The visual system reacts to this binocular rivalry in one of two ways: it either suppresses the image from one eye or the observer sees double.

Binocular disparity is measured by determining the angular deviation from both the left and right eye positions and then subtracting the two measures at each field angle. The errors in the vertical and horizontal directions are treated separately since they have distinctly different effects on vision. In the horizontal direction, the errors translate to vergence of the eyes. If the eyes have to rotate inward (toward the nose) in order to fuse the image of a distant object when viewing through the windscreen, this is called eye convergence. If the eyes must rotate outward, it is referred to as eye divergence. The eyes can tolerate considerable eye convergence but can only tolerate about 2 milliradians of eye divergence. Figures 3 and 4 show typical maps of eye vergence for F-16 windscreens.

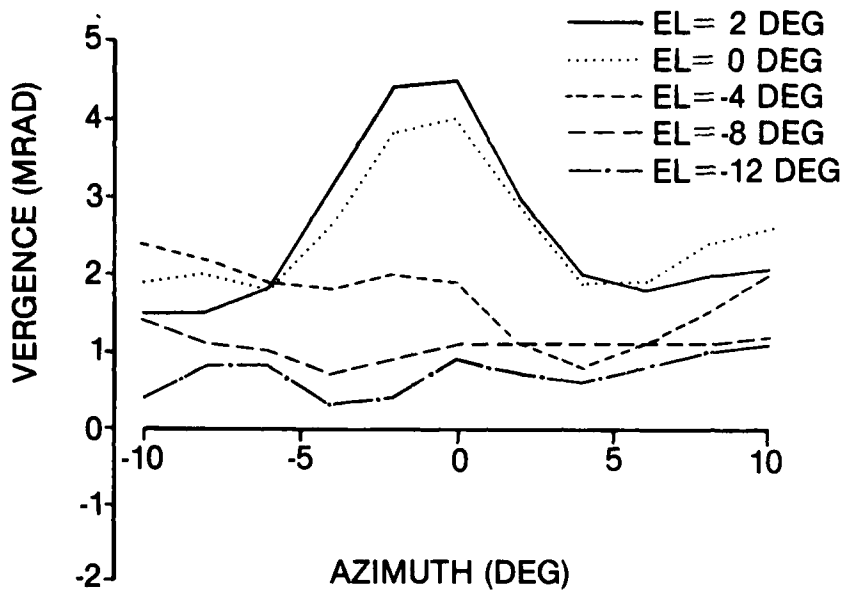


Figure 3. Graph of Binocular Vergence (Horizontal Direction) for an F-16 Windscreen

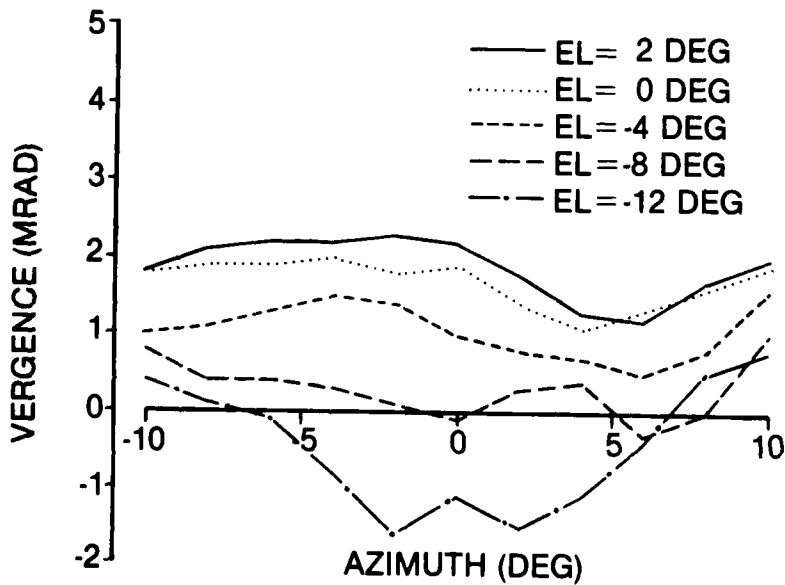


Figure 4. Graph of Binocular Vergence (Horizontal Direction) for another F-16 Windscreen

Angular deviation differences between the two eyes in the vertical direction are called vertical disparity. It is measured by subtracting the vertical (elevation) angular deviation errors for one eye position from the vertical angular deviation errors for the other eye. The difference between the two eyes in the vertical direction is referred to as dipvergence.

Just as in the case of divergence, the eyes have a relatively low tolerance for discrepancies in vertical position of an image between the two eyes. Typically, about 3 milliradians is the maximum permitted vertical disparity between right and left eyes.

The most accurate measure of binocular disparity is obtained by measuring the angular deviation of the windscreen from the two eye positions. However, there is an alternate method of documenting binocular effects that has been relatively recently promoted. This method uses a twin image projector system (like a slide projector) with a separation between the projection lenses equivalent to the average distance between the two eyes. This projection system is positioned at the pilot's head location with respect to the windscreen to simulate the view from his two eyes. One projector has a green color filter over it and the other has a red color filter. The projector system is set about 10 feet from a screen. A rectangular target grid with circles in the center of each square is projected from each of the eye positions onto the screen. With no windscreen in the way, the two images of the grid pattern are superimposed to produce a single yellow image on the screen.

With a windscreen in the path of the twin projector system, each projector will go through a different portion of the windscreen. Thus, if there is any difference in lateral displacement and/or angular deviation between the two portions of windscreen, it will cause a separation of the grid pattern into its red and green components. It has been suggested that the degree of separation, which can be easily measured, can be related to the quality of the windscreen.

The difficulty with this method is that the effects of lateral displacement and angular deviation are both included in the measurement process and cannot be separated. Thus, the separation between the red and green grids at the screen could be quite large, but there could be very little binocular disparity caused by angular deviation in the windscreen. Since, at normal viewing distances through the windscreen, only the binocular disparity due to angular deviation causes difficulties, the measurement could provide very misleading results.

The twin projector system can be adapted to field measurement by placing it in the seat of the aircraft to be tested while the aircraft is in a darkened hangar. A portable rear projection screen could be set up in front of the aircraft nose and the image of the twin grid pattern could be photographed from the screen.

## Distortion

Over the years, there have been several methods developed to try to characterize distortion. Almost all of these methods involve photographing a specific type of pattern through the windscreen followed by an analysis of the photograph to determine the level of distortion. Unfortunately, distortion in aircraft windscreens is usually due primarily to manufacturing difficulties. The distortion effects are, therefore, seldom uniform, symmetric or consistent from windscreen to windscreen and manufacturer to manufacturer. This makes it all the more difficult to characterize.

By far the most popular method of measuring distortion is based on American Society for Testing and Materials (ASTM) F 733-81. This test method was primarily developed for flat or nearly flat transparencies (such as commercial aircraft passenger windows) but variations of it are widely used for specifying permissible distortion levels in many other aircraft windscreens such as the B-1, F-16, F-111, F-15, F-18, and the A-10. This method is commonly referred to as the grid line slope test procedure.

A large pattern consisting of horizontal and vertical lines (about 1/16 inch wide) spaced typically about one inch apart is the test pattern. Usually, the lines are white (often made by stretching string) with a black background. The lines are sufficiently bright that they will show up quite well on photographs. The procedure is to position a camera at a specified distance from the test pattern (15 to 20 feet) and photograph the test pattern with no windscreen in the path. Then, without advancing the film in the camera, a second exposure is made with the windscreen in its installed orientation with respect to the camera such that the camera is in the pilot's eye position. All distortion analysis is then done on an enlarged print of this double exposure photograph.

Grid line slope is determined by inspecting the photograph and determining where the grid lines are sloped the greatest compared to the horizontal and vertical reference lines (the exposure with no windscreen in the path). This slope is usually expressed as a ratio such as 1 in 10 or 1 in 15 (see Figure 5). In practice, the slope can be accurately measured using a digital drafting board which measures the slope as an angle. This angle can then be converted to the traditional ratio by using the following equation:

$$\text{GLS} = 1 \text{ in } 1/\tan(a) \quad (1)$$

where: GLS = grid line slope

a = angle of grid line with respect to horizontal.

For example, if the slope angle is 5 degrees, the grid line slope would be 1 in 1/tan(5) or 1 in 11.4.

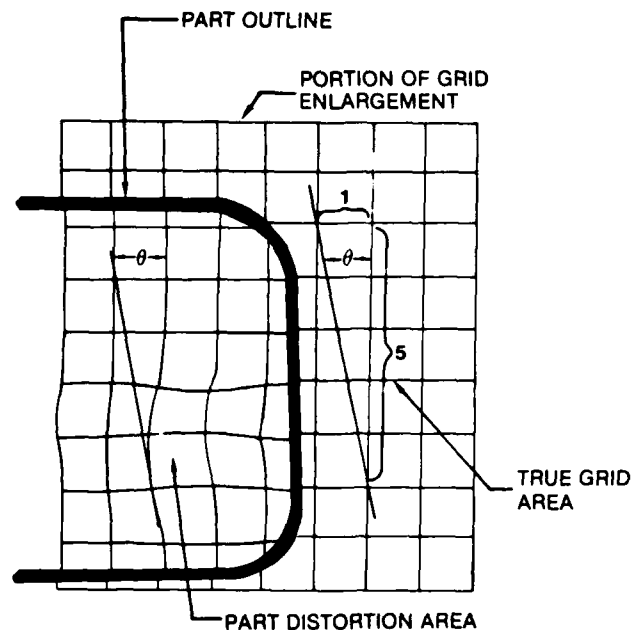


Figure 5. Determination of Grid Line Slope for Assessing Windscreen Distortion (from ASTM F733-81)

The grid line slope is the maximum slope that can be found in the photograph for the specified area or zone of the windscreen. Typically, the windscreen is divided into zones corresponding to how critical vision is through the particular area of the windscreen. The general area of the windscreen in the straight ahead direction is the most critical and is designated zone 1. Due to manufacturing difficulties, there is also normally an "optical free" zone in which the manufacturer is not held to any distortion specification. The optical free zone is on the order of one to two inches all around the edges of the windscreen. In some aircraft, the optical free zone in the very forward edge of the windscreen may be larger due to the extreme angle that the pilot is viewing through this portion of the windscreen. The extreme viewing angle significantly magnifies optical distortion effects.

A portable system for measuring grid line slope has been developed that permits some level of measuring distortion in the field. A string array mounted on a collapsible frame has been produced that can fit into a modest sized box for easy transport. The strings are spaced two inches apart instead of the customary one inch, but it is apparent from the field distortion measurements that this is sufficient.

Typical specification values for grid line slope are on the order of 1 in 10 to 1 in 16 for critical vision areas (low distortion desired) and about 1 in 6 to 1 in 9 for less critical portions of the windscreen. A value of 1 in 3 has been used for essentially optical free zone areas in an attempt to improve the distortion effects in these areas.

Two other measures of distortion based on the double exposure photographic procedure described above are lens factor and displacement grade. These have been used for a long time in specifying F-111 windscreens, but it is expected that these methods will be phased out in the future pending the outcome of studies to determine if they relate to pilot assessment of distortion.

For lens factor, the enlarged print of the photograph must be made of such a size that the grid board squares (with no windscreen in the way) number 16 per inch on the print. The windscreen is then divided into a relatively complex pattern of zones (NOT the same zone arrangement as described for the grid line slope). Each zone is then inspected (on the photograph) to determine areas in which the squares of the pattern have been compressed or expanded. The number of squares in one inch (on the photograph) are counted for area where it appears compression or expansion has taken place. If the number of squares is less than 16, then the number is divided into 16. If the number of squares in an inch is greater than 16, then 16 is divided into that number. Each of these will result in a number larger than unity indicated some average level of magnification of minification over the one inch areas measured. This number is then cubed (raised to the third power) to spread the numbers out more. This final number is referred to as the lens factor. It is determined for both horizontal and vertical directions and for several zones on the windscreen.

Displacement grade is another measure that is derived from the photographic procedure previously described. With the photograph on a drafting board, a reference horizontal is determined by aligning the drafting edge with one of the horizontal lines that was recorded with no windscreen in the path. Then, the drafting edge is moved about the photograph (keeping it horizontal) in a search for gridlines that show significant displacement over their length. For example, a grid line might gradually rise from left to right from its normal horizontal position. The drafting edge would then be aligned with the left end of the line and the maximum vertical excursion of the line from the drafting edge would be measured (in this example, it would be at the far right hand edge). This distance times 1000 is the displacement grade.

The displacement grade specification is based on a combination of vertical and horizontal displacements using a relatively complex system of zones for the windscreen. The current displacement grade for the F-111 is 120. The portable string board described earlier could be used to measure displacement grade and lens factor in the field but no attempt has yet been made to do so because of the questionable utility of these measures.

Probably the most comprehensive measure of distortion can be made by fully mapping the angular deviation (described earlier) over the entire windscreen. This has been done on a trial basis for F-111 windscreens and is under consideration as a specification that would replace the lens factor and displacement grade specifications. To date, no attempt has been made to convert the angular deviation maps to grid line slope format or other similar reduction of the large amount of data represented by the angular deviation mapping.

It is worthwhile to mention the other methods of measuring distortion that have been tried in the past but that are not currently in use or under consideration for use in specifying windscreens. These include Moiré photography, optical Fourier analysis and the three hole aperture camera methods.

Moiré photography has been demonstrated with aircraft windscreens, but no further work has been done to develop this method. The test pattern for this approach is a large square-wave design. In a vertical orientation, this consists of alternating black and white vertical stripes with a width of about 1/4 inch. This pattern is photographed with no windscreen in the viewing path. Without advancing the film, a second exposure is made on top of the first with the windscreen placed in its normal installed orientation. The resulting double photograph shows a Moiré pattern of interference fringes between the windscreen and no windscreen exposures. The number and spacing of these fringes, in general, corresponds to areas of higher distortion in the windscreen. A variation of this method is to produce a double exposure photograph from the two eye positions, thus obtaining a binocular disparity Moiré map of the windscreen.

A closely related technique that uses the same target pattern is the optical Fourier technique (US patent No. 4,299,482). A photograph of the square wave test pattern is produced with the windscreen in position. The film is developed but instead of printing a photograph from the negative, the negative is inserted in an optical Fourier analysis system. The diffraction pattern produced by the negative can be analyzed and has been shown to relate to subjective assessment of distortion in transparent panels (Self & Task, 1980). The disadvantage of this approach is the requirement of a special target pattern and optical Fourier analysis equipment. It is also not being pursued at this time.

An older technique for characterizing distortion is by the use of a three hole aperture in front of the camera. The standard one inch grid board pattern is photographed through the windscreen with the triangularly spaced apertures in front of the camera lens. An enlargement of the photograph was then inspected to determine if the grid lines split anywhere in the photograph. Acceptance criteria was based on the number of splits that were permitted. The technique was based on the assumption that, where the windscreen is distorted, it would also result in a blurred image when photographed with a low number lens. With the three apertures, however, instead of seeing a blurred grid line in areas of distortion, one would see a splitting of the lines. The intent was to make it simpler to determine acceptance criteria since it is easier to determine if the line splits than if it looks blurry. This procedure is not currently in use with any windscreens and is not being pursued.

Of all the methods to measure distortion, the grid line slope has become the standard. It is not a good measure of distortion but it has survived as the best available method that can be readily used to provide some indication of the level of distortion in a transparency. It is not likely that an alternate procedure will evolve any time in the near future.



## Haze/Diffraction

The phenomena of haze in a transparency is actually a manifestation of diffraction. Haze or halation is caused by diffraction of light by either microscopic surface imperfections, such as tiny scratches caused by cleaning, or by the material of the windscreen itself. The diffraction is essentially a scattering of a fraction of the light falling on the windscreen. The amount and distribution of the scattered light depends on what is causing the scattering, the intensity of the incident light, and the geometry of the viewing angle through the transparency. The effect is the appearance of a haze or veiling luminance that reduces the contrast of objects viewed through the windscreen.

Haze in new windscreens is relatively low and in glass windscreens is almost nonexistent. However, as plastic windscreens are repeatedly cleaned, even following recommended cleaning procedures, tiny micro-scratches are created on the surface. These micro-scratches act as diffraction gratings with random line orientation and spacing. The result is a scattering of light that appears as a haze. As the windscreen is cleaned more and more, the number of these scratches increases until the scattered light problem becomes severe enough that it is difficult to view through the windscreen under some illumination conditions. The worst viewing condition is in directions close to bright sources of light, such as the sun. The scattering of light is not uniform, but rather is much worse for small angles close to the source of the light. In general, the amount of scattered light decreases with the square of the angle between the line of sight and the light source.

The standard method of measuring haze is ASTM D 1003-16, which is based on a method developed by the National Bureau of Standards. This method is depicted in Figure 6. An incandescent, collimated light source directs a beam of light through a test area into an aperture in an integrating sphere. The beam is so aligned that it also exits the integrating sphere through an aperture at the opposite side of the sphere. The area between the beam source and the entrance to the integrating sphere is where the test specimen is placed. A photodetector in the integrating sphere measures the average amount of light bouncing around inside the sphere. With no sample in the way, the readout is adjusted to read zero. A reference plate, internal to the integrating sphere, is then positioned so as to cover the exit aperture of the sphere. The beam of light is then fully scattered within the sphere. With the reference plate in position, the sample is placed in the test area and the photodiode reading is adjusted to 100. This reading corresponds to the fact that all the light getting through the sample is collected and averaged by the sphere, but the scattered transmitted light has not yet been differentiated from the unscattered transmitted light.

## NBS HAZE MEASUREMENT

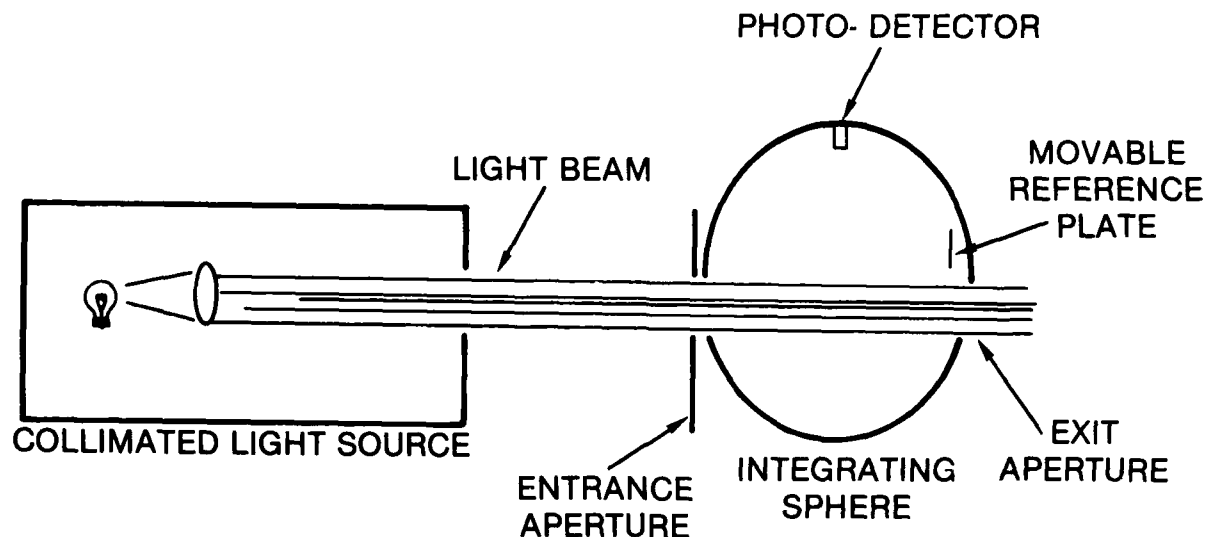


Figure 6. Instrumentation Measuring Haze Using ASTM D 1003-61 Test Method

Without changing any settings, the reference plate is removed from the exit aperture of the integrating sphere. If the test sample does not scatter light at all, then the entire beam exiting the sample and entering the sphere will exit through the exit aperture of the sphere. However, if the sample scatters some of the light, thus changing its direction, it will not pass through the exit aperture. The photodetector will then measure the average fraction of the light which enters the integrating sphere but does not exit the sphere. This fraction is read out directly on the display. In equation form:

$$H = \frac{S}{T + S} \times 100 \% \quad (2)$$

where: H = Haze in percent  
 S = Scattered light (that passes through the sample)  
 T = Transmitted light (only the unscattered transmitted light)

Commercially available instruments have been developed which can make this measurement very accurately. It is by far the most often used method to specify haze. However, it does have a significant drawback: it is difficult to use on other than small samples and virtually impossible to use on windscreens already installed on aircraft. Thus, while it is useful for specifying new parts, it is not useful for determining when a windscreen should be removed from an aircraft in the field because of too much haze.

In an attempt to develop a field usable method, an alternate approach to measuring haze has been devised and published as ASTM F 943-85. This approach has been applied to A-10 and F-16 windscreens with some success (Task & Genco, 1985), however, it is difficult to apply without suitable training and is probably not appropriate for routine (non-research) use.

This test method is based more on the effects of the haze on human visual capability. As light falls on the transparency it is absorbed, reflected, scattered or transmitted unaffected. For a fixed transparency and illumination angle, the amount of scattered light is directly proportional to the illumination falling on the surface. If the amount of incident illumination is doubled, then the amount of scattered illumination is doubled. Thus, the important factor is the ratio of the scattered light to the incident light. In equation form:

$$H_i = \frac{L}{E} \quad (3)$$

where:  $H_i$  = Haze index  
L = veiling luminance caused by scattered light  
E = illumination falling on windscreen surface.

The haze index is in units of luminance/illuminance such as foot-Lamberts per foot-candle. It should be noted that the haze value is highly dependent on the geometry of the illuminating source and the angle of view through the transparency. This may at first seem to be a disadvantage of this method compared to the nondirectional ASTM D 1003-61 test method. However, it does directly relate to the observed visibility through the transparency, which also varies with illuminating and viewing geometry.

The haze index can be measured both in the laboratory and in the field using similar techniques. For laboratory measurement, a semi-collimated light source is used to illuminate the transparency to be measured. A photometer is positioned at the design eye location of the windscreen to measure the amount of veiling luminance produced by the illuminating source. A black, light absorbing surface must be placed in the line of measurement to insure that the luminance being measured is only the scattered light and not a combination of scattered and transmitted light (see Figure 7).

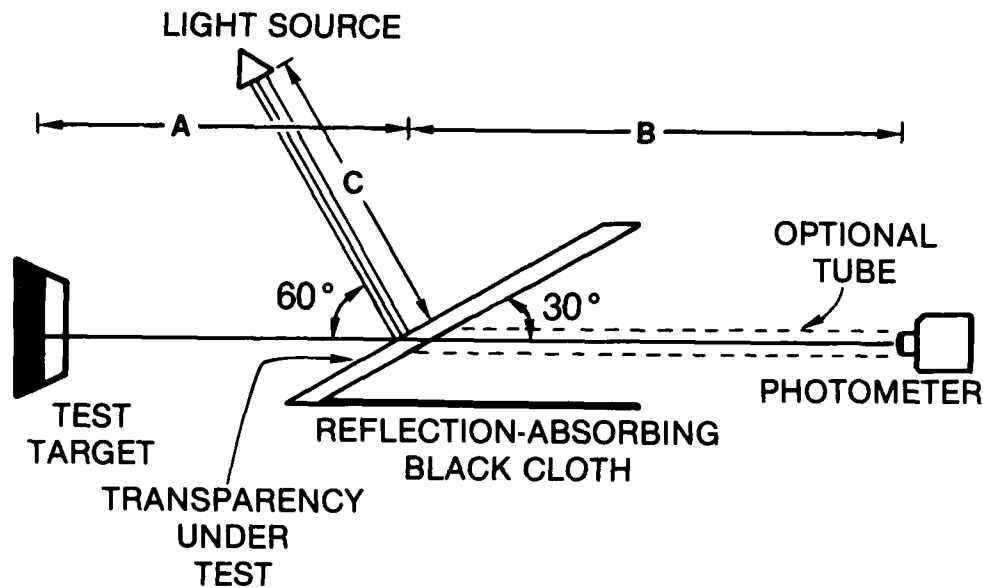


Figure 7. Haze Measurement Procedure Using ASTM F 773-81 Test Method

The illumination falling on the surface of the transparency can be measured using the same photometer by making use of a Lambertian reflector. A Lambertian reflector is a surface that reflectively scatters all incident light in a perfectly diffusing fashion. Because of the way in which foot-candles (illumination) and foot-Lamberts (luminance) are defined, the luminance of a perfectly diffusing reflector in foot-Lamberts is numerically equal to the illuminance in foot-candles falling on the surface. Thus, one can place a near Lambertian reflector (such as a flat white, Barium Sulphate plate) on the surface of interest and measure its luminance in foot-Lamberts. This value is numerically equal to the illumination falling on the surface in foot-candles. Once the veiling luminance and incident illumination are measured, the haze index can be calculated using Equation 3. To fully characterize the transparency, the haze index should be measured for all illuminating and viewing angles of interest.

The haze index can be measured on installed aircraft transparencies in a manner similar to that used in the laboratory with some modifications. Instead of using an artificial light source, one can use actual sunlight if the sun is oriented correctly for the desired measurement. Under field conditions, the black area of the black and white test pattern will probably not trap all of the light; it will reflect some light which may be enough that it needs to be accounted for when measuring the haze index. This is done by modifying Equation 3 slightly to compensate for the light that may be reflecting from the black target area. The modified equation is:

$$H_i = \frac{L - Bt}{E} \quad (4)$$

Where: B = luminance of the black area viewed directly  
t = transmission coefficient of the windscreen

It is possible to relate the haze index value to the amount of contrast loss that would be experienced by a pilot viewing through the transparency. Equation 5 describes the amount of contrast loss as a function of the haze index, transmission coefficient and the ambient illumination conditions:

$$CL = 1 - \frac{M}{M + EH_i/t} \quad (5)$$

where: CL = fraction of contrast loss  
M = Mean (average) target luminance  
E = illumination on the windscreen  
H<sub>i</sub> = haze index  
t = transmission coefficient of the windscreen

There are many families of curves that can be graphed based on Equation 5 that show the effects of the different ambient conditions and windscreen haze index on amount of contrast loss. It should be noted in Equation 5 that the haze index appears in conjunction with the transmission coefficient of the windscreen. For this reason, the quantity H<sub>i</sub>/t has been designated the haze ratio which is the critical quantity for comparison between windscreens. Table 2 is a summary of some haze index and haze ratio measurements that have been made for several aircraft along with pilot comments regarding the windscreens.

Table 2. Typical values of haze index and haze ratios for windscreens.

TRANSPARENCY	HAZE INDEX *	HAZE RATIO *	COMMENTS
F-111 Glass W/S	0.005	0.011	Good
F-111 Plastic W/S	0.040	0.080	Marginal
LANTIRN HUD Eyebrow	0.045	0.085	Marginal
LANTIRN HUD Center	0.013	0.020	Good
F-16 W/S (Plastic)	0.023	0.035	OK
F-16 W/S and LANTIRN			
HUD - Eyebrow	0.048	0.150	Poor
HUD - Center	0.033	0.078	Marginal
A-10 Plastic W/S	0.022	0.030	OK
A-10 W/Residue	0.110	0.158+	Unacceptable
A-10 W/S and HUD	0.042	0.080	Poor

\* Units are ft-Lamberts/ft-candle

These data were taken at different times on different efforts for different reasons, so it is somewhat difficult to establish exact guidelines from this table. However, it is apparent that the windscreens become

unacceptable somewhere in the neighborhood of about 0.16 ft-Lamberts/ft-candle of haze ratio.

A further advantage of this haze index approach to measuring halation in windscreens is that Equation 5 can be combined with basic vision data concerning the effects of contrast on performance to calculate the effects of the haze on pilot detection performance.

A third method of characterizing windscreen haze is currently under development. This method makes use of the fact that some of the scattered light from the windscreen is scattered back toward the direction of the illuminating source. If this rearward scattered light can be separated from the reflected light and measured, it would be possible to use it as a measure of haze in the windscreen. A prototype device using this approach has been designed, built and tested. The device worked reasonably well with new transparent parts where the scattering was primarily internal to the material as opposed to being caused by surface scratches. However, when the device was used to measure old windscreens, the linear micro-scratches on the surface of the windscreen produced a diffraction pattern that was not circularly symmetric. Since the prototype device sampled only a portion of the backscattered light in one direction, it did not produce reliable nor repeatable readings. Figure 8 shows the prototype device (US Patent No. 4,687,338).

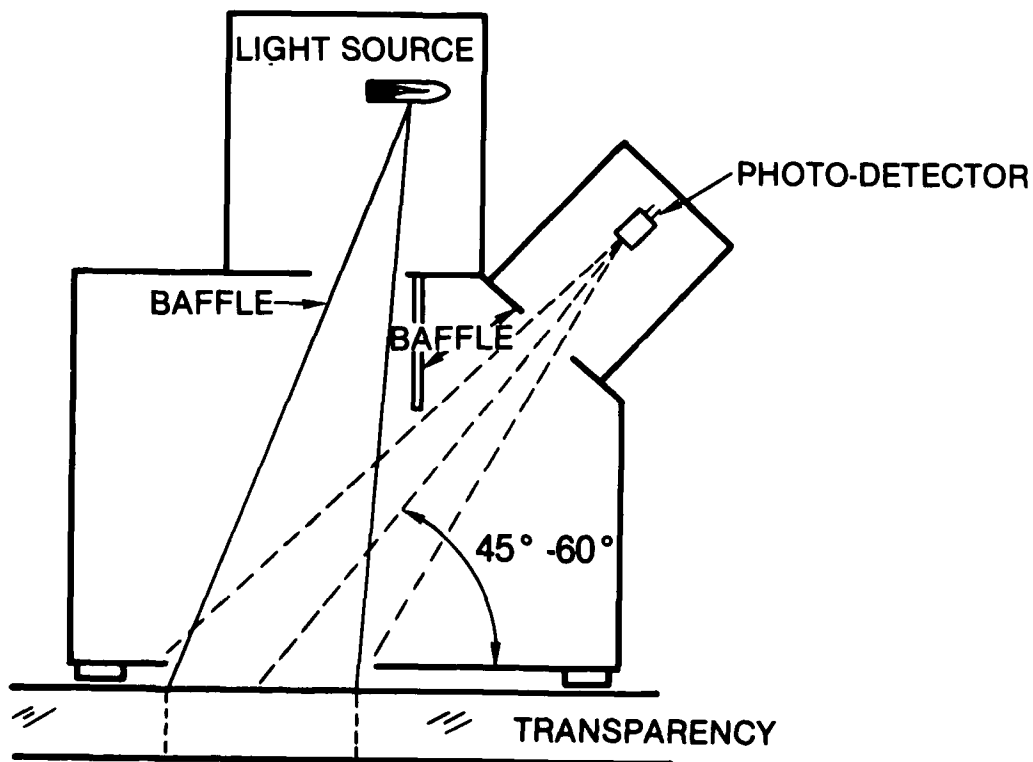
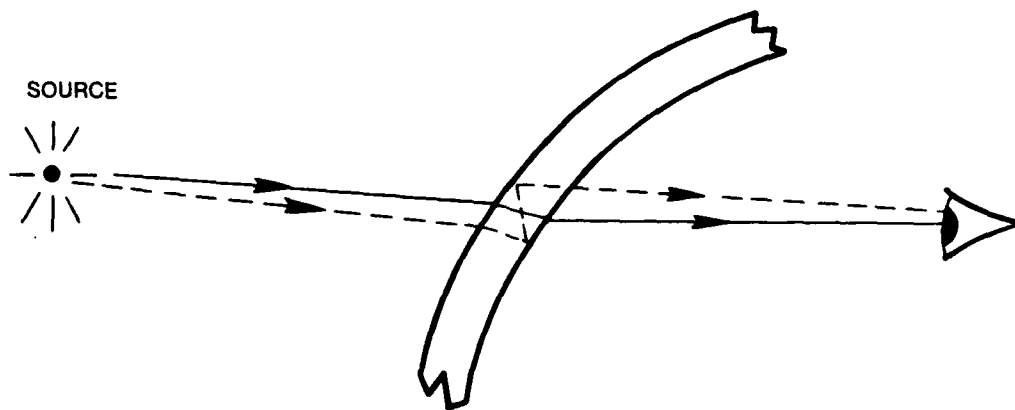


Figure 8. Diagram of Prototype Device to Measure Haze Making Use of the Backscattered Light

In order to correct this problem, an alternate design approach has been developed. This approach uses an integrating sphere to capture and average all of the backscattered light while providing sufficiently large apertures to permit the reflected light to escape from the sphere. This device is in the process of being fabricated and tested. The intent is to produce a device that can be easily used in the field to permit measurement of windscreen haze by minimally trained personnel. This would provide a quantitative means of determining when the windscreen should be removed from the aircraft due to haze.

### Multiple Imaging

Multiple imaging is typically only visible (and only a problem) during night flight, particularly night landings. Light from external sources, such as runway marker lights and the glide slope indicator lights, are seen both directly through the windscreen and as a secondary, and sometimes tertiary, image. The secondary image is caused by the light from the source coming through the outer surface of the windscreen, being partially reflected by the inside surface (surface closest to the pilot), then partially reflecting again from the outer surface and finally going to the pilot's eye (see Figure 9). The effect of this is to present two images of external light sources to the pilot. The position of the secondary and the intensity of the secondary images with respect to the primary, varies considerably depending on the parallelism of the inner and outer surfaces of the transparency and the angle of view through the windscreen.



**MULTIPLE IMAGING**

Figure 9. Ray Trace Showing the Reflections That Cause Multiple Imaging

There are two parameters of interest with regards to multiple imaging: the ratio of the intensity of the secondary image to the primary image, and the apparent angular separation between the secondary and the primary. A test procedure has been developed for each of these parameters. The test procedure to measure the angular separation between primary and secondary images is in the process of being accepted as a standard ASTM test procedure. It should be fully approved by late 1988.

The angular separation between primary and secondary images is determined by photographing a rectangular array of lights spaced about 16 inches apart and positioned about 23 feet from the design eye position of the windscreen. At this distance, the angular separation between the lights is approximately 3.3 degrees. On the photograph, the distance between the lights is measured in linear units. This provides a conversion factor to convert between distances on the photograph and angular distances from the design eye position. For example, if the separation on the photograph between the primary images of two adjacent lights is 20 mm, then one can convert from mm on the photograph to degrees of angular subtense by multiplying the photograph distances by  $3.3 \text{ degrees}/20 \text{ mm}$  or  $0.166 \text{ degrees/mm}$ . Then, a digital caliper can be used to measure the linear distances between the primary and secondary images on the photograph. These linear distances can then be changed to angular separations by using the conversion factor. From our limited experience so far with this metric, it appears that the pilots are reacting primarily to the angular separation between the primary and secondary images in the lower portion of the windscreen. This makes sense in that this area of the windscreen is the most critical during landings and the intensity of the secondary images is also the greatest in this area.

The intensity ratio between the secondary and primary images is measured using a custom designed incandescent point source projector. The device is just like a slide projector with the slide being an opaque sheet with a tiny pinhole in it. The projector is positioned about 15 feet from the windscreen and the image of the pinhole is focused through the windscreen at the design eye position of the windscreen. A secondary image of the point source also appears near the design eye position due to the multiple imaging effect in the windscreen. Typically, this secondary image is separated from the primary by a small distance due to the lateral displacement effect of the windscreen. The intensity of the primary and secondary images is measured using a photometer configured to measure illumination. The active area of the photometer must be sufficient to include all of the light (separately) in the secondary and the primary images. This typically corresponds to a circle of light about one centimeter in diameter. The intensity ratio is calculated by dividing the illumination in the secondary image by the illumination in the primary image. This value is calculated for all field angles of interest.

#### Minor Optical Defects

Minor optical defects refer primarily to small inclusions in the windscreen or small bubbles. The inclusions may be tiny bits of dirt or other impurities or even pieces of hair. Typically, most minor optical defects are not visible except under close visual inspection. Specifications for minor optical defects limit the number and size of defects that are permitted. Inspectors locate and optically measure the diameter of each defect that they can find. This is typically a time consuming and laborious process, but is a requirement as part of the acceptance test procedures for all new windscreens.



Most minor optical defects are probably not even noticed by aircrew members. At least one study (Kama & Genco, 1982) was done to look at the effects of minor optical defects on subject target detection performance. The results of this study indicated that specifications for minor optical defects should probably be relaxed since the size and density of defects investigated (which far exceeded the acceptance criteria) showed no loss in target detection performance. However, specification requirements have not been relaxed.

#### Rainbowing/Birefringence

Birefringence is a phenomenon that occurs with polycarbonate under stress. Stress causes the material to exhibit two indices of refraction depending on the polarization state of the incident light. The details are far too complex to cover here, but the result is that the windscreen may appear to have a pastel rainbow effect in some areas for clear sky conditions. Sky light can be as much as 80% polarized during a clear, blue sky day. This effect has been noted on all plastic aircraft windscreens. As yet, there is no procedure for quantifying the severity of the rainbowing pattern so it is usually not specified. The color pattern seen is usually due to unrelieved stress in the windscreen that occurs as part of the manufacturing process. Efforts to reduce this effect have not been very successful.

Although the rainbowing pattern may be easily visible, it is usually not considered to be a significant problem by aircrew members. The spatial pattern of the rainbowing remains fixed, but the colors that make up the pattern shift as the aircraft changes orientation with respect to the partially polarized skylight. It has been hypothesized that this swirling of the colors might cause a distraction, however, there has been no evidence to indicate that birefringence or rainbowing is a significant problem. Pilots wearing (unauthorized) polarized sunglasses would see this effect greatly exaggerated.

#### Reflectivity

Reflections occur at the interface between any two transparent media that have unequal indices of refraction. Thus, there is a significant reflection at the air/windscreen interface since the index of refraction of air is almost unity and the index of refraction of the plastic windscreen is typically on the order of 1.49 or 1.59. It should be noted that the reflectivity at the inside and outside surfaces of the windscreen is the basis for multiple imaging discussed earlier.

Reflections are of concern for several reasons: first, it is the basis for the multiple imaging problem; second, it causes a loss of contrast for daytime flight due to reflections of the glare shield in the windscreen; third, it is a source of distraction during daytime flight due to the reflection of the pilot's helmet in the windscreen; and fourth, reflections of internal cockpit lights during night flight are an annoyance.

There is no practical method as yet to reduce reflections on aircraft windscreens. All antireflection techniques are either too delicate for windscreen use or are wavelength and angle dependent, making them unsuitable for aircraft use. However, with the increased interest in reducing glint (also caused by reflection from the windscreen) and other unwanted reflections, there has been a draft ASTM test method to measure the reflection coefficient. Although not yet approved, it is expected that this test procedure will be validated before the end of 1988.

### Transmissivity

As noted above, some light is reflected from the surface of the transparency. Additionally, some light is absorbed by the windscreen material and some light is scattered. The remaining light is transmitted through the transparency and is usable for viewing the outside world. The transmission coefficient is the ratio of the transmitted light to the total incident light.

The present method of measuring transmissivity is based on ASTM D 1003-61 which uses an integrating sphere approach to the measurement. This method can only be used on relatively small samples (or coupons) of material and is designed to make measurements of transmissivity essentially perpendicular to the surface of the coupon. In addition, this method measures luminous transmittance which includes both scattered and unscattered transmitted light (only the unscattered transmitted light is useful for producing an image). Despite these shortcomings, this method is the standard method used for specifying transmissivity in aircraft windscreens and aircrew visors.

Since the reflectivity of the surface varies with angle, the amount of light transmitted also varies with angle. Thus, a measurement of transmissivity perpendicular to the surface of a material does not provide a good measure of the transmissivity apparent to the pilot viewing through the windscreen. For this reason, an alternate transmissivity measurement procedure is under development. This procedure requires a light emitting surface and a photometer. The luminance of the light emitting surface is measured both directly and through the windscreen. The ratio of the two readings is a measure of the windscreen transmissivity. Since the windscreen does not have to be mounted in any special orientation nor put in contact with an entrance aperture, it is possible to map the transmissivity of the entire windscreen as seen from the pilot's eye position. This can produce significantly different numbers than the currently accepted standard method. For example, the transmissivity of the B-1 windscreen using the standard, perpendicular method is about 65%. However, the actual transmissivity through the nose region of the B-1 (about 82 degrees angle of incidence) is closer to about 20%.

Field measurement of transmissivity is not possible using the ASTM D 1003-61 method but is relatively easy using the photometer and light source method. However, care should be taken when using the photometer and light source method to minimize sources of error. The windscreen should be shaded from direct light sources to prevent haze from confounding the

reading and a black light absorbing surface should be used to cover the glare shield to minimize reflections from this source. Either of these problems will tend to result in a higher reading of transmissivity than actually exists.

It is difficult to accurately quantify the effect of transmissivity on aircrew performance. A lower transmissivity does not decrease contrast but it does decrease the apparent brightness of objects viewed through the windscreen. A lower luminance level, in general, will result in a lower visual acuity of the pilot. This effect is probably not significant for most daytime flying conditions. Only on severely overcast days or during twilight would a loss of visual acuity due to lower windscreen transmissivity probably be measurable.

#### WINDSCREEN, VISOR, AND HUD INTEGRATION ISSUES

Many of the same characteristics and measurements can be applied to visors and HUD combiners as well as windscreens. Angular deviation, distortion, minor optical defects, haze, transmissivity and reflectivity all apply equally well to visors and HUD combiners. Of particular interest are angular deviation, haze and transmissivity. Since the pilot must view through all three transparencies (the visor, HUD combiner and windscreen), the effects of angular deviation, haze and transmissivity of each of these transparencies can combine to produce larger overall effects on vision.

Normally, angular deviation measurements are not made on visors. Instead, visors are typically characterized by the amount of prismatic deviation, spherical power and cylindrical power in the visor at different locations on the visor. If the visor deviations and the windscreen deviations happen to be in the same direction, the overall effect of viewing through the visor and windscreen together could produce visual problems.

Haze effects tend to reduce contrast of objects viewed through the transparency. Typically, visors have very low haze values (less than 1%) as measured using the ASTM D1003-61 test method. However, as visors age and are used, they get scratched and pitted thus increasing their haze effects much the same as the windscreens. Add to this increased haze in the HUD combiner due to dust or poor cleaning practices and the overall loss of contrast through the combination of visor, HUD combiner and windscreen can be very great for some viewing conditions. Contrast loss in excess of 90% has been measured for some aircraft windscreens and viewing conditions.

Since transmissivity ( $t$ ) is a multiplicative parameter, the amount of light that actually gets to the pilot's eyes depends on the product of the transmissivities of the visor, HUD combiner and windscreen (as well as the pilot's glasses, if worn). For example, if the pilot is wearing the clear visor ( $t=.92$ ) and has a conventional HUD combiner ( $t=.5$ ) and is viewing straight ahead through the F-16 solar coating windscreen ( $t=.65$ ), then the total transmissivity would be:  $t=(.92) \times (.5) \times (.65)=0.30$  or about 30%. For daylight conditions, this loss of luminance should not be a problem at all. However, during dusk and dawn and on heavily overcast days, this 30%

transmissivity will tend to reduce the pilot's visual acuity by some small but measurable amount.

Another area of concern for HUD/windscreen integration has to do with the optical distance at which the HUD symbology appears. HUDs are normally set so that the image produced by the HUD appears to be at optical infinity. That is, the eyes are looking straight ahead and are focused at infinity (or close to it). For the F-16, the forward portion of the canopy acts like a slight negative lens. This causes objects that are actually very far away to appear to be about 100 to 150 ft away in terms of eye convergence and focus. Since the HUD was designed to produce essentially a flat field at infinity, a mismatch occurs between the apparent optical distance of objects viewed through the windscreen and the apparent optical distance of the HUD symbology. This mismatch, at a minimum, causes an aiming error due to parallax (which is partially corrected by the angular deviation mapping and HUD symbology correction). At its worst, it could cause a pilot to see two targets and one aiming reticle (where there is only one target) or two aiming reticles and one target.

This condition has been somewhat corrected by decollimating the HUD image so that it appears at about the same optical distance as the object viewed through the windscreen. Since these corrective actions have been taken, there have been no further complaints about seeing double.

## REFERENCES

- ASTM D 1003-61. "Haze and luminous transmittance of transparent plastics". September 1961.
- ASTM F 733-81. "Optical distortion and deviation of transparent parts using the double-exposure method". August 28, 1981.
- ASTM F 943-85. "Measuring halation of transparent parts". July 26, 1985.
- Bauer, G., Huebner, H. J. and Sutter, E., "Measurement of light scattered by eye protection filters", Appl. Optics, 7(2), 1968, pp 325-329.
- Clark, B. A. J., "Veiling glare from spectacles and visors in aviation", Aust. J. Optom. 62,6, June 1979.
- Genco, L. V., "Angular deviation and its effect on HUD-equipped aircraft weapons sighting accuracy", Technical Report: AFAMRL-TR-82-43, August 1982.
- Genco, L. V., "Optical interactions of aircraft windscreens and HUDs producing diplopia", section of: Optical and human performance evaluation of HUD systems design, W. L. Martin, Ed., Technical Report: AFAMRL-TR-83-095 or ASD(ENA)-TR-83-5019, pp 20-27, December 1983.
- Genco, L. V., "Visual effects of F-16 canopy/HUD integration", paper in: Conference on aerospace transparent materials and enclosures, S. A. Morolo, Ed., Technical Report: AFWAL-TR-83-4154, pp 793-801.
- Genco, L. V. and Task, H. L., "Aircraft transparency optical quality: New methods of measurement". Technical Report: AFAMRL-TR-81-21, 1981.
- Harris, J. S. and Harding, K. G., "Study and evaluation of existing techniques for measuring aircraft windscreen optical quality: Development of new techniques for measuring aircraft windscreen optical distortion", Technical Report: AFAMRL-TR-81-25, February 1981.
- Kama, W. N., "Visual perception through windscreens: effects of minor occlusions and haze on operator performance", paper in: Conference on aerospace transparent materials and enclosures, S. A. Morolo, Ed., pp 825-847, December 1983.
- Kama, W. N. and Genco, L. V., "The effect of size and number (density) of minor optical occlusions on target detection performance", Technical Report: AFAMRL-TR-82-48, September 1982.
- Kraft, C. L., Anderson, C. D., Elworth, C. L. and Larry, C., "Windscreen quality and pilot performance", Technical Report: AMRL-TR-77-39, October 1977.
- MacLeod, S. and Eggleston, R. G., "Pilot reactions to optical defects found in F-111 bird impact resistant windscreens", Technical Report: AFAMRL-TR-80-4, December 1980.

Seid, R., "Computer analysis and correction of the optical distortion in the F-111 bird impact resistant windscreen", Technical Report: AFAMRL-TR-81-67, December 1981.

Self, H. C. and Task, H. L., "Potential of optical Fourier analysis for measuring windscreen distortion". Technical Report: AFAMRL-TR-80-104, December 1980.

Targove, B. D. and Seid, R., "Paraxial opticovisual analysis of the F-111E windscreen with generic application", Technical Report: AMRL-TR-79-107, December 1979.

Task, H. L., "Measurement of HUD optical quality", NAECON 1983 conference, mini-course notes, Dayton, Ohio, 17-19 May 1983.

Task, H. L., "Measurement of HUD optical quality", section of: Optical and human performance evaluation of HUD systems Design, W. L. Martin, Ed., Technical Report: AFAMRL-TR-83-095 or ASD(ENA)-TR-83-5019, pp 11-19, December 1983.

Task, H. L., "Optical effects of F-16 canopy-HUD integration", paper in: Conference on aerospace transparent materials and enclosures, S. A. Morolo, Ed., Technical Report: AFWAL-TR-83-4154, pp 809-824, December 1983.

Task, H. L. and Genco, L. V., "The measurement of aircraft windscreen haze and its effect on visual performance", Technical Report: AFAMRL-TR-85-016, February 1985.

Task, H. L., Genco, L. V., Smith, K. L. and Dabbs, A. G., "System for measuring angular deviation in a transparency", US Patent No. 4,377,341, March 22, 1983.

United States Patent #4,299,482. "Measurement of windscreen distortion using optical diffraction". H.L. Task. November 10, 1981.

United States Patent #4,687,338, "Method of measurement of haze in transparencies". H.L. Task and L.V. Genco. August 28, 1981.

Ward, F. E. and DeFrances, A. J., "Development of a visual inspection technique (optical assessment of aircraft transparencies)", Technical Report: AMRL-TR-79-67, October 1979.

MEASURES OF DISTORTION: ARE THEY RELEVANT?

William N. Kama  
Human Engineering Division  
AAMRL

## MEASURES OF DISTORTION: ARE THEY RELEVANT?

William N. Kama

Human Engineering Division  
Armstrong Aerospace Medical Research Laboratory  
Wright-Patterson AFB, Ohio 45433-6573

### ABSTRACT

Based on the results obtained from a pilot study, an experiment was conducted to determine how well current measures of optical distortion in aircraft transparencies (grid line slope, lens factor and displacement grade) related to the subjective assessment of this phenomenon by human operators. A total of 20 subjects were asked to perform several tasks, each of which would yield a measure (subjective and objective) of the "amount" of distortion present in 13 test windshields. The subjective tasks included a magnitude estimation task (using the actual windshields and photos of the windshields) - in which all windshields were compared to a "referee" windshield; and a ranking test, in which subjects ranked distortion photos of each windshield from the least objectionable to the most objectionable. The objective task consisted of measuring distortion using the measurement techniques of grid line slope, lens factor and displacement grade. The results obtained indicated no relationship between a human operator's qualitative assessment of a windshield and the quantitative measures obtained.



## INTRODUCTION

One of the optical characteristics of a transparency that can degrade an aircrew member's visual performance is distortion. Distortion occurs as a result of the differences in thickness or parallelism (prismatic or wedge effect) between the two surfaces of the windshield. If the distortion is severe, it can degrade the visual performance of an aircrew member by causing objects being viewed by them to appear in a location different from their actual position as well as causing straight lines to appear wavy.

Currently, the amount of distortion present in a windshield is determined by taking black and white photographs of a large grid board through the windshield. The grid board contains 1-inch squares made up of 1/16-inch wide, white lines on a dark background. The photographs are taken with the windshield mounted at its installed angle; the camera located at the design eye position; and the gridboard located at a specified distance from the windshield (200 inches from the design eye position for lens factor and displacement grade and 120 inches from the forward edge of the windshield for grid line slope.)

Each photo or print is enlarged so that the image size on each print is 16 grid squares per inch. After the photos are developed, a drafting table and equipment are utilized to obtain three measures that are used to characterize the amount of distortion present in a windshield. These measures are grid line slope, lens factor (lensing) and displacement grade.

**Grid Line Slope:** The determination of grid line slope yields a ratio of the slope of a deviated grid line to that of a nondeviated grid line. This ratio may be defined as the number of horizontal grids that is crossed by a straight edge before a complete vertical grid is crossed or as grid squares of run for one grid square of rise. Grid line slope is generally less stringent (1:3) for noncritical viewing areas of the windshields, but becomes more stringent (1:9, 1:10 or 1:12) for the critical viewing zones.

To determine grid line slope, the photo is placed on the drafting table and positioned until the upper and lower horizontal grid lines that extend outside of the boundary of the windshield are parallel with the horizontal scale of the drafting machine. When parallelism is attained, the photo is fastened to the table with tape so that it does not move during the measurement process. The straight edge of the drafting machine is then placed tangent to the horizontal grid line exhibiting the maximum slope in each of the viewing areas (see Figure 1). The number of horizontal grid lines (run) required for the straight edge to cross a vertical grid line (rise) is then determined. This yields the grid line slope or rise to run ratio. In Figure 1, the measured grid line slope is 1:3.

**Lens Factor (Lensing):** The following procedure is used to determine lens factor: Prior to affixing the photo to the drafting table, the horizontal grid lines in the upper and lower grid board areas outside the boundaries of the windshield (see Figure 2) are checked for parallelism with the horizontal scale of the drafting machine. Once parallelism is established, the photo is fixed to the table and the entire upper and lower

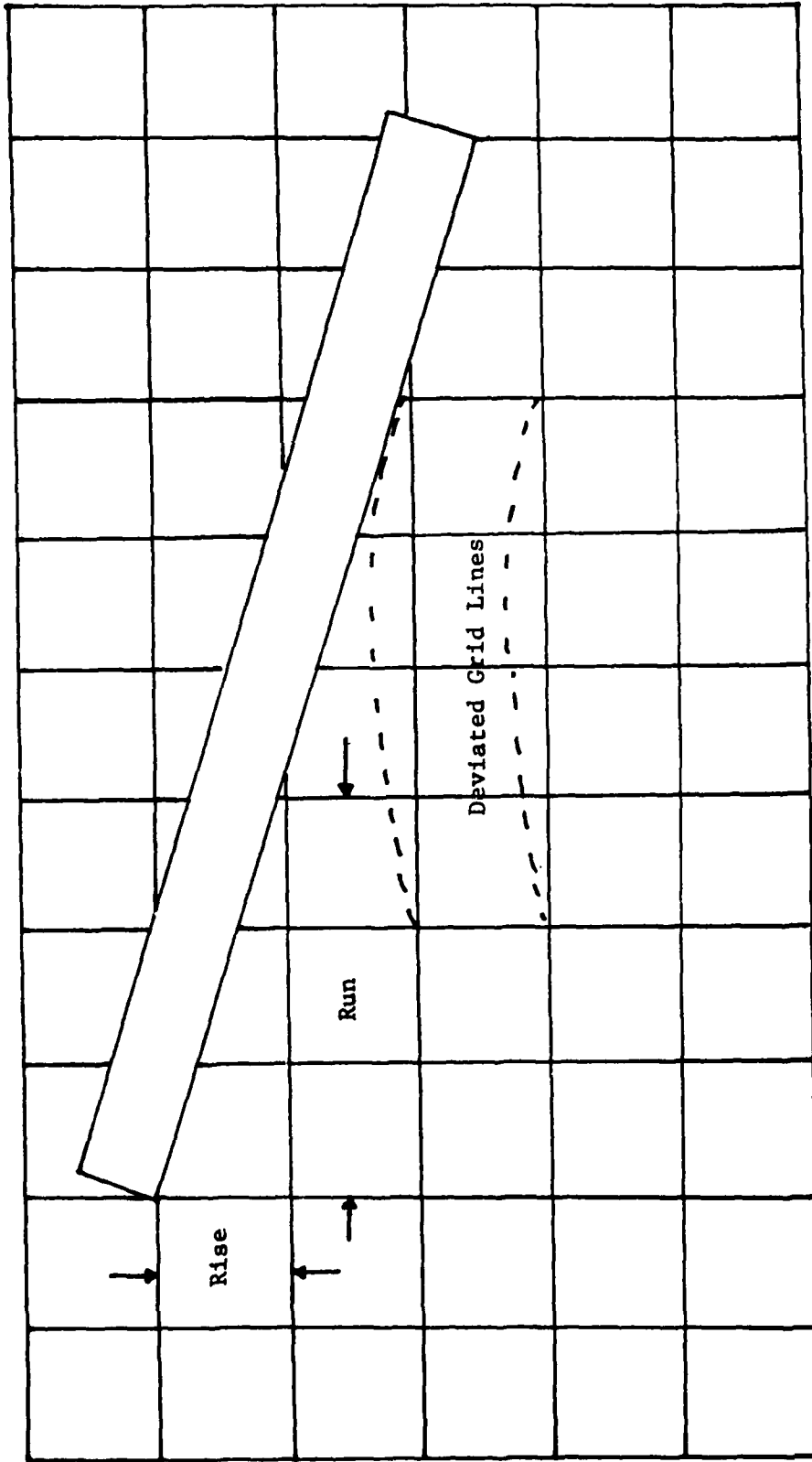


Figure 1. Method used to determine grid line slope. In this example, the grid line slope is 1:3.

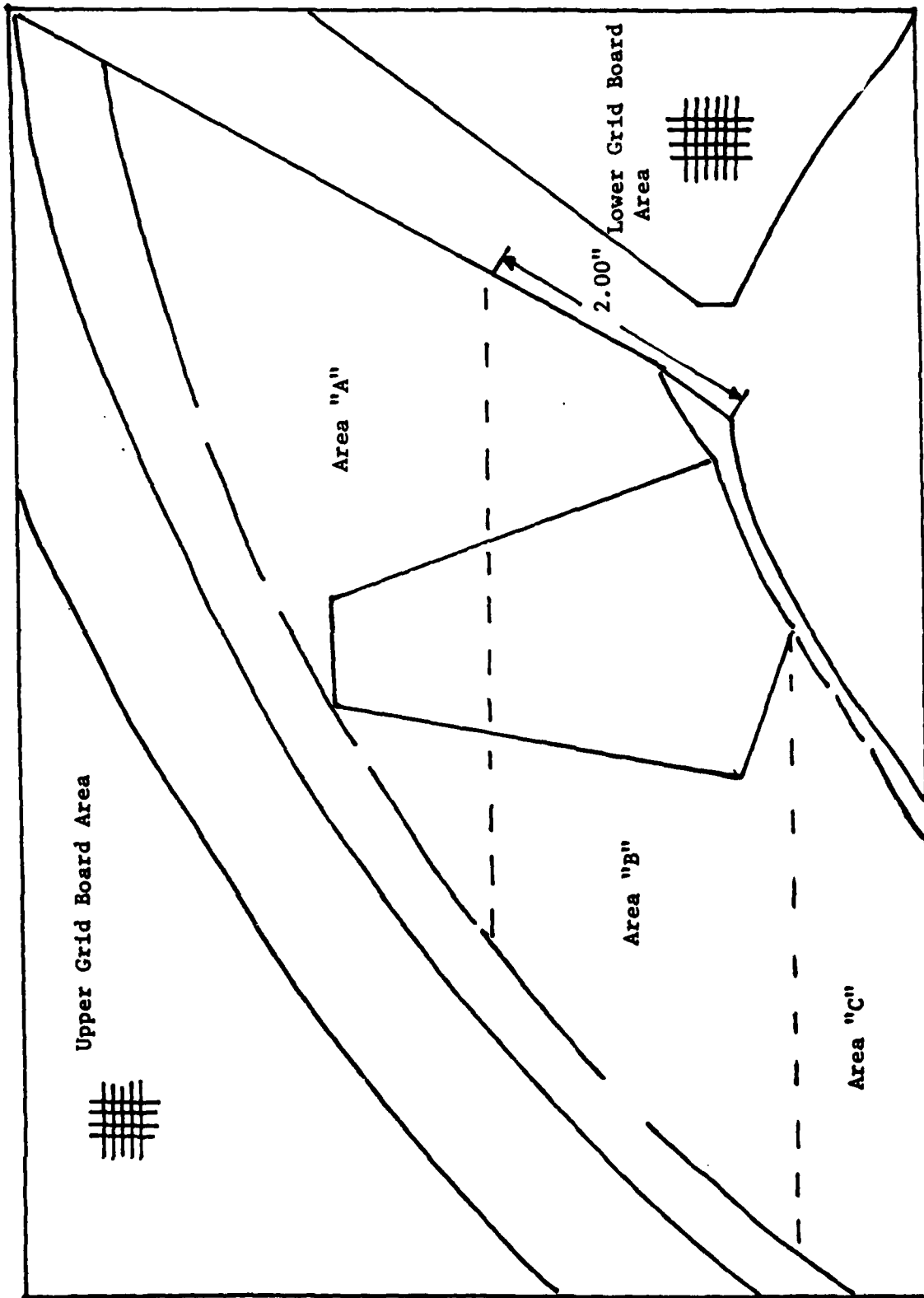


Figure 2. Areas of the windshield that is measured to determine Lens Factor and Displacement Grade.

grid board areas are then checked for parallelism with the horizontal drafting scale. In the upper grid board area, a specific grid line is allowed to deviate from horizontal parallelism a maximum of 1/4 of a grid square over a distance of 5 inches while in the lower grid board area this allowance is 1/8 of a grid square over a distance of 2.5 inches. Any deviation in excess of 1/4 of a grid square or any deviation in excess of 1/8 in the lower grid board area will be cause for rejecting the photograph from further evaluation.

After establishing the parallelism of the upper and lower grid board areas, the horizontal scale of the drafting machine is locked in place. The number of grid squares per horizontal inch (one inch is always used as the unit of measure) is then checked at several locations in both the upper and lower grid board areas. The number of grid squares per inch that is obtained is recorded and used as a reference for measurements made in the windscreens various areas.

Several horizontal "squares per inch" measurements are then made for each of the areas designated A, B and C in Figure 2. For each of these areas, the maximum deviation is recorded. Depending on whether this measure is larger or smaller than the reference measurement obtained previously, this measure is either divided by the reference measurement or is divided into the reference measurement. Doing this ensures that a value larger than 1.00 is obtained. This value is then cubed to obtain the lens factor for each of the areas A, B and C. The lens factor for the windshield is then represented by the lens factor obtained for either A or B, whichever is larger (the lens factor value for area C at this time is only for informational purposes). A lens factor of 1.10 or less represents a windshield that is optically acceptable with respect to distortion.

Displacement Grade: The photo used to measure lens factor is also used to measure displacement grade. The horizontal scale of the drafting machine and a 100th inch division scale (a digital caliper in this study) are used to determine the maximum vertical displacement of a horizontal grid line to the nearest 0.001 inch within the areas A, B and C as shown in Figure 2. The horizontal scale was aligned with a horizontal grid line in such a manner that it just touched the beginning of that grid line. The scale was then locked into position and the maximum displacement measured with the digital calipers to the nearest 0.001 inch.

Next, the maximum horizontal displacement of a vertical grid line is determined to the nearest 0.001 inch within the areas D and E (Figure 3) using the vertical scale of the drafting machine and a 100th division scale (digital caliper). As before, the vertical scale was aligned with a vertical grid line so that it just touched the beginning of that line. After the vertical scale was locked into position, the maximum displacement for that line was measured to the nearest 0.001 inch using the digital caliper.

The displacement grade for areas A, B and C are then determined in the following manner: For area A, the area A horizontal line displacement value is added to the vertical line displacement value of area D and the resultant value multiplied by 1000. For area B, the displacement grade is

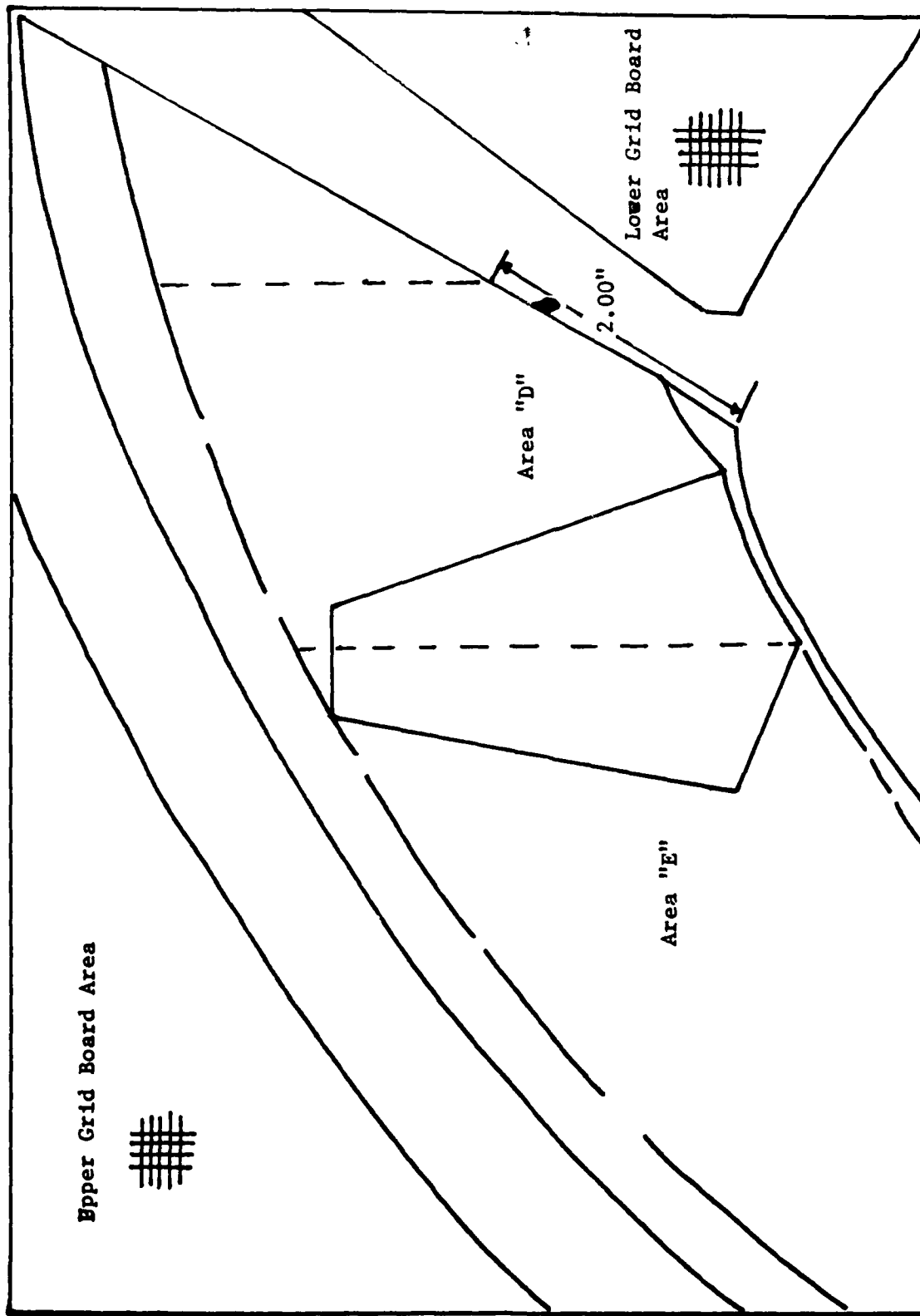


Figure 3. Areas D and E of the windshield that is measured for maximum horizontal displacement of a vertical gridline, Displacement Grade.

obtained by adding the horizontal line displacement value for area B to the vertical line displacement value for area D and multiplying the total by 1000. For area C, the horizontal line displacement value for area C is added to the vertical line displacement of area E and the resultant total multiplied by 1000. As with lens factor, the displacement grade measure for area C is for information only. A displacement grade of 120 or less in areas A or B indicates an acceptable windshield with respect to distortion.

From the preceding paragraphs, one can see that all three measures of distortion are not easily obtained and that special emphasis is placed on the photos used to obtain these measures. Additionally, there is apparently no "good" way to determine which of these three measures best characterize the distortion present in a given windshield.

A pilot study was therefore conducted in the Windscreen Facility at the Armstrong Aerospace Medical Research Laboratory to determine if there was any correlation between how human subjects assessed distortion in a windshield and these three measures of distortion. In this study, the subjects ranked distortion photos of 7 F-111 windshields in terms of the least objectionable to the most objectionable. Grid line slope, lens factor and displacement grade measures were then determined for each of these seven windshields. The results obtained indicated a fairly good correlation between subject ranking and lens factor ( $r = 0.88$ ,  $p < .01$ ) and subject ranking and displacement grade ( $r = 0.71$ ,  $p < .05$ ). However, the correlation between subject ranking and grid line slope was very low, a correlation of .09 being obtained. A comparison of the three measures of distortion yielded a correlation of 0.63 between lens factor and displacement grade; a correlation of 0.07 between grid line slope and displacement grade; and a negative correlation of -0.15 between grid line slope and lens factor. These results suggest that lens factor and displacement grade correlate highly with human assessment of distortion in windshields and appears to provide a fairly reliable measurement of distortion while grid line slope does not.

Based on the results of this pilot study, a larger study was devised to determine whether the associations found in the pilot study would also be found when a larger sample of windshields and a larger number of subjects were employed. In particular, to determine if one of the quantitative measures of distortion was related in some manner to a human operator's perceived quality of a windshield with respect to distortion.

## METHODOLOGY

### Test Samples

A total of 13 F-111 windshields were used in this study. Twelve had been removed from service for a variety of reasons (but none for distortion and hence all acceptable with respect to this characteristic) and one new F-111 windshield which did not meet current displacement grade specifications. Seven of the windshields were left-mounted and six were right-mounted. Each windshield was "masked" (see Figure 4) so that the area of

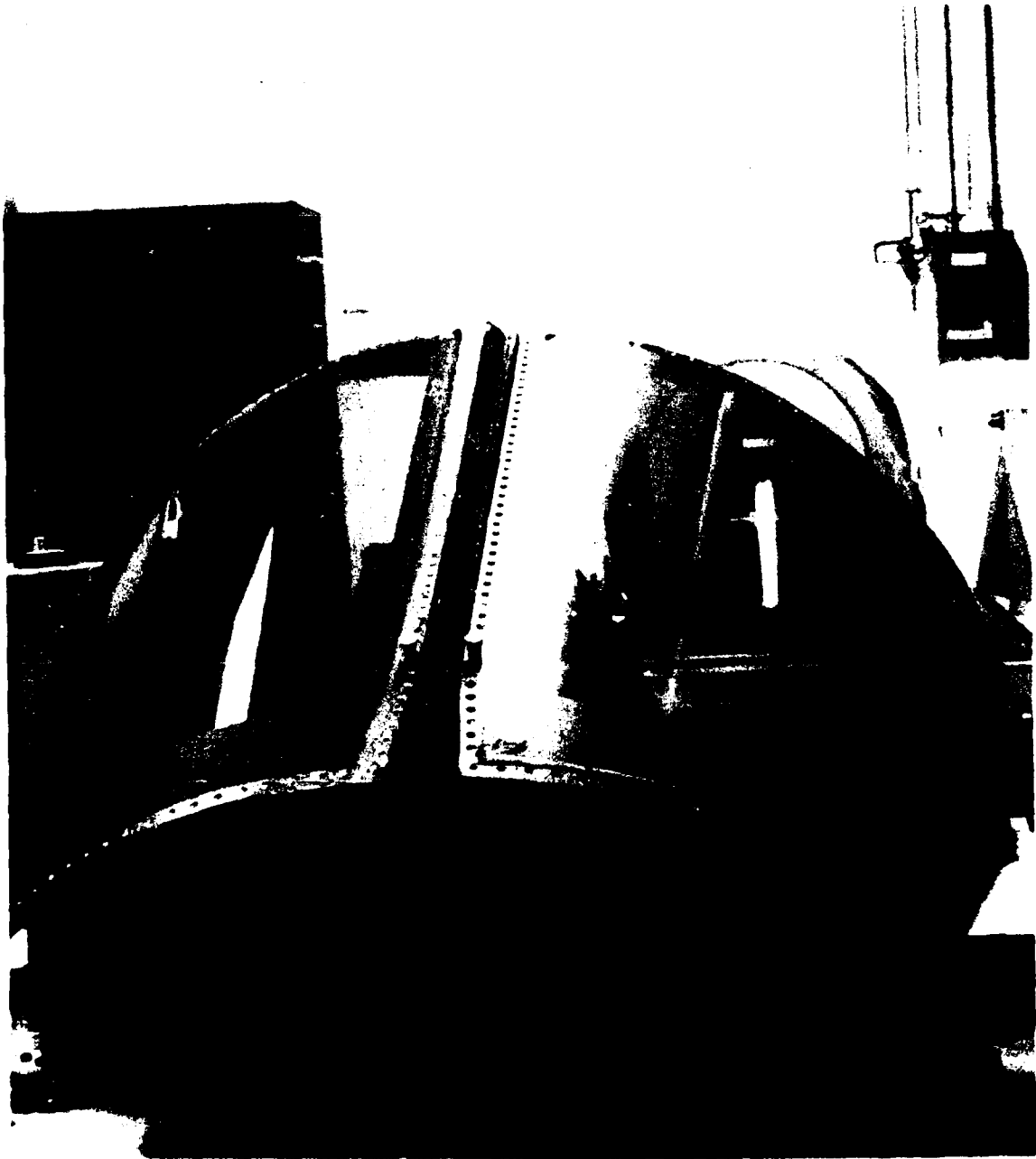


Figure 4. Photo of test windshields showing area that was "masked"

the windshield that was used for each test corresponded to the area seen through the camera's lens from the design eye position with the windshield at its installed angle. This was done to reduce the influence of the optical free zone on a subject's decision and to use the same area of each windshield as the basis of comparison.

Each windshield was photographed against the grid board to obtain the necessary photos for deriving grid line slope, lens factor and displacement grade. All of the photos were taken with the windshields in their installed position; the camera mounted at the design eye position; and the grid board at the appropriate distance from the design eye position for each requisite measure. Photos were also generated for use in two of the subjective tests to be performed. Figures 5 and 6 show the photos used.

### Tasks

The tasks used in this study consisted of two types: qualitative and quantitative. The qualitative tasks were comprised of a magnitude estimation task using the actual windshields [M.E.(WS)], a magnitude estimation task using photos of the windshields [M.E.(Photo)], and a distortion photo ranking task. The quantitative tasks consisted of the three distortion measurement techniques described earlier - grid line slope (GLS), lens factor (LF), and displacement grade (DG).

**Magnitude Estimation:** In this subtask, one of the thirteen windshields used in this study was selected as a standard or "referee" windshield. The subjects were then asked to compare each of the other 12 windshields to this standard windshield. Using a scale in which the standard windshield was arbitrarily assigned a value of 70, subjects indicated "how much better," "worse" or "equal to" the standard windshield each of the test windshields were by assigning a value to each of them. For example, if they felt that a windshield was slightly better than the standard windshield, they might assign that particular windshield a value of "75." Each of the values were assigned to each windshield after each subject had compared the test windshield with the standard (referee) windshield by alternately viewing the distortion grid board through each of them. Subjects were given as much time as required to reach a decision. Subjects performed this task twice (on different days) to determine their repeatability on this task.

Subjects also performed this task using the photos taken of the gridboard through each windshield. As with the first task, the procedure involved the subjects assigning values to each test windshield after comparing them with the standard windshield. Again, subjects performed the task twice to allow us the opportunity to determine the repeatability of their "measurement."

**Ranking Task:** In this task, each subject was asked to examine the distortion photos taken of each windshield. After studying them, they were to rank each of the photos in terms of order of acceptance, i.e., from the least objectionable to the most objectionable. They were allowed as much time as required to arrive at a final order of ranking. Again, subjects





Figure 5. Photo used to determine grid line slope

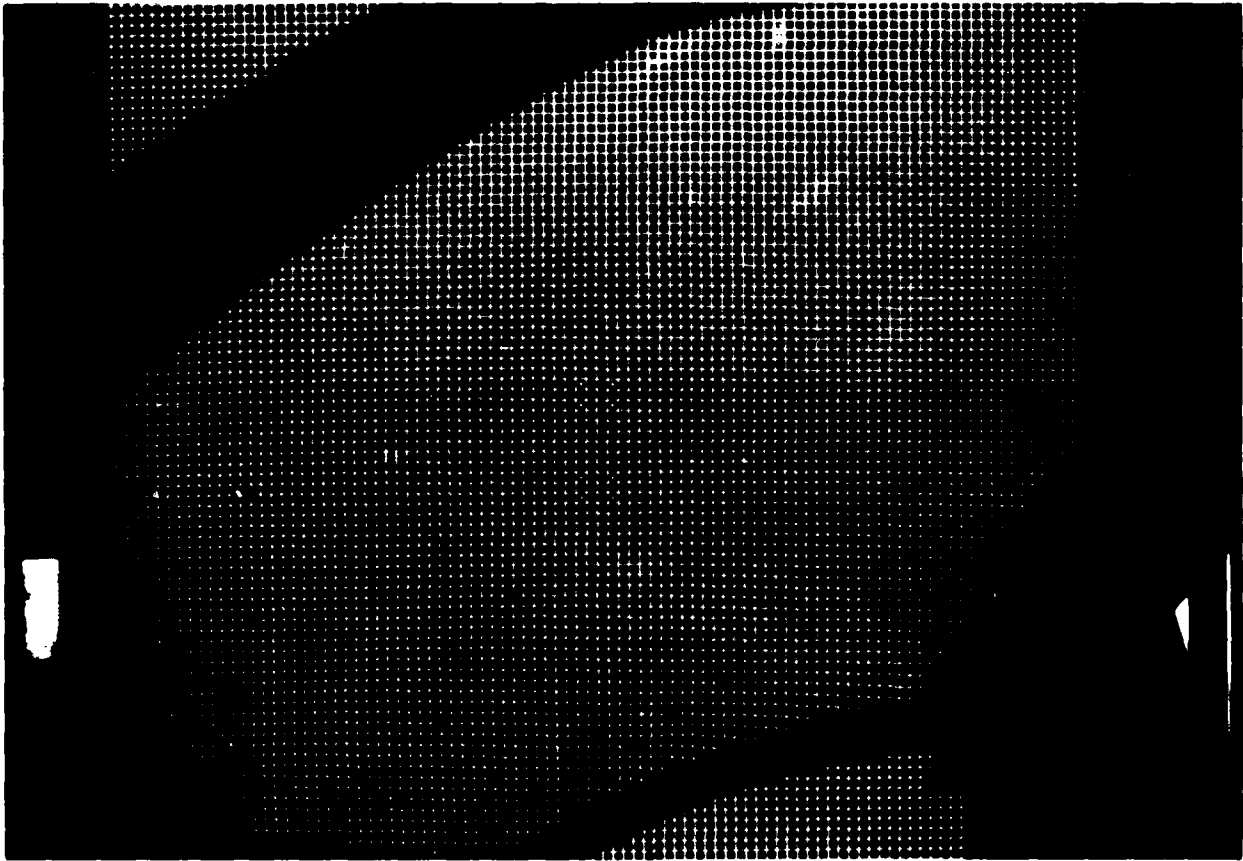


Figure 6. Photo used to determine lens factor and displacement grade

performed this task twice in order to get a determination of their repeatability on this task.

A total of 15 subjects participated in these qualitative tasks.

**Grid Line Slope:** A total of six subjects independently determined the GLS for each of the test windshields in accordance with the procedures described in the introductory section of this paper and as set forth in ATP 601E, "Acceptance Test Procedure for F-FB-111 Bird Impact Resistant Transparencies."

**Lens Factor:** The same six subjects determined LF for each of the test windshields in accordance with the procedures described in the introductory section of this paper and as set forth in ATP 601E.

**Displacement Grade:** Again, the same six subjects determined DG for each of the test windshields using the procedures described in the introductory section of this paper and as set forth in ATP 601E.

### Subjects

A total of 20 subjects from a voluntary and paid subject pool were used in this study. Fifteen of the subjects completed the qualitative tasks only - both magnitude estimation tasks and the ranking task. Six of the twenty subjects (including one from the previous 15) were considered "experienced" subjects who were familiar with and had formerly used the quantitative techniques (grid line slope, lens factor and displacement grade) in other studies conducted in the AAMRL Windscreen Test Facility.

The use of six experienced subjects to perform the quantitative measurement of distortion was deemed necessary at this point in time due to lack of time to provide the proper training to the naive subjects. Additionally, it was felt that the statistical comparisons between the two independent groups would not severely compromise the results of this study.

## RESULTS AND DISCUSSION

The data obtained in this study were subjected to the following analysis. For the qualitative data, the repeatability between the first and second sessions for each subject on each task was determined using regression and correlation techniques. Table 1 presents the coefficients of determination ( $R^2$ ) and the correlation coefficients ( $R$ ) obtained with each of the qualitative techniques.  $R^2$  yields the amount of variability or error that is reduced in  $Y$  given a linear relationship in our set of data and the value of  $X$ . It also gives us an indication of the strength of this relationship and the "goodness" of this linear rule to predict the value of  $Y$ . In this study,  $X$  is represented by the scores obtained in the first session and  $Y$  by the scores from the second session. Examination of Table 1 shows that the repeatability or consistency in scores from one session to the next was best achieved with the magnitude estimation technique using photos. An  $R^2$  value of 0.509 was obtained with a correlation coefficient

Table 1. Coefficient of Determination ( $R^2$ ) and Correlation Coefficient (R) for each Task

	$R^2$	R
Mag.Est. (WS)	0.126	0.355
Mag.Est. (Photo)	0.509	0.713
Photo Ranking	0.347	0.589

of 0.713. The first value indicates a moderate linear relationship between the first and second session scores (over half of the variability being accounted for) and indicates a fairly good prediction of the second score based on the score obtained in session one. The second value gives a good indication of the repeatability of this technique. The linear regression curve obtained for this technique is shown in Figure 7.

Based on the above result, i.e., a good repeatability, the magnitude estimation technique using the photos [Mag.Est.(P)] was selected for use in comparing "subjective quality" with the results obtained from the three quantitative or objective measurement techniques. However, prior to performing these comparisons, the data for three of the subjects used in the Mag.Est(P) task were discarded because they exhibited substantially poorer repeatability ( $R^2$ 's of less than 0.23) than the rest of the subjects. This action did not significantly change the  $R^2$  (0.538) or the R (0.733) of the group. Figure 8 depicts the regression curve for this data.

Table 2 shows the means that were obtained and used to compare the "subjective" measure of distortion with the objective measures of distortion. The regression curves obtained from these comparisons are shown in Figures 9, 10 and 11.

Table 2. Mean Scores Obtained for Each of the Tasks on Each Windshield

Window	Mag.Est. (P)	GLS	LF	DG
A	70.0	8.8	1.09	104.4
B	61.1	11.3	1.12	224.3
C	57.1	12.2	1.05	139.0
D	64.8	9.8	1.06	139.6
E	54.3	11.7	1.04	110.8
F	76.4	21.0	1.04	105.3
G	70.2	12.8	1.07	146.0
H	72.7	14.2	1.02	73.7
I	56.2	13.3	1.09	170.0
J	69.9	13.5	1.06	89.3
K	54.0	12.0	1.08	185.3
L	51.6	7.3	1.03	78.8
M	64.0	10.8	1.10	143.9

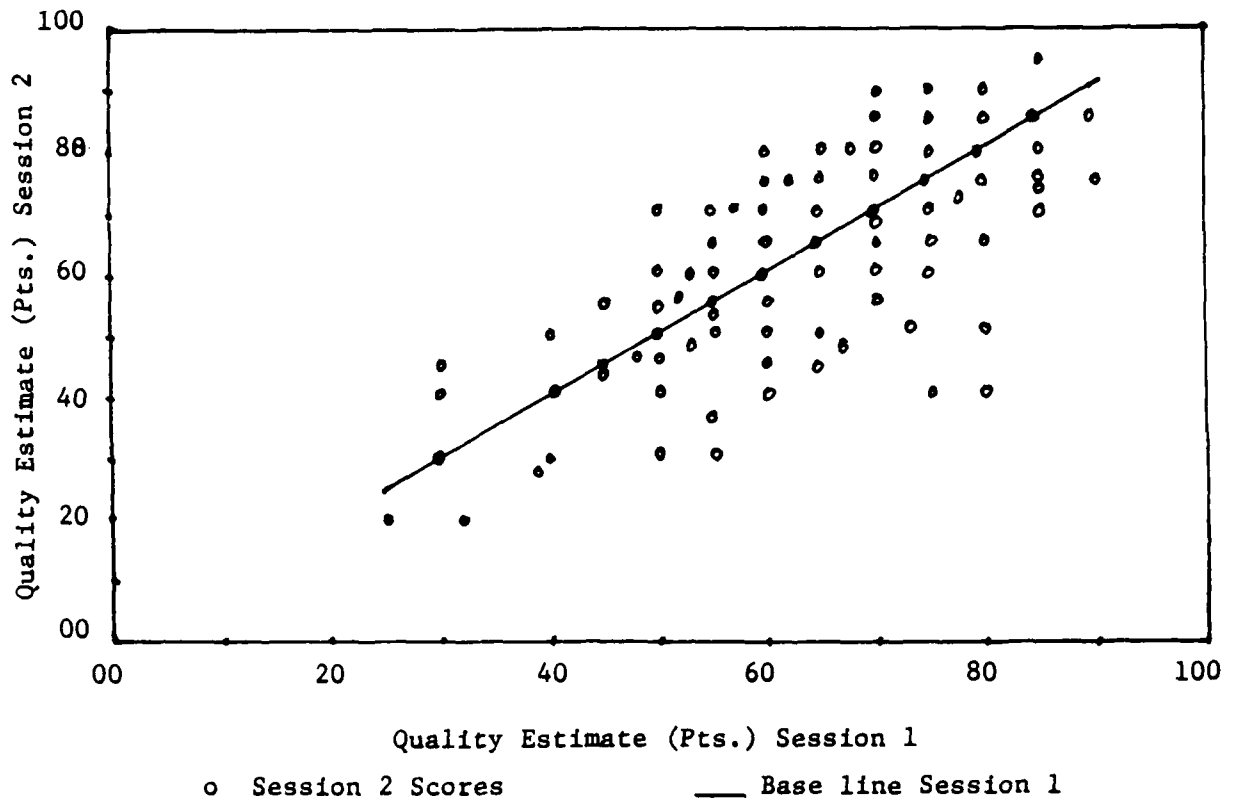


Figure 7. Correlation between quality estimates for session 1 and session 2 (15 Subjects)

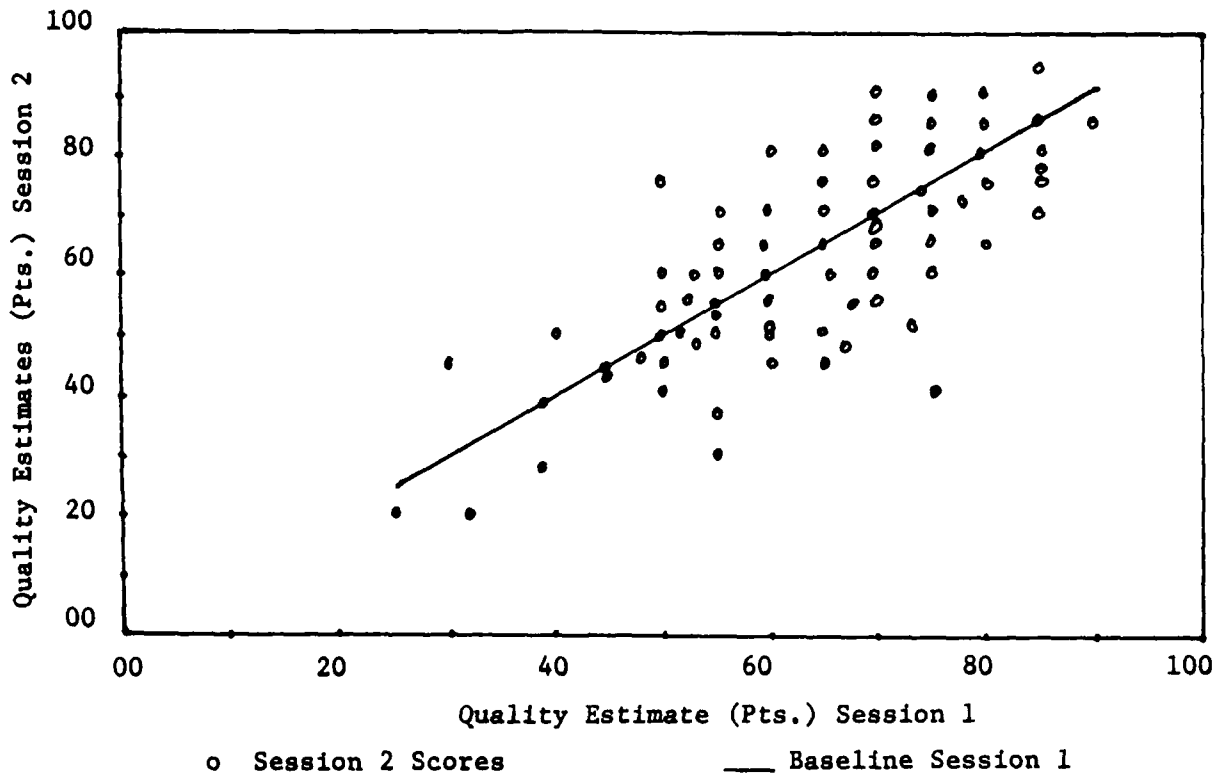


Figure 8. Correlation between quality estimates for session 1 and session 2 (12 Subjects)

Figure 9 shows the relationship obtained between Mag.Est.(P) and GLS. The  $R^2$  value obtained was 0.331 with a correlation coefficient of 0.575. For the relationship between Mag.Est.(P) and LF (Figure 10), the values obtained were 0.033 and 0.180 for  $R^2$  and R respectively. For Mag.Est.(P) versus DG (Figure 11), the values were 0.159 and 0.398. All of the  $R^2$  values obtained indicated no strong linear relationships existed between the subjective measure of distortion [Mag.Est.(P)] and the objective measures of GLS, LF and DG. The ability to predict a score on the objective measures based on a given subjective score was no better than chance.

Utilizing the data shown in Table 2, it was decided to rank each of the 13 windshields in accordance with the "score" that they had received for each task so we could determine if there were any strong associations between the subjective and objective measurement techniques. A Spearman rank difference correlation technique was employed for this analysis. For the Mag.Est.(P) technique, the windshield with the lowest point value was assumed to be the worst with the highest being the best and having a ranking of "1". For GLS, the windshield that had the highest score above "9" was ranked number one while the windshield with the lowest score below "9" was ranked the worst. For LF, the windshield with the smallest score below 1.10 was ranked first while the windshield with the largest score above 1.10 was ranked last. For DG, the windshield with the smallest score below 120 was ranked number one while the windshield with the largest score above 120 was ranked last. The rankings for each windshield under each measurement technique is shown in Table 3.

Table 3. Ranking of Each Windshield on Each Test Measure

Windshield	Mag.Est.(P)	GLS	LF	DG
A	4	12	10.5	4
B	8	9	13	13
C	9	6	5	7
D	6	11	6.5	8
E	11	8	3.5	6
F	1	1	3.5	5
G	3	5	8	10
H	2	2	1	1
I	10	4	10.5	11
J	5	3	6.5	3
K	12	7	9	12
L	13	13	2	2
M	6	10	12	9

A ranking of "1" was considered the most acceptable with the least acceptable receiving a ranking of "13."

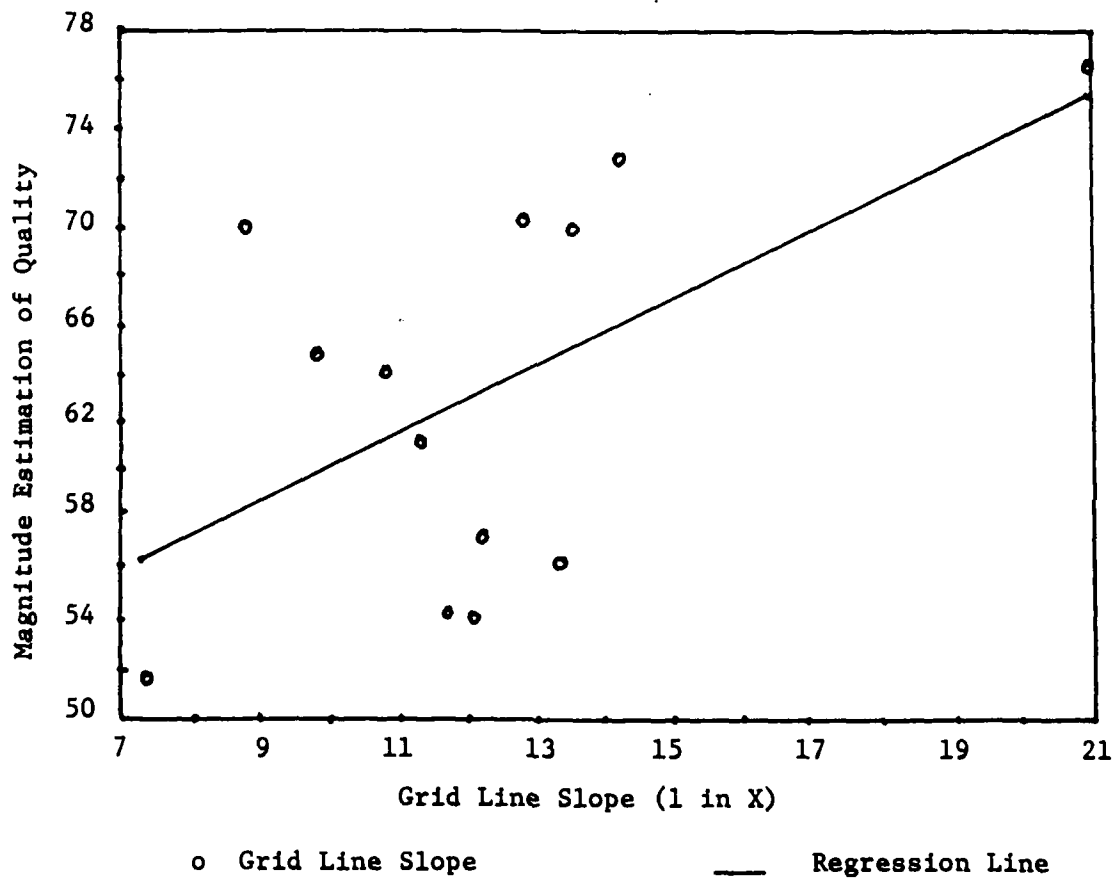


Figure 9. Correlation between Magnitude Estimation (Photo) and Grid Line Slope.



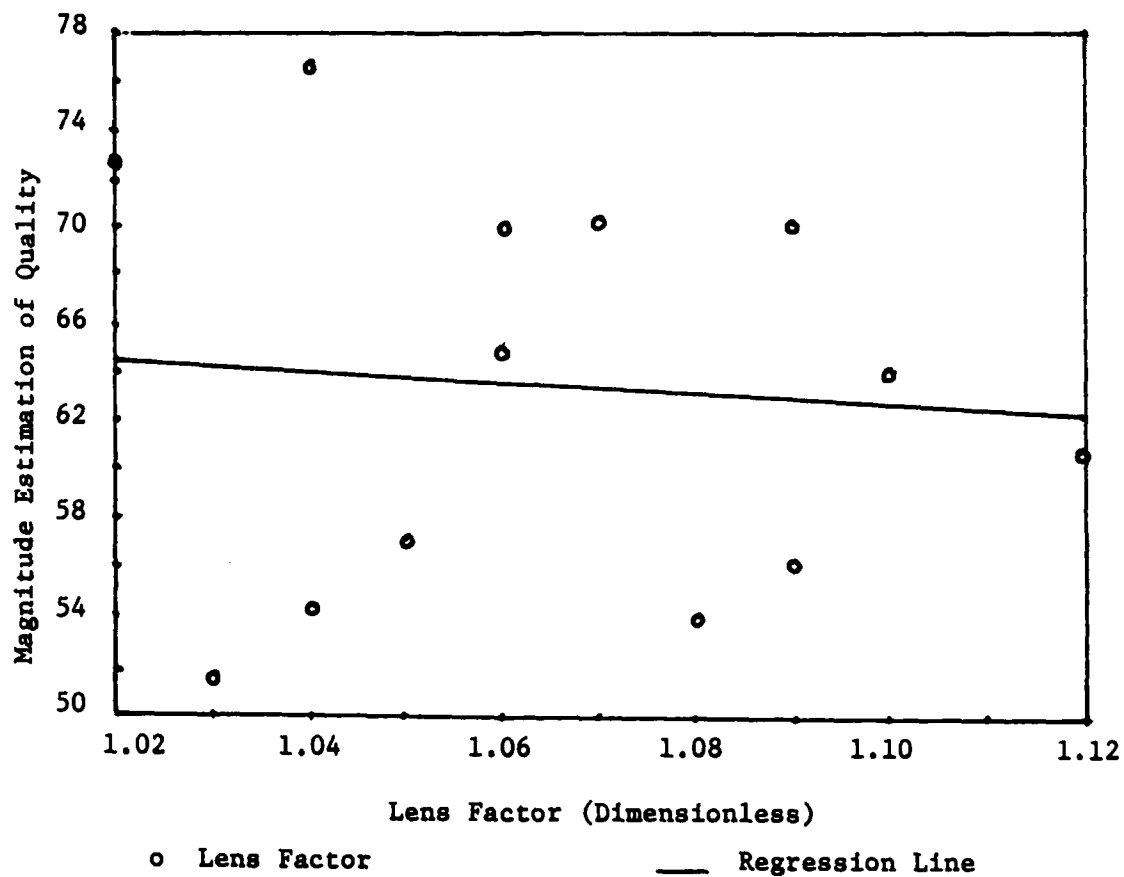


Figure 10. Correlation between Magnitude Estimation (Photo) and Lens Factor

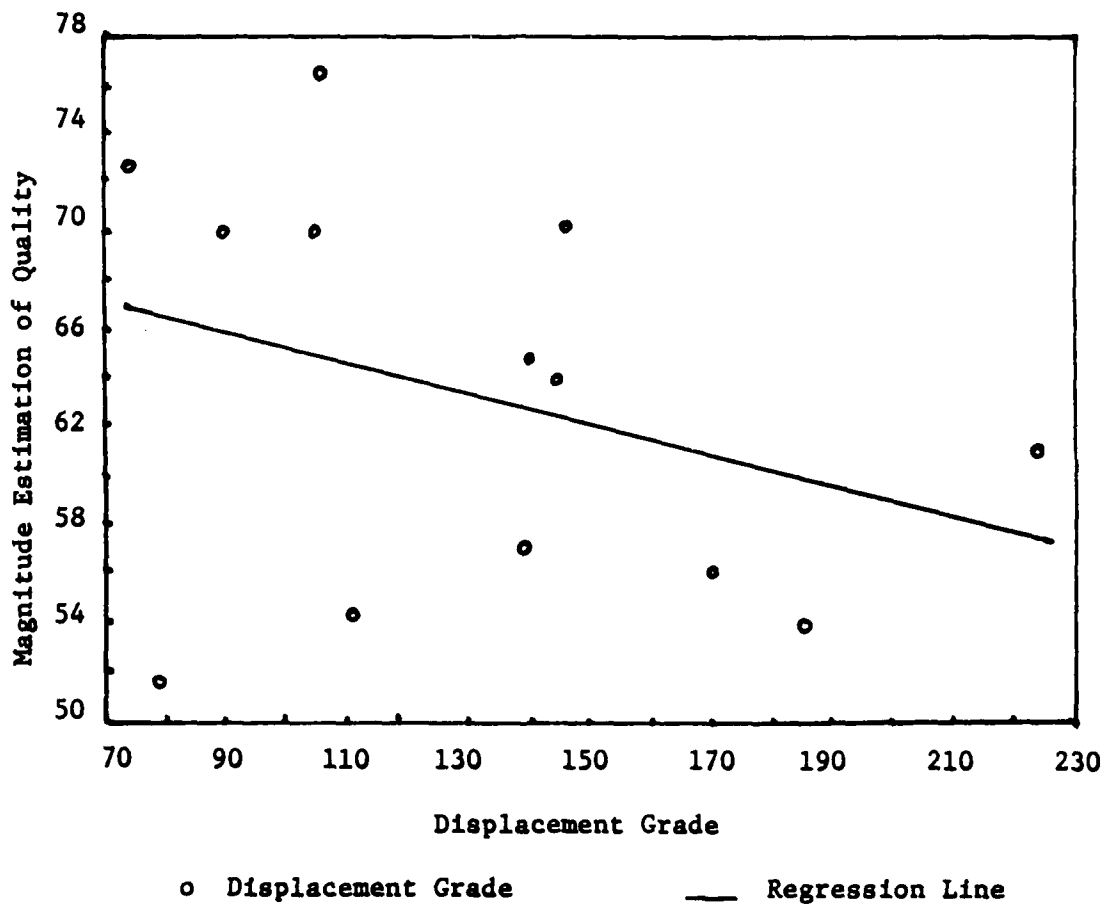


Figure 11. Correlation between Magnitude Estimation (Photo) and Displacement Grade.

The correlation matrix obtained from the rank scores are shown below:

	Mag.Est (P)	GLS	LF	DG
Mag.Est. (P)	--	0.448	0.062	0.288
GLS		--	0.287	0.088
LF			--	0.734
DG				--

As was the case with the regression analysis, the results obtained indicate no significant relationship between an observer's subjective perception of optical distortion quality and the objective measures of distortion that were obtained except for GLS. The correlation coefficient of 0.448 is found to be almost significant at the .05 level of confidence. The only significant correlation obtained was between the objective measures of LF and DG. The correlation coefficient obtained was 0.734 which was significant at the .01 level of confidence.

#### CONCLUSION

The major finding from this study is the lack of relationship between an observer's subjective rating of distortion in a windshield and that obtained by objective techniques. This finding is important as it indicates that the human observer is responding to some property of distortion that as yet is not being measured by the three currently employed measurement techniques. Unfortunately, we are unable, at this time, to ascertain what aspect or feature of distortion that is being responded to or even if such an aspect can be measured.

It is our intention, therefore, to continue to pursue work in this area in order to find, and hopefully, develop a metric that is related to a human observer's subjective assessment of distortion. Based on the fact that GLS showed a much stronger relationship (although not a significant one) than LF and DG with the subjective ratings, we plan to use this objective metric as our starting point. It is also our considered opinion that only GLS be used to assess the amount of distortion present in transparencies and that we eliminate the use of LF and DG.

With respect to the question asked by the title of our study "Measures of Distortion: Are they Relevant?", our answer must be in the negative. The results of this study offers no evidence to support the thesis that any one of the three objective measurement techniques provides a better metric of distortion than the other. Furthermore, none of them showed a strong linear relationship or capability of being predicted from a qualitative evaluation. As a matter of fact, it would seem that the use of a subjective evaluation technique would do as good a job (if not better) than the currently used objective measurement techniques. Such a technique would involve the comparison of a distortion photo of the windshield being evaluated with that of a photo of the referee windshield for a given production run. Any windshield deemed to be equal to or better than the referee windshield would be optically acceptable with respect to distortion.

REFERENCE

ATP 601E, "Acceptance test procedures for F-FB-111 bird impact resistant transparencies."

RECENT ADVANCES IN OPTICAL MEASUREMENTS OF TRANSPARENCIES

Capt Harold S. Merkel  
AAMRL/HEF

# Recent Advancements in Optical Measurements of Transparencies

Captain Harold S. Merkel  
AAMRL/HEF  
Wright-Patterson AFB, Ohio

## Abstract

In recent years new procedures have been developed for measuring transparency optical parameters. This paper discusses four procedures which have provided new means by which manufacturers and users of transparencies may quantify critical optical parameters. For each procedure three factors will be addressed: 1) the background of the procedure; 2) the requirement for the procedure and considerations made in its development; and 3) a summary of the procedure. The final section of the paper will discuss some areas of current investigation which are likely to lead to enhancements of existing measurement procedures.

## 1 Introduction

The aerospace transparency community is diverse, consisting of materials suppliers, transparency manufacturers, airframe manufacturers, government and private laboratories, airlines, agencies of the military services, and other associated organizations. In such a group many individuals and organizations have a focused area of interest and often are not aware of developments in other areas of transparency technology. The purpose of this paper is to update the transparency community on developments in the area of optical measurements of transparencies.

In the five years since the last Air Force Conference on Aerospace Transparent Materials and Enclosures several new methods have been established for measuring optical parameters of transparent parts. These methods are typically developed by task forces of the American Society of Testing and Materials (ASTM) F 7.08 Subcommittee on Aerospace Transparent Enclosures and Materials and published as ASTM Standard Test Methods. The new test methods discussed in this paper are those for measuring multiple imaging, reflectivity, transmissivity, and binocular disparity.

## 2 Multiple Imaging

### 2.1 Background

Multiple imaging occurs when light rays from an object outside the cockpit reflect off the inner and outer surfaces (and sometimes the interlayers) of the transparency and form two or more images of the object (see figure 1).

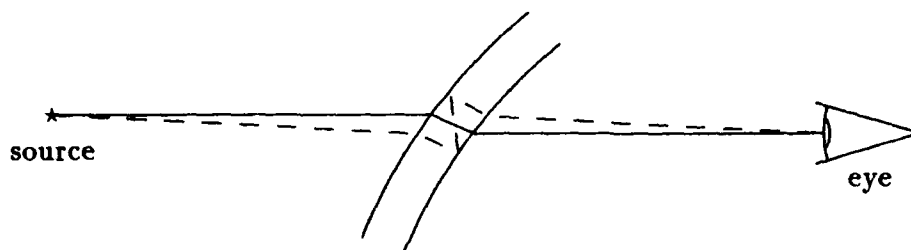


Figure 1: Multiple Imaging

Because the intensities of the secondary images are very low compared to the primary image, multiple images are usually only observed at night when looking at luminous objects. In the daytime, multiple images are not observed because they are washed out by ambient light.

Multiple imaging occurred in aircraft transparencies for many decades without seriously interfering with pilots' vision. This was because virtually all early transparencies were thin flat (or nearly flat) plates of a single transparent material. The multiple images from these flat transparencies were uniformly displaced from the primary image, and if the angle between the surface of the transparency and the pilot's line of sight was large (as was often the case), this displacement was very small. Also, nighttime flying was less frequent, so the occasions to observe multiple imaging were fewer.

As aircraft technology and performance advanced over time, transparencies evolved from flat plates to large, thick, curved parts constructed of several layers of materials. This complexity in transparency design sometimes resulted in objectionable multiple imaging. In today's environment, where aerodynamic design and bird strike resistance impose significant curvature and thickness constraints on transparencies, it is becoming increasingly difficult to control the multiple imaging characteristics of a transparency. Since it is unlikely that the design and manufacturing methods of transparencies for high performance aircraft will change radically in the near future, multiple imaging is likely to remain a concern.

Cases in which transparencies were removed from aircraft because of objectionable multiple imaging are largely attributable to manufacturing defects. Often it is not solely the multiple imaging characteristics of the transparency, but the combination of multiple imaging with distortion that is objectionable. Distortion can increase the angular displacement of secondary multiple images from their primary images and also cause the multiple images to occur in different positions relative to the primary image for different locations on the windscreen. This can result in a distracting swirling effect as a light source passes across the pilot's field of view. Multiple images that might be acceptable for a transparency with low distortion become objectionable in a more distorted transparency. Thus a key to preventing objectionable multiple imaging is to produce transparencies with low distortion.

Multiple images seem to be especially noticeable in the forward areas of a windscreen; there are two reasons for this. First, the forward area of the transparency is the area that is used during landing, a critical and visually intensive task. Second, the angle between the windscreen surface and the pilots line of sight is smaller in the forward area of the windscreen. This results in lower image intensity ratios (i.e., brighter secondary images.)

## 2.2 Requirement

When the first B-1B aircraft became operational in 1985 at Dyess Air Force Base, Texas, aircrews voiced concerns about severe multiple imaging in the forward 30 - 40 % of some of the windscreens. As a result several aircraft were temporarily prohibited from nighttime flying. This incident alerted the Air Force and other members of the transparency community to the seriousness of multiple imaging and its potential impact on flight safety. Multiple imaging has been a problem in other aircraft, but usually in isolated cases. The most notable cases were some F-111 aircraft that had windscreens removed for excessive multiple imaging. Currently the attention on multiple imaging problems has subsided, but the multiple imaging characteristics of high performance aircraft remain relatively unchanged.

In response to the B-1B problem the Air Force launched an investigation to determine the critical parameters of multiple imaging to which the aircrew were objecting. Through a comparison of windscreens that were and were not objectionable and a series of laboratory and field measurements of the optical characteristics of the B-1B windscreen, researchers discovered that the difference between the objectionable and acceptable windscreens was in the angular displacement of the secondary from the primary images in the forward portion of the windscreen. The relative intensity ratios of the multiple images were not significantly different between the two groups. Because of this finding, a technique for measuring the angular displacement of multiple images was developed.

Several factors were considered in developing the angular displacement measurement procedure. First of all, it had to accurately measure the parameter of interest. Also, the measurement procedure had to work in the field with the windscreen installed on the aircraft as well as in the laboratory with the windscreen mounted on a fixture. Other considerations were to keep the necessary equipment portable and low in cost.

## 2.3 Summary of Procedure

The procedure for measuring the angular displacement of secondary images involves photographing an array of lights of known size and distance from the transparency. If the procedure is performed in the field, the light array is placed 23 ft in front of the aircraft and elevated so the center light of the array is aligned on the 0 azimuth and 0 elevation pilot's line of sight. If the procedure is performed in a laboratory the windscreen is mounted in a fixture at the installed angle and the light array is placed in the same relative position to the transparency as for the field measurements (see figure 2).

With the light array positioned, photographs of the array are taken with the camera in the design eye position. These photographs contain images of the lights of the array as well as the multiple images of the lights caused by the transparency. The linear separation of the secondary image from the primary image is measured on the photograph using a ruler or a caliper. This linear separation is converted to angular displacement by multiplying by a scale factor, which is calculated from the known geometry of the test apparatus.



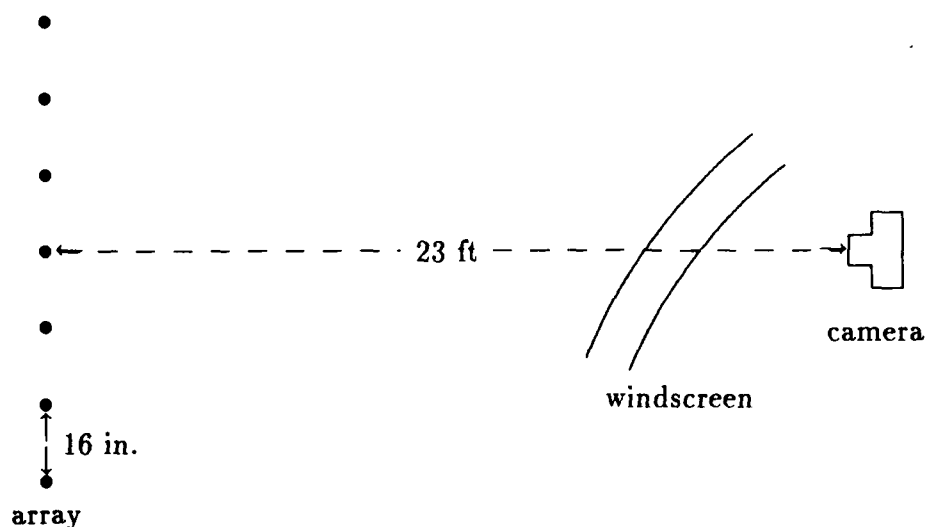


Figure 2: Apparatus set-up for measuring the angular displacement of multiple images

### 3 Reflectivity

#### 3.1 Background

Reflections from aircraft transparencies are often considered more of an annoyance than a serious impairment to a pilot's visual performance. However, these reflections are still undesirable and hinder out-of-the-cockpit vision. During daytime flight reflections from the glare shield, pilot's flight suit and helmet, or other cockpit objects may be distracting and reduce the contrast of objects viewed through the transparency. At night the reflections of internal cockpit lights may have a similar effect.

#### 3.2 Requirement

There is currently no practical way to reduce or eliminate reflections at the transparency surface. The use of antireflective coatings is promising, but as yet the coatings cannot be practically applied to aircraft transparencies. For manufacturers and researchers to objectively evaluate reflections on transparencies, a procedure which quantitatively measures the reflection is required. This procedure must take into consideration the spectral distribution of the light source, the spectral sensitivity of the observer, and the relative geometry of light source, transparency, and observer.

For the past two years a task force of the American Society of Testing and Materials F 7.08 subcommittee on Aerospace Transparencies and Enclosures has been developing a procedure to measure the reflectivity of transparencies which meets the above requirements. This measurement procedure was approved by the F 7.08 committee in October 1988 and should be published in late 1989.

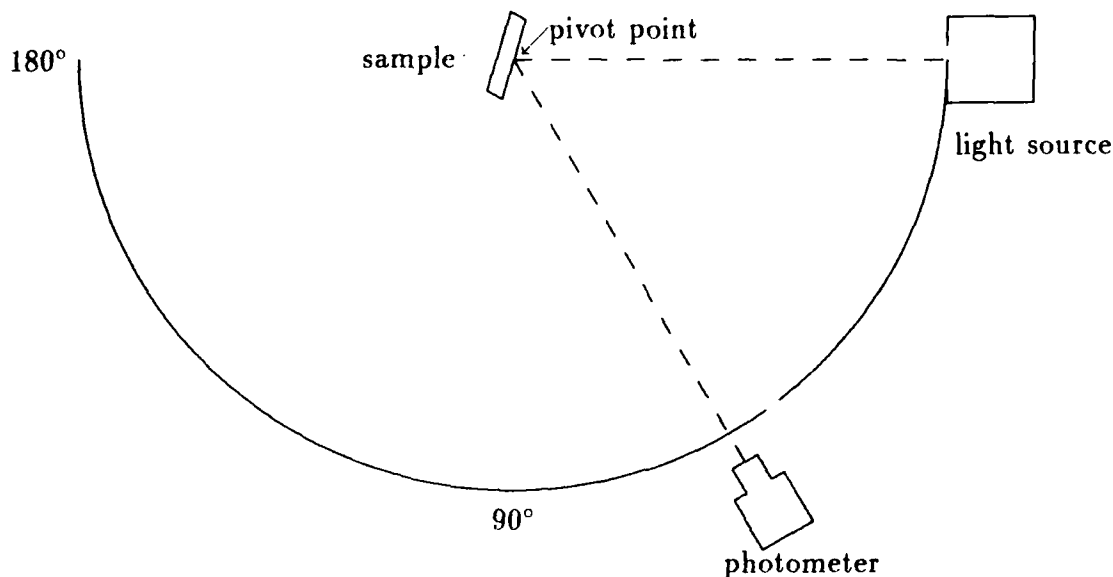


Figure 3: Apparatus set-up for measuring reflectivity.

### 3.3 Summary of Procedure

The luminance of a specified diffuse light source is measured directly with a photometer. Then the luminance of the reflection of the source off the transparent specimen is measured at the desired geometry (see figure 3). The luminance of the reflection of the source is divided by the luminance of the the source measured directly to obtain the reflectivity of the specimen. Since the reflectivity depends upon spectral distribution of the light source and the geometry of the test apparatus these factors must be recorded as part of the test results. The test procedure also has provisions to measure the reflectivity of a standard sample and to check for polarization effects.

The light source specified by the test method is the National Bureau of Standards Illuminant C. The C standard is a broad band white light source with a high color temperature. If other sources are used in place of the standard C source this should be reported as part of the test results. For example, one might wish to use a narrow band source to represent reflections from a particular cockpit display.

## 4 Transmissivity

### 4.1 Background

Transmissivity is the relative amount of light that is transmitted through a transparency. Light not transmitted may be absorbed, scattered, or reflected by the transparent material. The transmission coefficient may have values ranging from 1.0 (all of the light is transmitted) to 0.0 (none of the light is transmitted), but for aircraft transparencies transmissivity is

ordinarily between 0.65 and 0.90 (when measured perpendicular to the surface).

The transmissivity of aircraft transparencies is usually measured by the ASTM Test Method D 1003. This method uses the Gardner Hazemeter, which was originally designed to measure the transmissivity and haze of flat, relatively thin samples. The D 1003 method requires alignment of apparatus on both sides of the transparency and can only make measurements using a line of sight perpendicular to the surface of the transparency. Also, because it uses an integrating sphere to measure the transmitted illuminance, it does not differentiate between image forming and scattered light. However, D 1003 is a relatively simple test to perform and it yields accurate results for its intended application of thin, flat parts. Though this method has been popularly used for measuring thick curved transparent parts, these results are not as accurate as for thin parts nor are they representative of the pilot's visual situation. ASTM D 1003 has been used simply because it has become the accepted method and until recently there was no other convenient alternative.

## **4.2 Requirement**

Because of the limitations of the D 1003 method a new procedure for measuring transmissivity was developed that yielded accurate results for measuring thick curved parts at any angle. The new procedure does not require critical alignment of apparatus on both side of the transparency, so parts may be measured while installed in the aircraft as well as in the laboratory.

## **4.3 Summary of Procedure**

A diffused light source is placed on one side of the transparent part to be measured. A black, light absorbing reference surface is placed next to the light source. A photometer is used to measure the luminance of the light source and black reference directly and through the transparency. The black reference reading measured through the transparency is subtracted from the light source reading measured through the transparency. This difference is then divided by the light source measured directly minus the black reference measured directly. This ratio is the transmission coefficient. The subtraction of the black reference from the light source readings corrects the measurement for scattered and reflected light. Thus only the image forming light contributes to the value of the transmission coefficient.

# **5 Binocular Disparity**

## **5.1 Background**

Binocular disparity is the difference between the two images that are formed on the retinas of the two eyes. A certain amount of binocular disparity is natural since the eyes are physically separated, and this disparity is used for the perception of depth. However, when the amount of disparity exceeds the visual system's ability to fuse, or combine, the images from the two

eyes into one perceived image, diplopia (doubling of vision) may occur. Besides diplopia, binocular disparity can also cause headaches, eye strain, and fatigue.

One situation which may cause sufficient binocular disparity to induce diplopia is the observation of two objects at different distances. Focusing on one object will cause the other to appear doubled. This may be easily demonstrated by looking at a distant object while holding your thumb in the line of sight. Focusing on the distant object, the thumb will appear doubled; focusing on the thumb, the object will appear doubled.

## **5.2 Requirement**

Pilots flying aircraft equipped with a head-up display (HUD) are (for certain tasks) required to simultaneously focus on the HUD symbology and on a target outside the aircraft. If these two objects are optically at different distances this can result in diplopia, where either the HUD symbology or the target appears double. To avoid excessive binocular disparity the HUD symbology must be placed at or near the same optical distance at which the targets occur. Almost all aerial targets are a large distance away, and occur naturally at what is considered optical infinity. However, the transparency acts as a weak lens and changes the optical distance of the target. If this perceived distance of the target is substantially different than the optical distance of the HUD symbology, the pilot may experience diplopia.

Since the transparency is a critical optical element in the above situation, it is desirable to quantify the binocular disparity effects of the transparency. Thus a procedure was developed which measures the amount of binocular disparity introduced by the transparency at different locations on the windscreen.

## **5.3 Summary of Procedure**

The procedure for measuring the binocular disparity of a transparent part uses the ASTM Standard Method F 801 for measuring optical angular deviation. This procedure uses an electro-optical device commonly called an angular deviation device. It consists of a transmitter and receiver, which are placed on opposite sides of the windscreen and can measure the angular deviation of a collimated light beam as it is transmitted through the transparency.

To measure binocular disparity, two sets of angular deviation measurements are taken at specified intervals over the windscreen. (Usually measurements are taken every two degrees of azimuth and elevation.) One set of measurements is made with the transmitter in the pilot's left eye position and the other set is made with the transmitter in the pilot's right eye position. These two locations are separated by 2.5 inches, the typical interpupillary distance between human eyes. To obtain the binocular disparity at each measurement point, the angular deviation taken from the left eye position is subtracted from the angular deviation taken from the right eye position.

## 6 Areas of Current Development

There are several established procedures for measuring optical parameters that, although they have not been revised as yet, are under investigation and may be revised within the next one to two years.

- *Distortion* – The current published method for measuring distortion is ASTM Standard Method F 733-81, Measuring Optical Distortion and Deviation of Transparent Parts using the Double-exposure Method. There are two reasons that require revising this method. First, a survey of members of the Distortion task force at the October, 1988 ASTM F 7.08 meeting indicated that no one followed this method for measuring distortion. (A couple members indicated that their company did use the method for measuring deviation.) Second, the distortion metric the method uses, grid line slope, does not correlate well with subjective determinations of windscreen distortion. (see the paper entitled "Measures of Distortion: Are they relevant?" in this publication).
- *Haze* – There are two accepted methods for measuring haze: ASTM D 1003-61 and ASTM F 943-85. The D 1003 method uses a collimated light source and integrating sphere and the F 943 method uses a hand held photometer, light source, and a set of black and white targets. D 1003 has the disadvantage that measurements cannot be made on installed transparencies, and F 943 has the disadvantage that it is a rather involved measurement procedure and is sensitive to alignment of the measuring apparatus. Some work has been performed to develop a haze measurement device that overcomes the disadvantages of both methods. A prototype device that samples the amount of backscattered haze shows promise, but needs further development to account for different thicknesses of transparencies. Other alternatives are also being examined.

## 7 Discussion

It is difficult to overstate the importance of maintaining high quality vision for Air Force pilots. Quality vision is important for safe flying, but it is *essential* to win in aerial combat. Even with the current electronic and electro-optical aids that the pilot has at his disposal, winning in combat often depends on visually acquiring the bogie before he sees you, and shooting your weapons more accurately than your adversary. The transparency is a fundamental element in the pilot's visual path, and the optical quality of the transparency directly impacts his ability to perform. Haze and reflections reduce the contrast and detection distance of enemy aircraft. Distortion may make it difficult to judge closure rates, angular deviation causes inaccurate weapons aiming, multiple imaging makes nighttime landings more difficult, and binocular disparity may cause eye strain and fatigue.

A necessary part of developing procedures for measuring optical parameters is determining which parameters are relevant to visual performance and which metrics of these

parameters correlate with either performance or subjective measures of quality. Procedures which measure parameters with metrics unrelated to visual performance are easy to generate, but useless. The difficult aspect of developing measurement procedures is to relate the results of the procedures to visual performance. The procedures discussed in this paper are significant in that they quantify optical parameters relevant to visual performance and hence permit meaningful evaluation of the acceptability of transparencies. Additionally, they are part of a feedback mechanism to the manufacturing process, so further improvements in transparency optical parameters might be realized in the future.

## References

- [1] ASTM F 733-81. *Optical distortion and deviation of transparent parts using the double-exposure method*. August, 1981.
- [2] ASTM F 1165-88. *Standard Test Method for Measuring Angular Displacement of Multiple Images in Transparent Parts*. October, 1988
- [3] ASTM F 943-85. *Measuring halation of transparent parts*. July 26, 1985.
- [4] *Standard Test Method for Measuring Optical Reflections from Transparent Materials*. Draft ASTM Standard Test Method (unpublished).
- [5] *Measurement of Transmissivity of Transparent Parts*. Draft ASTM Standard Test Method (unpublished).
- [6] *Standard Test Method for Measuring Binocular Disparity in Transparent Parts*. Draft ASTM Standard Test Method (unpublished)
- [7] Task, H.L., "Vision through aircraft transparencies." paper in: AGARD Lecture Series No. 156, *Visual effects in the high performance aircraft cockpit*. April, 1988.
- [8] Kama, W.N., "Visual perception through windscreens: effects of minor occlusions and haze on operator performance", paper in: *Conference on aerospace transparent materials and enclosures*, S. A. Morolo, Ed., pp 825-847, December 1983.
- [9] Genco, L.V. and Task, H.L., *Aircraft transparency optical quality: New methods of measurement*. Technical Report: AFAMRL-TR-81-21, 1981.

TRANSPARENCY OPTICAL PERFORMANCE PREDICTION

John W. Fielman  
Dr. John S. Loomis  
University of Dayton



# Transparency Optical Performance Prediction

John W. Fielman  
Dr. John S. Loomis  
University of Dayton Research Institute  
Dayton, Ohio 45469

## Abstract

This paper describes a system of computer codes currently under development to analytically predict the optical performance of aircraft transparencies as designed and under load. The architecture of the codes and the theoretical approach are described.

The ray trace optical code is being interfaced to finite element thermal and stress codes to permit the effects of operational loads to be modeled. Thermal, displacement, and stress field definition data computed by the finite element codes are input to the optics code. This information is required to compute the orthotropic indices of refraction throughout the material volume of the aircraft transparency. This computation is performed at each step along the propagation path of each ray. Stress optics effects are included in the mathematical model.

A mesh of rays at several frequencies from one or two eye positions is traced through the windows to map the optical distortion effects. The code computes polarization effects as well as path deviation. Effects of multipath reflections are accounted for by subdividing rays at material boundaries into reflected and refracted rays as a function of the angle of incidence. Ray subdivisions whose intensity is above a specified minimum are then traced.

Post-processing graphics codes are being developed to display distortion effects and compute focus and astigmatism for specified regions of the transparency. Plots of displacement vectors and deformed grids will be generated.

## Introduction

Code is being developed to analytically predict the optical quality of high performance aircraft transparencies subjected to operational loads. An optical ray trace code originally developed for the analysis of high-energy laser windows is being modified for application to multilayer canopy designs. The code will accept temperature and stress data as input to permit the computation of varying birefringent indices of refraction as a function of

these parameters. Plans include using the STAPAT thermal analyzer to obtain aircraft transparency temperature data and the MAGNA finite element code to compute the transparency stress and displacement data.

The PATRAN finite element pre- and post-processing software system will be used to provide a common interface between the thermal, stress, and optics codes.

The optics code will track rays of various wavelengths through the transparency. The deformed geometry generated by the stress analysis will be used to determine angles of reflection and refraction at transparency layer boundaries. Birefringent indices of refraction will be computed as a function of material, temperature, and stress state at the refracting surfaces and within the transparency material.

Graphics software will be developed to display the results of the optical analysis. This will include deformed grids, contour plots of phase variations, and other optical parameters.

## **STAPAT and MAGNA Interfaces**

STAPAT (Specific Thermal Analyzer Program for Aircraft Transparencies) [1] will be used to compute the temperature field within the transparency which is part of the input required by MAGNA (Materially and Geometrically Nonlinear Analysis) [2] to perform transparency finite element stress analysis. The results of both the thermal analysis and the stress analysis will be input to the new OPTRAN (Optical analysis of aircraft Transparencies) optical analysis code currently under development.

It is planned that the PATRAN [3] finite element modeler will provide a common interface between the STAPAT, MAGNA, and OPTRAN. PATRAN is a software product of the PATRAN Division of PDA Engineering. There are numerous reasons for selecting PATRAN to provide an the interface between the codes. There is an existing commitment for using PATRAN to support the operation of STAPAT and MAGNA. MAGNA interfaces are available and a PATRAN to STAPAT interface has been written. A STAPAT to PATRAN interface is under development.

PATRAN software is available for many computer systems and offers device drivers for many interactive graphics terminals. PATRAN provides excellent tools for defining the model geometries and generating graphic displays of the models. It is widely used, well supported, and interfaced to many of the more popular finite element codes, thus offering the opportunity of using other analysis tools in conjunction with OPTRAN.

Isoparametric tricubic hyperpatches defined by the same mathematical formulation as those used by PATRAN [3][Chapter 37] will be used in OPTRAN. They will be used

to model the deformed transparency layer solid geometry and map the temperature and stress parameters within the transparency material layers. The temperature (T) and the six orthogonal stress parameters ( $\sigma_{xx}$   $\sigma_{yy}$   $\sigma_{zz}$   $\tau_{xy}$   $\tau_{yz}$   $\tau_{zx}$ ) are required at each incremental step along the optical ray trace paths to compute continuously varying orthotropic indices of refraction. Displacements are critical in determining reflected and refracted optical ray path directions at layer boundaries. Temperature, pressure, and density fields in the surrounding air stream will be mapped using the same isoparametric hyperpatches. These parameters determine index of refraction in the atmosphere.

The flow of data between PATRAN and STAPAT is indicated in Figure 1. The STAPAT to PATRAN interface will convert computed temperatures to data hyperpatches. Mapping the temperature field with hyperpatches will offer important flexibility in interpolating temperatures at arbitrary finite element node locations. This permits stress models to be generated independently of the thermal analysis models used.

The temperature data will be included in models created for the stresses analysis. The PATRAN to MAGNA translator and MAGNA to PATRAN translator are indicated in Figure 1. Code exists to compute the averaged stress values at MAGNA analysis nodal locations required by the optics code but the current version of the MAGNA to PATRAN translator (MAGPAT) is not programmed to process this information. Either MAGPAT will be modified or provisions will be made in the optics code to map these values onto hyperpatches, as shown in Figure 2.

Figure 3 is a PATRAN-generated display of the hyperpatch geometry of a hypothetical three-layer transparency section with a 10x10 matrix of incident optical rays entering one of the hyperpatches. The matrix of rays was generated using a grid point at a hypothetical eye location and generating a 10x10 mesh of grid points on the incident face of the hyperpatch, which are connected by PATRAN lines to the grid point at the eye location. It is planned that the user will have the option of generating ray matrices for input to OPTRAN using PATRAN.

Figure 4 shows the same transparency section from a different view with each of the hyperpatches subdivided into a 5x5x3 matrix of hexagonal solid finite elements as might be used for a STAPAT thermal analysis.

## Optical Ray Trace

The ray trace program OPTRAN uses the isoparametric surface geometry definitions from PATRAN to locate boundaries for ray refraction and reflection. The results of finite-element heat and stress programs define the volumetric temperature and stress states of the transparency. Stress and temperature affect light rays in two ways. First, the surfaces of the transparency deform as a result of stress and temperature changes,

PATRAN - STAPAT - MAGNA - DATA FLOW

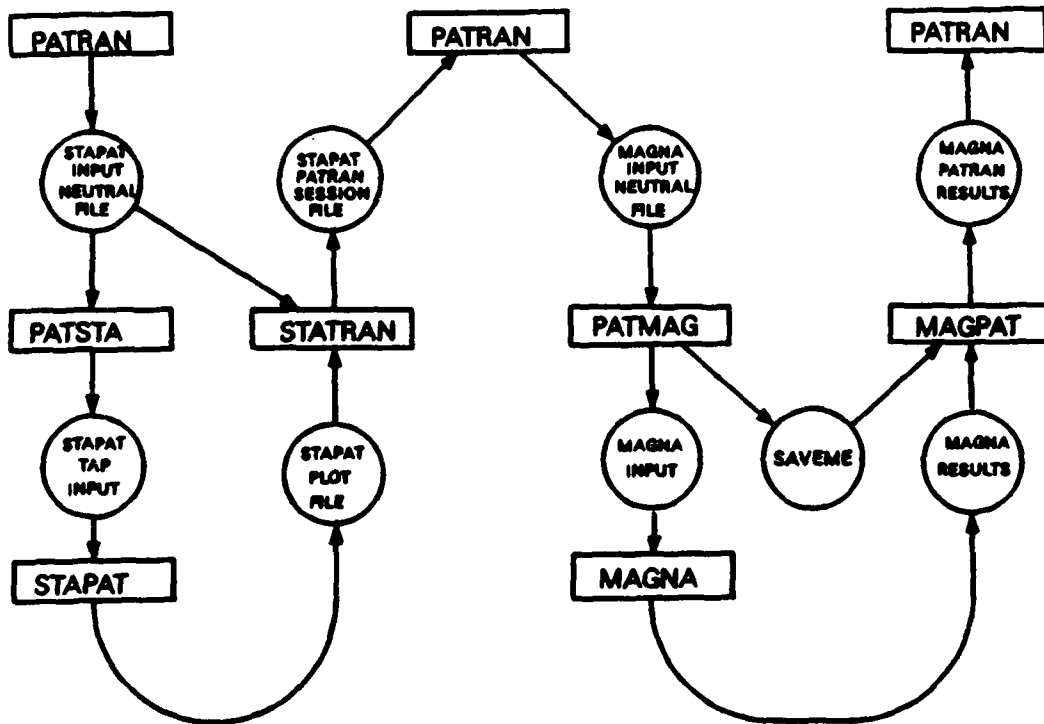


Figure 1: PATRAN-STAPAT-MAGNA Data Flow

## PATRAN - OPTRAN - OPTINT - DATA FLOW

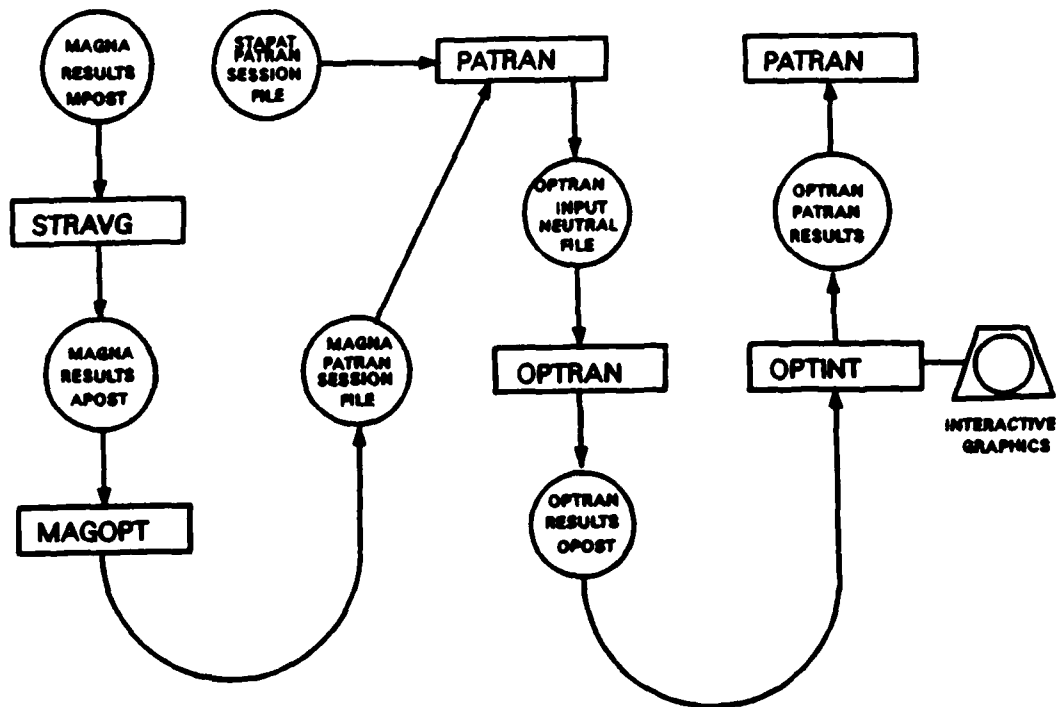
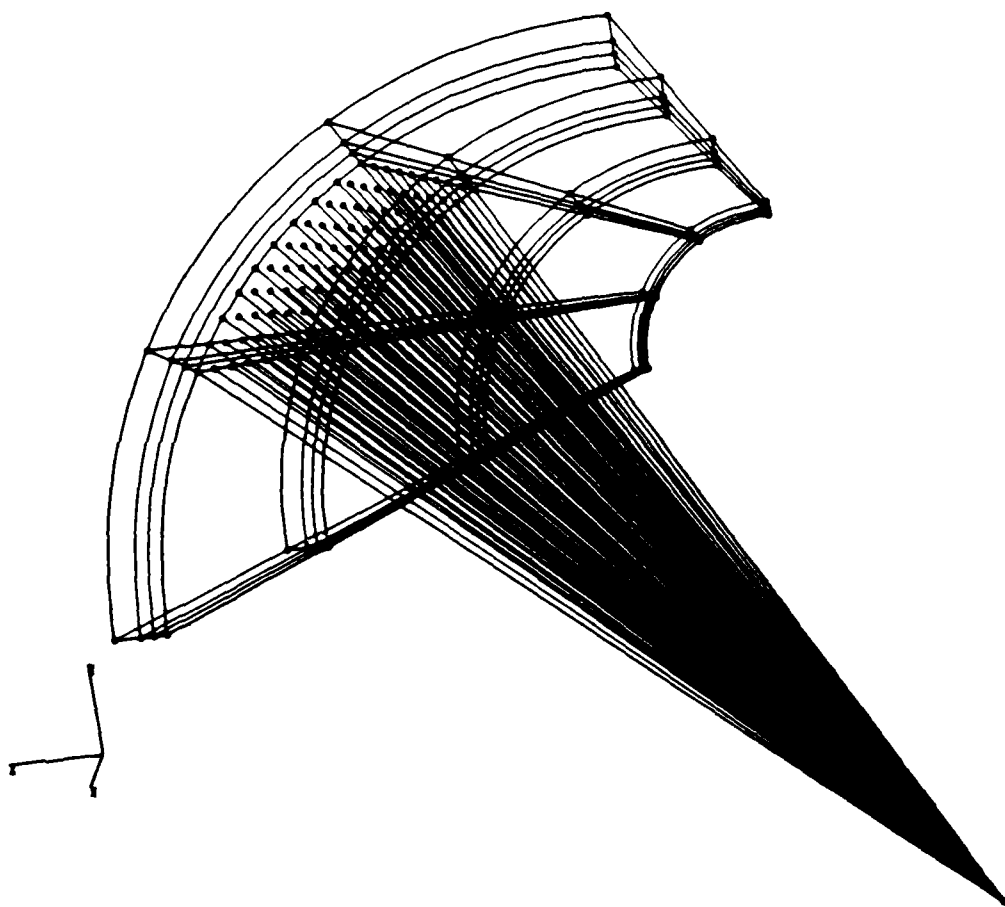
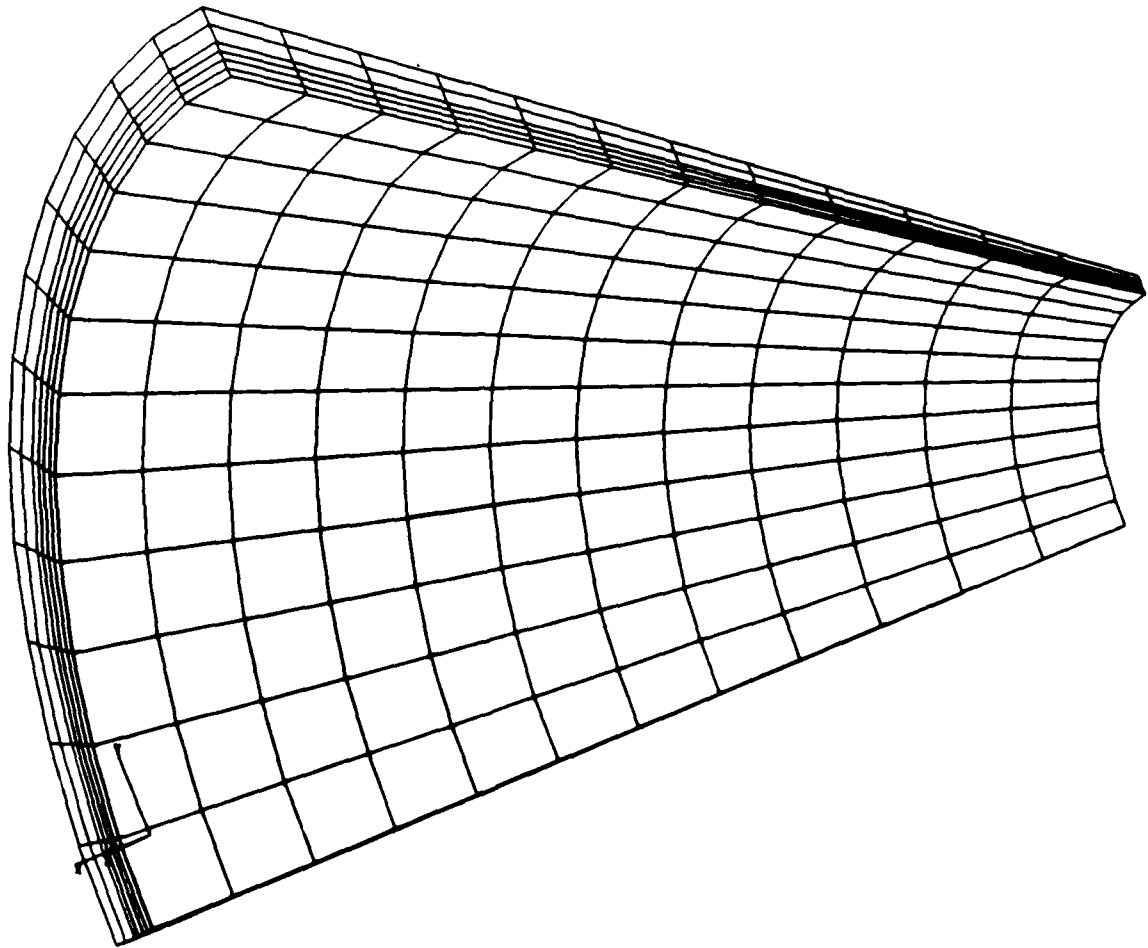


Figure 2: PATRAN-OPTRAN-OPTINT Data Flow



**Figure 3: Transparency Hyperpatch and Raytrace Model**



**Figure 4: Transparency Hexagonal Finite Element Model**

so that the geometry of the transparency changes. Second, the index of refraction of the transparency layers depends on both temperature and stress.

At an interface between two dielectric materials, a plane of incidence is defined by the normal vector to the surface and the direction vector of the incident ray. The light ray is split into reflected and refracted rays, propagating in the plane of incidence. Snell's law determines the direction of propagation. The polarization of the incident ray, defined by the electric field vector, is decomposed into components parallel and perpendicular to the plane of incidence. The Fresnel equations determine the reflectance and transmittance of each polarization component.

Within a birefringent material, the electric field vector must be decomposed into components parallel to the principal axes of the dielectric material, as determined by the dielectric tensor. The components propagate in slightly different directions, creating the phenomenon of double refraction.

A single light ray passing through a layered transparency will fan out into a multiplicity of rays of differing energy. The observer sees a primary image, corresponding to the ray transferring the most energy, and perhaps one or more secondary images.

### Ray Description

The following information is needed to describe a ray. The light ray intersects the surface  $F(x, y, z) = 0$  at a position  $p$ . Let the normal to the surface at that point be  $q$  and the direction of propagation in the medium following the surface  $F$  be given by the unit vector  $t$ . We suppose orthogonal axes of polarization  $r$  and  $s$  for the complex electric field vectors. The unit vectors  $(r, s, t)$  form a right-handed coordinate system. The complex electric fields corresponding to the two orthogonal polarization states form a column vector  $\mathbf{J}$  known as the Jones vector. [5][Chapter 8]

$$\mathbf{J} = \begin{pmatrix} E_r \\ E_s \end{pmatrix}.$$

### Wave Propagation in a Birefringent Medium

In a birefringent medium whose principal axes are  $(x, y, z)$ , with the direction of propagation in the  $z$ -direction, the associated indices of refraction is given by  $n_x$  and  $n_y$ . The Jones matrix for the propagating wave is then

$$\mathbf{J}' = \begin{pmatrix} e^{-2\pi j n_x d/\lambda} & 0 \\ 0 & e^{-2\pi j n_y d/\lambda} \end{pmatrix} \mathbf{J}$$



where  $d$  is the distance propagated. This relationship may be factored by defining

$$n = \frac{n_x + n_y}{2}$$

$$\delta_n = \frac{n_x - n_y}{2}.$$

The optical path  $\delta$  along the ray is given by

$$\delta = nd$$

and the Jones matrix is now given by

$$\mathbf{J}' = \begin{pmatrix} e^{-2\pi j \delta_n d / \lambda} & 0 \\ 0 & e^{2\pi j \delta_n d / \lambda} \end{pmatrix} \mathbf{J}.$$

If the direction of propagation is  $\mathbf{t}$ , the birefringent indices are calculated as follows. [7] The intersection of the dielectric ellipsoid with a plane through the origin and perpendicular to  $\mathbf{t}$  defines an ellipse whose major and minor axes are the birefringent indices of refraction (Appendix C). If this ellipse is oriented at an angle  $\omega$  with the  $r$ -axis, the Jones vector transforms as

$$\mathbf{J}' = \begin{pmatrix} \cos \delta_n - j \sin \delta_n \cos 2\omega & j \sin \delta_n \sin 2\omega \\ j \sin \delta_n \sin 2\omega & \cos \delta_n + j \sin \delta_n \cos 2\omega \end{pmatrix} \mathbf{J}.$$

The ray coordinates  $\mathbf{p}'$  after propagation a distance  $d$  from  $\mathbf{p}$  in the direction  $\mathbf{t}$  are given by

$$p'_x = p_x + t_x d$$

$$p'_y = p_y + t_y d$$

$$p'_z = p_z + t_z d.$$

Generally the point  $\mathbf{p}'$  will be the intersection with the next refracting or reflecting surface.

### Ray Tracing Parametric Surfaces

A general discussion of geometric modeling based on parametric cubic surfaces is found in Mortenson [6]. Raytracing of parametric surfaces has been applied to studies of computer graphics [8,9,10]. Given the parametric surface

$$\mathbf{S}(u, v) = ( X(u, v) \quad Y(u, v) \quad Z(u, v) )$$

and a ray defined by the point  $\mathbf{p}$  and the unit direction  $\mathbf{t}$ , we obtain the square of the distance from the surface to the ray by

$$\sigma^2 = |\mathbf{V}|^2 - (\mathbf{V} \cdot \mathbf{t})^2$$

where

$$\mathbf{V} = \mathbf{S}(u, v) - \mathbf{p}$$

and the distance  $d$  along the ray where the minimum is achieved, is given by

$$d = \mathbf{V} \cdot \mathbf{t}.$$

A local minimum of  $\sigma^2 = 0$  corresponds to a point  $(u, v)$  where the ray intersects the surface. Those points where  $\sigma^2$  is a minimum, but  $\sigma^2 > 0$ , indicate that the ray missed the surface by a finite distance. Thus a minimization algorithm will still converge near a "silhouette edge" of the surface, but will give a non-zero minimum.

At any point  $(u, v)$  on the parametric surface, we can construct a vector  $\mathbf{q}$  perpendicular to the patch by computing the cross product of the tangent vectors  $\mathbf{S}^u$  and  $\mathbf{S}^v$ .

$$\mathbf{q} = \frac{\mathbf{S}^u \times \mathbf{S}^v}{|\mathbf{S}^u \times \mathbf{S}^v|}$$

where

$$\begin{aligned} \mathbf{S}^u &= \frac{\partial \mathbf{S}(u, v)}{\partial u} = \left( \frac{\partial X(u, v)}{\partial u} \quad \frac{\partial Y(u, v)}{\partial u} \quad \frac{\partial Z(u, v)}{\partial u} \right) \\ \mathbf{S}^v &= \frac{\partial \mathbf{S}(u, v)}{\partial v} = \left( \frac{\partial X(u, v)}{\partial v} \quad \frac{\partial Y(u, v)}{\partial v} \quad \frac{\partial Z(u, v)}{\partial v} \right). \end{aligned}$$

## Ray Refraction

Refraction at a boundary between two dielectric media is determined by Snell's law, that

$$n(\mathbf{q} \times \mathbf{t}) = n'(\mathbf{q} \times \mathbf{t}')$$

where  $\mathbf{q}$  is the surface normal vector and  $\mathbf{t}$  the unit vector in the direction of propagation. After refraction, the ray vectors  $(\mathbf{r}, \mathbf{s}, \mathbf{t})$  will have been rotated through an angle  $\theta$  about an axis defined by the vector  $\mathbf{t} \times \mathbf{t}'$ , where

$$\sin \theta = |\mathbf{t} \times \mathbf{t}'|$$

gives the rotation angle (Appendix A).

If the plane of incidence is aligned with the  $(\mathbf{r}, \mathbf{s})$  axes, then the Fresnel losses can be included in the Jones vector,

$$\mathbf{J}' = \begin{pmatrix} \tau_p & 0 \\ 0 & \tau_s \end{pmatrix} \mathbf{J}$$

where  $\tau_p$  and  $\tau_s$  are the amplitude transmittance coefficients parallel (p) and perpendicular (s) to the plane of incidence.

In general, the plane of incidence is perpendicular to  $\mathbf{q} \times \mathbf{t}$ , and oriented with respect to the  $r$ -axis by the angle  $\omega$  given by

$$\cos \omega = \frac{\mathbf{q} \times \mathbf{t} \cdot \mathbf{r}}{|\mathbf{q} \times \mathbf{t}|}.$$

### Stress Birefringence

When a stress is applied to a material, the index ellipsoid is modified, and the changes in the components of the dielectric tensor are linearly related to the six stress components. [7][p. 703-704] The equation for the index ellipsoid of an unstressed material with respect to the principal axes of the material ( $x, y, z$ ) is given by

$$\frac{x^2}{n_x^2} + \frac{y^2}{n_y^2} + \frac{z^2}{n_z^2} = 1.$$

On applying stress, this ellipsoid is changed into another whose equation is

$$a_{xx}x^2 + a_{yy}y^2 + a_{zz}z^2 + 2a_{xy}xy + 2a_{yz}yz + 2a_{zx}xz = 1.$$

The coefficients of the ellipse are defined by

$$\{A\} = \{A_0\} + [q]\{\sigma\}$$

where

$$\{A\} = \begin{pmatrix} a_{xx} \\ a_{yy} \\ a_{zz} \\ a_{xy} \\ a_{yz} \\ a_{zx} \end{pmatrix}, \quad \{A_0\} = \begin{pmatrix} 1/n_x^2 \\ 1/n_y^2 \\ 1/n_z^2 \\ 0 \\ 0 \\ 0 \end{pmatrix} \quad \text{and} \quad \{\sigma\} = \begin{pmatrix} \sigma_{xx} \\ \sigma_{yy} \\ \sigma_{zz} \\ \tau_{xy} \\ \tau_{yz} \\ \tau_{zx} \end{pmatrix}.$$

The first term contains the orthotropic indices of refraction and associated temperature coefficients:

$$\begin{aligned} n_x &= \hat{n}_x + \frac{dn_x}{dT} \Delta T \\ n_y &= \hat{n}_y + \frac{dn_y}{dT} \Delta T \\ n_z &= \hat{n}_z + \frac{dn_z}{dT} \Delta T \end{aligned}$$

where  $(\hat{n}_x, \hat{n}_y, \hat{n}_z)$  is a set of orthotropic indices of refraction and  $(dn_x/dT, dn_y/dT, dn_z/dT)$  is a set of orthotropic  $dn/dT$ 's along the same axes, and  $\Delta T$  is the temperature change. The second term contains stress-related terms where  $\{\sigma\}$  is the stress tensor and  $[q]$  is a set of 36 stress-optical coefficients.

Although all the stress-optic coefficients may have unique non-zero values, symmetry considerations for crystalline or isotropic materials prescribe relationships among the coefficients and reduce the number of independent values that must be specified. For cubic crystals, the three principal axes (x, y, z) are equivalent, and consequently the following relations hold among the stress-optics coefficients:

$$\begin{aligned} q_{11} &= q_{22} = q_{33} \\ q_{12} &= q_{21} = q_{23} = q_{32} = q_{13} = q_{31} \\ q_{44} &= q_{55} = q_{66} \end{aligned}$$

with all the remaining coefficients being zero.

For isotropic materials, the above relations must remain unaltered for any change of axes. This is only possible if the stress-optical coefficients satisfy the additional relation

$$q_{44} = q_{11} - q_{12}.$$

If the reference coordinate system is different from that of the dielectric material, the stresses must first be converted to the material coordinates (see Appendix B). Then the resulting dielectric tensor must be transformed into the reference coordinate system. If  $\{\sigma\}'$  denotes material coordinates and  $\{\sigma\}$  reference coordinates, then

$$\{\sigma\}' = [s]\{\sigma\}$$

where  $[s]$  is the coordinate transformation matrix. In material coordinates,

$$\{A\}' = \{A_o\}' + [q]'\{\sigma\}'$$

which may be written in reference coordinates as

$$\{A\} = [s]^{-1}\{A_o\}' + [s]^{-1}[q]'[s]\{\sigma\}.$$

The matrix  $[s]^{-1}[q]'[s]$  is not a function of stress and in many cases is not a function of location, and therefore can be precomputed.

## Output Data

The result of a ray trace is a set of ray data, consisting of the following information:

<b>p</b>	vector	ray position
<b>q</b>	vector	surface normal
<b>r</b>	vector	r-polarization direction
<b>s</b>	vector	s-polarization direction
<b>t</b>	vector	direction of propagation
<b>C</b>	tensor	surface curvature
<b>N</b>	tensor	index of refraction
<b>K</b>	tensor	extinction coefficient
<b>d</b>	scalar	distance to next surface

This data is calculated for the object surface, each intermediate surface intersected by the ray, and finally for the image surface.

Tensor variables are defined as follows. A tensor is a symmetric matrix **A**. Associated with the tensor are a set of principal axes rotated about the t-axis of the (r, s, t) coordinate system. If the principal axes of the tensor are (u, v), the principal components of **A** are given by (  $a_u, a_v$  ). The (u, v, t) coordinate system is right-handed, such that the u-axis makes an angle  $\omega$  with the r-axis. Then the tensor components are given by

$$a_{rr} = a + \delta_a \cos(2\omega)$$

$$a_{ss} = a - \delta_a \cos(2\omega)$$

$$a_{rs} = \delta_a \sin(2\omega)$$

where

$$a = \frac{a_u + a_v}{2}$$

$$\delta_a = \frac{a_u - a_v}{2}$$

Tensor data consists of the following four scalar variables:

$$a_1 = a$$

$$a_2 = \delta_a$$

$$a_3 = \cos(2\omega)$$

$$a_4 = \sin(2\omega).$$

## Optical Analysis

Rays are traced from an eye point toward the outer world. Azimuth and elevation angles are used to specify the perceived direction **t**. The direction of the exit ray **t'** shows the true direction. Azimuth and elevation deviation angles **e** are calculated from  $e = t - t'$ .

Typically deviation angles are expressed in milliradians. Deviation causes objects to be seen at other than their true direction from the observer.

The data from a square array of rays, equally spaced in azimuth and elevation, can be displayed in single cross-sections of elevation or azimuth error or as deformed grids, emulating the typical grid board photograph.

The ray data output files will contain sufficient information to allow differential ray traces for each primary ray traced through the transparency. Differential rays allow the magnification, focus shift, and astigmatism to be calculated for specified regions of the transparency.

## References

- [1] M. O. Varner, J. C. Adams, D. E. Boylan, A. F. Gwinn, Jr. R. A. LeMaster, W. R. Martindale, and V. Noprattvarkorn, "Specific Thermal Analyzer Program for High-Temperature Resistant Transparencies for High-Speed Aircraft (STAPAT)," AFWAL-TR-84-3086, Wright-Patterson Air Force Base, Dayton, Ohio, 1984.
- [2] R. A. Brockman, "MAGNA (Materially and Geometrically Nonlinear Analysis)," AFWAL-TR-82-3098, Wright-Patterson Air Force Base, Dayton, Ohio, 1982.
- [3] "PATRAN Plus User Manual," PDA Engineering, PATRAN Division, Costa Mesa, California, 1987.
- [4] R. A. Brockman, T. W. Held, and V. G. Dominic, "MAGNA-to-PATRAN Data Interface User's Guide," University of Dayton, Dayton, Ohio 1986.
- [5] Eugene Hecht, *Optics*, Second Edition, Addison-Wesley, 1987.
- [6] Michael Mortenson, *Geometric Modeling*, John Wiley & Sons, 1985.
- [7] Max Born and Emil Wolf, *Principles of Optics*, Fifth Edition, Pergamon Press, 1975.
- [8] Kenneth I. Joy and Murthy N. Bhetanabhotla, "Ray Tracing Parametric Surface Patches Utilizing Numerical Techniques and Ray Coherence," *Computer Graphics*, Proceedings of SIGGRAPH 1986, volume 20, number 4, pp.279-285, (July, 1986).
- [9] J. T. Kajiya, "Ray Tracing Parametric Patches," *Computer Graphics*, Proceedings of SIGGRAPH 1982, volume 16, number 3, pp. 245-254, (July, 1982).
- [10] Mikio Shinya, Tokiichiro Takahashi, and Seichiro Naito, "Principles and Applications of Pencil Tracing," *Computer Graphics*, Proceedings of SIGGRAPH 1987, volume 21, number 4, pp. 45-54, (July, 1987).

## Appendices

### A Three-Dimensional Rotations about an Arbitrary Axis

We wish to rotate the point  $\mathbf{p} = (x, y, z)$  through an angle  $\theta$  about an axis of rotation  $\mathbf{a} = (a_x, a_y, a_z)$  passing through the origin, with positive rotations following the right-hand rule. The rotated point  $\mathbf{p}'$  is given by

$$\mathbf{p}' = \mathbf{pR}$$

where  $\mathbf{R}$  is the following matrix

$$\begin{bmatrix} a_x^2 + (1 - a_x^2) \cos \theta & a_x a_y (1 - \cos \theta) + a_x \sin \theta & a_x a_z (1 - \cos \theta) - a_y \sin \theta \\ a_x a_y (1 - \cos \theta) - a_x \sin \theta & a_y^2 + (1 - a_y^2) \cos \theta & a_y a_z (1 - \cos \theta) + a_x \sin \theta \\ a_x a_z (1 - \cos \theta) + a_y \sin \theta & a_y a_z (1 - \cos \theta) - a_x \sin \theta & a_z^2 + (1 - a_z^2) \cos \theta \end{bmatrix}$$

### B Tensor Rotation Transformation

Given a point expressed in  $(x, y, z)$  coordinates, we find the corresponding representation in  $(r, s, t)$  coordinates. Let  $k_i$  be the direction of the  $(r, s, t)$  axes in  $(x, y, z)$  coordinates. Then

$$\begin{pmatrix} r & s & t \end{pmatrix} = \begin{pmatrix} x & y & z \end{pmatrix} \begin{bmatrix} r_x & s_x & t_x \\ r_y & s_y & t_y \\ r_z & s_z & t_z \end{bmatrix}$$

The reverse transformation is

$$\begin{pmatrix} x & y & z \end{pmatrix} = \begin{pmatrix} r & s & t \end{pmatrix} \begin{bmatrix} r_x & r_y & r_z \\ s_x & s_y & s_z \\ t_x & t_y & t_z \end{bmatrix}$$

The transformation of a tensor from  $(x, y, z)$  to  $(r, s, t)$  coordinates is given by

$$\begin{pmatrix} a_{rr} \\ a_{ss} \\ a_{tt} \\ a_{rs} \\ a_{st} \\ a_{rt} \end{pmatrix} = \begin{bmatrix} r_x^2 & r_y^2 & r_z^2 & 2r_x r_y & 2r_y r_z & 2r_z r_x \\ s_x^2 & s_y^2 & s_z^2 & 2s_x s_y & 2s_y s_z & 2s_z s_x \\ t_x^2 & t_y^2 & t_z^2 & 2t_x t_y & 2t_y t_z & 2t_z t_x \\ r_x s_x & r_y s_y & r_z s_z & (r_x s_y + s_x r_y) & (r_y s_z + s_y r_z) & (r_z s_x + s_z r_x) \\ s_x t_x & s_y t_y & s_z t_z & (s_x t_y + t_x s_y) & (s_y t_z + t_y s_z) & (s_z t_x + t_z s_x) \\ r_x t_x & r_y t_y & r_z t_z & (r_x t_y + t_x r_y) & (r_y t_z + t_y r_z) & (r_z t_x + t_z r_x) \end{bmatrix} \begin{pmatrix} a_{xx} \\ a_{yy} \\ a_{zz} \\ a_{xy} \\ a_{yz} \\ a_{zx} \end{pmatrix}$$

## C Principal Axes of Projected Ellipse

Given an ellipsoid **A** in the  $(x, y, z)$  coordinate system and an axis of projection given by the unit vector  $(u, v, w)$ . Then

$$ux + vy + wz = 0$$

is the equation of a plane through the origin and perpendicular to the projection axis. The intersection of this plane with the ellipsoid is an ellipse. We want to find the major and minor axes of this ellipse.

We find the lengths of the axes by finding the extrema of  $r^2 = x^2 + y^2 + z^2$  subject to the constraints that the extrema lies on the plane and the ellipsoid.

By using Lagrange's method of undetermined multipliers ( $\lambda_1$  and  $\lambda_2$ ), we define the following:

$$h(x, y, z) = x^2 + y^2 + z^2 + \lambda_1 h_1(x, y, z) + \lambda_2 h_2(x, y, z)$$

where

$$\begin{aligned} h_1(x, y, z) &= a_{xx}x^2 + a_{yy}y^2 + a_{zz}z^2 + 2a_{xy}xy + 2a_{yz}yz + 2a_{zx}xz - 1 \\ h_2(x, y, z) &= ux + vy + wz. \end{aligned}$$

Then setting the partial derivatives of  $h(x, y, z) = 0$  gives

$$\begin{aligned} \frac{\partial h}{\partial x} &= 2x + 2\lambda_1 [a_{xx}x + a_{xy}y + a_{xz}z] + \lambda_2 u = 0 \\ \frac{\partial h}{\partial y} &= 2y + 2\lambda_1 [a_{yy}y + a_{xy}x + a_{yz}z] + \lambda_2 v = 0 \\ \frac{\partial h}{\partial z} &= 2z + 2\lambda_1 [a_{zz}z + a_{xz}x + a_{yz}y] + \lambda_2 w = 0. \end{aligned}$$

Then we may obtain

$$x \frac{\partial h}{\partial x} + y \frac{\partial h}{\partial y} + z \frac{\partial h}{\partial z} = 2r^2 + 2\lambda_1 = 0$$

and

$$u \frac{\partial h}{\partial x} + v \frac{\partial h}{\partial y} + w \frac{\partial h}{\partial z} = 2\lambda_1 [ua_x + va_y + wa_z] + \lambda_2 = 0$$

where

$$\begin{aligned} a_x &= a_{xx}x + a_{xy}y + a_{xz}z \\ a_y &= a_{xy}x + a_{yy}y + a_{yz}z \\ a_z &= a_{xz}x + a_{yz}y + a_{zz}z. \end{aligned}$$



Then

$$\begin{aligned}\frac{\partial h}{\partial x} &= 2x - 2r^2 a_x + 2r^2 u [ua_x + va_y + wa_z] = 0 \\ \frac{\partial h}{\partial y} &= 2y - 2r^2 a_y + 2r^2 v [ua_x + va_y + wa_z] = 0 \\ \frac{\partial h}{\partial z} &= 2z - 2r^2 a_z + 2r^2 w [ua_x + va_y + wa_z] = 0.\end{aligned}$$

Factoring gives the following system of homogeneous equations.

$$\begin{aligned}x[r^{-2} - a_{xx} + ua_u] + y[-a_{xy} + ua_v] + z[-a_{xz} + ua_w] &= 0 \\ x[-a_{xy} + va_u] + y[r^{-2} - a_{yy} + va_v] + z[-a_{yz} + va_w] &= 0 \\ x[-a_{xz} + wa_u] + y[-a_{yz} + wa_v] + z[r^{-2} - a_{zz} + wa_w] &= 0\end{aligned}$$

where

$$\begin{aligned}a_u &= a_{xx}u + a_{xy}v + a_{xz}w \\ a_v &= a_{xy}u + a_{yy}v + a_{yz}w \\ a_w &= a_{xz}u + a_{yz}v + a_{zz}w.\end{aligned}$$

The determinant of coefficients of this set of three homogeneous equations must vanish for there to be a non-trivial solution for  $x$ ,  $y$ , and  $z$ . Using this requirement gives

$$\begin{vmatrix} [r^{-2} - a_{xx} + ua_u] & [-a_{xy} + ua_v] & [-a_{xz} + ua_w] \\ [-a_{xy} + va_u] & [r^{-2} - a_{yy} + va_v] & [-a_{yz} + va_w] \\ [-a_{xz} + wa_u] & [-a_{yz} + wa_v] & [r^{-2} - a_{zz} + wa_w] \end{vmatrix} = 0$$

Expanding the determinant gives

$$ar^4 + br^2 + 1 = 0$$

where

$$a = (a_1 - a_2) - (a_3 - a_4)$$

$$\begin{aligned}a_1 &= a_{xx}a_{yy} + a_{yy}a_{zz} + a_{xx}a_{zz} \\ a_2 &= a_{xy}^2 + a_{yz}^2 + a_{xz}^2 \\ a_3 &= a_{xx}(va_v + wa_w) + a_{yy}(ua_u + wa_w) + a_{zz}(ua_u + va_v) \\ a_4 &= a_{yz}(va_w + wa_v) + a_{xy}(va_u + ua_v) + a_{xz}(ua_w + wa_u),\end{aligned}$$

and

$$b = ua_u + va_v + wa_w - a_{xx} - a_{yy} - a_{zz}.$$

This equation is a simple quadratic in  $r^2$ . The solutions are the major and minor axes. The system of homogeneous equations can then be solved for the direction of the respective principal axes.

SESSION VIII

OPTICS (PART B)

Chairman: H. L. Task  
Armstrong Aerospace Medical  
Research Laboratory  
Wright-Patterson AFB, Ohio

Co-Chairman: LTC L. V. Genco  
Armstrong Aerospace Medical  
Research Laboratory  
Brooks AFB, Texas

Coordinator: W. N. Kama  
Armstrong Aerospace Medical  
Research Laboratory  
Wright-Patterson AFB, Ohio

THE SWITCHABLE TRANSPARENCY - WHAT WILL IT BE?

Charles B. Greenberg  
PPG Industries, Inc.

**THE SWITCHABLE TRANSPARENCY - WHAT WILL IT BE?**

**BY**

**CHARLES B. GREENBERG**

**PPG INDUSTRIES, INC.**

**P. O. Box 11472**

**PITTSBURGH, PA. 15238-0472**

## THE SWITCHABLE TRANSPARENCY - WHAT WILL IT BE?

By

Charles B. Greenberg  
PPG Industries, Inc.  
P. O. Box 11472  
Pittsburgh, PA 15238-0472

### ABSTRACT

When one dreams the ultimate about a transparency, at least in terms of glare attenuation and solar control, it is of variable transmission and reflection. Such visions have supported research programs worldwide on photochromism, thermochromism and electrochromism. Photochromic and thermochromic materials, sometimes as thin films, suffer fundamentally in that they do not combine (1) deep visible and solar IR switching, (2) user control and (3) field stability. User control is necessary, in particular, for aerospace transparencies. Electrochromism does offer deep and broad spectral switching, and it also has the advantage of being electronically controlled. Field stability remains to be proven.

Solid-state electrochromic transparencies have been made which switch very dramatically over the whole of the solar spectrum. Engineering calculations of solar shading, based on ASHRAE practice in architectural industries, give very favorable results. The active thin film for which this has been demonstrated, also the best known of electrochromic materials, is tungsten oxide. It is formed by deposition in vacuum and is one member of a configuration which is best described generally as a "transparent battery." A unique version has been developed which addresses two needs that have heretofore constrained technological development: (1) to carry current efficiently over a large area and (2) to provide a counter electrode half cell reaction without loss of transparency. Results with this configuration, so far, support the view that electrochromism is conceptually right for a switchable transparency.

## Introduction

In a modern world of many remarkable solid-state achievements, the ordinary glass transparency is no longer the wonder that it once was. The roots of that novelty are as distant as imperfect windows and mirrors in a 17th century Palace of Versailles. Yet, this frozen-in, amorphous solid is still one of the most astonishing materials. In its modern form, it serves as a chemically and physically durable windscreen which provides nearly perfect visual acuity. Without it, neither architecture nor the automobile nor the airplane could have evolved as each has in the 20th century. However, it is not enough to be a transparent windscreen; additionally, the issue is solar control.

A great deal has been done in the past half century to tailor the spectral properties of transparencies in the solar range. At first this was done by simply making glass more absorbing, particularly in the solar infrared region. In the last 25 years, more effective solar control has been achieved by using reflecting metal and metal oxide thin films on clear and partially absorbing glass substrates. Heretofore, the impact of this has largely been in architecture, but similar opportunities exist in the transportation sectors. Films have usually been chosen to lessen heat buildup under high solar loading; in aircraft, glare reduction might be equally important. Obviously, there are times when high visibility or solar loading is desired; so, now the dream, for the glass itself or a thin film on it, is a switchable or variable transparency. This goal needs to be considered in a realistic way, which is largely what this paper is about. It is also about electrochromic transparencies in particular, because these will be shown to be especially suitable in certain critical respects.

## Switchable Materials - The Choice

Potentially, there are three important types of switchable materials. These are highlighted in Table 1, with general comments to summarize key points.

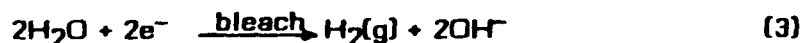
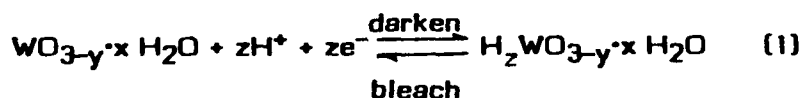
Table 1 - Switchable Materials

<b>Optical Response</b>	<b>Stimulus</b>	<b>Best Candidate</b>	<b>General Comments</b>
Thermochromic	absorbed solar energy	doped VO <sub>2</sub> thin film	(1) simple in principle (2) architectural concept; no user control
Photochromic	solar UV and visible	silver halide-containing glass	(1) thermally bleached (2) eye wear exists
Electrochromic	electrical, user controlled	tungsten oxide thin film	(1) multilayered (2) automotive and aircraft potential (3) displays of long-standing interest

There are fundamental issues which detract from thermochromism and photochromism, relative to electrochromism, for a transparency. For thermochromism, it is the limited spectral distribution of switching. Figure 1 shows a very typical result for a thermochromic, VO<sub>2</sub>-containing thin film on a 4 mm thick, low-iron, glass substrate. The substrate contributes relatively low infrared absorption relative to the commonly used, higher-iron, clear float glass composition. The film was prepared by chemical vapor deposition after SnO<sub>2</sub>-priming of the substrate<sup>1</sup>. It exhibits little transmittance switching in the important visible region. Spectral switching occurs most effectively in the far solar infrared, a result already anticipated by others<sup>2,3</sup> for VO<sub>2</sub> crystals and films deposited on crystalline substrates in vacuum. Doping does not alter the result<sup>1</sup>, though the switching temperature can be shifted towards room temperature<sup>4-6</sup>. The switching temperature for a VO<sub>2</sub> film is nearer to room temperature than for any other inorganic compound, which has accounted for interest in it. Another material, namely (V<sub>0.99</sub>Cr<sub>0.01</sub>)<sub>2</sub>O<sub>3</sub>, has failed to exhibit the expected switching near room temperature when prepared in thin film form<sup>7</sup>.

Photochromic glasses containing silver halides are known to be quite effectively switched in the visible region, at or near room temperature, by UV and visible energy<sup>8</sup>. One concern, however, is that the color centers are bleached thermally, and, of course, transparencies can become quite hot in use. Without convective cooling, a stationary surface can reach 90°C in extreme conditions. Additionally, the darkening and bleaching responses cannot be controlled by an operator, a distinct disadvantage, which is especially important to aircraft.

Electrochromic switching<sup>9,10</sup> of poorly crystallized WO<sub>3-y</sub>·xH<sub>2</sub>O, often referred to simply as amorphous WO<sub>3</sub> or WO<sub>3</sub>·xH<sub>2</sub>O, suffers from none of the above disadvantages. As Table 1 indicates, switching is accomplished electrically by user control of a multilayered configuration, which is essentially a transparent battery. Figure 2 shows the excellent spectral switching of transmittance for an approximately 4000 Å thick film coupled to the electrolysis of water in a polymer-electrolyte. The clear, solid electrolyte was prepared with poly-2-acrylamido-2-methyl propanesulfonic acid<sup>11,12</sup>. The configuration of the cell is NESA<sup>®</sup> glass/WO<sub>3-y</sub>·xH<sub>2</sub>O/electrolyte/NESA glass. The conductive clear float glass is 3 mm thick with a sheet resistance of 25 ohms/sq, and the electrolyte is 0.76 mm thick. Probable electrochemical reactions for this cell are:



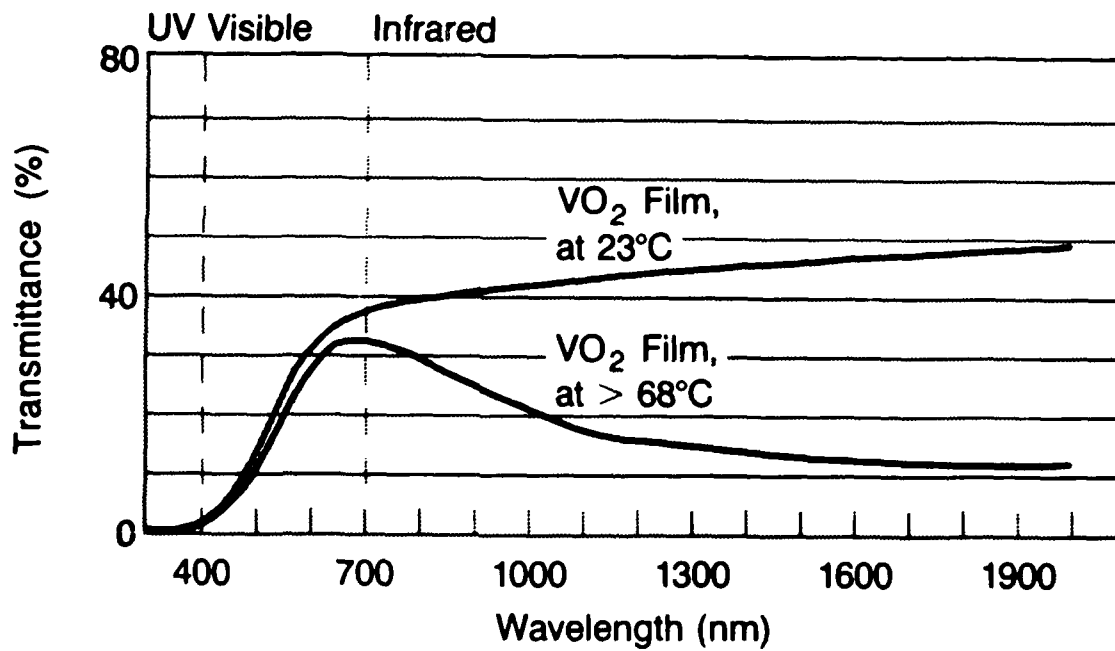


Figure 1. Thermochromic Switching of  $\text{VO}_2$  in the Solar Region; Estimated Film Thickness is  $0.1\mu\text{m}$ .

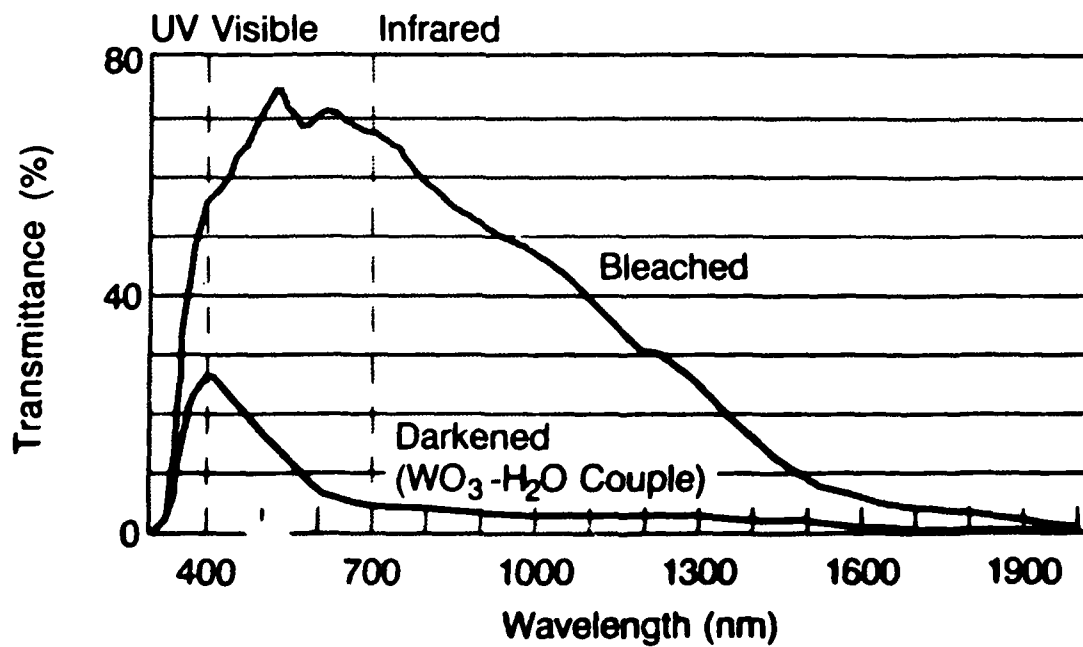


Figure 2. Electrochromic Switching in the Solar Range of a Model Cell Containing a Tungsten Oxide Thin Film.



The formation of gases for the counter electrode reactions makes this particular cell impractical, except for modelling purposes. It is used here for the sole purpose of generating the data shown in Figure 2. The results were obtained before gas evolution became evident. The data show the very good optical switching in both the visible and near infrared spectral regions. In Table II below, the data are reduced to selected solar performance values and compared to two popular architectural glasses. The first has a titanium nitride/stainless steel film on the interior surface of 6 mm clear float glass. The second has a spinel film on the exterior surface of 6 mm bronze-colored glass; it has been described elsewhere<sup>13</sup>.

Table II Comparative Solar Performance

Sample	T <sub>vis</sub> (%)	T <sub>tot</sub> (%)	S.C. (Summer)
<b>A. Architectural Glass</b>			
SOLARBAN® 560-14 (2) Clear	14	11	0.30
SOLARCOOL® (1) Bronze	21	26	0.45
<b>B. Electrochromic (WO<sub>3</sub>-H<sub>2</sub>O couple)</b>			
Bleached	69	54	0.74
Darkened	12	8	0.38

The shading coefficient, S.C., has been defined by ASHRAE for AM-2 insolation, and specific summertime conditions<sup>14</sup>. It is the solar heat gain normalized to the heat gain through 3 mm thick clear float glass. Reradiated energy is included. Transmittances in the visible and total solar ranges are given, also for AM-2 insolation, by T<sub>vis</sub> and T<sub>tot</sub>, respectively.

As Table II shows, the darkened electrochromic sample has a shading coefficient which is intermediate to those of the architectural samples. The transmittance in the visible is 12%, while the total solar energy transmitted is 8%. Overall, these are very good performance characteristics. It is this user controlled solar attenuation which makes electrochromism the preeminent candidate.

## Solid-State Electrochromic Window

There are no practical, solid-state, electrochromic transparencies in the published literature which exhibit true deep, visible switching repetitively, with reasonable stability. Deep switching means varying the transmittance between about 70% and 20% at least. Figure 3 shows a configuration<sup>15</sup> which is solid-state and which does deep switch. The preceding cell equation (1) applies and is, in this case, coupled with



The electroformed grid<sup>16</sup> shown in Figure 3 is the site for equation (4). It is also one of two conductive and transparent members of the battery. It is imbedded in a solid, H<sup>+</sup>-conducting polymer-electrolyte of poly-2-acrylamido-2-methylpropane sulfonic acid. An actual assembly has bus bars on all four sides of the tungsten oxide-coated member. The vacuum evaporated film's thickness ranges from about 3200 to 4200 Å. The electrolyte is 0.43 mm thick. The 25 ohms/sq NESA glass and clear float glass are 5 mm and 3 mm thick, respectively.

Optical switching of a 14 cm x 28 cm viewing area is shown in Figure 4. This occurs quite uniformly and with very good visual acuity, which Figure 4 accurately depicts.

The first three electrochromic cycles of a like transparency are shown in Figure 5 for powering at room temperature with low applied voltage of alternating polarity. This was continued for 10,000 cycles, with some subsequent, unexplained drifting especially notable up to 250 cycles. The first two cycles after reaching 10,000 cycles are shown in Figure 5. These show the drift as accelerated darkening and bleaching, but in other ways the sample exhibits virgin characteristics. There is little loss in visual uniformity of response or acuity. No bubbles have been generated, nor is the Cu grid degraded in any way visually under optical microscopy. The small loss of bleached state transmittance after long cycling may be an indication of some transfer of Cu metal to the WO<sub>3-y</sub>·xH<sub>2</sub>O film. This has been easily observed with lower viscosity electrolytes. Overall, the solid-state transparency response is very encouraging.

## Conclusion

Figures 4 and 5 demonstrate deep switching and reasonable stability in the solid state for room temperature. In the fullest sense, however, "reasonable stability" must include behavior at higher temperatures especially. It is still premature to judge that. However, it is not too soon to judge the general question posed by the title of this paper about the switchable transparency. What will it be? Three characteristics of the solid-state configuration shown here suggest that electrochromic switching is the likely best candidate for a variable transmission transparency. These are: (1) user control; (2) deep solar and visible switching; and (3) reasonable cycling stability at room temperature at least.

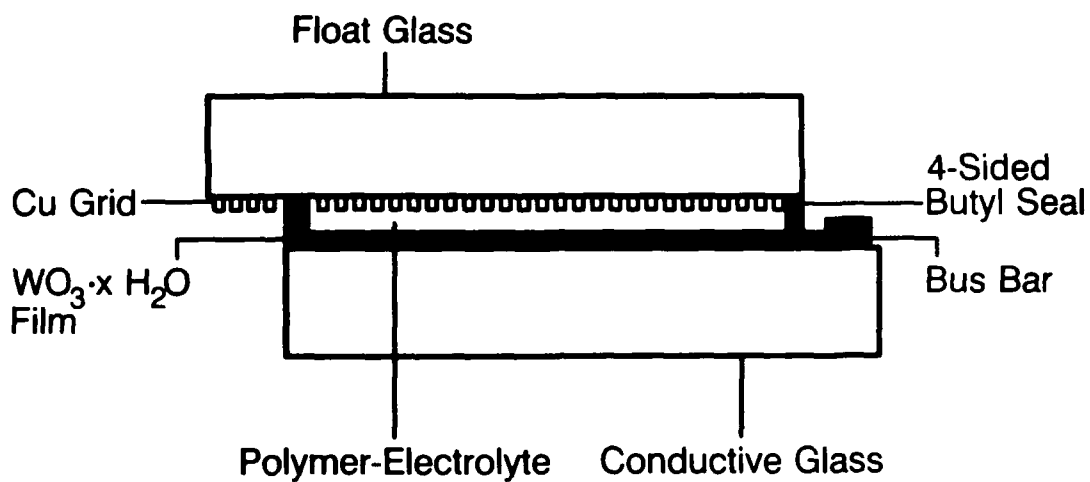


Figure 3. Solid-State, Electrochromic, Transparency Configuration with a Tungsten Oxide Film, Copper Grid and Coupled Gas-Free Half-Cell Reactions<sup>15</sup>.



Figure 4. Electrochromically Switching Sample of the Preferred Configuration.

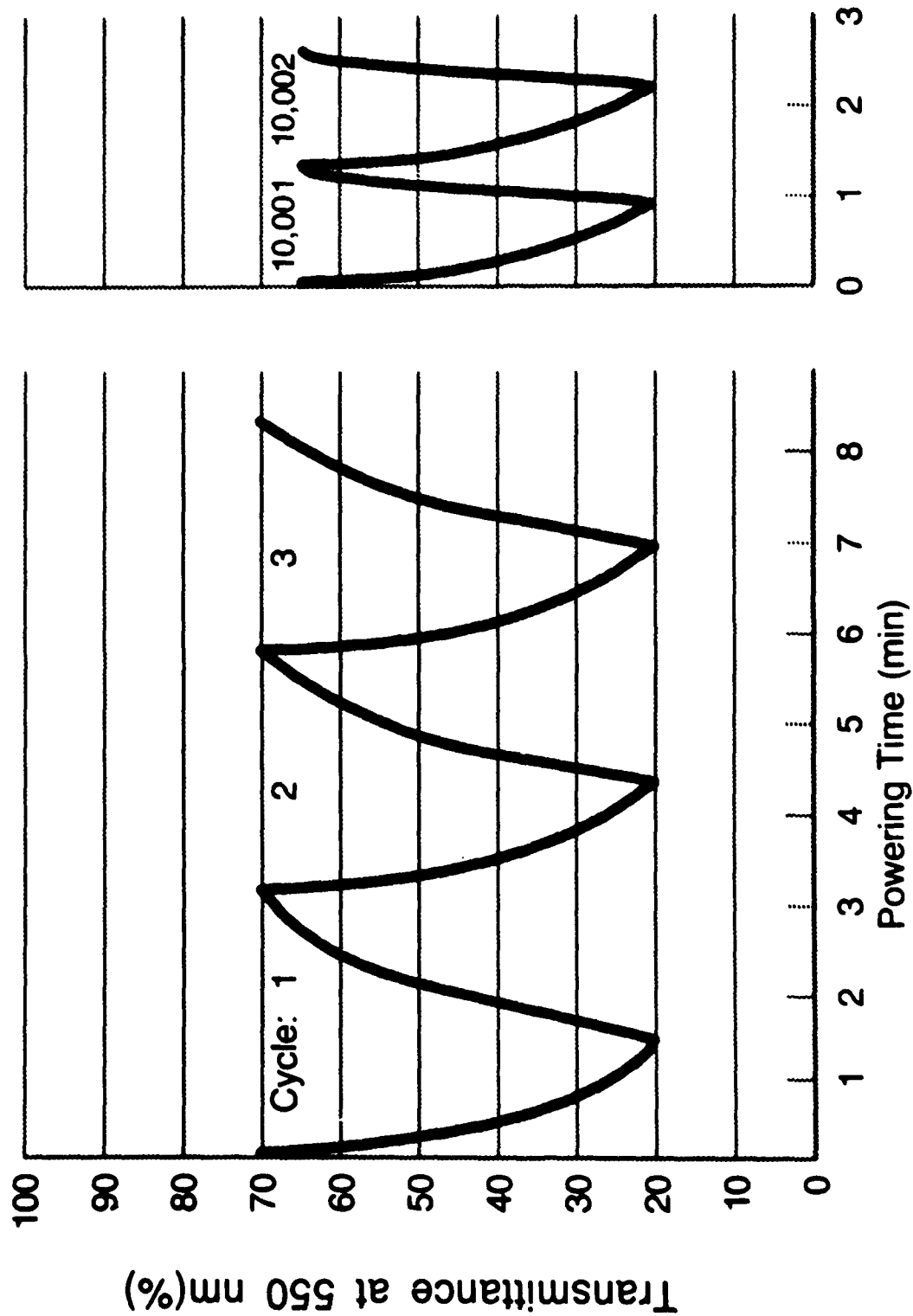


Figure 5. Electrochromic Cycling at Room Temperature, Alternately -0.50 Volt for Darkening and 0.60 Volt to Bleach; Active Area = 14 cm x 28 cm.

### Acknowledgements:

For collecting some of the data used for the central point of this presentation, I am indebted to my colleague D. E. Singleton. Both of us continue to enjoy the excellent support of our assistants, I. S. Tanowitz, J. B. McCandless and D. L. Backfisch. They have done outstanding jobs in sample preparation. I am also indebted to T. G. Rukavina for guidance in the preparation of electrolytes, and to M. E. Helzel for data on solar performance.

### REFERENCES

1. C. B. Greenberg, *Thin Solid Films*, 110, 73 (1983).
2. A. S. Barker, Jr., H. W. Verleur and H. J. Guggenheim, *Phys. Rev. Lett.*, 26, 1286 (1966).
3. H. W. Verleur, A. S. Barker, Jr. and C. N. Berglund, *Phys. Rev.*, 172, 172 (1968).
4. M. Nygren and M. Isrealsson, *Mat. Res. Bull.*, 4, 881 (1969).
5. T. Horlin, T. Niklewski and M. Nygren, *Mat. Res. Bull.*, 7, 1515 (1972).
6. C.N.R. Rao, M. Natarajan, G. V. Subba Rao and R. E. Loehman, *J. Phys. Chem. Solids*, 32, 1147 (1971).
7. C. B. Greenberg and D. E. Singleton, *Solar Energy Mat.*, 16, 501 (1987).
8. W. H. Armistead and S. D. Stookey, *Science*, 144, 150 (1964).
9. S.K. Deb, *Phil. Mag.*, 27, 801 (1973).
10. B. W. Faughnan and R. S. Crandall, *Topics in Appl. Phys.*, 40, 181 (1980).
11. R. D. Giglia and G. Haacke, *Soc. Inf. Display Digest*, 12, 76 (1981).
12. J. P. Randin, *J. Electrochem. Soc.*, 129, 1215 (1982).
13. C. B. Greenberg, *J. Electrochem. Soc.*, 132, 1394 (1985)
14. *ASHRAE Handbook, 1985 Fundamentals*, Chap. 27.13-27.28.
15. C. B. Greenberg and D. E. Singleton, U. S. Patent No. 4,768,865 (Sept. 6, 1988).
16. D. S. Postupack and J. P. Pressau, ITEM<sup>TM</sup> update 1988, 40 (1988).

GRUMMAN/FAA LIGHTNING STUDY: A POTENTIAL COUNTERMEASURE  
FOR LIGHTNING INDUCED FLASHBLINDNESS OF AIRCREW MEMBERS

H. D. Kivlighn, Jr.  
Grumman Corporation

PAPER WAS WITHDRAWN

A NEW APPROACH TO LASER FILTERS

John A. Brown  
William A. Thornton

John Brown Associates

---

## A NEW APPROACH TO LASER FILTERS

---

John A. Brown and William A. Thornton  
John Brown Associates, Inc.

---

Prime-Color laser filters block the entire visible spectrum except for three narrow bands at approximately 450 nm, 530 nm and 610 nm (the "Prime Colors"). All currently-identified laser threat wavelengths are blocked, and vision through the filter is bright and clear and in full natural color.

---

There is a growing need to provide eye protection to air and ground personnel at risk from laser beams, many of which have the ability actually to blind a person by burning the retina, and a number of approaches have been explored.

Most approaches to date have been notch filters designed to be opaque to specific laser wavelengths but to transmit as much of the rest of the visible spectrum as possible. Examples include holographic interference filters such as the one illustrated in Figure 1 and absorptive dyes such as the one illustrated in Figure 2 (the wavelength scales are omitted in the interests of security). But a notch filter is not a complete answer to the problem, because hostile laser beams may be at unexpected wavelengths. In fact, it seems that a new threat is identified almost every week as new lasers are developed!

We have demonstrated a completely different answer: an interference filter that blocks all of the visible spectrum except for three narrow transmission bands (the "Prime-Color" bands) as shown in the transmission spectrum in Figure 3. This filter blocks ALL of the currently-identified threat wavelengths as well as some that have not (yet) been identified as threats. The measured optical density between the passbands, especially at the threat wavelengths, is six or better.

The difference between a Prime-Color filter and a conventional notch filter is vividly seen by viewing a visible spectrum display and an outdoor scene through the different filters. The notch filter shows a wide black line in the spectrum, and gives a strong color cast to the outdoor scene. In contrast, the Prime-Color filter shows only three



bright lines (blue, green and red-orange) in an otherwise completely black spectrum, but shows the outdoor scene in full natural color.

The above Prime-Color filter has been incorporated into an experimental pair of goggles and tested on the highway behind the wheel of an automobile. Vision was excellent, and driving was easy. Outdoor scenes were bright and clear and in full natural color. Red lights were red, the yellow line was yellow, the blue sky was blue, and the green grass was green. It has to be seen to be believed.

Why does it work? Because the human visual system does not respond equally to all wavelengths. It responds best to the ones we call "Prime-Colors" - so much so that human vision can be thought of as "sampling" the spectrum at the Prime wavelengths and relatively ignoring the rest of the spectrum. That's not absolutely true, but it's true enough to make a good model. It's similar to the process by which a color television CRT produces a full color picture with only three rather narrow-band phosphors (approximately red, green and blue).

It's not exactly the same; we see natural scenes in full color through the Prime-Color filter because natural pigments (and man-made ones, too) are rather broad-band, and the visual system reconstructs their colors from the three samples. An especially clear illustration of that is the fact that one sees yellow objects as yellow through the filter even though the filter transmits no spectral yellow light at all.

There is a problem - one shared by all interference filters including notch filters: the pass-band or stop-band shifts toward the blue if the incoming beam comes in off-normal. Thus, a notch filter with a narrow stop-band centered on a threat wavelength may pass that wavelength if the threat comes in at, say,  $60^\circ$  from the side, because the stop-band will have shifted enough to let the threat wavelength through. Similarly, in a Prime-Color filter designed to pass the P-43 phosphor emission line but block the nearby threat wavelength, the angle shift can move the passband right onto the threat wavelength. This problem is fundamental to all interference filters.

There are several potential solutions to the "angle" problem. One is to avoid it by using a wrap-around filter so situated that oblique rays will always miss the eye behind the filter, somewhat like the sketch in Figure 4. In this arrangement, any incoming ray normal to the filter lens would be blocked; and any oblique ray that got through would miss the eye. The design and fabrication of a wrap-around filter is not simple, but it can be done.

Another approach is to exclude oblique rays by restricting the wearer's peripheral vision with a shallow honeycomb screen on the front of the filter. The resulting tunnel vision is annoying at first, but one adapts to it quite rapidly just as one adapts to the tunnel vision experienced when first putting on ordinary eyeglasses.

Still another approach is to use narrow-band dyes as supplemental threat-blockers. The dyes would have no effect on light coming in normally, because they would absorb at wavelengths where the filter was already opaque; but they would shut the window that the angle shift would otherwise open. The problem with this approach is that there are few if any dyes yet available with sharp absorption edges in just the right places. We are working on better ones.

The Prime-Color filter described herein is a preliminary development, supported entirely in-house. We currently have three contracts to adapt it to practical military eyewear, and we hope to have much more to report in the near future.

---ooOoo---

Beckman DK-2 CHART

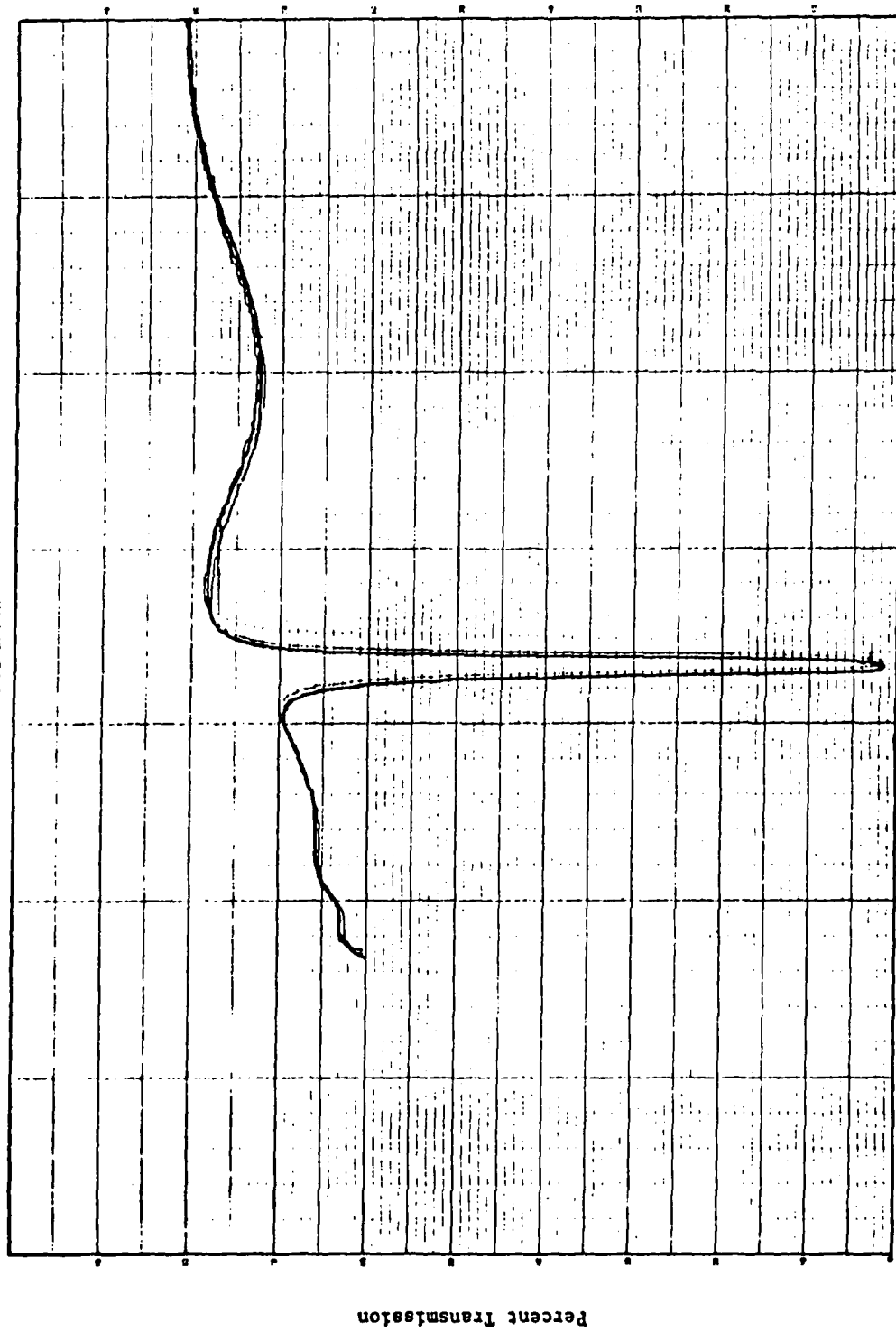


FIGURE 1 - Holographic Notch Filter

Beckman DK-2 CHART

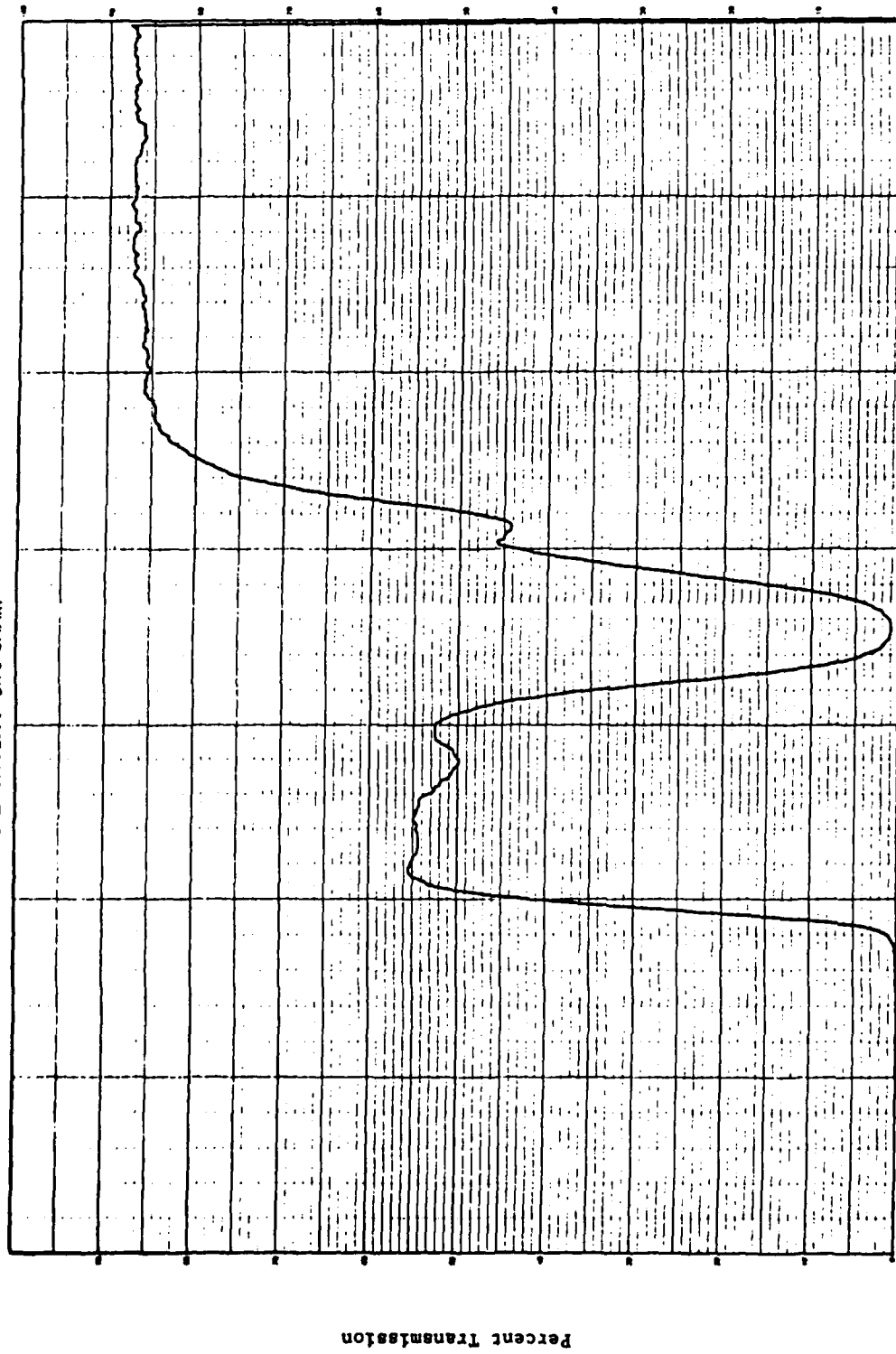


FIGURE 2 - Absorptive Dye Notch Filter

Beckman DK-2 CHART

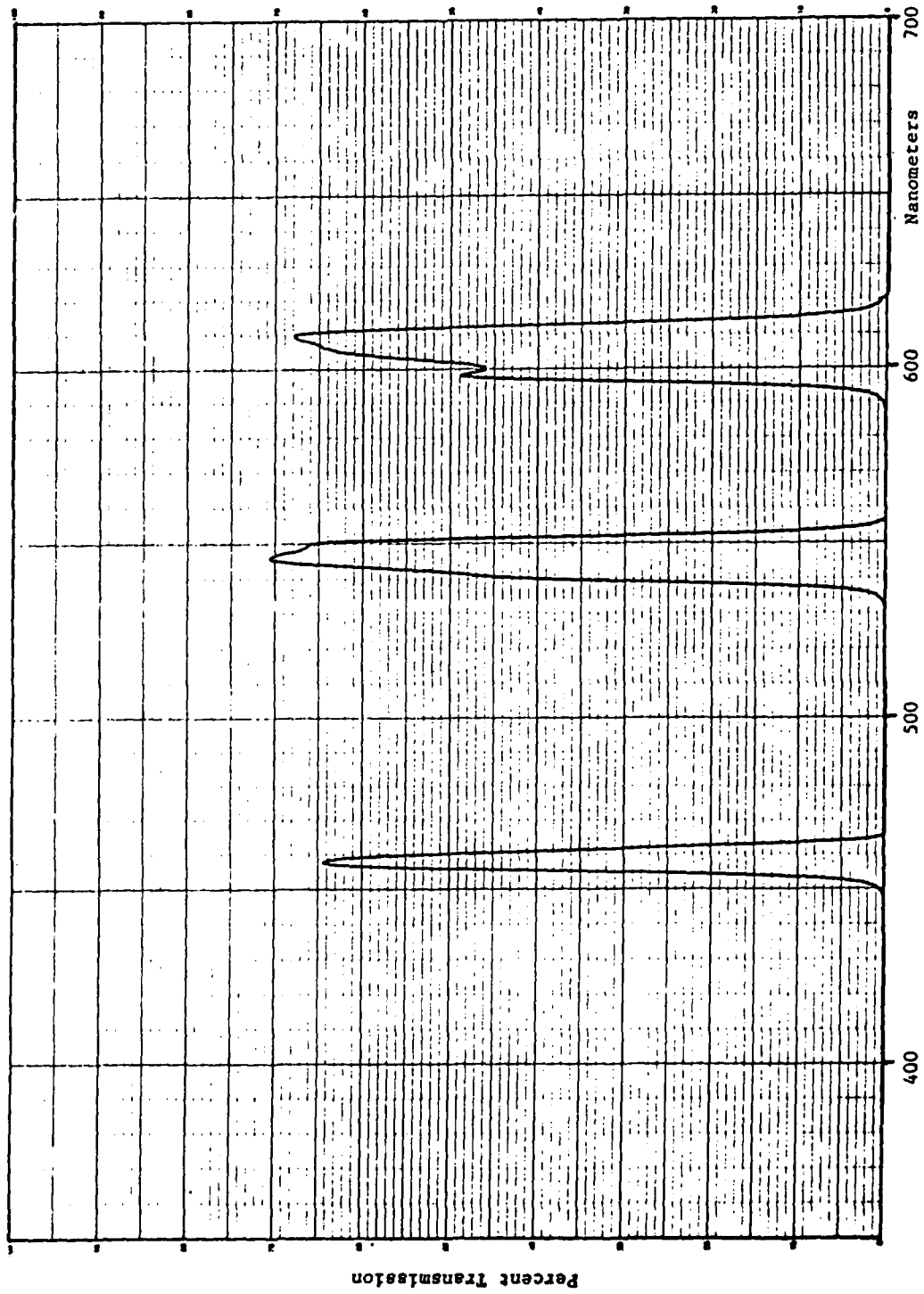


FIGURE 3 - Prime-Color Filter

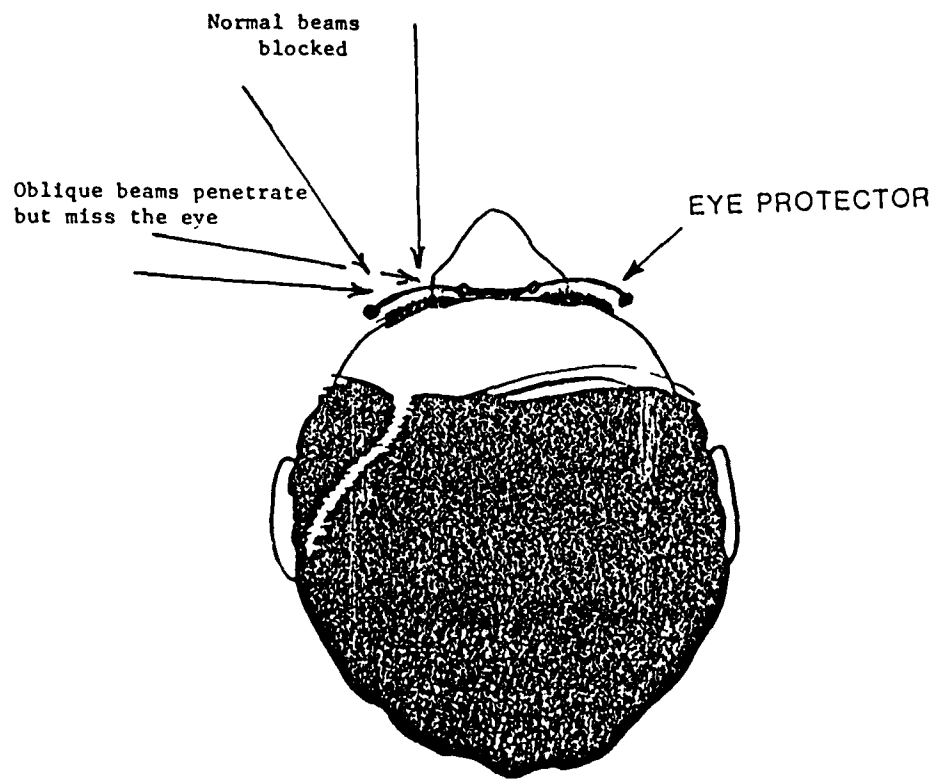


FIGURE 4 - Wraparound Concept

LARGE-AREA OPTICAL FILTER FABRICATION  
BY PLASMA POLYMERIZATION

Roy F. Wielonski  
Battelle

# LARGE-AREA OPTICAL FILTER FABRICATION BY PLASMA POLYMERIZATION

Roy F. Wielonski  
Battelle  
505 King Avenue  
Columbus, Ohio 43201

## Abstract

Optical filters for controlling the transmission of light at one or more wavelengths have been developed to a high degree of sophistication. Filter designs for these applications range from single quarter-wave antireflection coatings to multilayer coatings with high rejection capability in specific spectral regions. The fabrication of these optical filters requires precise control of coating thickness and refractive index over the surface of the desired substrate.

The optical performance of aircraft transparencies could be improved by incorporating either single or multilayer coatings in the design and fabrication stage. Transparencies, however, used on aircraft can range in size from 1 ft<sup>2</sup> to over 10 ft<sup>2</sup>. These components are not usually planar but contain compound curves making coating difficult. Incorporating optical filters on these large-area highly contoured surfaces can be accomplished through the use of plasma polymerization technology. Experiments are in progress directed toward producing multilayer quarter-wave coatings for reflection modification on these large-area components. These experiments are being extended to include optical designs which require graded index materials. Materials being investigated for both quarter-wave and graded index design filters include those which have refractive index values from 1.5 to 2 in a wavelength range of 400 nm to 800 nm. In addition to controlling light transmission, the coatings deposited by plasma polymerization can improve the weatherability and abrasion resistance of the transparency which is often a polymeric material.

Results of the current research will be reported in two categories: (1) optical performance, and (2) material performance. The items in the optical performance area include filter design, optical characterization of deposited materials, and performance data for one of the large-area filters fabricated. The items in the material performance area include data on the durability of these type of coatings.

## Background

The application of coatings to control the optical properties of glass or plastic substrates is usually implemented through the use of sputtering, resistance evaporation or low pressure chemical vapor deposition methods. The former two methods are highly developed and used commercially. Each



technique though has advantages and disadvantages based on deposition rate, composition control or limitation on the substrate temperature under which the deposition can take place. Usually the coating is required to either lower light reflection or provide narrow-band transmission for specific optical wavelengths. Substrate size often becomes an issue when these effects are required over surfaces approaching many square feet in area. The problem is further complicated when the large area substrate is curved. Researchers in this field often spend considerable time in designing tooling fixtures to insure uniform coating coverage over these parts.

Aircraft transparencies sometimes can be categorized as large area, complex, contoured components. These transparencies are either glass, plastic, or combinations of glass and plastic. The problem of coating these parts uniformly with reflection reducing or enhancing coatings can be made easier by the use of a technology known as plasma polymerization. This technology takes advantage of plasma-assisted deposition methods that can ensure that coatings will conform and adhere to the substrate whether planar or curved.

### Introduction

Plasma polymerization is a vacuum coating technology that permits the coating of substrates using polymer precursors which reacted in a low-pressure gas plasma and form coatings. The process takes place in a partial vacuum where the "coating" plasma created by an applied electric field conforms to the surface area of the part to be coated. This plasma can also be used to prepare the substrate for coating by performing a cleaning action through inert gas ion bombardment. Standard polymeric precursors, e.g., methyl methacrylate, propylene, and styrene can be polymerized into highly crosslinked coatings. Non-standard precursors, e.g., methane, organosiloxanes, can also be polymerized into coatings such as diamond-like carbon or silicon dioxide materials.

A variety of these precursors can be combined or deposited sequentially to form barrier layers or protective coatings for other plastics, i.e., polycarbonate or acrylic, giving them abrasion resistance and unique optical characteristics.

Plasma polymerized coatings can be applied with equal ease to both small and large area components by contouring the plasma to these parts. Flat and curved substrates with surface areas up to 8 ft<sup>2</sup> have been routinely coated with crosslinked films in excess of 5 micrometers. Generally, much thinner films (2 to 3 micrometers) are sufficient.

The application of optical coatings to aircraft transparencies offers a unique challenge since the components of interest are usually large-area, curved, plastic components. Several potential uses for these optical coatings on transparencies include enhanced light transmission, glare reduction, solar heat control and band pass or band reject filters for eye protection. Methods for applying these coatings by commercially developed vacuum processes rely on carefully tailoring the vapor stream or atom flux to control the coating uniformity which is essential in order to meet

performance goals. Additionally, the use of substrate motion is often needed to control uniformity. The formerly mentioned process methods to control coating uniformity are less critical in plasma polymerization coating work.

### Coating of Large-Area Substrates

Large-area substrates (glass or plastic) referenced in this work include those that have surface areas from 8 in.<sup>2</sup> to 2000 in.<sup>2</sup>. Planar and curved substrates like this can be coated uniformly with crosslinked polymer films without the need for motion relative to the deposition source. The plasma polymerization approach lends itself well here since motion or multiple source placement is not needed; in fact, the vacuum chamber volume contains and is the source of material for the coating [1].

Film thickness uniformity requirements for optical coatings, i.e.,  $\pm 5$  to 10 nm over large areas are more stringent than for abrasion or chemical resistant coatings over the same surface area where the tolerance for the latter may be widened to at least  $\pm 100$  to 200 nm. Presently, our data on coating uniformity is for abrasion resistant coatings deposited by plasma polymerization on large areas of at least 1500 in.<sup>2</sup>. Nine measurements of coating thickness were performed on a substrate (of the size mentioned above) in a central region covering an area of approximately 430 in.<sup>2</sup>. The coating applied to this substrate had a thickness with a mean value of 2812 nm, a variance from the mean of 11.4 nm and a standard deviation of 107 nm.

These data are not meant to imply limits on thickness uniformity achievable but rather to provide a base line for current work. Past research dealing with coating optical discs (12-in. diameter) though was successful in obtaining a very uniform coating thickness of 800 nm  $\pm 3.0$  nm across the disc surface by the plasma polymerization technique. Our research is now proceeding along two paths, one being the basic process development to implement multilayer optical filter coatings by plasma technology and the other being the large area processing research required in preparation for implementing the multilayer concept on large-area substrates. An SiO<sub>x</sub>-type coating applied by plasma polymerization for use on large area surfaces is currently much further developed than other materials needed for filter fabrication. This coating has demonstrated antireflection and abrasion resistant qualities when applied over higher index materials such as transparent semiconducting films like indium-tin oxide. Experience in applying these single layer optical coatings is helping to provide the data, and solve process problems needed for uniformly applying multilayer coatings over large areas.

The test case chosen for this paper is a multilayer coating consisting of alternating layers of high and low index materials deposited by plasma polymerization. The substrates are both glass and polycarbonate since these are often materials used in transparencies. The use of polycarbonate material demonstrates the ability of the process to coat without thermally damaging typical aircraft transparency materials.

## Material Selection for Filter Fabrication

Successful demonstration of multilayer optical film deposition by plasma polymerization requires two materials with dissimilar refractive indices at the design wavelength of the optical device. We chose two materials derived from precursors known to yield silicon dioxide- ( $\text{SiO}_2$ ) and titanium dioxide- ( $\text{TiO}_2$ ) like films. The refractive index value targets were 1.45 ( $\text{SiO}_2$ ) and 2.3 ( $\text{TiO}_2$ ) at a wavelength of 550 nm for the plasma deposited coatings.

The  $\text{SiO}_x$  and  $\text{TiO}_x$  materials are generated using low vapor pressure liquid (<1 mm Hg) precursors, unlike the traditional materials source used in the preparation of optical films by evaporation and sputtering techniques, as practiced in many laboratories. Other potential materials for plasma deposition of optical coatings being evaluated include those in the silicon nitride and silicon oxynitride category.

## Optical Design

A low transmission band reject filter consisting of alternating quarter wave optical thickness (QWOT) films to form a multilayer stack was selected. The design originally chosen was to be comprised of 8 to 10 high ( $n = 2.3$ ) and low index ( $n = 1.45$ ) (at 550 nm) pairs of QWOT films. The original design mentioned would have had less than 5 percent transmission at the design wavelength of 550 nm. A final design evolved based on the materials which could be prepared and their refractive indices. This design actually consisted of 20 to 40 layers of QWOT films. Optical filters of this type and using plasma polymerization techniques (but with fewer layers) have been prepared by previous researchers [2]. The goal for the present work was to apply this concept to large-area substrates using our prototype production equipment. The optical multilayer design criteria, including such items as film thickness and index grading information, was generated on a Hewlett-Packard 300 Series computer system using commercial software for filter design [3]. Theoretical performance curves have been prepared for both the multilayer filters discussed here as well as for other types of filters such as those of the Rugate type. A multilayer optical filter consisting of 27 QWOT films was studied as a result of our preliminary experimental work using a design based on  $\text{TiO}_2$  (H)/ $\text{SiO}_2$  (L) combinations. The expected bandpass for this filter is shown in Figure 1.

This filter characteristic assumes the index of refraction values for  $\text{SiO}_2$  (1.45) and  $\text{TiO}_2$  (2.3). The performance of this filter is related to the index ratio of the materials. As this ratio decreases the stop band as well as the transmission of the multilayer changes.  $\text{TiO}_2$  and  $\text{SiO}_2$  have an index of refraction ratio of 1.62. This ratio provides a stop band (width of low transmission region) close to 10% [4]. Stop bands of less than 5% can be realized as the index ratio approaches unity. An example of this is shown in Figure 2 for assumed values of high index material (1.54) and low index material (1.45).

## Rugate Filters

It should be possible to fabricate optical filters of the Rugate variety over large areas as well by varying the various gas precursors to grade the refractive indices. This type of precursor variation is planned for future experiments. At the present time, computer software and data acquisition equipment have been installed on our large-area coating system which can be used in these studies. A demonstration of periodic dopant concentration variation has been achieved in preliminary tests using argon gas as the dopant varied. This dopant variation is shown in Figure 3. A residual gas analyzer was used to monitor the mass peak being varied.

## Preparation of Optical Filters by Plasma Polymerization

Processing coatings for the purpose of producing optical filters requires precise control of such parameters as precursor flow rate into and out of the vacuum chamber, plasma power, residual background gas environment, and in particular, the optical thickness of the coating as it is being deposited. The precursors for these experiments are liquids and require special control methods. Precision flow control devices were used which maintain the flow of the low-vapor-pressure materials into the chamber to within 5-10 cc/min or less. The flow rate is maintained constant while the total pressure is controlled at set pressure points in a range of less than 100 mtorr by a downstream variable conductance valve. This valve responds to set points and the true pressure readings of a capacitance manometer gauge system. Since the precursor material is not a simple material, specialized techniques are being used to monitor the process. These techniques are capable of providing the data for process control and analysis.

All of the parameters mentioned above are fed to a computer controlled data acquisition system used in conjunction with an optical monitoring system. The optical monitoring system is used either in a reflection or transmission mode to measure the actual film growth rate and aid in establishing plasma power needs. Once the rate of growth is known and controlled, the cut points for total film thickness or optical quarter wave point termination can be made. The measurements can be carried out at various wavelengths. This procedure is used to monitor the film growth which is very stable (change in growth rate is less than 20 nm/min. in two hours). Deposition experiments have been carried out over longer periods of time (>3 hours) with similar results. Measurements made by this method can also provide information as to the film homogeneity, optical quality and growing rates when two sides of a substrate are being coated.

## Analysis of Film Properties

The coatings deposited by the plasma polymerization process were evaluated in terms of their optical and physical properties. Optical measurements were made on the SiO<sub>2</sub>-type coatings using ellipsometric techniques over a spectral

region from 300 nm to 800 nm. Spectral measurements in addition to providing refractive index data provides necessary information on the dispersion qualities of the material. The  $TiO_2$ -type coating has not yet been characterized by this method. Refractive index data for this material is being obtained by depositing QWOT thick coatings on both glass and silicon wafers at one wavelength (550 nm) for comparison with calculated predictions of light reflection for QWOT films using index values of 1.5 to 1.8 for these same substrates.

### Optical Properties

The plasma-deposited material based on the organosiloxane precursor resembles  $SiO_2$  in terms of the refractive index, i.e., 1.45 to 1.46 at 550 nm. Figure 4 shows the dispersion curve for this material.

As mentioned earlier, plasma-deposited  $TiO_2$  films based on titanium organometallics have not been characterized as thoroughly since the preparation of films with this material has just started. Preliminary reflection measurements indicate that films can be formed which have refractive index values in a range from 1.5 to 1.8 at 550 nm. The index controlling parameters believed to be important are: (1) concentration ratios of titanium precursor and oxygen in the reaction chamber, (2) pressure of the previous molar ratio concentration in the vacuum chamber, and (3) plasma power density.

Two multilayer film combinations were prepared using the organosiloxane and titanium organometallic precursors. The total number of layers to be deposited was guided by the reflection measurements which were made in-situ and simultaneous with the deposition process. The first experimental multilayer coating consisted of 27 layers, each a quarter-wave- optical thickness at 550 nm. This filter was measured using a Perkin-Elmer spectrophotometer. Its transmission characteristics are shown in Figure 5. The transmission characteristics for a filter consisting of 27 layers (like the one fabricated) using materials with refractive indices like  $SiO_2$  (1.45) and  $TiO_2$  (2.3) should have been similar to that predicted by a design shown in (Figure 1). Discrepancies in actual versus predicted performance are believed to rest in differences between refractive index data used to calculate the filters performance (Figure 1) and the actual refractive index values of the deposited films (primarily the  $TiO_2$ ). The polymerized material used to obtain the  $SiO_2$  coating was independently characterized to determine its refractive index across the spectral region from 300 nm to 800 nm. The data shown in (Figure 4) indicates a good match to the data for stoichiometric  $SiO_2$ . Since no refractive index data (of the type in Figure 4) was available for the deposited  $TiO_x$  material, an indirect iterative computer-assisted design technique was used to match the actual performance curve with various values of  $n$  for the  $TiO_x$  layer (assuming a value of 1.45 for the  $SiO_x$  material). Using this procedure, a performance curve was obtained which matched the actual characteristics of the 27-layer coating (Figure 2). From this analysis technique, an estimated refractive index value of 1.54 at 550 nm was assigned to the deposited  $TiO_x$  material in the first multilayer coating rather than a value of 2.3 at 550 nm.

A second multilayer film was attempted in which changes were made in the formation of the  $TiO_2$  QWOT films. In this experiment, the reflection from the glass surface for the same optical thickness as above (i.e., at the 27th QWOT point) increased by 23 percent over the previous multilayer, at the same QWOT point, indicating a higher index of refraction value for the  $TiO_2$  film being deposited. This multilayer when complete consisted of 37 layers. The resultant film had a reflectance greater than 50% at a wavelength of 550 nm.

This second 37-layer film combination was measured to determine percent transmission using a Perkin-Elmer spectrophotometer. It has lower transmission in the 550 nm region, as well as lower transmission overall across the same spectral region when compared with the previous 27-layer film. The reason for this lowered transmission is not fully understood but it implies higher absorption or film inhomogeneity. Figure 6 shows the resultant plot obtained.

### Physical Properties

Some of the physical properties for these plasma-deposited coatings of interest to the aerospace transparency community are: (1) solvent and chemical resistance, (2) weathering and ultraviolet resistance, and (3) chemical stability.

The materials discussed in this paper if they are to find their way into transparency applications should meet several of the above general criteria. Our  $SiO_x$ -type material has undergone testing in many of the categories mentioned and meets most of these requirements. In particular, polycarbonate plastics which are damaged by solvents, i.e., acetone can be protected by plasma polymer coatings. Physical damage to polymers due to abrasive action can also be minimized by these coatings, in particular, a plasma polymer film can limit light loss due to optical haze resulting from inadvertent abrasive exposure. Tests performed on coated polymer sheet material using the Bayer test procedure had the following result: haze increased to only 4% following 900 cycles of testing. This result, coupled with improved transparency performance, suggest continued research is desirable and that incorporation of these coatings into the overall transparency design strategy may be warranted.

### Future Work

Work in this area is continuing both in the optical and materials performance categories. Results as they are obtained will be made available to the Aerospace community.

### References

- (1) "Coatings Deposited by Plasma Polymerization", R. Wielonski and E. Drauglis, Presented at Society of Vacuum Coaters' 28th Annual Technical Conference (April 1985).
- (2) J. C. Lee, "Multilayer Optical Interference Coatings Via Glow Discharge Polymerization", Applied Optics, Vol. 17, No. 16, Aug. 15, 1978.
- (3) Thin Film Designer Software , Computer-Assisted Design of Optical Filters.
- (4) Optical Thin Films: Users' Handbook, James D. Rancourt, MacMillan Publishing Company (1987), pp 61-62.

### Acknowledgements

William Ivancic, Research Scientist, Battelle, for his invaluable assistance in developing computer software and implementing the hardware for process data acquisition and spectrophotometric analysis.

Mecky Puiu, Instrument Specialist, Rudolph Research, for optical characterization of sample material by ellipsometric methods.

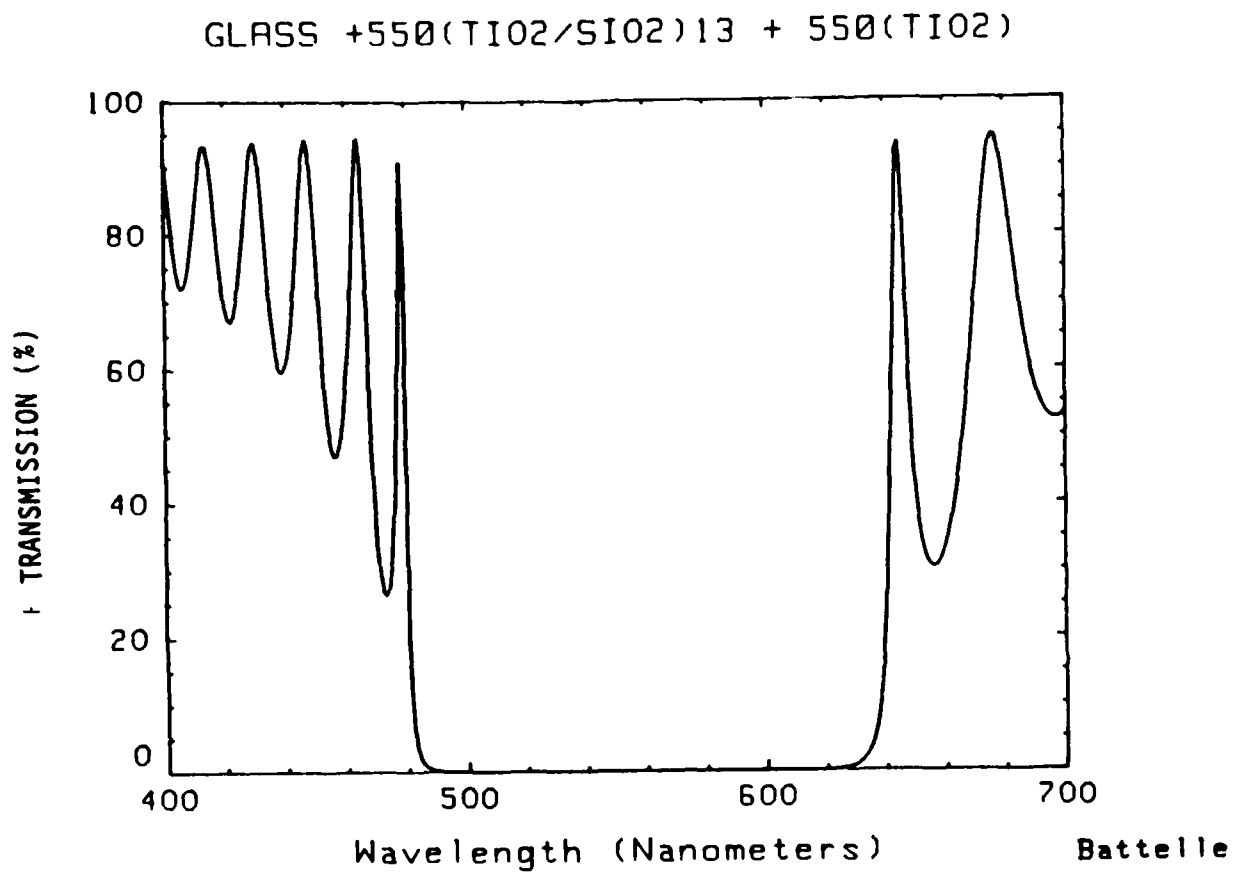


Figure 1. Performance of an Optical Filter Using 27 QWOT Films Based on TiO<sub>2</sub>/SiO<sub>2</sub> According to the Design 550 [(HL) 13 + (H)].



GLASS+550(1.54/1.45)13+550(1.54k=.001)

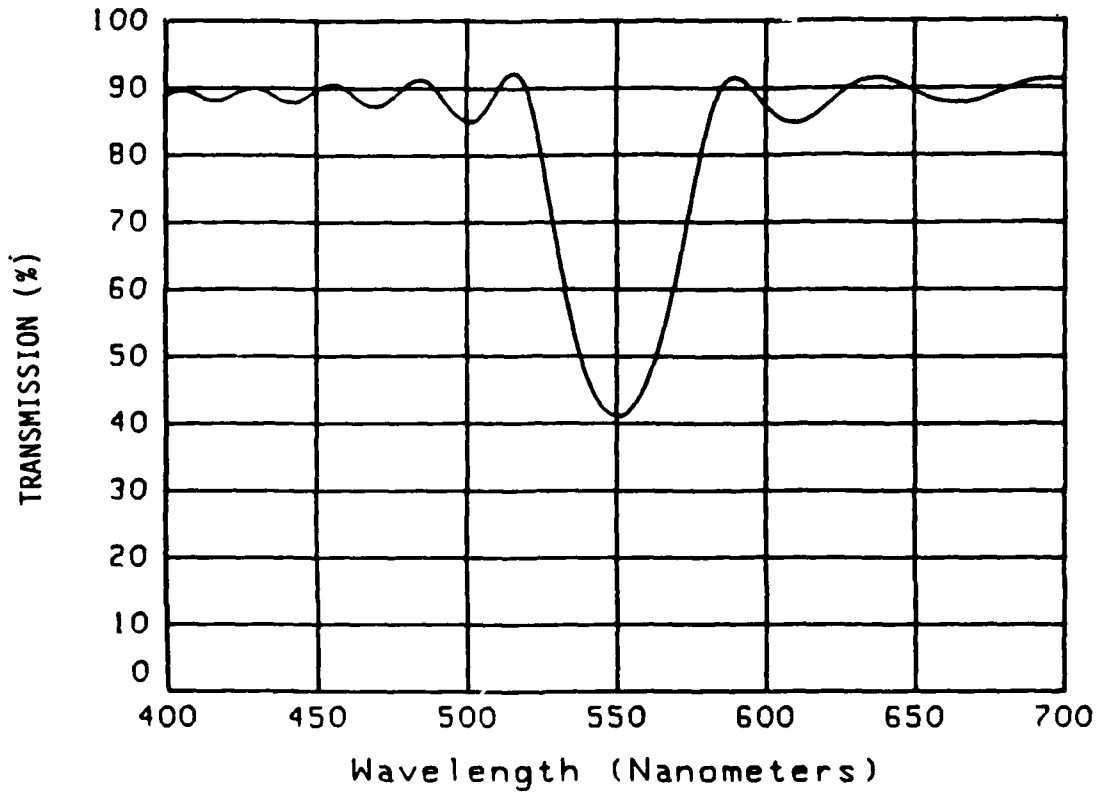


Figure 2. Performance of an Optical Filter Using 27 QWOT Films Based on Values for H(1.54) and L(1.45) According to the Design 550 [(HL) 13 + (H)].

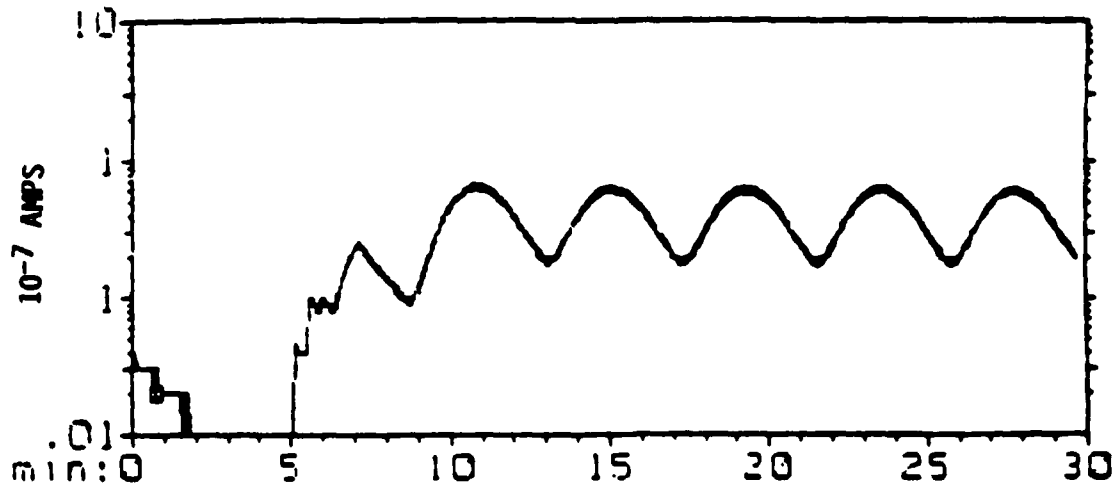


Figure 3. Argon Doping Gas Concentration Varied by Computer Control.

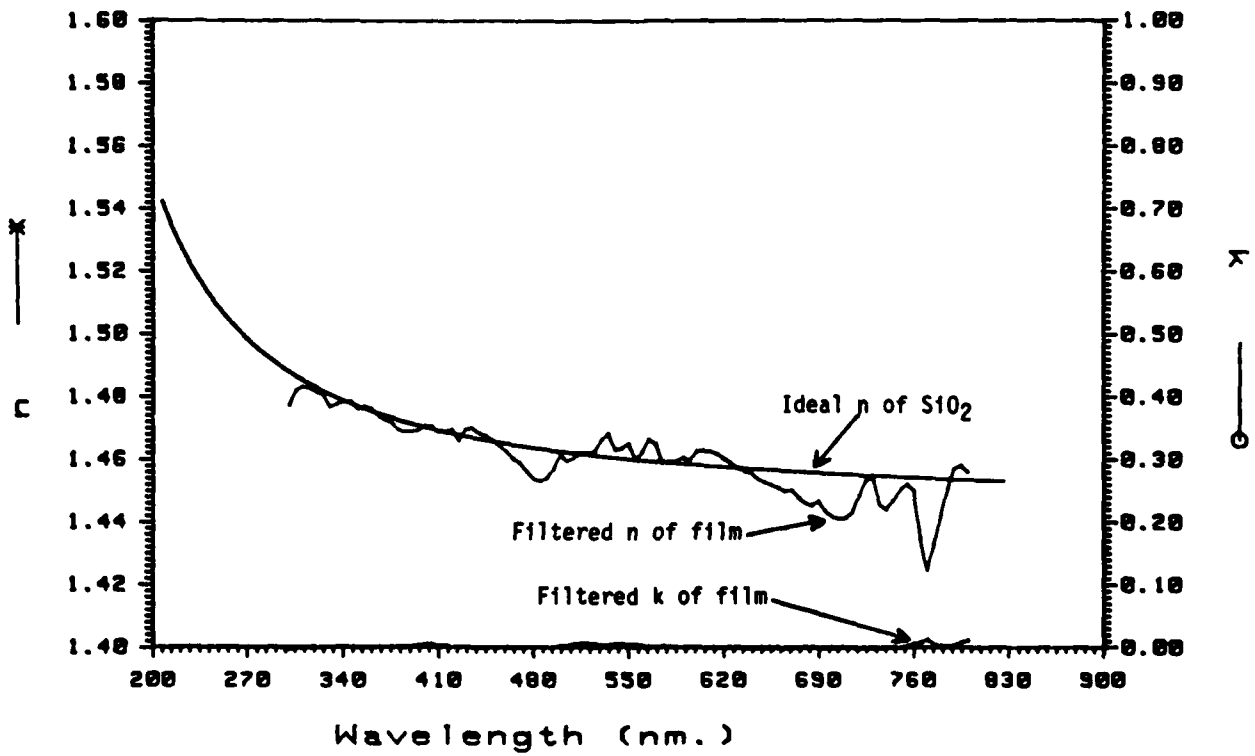


Figure 4. Spectrum Comparison of Ideal SiO<sub>2</sub> to Plasma-Deposited Film (Sample No. 43543-34, Film Thickness 36,759Å.)

Performance of Deposited QWOT Coating  
(27 layers of  $TiO_x/SiO_x$ )

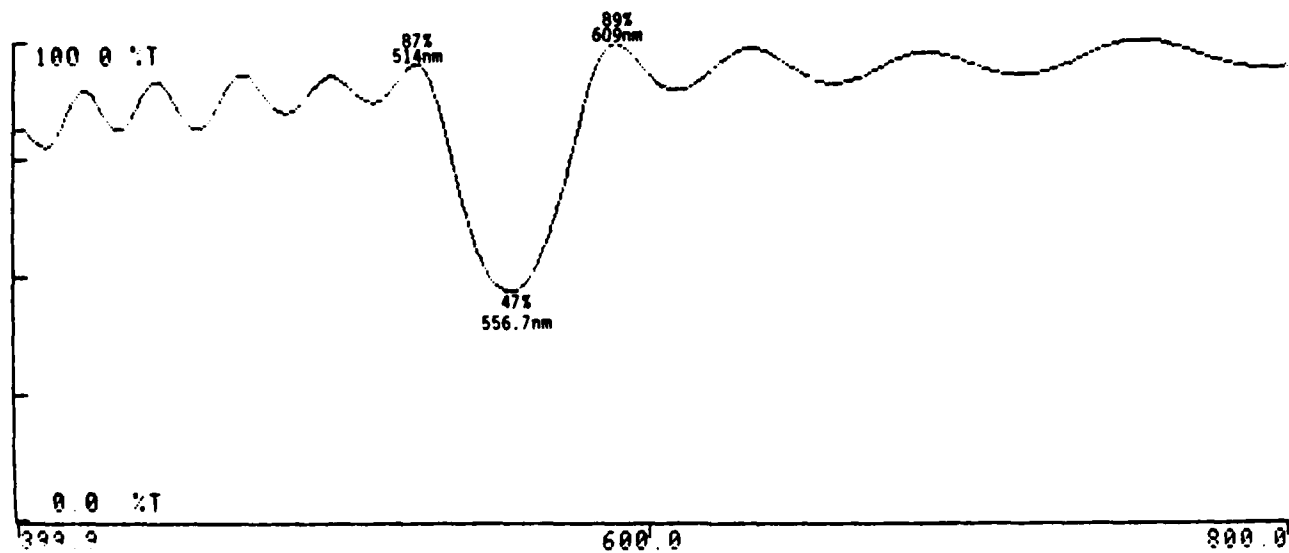


Figure 5. Transmission Characteristics of Multilayer/Wavelength.

Performance of Deposited QWOT Coating  
(37 layers of  $TiO_x/SiO_x$ )

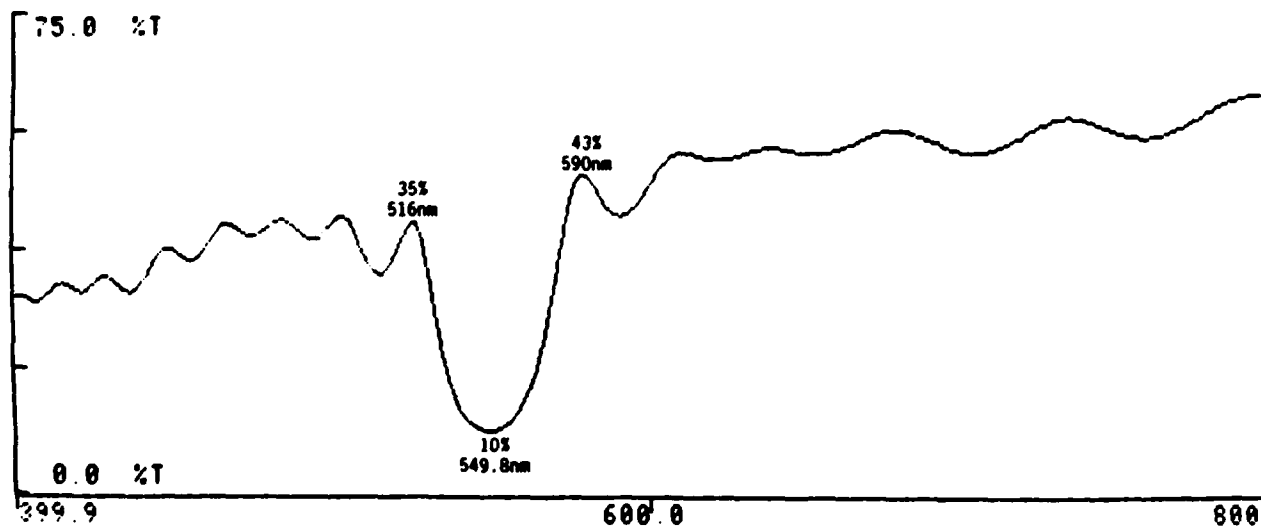


Figure 6. Transmission Characteristics of Multilayer/Wavelength.

SESSION VIII

COMPUTER AIDED ANALYSIS (PART A)

Chairman: R. E. McCarty  
Flight Dynamics Laboratory  
Wright-Patterson AFB, Ohio

Co-Chairman: C. Smith  
Flight Dynamics Laboratory  
Wright-Patterson AFB, Ohio

Coordinator: M. G. Gran  
Flight Dynamics Laboratory  
Wright-Patterson AFB, Ohio

HIGH PERFORMANCE TRANSPARENCY DESIGN

F. F. Abdi  
G. L. Savoni  
G. Clark  
Rockwell International

R. A. Smith  
Flight Dynamics Laboratory

## HIGH PERFORMANCE TRANSPARENCY DESIGN

F.F. ABDI, G.L. SAVONI, and G. CLARK  
Rockwell International  
and  
R.A. SMITH  
Flight Dynamics Laboratory

AEROSPACE TRANSPARENT MATERIAL AND ENCLOSURES  
16- 20 JANUARY 1989 Monterey, California

### ABSTRACT

An integrated design methodology to replace the trial and error techniques used in high performance transparency design is presented. The methodology, based on an integrated application, provides more efficient, cost effective design iteration and reduces the number of developmental specimens which must be fabricated and tested.

A transparency design and analysis methodology for high performance aircraft crew compartment enclosures was developed and demonstrated through the use of computerized analysis tools. At the conceptual stage, an initial cross-section code was developed to achieve a minimum weight design while considering all flight constraints. Subsequent use of STAPAT (thermal analysis) and MAGNA (thermal stress and bird strike analysis) codes in an iterative analysis cycle resulted in a TF-15 transparency design to meet bird strike and thermal requirements. The integrated cross-section design methodology provides rules and procedures for using STAPAT and MAGNA in an iterative cycle for defining a cross section which meets all failure criteria.

### INTRODUCTION

The overall objective is to develop and demonstrate an integrated design methodology to replace the trial and error techniques commonly used in transparency design. It is believed that valid analytical tools would reduce significantly the level of full-scale testing required for three-dimensional, geometrically and materially nonlinear structural dynamic systems. A computational design study of a TF-15 fighter crew compartment enclosure was developed and demonstrated for bird strike and thermal analysis methodology for high performance aircraft. Since both STAPAT and MAGNA require great amounts of computer resources (the CRAY supercomputer is recommended for MAGNA analysis), an initial cross-section code (ICS) was developed to estimate the required bird strike structural requirements using handbook equations, to size the interlayers to provide the required thermal protection, and to predict the visible transmission through the preliminary cross section.

The integrated cross section design methodology provides rules

and procedures for using STAPAT and MAGNA in an iterative cycle for defining a cross-section which meets all failure criteria. The procedure minimizes the number of iterations needed to meet the various requirements.

The results of a literature and industry materials survey were used to identify a number of candidate high temperature or high performance material available in the near future. The impact of these advanced materials on the design weight, optics, and thermal and bird strike capability of the best design was evaluated. An assesment of the state-of-the-art in transparency materials concluded that polycarbonate remains the chief structural candidate for aircraft transparencies for the near term. Polyester carbonates and polyarylates show promise but will not be produced in the quantities needed. The fluorepoxies are clear and can withstand high temperatures but are still developmental: however, additional property characterizations are warranted.

### TRANSPARENCY DESIGN GOALS

Transparency design goals can be summarized as achieving a minimum weight design while considering: optics (high visible transmission, low distortion), bird strike resistance (e.g., 4 pound bird at 500 knots), thermal resistance (high supersonic capability, thermal stress during transients, impact of temperature on material properties), and pressurization/flight loads [1].

Figure 1 represents an integrated analysis optimization methodology for the preliminary design concepts. As shown, this process can be used to provide an efficient turnaround in design analysis. A lofting generation code can be used to define the initial lines. This moldline description can be converted to develop the nodal and finite element models needed by STAPAT and MAGNA. The optics evaluation requires a smooth representation of the transparency geometry such as discrete curve fitting. The thermal, structural, and optical results can be combined to optimize the best achievable design.

### CONCEPTUAL DESIGN METHODOLOGY

Conceptual design optimization methodology provides a means of developing an initial cross section for preliminary design. A PC-based initial cross section code (ICS) was written to define heating and maximum temperature, to define the bird strike structural requirements using handbook equations, to define the pressurization structural requirements, to size the interlayers to provide the thermal protection required by the structural plies, and to predict visible transmission through the preliminary cross section. This code has been designed to achieve a minimum weight design subject to structural, thermal, and optical constraints. Figure 2 is a flow diagram of the ICS code. The systematic approach for initial sizing (thermal, bird strike, and pressurization) is based on: (1) material selection and configuration which consists of the selection of material allowed in a temperature range (default and/or user defined, interactively modify built-in values), monolithic or laminated construction, and balanced or unbalanced structural plies, (2) ICS



aeroheating option, which, after the user defines the forebody and windshield as either cones or wedges, calculates the heating rates and adiabatic wall temperature based on local flow properties, (3) sizing for bird strike, which is based on handbook equations for glass, stretched acrylic, and polycarbonate. Weight is minimized subject to a known applied impact defined by bird weight, aircraft velocity, and impact angle while satisfying critical stress and design criteria. A 15-percent thickness reduction for double-ply configuration is also considered. , (4) sizing for pressurization in which the minimum transparency thickness required to satisfy the internal cabin pressure loads are calculated (sizing options include flat, curved, monolithic, or multi-ply designs), and (5) sizing for temperature which determines the interlayer thickness required to maintain structural ply temperatures below their allowables. (This is based on a transient technique (a steady state technique is too conservative) which utilizes the temperature response of an insulated thick plate after sudden exposure to a uniform convective environment. Solutions are coded in the form of temperature ratio as a function of the Fourier and Biot moduli.

### PRELIMINARY DESIGN METHODOLOGY

The methodology is based on an integrated application of the STAPAT (thermal analysis) and MAGNA (thermal stress and bird strike analysis) codes, providing a more efficient, cost effective design iteration, and reducing the number of developmental specimens which must be fabricated and tested [2].

STAPAT and MAGNA analysis begins after the initial cross section has been defined. Figure 3 illustrates the process that is used to provide an efficient turnaround in design analysis.

The MAGNA finite element code is used to predict the nonlinear bird strike response of the transparency design and to perform thermal stress analysis using temperature predictions from STAPAT [3]. MAGNA analysis also considers large displacement/rotation, finite strains, and elastic-plastic behavior. To perform a MAGNA thermal stress analysis, the STAPAT nodal temperature grid was transformed onto the MAGNA grid using a three-dimensional interpolation which generates the required MAGNA nodal temperature distribution, as shown in Figure 4.

### BIRD IMPACT CRITERIA

Bird impact load definition is based on: (1) the bird behaves as a fluid during impact, (2) the impulse delivered to the structure is equal to the component of the bird's linear momentum which is normal to the target surface, (3) the average density of the bird material is  $1.86 \text{ sl/ft}^3$ , (4) the period of the impact event is best characterized as the time required for the bird to travel its own length, [4] and (5) the pressure resulting from bird impact can be calculated from a nominal force that is constant over the impact period [5].

### REMODEL TRANSPARENCY

More complete definition of the structural concepts will require remodeling of the transparency for two or more components such as

the aft arch and canopy [6]. The remodeling can be a tedious, time-consuming process requiring an extensive amount of iteration. However, this process can be shortened by the following criteria: (1) Include the stiffness of the aft arch model in the baseline MAGNA analysis (realistic boundary conditions). The use of simplified beam elements will not require extra nodes within the finite element model and the exact cross sectional properties will be represented; (2) match the stiffness of the two components; (3) perform thermal/structural analysis of the edge member aft component; and (4) use the maximum stress to generate a new design thickness, if necessary.

#### AFT ARCH EFFECT ON THE WINDSHIELD

The aft arch effect on the windshield design was considered using an approach different from standard trial and error methods. This technique is described as follows: (1) model the aft arch using MAGNA finite element modeling technique, (2) refine every aft element of the windshield to include the aft arch model, (3) generate surface data files, (4) expand the surface models to solid substructures, (5) merge the substructures into an aft arch model, (6) reduce the material properties of the aft arch caused by the temperature effect, (7) run natural frequency to estimate the stiffness of the aft arch, (8) estimate the weight of the aft arch, (9) compare the mode shapes (as shown in Figure 5) natural frequencies, and the stiffness of the aft arch and the windshield, and (10) merge the aft arch with baseline and rerun MAGNA nonlinear dynamic analysis with appropriate boundary conditions. Figure 6 represents the integrated design concepts.

#### TRANSPARENCY MATERIAL EVALUATION

Key properties for selection of advanced transparency materials are good optics and structural and thermal capability [7]. Improved protection of aircraft transparencies against natural and induced environments has been demonstrated to be necessary. Higher temperature capability is required for application to next generation aircraft. Increased strength and retention of bird strike protection after exposure to these high temperatures are essential for aircraft which fly at altitudes where bird strikes are possible. At the same time, it is imperative that excellent vision is retained to allow the crew to effectively accomplish mission goals. A summary of state-of-the-art materials is presented in Table 1. These materials are used either as structural monolithic plies or as structural or face plies in a composite site laminated design using appropriate interlayer. Coatings are as required for heating, reducing radar cross section, improving abrasion resistance, and providing anti-static, anti-reflection, or electromagnetic pulse (EMP) protection. An assesment of the state-of-the-art in transparency materials concluded that polycarbonate remains the chief structural material for aircraft transparencies for the near term. Polyester carbonates and polyarylates show promise, but will not be produced in the quantities necessary. The fluorepoxies are clear and can withstand high temperatures but are still developmental; however, additional property characterizations are warranted. Figure 7(a) represents the visible transmittance and heat deflection temperature, and Figure 7(b) represents the temperature effect on impact resistance of

the various transparent materials. [7]

## RESULTS

A monolithic structural design was selected for this methodology study because of its simplifying attributes in finite element analysis. A structural weight reduction of approximately 15 percent would result for a multi-ply structural design. Figure 8 represents the TF-15 windshield construction analysis results. It compares the thickness of the structural layer to the initial thickness of the structural layer, obtained for different stages of the design process. Also shown in the Figure 8 is a weight summary of the transparency system. The best transparency design was obtained for 0.120-inch glass, 0.505-inch silicon, and 1.448-inch polycarbonate. The aft arch design was constructed using Ti-6Al-4V material and it was not changed from the initial sizing during the design process. The weight of the aft arch was estimated as 8.14 pounds. Figure 9 shows the stress postprocessing results from a bird strike analysis on the windshield/aft arch finite element model.

### AFT ARCH THERMAL ANALYSIS

An additional thermal analysis of the edge member was performed to account for the effect of the edge member and bolt on local thermal distribution. This was accomplished by modeling a typical (high temperature location) member geometry and bolt design. The maximum thermal gradient occurred at the end of the first high altitude, high velocity cruise ( $t = 865$  seconds). Figure 10 represents the transient plot of temperature versus time of the aft arch model. The thermal/structural analysis results ensured the non-existence of a failure mode in any component of the model.

### SUMMARY and CONCLUSION

The advantage of the high performance transparency design methodology can be summarized as follows: (1) it established a new conceptual design methodology (ICS) code which can provide excellent results for sizing the thickness of the interlayer (prediction of maximum temperature of the structural layer) and also sizing the thickness of the structural layer, and (2) the STAPAT and MAGNA codes were used together and provided capabilities such as finite element based thermal analysis and finite element linear/nonlinear static/dynamic analyses. The methodology procedures were examined for the selected fighter canopy. Based on the results it was concluded that continued development is recommended for MAGNA/STAPAT model generation and postprocessing. It is also recommended that the optimization methodology development be continued at the conceptual and preliminary design level.

### ACKNOWLEDGEMENT

This work was supported by the Air Force AFWAL/FDER Contract F33615-C-3414. The authors express special thanks to Dr. Trent Logan for his valuable support of the program and for his encouragement.

## REFERENCES

1. Mayer, A. H., and Smith, R., "Aircraft Windshield Design with Large Structural Analysis Codes," Aerospace Transparent Material and Enclosures conference, Monterey, CA, January 1989.
2. Edelstein, K.S., and McCarthy, R. E., "Space Shuttle Orbitor Windshield Bird Impact Analysis," ICAS-5.8.3, Jerusalem, Israel, September 1988.
3. Dote, H., and Theodore, K. T., "Structural Analysis and Testing of the Space Orbitor Window System," AIAA 90-qb10r 21st SDM Conference, Seattle, WA, 12-14 May 1980
4. McCarthy, R. E., "MAGNA Computer Simulation of Bird Impact on the TF-15 Aircraft Canopy," 14th Conference on Aerospace Transparent Materials and Enclosures, Scottsdale AZ, July 1983.
5. Soni, M. L., "Finite Element Modeling of Aircraft Transparencies for Bird Impact Response Analysis Using MAGNA," University of Dayton Research Institute, February 1987.
6. McCarthy, R. E., and Gran, M. G., "MAGNA Nonlinear Finite Element Analysis of T-46 Aircraft Windshield Bird Impact," AIAA/AHS/ASEE Aircraft systems, Design & Technology Meeting, Dayton Ohio, October 20-22 1986.
7. "Advanced Transparency Materials," Rockwell International Internal Report NA-88-1639, 20 August 1988.

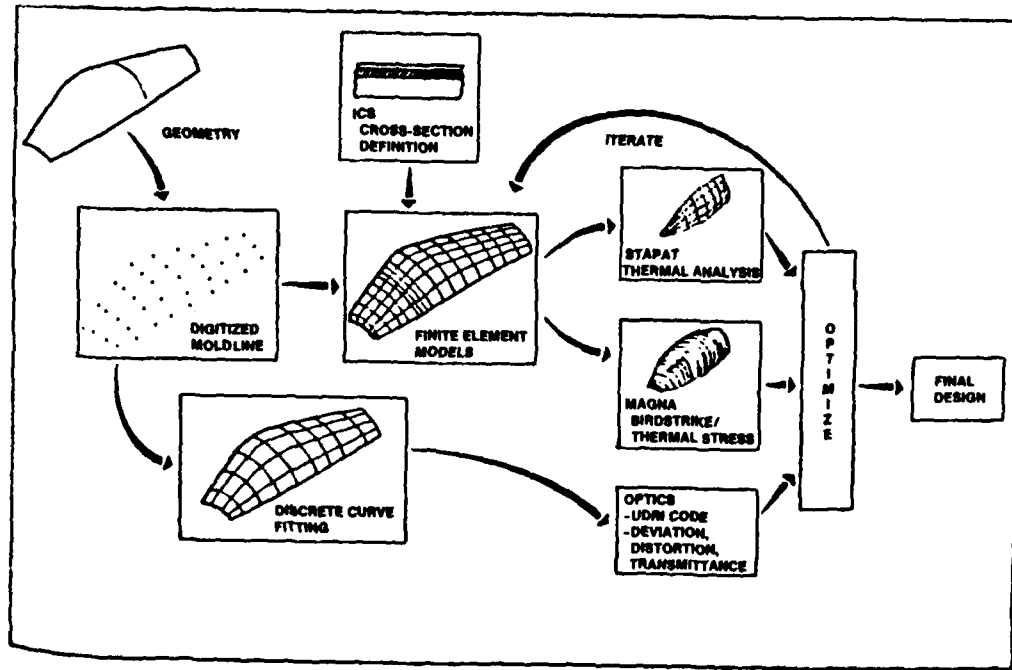


Figure 1. INTEGRATED ANALYSIS METHODOLOGY FOR PRELIMINARY DESIGN

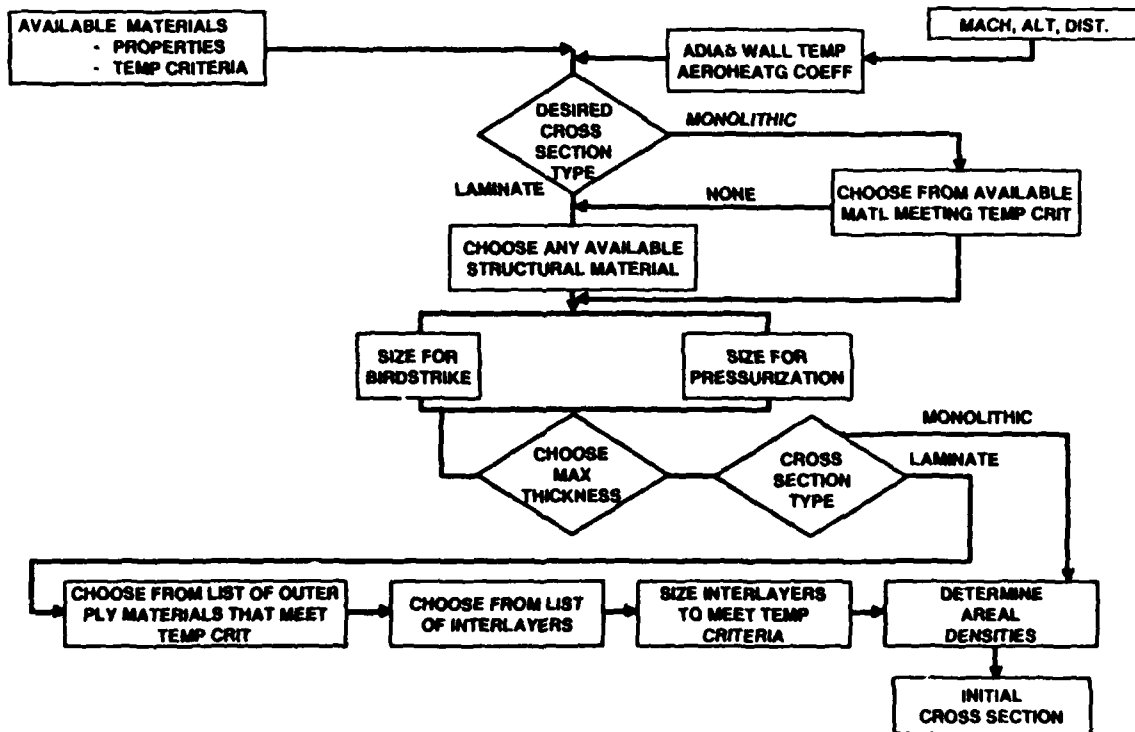


Figure 2. INITIAL CROSS-SECTION FLOW DIAGRAM

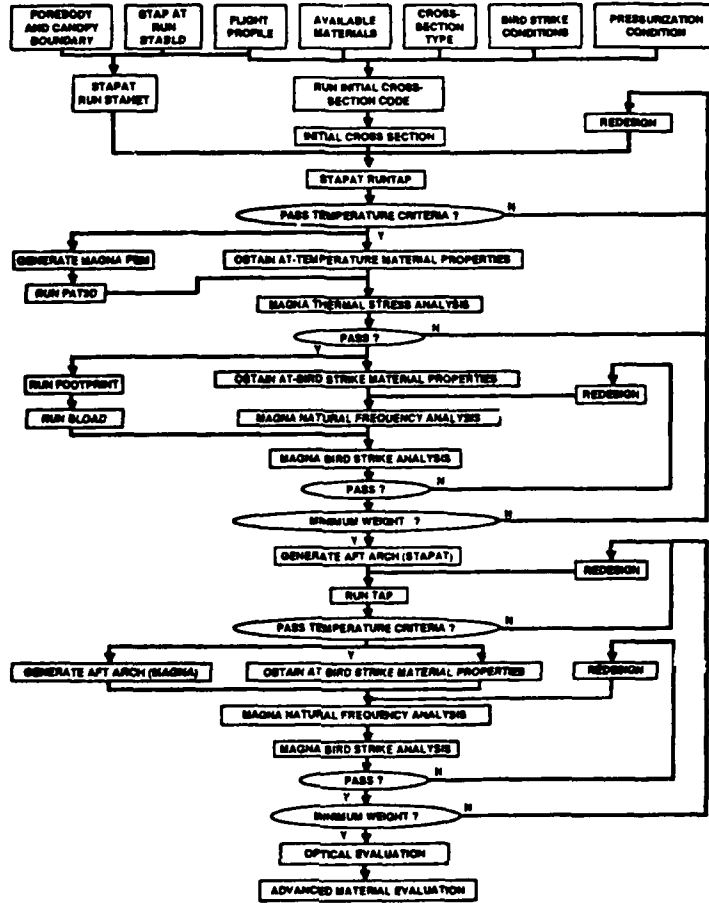


Figure 3. TRANSPARENCY DESIGN METHODOLOGY

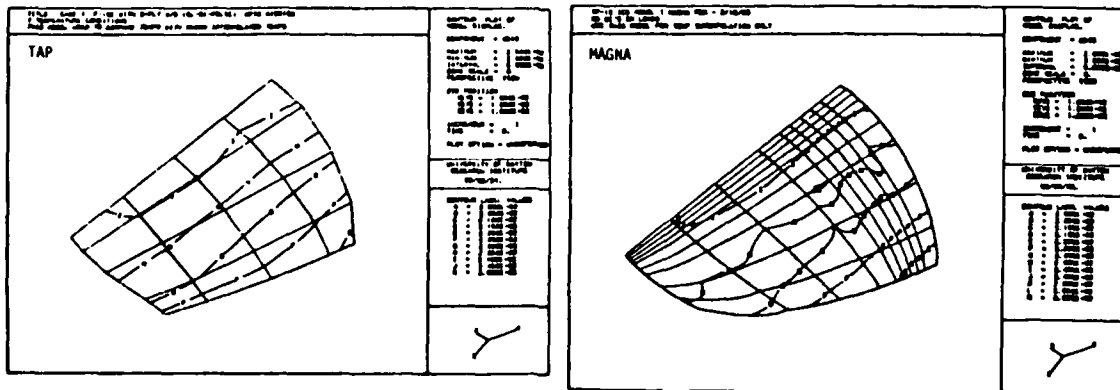


Figure 4. COMPARISON OF STAPAT AND MAGNA TEMPERATURE DISTRIBUTION

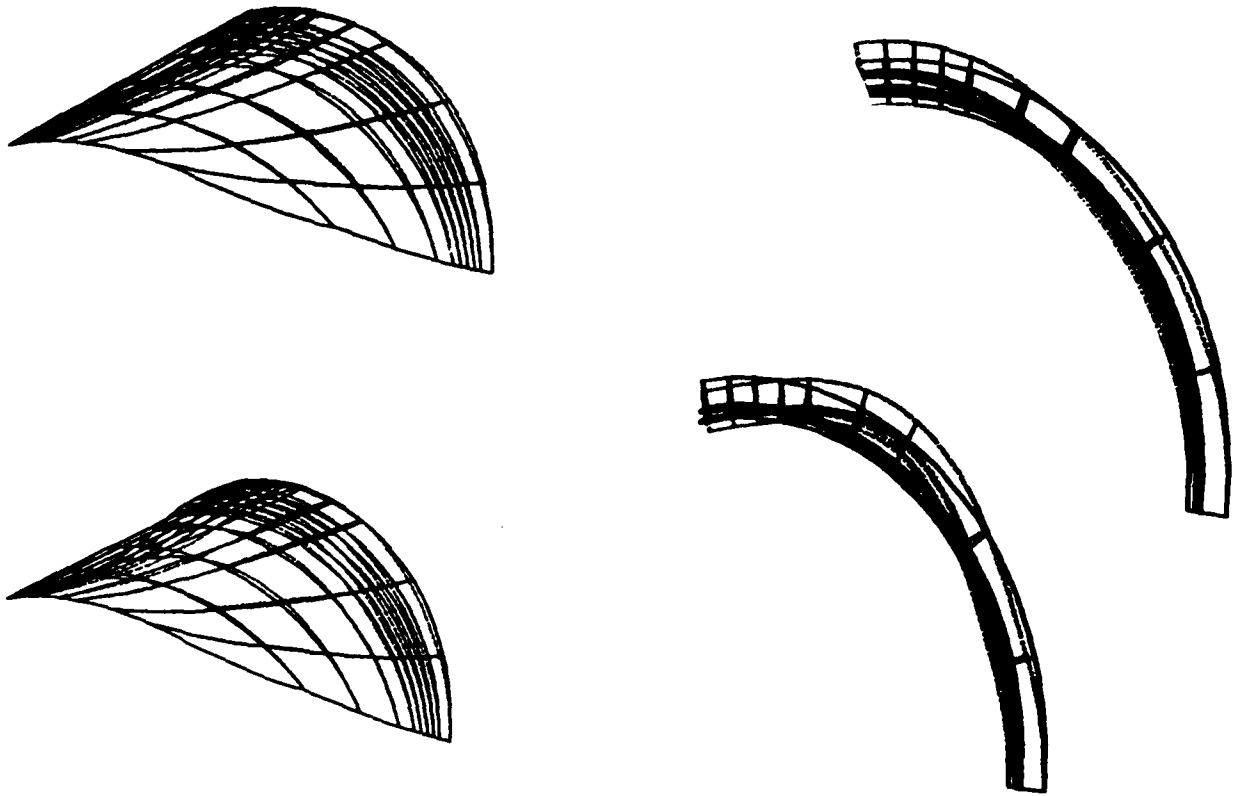


Figure 5. MODE SHAPES FOR TRANSPARENCY AND AFT ARCH

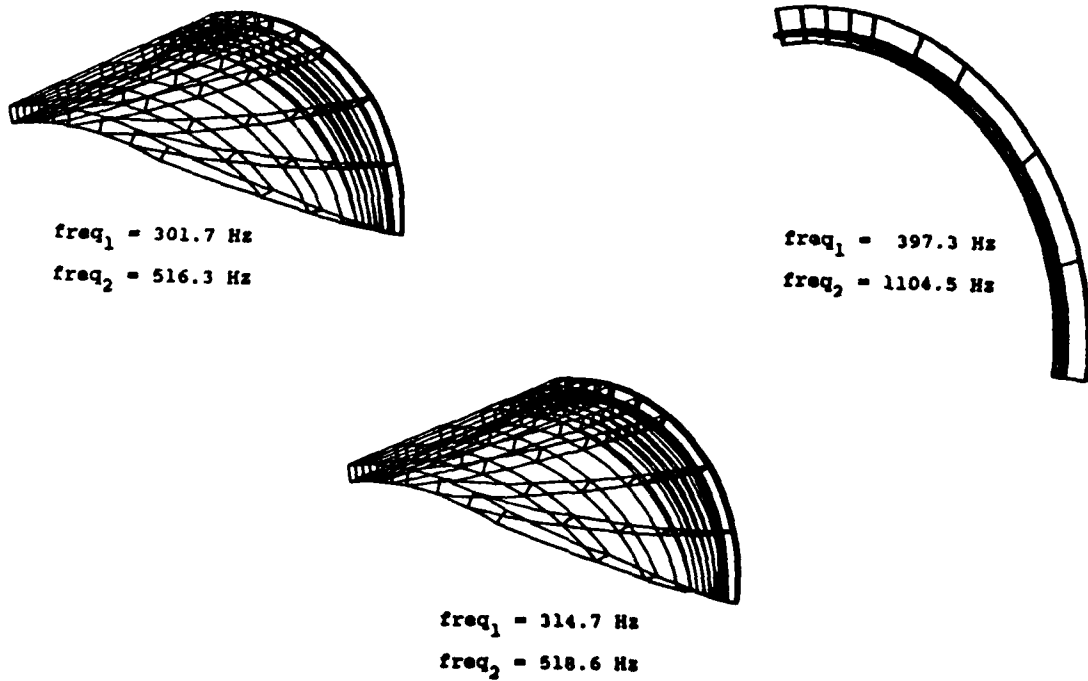
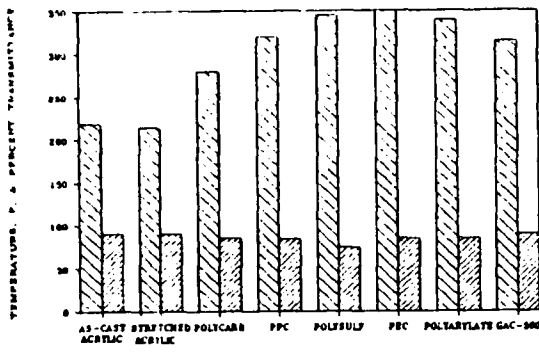
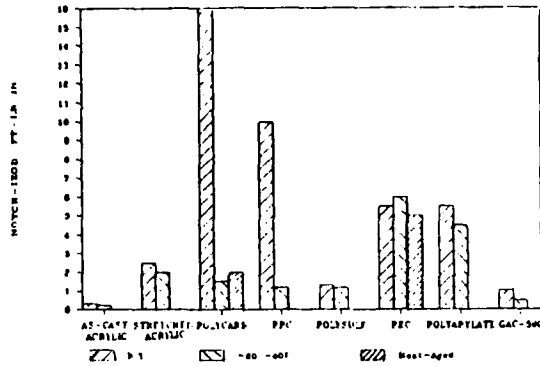


Figure 6. INTEGRATED DESIGN CONCEPT



HEAT DEFLECTION AND TRANSMISSIVITY



TEMPERATURE EFFECT ON IMPACT RESISTANCE

Figure 7. MATERIAL SURVEY TO IDENTIFY THE BEST PRESENT AND NEAR FUTURE CANDIDATES

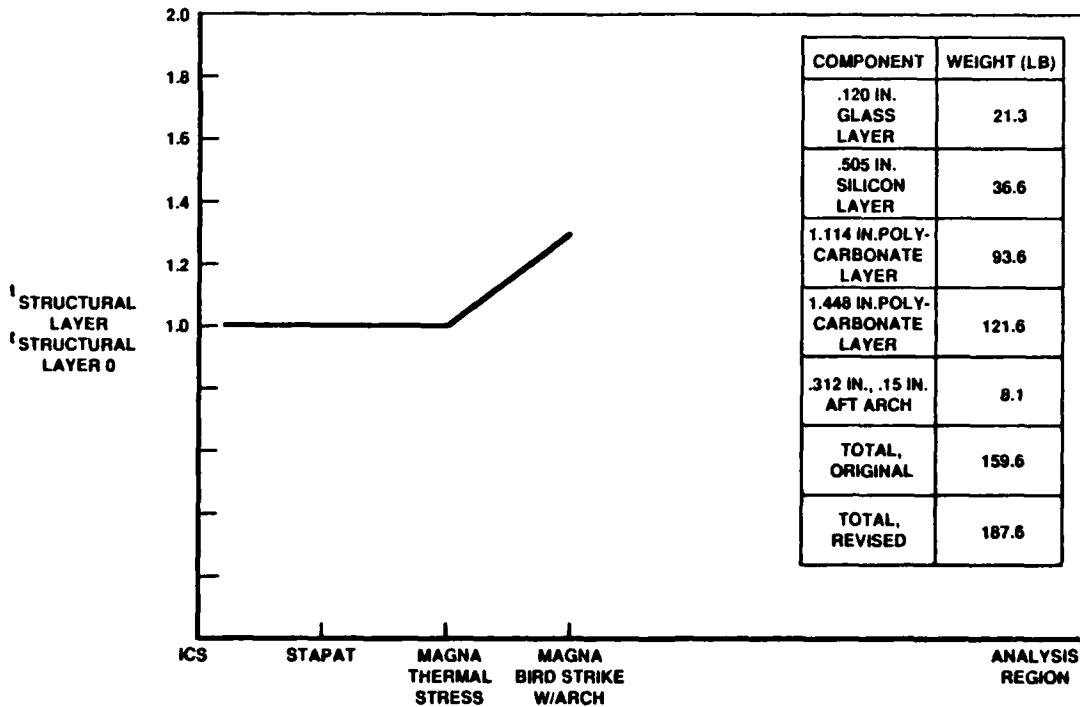


Figure 8. TF-15 WINDSHIELD CONSTRUCTION



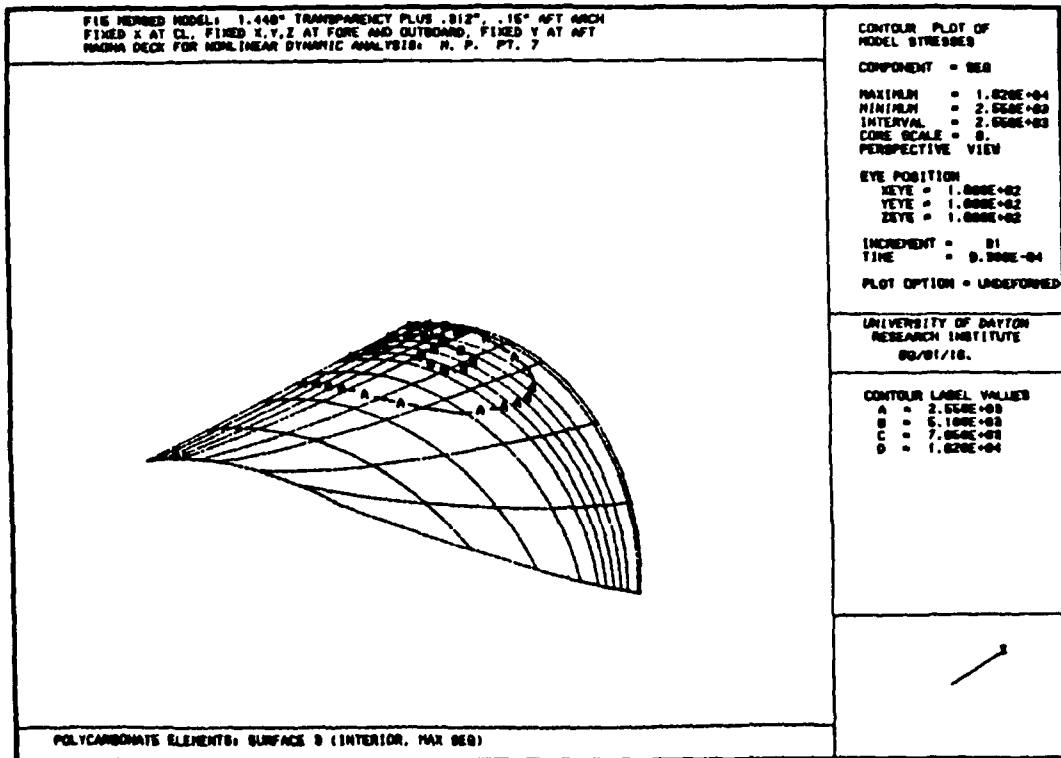


Figure 9. CONTOUR PLOT OF STRESSES FROM BIRD STRIKE

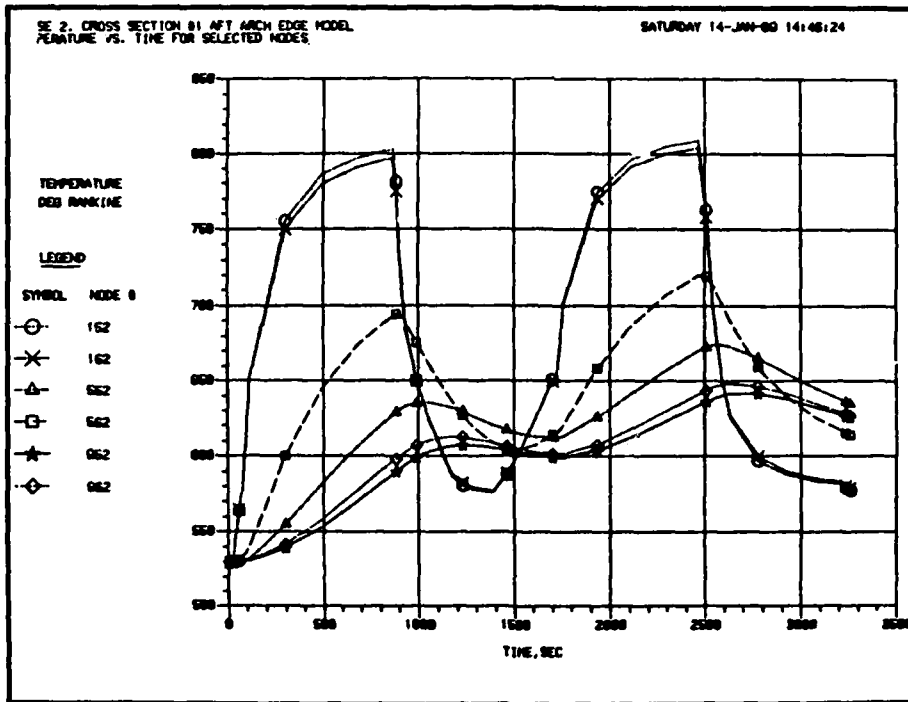


Figure 10. AFT ARCH: TEMPERATURE AS A FUNCTION OF TIME

TABLE 1. SUMMARY OF STATE-OF-THE ART MATERIALS

STRUCTURAL	INTERLAYERS	COATINGS
As-cast acrylic Modified as-cast acrylic Stretched acrylic Polycarbonate Thermal/Strength glass Chemical/Strength glass Borsilicate glass	Sheet Polyvinyl- butyral (PVB) Sheet and cast-in-place urethanes Sheet and cast-in-place silicones	Hard coating for abrasion/Weathering Anti-static and Anti-reflection Conductive coating: gold, indium-oxide indium-tin-oxide

EXPLICIT FINITE ELEMENT TECHNIQUES FOR  
TRANSPARENCY IMPACT ANALYSIS

R. A. Brockman  
T. W. Held

University of Dayton

## EXPLICIT FINITE ELEMENT TECHNIQUES FOR TRANSPARENCY IMPACT ANALYSIS

R. A. Brockman and T. W. Held  
University of Dayton Research Institute  
Dayton, OH 45469 USA

---

### ABSTRACT

Recent advances in computer hardware and vectorization methods make the explicit class of time integration methods attractive for analyzing structural dynamic impact response. Explicit solution methods, which avoid large matrix operations, exploit the characteristics of vector processors such as the CRAY computers. Secondly, these techniques permit relatively sophisticated material and failure modeling as compared with more conventional solution strategies.

This paper reviews the current status of explicit solution techniques for use in birdstrike simulation, and describes recent development activity in this area at the University of Dayton. Items which present particularly difficult challenges include: the formulation of explicit elements capable of representing laminated transparency constructions with very flexible interlayers; constitutive modeling of rate-sensitive transparent materials and interlayers; and modeling of the impacting body and/or the resulting impact loading history. The paper summarizes new developments in finite element technology which remove the most serious disadvantages of explicit solution algorithms.

### INTRODUCTION

Impact phenomena encompass a broad range of structural behavior and response times, which depend upon the stiffness, strength, mass, geometry, velocities, and failure characteristics of the bodies involved. Soft body impacts, such as transparency birdstrikes, are distinctive among impact problems: while the response is often highly nonlinear, critical features of the response may occur either at early times or long (milliseconds) after the impact is finished.

The current generation of birdstrike analysis software [1] has been in use for about ten years, and has been employed in a number of successful applications [2-5]. However, practical transparency analysis remains a time-consuming and laborious process, and in some circumstances the present inventory of analysis tools may not be optimal. For instance, an impact solution may be dominated by complicated contact conditions which preclude the use of large time steps, so that the advantages of an implicit solution are lost. Much of the material in this paper reflects our continuing search for new methods which apply to unusual or more highly nonlinear situations.

This paper discusses explicit finite element solution methods, which are used widely for the numerical solution of shock and wave propagation

problems. This class of algorithms is attractive because it is readily adapted to high performance on the current generation of supercomputers, which combine parallel or pipelined processors, moderate amounts of high-speed memory, and relatively slow disk performance. An added benefit is the ability to implement more detailed material and failure models. In subsequent sections, we present the underlying theory of the explicit technique, compare the characteristics of implicit and explicit integration algorithms, and address some of the problems which remain in the application of these methods to birdstrike simulation.

### THEORETICAL BACKGROUND

This section presents a brief introduction to the theoretical aspects of the explicit finite element solution. The reader familiar with the more traditional implicit finite element solutions implemented in general purpose analysis codes will recognize most of the steps in this development. We begin with the principle of virtual work, and outline the process of spatial discretization common to all transient finite element solution techniques. The result of this step is a semidiscrete system which may be analyzed by numerous time integration algorithms [6]. The remainder of the discussion shows how implicit and explicit time integration schemes derive from the same semi-discretized system of equations.

#### Principle of Virtual Displacements

The starting point for the explicit finite element solution consists of the momentum equations in spatial (Eulerian) coordinates [7]:

$$\sigma_{ji,j} + \rho \bar{b}_i = \rho \dot{v}_i$$

Here  $\sigma_{ij}$  is the Cauchy stress (true stress),  $\rho$  is the current density,  $\bar{b}_i$  is the prescribed body force per unit mass, and  $v_i$  are the velocity components. A superimposed dot denotes a material time derivative. The boundary conditions state that either the displacement assumes a prescribed value, or that the traction condition

$$n_j \sigma_{ji} = \bar{t}_i$$

is satisfied. The prescribed tractions are denoted by  $\bar{t}_i$ , and  $n_i$  are the components of the outward normal to the boundary. One and only one of these conditions applies at every point of the boundary, in each of three linearly independent directions. On contacting surfaces (which we identify by superscripts  $\alpha$  and  $\beta$ ), the velocities satisfy the unilateral constraint:

$$(v_i^\beta - v_i^\alpha) n_i^\alpha \geq 0$$

Whenever the geometric constraint is an equality, the normal component of the tractions on the opposing surfaces must be equal and opposite:

$$\sigma_{ij}^{\alpha} n_i^{\alpha} n_j^{\alpha} + \sigma_{ij}^{\beta} n_i^{\beta} n_j^{\beta} = 0$$

We will assume that the kinematic boundary conditions are satisfied, including the unilateral contact constraints. The weak form of the system above is [8]:

$$\int_V (\sigma_{ji,j} + \rho \bar{b}_i - \rho \dot{v}_i) \delta v_i \, dV + \int_{A_{\sigma}} (\bar{t}_i - n_j \sigma_{ji}) \delta v_i \, dA - \int_{A_{\alpha}} (\sigma_{ij}^{\alpha} n_i^{\alpha} n_j^{\alpha} + \sigma_{ij}^{\beta} n_i^{\beta} n_j^{\beta}) \delta v_i^{\alpha} \, dA = 0$$

The test functions  $\delta v_i$  must vanish where the displacements are prescribed but are arbitrary and independent elsewhere. If  $\delta v_i$  are interpreted as a virtual velocity field, the weak form above represents the rate at which existing forces do work and corresponds to the principle of virtual work. Applying Gauss' divergence theorem and noting that every point of the boundary must belong to  $A_{\sigma}$ ,  $A_{\alpha}$ , the segment  $A_{\beta}$  corresponding to  $A_{\alpha}$ , or  $A_u$  on which  $\delta v_i$  vanishes, one obtains:

$$\int_V \sigma_{ji} \delta v_{i,j} \, dV + \int_V \rho \dot{v}_i \delta v_i \, dV - \int_V \rho \bar{b}_i \delta v_i \, dV - \int_{A_{\sigma}} \bar{t}_i \delta v_i \, dA = 0$$

The unknown quantities in the virtual work equation are the velocity components  $v_i$ , which are the fundamental unknowns, and the stresses  $\sigma_{ij}$ , which are determined from  $v_i$  using the appropriate constitutive relations.

The interpretation of the virtual work principle  $\delta W = 0$  is as follows: among all kinematically admissible velocity fields  $v_i(\mathbf{x}, t)$ , the velocity field which makes  $\delta W = 0$  vanish for arbitrarily chosen test functions  $\delta v_i$  is the true velocity field.

### Finite Element Discretization

Constructing a finite element approximation of the principle involves the following steps:

- express  $\delta W$  as the sum of contributions from individual finite elements:

$$\delta W = \sum_{e=1}^N \delta W^{(e)}$$

- approximate the velocity field within each element in terms of discrete nodal values:

$$v_i^{(e)}(\mathbf{x}, t) = N_J(\mathbf{x}) \cdot V_{iJ}(t)$$

□ approximate the arbitrary test functions  $\delta v_i$  within an element in terms of discrete nodal values:

$$\delta v_i^{(e)}(\mathbf{x}, t) = N_J(\mathbf{x}) \cdot \delta V_{iJ}(t)$$

in which  $\delta V_{iJ}$  are arbitrary and independent.

The  $N_J(\mathbf{x})$  are known functions of position, called shape functions; with this approximation, the unknowns are reduced to the set of nodal values  $V_{iJ}$ , which are functions solely of time. Therefore the resulting system will consist of ordinary differential equations, with time the independent variable. The division of the virtual work expression into contributions from disjoint elements requires that either  $v_i$  be continuous across the element boundaries, or that jump conditions be introduced to account for the unboundedness of the derivatives  $v_{i,j}$ . We choose to select the shape functions  $N_J(\mathbf{x})$  so that the velocity field remains continuous everywhere.

Introducing the finite element approximations in the virtual work expression gives the semidiscrete equation:

$$\sum_{e=1}^N \left[ \int_{V^{(e)}} \sigma_{ji} N_{K,j} \, dV + \int_{V^{(e)}} \rho N_K N_L \dot{V}_{iL} \, dV \right] \delta V_{iK} - \sum_{e=1}^N \left[ \int_{V^{(e)}} \bar{\rho} b_i N_K \, dV + \int_{A_\sigma^{(e)}} \bar{\tau}_i N_K \, dA \right] \delta V_{iK} = 0$$

Since the nodal test function values  $\delta V_{iK}$  are arbitrary and independent, the coefficient of  $\delta V_{iK}$  (consisting of the sum of all bracketed terms) must vanish. This condition yields one equation corresponding to each unconstrained nodal value  $\delta V_{iK}$  (or  $V_{iK}$ ).

We define the internal nodal force vector,

$$F_{iK}^{int} = \sum_{e=1}^N \int_{V^{(e)}} \sigma_{ji} N_{K,j} \, dV$$

the mass matrix,



$$M_{KL} = \sum_{e=1}^N \int_{V(e)} \rho N_K N_L dV$$

and the external force vector,

$$F_{iK}^{ext} = \sum_{e=1}^N \int_{V(e)} \rho \bar{b}_i N_K dV + \int_{A_\sigma(e)} \bar{t}_i N_K dA$$

Then the semidiscrete equations of motion for the finite element model are simply:

$$M_{KL} \ddot{v}_{iL} = F_{iK}^{ext} - F_{iK}^{int}$$

subject to the initial conditions and the prescribed displacement/velocity boundary conditions. To this point, the formulation of both implicit and explicit solution techniques is the same, although the best choice for the element shape functions often is different for the two classes of temporal solutions.

#### Implicit Solution

The most common approach to solving the semidiscrete equations of motion in structural dynamic (as opposed to wave propagation) problems is to adopt an implicit finite difference approximation in time for each degree of freedom. A favorite choice is the trapezoidal rule [10]:

$$\frac{v_{iK}(t+\Delta t) + v_{iK}(t)}{2} \approx \frac{U_{iK}(t+\Delta t) - U_{iK}(t)}{\Delta t}$$

$$\frac{\dot{v}_{iK}(t+\Delta t) + \dot{v}_{iK}(t)}{2} \approx \frac{v_{iK}(t+\Delta t) - v_{iK}(t)}{\Delta t}$$

When the equation of motion is applied at time  $t+\Delta t$  (assuming the state at time  $t$  is known), the difference formulas can be used to eliminate all of the unknowns except  $U_{iK}(t+\Delta t)$ , the nodal displacements at the end of the time step:

$$\frac{4}{\Delta t^2} M_{KL} U_{iL}(t+\Delta t) + F_{iK}^{int}[U(t+\Delta t)] = F_{iK}^{ext} + M_{KL} (\dot{v}_{iL}(t) + \frac{4}{\Delta t} v_{iL}(t) + \frac{4}{\Delta t^2} U_{iL}(t))$$

If  $F_{iK}^{int}$  depends linearly on the nodal displacements at time  $t+\Delta t$ , that is,

$$F_{iK}^{int}[U(t+\Delta t)] = K_{iKjL} U_{jL}(t+\Delta t)$$

then the system resembles an equilibrium system with the "effective" stiffness coefficients

$$K^{eff} = K + \frac{4}{\Delta t^2} M$$

which remain constant unless properties or constraints change or the time step is modified. If the system is nonlinear, the algebraic system must be solved iteratively (usually by some variant of Newton's method).

Since the balance equations at time  $t+\Delta t$  determine the state of the system at  $t+\Delta t$ , the stability properties of the implicit technique are quite good. For linear systems, the trapezoidal rule used above is known to be unconditionally stable; that is, the numerical integration remains stable for any choice of the time step. The method is accurate for frequency components whose period is much larger than  $\Delta t$ ; when the period and time step are similar in magnitude, accuracy degrades quickly (Figure 1). This "low-pass filter" behavior is responsible for the favorable stability properties of the implicit family of integration methods [11].

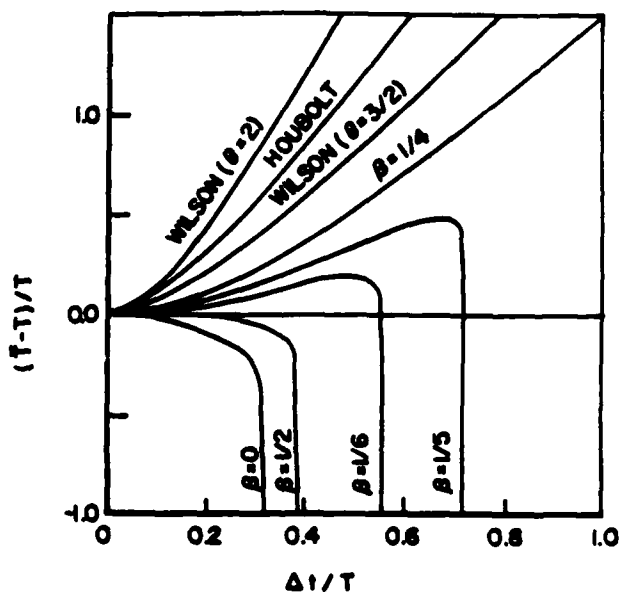


Figure 1. Truncation Error Properties of Several Implicit Methods.

A transparency model of moderate size may contain from 5,000 to 10,000 degrees of freedom, and the stiffness  $K$  (stored in sparse format) occupies several million words of computer storage. While the computational effort required to form, triangularize, and solve the matrix at each iteration is considerable, the most serious problems with efficiency involve input and output. Present-day supercomputers are still too small to cope with the system in high-speed memory, so that disk transfers become the limiting factor in problem throughput.

### Explicit Solution

The explicit solution approach is preferred in the solution of problems of wave propagation and short-duration impact response. The temporal discretization uses the central difference formulas:

$$V_{iK}^{(t+\frac{1}{2}\Delta t)} \approx \frac{U_{iK}^{(t+\Delta t)} - U_{iK}^{(t)}}{\Delta t}$$
$$\dot{V}_{iK}^{(t)} \approx \frac{V_{iK}^{(t+\frac{1}{2}\Delta t)} - V_{iK}^{(t-\frac{1}{2}\Delta t)}}{\Delta t}$$

A typical step in the solution consists of applying the equations of motion at time  $t$  to determine the accelerations:

$$M_{KL} \dot{V}_{iL}^{(t)} = F_{iK}^{ext} - F_{iK}^{int}$$

and then using the finite difference formulas to obtain new velocities

$$V_{iK}^{(t+\frac{1}{2}\Delta t)} = V_{iK}^{(t-\frac{1}{2}\Delta t)} + \dot{V}_{iK}^{(t)} \Delta t$$

and positions:

$$U_{iK}^{(t+\Delta t)} = U_{iK}^{(t)} + V_{iK}^{(t+\frac{1}{2}\Delta t)} \Delta t$$

In practice, the mass matrix  $M_{KL}$  is lumped (made diagonal), so that no equation-solving is required, and in fact the system matrices need never be formed. Krieg and Key [12] show that mass lumping is desirable in explicit solutions, since it tends to counteract the temporal discretization error.

The integration process in this case is conditionally stable; that is, stability is assured only if the time step is less than a critical value. For the central difference method:

$$\Delta t \leq \frac{2}{\omega_{max}}$$

where  $\omega_{max}$  is the highest natural frequency of the discrete system. In practice we bound the highest frequency by determining the maximum element frequency [6], a calculation which can be performed very quickly at each time step.

Because explicit techniques are best suited for solving short-duration dynamic problems, which typically involve nonlinear response, they are less familiar to most engineers than the implicit methods used most commonly for statics and structural dynamics. Explicit finite element methods were first used in the early 1970's [13,14] and now are used extensively for

analyzing ballistic and hypervelocity impact, detonation physics, crash response, forging and high-speed forming, and other highly nonlinear dynamic events [15-18].

### COMPARISON OF IMPLICIT AND EXPLICIT SOLUTIONS

The most effective means of analyzing an impact problem varies with the situation. For short-duration problems which exhibit strong nonlinearity, explicit solution techniques and simple finite elements are preferred. For computing extended-time responses dominated by low-frequency motion, implicit methods and higher-order elements tend to be more effective. Table 1 compares some of the important features of these two families of algorithms.

Given that both methods are capable of achieving correct results, the most "effective" method consumes the least resources: engineering time, modeling and data reduction effort, and computer costs. Some examples may help to illustrate the many factors involved:

- explicit methods may be unsuitable for calculating long-time response if the model contains a few very small elements, since these few elements limit the allowable time step to small values; with implicit methods, no such problem exists;
- the occurrence of contact or strong material nonlinearity in the implicit solution may dictate the use of time steps comparable to those of the explicit solution, destroying the key advantage of the implicit approach; these factors have little or no effect on the explicit solution;
- if the critical response occurs early in the computation, the advantage lies with the explicit solution; as the simulated time increases, implicit techniques become more competitive.

The relative efficiency of competing time integration methods also depends upon the computing environment. Recent developments in supercomputer architecture favor the explicit technique, which is more highly vectorizable and less I/O intensive. In practice, this means that the "break even" point (circumstances for which the two methods are equally effective) has shifted, with some transparency impact problems remaining on each side of the dividing line.

Historically, explicit methods have been handicapped in transparency impact analysis because of the need to analyze layered constructions with widely varying layer moduli [19]. The need to capture the high transverse shear flexibility of these laminated designs required three-dimensional modeling of individual layers, which in turn limited the allowable explicit time step to very small values. The next section of the paper discusses a recent development in element technology which promises to circumvent this problem.

Table 1. Comparison of Implicit and Explicit Solution Methods.

Characteristic	Explicit	Implicit
<b>SOLUTION TIME STEP</b> <ul style="list-style-type: none"> <li>• Allowable step size</li> <li>• Typical time step (ms)</li> <li>• Number of time steps (typical)</li> <li>• Step size limited by</li> </ul>	Small 0.001 10-100K Stability	Large 0.1 100-1000 Accuracy
<b>TREATMENT OF NONLINEARITIES</b> <ul style="list-style-type: none"> <li>• Geometric nonlinearities</li> <li>• Analysis of contact &amp; impact</li> <li>• Material model</li> <li>• Equation of state</li> <li>• Failure model implementation</li> </ul>	Arbitrary Straightforward Arbitrary Arbitrary Straightforward	Arbitrary Difficult Usually simple Linear Difficult
<b>FINITE ELEMENTS</b> <ul style="list-style-type: none"> <li>• Finite elements (typical)</li> <li>• Integration points per element</li> <li>• Element code vectorizable</li> </ul>	Low order 1 Yes	Higher order 8-27 Somewhat
<b>SOLUTION TECHNIQUE</b> <ul style="list-style-type: none"> <li>• Simultaneous equation solution</li> <li>• Model numbering, bandwidth</li> <li>• I/O effort per solution cycle</li> <li>• Basic solution vectorizable</li> </ul>	None Unimportant Small Yes	Every cycle Crucial Large Partially
<b>PROBLEM SIZE STATISTICS</b> <ul style="list-style-type: none"> <li>• CPU time versus model size</li> <li>• CPU time versus numbering</li> <li>• I/O time for complete solution</li> <li>• Routine problem size (Cray X/MP)</li> </ul>	Linear Independent Small 100,000 DOF	Variable Variable Large 10,000 DOF
<b>IMPLEMENTATION</b> <ul style="list-style-type: none"> <li>• Data structure and handling</li> <li>• Overall program complexity</li> <li>• Program size (FORTRAN lines)</li> </ul>	Simple Low 10-50,000	Complex High 100,000+

## FINITE ELEMENTS FOR LAYERED CONSTRUCTIONS

This section presents a new finite element approximation for plates and shells having large stiffness variations from layer to layer. Layered structures of this type often require detailed and expensive models, since conventional plate and shell finite elements fail to reproduce the correct transverse shear strain distributions through the wall thickness. The present approach requires a single layer of elements having six engineering freedoms per node, regardless of the number of layers. The approximation discussed here uses closed-form elasticity solutions to develop transverse shear flexibility corrections, which bring this contribution to the energy into line with that caused by pure bending, twisting, and extension. For large displacement problems, the technique may be applied in corotational coordinates. Changes in stiffness caused by plasticity can be accounted for by recomputing the flexibility corrections based upon instantaneous moduli.

After a brief summary of the shear-flexible plate theory, we describe the basic aspects of the shear flexibility correction as it applies to layered isotropic materials. The method is applied to nonlinear problems through the use of a suitable corotational coordinate system. Numerical examples demonstrate the application of the proposed technique to thick composite laminates, as well as sandwich panels with extreme variations in layer stiffness.

### Mindlin-Reissner Plate Theory

The Mindlin-Reissner theory of plates [20] is based upon kinematic assumptions through which the displacement components (U,V,W) at a generic point in the plate are determined by the midsurface components (u,v,w) and two cross-sectional rotations ( $\theta_x, \theta_y$ ). If z is the direction normal to the plate midsurface, then:

$$\begin{aligned} U(x,y,z) &= u(x,y) + z\theta_y(x,y) \\ V(x,y,z) &= v(x,y) - z\theta_x(x,y) \\ W(x,y,z) &= w(x,y) \end{aligned}$$

We define the generalized displacement, strain, and stress vectors by:

$$\begin{aligned} \mathbf{u}^T &= [ u, v, w, \theta_x, \theta_y ] \\ \boldsymbol{\epsilon}^T &= [ \epsilon_x, \epsilon_y, \gamma_{xy}, \kappa_x, \kappa_y, \kappa_{xy}, \gamma_{xz}, \gamma_{yz} ] \\ \boldsymbol{\sigma}^T &= [ N_x, N_y, N_{xy}, M_x, M_y, M_{xy}, Q_{xz}, Q_{yz} ] \end{aligned}$$

In linear situations, the three quantities above are related linearly; that is,  $\boldsymbol{\epsilon} = \mathbf{B}\mathbf{u}$  and  $\boldsymbol{\sigma} = \mathbf{C}\boldsymbol{\epsilon}$ , in which:

$$B = \begin{bmatrix} \partial/\partial x & 0 & 0 & 0 & 0 \\ 0 & \partial/\partial y & 0 & 0 & 0 \\ \partial/\partial y & \partial/\partial x & 0 & 0 & 0 \\ 0 & 0 & 0 & 0 & \partial/\partial x \\ 0 & 0 & 0 & -\partial/\partial y & 0 \\ 0 & 0 & 0 & -\partial/\partial x & \partial/\partial y \\ 0 & 0 & \partial/\partial x & 0 & 1 \\ 0 & 0 & \partial/\partial y & -1 & 0 \end{bmatrix}$$

and

$$C = \begin{bmatrix} A_{11} & A_{12} & A_{16} & B_{11} & B_{12} & B_{16} & 0 & 0 \\ A_{12} & A_{22} & A_{26} & B_{12} & B_{22} & B_{26} & 0 & 0 \\ A_{16} & A_{26} & A_{66} & B_{16} & B_{26} & B_{66} & 0 & 0 \\ B_{11} & B_{12} & B_{16} & D_{11} & D_{12} & D_{16} & 0 & 0 \\ B_{12} & B_{22} & B_{26} & D_{12} & D_{22} & D_{26} & 0 & 0 \\ B_{16} & B_{26} & B_{66} & D_{16} & D_{26} & D_{66} & 0 & 0 \\ 0 & 0 & 0 & 0 & 0 & 0 & A_{44} & A_{45} \\ 0 & 0 & 0 & 0 & 0 & 0 & A_{45} & A_{55} \end{bmatrix}$$

The elastic stiffness resultants  $A_{ij}$ ,  $B_{ij}$ , and  $D_{ij}$  are defined as is usual in laminated plate theory [21]; that is:

$$(A_{ij}, B_{ij}, D_{ij}) = \int_{-t/2}^{t/2} \bar{Q}_{ij}(1, z, z^2) dz$$

in which  $\bar{Q}_{ij}$  are components of the elasticity tensor at a point, corrected to reflect the constraint of zero normal stress, and referred to a common system of coordinates.

The assumption that the tangential displacements (U,V) vary linearly through the plate thickness provides an extremely crude representation of the transverse shear strain field. For monolithic, isotropic elements, a uniform reduction factor often is applied to the shear strain energy to obtain more realistic behavior. Equating the transverse shear strain energy consistent with the assumed displacements to that of a parabolic strain field satisfying the equilibrium conditions yields the correction factor of 5/6, which is used commonly for isotropic plates and shells.

In the present work, we rely on a generalization of this idea first proposed by Whitney [22] for arbitrary wall constructions. The correction is approximate, but proves sufficient to bring the shear strain energy into line with that of other modes of deformation, in a way which reflects the relative flexibility of these modes for a given material layup. Several investigators have employed a similar concept for fiber-reinforced composite laminates [23-27].

Consider first a layered construction for which the shear strains and resultant forces are related by:

$$\begin{bmatrix} Q_{xz} \\ Q_{yz} \end{bmatrix} = \begin{bmatrix} k_1 A_{44} & 0 \\ 0 & k_2 A_{55} \end{bmatrix} \begin{bmatrix} \gamma_{xz} \\ \gamma_{yz} \end{bmatrix}$$

Based solely on the elastic stress-strain relationship of the material, factors  $k_1$  and  $k_2$  should both equal one. However, due to the excessive constraint imposed by the kinematic assumptions of the plate theory, the strains  $\gamma_{iz}$  produced by given shear forces  $Q_{iz}$  are too large over much of the plate thickness. Accordingly, the total strain energy predicted is too large, and the approximation appears "too stiff." This error does not respond to mesh refinement, since the displacement field approximation through the thickness remains linear. Our intent is to select values for  $k_1$  and  $k_2$  which lead to stored energies of a more reasonable magnitude, and thus yield better element behavior.

Since the shear resultants are uncoupled for the case noted above, the basic aspects of the method can be outlined within a single plane. Below, we discuss the determination of  $k_1$ , the shear correction factor for the (x,z) plane.

The shear corrections suggested by Whitney [22] depend upon the assumption of cylindrical bending, for which an analytical relationship may be established between the local bending stress and the transverse shear force resultant [28]:

$$\sigma_{x,x}^{(m)} = \frac{-Q_{11}^{(m)}}{D} (B_{11} - A_{11}z) Q_{xz}$$

The superscript (m) refers to a particular layer within the laminate cross-section, and parameter D is defined by:

$$D = D_{11} A_{11} - B_{11}^2$$

When combined with the analytic solution, the equilibrium equation

$$\sigma_{x,x}^{(m)} + \sigma_{xz,z}^{(m)} = 0$$



can be integrated through the plate thickness to obtain the shear stress within a layer:

$$\sigma_{xz}^{(m)} = \frac{1}{2D} [a^{(m)} + Q_{11}^{(m)} z (2B_{11} - A_{11} z)] Q_{xz}$$

The constants of integration  $a^{(m)}$  are determined by the condition that  $\sigma_{xz}$  be continuous at the layer interfaces, and from the free surface boundary condition at either the upper or lower surface. From the condition that  $\sigma_{xz} = 0$  at  $z = -t/2$ , we obtain:

$$a^{(1)} = \frac{1}{4} Q_{11}^{(1)} t (A_{11} t + 4B_{11})$$

in which  $m=1$  refers to the bottom layer of the laminate. Letting  $z_\ell^{(m)}$  be the lower surface of layer  $m$ , the interface continuity conditions for  $m=2, 3, \dots$  give:

$$a^{(m)} = a^{(m-1)} + [Q_{11}^{(m)} - Q_{11}^{(m-1)}] (A_{11} z_\ell^{(m)} - 2B_{11}) z_\ell^{(m)}$$

With the above definitions, the strain energy density in any layer may be written in the form:

$$v^{(m)} = \frac{1}{2} g^{(m)}(z) Q_{xz}$$

with

$$g^{(m)}(z) = \frac{1}{G_{xz}^{(m)}} \left[ \frac{a^{(m)}}{2D} + \frac{Q_{11}^{(m)} z}{2D} (2B_{11} - A_{11} z) \right]^2$$

Integrating the shear strain energy through the laminate thickness, and equating the result to the total strain energy per unit area obtained from the plate theory resultants,

$$V = \frac{Q_{xz}^2}{2k_1 A_{55}}$$

we obtain for the shear correction factor:

$$k_1 = \left[ A_{44} + \int_{-t/2}^{t/2} g^{(m)}(z) dz \right]^{-1}$$

The remaining factor  $k_2$  may be found in a similar fashion, using the appropriate elastic constants for the  $(y, z)$  plane.

### Example: Cylindrical Bending of a [0/90] Laminate

The semi-infinite thick plate shown in Figure 2 is subjected to a sinusoidal pressure load  $q(x) = q_0 \sin(\pi x/a)$ , and is simply supported on its lateral edges. The  $0^\circ$  direction is the fiber direction in the upper layer, and corresponds to the infinite ( $y$ ) direction. The material properties are  $E_L/E_T=25$ ,  $G_{LT}/E_T=0.5$ ,  $G_{TT}/E_T=0.2$ , and  $\nu_{LT}=\nu_{TT}=0.25$ . The plate has a width  $2a=24$  and thickness  $t=6$ . An exact elasticity solution of this problem has been presented by Pagano [29], and finite element results using independent layer rotations are reported by Palazotto and Witt [30].

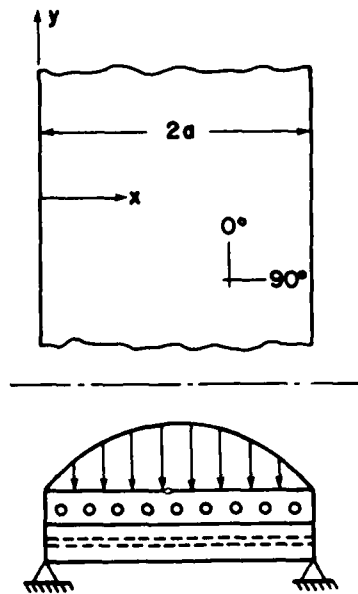


Figure 2. Thick [0/90] Laminated Plate.

The plate is modeled using ten elements over half the width, with symmetry conditions applied at the centerline. Transverse shear stresses in the element nearest the support are shown in Figure 3. The results are in reasonable agreement with the exact solution, with the peak shear stress being overestimated by about eight percent. The finite element solution of Ref. [29], using 30 elements with independent rotational degrees of freedom in each layer, appears to overestimate the maximum shear stress by three to four percent, based on graphical results.

This example demonstrates the effectiveness of the shear-corrected plate element in modeling the flexibility of a very thick laminate. A fringe benefit of the method is the detail with which transverse stresses may be determined within the cross-section. Notice that the stress data shown in Figure 3 are obtained from a single sampling point within a four-node quadrilateral element.

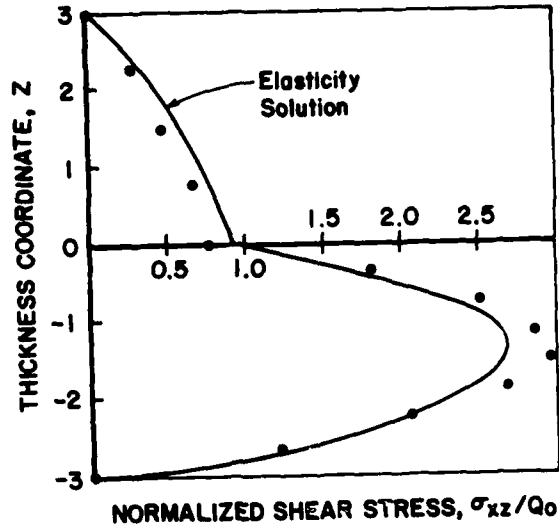


Figure 3. Transverse Shear Stresses in Thick [0/90] Plate.

Example: Rectangular Sandwich Plate

A square sandwich panel (Figure 4) is subjected to a uniform pressure load  $q_0$ . The three-layer plate is 50 inches on each side, with identical aluminum face sheets ( $E=10.5 \times 10^6$ ,  $\nu=0.3$ ,  $\tau_f=0.015$ ) and a cellular honeycomb core ( $G=50,000$ ,  $\tau_c=1.0$ ). All edges of the panel are completely fixed.

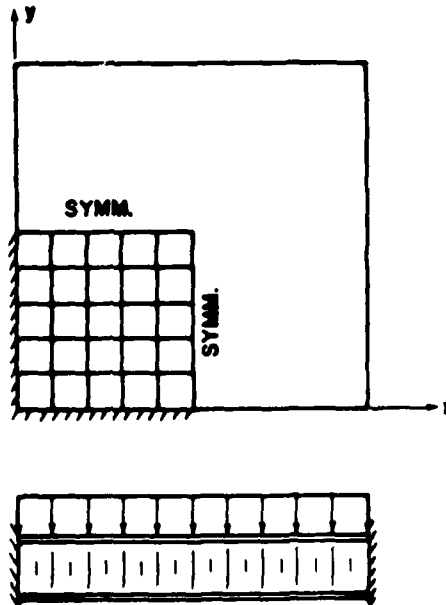


Figure 4. Rectangular Sandwich Panel.

The present solution uses a 5x5 mesh of four-node quadrilateral finite elements in one quadrant of the plate. The linear static solution yields a transverse deflection at the center  $w_c = 0.09285$ . This value compares well (2.2%) with the analytical solution obtained by Kan and Huang [31], which gives  $w_c = 0.09497$ . The finite element solutions presented in [32] and [33] achieve comparable accuracy with more than twice as many degrees of freedom and considerably more complicated elements.

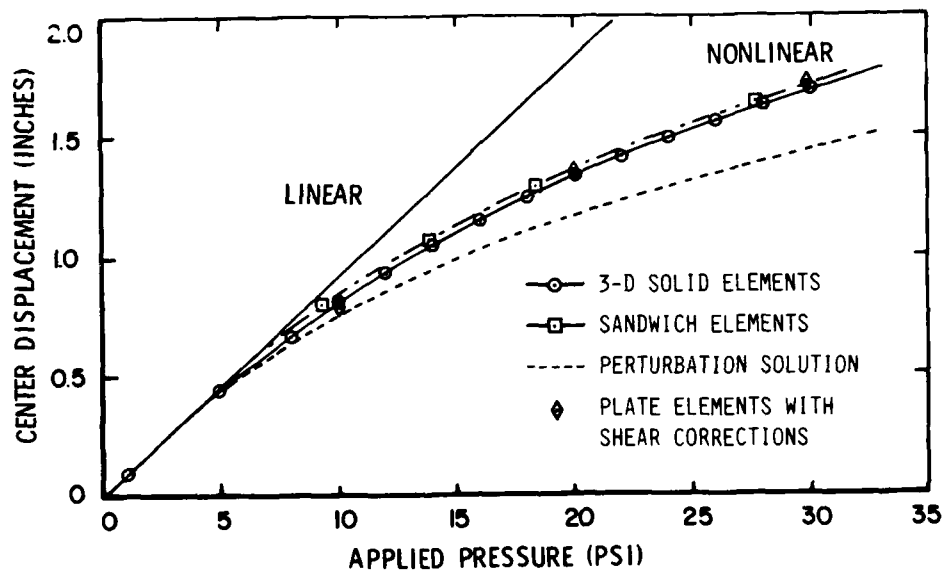


Figure 5. Nonlinear Static Response of Sandwich Panel.

Figure 5 shows the nonlinear response of the panel for pressures up to 30 psi. Notice that the analytical solution and the shear-corrected shell results are in good agreement until the deflection of the plate approaches its thickness, which represents the approximate limit of validity of the perturbation solution in [31]. The nonlinear analysis uses a corotational coordinate system to account for finite displacements and rotations, with shear corrections being applied in a coordinate system which rotates with each finite element.

#### Dynamic Solutions

A number of dynamic solutions have been performed as well with the shear-corrected plate/shell formulation, but are not presented here due to space limitations. The natural frequencies of composite laminates, thick sandwich panels, and layups typical of operational transparency laminates have been predicted successfully, with accuracy comparable to that of solid models with distinct elements in each layer. Presently we are investigating the performance of the shear-corrected elements in transient problems, both linear and nonlinear.

## SOFT-BODY IMPACT MODELING

One other troublesome aspect of transparency impact simulation is the need to predict the impact loading distribution as a function of both time and spatial position. The loading and structural response are known to be strongly coupled in certain cases [34,35], so the impact pressures cannot be predicted independently of the transparency motions.

The most common procedure in birdstrike analysis applications has been to use ad hoc loading models based upon experimental soft-body impact data [36]. The techniques described in References 34 and 35 are typical of this approach. While this general approach has been used successfully in several applications, the simulation cannot be performed with high confidence without experimental birdstrike data. Typically, these data are used to estimate the duration of loading and the spatial distribution of the impact pressure, and to substantiate the results of the computation. Such a heavy dependence upon experimental information limits the extent of structural modifications which can be studied without further testing.

Thus far, no modeling techniques have been developed which permit an accurate modeling of the soft-body deformation during bird impact analysis. The approach used in [37] has been used successfully in the solution of some relatively simple test cases, but has yet to be used and validated for realistic applications. The primary source of the difficulty is the fluid-like behavior of the impacting body. Treated as a "solids" (Lagrangian) problem, the mesh may become tangled due to the extremely large deformation which occurs. As a fluid dynamics problem cast in Eulerian terms, the entire boundary presents severe computational difficulties, since each point must satisfy either a free-surface condition or a contact constraint with the (Lagrangian) structure mesh.

Recent activity in this area at UDRI has focused upon Lagrangian (moving) meshes for the soft body, used with explicit time integration. Although several open questions remain concerning the constitutive model for the impacting body, we have had some success using a solid model with very low shear strength and a nonlinear equation of state. Figure 6 shows some typical results for oblique impact of an idealized cylindrical "bird" on a rigid wall.

### SUMMARY

Explicit time integration methods offer several advantages for impact analysis of aircraft transparency systems. Recent developments in finite element approximations have removed some restrictions which historically have discouraged the use of explicit solvers, particularly for laminated transparencies. This paper discusses the basic foundations of explicit finite element solution methods, recent developments in linear and nonlinear finite elements for layered structures, and some current activities in soft-body impact modeling.

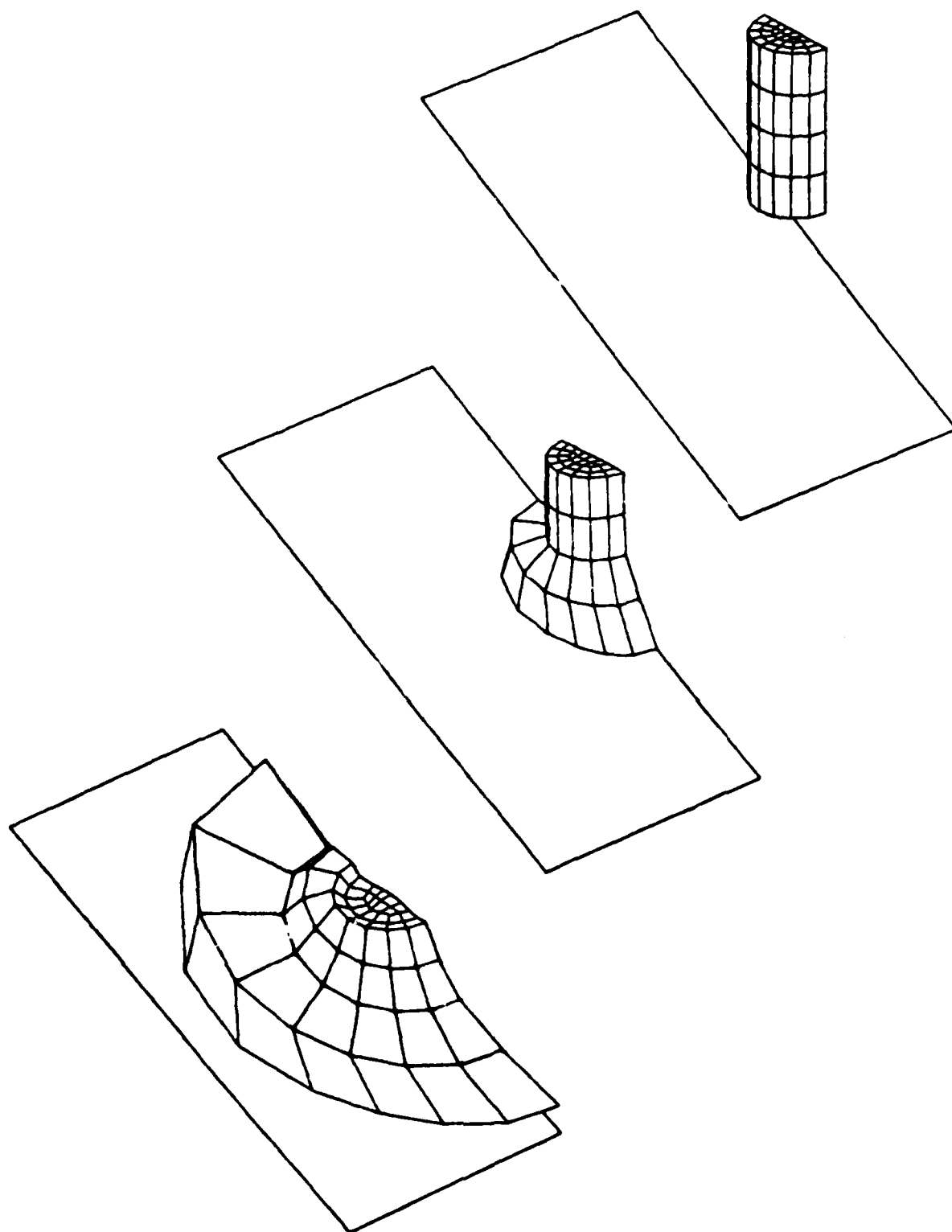


Figure 6. Simulation of Soft Body Impact on a Rigid Surface.

## REFERENCES

1. R. A. Brockman, MAGNA (Materially And Geometrically Nonlinear Analysis), Part I - Finite Element Analysis Manual, AFWAL-TR-82-3098, Part I, Air Force Wright Aeronautical Laboratories, Wright Patterson Air Force Base, Ohio (1982)
2. R. E. McCarty, MAGNA Computer Simulation of Bird Impact on the TF-15 Aircraft Canopy, in S. A. Morolo (ed.), Proceedings of the 14th Conference on Aerospace Transparent Materials and Enclosures, AFWAL-TR-83-4154, Air Force Wright Aeronautical Laboratories, Wright-Patterson Air Force Base, Ohio, 973-1008 (1983)
3. R. E. McCarty, Analytic Assessment of Bird Impact Resistant T-46A Aircraft Windshield System Designs using MAGNA, 15th Conference on Aerospace Transparent Materials and Enclosures, Monterey, CA (1989)
4. M. P. Bouchard, Finite Element Analysis of the B-1B Windshield System, 15th Conference on Aerospace Transparent Materials and Enclosures, Monterey, CA (1989)
5. R. E. McCarty, MAGNA Analysis of Space Shuttle Orbiter Windshield System Bird impact Protection, 15th Conference on Aerospace Transparent Materials and Enclosures, Monterey, CA (1989)
6. T. Belytschko, An Overview of Semidiscretization Procedures, in T. Belytschko and T. J. R. Hughes (eds.), Computational Methods for Transient Analysis, Chapter 1, North-Holland Co., Amsterdam (1983)
7. L. E. Malvern, An Introduction to the Mechanics of a Continuous Medium, Prentice-Hall Co., Englewood Cliffs, N.J. (1969)
8. J. N. Reddy, Introduction to the Finite Element Method, McGraw-Hill Co., New York (1984)
9. J. N. Reddy, Energy and Variational Methods in Applied Mechanics, John Wiley & Sons, New York (1984)
10. N. M. Newmark, A Method of Computation for Structural Dynamics, J. Eng. Mech. Div. 85, 67-94 (1959)
11. T. J. R. Hughes, Analysis of Transient Algorithms with Particular Reference to Stability Behavior, in T. Belytschko and T. J. R. Hughes (eds.), Computational Methods for Transient Analysis, Chapter 2, North-Holland Co., Amsterdam (1983)
12. R. D. Krieg and S. W. Key, Transient Shell Response by Numerical Time Integration, Int. J. Num. Meth. Engng. 17, 273-286 (1973)
13. R. Chiapetta, T. Belytschko, and J. Rouse, A Computer Code for Dynamic Stress Analysis of Media-structure Problem with Nonlinearities (SAMSON), AFWL-TR-72-104, Air Force Weapons Laboratory, Kirtland AFB, New Mexico (1973)

14. S. W. Key, HONDO - A Finite Element Computer Program for the Large Deformation Dynamic Response of Axisymmetric Solids, SLA-74-0039, Sandia National Laboratories, Albuquerque, New Mexico (1974)
15. J. A. Zukas, T. Nicholas, H. F. Swift, L. B. Greszczuk, and D. R. Curran, Impact Dynamics, John Wiley & Sons (1982)
16. G. R. Johnson, D. D. Colby, and D. J. Vavrick, Three Dimensional Computer Code for Dynamic Response of Solids to Intense Impulsive Loads, Int. J. Num. Meth. Engng. **14**, 1865-1871 (1979)
17. G. L. Goudreaux and J. O. Hallquist, Recent Developments in Large-Scale Finite Element Lagrangian Hydrocode Technology, Comp. Meth. Appl. Mech. Engng. **33**, 725-757 (1982)
18. C. E. Anderson, Jr., An Overview of the Theory of Hydrocodes, Int. J. Impact Engng. **5**, 33-59 (1987)
19. R. A. Brockman, Current Problems and Progress in Aircraft Transparency Impact Analysis, in S. A. Morolo (ed.), Proceedings of the 14th Conference on Aerospace Transparent Materials and Enclosures, AFWAL-TR-83-4154, Air Force Wright Aeronautical Laboratories, Wright-Patterson Air Force Base, Ohio, 1058-1082 (1983)
20. R. D. Mindlin, Influence of Rotatory Inertia and Shear on the Bending of Elastic Plates, J. Appl. Mech. **18**, 1031-1036 (1951)
21. R. M. Jones, Mechanics of Composite Materials, Scripta Book Co., Washington, D. C. (1975)
22. J. M. Whitney, Shear Correction Factors for Orthotropic Laminates under Static Load, J. Appl. Mech. **40**, 302-304 (1973)
23. T. S. Chow, On the Propagation of Flexural Waves in an Orthotropic Laminated Plate and its Response to an Impulsive Load, J. Comp. Mats. **5**, 306-319 (1971)
24. T. S. Chow, Theory of Unsymmetric Laminated Plates, J. Appl. Physics **46**, 219-221 (1975)
25. A. K. Noor, Stability of Multilayered Composite Plates, Fibre Sci. Tech. **8**, 81-89 (1975)
26. S. N. Chatterjee and S. V. Kulkarni, Shear Correction Factors for Laminated Plates, AIAA J. **17**(5), 498-499 (1979)
27. A. K. Noor and W. S. Burton, Stress and Free Vibration Analyses of Multilayered Composite Plates, Compos. Struc. **11**(2), (1989)
28. J. M. Whitney and N. J. Pagano, Shear Deformation in Heterogeneous Anisotropic Plates, J. Appl. Mech. **37**, 1031-1036 (1970)
29. N. J. Pagano, Exact Solutions for Rectangular Bidirectional Composites and Sandwich Plates, J. Comp. Mats. **4**, 20-34 (1970)



30. A. N. Palazotto and W. P. Witt, Formulation of a Nonlinear Compatible Finite Element for the Analysis of Laminated Composites, Comput. Struct., 21, 1213-1234 (1985)
31. H. P. Kan and J. C. Huang, Large Deflection of Rectangular Sandwich Plates, AIAA J., 5, 1706-1708 (1967)
32. G. R. Monforton, Discrete Element, Finite Displacement Analysis of Anisotropic Sandwich Shells, Ph.D. thesis, Case Western Reserve Univ., (1970)
33. R. A. Brockman, MAGNA: A Finite Element System for Three-Dimensional Static and Dynamic Structural Analysis, Comp. Struct., 13, 415-423 (1981)
34. B. S. West and R. A. Brockman, Evaluation of Bird Load Models for Dynamic Analysis of Aircraft Transparencies, AFWAL-TR-80-3092, Air Force Wright Aeronautical Laboratories, Wright-Patterson Air Force Base, OH (1980)
35. R. E. McCarty, Three Dimensional Nonlinear Dynamic Finite Element Analysis for the Response of a Thick laminated Shell to Impact Loads, Proc. AIAA/ASME/ASCE/AHS 26th Structures, Structural Dynamics, and Materials Conference, Orlando, Florida (1985)
36. J. R. Barber, H. R. Taylor, and J. M. Wilbeck, Bird Impact Forces and Pressures on Rigid and Compliant Targets, AFFDL-TR-77-60, Flight Dynamics Laboratory, Wright-Patterson Air Force Base, Ohio (1978)
37. R. A. Brockman, Finite Element Analysis of Soft-Body Impact, AFWAL-TR-84-3035, Air Force Wright Aeronautical Laboratories, Wright-Patterson Air Force Base, OH (1985)

FINITE ELEMENT ANALYSIS OF THE B-1B AIRCRAFT  
WINDSHIELD SYSTEM

Michael P. Bouchard  
William R. Braisted

University of Dayton

## Finite Element Analysis of the B-1B Aircraft Windshield System

Michael P. Bouchard  
William R. Braisted

University of Dayton Research Institute  
Dayton, Ohio

January 1989

### ABSTRACT

This paper discusses analyses which supported a study aimed at eliminating B-1B windshield problems which surfaced when the aircraft became operational. Optics and durability were immediately degraded by delamination. The many edge attachments made windshield changeout difficult and time-consuming, thereby affecting supportability. The objective of these analyses was to evaluate the impact of design configuration changes proposed to alleviate the in-service problems on the structural performance of the windshield system when subjected to birdstrike or internal cabin pressure. The MAGNA finite element analysis code was used to evaluate the structural performance of the current production configuration, which served as a baseline, and the alternate design configurations. The fasteners were evaluated based on the MAGNA output using additional computer programs. Computations were made first assuming all fasteners were present, then assuming every other fastener was removed. The models and analyses are discussed and summary results for each design configuration presented. Conclusions are drawn regarding the viability of the proposed alternate design configurations in view of their impact on the structural performance of the windshield system.

## INTRODUCTION

This paper discusses structural analyses performed in support of a study aimed at eliminating B-1B windshield problems which surfaced when the aircraft became operational (Ref. 1). Optics and durability were immediately degraded by delamination. The many edge attachments made windshield changeout difficult and time-consuming, thereby affecting supportability. The overall objective of this study was to evaluate the impact of design configuration changes proposed to alleviate the in-service problems on the structural performance of the windshield system when subjected to birdstrike or internal cabin pressurization.

The study was conducted in two phases. The objective of Phase 1 was to establish the structural performance of the current production B-1B windshield system when subjected to internal pressure loading or birdstrike by a four pound bird impacting at either of two locations at 650 mi/hr. Birdstrike results were compared to birdstrike test results of the B-1A windshield system (no birdstrike tests of the B-1B system had been performed). In addition, the analytical results were reviewed to determine the more critical of the two bird impact locations (the near-center location, denoting a position near the windshield panel geometric center, or the upper corner location near the connection between the centerpost and the eyebrow frame). The Phase I results served as a baseline for the Phase 2 effort. The objectives of Phase 2 were to determine the structural performance of alternate configuration windshields subjected to the internal pressure loading or birdstrike at the critical location determined in Phase I, and to compare the results with those of the baseline windshield system.

In evaluating the structural performance of the various windshield configurations, several items were deemed important. First, deflections and stresses in the windshield panel (particularly in the structural polycarbonate plies) were important since the primary birdstrike protection is provided by this component. Second, the stresses in the frame members supporting the windshield were important, especially since fracture of a large portion of the eyebrow frame had occurred during testing of the B-1A windshield system (Ref. 2). Third, stresses in the fasteners joining the windshield to the immediate support structure were of importance since the fasteners must provide load transfer from the windshield to the frames and maintain the windshield pressure seal. Of special interest was checking the structural feasibility of removing every other fastener and of increasing the associated hole tolerances, both of which would significantly reduce windshield change-out time.

The study was performed using the MAGNA nonlinear finite element analysis program (Ref. 3) as the major analysis tool. Additional computer programs were written or modified from existing ones to aid in analyzing the windshield fasteners. Due to the large finite element model sizes, the ASD CRAY X-MP located at Wright-Patterson Air Force Base, Ohio was used for all MAGNA analyses. Preprocessing (model development), post-processing (data reduction), and fastener analysis were performed using the ASD CDC Cyber computers located at WPAFB and the UDRI Research VAX located at the University of Dayton in Dayton, Ohio.

## MODELING

Figure 1 is a schematic representation of the B-1B windshield system, showing the large left and right windshield panels, the aft windows, and the immediate support structure. Figure 2 depicts the cross sections of the various windshield panel configurations that were analyzed. The baseline windshield consisted of an outer thermally tempered glass ply, a single thick structural polycarbonate ply, and an inner spall polycarbonate ply, bonded together by silicone interlayers. The trade study alternate configuration windshield concepts included substituting acrylic for the glass outer ply, substituting urethane for silicone, substituting a coating for the inner spall polycarbonate ply, and splitting the single structural polycarbonate ply into two polycarbonate plies bonded together by a 0.060 inch layer of silicone.

The bird impact problem was non-symmetric since the impact sites were not located along the windshield centerline. Both windshield panels were therefore modeled, along with the immediate support structure, which included the centerpost, eyebrow frame, and aft arch. Some additional structure aft of the windshield panels, including the aft left-side window and its supporting frame and the aft portion of the centerpost, was also modeled since the stiffness of this structure was believed to have an influence on the dynamic results. Figure 3 presents the windshield system geometry.

Modeling commenced with creating a coarse grid model of the left windshield panel using the MAGNA preprocessor module IJKGEN (Ref. 4) and modified versions of user subroutines CRDTRN, SURFAC, and UINPUT, which were originally written by AFWAL/FIER (Ref. 5). The model was then reflected and subsequently refined using the PREP module (Ref. 4) of MAGNA to obtain the desired element mesh. A model of the aft window was created manually to complete the geometry of the transparencies. The transparency geometry remained unchanged except for the analyses involving the split structural ply, which required additional refinement through the thickness of the windshield panels.

To achieve accurate stresses as well as accurate deflections near the impact site, each layer of the left windshield panel was modeled with a layer of solid (Type 8) elements. Since stresses in the right windshield panel and aft window were of less importance, Type 11 laminated shell elements were employed. This element type provided accurate deflections and was economical, since only one layer of elements was required to model all of the multiple windshield and window layers.

The centerpost and eyebrow frames in the vicinity of the impact sites were created manually using solid (Type 6, 7, 8) elements to ensure accurate modeling of local effects such as flange bending. Support structure located away from the impact site, including the aft arch, far-forward and aft centerpost, right eyebrow, and aft window frame were modeled with Type 12 curved beam elements, which provided accurate overall (but not localized) bending, twisting, and axial stresses as well as accurate deflections. The resulting models were large, with the baseline model

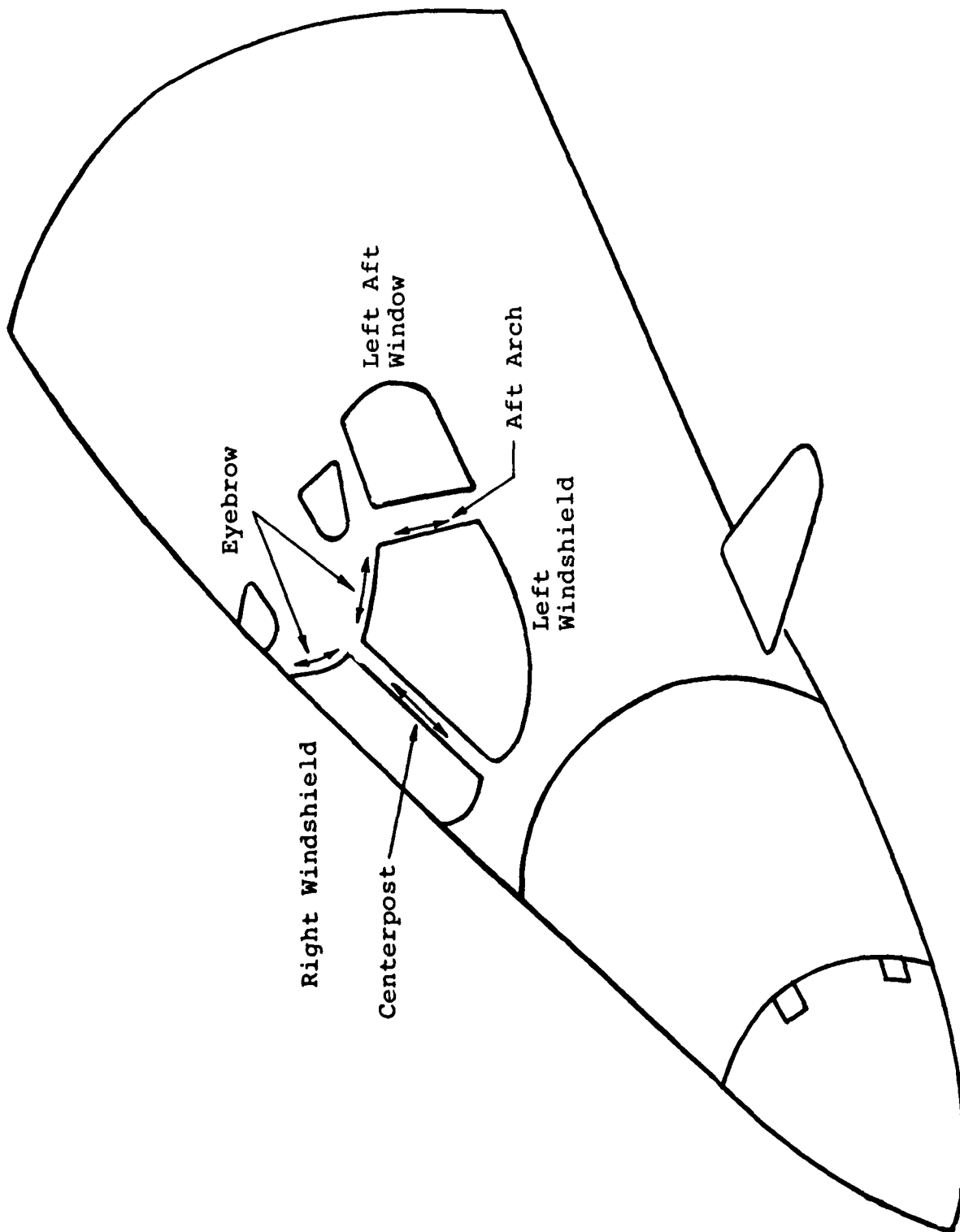
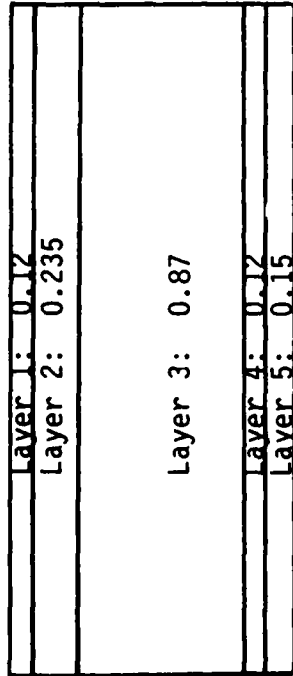
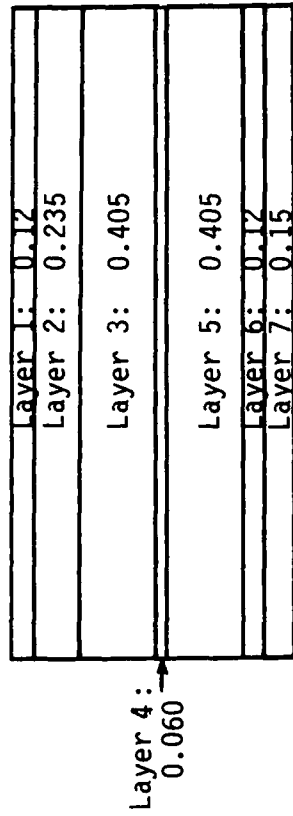


Figure 1. Schematic of B-1B Windshield System.

CASES 1-7



CASES 8-9



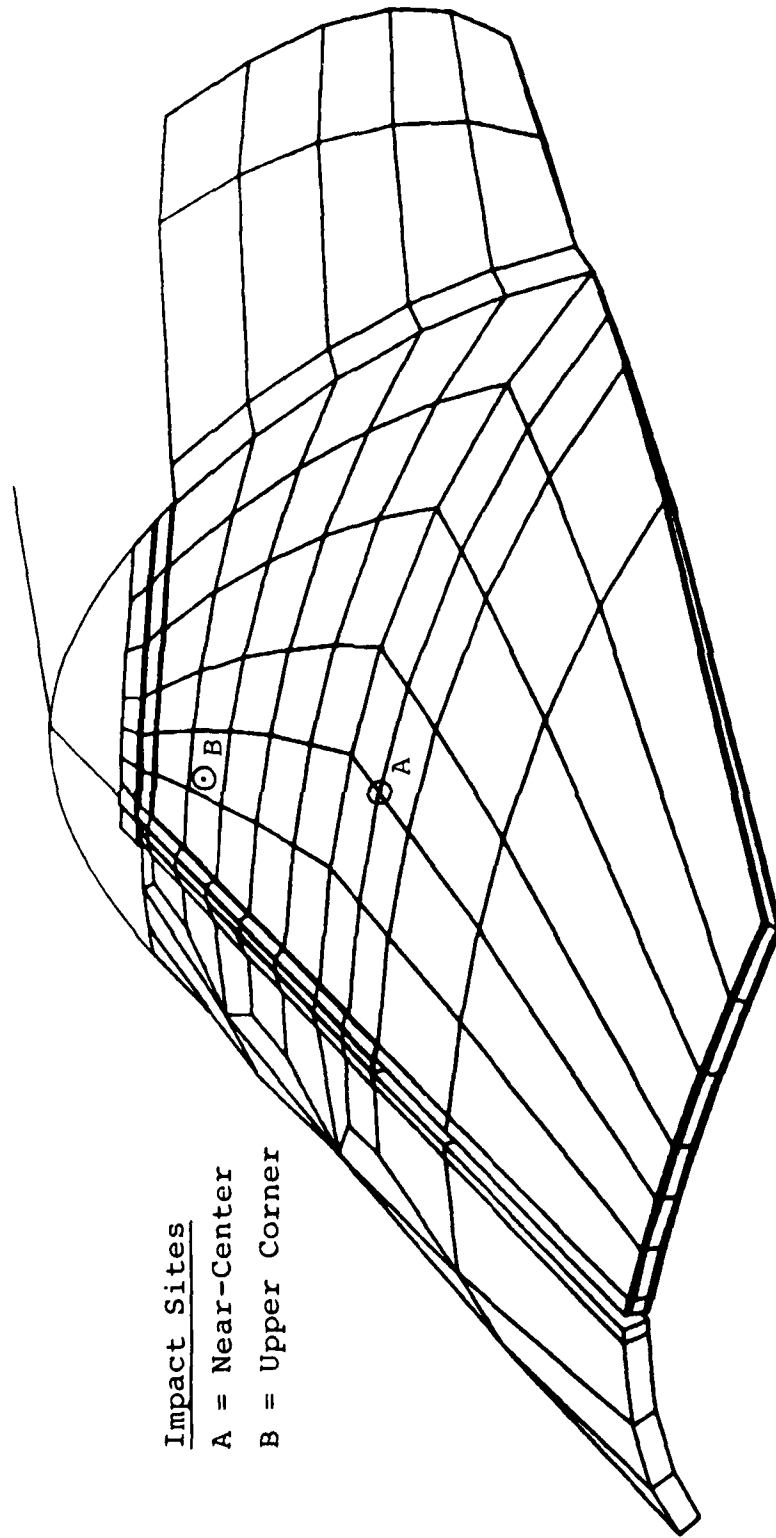
all dimensions in inches

Layer	Case 1-4	Case 5	Case 6	Case 7
1	GL	AC	GL	GL
2	SI	SI	UR	SI
3	PC	PC	PC	PC
4	SI	SI	UR	-
5	PC	PC	PC	-

Layer	Material
1	GL
2	SI
3	PC
4	SI
5	PC
6	SI
7	PC

AC = As-Cast Acrylic  
 GL = Thermally Tempered Glass  
 PC = Polycarbonate  
 SI = Silicone  
 UR = Urethane

Figure 2. Windshield Cross-Section Geometry.



Impact Sites  
A = Near-Center  
B = Upper Corner

Figure 3. MAGNA Model for the Current Production Windshield System.



having 589 solid elements, 46 laminated shell elements, and 46 beam elements, while the split structural ply model had 729 solid elements and the same number of shells and beams. The models were approximately three times larger than the largest models successfully analyzed on the ASD Cyber 845 computer (Ref. 5). To reduce the memory requirements needed for the model, the nodal bandwidth was minimized by executing the RENUMBER option in PREP and then running the model through a wavefront minimization code developed originally by Hoit and Wilson (Ref. 6) and modified by UDRI for use with MAGNA.

Table 1 summarizes the elastic material properties for the various components of the model. Isotropic properties were input for all solid and beam elements, except for the interlayer solid elements. The tensile modulus, shear modulus, and Poisson's ratio were independent of each other for the interlayer materials. Therefore these properties were input in orthotropic format, which allowed for their independent entry. Finally, due to the assumption of perfect shear coupling between layers, the response of the Type 11 element is generally too stiff when the tensile moduli vary considerably between adjacent layers. The layer-to-layer variation was large for the B-1B windshield, with the glass modulus being 3450 times larger than the silicone modulus. The appropriate tensile and shear modulus values were therefore multiplied by shear correction factors computed in accordance with Reference 7. Table 2 summarizes the correction factors and revised properties. Note that the current version of MAGNA does not properly recover stresses for shear corrected elements, making the Type 11 element inappropriate for accurate stress analysis of laminated windshields.

Other revisions to the basic elastic material properties given in Table 1 were also needed. First, each layer of the peripheral elements of all of the left windshield models was assigned the tensile modulus of polycarbonate and a high yield strength (chosen to ensure yielding did not occur) in an effort to simulate the restraint imposed by the fasteners. Without the restraint, the structural ply would pull out since the only restraint would be from the soft interlayers, leading to incorrect calculation of fastener edge loads. Linear constraints were considered but not used because they are applied at points, rather than being distributed, leading to higher-than-actual stresses. Second, to simulate removal of the spall ply, the inner ply was assigned a low tensile modulus (1000 psi) and density (0.000429 lb./cu.in.) to ensure its stiffness and mass would be negligible. (This approach was a fast and accurate alternative to reconstructing the windshield models with the spall ply removed.) Third, the silicone plies for the acrylic outer ply trade study were stiffened with a revised tensile modulus of 10,000 psi. This was done to prevent the acrylic ply from deflecting all the way through the interlayer into the structural ply, turning the interlayer inside out, thus causing numeric instabilities. No adverse effects on the results were expected since the added interlayer stiffness was still relatively small compared to that of the structural polycarbonate ply (tensile modulus ratio of 35.5 to 1 for polycarbonate compared to the revised silicone). Fourth, the tensile modulus of the glass layer on the left side windshield model was also revised. Preliminary MAGNA birdstrike results showed the glass to fail in ductile fashion rather than shattering, which was the expected failure mode (for example, impact of B-1A simulated windshield test articles - Ref. 8). The glass ply was in essence behaving like a sheet of aluminum, which has

TABLE 1

## ELASTIC MATERIAL PROPERTIES

Material	Tensile Modulus (kpsi)	Shear Modulus (kpsi)	Poisson's Ratio	Density (lb/in <sup>3</sup> )	Yield Strength (kpsi)	References
Windshield Outer Ply	10,000	4,070	0.23	0.091	18.0	19,22
	Tempered Glass					
Windshield Outer Ply	450	167	0.35	0.043	10.0	19,20
	As-Cast Acrylic					
Windshield Structural Ply	355	130	0.37	0.043	12.1	19,20,21
	Polycarbonate					
Windshield Interlayer	2.9	0.145	0.33	0.0385	*	19,23
	Silicone					
Windshield Interlayer	8.7	0.895	0.43	0.0385	*	19,23
	Urethane					
Forward Centerpost and Aft Window Frame	10,600	3,980	0.33	0.1	50.	18
	2024-T62 Aluminum					
Aft Arch and Aft Centerpost	10,400	3,910	0.33	0.1	56.	18
	2124-T851 Aluminum					
Eyebrow	10,000	3,760	0.33	0.1	56.	18
	7075-T73 Aluminum					

\*Arbitrarily large value of  $1 \times 10^{12}$  psi used--see text.

TABLE 2

## SHEAR CORRECTED MATERIAL PROPERTIES FOR TYPE 11 ELEMENTS

CASE 4: CURRENT PRODUCTION CONFIGURATION  
CORRECTION FACTOR = 0.00095

Material	E <sub>1</sub> psi	E <sub>2</sub> psi	E <sub>3</sub> psi	G <sub>12</sub> psi	G <sub>13</sub> psi	G <sub>23</sub> psi	ν <sub>12</sub>	ν <sub>13</sub>	ν <sub>23</sub>
Glass	10x10 <sup>6</sup>	10x10 <sup>6</sup>	10x10 <sup>6</sup>	4.07x10 <sup>6</sup>	3867	3867	.23	0.	0.
Polycarbonate	355000	355000	355000	130000	124	124	.37	0.	0.
Silicone	2900	2900	2900	145	0.138	0.138	.33	0.	0.

CASE 5: ACRYLIC OUTER PLY CONFIGURATION  
CORRECTION FACTOR = 0.0093493

Material	E <sub>1</sub> psi	E <sub>2</sub> psi	E <sub>3</sub> psi	G <sub>12</sub> psi	G <sub>13</sub> psi	G <sub>23</sub> psi	ν <sub>12</sub>	ν <sub>13</sub>	ν <sub>23</sub>
Acrylic	450000	450000	450000	167000	1561	1561	.35	0.	0.
Polycarbonate	355000	355000	355000	130000	1215	1215	.37	0.	0.
Silicone	2900	2900	2900	145	1.356	1.356	.33	0.	0.

CASE 6: URETHANE INTERLAYER CONFIGURATION  
CORRECTION FACTOR = 0.0057993

Material	E <sub>1</sub> psi	E <sub>2</sub> psi	E <sub>3</sub> psi	G <sub>12</sub> psi	G <sub>13</sub> psi	G <sub>23</sub> psi	ν <sub>12</sub>	ν <sub>13</sub>	ν <sub>23</sub>
Glass	10x10 <sup>6</sup>	10x10 <sup>6</sup>	10x10 <sup>6</sup>	4.07x10 <sup>6</sup>	23603	23603	.23	0.	0.
Polycarbonate	355000	355000	355000	130000	754	754	.37	0.	0.
Urethane	8700	8700	8700	895	5.19	5.19	.43	0.	0.

CASE 7: NO SPALL PLY CONFIGURATION  
CORRECTION FACTOR = 0.00073913

Material	E <sub>1</sub> psi	E <sub>2</sub> psi	E <sub>3</sub> psi	G <sub>12</sub> psi	G <sub>13</sub> psi	G <sub>23</sub> psi	ν <sub>12</sub>	ν <sub>13</sub>	ν <sub>23</sub>
Glass	10x10 <sup>6</sup>	10x10 <sup>6</sup>	10x10 <sup>6</sup>	4.07x10 <sup>6</sup>	3008	3008	.23	0.	0.
Polycarbonate	355000	355000	355000	130000	96	96	.37	0.	0.
Silicone	2900	2900	2900	145	0.107	0.107	.33	0.	0.

CASE 9: SPLIT STRUCTURAL PLY CONFIGURATION  
CORRECTION FACTOR = 0.00084879

Material	E <sub>1</sub> psi	E <sub>2</sub> psi	E <sub>3</sub> psi	G <sub>12</sub> psi	G <sub>13</sub> psi	G <sub>23</sub> psi	ν <sub>12</sub>	ν <sub>13</sub>	ν <sub>23</sub>
Glass	10x10 <sup>6</sup>	10x10 <sup>6</sup>	10x10 <sup>6</sup>	4.07x10 <sup>6</sup>	3454	3454	.23	0.	0.
Polycarbonate	355000	355000	355000	130000	110	110	.37	0.	0.
Silicone	2900	2900	2900	145	0.123	0.123	.33	0.	0.

the same modulus as glass. The model was therefore too stiff (deflection was less than 1 inch, which was less than half the deflection for the B-1A - Ref. 9), so the glass was assigned a low tensile modulus of 1000 psi to represent the reduction in stiffness in the shattered state. The density was not changed since the glass was assumed to remain bonded to the interlayer, allowing its inertia to influence the dynamic response of the windshield.

In addition to elastic material properties, it was important that the plastic stress-strain behavior be input for those materials for which yielding was a possibility. Table 3 summarizes the pertinent data. Acrylic was treated as an elastic-perfectly plastic material even though it tends to load up directly to failure without yielding. This was done because MAGNA cannot "turn off" an element once it reaches its ultimate strength, nor can it accept a negative stress-strain slope (strain softening). The model acrylic thus performed better than actual acrylic although it did not adversely affect the results since the soft, thick interlayer immediately below it tended to uncouple its response from the remainder of the windshield. Plasticity was not incorporated into the interlayer models. These layers were viewed strictly as load transfer mediums since modeling of their response would have been imprecise (due to the lack of accurate material properties and limitations in MAGNA for modeling the bulk behavior of such materials).

Nodal constraints applied to the models consisted of boundary conditions and linear constraints. Rigid connections were modeled along the sill, forward arch, and at either end of the centerpost by pinning all nodes through the windshield thickness and by constraining all translations and rotations at the ends of the centerpost beam elements. Linear constraints were necessary to properly couple the rotation (twisting or bending) of the beam elements to the translation of the solid elements, which did not have rotational degrees of freedom. Computer codes were written to compute the constraints in local coordinates, transform them into global coordinates, and then write them in MAGNA format to files which were later merged into the MAGNA models.

The applied loads included internal static pressures and birdstrike dynamic pressures. For the internal pressure analyses, the windshields were subjected to three different pressure loads, as outlined in Table 4. All pressures were gauge pressures, that is, pressure above atmospheric (essentially the pressure difference between the cockpit and outside the aircraft). All interior, inward-facing solid and layered shell element surfaces were loaded.

Two bird impact sites were used for the baseline birdstrike analyses, as shown in Figure 3. Site "A" was located near the geometric center of the left side windshield while site "B" was located in the upper corner near the joint between the centerpost and eyebrow frames. For the trade studies, only the "worst case" site was used, which was determined from the baseline analyses. Bird impact was by a four pound bird impacting at 650 mi/hr. Two user subroutines, ULOAD and USRLOD, were developed using the method discussed in Reference 10 to compute and apply to the models the loads due to birdstrike. The method computed loads based on the results of flat panel testing (Ref. 11, 12), and featured the correct spatial and time

TABLE 3  
POST-YIELD STRESS-STRAIN CURVES

Material	Total Strain <sup>a</sup> μin/in	Plastic Strain μin/in	Stress <sup>b</sup> kpsi
2024-T62 Aluminum	4728.	0.	49.8
	5214.	290.	52.2
	5616.	550.	53.7
	6018.	860.	54.7
	7025.	1760.	55.8
	8032.	2680.	56.7
	9041.	3620.	57.5
	10050.	4520.	58.2
	105000.	99510.	58.7
7075-T73 Aluminum	5616.	0.	55.7
	5817.	60.	57.6
	6018.	120.	59.0
	6219.	230.	59.9
	6622.	530.	61.0
	7025.	850.	61.7
	8032.	1700.	63.3
	9041.	2630.	64.1
	10050.	3560.	64.9
116050.	109560.	64.9	
Polycarbonate	35150.	0.	12.0
	644368.	605700.	13.7
Acrylic	22222.	0.	10.0
	10022222.	10000000.	10.0

<sup>a</sup> Green-St. Venant Strain

<sup>b</sup> Second Piola-Kirchoff Stress

TABLE 4  
LOADS

Internal (Cabin) Pressures

Designation	Pressure (psig)	Structural Pass/Fail Criterion
Limit Pressure	10.6	Maintain pressure without yielding of windshield or support structure
Proof Pressure	14.1	Maintain pressure without significant yielding of windshield or support structure
Ultimate Pressure	21.2	Maintain pressure

Birdstrike Loads

	Near Center Impact	Upper Corner Impact
Impact Angle (deg)	20.5714	25.0
Bird Diameter (in)	4.201672	4.20167
Effective Bird Length (in)	19.5987	17.4139
Max. Footprint Length (in)	30.3068	25.7243
Impact Velocity (in/sec)	11,447.8	11,447.8
Normal Velocity (in/sec)	4,022.47	4,838.06
Tangential Velocity (in/sec)	10,717.9	10,375.3
Impact Duration (msec)	1.712	1.52115
Pressure Rise Time (msec)	0.3424	0.30423
Peak Total Force (lb)	48,695.9	65,917.8
Peak Pressure (psi)	1,483.2	2,395.5

distribution of pressure and force (see Figure 4), as well as "hands-off" operation by the user during MAGNA runs. The method assumed that the bird was a right, circular cylinder having a length-to-diameter ratio of 2:1 and density of 0.03433 lb/cu.in., that the maximum pressure point (located at the first point of contact between the bird and windshield) remained stationary, and that no transverse bird spreading occurred (constant width footprint). Table 4 presents the pertinent data describing the geometry, magnitude, and timing of both the near-center and corner impact load.

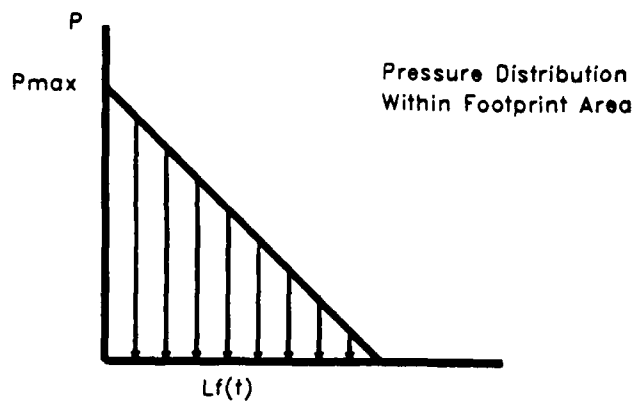
#### ANALYTICAL PROCEDURE

Table 5 summarizes the various MAGNA analyses that were conducted. The Phase I baseline effort consisted of Cases 1-4, while the Phase II trade study effort consisted of Cases 5-9. Three different types of MAGNA analyses were performed and are briefly discussed below: eigenvalue (natural frequency), nonlinear static (internal pressurization), and nonlinear dynamic (birdstrike). Fastener analysis, which is not directly performed by MAGNA, is also discussed.

Eigenvalue analysis (natural frequency analysis) was performed as a means to check the MAGNA models and as an aid in selecting/checking a time step for nonlinear dynamic birdstrike analysis. The frequency and mode shapes generated were studied to reveal any errors in boundary conditions, linear constraints, or material properties. The period of the lowest vibration mode of the left side windshield panel was divided by 100 to give an estimate of the time step for nonlinear dynamic analysis. The consistent mass matrix formulation was used in the analyses.

Nonlinear static analysis was performed for the internal pressure loading cases. The material nonlinearity option was selected because, as noted in Table 4, the proof and ultimate pressure definitions included the possibility of yielding. Displacements were, however, expected to be small. Static analysis was appropriate since the time history of the loading and response was not important. The internal pressure was applied in four successive increments of 5.3 psi, 5.3 psi, 3.5 psi, and 7.1 psi, resulting respectively in total internal pressures of 5.3 psi, 10.6 psi, 14.1 psi, and 21.2 psi. Iteration was performed at every increment to obtain convergence of the solution. The combined Newton-Raphson iteration technique and default displacement and residual force tolerances were used.

Nonlinear dynamic analysis was performed for all birdstrike analyses. The large displacement and material nonlinearity options were required in anticipation of deflections of approximately two inches (similar to deflections of the B-1 windshield panel noted in Reference 9) and yielding of the windshield plies and/or frame members. The time step for all analyses was 0.04 milliseconds, which was chosen based on the time of contact of the bird on the windshield. The time step estimate based on the eigenvalue analysis was 0.061 milliseconds, which verified the magnitude of the chosen time step. Combined Newton-Raphson iteration was performed during every fifth increment to ensure convergence of the solution. Default



$P$  = Pressure  
 $F$  = Force  
 $t$  = Time  
 $L_f$  = Footprint Length

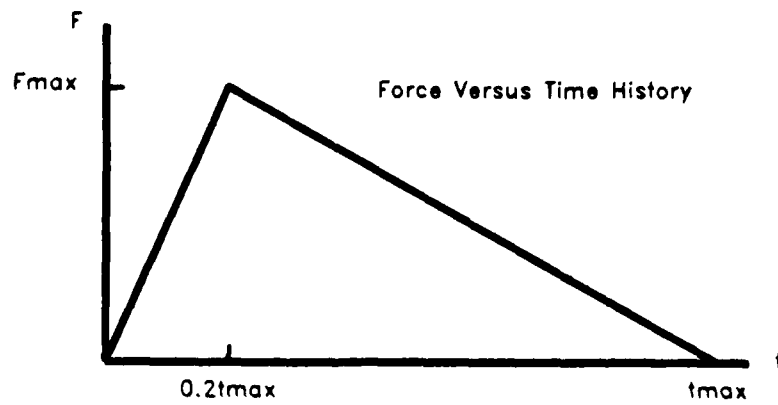


Figure 4. Birdstrike Load Distributions.



TABLE 5  
MAGNA ANALYSIS CASES

Case	Windshield Configuration	Loads
1	Current Production	Natural Frequency
2	Current Production	Internal Pressure
3	Current Production	Bird Impact at A <sup>a</sup>
4	Current Production	Bird Impact at B <sup>b</sup>
5	Acrylic Outer Ply	Bird Impact at B
6	Urethane Interlayer	Bird Impact at B
7	No Spall Ply	Bird Impact at B
8	Split Structural Ply	Internal Pressure
9	Split Structural Ply	Bird Impact at B

NOTES:

<sup>a</sup>Location A is near the windshield geometric center.

<sup>b</sup>Location B is near the centerpost-to-eyebrow joint.

displacement and residual stress convergence tolerances were used. The analyses were stopped and restarted after every fifth increment so that the convergence and results (displacements and stresses) could be checked. The analyses were terminated when the displacements and stresses in the structural polycarbonate ply began to decrease after having reached their maximum values.

Analysis of the NAS1580C4 fasteners used to attach the windshield to the support structure was conducted for all pressurization and birdstrike analyses. Since the fasteners joining the windshield to the supporting structure were not explicitly modeled, MAGNA could not directly provide loads acting on the fasteners. However, it was possible to reduce the available MAGNA data into the desired fastener loads. The process outlined in Figure 5 required that several computer programs be written or modified. The procedure and programs are briefly described below, with a more complete explanation being provided in Reference 13.

Integration point stresses obtained from the MAGNA analyses were collected on MAGNA post-processor, or MPOST, files at each time increment during each analysis. However, integration point stresses were not appropriate for subsequent data reduction; nodal stresses were necessary. Extrapolation from integration point stresses to nodal stresses occurred in the stress averaging program, STRAVG, which is a utility in the MAGNA post-processing software package (Ref. 14).

The next step in fastener analysis was to convert the nodal stresses at the windshield perimeter into stress resultants. The computer program STRSLT, which was modified from a previous version, converted node point stresses into equivalent forces and moments per unit length (stress resultants) by integrating the nodal stresses through the transparency thickness.

Written for this analysis, the computer program XFER converted STRSLT stress resultant information into loads acting on the fasteners. The stress resultants acting along the windshield edge were assumed to cause bushing rotation relative to the fastener due to the clearance between these components. Such rotation produced shear forces on the upper and lower portions of the fastener grip length as indicated in Figure 6. Shear resultants acting through the transparency thickness were transferred to the frame flanges through the fasteners, resulting in an axial force in the fastener as shown in Figure 6. The loads (axial, upper shear, and lower shear) were calculated as a combination of the stress resultants for each of the five plies in the transparency (seven plies for Case 9) along the entire windshield perimeter.

Plot files written by XFER contained the axial and shear load components as functions of the location along the perimeter of the windshield. A commercially available scientific graph plotting program for IBM PC and compatible computers (Ref. 15) was used to display the load resultants graphically. One plot was generated for each fastener load component (axial, upper shear, and lower shear) for each baseline and trade study analysis. Note that since the fasteners were always loaded in tension, negative axial loads did not indicate compression. The sign of the

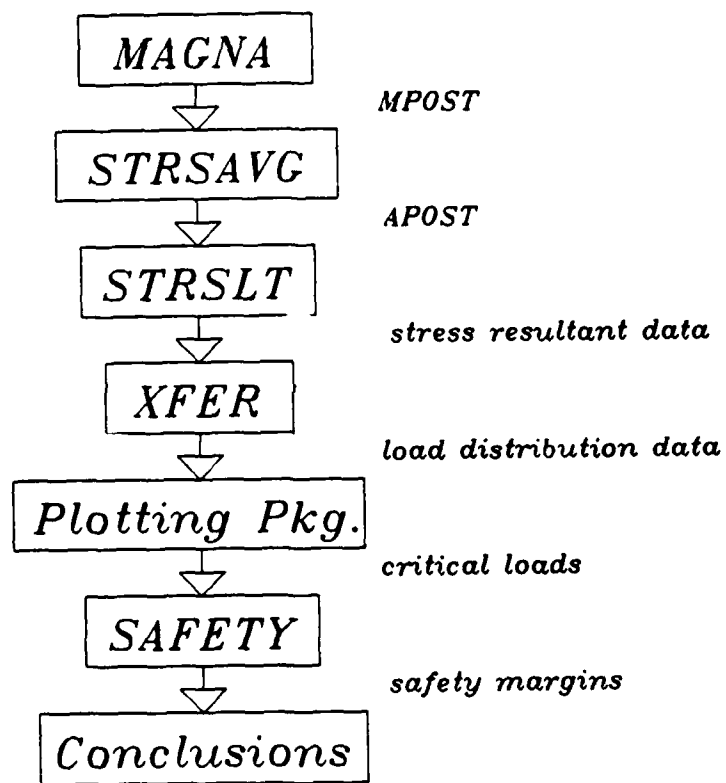


Figure 5. Fastener Analysis Procedure.

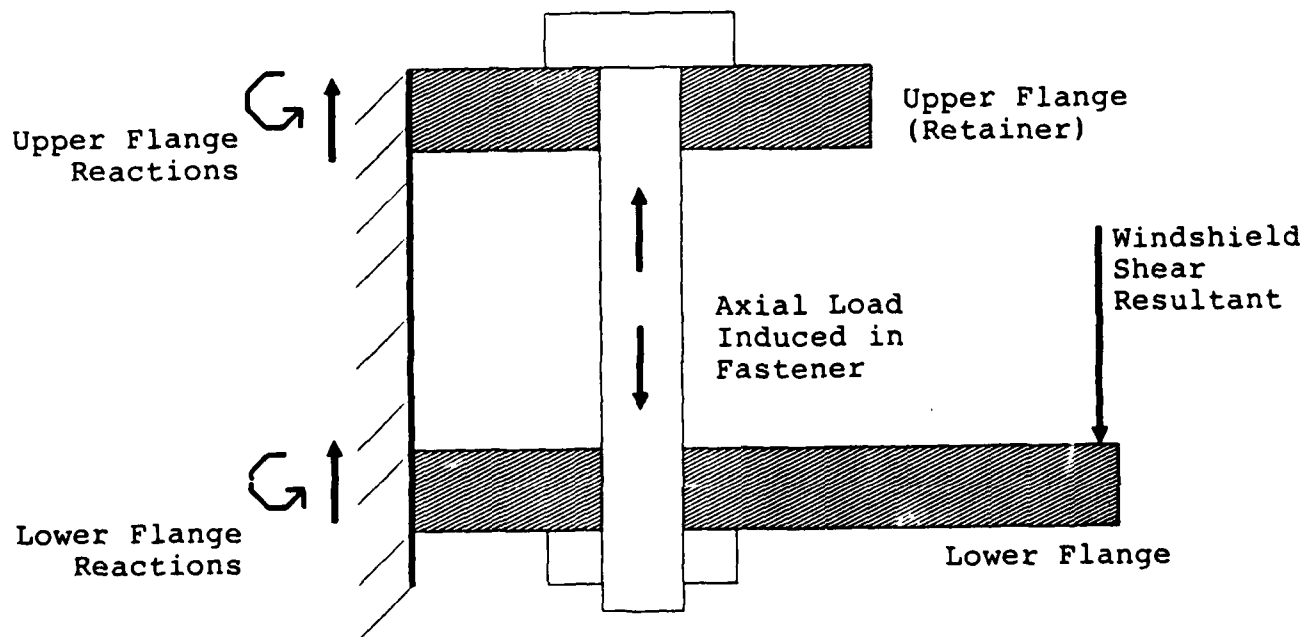
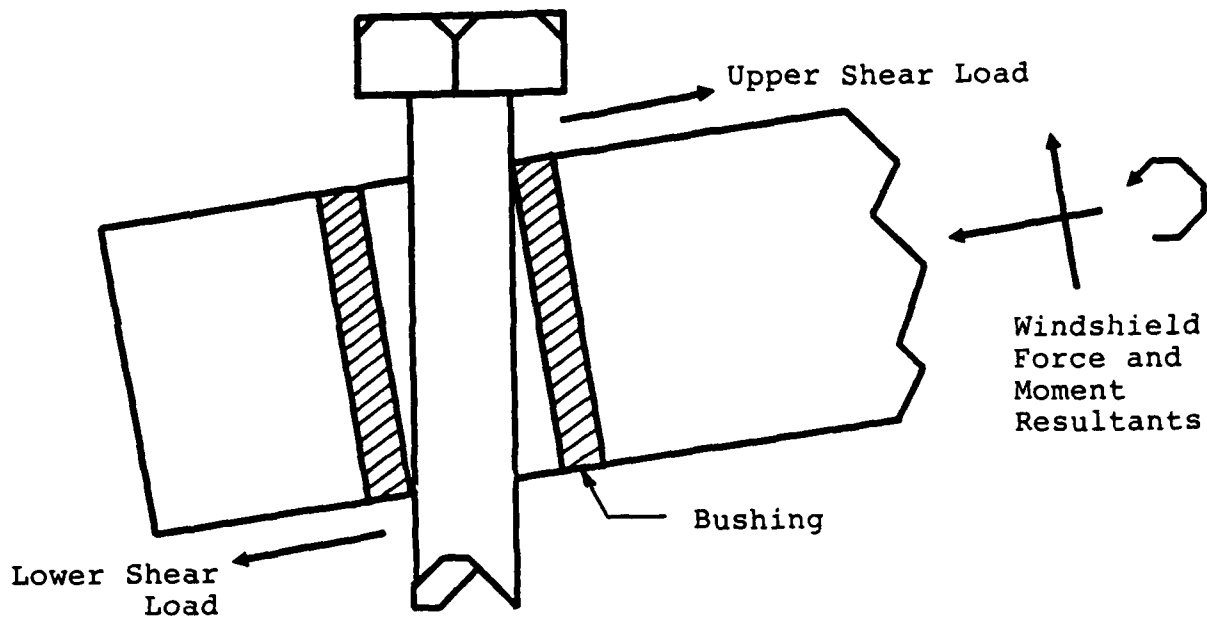


Figure 6. Shear and Axial Forces Acting on Fastener.

axial load only indicated the direction of load application, which was the direction of the windshield shear load shown in Figure 6.

The critical loads acting on the fasteners were taken directly from the plots. Shear and axial effects were considered both independently and together. The combined effects of shear and tension were accounted for using the following interaction equation:<sup>24</sup>

$$(S_t/S_t')^2 + (S_s/S_s')^3 \leq 1$$

where  $S_t$  = Actual fastener tensile stress,

$S_t'$  = Allowable fastener tensile stress, psi,

$S_s$  = Actual fastener shear stress, psi, and

$S_s'$  = Allowable fastener shear stress, psi.

The computer program SAFETY was written to determine the margins of safety against various failure modes for given geometry and critical load conditions. Four failure modes were considered in the analysis: fastener tension, fastener shear, structural ply bearing, and structural ply rupture (tensile failure between adjacent fastener holes). In addition, SAFETY also computed fastener margins assuming every other fastener was deleted. Note that fastener preload was considered in performing all calculations.

### RESULTS AND DISCUSSION

Table 6 and Figures 7-9 summarize the MAGNA results for the baseline (current production) and trade study (split structural polycarbonate ply) internal pressurization analyses. Because the other trade study configurations utilized the same structural ply as the baseline, and because this ply bears 70% - 80% of the applied load, the performance of these other trade studies was judged to be similar to that of the baseline configuration. The results therefore showed that the current production windshield system and each of the trade study windshield system configurations were sufficiently designed to resist internal cabin pressures of up to 21.2 psi above outside atmospheric pressure without permanent deformation to any of the windshield components.

Table 6 and Figures 7-9 also summarize the MAGNA results for the baseline and trade study birdstrike analyses. The baseline (current production) analyses indicated that bird impact at the upper corner location was more severe than impact at the near-center location, resulting in permanent deformation of the eyebrow frame and the structural polycarbonate ply. Figures 10 and 11 show the high stress regions on the structural polycarbonate ply and in the eyebrow web for Case 4. The analyses indicated, however, that the current production windshield system was capable of defeating a four pound bird at 650 mi/hr impacting at the upper corner site as well as at the near-center site.

TABLE 6  
SUMMARY OF RESULTS FOR MAGNA BIRDSTRIKE ANALYSES

Case Number Category	2	3	4	5	6	7	8	9
Model Description	Baseline Current Production	Baseline Current Production	Baseline Current Production	Trade Study Acrylic Outer Ply	Trade Study Urethane Interlayer	Trade Study Remove Spall Ply	Trade Study Split Structural Ply	Trade Study Split Structural Ply
Lloads	P	A	B	B	B	B	P	B
Maximum Deflection (in.)	0.104	1.399	1.05	0.919	0.988	1.171	0.107	1.364
Maximum Structural Polycarbonate Stress (kpsi) (Yield - 12 kpsi)	0.5	5	12	12	12	12	0.105	12
Maximum Structural Polycarbonate Strain (%) (Yield=3.38%, Failure=120%)	0.14	1.4	8	7.5	7.5	9.	0.14	16.
Maximum Centerpost Stress (kpsi) (Yield - 50 kpsi)	1.5	14.	40.	40.	40.	45.	4.	50.
Maximum Centerpost Strain (%) (Yield - 0.47%, Failure - 5.0%)	0.014	0.13	0.38	0.38	0.38	0.42	0.038	1.3
Maximum Eyebrow Stress (kpsi) (Yield - 65 kpsi)	7.	7.	70	70	70	70	0.2	70
Maximum Eyebrow Strain (%) (Yield - 0.56%, Failure - 8.0%)	0.07	0.06	3.5	3.5	3.5	4.0	0.002	4.0

NOTES:  
A - Impact at Site A  
B - Impact at Site B  
P - Internal Pressure

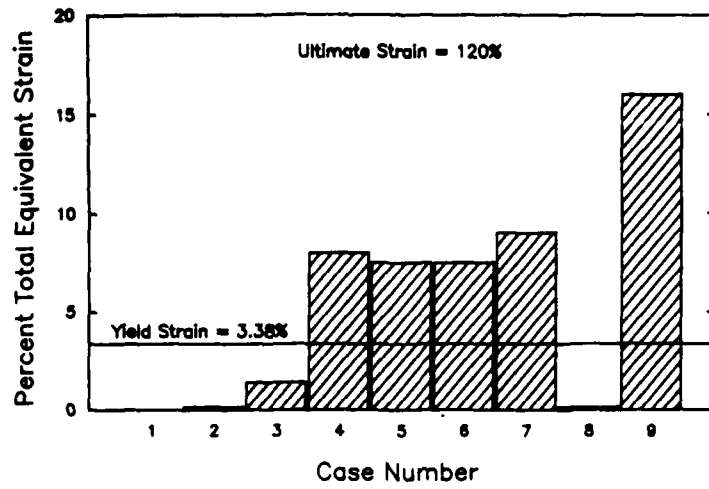


Figure 7. Strain Summary, Structural Polycarbonate Ply.

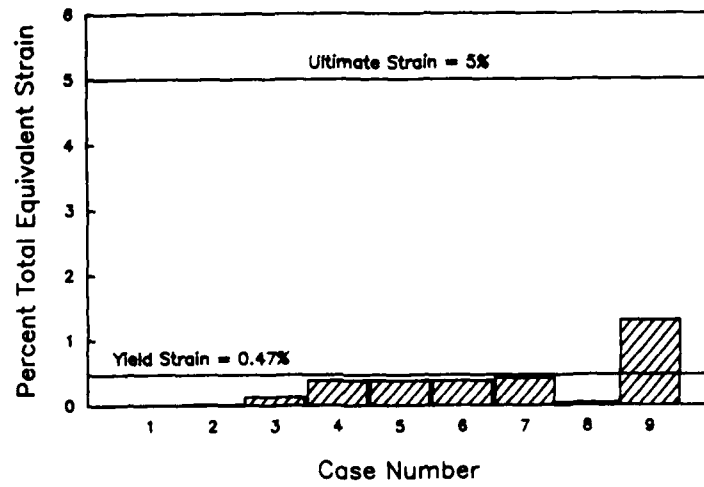


Figure 8. Strain Summary, Centerpost.

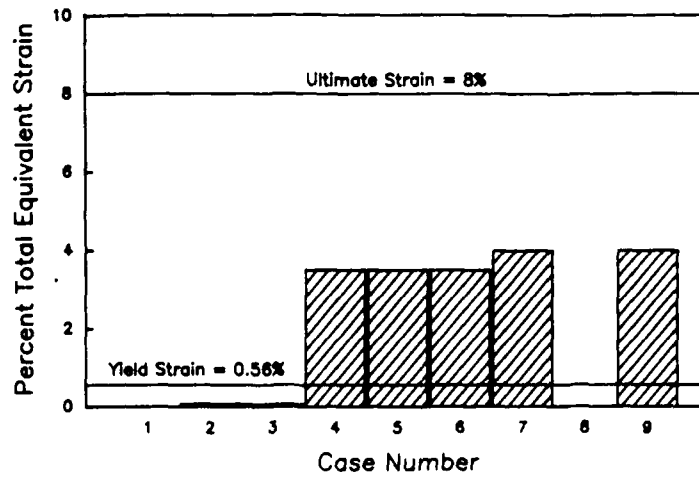


Figure 9. Strain Summary, Eyebrow.

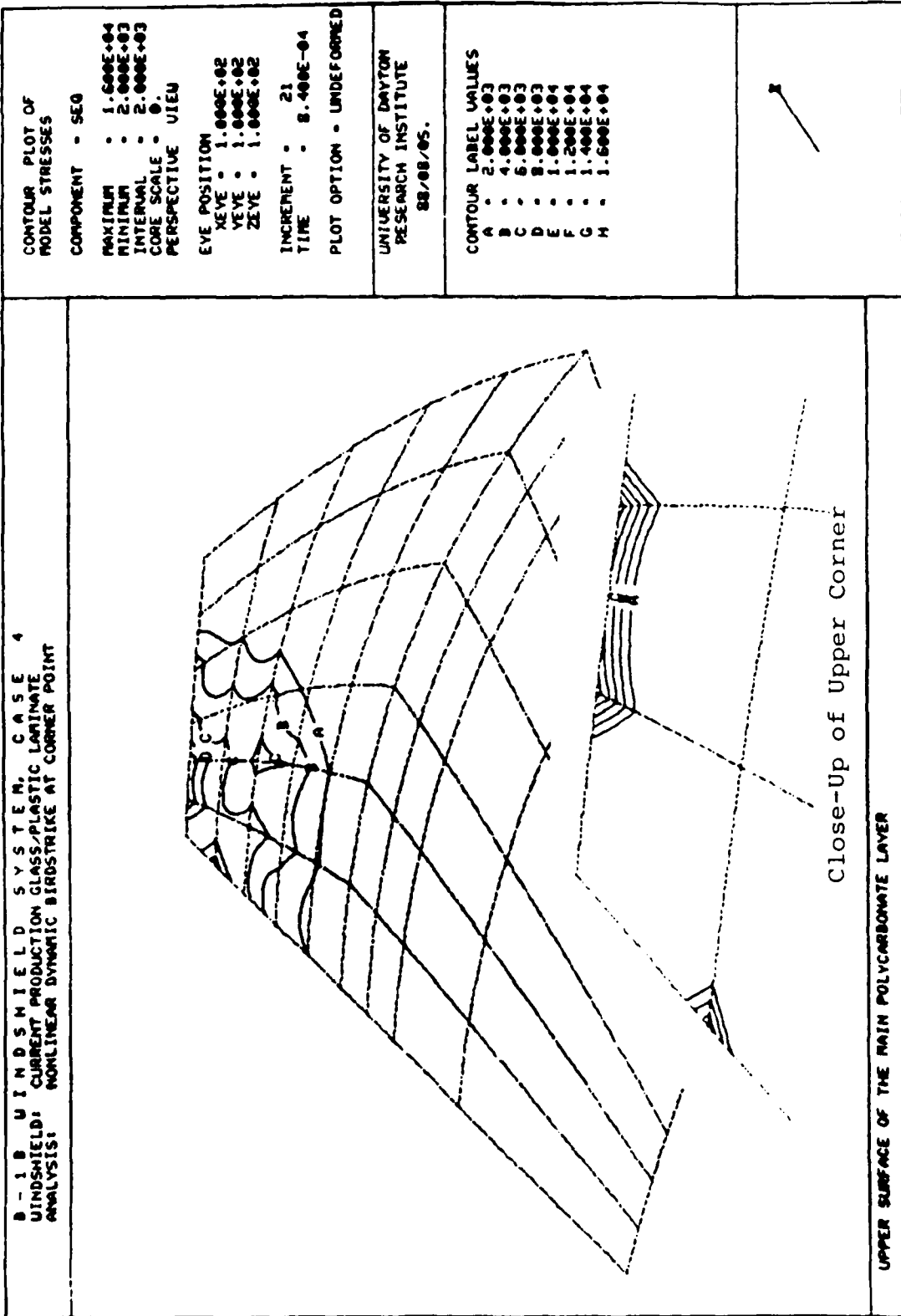


Figure 10. Equivalent Stress Contours on the Outer Surface of the Structural Ply, Case 4.



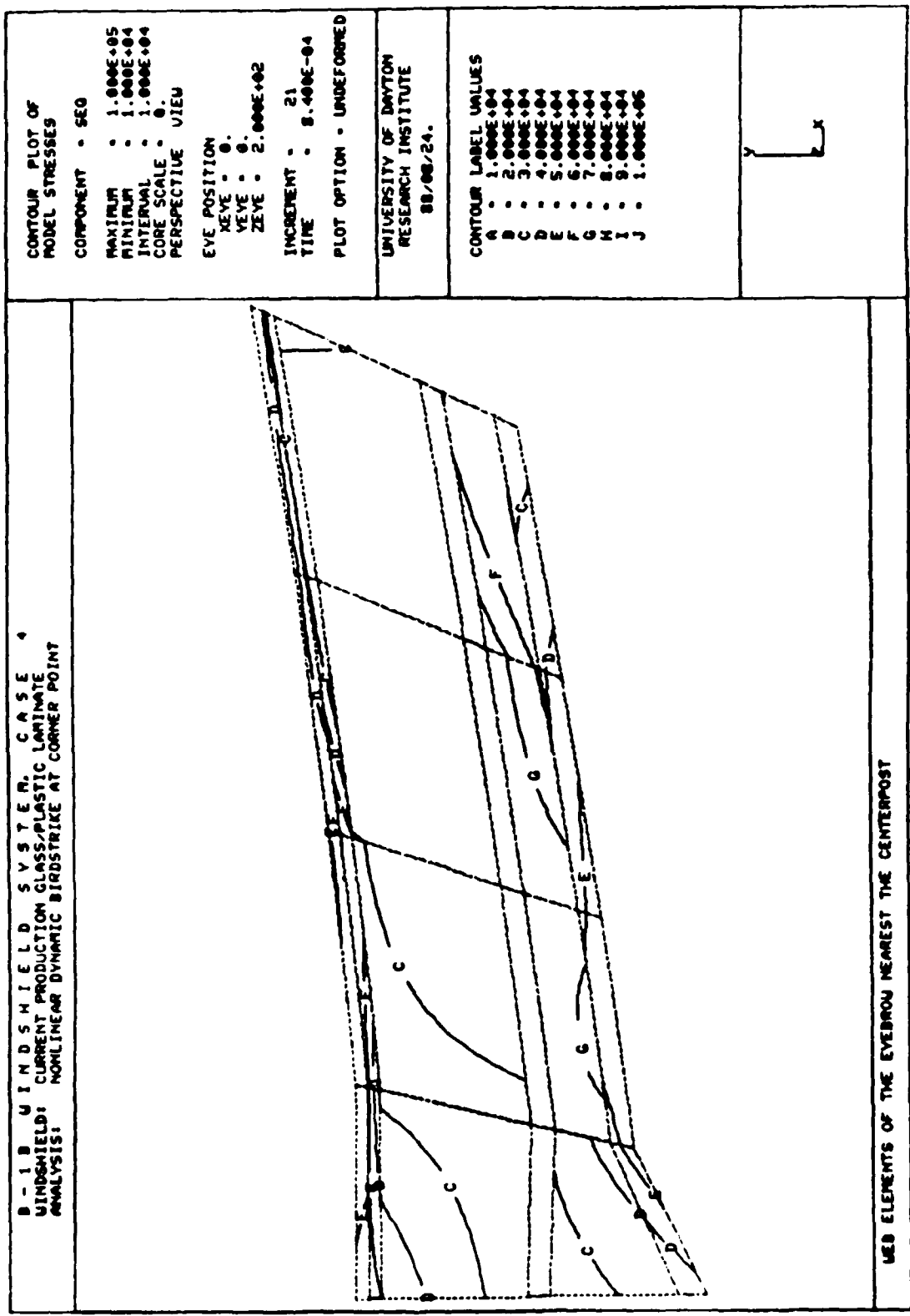


Figure 11. Equivalent Stress Contours on the Eyebrow Web, Case 4.

The birdstrike analyses also indicated that, in addition to the current production configuration, all trade study configurations were capable of defeating a four pound bird impacting at the upper corner location at 650 mi/hr. Since this location was determined to be more severe than the near-center impact site, all windshield configurations should also have been capable of defeating a four pound bird impacting at the near-center site at 650 mi/hr. The performance of the various configurations was similar, although, compared to the other configurations, the split polycarbonate ply configuration resulted in a 0.23 - 0.48 inch increase in maximum windshield deflection, a 0.07 - 0.08 in./in. increase in structural ply plastic strains, and plastic deformation of the centerpost. Its performance was still more than adequate to prevent failure of the windshield system.

The MAGNA birdstrike results indicated that, for the upper corner birdstrike, the structural polycarbonate ply (plies) and the eyebrow frame deformed permanently. Figures 12 and 13 show the equivalent strains along the back edge of the structural polycarbonate ply at the eyebrow interface and in the eyebrow web for Case 4. Contours for the trade study cases were similar. As presented in Table 6 and Figures 7 and 9, the maximum equivalent strains in the eyebrow web (4%) and polycarbonate structural ply (7.5% - 16%) were below the elongations to failure of 8% (Ref. 18) and 120% (Ref. 16), respectively. The centerpost folit structural ply case also deformed permanently (but not for the other cases). The location of the highest stresses in the eyebrow frame (in the web between the bottom two flanges) was the same location where fracture occurred during upper corner birdstrike testing of the B-1A. Fracture of the B-1B eyebrow frame or the structural polycarbonate ply (plies) should not occur unless the elongation to failure of the materials used for these components is degraded (for example, by improper processing, embrittlement, or stress concentration).

Table 7 and Figure 14 summarize the results of the baseline and birdstrike fastener analyses for both the pressurization and birdstrike loading. Note that values inside (below) the curve of Figure 14 indicate fastener pass while values outside the curve indicate fastener failure. Figure 15 presents typical fastener load distributions from which Table 7 was compiled. The safety margins for the pressurization analyses were large, indicating that the current production and trade study windshield fasteners were sufficiently designed to resist internal cabin pressures of up to 21.2 psi above the outside atmosphere. (Note that the trade study configurations for which no pressurization margins are given were expected to give similar results since they utilized the same structural polycarbonate ply, which transfers 70% - 80% of the applied load to the fasteners.)

With all fasteners present, all birdstrike fastener margins are positive, indicating that the fasteners were sufficient to resist both near-center and upper corner birdstrikes without failure. (Note that, since the upper corner impact was more critical than the near-center impact, and since the fastener performance was acceptable for all upper corner impacts, it was inferred that the fastener performance would also be acceptable for near-center impact on those trade study configurations that were not explicitly analyzed for this impact condition.) The use of acrylic for the outer ply or urethane for the interlayers improved the fastener margins

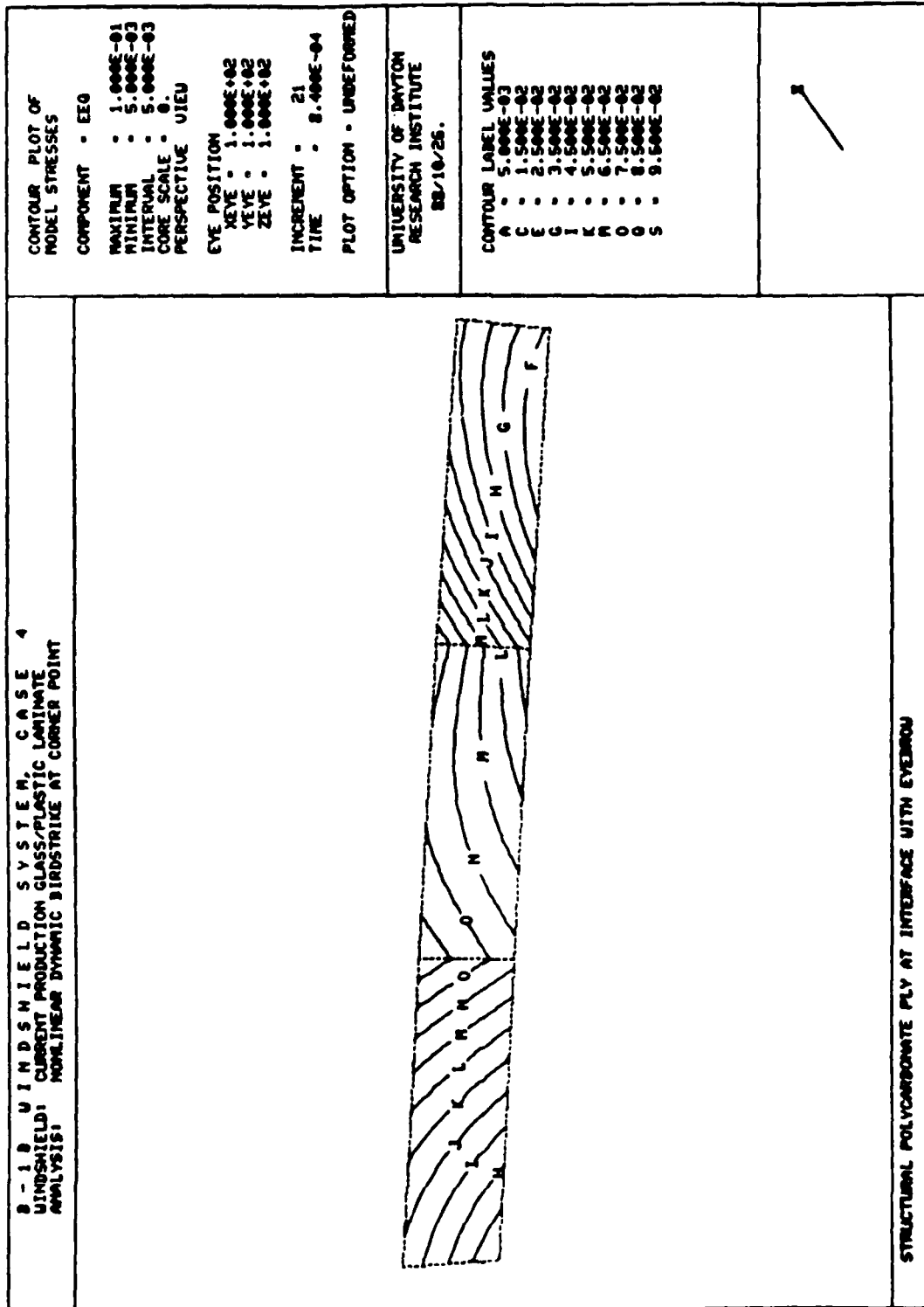


Figure 12. Equivalent Strain Contours Through the Thickness of the Structural Ply at the Upper Corner Windshield/Eyebrow Interface, Case 4.

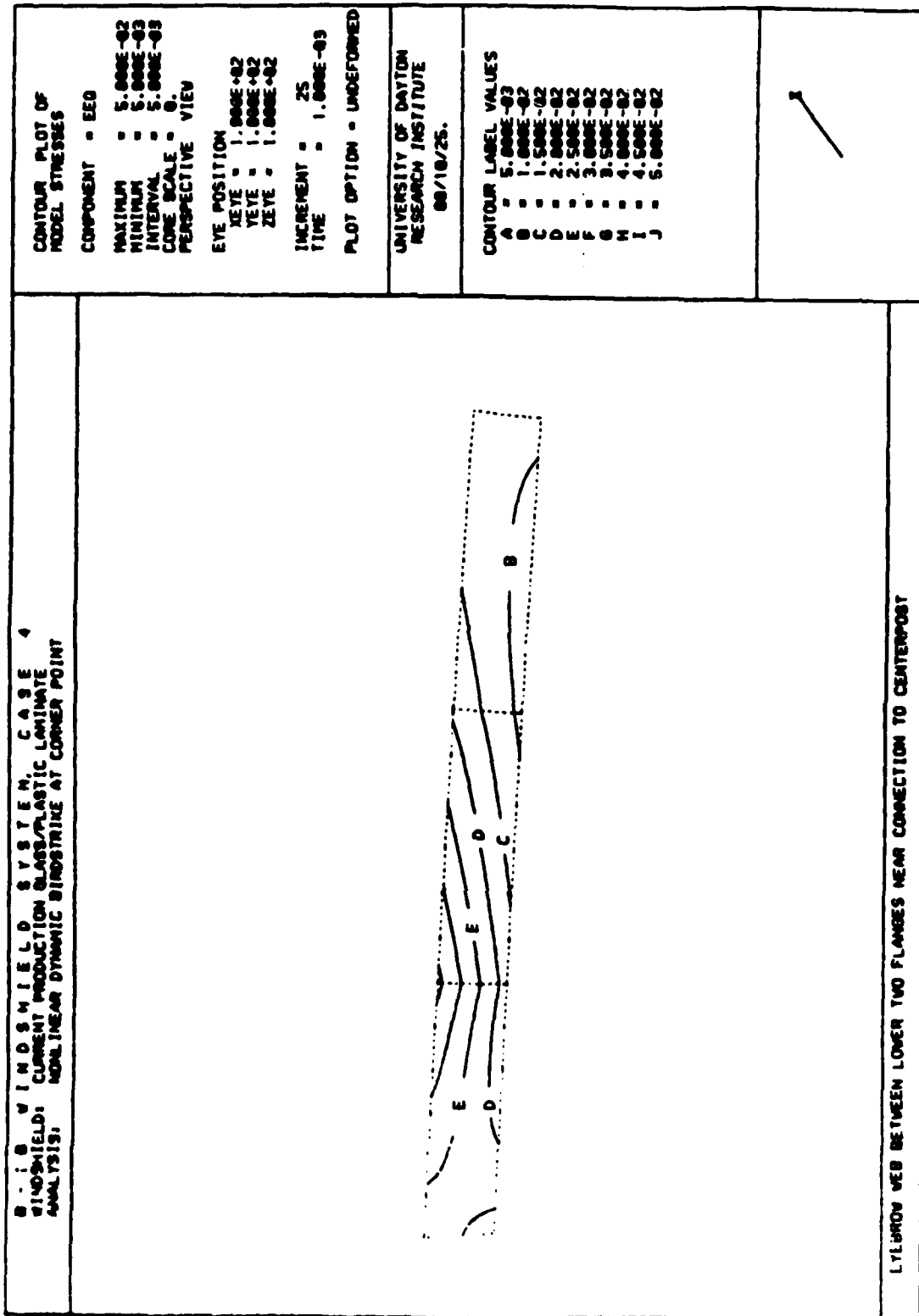


Figure 13. Equivalent Strain Contours on Lower Portion of Eyebrow Web, Case 4.

TABLE 7  
Fastener Analysis Summary

Case No.	Category	Model Description	Loads	Safety Margins <sup>C</sup> Tension Shear Bearing Rupture	Safety Margins (50% fastener removal) Tension Shear Bearing Rupture	Interaction Relation Values <sup>d</sup> All Present 50% Removal
1	Baseline	Current Production Windshield	Natural Frequency	-	-	-
2	Baseline	Current Production Windshield	Internal Pressure	3.12 4.64 6.50 20.91	1.06 1.82 2.75 24.66	0.06 0.28
3	Baseline	Current Production Windshield	Impact at A	2.18 2.55 3.72 12.78	0.59 0.77 1.36 15.14	0.12 0.57
4	Baseline	Current Production Windshield	Impact at B	0.99 0.98 1.63 6.68	-0.01 -0.01 0.32 8.00	0.38 2.05
5	Trade Study	Acrylic Outer Ply	Impact at B	1.16 1.44 2.25 8.48	0.08 0.22 0.62 10.10	0.28 1.41
6	Trade Study	Urethane Interlayer	Impact at B	1.15 1.31 2.07 7.97	0.07 0.15 0.54 9.51	0.30 1.52
7	Trade Study	Remover Inner (Spall) Ply	Impact at B	1.15 0.84 1.45 6.15	0.07 -0.08 0.22 7.37	0.38 2.15
8	Trade Study	Split Main Structural Ply	Internal Pressure	3.30 6.17 8.53 21.84	1.15 2.58 3.77 31.61	0.06 0.24
9	Trade Study	Split Main Structural Ply	Impact at B	1.47 0.68 1.23 5.52	0.23 -0.16 0.12 6.64	0.38 2.35

- Notes:
- a. Point A is center-center location of windshield
  - b. Point B is adjacent to the corner connection between the centerpost and eyebrow.
  - c. Safety margins < 0.0 indicate failure
  - d. Interaction Relation values > 1.0 indicate failure

# FASTENER STRESS SUMMARY

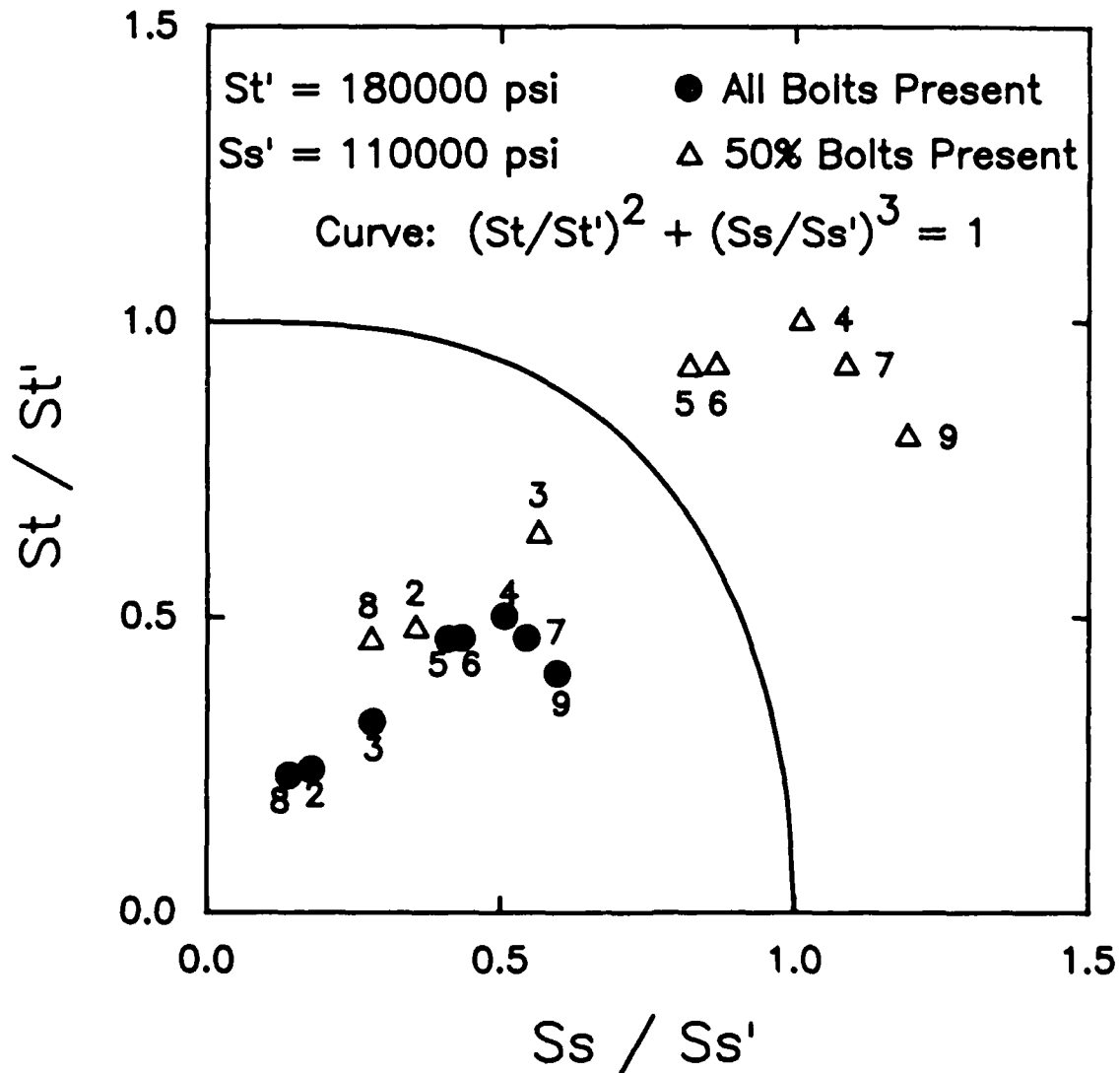


Figure 14. Fastener Stress Summary.

# B-1 B Case 4 Incr 21

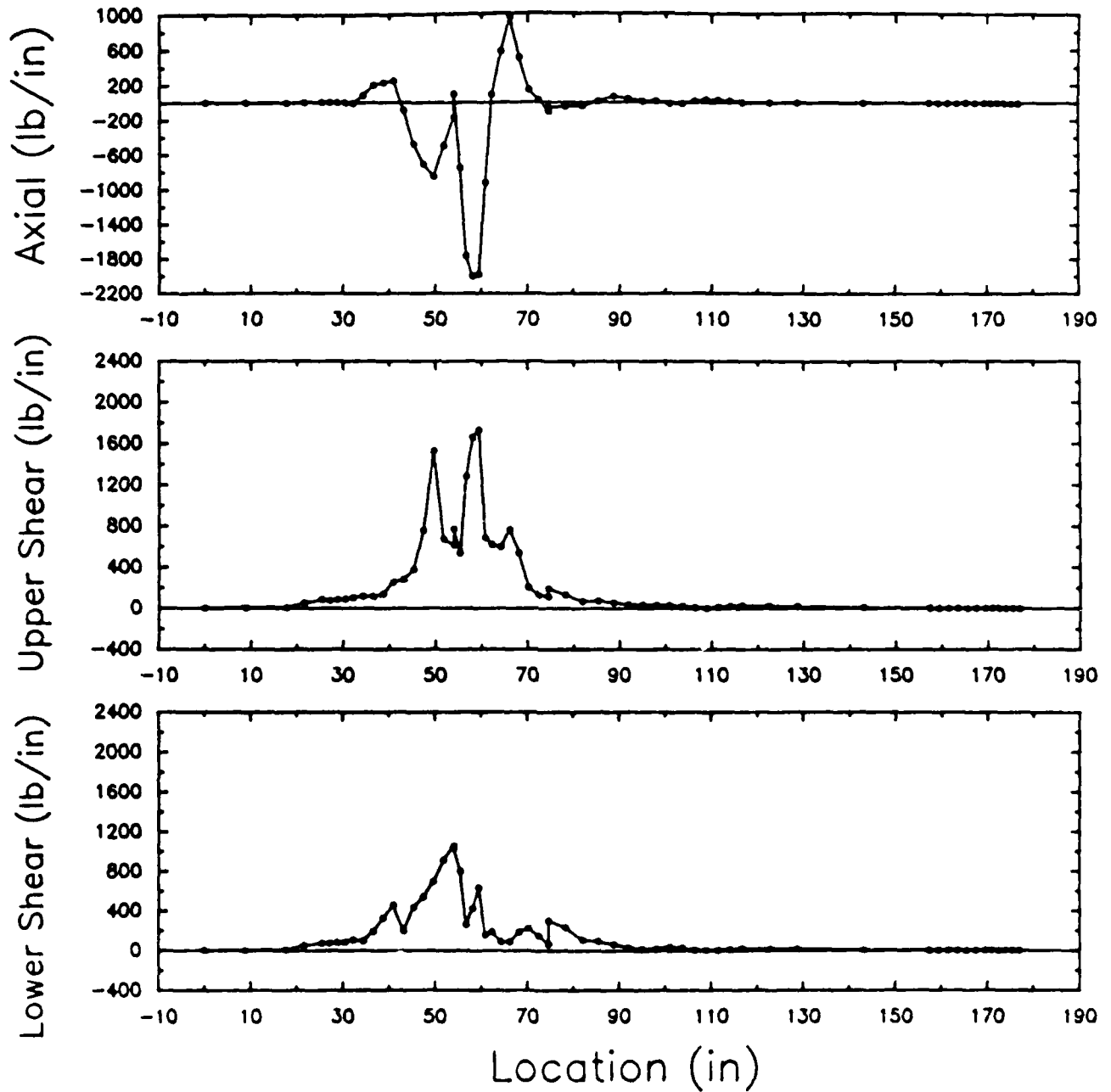


Figure 15. Fastener Load Distribution, Case 4.

somewhat, while removing the spall ply or splitting the structural ply reduced the margins somewhat. With every other fastener removed, the safety margins were still acceptable for the near-center impact, but were approximately zero for upper corner impact, meaning that fastener failure occurred. Any attempt to eliminate fasteners from the various windshield configurations must therefore be selective in both the quantity and the location of the fasteners removed.

Finally, based on a review of B-1B and B-1A fastener system drawings, it appears that the existing B-1B fastener-to-bushing tolerance is adequate to facilitate windshield changeout. As shown in Figure 16, the minimum clearance is 0.010 inches between the fastener and frame member. Based on B-1A birdstrike test results for windshields having bushings with the as-specified fastener-to-bushing tolerance and windshields having bushings with an oversize tolerance (Ref. 8, 17), the existing B-1B tolerance should not change the structural behavior of the windshield system. All results reported herein should therefore be representative of the full-scale B-1B windshield system performance.

### CONCLUSIONS

As a result of the MAGNA analyses, the following conclusions concerning the structural performance of the current production and alternate configuration B-1B windshield systems were reached:

1. The current production and the split polycarbonate structural ply windshield configurations resisted internal cabin pressures of up to 21.2 psig (ultimate pressure) without permanent deformation to the windshield panel or the immediate support structure. Similar performance is to be expected for all of the other trade study configurations.

2. The current production windshield configuration was capable of resisting impact by a four pound bird at the near-center location at 650 mi/hr without fracture of the windshield panel or immediate support structure. Similar performance is to be expected for the trade study configurations.

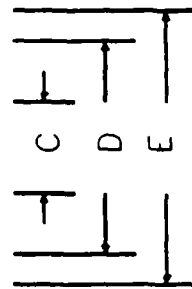
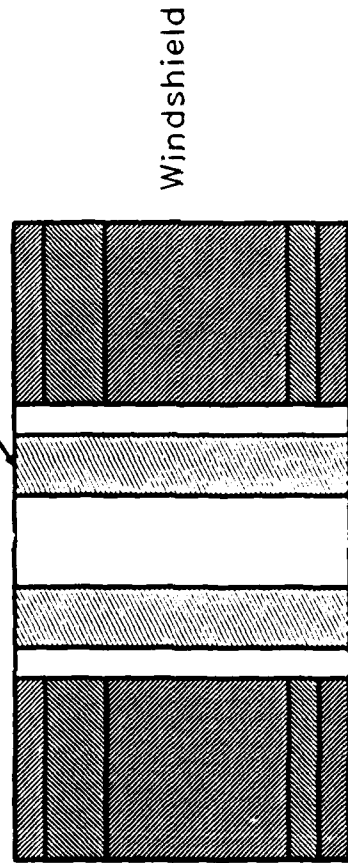
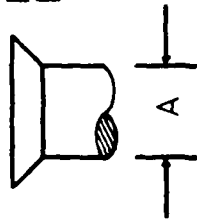
3. All windshield configurations were capable of resisting impact by a four pound bird at the upper corner location at 650 mi/hr without fracture of the windshield panel or immediate support structure.

4. The upper corner impact location was more critical than the near-center location, resulting in higher stresses and local yielding in the windshield structural ply (plies) and the supporting framework.

5. All of the various windshield configurations demonstrated similar resistance to upper corner birdstrike except for the split polycarbonate ply configuration, which exhibited somewhat more windshield



NAS1580C4  
Fastener



Dimensions for B-1B (inches)

- A = 0.2490 - 0.2495
- B = 0.261 +.004/-0.001
- C = 0.266 +/-0.001
- D = 0.4005 +/-0.0010
- E = 0.4063 +.0005/-0.0043
- F = 0.261 +.004/-0.001

Note: C = 0.257 for B-1A

Figure 16. B-1B Fastener System Dimensions.

deflection (0.23 - 0.48 inch increase) and structural polycarbonate yielding (0.07 - 0.08 in./in. increase).

6. The yielded region in the eyebrow frame (the web between the bottom two flanges near the connection to the centerpost) due to upper corner birdstrike was the same region that fractured in upper corner birdstrike testing of the B-1A windshield system. Apparently the redesign of the crew enclosure from B-1A to B-1B did not eliminate the presence of high stresses in this region due to upper corner bird impact. Strains of up to 4% were present, half of the ultimate (fracture) strain of 8% for the 7075-T73 aluminum. Fracture should not occur in the B-1B eyebrow unless the strain to failure is degraded (due, for instance, to improper material processing, embrittlement, or stress concentration).

7. The total strain present in the structural polycarbonate ply (plies) due to upper corner birdstrike was well below the elongation to failure for polycarbonate. Fracture of these plies during upper corner bird impact should therefore not occur unless the polycarbonate elongation is degraded.

8. The current production and trade study fasteners resisted internal cabin pressures up to 21.2 psig without failure.

9. Analysis of the current production windshield revealed that the upper corner impact produced fastener safety margins which were 50% less than those resulting from the near-center impact.

10. All fasteners in the current production and trade study windshield configurations withstood near-center and upper corner impact by a four pound bird at 650 mi/hr without failure.

11. With every other fastener deleted, the remaining fasteners were sufficiently strong to resist failure when the current production windshield was subjected to impact by a four pound bird at the near-center location. Similar fastener performance is to be expected for the trade study configurations.

12. When every other fastener was removed from the current production and trade study windshield configurations, the resulting safety margins for upper corner impact were reduced to approximately zero, implying that fastener failure was probable. Deletion of fasteners to facilitate windshield changeout must therefore be more selective as to the quantity and location of the deleted fasteners.

13. The critical fastener tolerance for windshield changeout was identified to be the fastener-to-frame tolerance. This tolerance (0.010 - 0.015 inches) was larger than the B-1A tolerance (0.007 inches) and was judged to be adequate to facilitate windshield changeout. The existing B-1B tolerance does not change the results reported herein, that is, the structural performance is not degraded or improved by this tolerance.

## REFERENCES

1. Bouchard, Michael P. and Braisted, William R., B-1B Improved Windshield Development, Volume II: MAGNA Analysis: Baseline and Parametric, UDR-TR-88-129, University of Dayton Research Institute, Dayton, Ohio, November 1988.
2. Sanders, Eugene J., Results of Qualification Testing of Bird Resistant Windshields for the B-1 Aircraft, AEDC-DR-75-87, Arnold Engineering Development Center, Arnold Air Force Station, Tennessee, September 1975.
3. Brockman, R.A., MAGNA (Materially and Geometrically Nonlinear Analysis, Part I - Finite Element Analysis Manual, AFWAL-TR-82-3098, Part I, Air Force Wright-Aeronautical Laboratories, Wright-Patterson Air Force Base, Ohio, March 1984.
4. Bruner, T.S., Brockman, R.A., and Primrose, K.A., MAGNA (Materially and Geometrically Nonlinear Analysis, Part II - Preprocessor Manual, AFWAL-TR-82-3098, Part II, Air Force Wright-Aeronautical Laboratories, Wright-Patterson Air Force Base, Ohio, March 1984.
5. McCarty, R.E. and Hart, 2nd Lt. J.L., "Validation of the MAGNA Computer Program for Nonlinear Finite Element Analysis of Aircraft Transparency Bird Impact," from AFWAL-TR-83-4154, Proceedings for Conference on Aerospace Transparent Materials and Enclosures, pp. 921-972, Air Force Wright Aeronautical Laboratories, December 1983.
6. Hoit, Marc and Wilson, E. L., "An Equation Numbering Algorithm Based on a Minimum Front Criteria," Computers and Structures, Vol. 16, Nos. 1-4, pp. 225-239, 1983.
7. Brockman, R.A., Simple Finite Elements for Layered Plates and Shells, UDR-TR-87-111, University of Dayton Research Institute, Dayton, Ohio, August 1987.
8. Sanders, Eugene J., Results of Bird Impact Testing of Prototype B-1 Windshields and Supporting Structure Design, AEDC-DR-76-100, Arnold Engineering Development Center, Arnold Air Force Station, Tennessee, December 1976.
9. Sanders, Eugene J., Results of Further Tests to Evaluate the Bird Impact Resistance of Windshields for the B-1 Aircraft, AEDC-DR-76-43, Arnold Engineering Development Center, Arnold Air Force Station, Tennessee, May 1976.
10. Brockman, R.A. and West, B.S., Bell-Boeing V-22 Birdstrike Loads Estimation, UDR-TM-86-12, University of Dayton Research Institute, Dayton, Ohio, July 1986.
11. Barber, John P., Taylor, Henry T., and Wilbeck, James S., Bird Impact Forces and Pressures on Rigid and Compliant Targets, AFFDL-TR-77-60,

Air Force Wright Aeronautical Laboratories, Wright-Patterson Air Force Base, Ohio, May 1978.

12. West, Blaine S. and Brockman, Robert A., Evaluation of Bird Load Models for Dynamic Analysis of Aircraft Transparencies, AFWAL-TR-80-3092, Air Force Wright Aeronautical Laboratories, Wright-Patterson Air Force Base, Ohio, August 1980.
13. Braisted, William R., Transparency Fastener Study Based on MAGNA Finite Element Analysis Results, UDR-TM-88-35, University of Dayton Research Institute, Dayton, Ohio.
14. Brockman, R.A., Bruner, T.S., Hecht, M.J., Bouchard, M.P., and Wright, M.E., MAGNA (Materially and Geometrically Nonlinear Analysis, Part III - Postprocessor Manual, AFWAL-TR-82-3098, Part III, Air Force Wright-Aeronautical Laboratories, Wright-Patterson Air Force Base, Ohio, March 1984.
15. Rubenstein, Steve, Norby, John, and Mitchell, Dick, Sigma Plot - Scientific Graph System, Version 3.0, Jandel Scientific, Sausalito, California, 1986.
16. \_\_\_\_\_, Merlon Polycarbonate Design Manual, Plastics Division, Mobay Chemical Corporation, Pittsburgh, Pennsylvania.
17. Magnusson, R.H., High Speed Bird Impact Testing of Aircraft Transparencies, AFFDL-TR-77-98, Air Force Wright Aeronautical Laboratories, Wright-Patterson Air Force Base, Ohio, June 1978.
18. \_\_\_\_\_, Military Standardization Handbook - Metallic Materials and Elements for Aerospace Vehicle Structures, MIL-HDBK-5D, Volume 1, Department of Defense, Washington, D.C., June 1983.
19. Lawrence, James A. Jr., Guidelines for the Design of Aircraft Windshield/Canopy Systems, AFWAL-TR-80-3003, Air Force Wright Aeronautical Laboratories, Wright-Patterson AFB, OH, February 1980.
20. Greene, F. E., Testing for Mechanical Properties of Monolithic and Laminated Polycarbonate Materials--Part I: Test Results and Analysis, AFFDL-TR-77-96, Part I, Air Force Wright Aeronautical Laboratories, Wright-Patterson AFB, OH, October 1978.
21. \_\_\_\_\_, Military Standardization Handbook, Plastics for Aerospace Vehicles--Part II: Transparent Glazing Materials, MIL-HDBK-17A, Part II, June 1977.
22. Rockwell B-1B Drawing L 3051091, note for Parts -007 and -008.
23. Clayton, Kenneth I., Milholland, John F., and Stenger, Gregory J., Experimental Evaluation of F-16 Polycarbonate Canopy Material, AFWAL-TR-81-4020, Air Force Wright Aeronautical Laboratories, Wright-Patterson AFB, OH, April 1981.

24. \_\_\_\_\_, Military Standardization Handbook - Metallic Materials and Elements for Aerospace Vehicle Structures, MIL-HDBK-5D, Volume II, Department of Defense, Washington D.C., June 1983, p. 8-91.

AIRCRAFT WINDSHIELD DESIGN WITH LARGE STRUCTURAL ANALYSIS CODES

Arnold H. Mayer  
Richard A. Smith

Flight Dynamics Laboratory

## Abstract

### Aircraft Windshield Design with Large Structural Analysis Codes

Arnold H. Mayer, Branch Chief  
Richard A. Smith, Project Engineer

Aircrew Protection Branch

Vehicle Subsystems Division

Flight Dynamics Laboratory

Wright Research and Development Center, WPAFB, OH 45433

This paper deals with the analytical design of military aircraft windshields and transparent crew enclosures. Trends are discussed that make a more analytically based, as opposed to empirically based, design practice desirable. The role of large codes especially large finite element structural dynamics analysis codes in meeting the accuracy requirements with respect to modeling performance under specified use environments is sketched and their consequent value for design purposes suggested. A recent instance in which structural analysis code MAGNA was applied to the structural design of a new transparency systems is cited and that experience is used to anticipate the situation in which a set of codes of comparable complexity might be used to analytically design a transparency to meet multiple interdependent performance requirements.

The contemplation of this situation suggests that it represents a prohibitively expensive approach to design. Several ideas are proposed regarding how such a collection of accurate large codes can be used to design transparencies without incurring this excessive cost. One of the proposals is illustrated with respect to the structural impact design aspect. This employs text book solution techniques for canonical structural shapes to aid in the initial guessing and design convergence process requiring only a small number of iterations. Experience and results obtained to date in an application to an irregularly shaped Space Shuttle window are reported and extensions to include additional design attributes such as thermal response, optics and radar cross section are outlined.

Aircraft Windshield Design With Large Structural Analysis Codes  
Arnold H. Mayer, Richard Smith, AFWAL Flight Dynamics Laboratory

This paper deals with the analytical design of complex fighter aircraft windshields and transparent crew enclosures. The paper seeks to contribute to the creation of a product development process capable of bringing to market military aircraft windshields and canopies which feature a balanced mix of high performance levels in an increasing multiplicity of important functions and qualities which these subsystems are expected to perform and manifest. Goal benefits of the capability being pursued are significant reductions in development cost and schedule over what would result if current windshield development practice were to be applied to the more complex military transparent subsystems of tomorrow.

An overview of the many functions transparent enclosures are required to perform is presented first with some indications regarding which functions are currently emphasized and which will become more important in the future. Current development practice is described, and anticipated shortcomings with respect to developing future high complexity transparent enclosures are identified. Trends being set in the evolution of a transparency development process as a result of the directions of Air Force sponsored research and technology development are outlined next and some anticipated problems which may result in a prohibitively expensive process are indicated. Current deficiencies of existing tools and methods are also discussed. Alternative approaches are then proposed that could lead to significant cost reductions and to an appropriate ultimate transparency development process. A sample application of one approach to reduced cost design for the impact structural aspect of windshields is described, and the possible payoff of extensions of this approach that would address all windshield design requirements is forecast.

#### Aircraft Transparency Functions and Quality Requirements

Table I summarizes the many required functions and qualitative factors of military aircraft transparencies. A more detailed discussion of these also may be found in the Aircraft Transparency Design Guide AFWAL TR-80-3003. (1)

In the past, concern centered mainly on the safety-of-flight issue and bird-impact tolerance. More recently there has been an awakening to the service life durability issue and interest in the optical interplay of windshields with Head-Up-Displays and targeting/weapon aiming functions. Currently attention is being drawn to the low-observability aspects. In the future, vulnerability to various advanced weapons such as lasers, high power microwave and chemical-biological threats are expected to become firm requirements.

#### Current Windshield Development Process

The traditional and dominant current development practice is empirically based, (1) relying heavily on prior bird impact test results on flat panels or similarly shaped windshields of the same material or cross sectional



constructions of interest. More recently, successful attempts have been seen to design complex windshields through the use of finite element structural dynamics analysis codes. (2) This analytical design approach for the structural requirement appears to offer at least a factor of ten reduction in development costs relative to a purely empirical approach when relevant prior data specific to the particular design problem are unavailable. The current development process, then, is seen to be a largely empirical one, which makes heavy use of experimental correlations developed for flat plates and birdstrike testing results from previous designs, coupled with shrewd engineering guesswork. The role of computer analysis is relegated for the most part, if it is done at all, to checking a final design.

Moreover, all windshield design approaches used to date, whether they be empirically or analytically based, yield what may be termed feasible designs that have no pretensions to be in any sense optimal, or minimum weight designs.

An important source of the high costs in an empirically based design approach is the costly requirement to fabricate a test article to prove the birdstrike resistance of each design iteration. Due to this cost, an empirically developed design will have been able to afford only a small number of design iterations, thus resulting in a feasible or suboptimal design that may usually embody both greater strength margin and weight than necessary.

The structural design problem for aircraft transparencies requires that a number of structural considerations be satisfied. Important among these are impact strength, bounded maximum deflection and a non-simple constraint function involving the slope and deflection time histories (during the impact event) of the windshield aft arch. This last constraint addresses the injury potential of bird debris that enters the cockpit through transient openings created between the windshield aft arch and the canopy and limits the impulse of admitted debris on the pilot's head.

Many other attributes and qualities of windshields are important to their successful functioning. These include temperature tolerance due to aeroheating, high power microwave and laser irradiation; visual optical characteristics such as optical clarity, efficient light and distortion-free image transmission; suppression of radar cross section due to electromagnetic wave scattering from the cockpit; suppression of sunlight reflections as an unwanted telltale signature; and, durability with respect to undesired manifestations of weathering, aging, wear, impact and maintenance induced phenomena. Many of these performance aspects are amenable to analysis; some, primarily, the durability characteristics, are not as yet. Neither are the effects of these and locked-in manufacturing stresses on each other and the various kinds of desired performance. Where these attributes are amenable to analysis, experience has found that large computer codes are necessary to achieve the desired accuracy.

With the incorporation of design features in transparencies that address the many new and important hostile threats and environmental factors comes a complexity stemming from the interdependence of these many desired attributes. The result of this is that any single design attribute can no longer be enhanced other than at the expense of the others. The fabrication cost of a complete product accordingly tends to increase significantly due to the many diverse features that may need to be incorporated.

Because of the above considerations, a purely empirical approach is out of the question, being too costly, and will, because of the mutual interference of attributes result in a number of these being marginal relative to their desired levels. Recourse to more reliance on analysis definitely is indicated and especially accurate analysis since we are looking for the attainable optimum balance of attributes. This approach, unless carefully executed, runs the risk of being also a high cost approach as will be shown. A recent instance of using a large finite element analysis code to design for the structural impact attribute alone found that an \$18,000 computer cost was incurred. (2)

The case in point involved 20 design iterations to arrive at an acceptable (not necessarily an optimum) design for the T-46 windshield and aft arch and cost \$18,000 in computer charges utilizing the MAGNA structural analysis code. Let us analyze the cost of designing a transparency with respect to M different design variables using a hypothetical collection of N large stand-alone computer codes. The cost function reflects the total cost as being the product of the cost per iteration and the number of iterations

$$C = c(i) * I$$

In the above example the cost per iteration was

$$c(i) = \$18,000/20 = \$900$$

When designing for M variables with N large stand-alone programs, the total number of iterations would be

$$I = \text{PROD} (N * i(j)), j = 1,2,3, \dots, M \quad (3)$$

the product of the number of iterations required to optimize for each variable alone. Let us see what the cost would be to optimize a windshield with respect to structural, thermal, optical, and radar cross-section features. Assume that appropriate materials and a material stackup order already have been selected and that the structural, thermal, optical, and low observability properties may be optimized by determining the thicknesses of 3, 1, 1 and 1 plies associated respectively with these four performance categories. As this involves six design variables, assume also that six iterations are required for each variable for each computer code at a cost of \$500 per execution. This would amount to a total cost of

$$C = c(i) * (N1) ** M \quad (4)$$

$$C = \$500 (4 \times 6) ** 6 = \$9.55E10 \quad (5)$$

or almost 100 billion dollars. If  $i = 3$ ,  $C = \$1.493 \times 10^9$  (6)

This is obviously a prohibitive cost. Something drastic certainly is required to reduce this cost to an affordable level before widespread use of computer codes to design the many features of a transparency becomes a reality.

After having discussed the trend of multiplying design requirements for military aircraft windshields, the concomitant complexity, and difficulty of developing transparencies that simultaneously offer high levels of capability with respect to the many performance aspects, the need for accurate but inexpensive analytical design tools is brought into focus. The accurate design tools on hand and under projected development are not inexpensive to acquire or operate, although the US Air Force continues to bear the cost of developing these tools.

#### Serial Optimization with respect to M Design Variables

A two dimensional illustration of the serial optimization approach may be considered. See Figure 1. The hypothetical objective function, Z, is an elliptic paraboloid, with major and minor axes skewed at some angle to the X and Y axes. The objective function has its minimum at the origin. The independent variables are represented by the X and Y coordinates respectively. The first design guess is the point (X1, Y1). The optimization process follows this guess with an evaluation of the objective function at this point, and i additional guesses, each followed by an evaluation of the objective function in order to arrive at a value of Y = Y2, that minimizes Z to an acceptable level of accuracy while keeping X constant at its first guessed value of X=X1. The next step consists of incrementing X to a new value X=X2 while keeping Y=Y2. This is followed by i iterations of guessing Y to minimize Z while holding X=X2. If the value of Z after these last two operations has increased rather than decreased, the previous value of Z, then the increment in X leading to X2 must be reversed in sign. It is easily seen that for every one of the i increments of X needed to reach Z=0, that is, the optimum value of X, there will be at least i increments of Y needed to find the optimum value of Y while X is being held constant. Therefore, in a serial optimization process, using N stand-a-lone computer codes, the total number of iterations required to optimize M design variables will be greater or equal to

$$I = (N \cdot i) ** M \quad (7)$$

#### Parallel Optimization with Respect to M Design Variables

Assume that a design is acceptable if N measures of performance,  $\text{PHI}(i)$ ,  $i=1,2,\dots,N$ , are maximized or constrained to exceed or not to exceed certain specified values,  $\text{PHIO}(i)$ . The N performance measures depend on M design variables  $X(j)$ ,  $j=1,2,\dots,M$ . The desired balance among these performance

measures is expressed by the way they enter into an objective function, F, where  $F=F(\text{PHI}(i))$ . The design is considered optimum when the function F is an extremum, i.e. maximum or minimum. (3) Because of the dependence of the performance measures on the design variables, the objective function also depends on the design variables. A popular form of the objective function is

$$F = \text{SUM } [i,1:M] w(i) * \text{PHI}(i) \quad (8)$$

where the  $w(i)$  are relative weights attached to the various performance measures.

Now the gradient of the function F with respect to the design variables represents the greatest possible rate of change of F with respect to all possible combinations of changes in the design variables,  $X(j)$ . Thus

$$\text{grad } F = \text{SUM } [j,1:M] \frac{\partial F}{\partial X(j)} = \text{SUM } [i,1:N] \text{SUM } [j,1:M] \frac{\partial F}{\partial \text{PHI}(i)} * \frac{\partial \text{PHI}(i)}{\partial X(j)} \quad (9)$$

The particular design vector increment that produces the greatest change in F is parallel to the gradient of F. (3)

$$\text{or } dX(j) = \frac{\partial F}{\partial X(j)} * ds / \text{ABS } [\text{grad } F] \quad (10)$$

where ds is the size of the design vector increment.

It is of interest to estimate the cost of applying a parallel optimization process to a design problem involving N performance measures which are evaluated by N large computer programs and which depend on M design variables while i is the number of iteration steps required to converge for a single variable. The number of computer runs will be  $I = N(M+1)*i$  with a cost  $C = c(i) * I = c(i) * N(M+1) * i$ . Thus the total cost for the previous example would be

$$C = \$500 * 4 * 7 * 6 = \$84,000 \quad (11)$$

which might be considered an affordable number given the value of the end result achieved. If  $i = 3$ ,  $C = \$42,000$  (12)

This parallel process cannot be accomplished today without development of a super executive computer program that causes the direction and magnitude of the design vector increment at each iteration to be computed and that then causes the N computer programs to evaluate the objective function at the new design variable values.

Since the large analysis computer programs are not set up to calculate sensitivities, it would take an additional run of each computer program to compute the corresponding sensitivity for each variable, so that again we run into increased costs.

We have shown that multi dimensional optimization is only practical if it is conducted as a parallel process in which each iteration of the convergence process toward an optimum design involves updated guesses of the optimum values for all the design variables simultaneously. To be totally practical the parallel process itself should be implemented using an executive computer program to orchestrate the computation of the objective function, its gradient, and the components of the steepest ascent vector increments and each execution of the set of performance codes.

It should be pointed out that, since the performance functions are not given analytically, computation of numerical estimates of the partial derivatives that enter into the gradient will require one execution of each performance code for each design variable increment plus one execution per code to compute the performance at the value of the new design vector at each iteration step.

Therefore the total number of computer runs required will be

$$I = N (M + 1) I \quad (13)$$

For the previous example, the cost will be

$$C = 4 \times 7 \times 6 \times 500 = \$84,000 \quad (14)$$

By employing simple analytical models to estimate the sensitivities of the various performance factors, the number of computer runs may be further reduced to  $1/(M + 1)$  of the above value

$$\text{or } I = N I \quad (15)$$

The cost for the previous example now will be

$$C = 4 \times 6 \times 500 = \$12,000 \quad (16)$$

which certainly, represents a significant cost reduction.

$$\text{If } i = 3, C = \$6,000 \quad (17)$$

Costs associated with the various optimization strategies as applied to the design of a laminated windshield are compared in tables 2 and 3.

The use of the simple analytical models for the structural dynamic performance will now be illustrated for several selected cases.

- (1) Design of a monolithic quartz window for the space shuttle;
- (2) Design of a monolithic polycarbonate window for the space shuttle;
- (3) Combined thermal/structural design of a laminated structural element;
- (4) Design of a monolithic canopy for the F-4.

Design of a monolithic quartz window for the space shuttle.

The irregular shape of the shuttle window is shown in Figure 2. The fused quartz material to be used represents a linear elastic material that fails in brittle fracture at a particular value of tensile stress.

The approach to developing an approximate analytical design model for this window consists of approximating it by a circular, simply supported elastic plate loaded at its center over a circular area by a constant pressure load which represents a rectangular pulse in the time domain. Simple plate theory was used with the usual assumption that cross-sections perpendicular to the thicknesses remain plane.<sup>(4)</sup> The problem is reduced to the vibration of a one dimensional linear oscillator (lumped spring-mass system) by equating the power of the forces to the time-rate of change of kinetic and potential energies.<sup>(5)</sup> The one-dimensionality of the problem and the calculation of the kinetic and potential energies is facilitated by assuming the system oscillates in its fundamental mode with the eigenfunction being approximated by half of a period of a cosine function in which the plate radius represents a quarter of a wavelength. The maximum bending moment and stress are found at the center and set equal to the fracture stress to determine the plate thickness. The failure curve connecting dimensionless plate thickness, stress and bird velocity versus dimensionless bird mass is shown in Figure 3. The derivation of the design equation is summarized in Figure 4.

The analytical expression corresponding to this curve was used to guess the plate thickness at fracture for a four pound bird impacting at the center with a closing velocity of 100 knots. Then the MAGNA program (6, 7, 8) was executed with a finite element model of the actual plate shape for this thickness and the true bending stress determined. A correction factor for the circular plate stress expression was then calculated so that it would predict the stress computed by the MAGNA program. The corrected expression was then used to calculate a new plate thickness corresponding to the failure stress. Reanalysis of the stress corresponding to the corrected guess of plate thickness using the MAGNA program then yielded a value sufficiently close to but less than the failure stress, demonstrating convergence of guesses had been achieved. The sequence of thickness guesses and corresponding stresses is shown in Table 4. Typical output from a Magna Program execution is shown in Figure 5.

#### Design of a monolithic polycarbonate window for the space shuttle.

This design problem is similar to the foregoing problem except that the material is a nonlinear elastic material that fails in yielding.<sup>(14)</sup> The criterion of yielding used was that of Hencky and Von Mises which is equivalent to stating that the octahedral shear stresses are equal to 47% of the tensile stress at yielding from a uniaxial tensile test.<sup>(9)</sup> The same fundamental eigenfunction was assumed as in the last problem. The energy equation<sup>(10)</sup> approach this time led to a non-linear oscillation equation of motion for the center deflection which was solved by assuming the deflection at the instant of cessation of the pressure pulse could be given with sufficient accuracy by the solution to the equation of motion using a linearized stress-strain curve.

A more realistic treatment of the deformation was used this time and assumed that the latter consisted of a combination of simple plate bending and midplane stretching using small deflection mathematical approximations following an approach described by Den Hartog. (11) The deformation energies for these two deformation modes were calculated independently of each other and then added to approximate the total elastic energy.

The same iteration process approach was employed as in the previous problem. The sequence of guesses and stresses is shown in Table 5.

More iterations were required than in the linear material example, but the advantage remains.

#### Combined Thermal Structural Design of a Layered Structural Element

Thermophysical properties are an equally important class of design variables besides those consisting of purely geometric entities like shape and dimensions.

These former variables cannot be varied independently of one another, in general. Each choice of a different material implies a certain fixed combination of values of the thermo physical properties belonging to it.

In order to learn how to treat transparency optimization problems in which multiple thermophysical properties are involved and to which appropriate choices of materials hold the key, it was decided to study a much simpler structural element. Instead of a dynamic plate impact problem, a statically loaded rod in tension having a constant cross-section and layered construction along its length was studied. This system was required to satisfy both structural and thermal requirements. The solution to this combined functions and environments optimization problem was expected to suggest a correspondingly appropriate approach to the multi functions/environments optimization problem for more complex structural systems, like plates and shells, which are representative of aircraft transparencies.

First we study the material choice problem without the thermal requirements. Therefore, assume a rod of linear elastic material subject to a maximum tensile load  $P_0$ . The stress in the rod must remain below the yield stress,  $S_y$  and the deflection is to be limited to  $d_{max}$ . Consider first only the structural function independent of temperature and lets require to find the structural material that leads to a rod of minimum weight. It is easily shown that the material possessing the lowest value for the following figure-of-merit,  $F.O.M = \rho E / S_y^2$  will lead to the rod of minimum weight.

Turning now to the combined structural-thermal problem we add the requirement that the ends of the rod be exposed to the temperatures  $T_1$ , and  $T_2$  respectively and that the heat transfer through the rod must be limited to the rate,  $Q$ . The important consideration in this problem is that materials be used only within temperature ranges below their maximum service

temperature. The approach to assuring this and picking the optimum material for each layer that minimizes the weight of the rod is as follows.

Plot the upper service temperature limit of each material on a temperature scale showing the maximum and minimum service temperatures of interest. Then define temperature intervals

$$T_{s1} - T_1, T_{s2} - T_{s1}, \dots, T_2 - T_{sn} \quad (18)$$

within each of which one material is to be selected. All materials with service temperatures exceeding the lower limit of a given temperature interval may be used in that interval. For each interval rank the applicable materials with respect to the appropriate figure of merit.

The figure of merit in this case turns out to be  $\rho/K$  the product of density and thermal conductivity. The value of the constant area is then determined by the material in the set of materials of lowest figures of merit which has the least yield stress,  $S_y$ . The above analysis is summarized in Figure 6.

#### Design of a Monolithic Canopy for the F-4

The detailed approximate symbolic analytical design expression for this case has not yet been worked out and therefore was not available for use with MAGNA. There appears to be no difficulty in principle however. In fact according to theoretical treatises on this subject simple, flat plate models are applicable here and represent legitimate approximations to curved shell bending problems when mid-plane strain may be neglected. Moreover, this paper has extended the application of theories for static large deflections of flat plates which include mid-plane stretching to the dynamic impact case. In light of the preceding considerations, this then should also work for the dynamic impact of curved shells representative of aircraft canopies such as the F-4.

#### Combined Windshield and Aft-Arch Optimization Problem

For the case in which the windshield and the aft-arch each may be treated separately as linear one or two dimensional systems, their combination would result in a single multidimensional system whose motion is described by a set of ordinary linear differential equations, whose solution in terms of symbolic expressions is basically a matter of Algebra but which becomes a tedious matter for the analyst if the dimensions are greater than two. Symbolic computer programs<sup>(12,13)</sup> now exist that can perform these tedious Algebraic manipulations as well as integrate all differential equation systems for which the solution can be expressed in terms of the known functions of analysis. These symbolic program should become increasingly useful as symbolic analytical design expressions are combined with numerical analysis to perform the challenging design optimization associated with aircraft transparencies.



## Conclusions

It is concluded that accurate, efficient, low cost, balanced design optimization of aircraft transparencies with respect to multiple functions is possible and practical if large numerical codes which analyze the various performance aspects of transparencies are used in conjunction with simple approximate analytically derived symbolic design expressions in a total parallel design process. The process requires for its operation a super-executive program, not yet developed, to orchestrate the execution of each large analysis program and to cause the systematic updating of the vector of guessed optimal values of the design variables. A design variable guess improver module is also needed which should embody a steepest ascent (descent) algorithm as suggested in this paper.

The advantages that accrue from the use of the simple symbolic analytical models are:

- (a) they can perform the function of a design guess improver;
- (b) they provide insight, by inspection, into the effect of the design variables on the design;
- (c) they help reduce the number of design variables by identifying a smaller number of dimensionless groups;
- (d) they dramatically lower the cost and convergence power per iteration.

Feasible approaches are shown for treating the optimal material selection problem in multi-material designs while taking account of the environmental tolerances of the materials.

The approach works in terms of selecting materials for application to various portions of the design according to extreme values of appropriate figures of merit. This material selection problem has always been considered one of the most challenging problems associated with design.

## REFERENCES

### Aircraft Windshield Design With Large Structural Analysis Codes

1. Lawrence, James Jr., Guidelines for the Design of Aircraft Windshield/Canopy Systems, Flight Dynamics Laboratory, Wright-Patterson Air Force Base, Ohio 45344-6553, AFWAL-TR-80-3003, February 1980.
2. McCarty, R.E., Analytic Assessment of Bird Impact Resistant T-46 Aircraft Windshield Designs Using MAGNA, 15th Aerospace Transparent Materials and Enclosures Conference, Monterey, California, January 1989.
3. Pierre, Donald A., Optimization Theory With Applications, Dover Publications, Inc., New York, 1986.
4. Timoshenko, S., and Woinowsky-Krieger, S., Theory of Plates and Shells, McGraw Hill Co., Inc., New York, 1959.
5. Tong, Theory of Mechanical Vibrations, McGraw Hill Co., Inc., New York, 1959.
6. Brockman, R.A., MAGNA (Materially and Geometrically Nonlinear Analysis) Part I - Finite Element Analysis Manual, Flight Dynamics Laboratory, Wright-Patterson Air Force Base, Ohio 45344-6553, AFWAL-TR-82-3098 Part I, December 1982.
7. Brockman, R.A., MAGNA (Materially and Geometrically Nonlinear Analysis) Part III - Postprocessor Manual, Flight Dynamics Laboratory, Wright-Patterson Air Force Base, Ohio 45344-6553, AFWAL-TR-82-3098 Part III, December 1982.
8. Brockman, R.A., MAGNA (Materially and Geometrically Nonlinear Analysis) Part IV - Quick Reference Manual, Flight Dynamics Laboratory, Wright-Patterson Air Force Base, Ohio 45344-6553, AFWAL-TR-82-3098 Part IV, December 1982.
9. Collins, J.A., Failure of Materials in Mechanical Design, John Wiley and Sons, New York 1981.
10. Timoshenko, S., and Goodier, J.N., Theory of Elasticity, McGraw Hill Co., Inc., New York 1951.
11. Den Hartog, J.P., Advanced Strenght of Materials, McGraw Hill Co., Inc., New York, 1952.
12. MAXIMA, Users Manual, Symbolics, Inc, Cambridge, Mass, 1986.
13. MATHCAD, Users Manual, Math Soft, Inc, Cambridge, Mass, 1987.
14. Plastics Polymer Science and Technology, Mahendra D. Baijal, Editor, John Wiley and Sons, New York, 1982.

TABLE 1

Functions of Aircraft Transparencies

Pilot Ingress/Egress	
Windscreen	Lightning Strike Tolerance
Pressure Containment	Anti Icing
Birdstrike Protection	Anti Fogging
Optical Functions	Rain Removal
Radar Signature Attenuation	
Projectile Penetration Resistance	
Laser Damage Resistance	
Nuclear Flash Protection	
Nuclear Blast Pressure/Temperature Pulse Hardness	
High Power Microwave Protection	
Particle-Beam Weapon Protection	

Qualities

Environmental Durability (Natural and Induced)  
Maintainability (Ease of and Durability under Maintenance)  
Thermal/Aerothermal Environment Tolerance

# Design Optimization

## Nomenclature:

$x(i)$  - Design Variable

$f(j)$  - Performance Measure;  $f(j) = f[j, x(i)]$

$F$  - Objective Function;  $F = \text{SUM } w(j)f(j)$

$w(j)$  - Relative Weights

$i(j)$  - Number of Iterations of Variable  $x(j)$

$I$  - Total Number of Iterations

$N$  - Number of Design Variables

$M$  - Number of Performance Measures

$C$  - Cost

$c(j)$  - Cost Per Iteration of  $j$ th Design Variable

TABLE 2

## Optimization Strategies

**Serial Approach - Stand-alone Analysis Codes Only**

$$C = c(j) * I = c(j) * (Ni)^M$$

**Parallel Approach - Analysis Codes Plus Executive Program  
Steepest Descent Algorithm**

$$dx(j) = ds * \frac{dF/dx(j)}{ABS(grad F)}$$

$$C = c(j) * I = c(j) * (M+1) * N * i$$

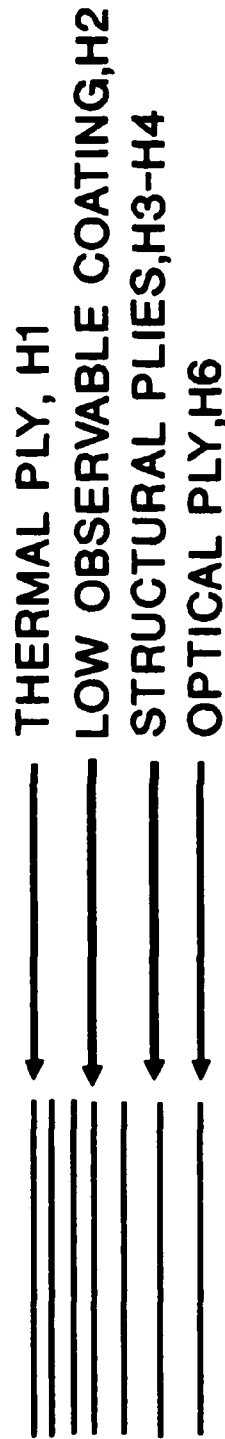
**Parallel Approach - Analysis Codes Plus Executive Program  
Steepest Descent, Design Formulas**

$$C = c(j) * I = c(j) * N * I$$

TABLE 3

# Design Cost Comparison

Design Example: Windshield Cross-section



Design Approach	No. Iterations	Cost (\$)
Serial	191E8	\$9.5E10
Parallel	168	\$84,000
Design Formulas	24	\$12,000

No. of Codes = 4  
 No. of Design Variables = 6  
 No. of Iterations Per Variable = 6  
 Cost Per Code Execution = \$500

TABLE 4

SPACE SHUTTLE WINDOW  
DESIGN PROCESS RESULTS  
 (BRITTLE LINEAR ELASTIC MATERIAL)

ITERATION NO.	DESIGN FORMULA (THICKNESS, INCHES)	MAGNA ANALYSIS STRESS RATIO ( $\sigma/\sigma_{CRIT}$ )
1	1.097	1.325
2	1.263	1.00

TABLE 5

SPACE SHUTTLE WINDOW  
DESIGN PROCESS RESULTS  
 (DUCTILE NON-LINEAR ELASTIC MATERIAL)

ITERATION NO.	DESIGN FORMULA THICKNESS (INCHES)	MAGNA ANALYSIS STRESS RATIO ( $\sigma/\sigma_{CRIT}$ )
1	.923	.335
2	.534	.530
3	.389	1.170
4	.421	.980



FIGURE 1.  
SERIAL OPTIMIZATION

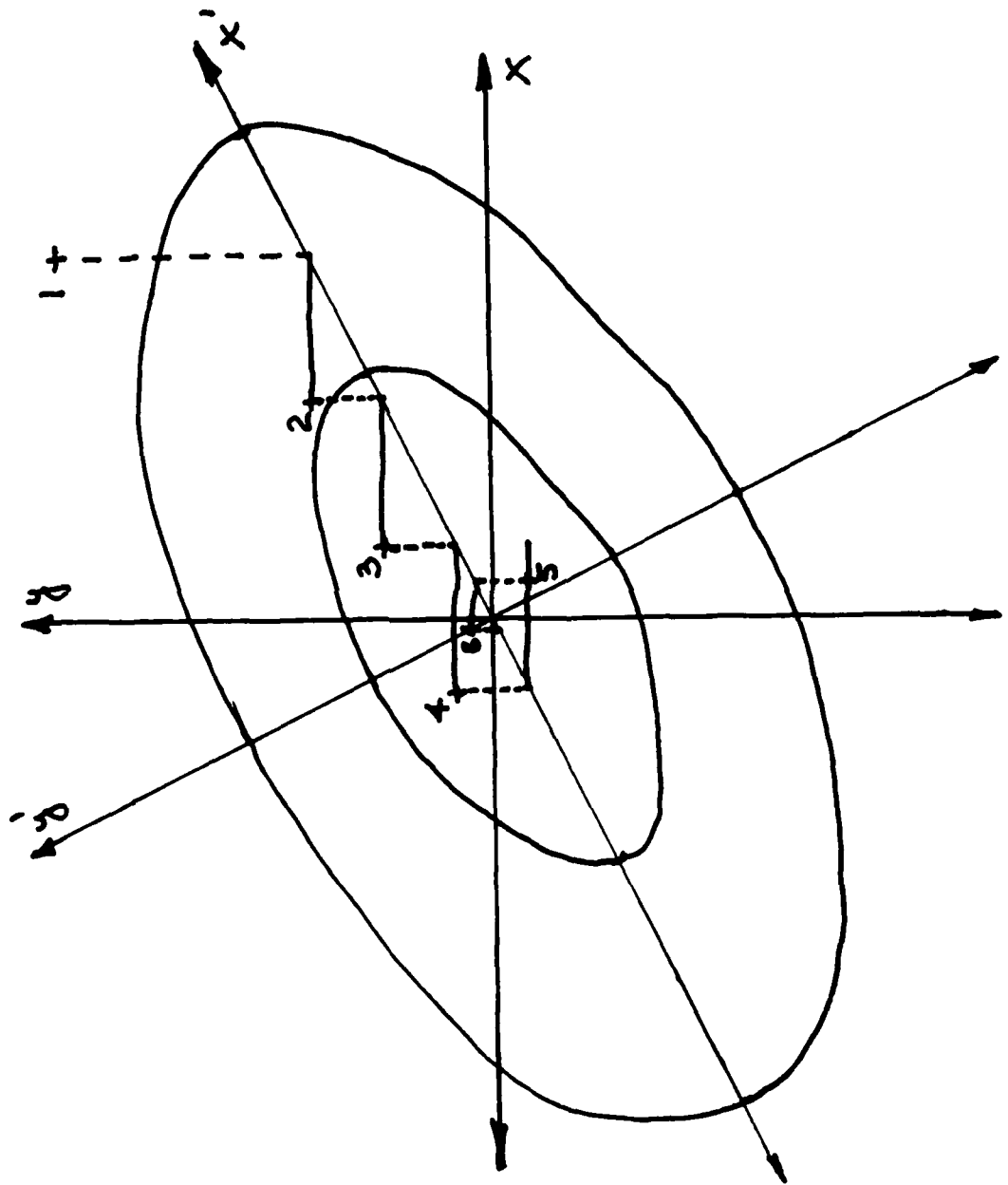
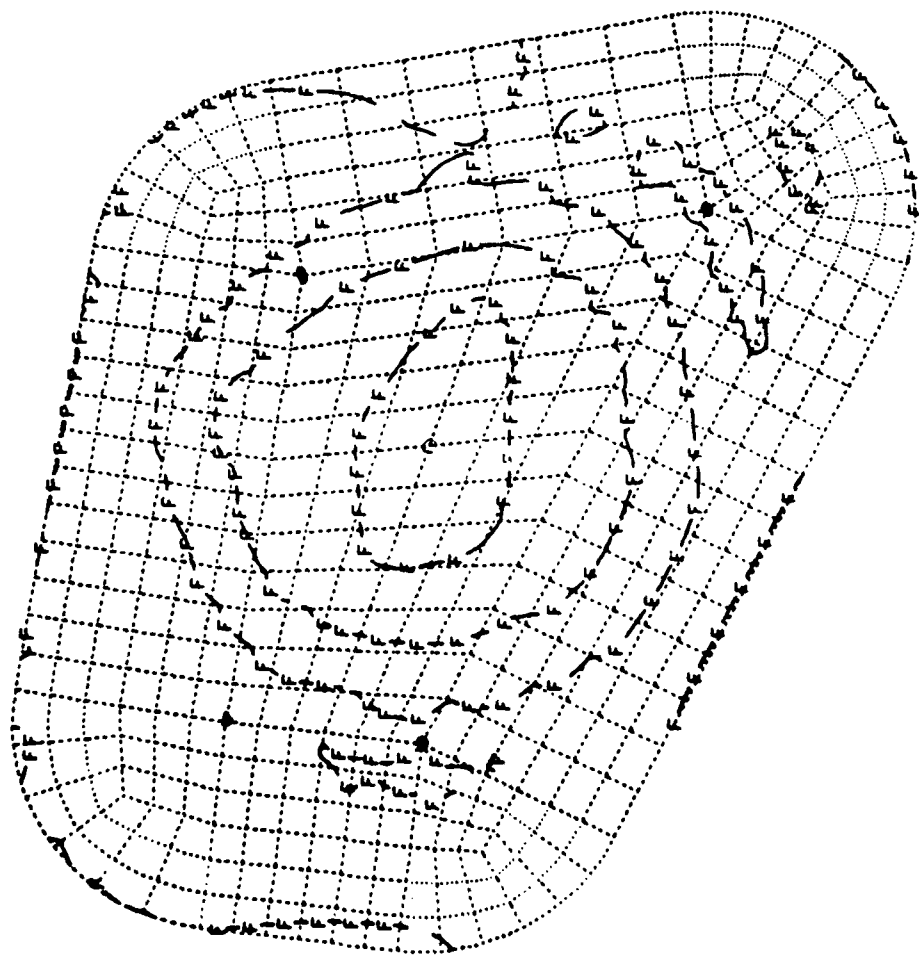
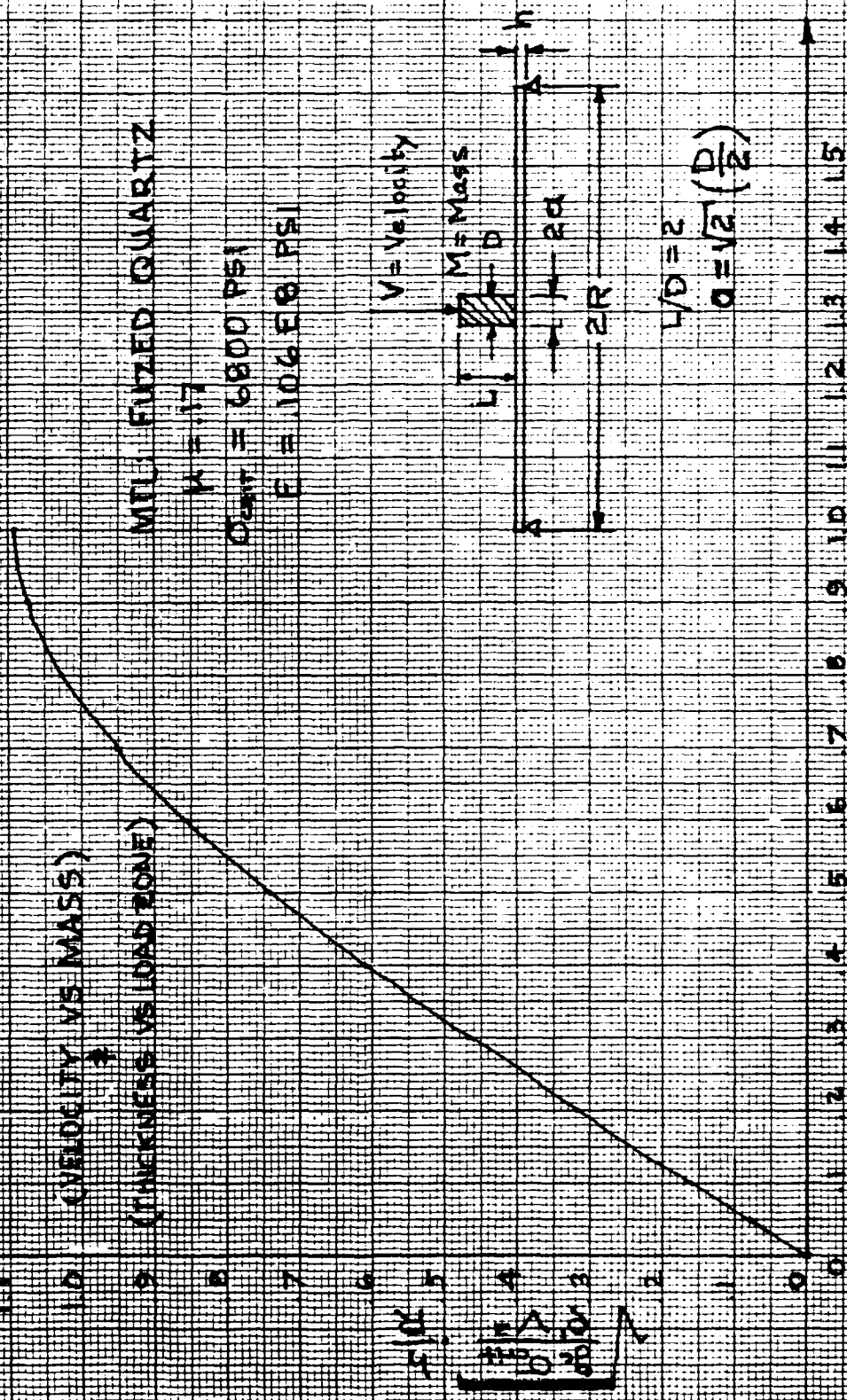


FIG 2 SHUTTLE WINDOW



**FIG 3 DIMENSIONLESS  
FAILURE CURVE  
BIRD IMPACT AT CENTER OF CIRCULAR PLATE**



10. (VELOCITY VS MASS)

9. (THICKNESS VS LOAD ZONE)

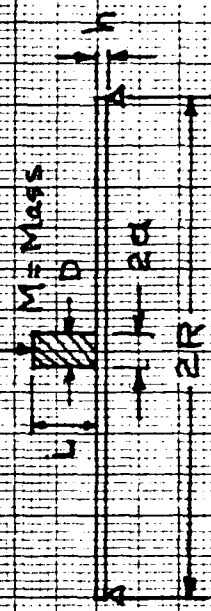
MTL FUSED QUARTZ

$\mu = .17$

$\sigma_{\text{quartz}} = 6800 \text{ PSI}$

$E = 1.06 \text{ EB PSI}$

V = Velocity



$L/D = 2$   
 $a = \sqrt{2} \left(\frac{D}{2}\right)$

$\frac{F}{R} = 6083 \left[ \frac{M^{1/3}}{R} \right] / R$

FIGURE 4

DESIGN FORMULA THEORY

$$\frac{d}{dt} [T+V] = \int_A \rho \dot{u} dA$$

$$u = q(t) \cdot \phi(r) ; \phi(r) = \cos \frac{\pi r}{2R}$$

$$\theta = \frac{1}{2} \rho' V_c^2 ; |r| \leq a ; a = \sqrt{2} \left( \frac{D}{2} \right)$$

$$M \ddot{q} + K q = F_0 [U(t) - U(t-\tau)] ; \tau = l/v$$

$$q_{max} = \frac{F_0}{K} \sqrt{2(1-\cos \omega \tau)} ; \omega \tau < \pi$$

$$q_{max} = 2 F_0 / K ; \omega \tau \geq \pi$$

$$\sigma = \frac{6D}{h^2} \left[ \frac{\partial^2 \phi}{\partial r^2} + \mu \cdot \frac{1}{r} \frac{\partial \phi}{\partial r} \right] q(t) ; D = \frac{E h^3}{12(1-\mu^2)}$$

$$\sigma_{max} = \frac{\pi^2 E h}{8(1-\mu)} \frac{q_{max}}{R^2}$$

$$\frac{\sigma}{\sigma_{crit}} \cdot \frac{\sigma_{crit} q_c}{\rho' V_c^2} \left( \frac{h}{R} \right)^2 = \frac{3(1+\mu)}{(2.94+2.47\mu)} \left[ \cos \frac{\pi a}{2R} - 1 + \frac{\pi a}{2R} \sin \frac{\pi a}{2R} \right]$$

$$\sqrt{.2(1-\cos \left\{ 2.12 \sqrt{\frac{(2.94+2.47\mu)}{(1-\mu^2)}} \cdot \sqrt{\frac{\sigma_{crit} q_c}{\rho' V_c^2}} \cdot \frac{h}{R} \cdot \sqrt{\frac{E \rho'}{\sigma_{crit} \rho}} \cdot \frac{a}{R} \right\}}}$$

FIGURE 5  
 SPACE SHUTTLE THERMAL PANE RESULTS  
 NORMAL IMPACT ON A 1.25 INCH THICK PANE

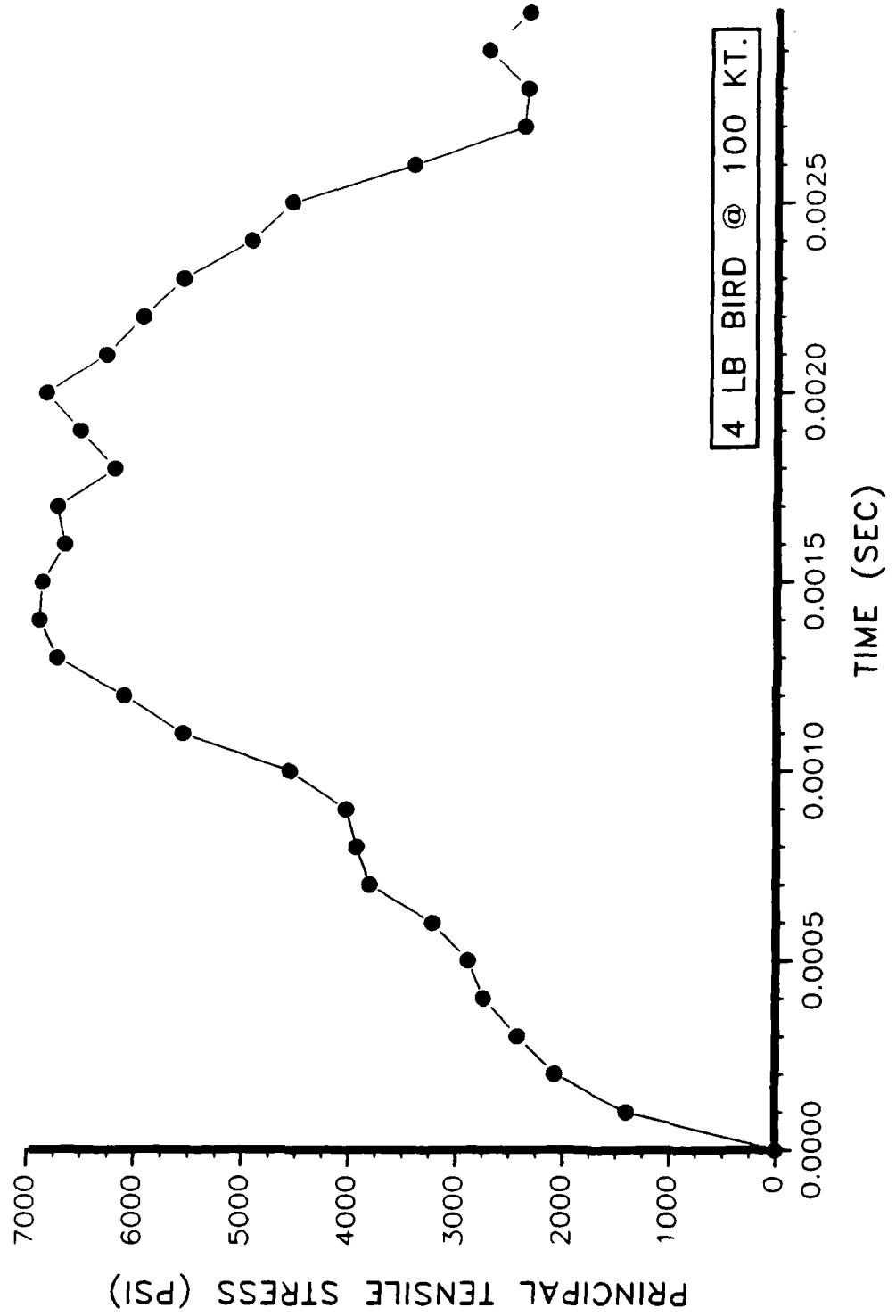


FIGURE 6  
COMBINED THERMAL/STRUCTURAL DESIGN  
LAMINATED TENSION MEMBER



CONSTRAINTS:

$$P \leq P_0$$

$$\sigma_i \leq \sigma_{y_i}$$

$$\delta = \sum \delta_i \leq \delta_{max}$$

$$A = \text{CONST.}$$

$$Q \leq Q_0$$

$$T(0) = T_1; T(l) = T_2$$

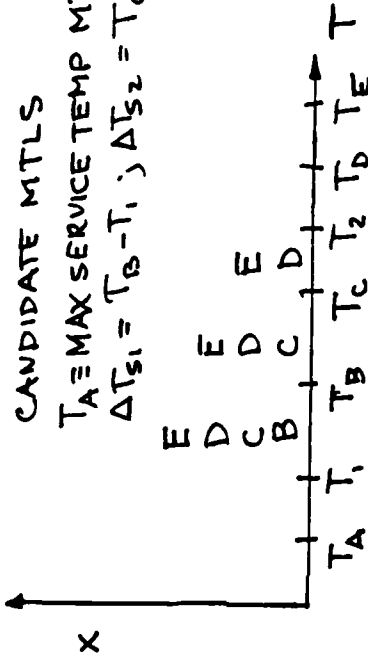
MINIMIZE MASS

$$M = \sum \rho_i A_i l_i$$

SOLUTION:

$$M = \sum \frac{\rho_i^2}{\text{Min}[\sigma_{y_i}^2]} \cdot \frac{\Delta T_{s_i} \rho_i K_i}{Q_0}$$

SELECT MTL IN EACH TEMP RANGE FOR  $\text{MIN}\{\rho_i K_i\}$   
FIGURE-OF-MERIT =  $\rho_i K_i$  [DENSITY X CONDUCTIVITY]



MAGNA ANALYSIS OF BIRD IMPACT ON AN F-4 SINGLE PIECE WINDSHIELD  
USING SHEAR CORRECTION AND ON AN F-4 FORWARD CANOPY

Michael G. Gran  
Flight Dynamics Laboratory

MAGNA ANALYSIS OF BIRD IMPACT ON AN F-4 SINGLE PIECE  
WINDSHIELD USING SHEAR CORRECTION AND ON AN  
F-4 FORWARD CANOPY

Michael G. Gran  
Aircrew Protection Branch  
Flight Dynamics Laboratory  
Air Force Wright Aeronautical Laboratories  
Wright-Patterson Air Force Base, Ohio

Abstract

MAGNA analysis has been completed on the F-4 single piece windshield, and on a new design of the F-4 forward canopy. All of these tasks were completed in-house in the Flight Dynamics Laboratory using the MAGNA finite element code developed at the University of Dayton Research Institute. All of the analyses were run on a CRAY/XMP 12 located at Wright-Patterson Air Force Base. The simulations were all for four pound bird impacts at different locations to predict the threshold of the new F-4 designs. The F-4 windshield model used a layered shell element that allows the element to be divided up into different layers to represent the different layers in the laminated design. This method is more cost effective because it allows one element to represent the cross section of the transparency, where in the past each layer had to be represented by a layer of solid elements. The cost of the analysis is large when there are so many elements because of the large number of layers. This is an attempt to cut the cost of the analysis substantially and still have reasonable results. An attempt was made with MAGNA to design a new F-4 forward canopy. This is the first time that the program was used explicitly to design a new part, without the aid of any previous full scale testing high speed film, and try to predict the threshold of a four pound bird impact at the most critical point on the canopy.



## INTRODUCTION

### Background

In the late 1960's, the tactical mission profile of Air Force aircraft changed substantially. With the advent of new radars and surface-to-air missile systems, it became necessary for flight operations to be conducted at very low altitudes and high speeds. The transparent crew enclosures, both windshields and canopies, installed on operational aircraft at the time had not been designed to provide enough bird impact protection. As a result of these more frequent low level missions unacceptable losses of aircraft and crewmembers occurred. The F-4 is an example of an older design that was not able to provide the proper protection at those high speeds and low altitudes.

In 1972, the then Air Force Flight Dynamics Laboratory formed an Advanced Development Program Office to lead the development of improved transparent crew enclosure systems. Since that time, this office has participated in the successful development of many bird impact resistant aircraft transparency systems. Methods employed in the development of these systems however were largely empirical, and as a result were very costly in terms of time and dollars. The first development of bird impact resistant transparencies for the F-111 aircraft involved about 50 iterations at a cost of \$100,000 each, for a total of \$5 million, and required about four years. The principle cause of this high cost was the need to build and test various full scale versions of the transparency systems being developed.

To help reduce those high cost of development, a second office was formed in 1976 in the Flight dynamics Laboratory, the Subsystems Development Group (AFWAL/FIER). This office conducted exploratory programs in an effort to develop computer analysis tools which could accurately predict the dynamic response of transparency structures to bird impact loading. Such analysis tools would significantly reduce the level of full scale bird impact testing required during the development of improved transparent systems.

By 1979 the Subsystems Development Group had taken delivery of a three-dimensional nonlinear finite element analysis system called MAGNA to address the aircraft transparency bird impact problem. Since the initial development and delivery of MAGNA, an intensive work effort has been mounted to validate the code for the bird impact application.[1-8] In each case, these attempts to validate MAGNA involved computer simulation of full scale bird impact tests. Computed results for strain, deflection, or mechanical failure were compared to test results in order to define a correlation between the two. Test results were employed for a number of different transparency system types including flat laminated glass bomber windshields, monolithic plastic bubble fighter canopies, thick monolithic plastic fighter

windshields, and laminated plastic trainer windshields.

These validation studies conducted with MAGNA have been successful, permitting a number of Air Force aircraft applications to have been conducted during the same period of time. Some of these work efforts involved dynamic response to bird impact loading, while the remainder involved a variety of other mechanical loads.[9-12]

The analyses that were completed for this paper were basically two different problems. The first analysis looked at the birdstrike resistance of an F-4 single piece windshield. This analysis was conducted in 1986 and was for the original design of the one piece wrap-around. Then the analysis was repeated using the shear correction factors on the same model. The next analysis attempted to design a new F-4 forward canopy for birdstrike resistance. This was completed in November 1988 and was the first time that a totally new design was accomplished, without the use of previous full scale testing results, using the MAGNA code.

The name of the Subsystems Development Group was changed to the Aircrew Enclosures Group in the fall of 1988. These two names are used throughout the paper. The symbols of the group also changed, in February 1989, from the Air Force Wright Aeronautical Laboratories (AFWAL/FIER) to Wright Research Development Center (WRDC/FIVR).

#### MAGNA Computer Program

The MAGNA nonlinear finite element analysis system was developed by the University of Dayton Research Institute, Dayton, Ohio and first became operational during the summer of 1978. The first edition of MAGNA for US Air Force aircraft transparency applications was delivered in late 1979. MAGNA was designed from the ground up for the analysis of large scale problems involving three-dimensional structures. It can account for the effects of both geometric nonlinearity (large displacements and rotations) and material nonlinearity (elastic-plastic behavior). The static, dynamic or free vibration response of a structure can be analyzed using MAGNA. Special features such as contact analysis (e.g. bird/canopy contact), full restart capabilities, and convenient interactive graphics make it a powerful analysis tool which is easy to use. Another feature is that live pressure loading is available and becomes an especially useful feature in the simulation of bird impact problems. The interactive graphics are provided in two packages: the first, a preprocessor, enables rapid finite element modeling of transparency structures. The second, a postprocessor, permits quick visualization of the results of an analysis including structural deformation, stress, and strain. The capabilities of MAGNA are documented in more detail elsewhere.[13-16]

## F-4 One Piece Windshield Analysis

The F/RF-4 aircraft frequently fly missions at low level and extremely high speeds which place the aircraft and crew in a flight regime that is very vulnerable to birdstrikes. As a result of this danger an improved one piece windshield was developed. In 1984 McDonnell Douglas, along with Goodyear Aerospace, provided the new transparency system to be tested. The objective of the development program was to: provide protection from a four pound birdstrike at 500 knots, maintain or improve the optical qualities and to provide for a low cost of ownership. Goodyear designed and fabricated the transparent panel, while McDonnell Douglas designed and built the aft arch. This design was very unique because the transparency was not bolted to the frame, but bonded along the edges. The F-4 one piece windshield design is shown in Figures 1-4. The windshield system was bird impact tested at Arnold Engineering Development Center (AEDC). The result of the 500 knot impact, at the most critical point, was that the transparency pulled out from the arch. The Subsystems Development Group was then tasked to do analysis on the system to understand why the transparency pulled out and to improve the system so it could meet the 500 knot requirement.

### Triangulation

The first thing that had to be accomplished was reducing the deflection data from the full scale test performed at AEDC. This was accomplished by using the triangulation method developed by the Subsystems Development Group.[17] The triangulation method is a computer program that uses coordinate data to come up with the deflections at known points on the transparency system. The method involves the use of high speed cameras that were employed during the test. There were two cameras placed inside the cockpit at known locations with respect to a reference point. The transparency was marked at the locations where deflection data was desired. These points were measured for their coordinates with respect to the same reference point as the cameras. The most desired way of using this method was to pick points on the transparency that corresponded to nodes on the finite element model that was being developed. The finite element grid pattern was placed on the inner surface of the prototype windshield before the test. This allowed the specific points to be monitored by the high speed cameras. The film was then evaluated to determine the best test for the reduction of the deflection data. It was determined that the 392 knot shot on the centerline, 8 inches from the aft arch, would be used for the triangulation method. The calibration of the two cameras were performed to determine the exact speed at which they functioned during the test. The ideal speed of the cameras is 5000 frames per second, but usually the speeds are slightly

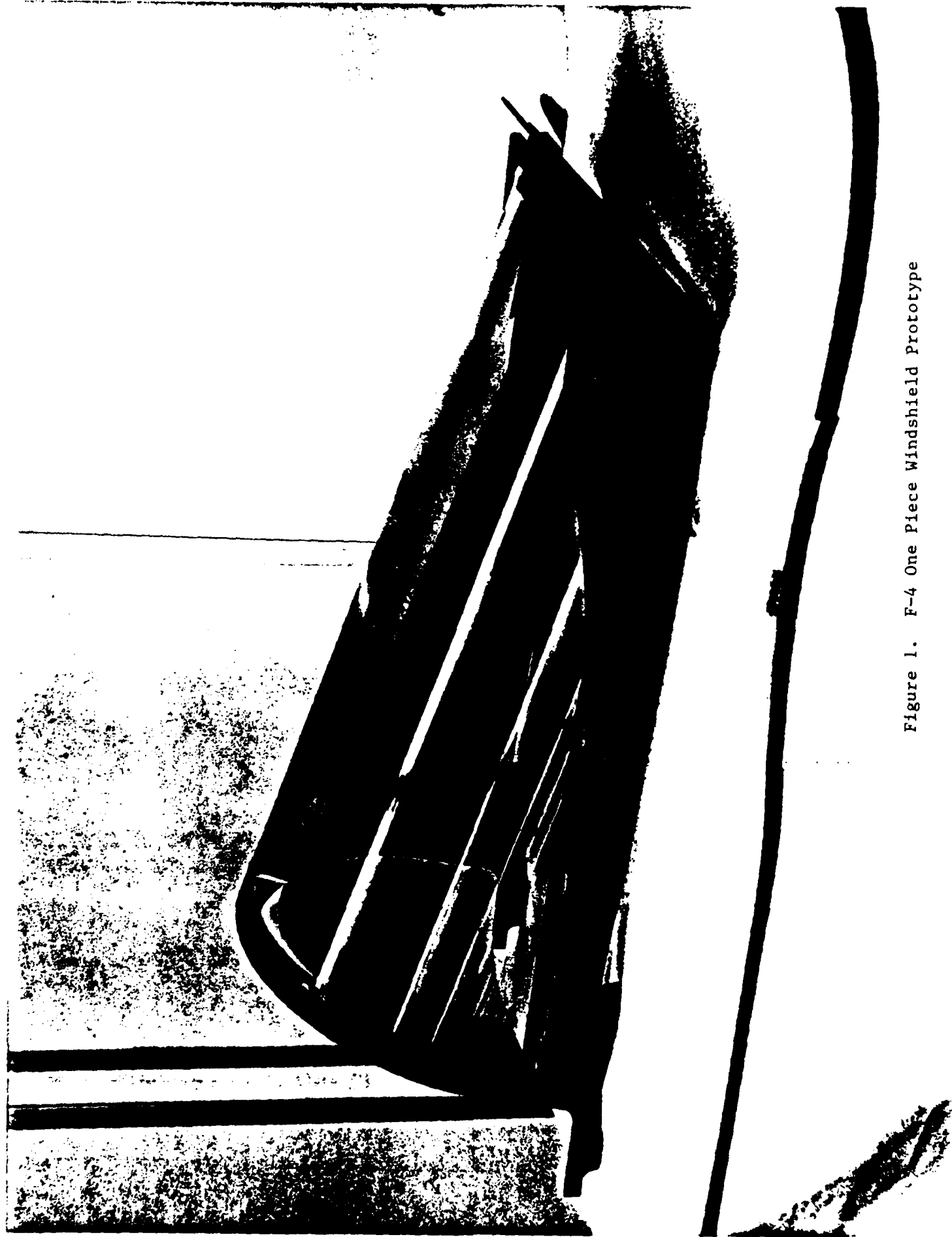


Figure 1. F-4 One Piece Windshield Prototype

F-4 PHANTOM II ONE PIECE WINDSHIELD



# One-Piece Windshield Construction

53-070682-1 Windshield

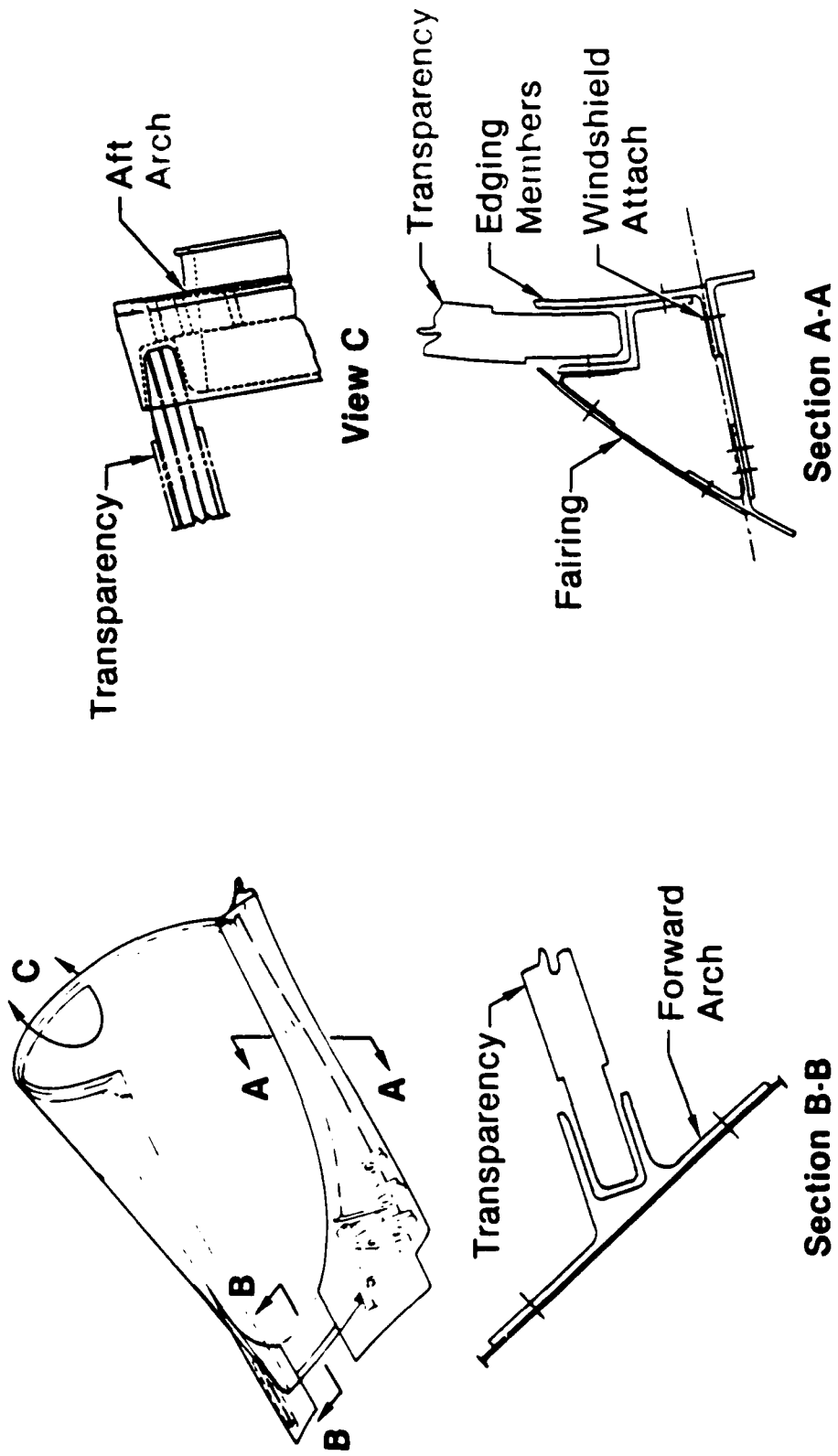


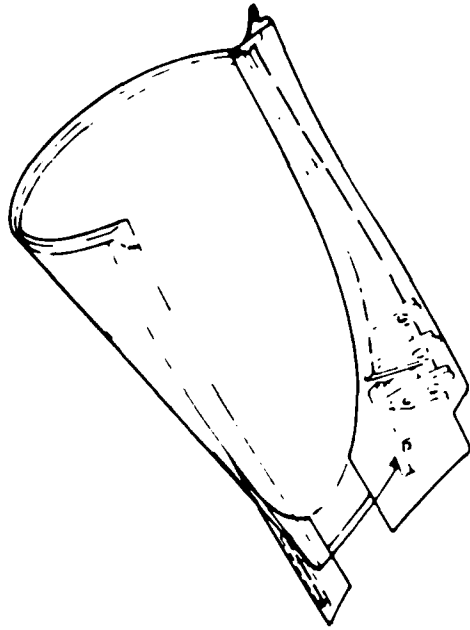
Figure 2. F-4 One Piece Windshield Construction



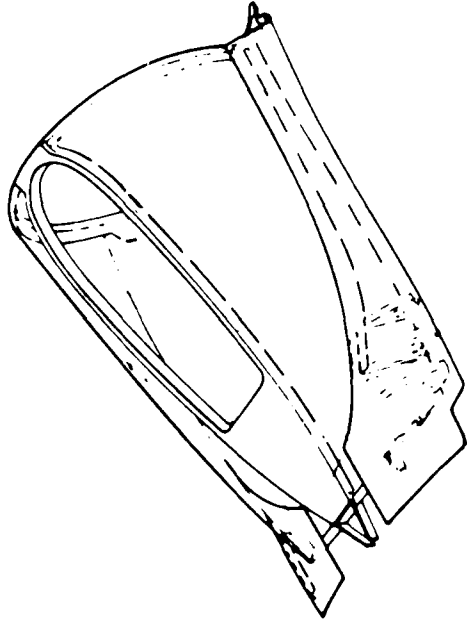
**F-4 PHANTOM II ONE PIECE WINDSHIELD**

## **Windshield Comparison**

**One-Piece Windshield**



**Existing  
Three-Piece Windshield**

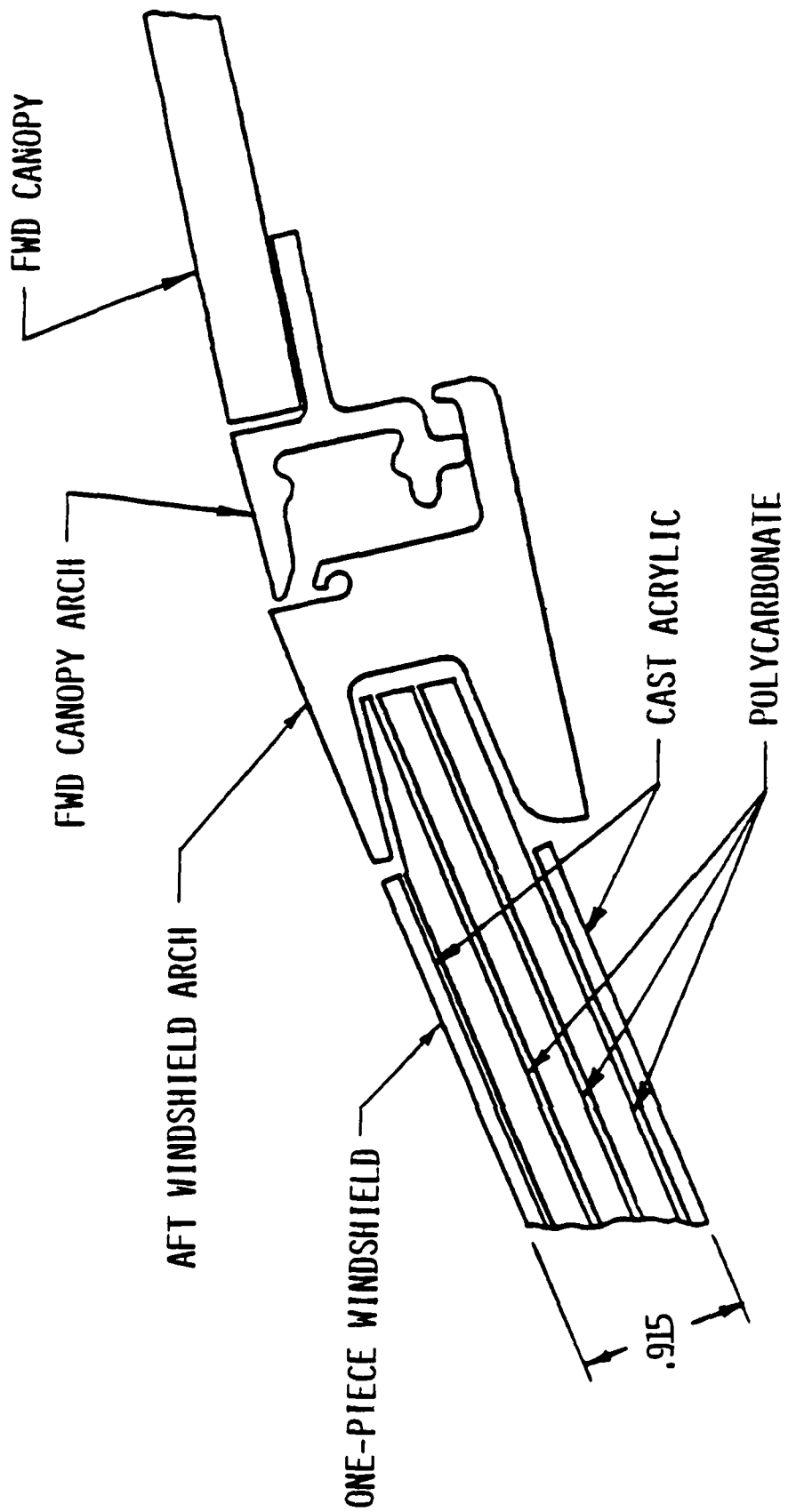


### **One-Piece Windshield Features**

- Prevent Cockpit Penetration — 4 lb Bird @ 500 kts
- Improved Pilot Forward Vision
- Fewer Parts
- Windshield Assemblies Replaceable at Cockpit Sill
- Provides Space for HUD

Figure 3. Comparison of F-4 One Piece Windshield with the Existing F-4 Windshield

# F-4 ONE-PIECE WINDSHIELD



- 0 500 KT - 4 LB BIRD IMPACT CAPABILITY
- 0 AFT WINDSHIELD ARCH WILL BE TITANIUM

Figure 4. F-4 One Piece Windshield Cross Section

lower than that. The two cameras inside the cockpit are shown in Figure 5.

This triangulation case was run on a Hewlett-Packard 85 computer. The two cameras were determined to be right at 5000 frames per second, so no scaling was performed on the camera speeds. The projection of each desired point, at each frame, was made on a piece of paper. This paper was then placed on a plotter and the computer digitized these points. The HP 85 computer then performed the analysis to determine the normal deflections of the desired points on the transparency. This program has now been expanded to PC computers and the VAX machines. The program is simple to run and gives results to an accuracy of a tenth of an inch. The results showed that the maximum, normal deflection occurred 2.3 inches aft of the impact point on the centerline. The maximum deflection was 2.34 inches and occurred at 0.002 sec after the initial impact. Three points were analyzed using the triangulation method. All the points lie on the centerline, one point was the impact point and the other two were forward 2.4 inches and aft 2.3 inches with respect to the impact point. The results for the three points analyzed are shown in Figures 6-8. The results were used to determine the accuracy of the computer simulations.

## Structural Modeling

### Geometry

The F-4 one piece windshield system was not an easy analysis to complete because of the design of the transparency and the geometry of the aft arch. The modeling was a cooperative effort between the University of Dayton Research Institute (UDRI) and the Subsystems Development Group. UDRI was responsible for modeling the transparent panel, while the Subsystems Development Group modeled the aft arch, last two rows of the transparent panel and merged the two models together. The fairings and frame structure along the sills and forward area of the windshield system were ignored in this analysis. The impact point was on the centerline, near the aft arch, so this assumption is valid and has been used in other similar applications successfully. The system is installed on the aircraft inclined at an angle of 29 degrees relative to the longitudinal axis of the vehicle. The transparency involves a nine ply design, three structural plies fabricated from polycarbonate, four thin polyurethane interlayers, and two as cast acrylic face plies. The cross section is shown in Figure 9. The overall thickness of this transparency system is .915 inches. The polycarbonate plies are each 3/16 inches, while the acrylic face plies are each .1 inches. The transparency was bonded to the frame and aft arch using PR 1725. This sealant is made by Products Research from California. The aft arch was basically a C channel with support areas and was made from titanium.





Figure 5. F-4 One Piece Birdstrike Test with Two High Speed Cameras Inside the Cockpit That Will Be Used for Triangulation.

# F-4 WINDSHIELD DEFLECTIONS

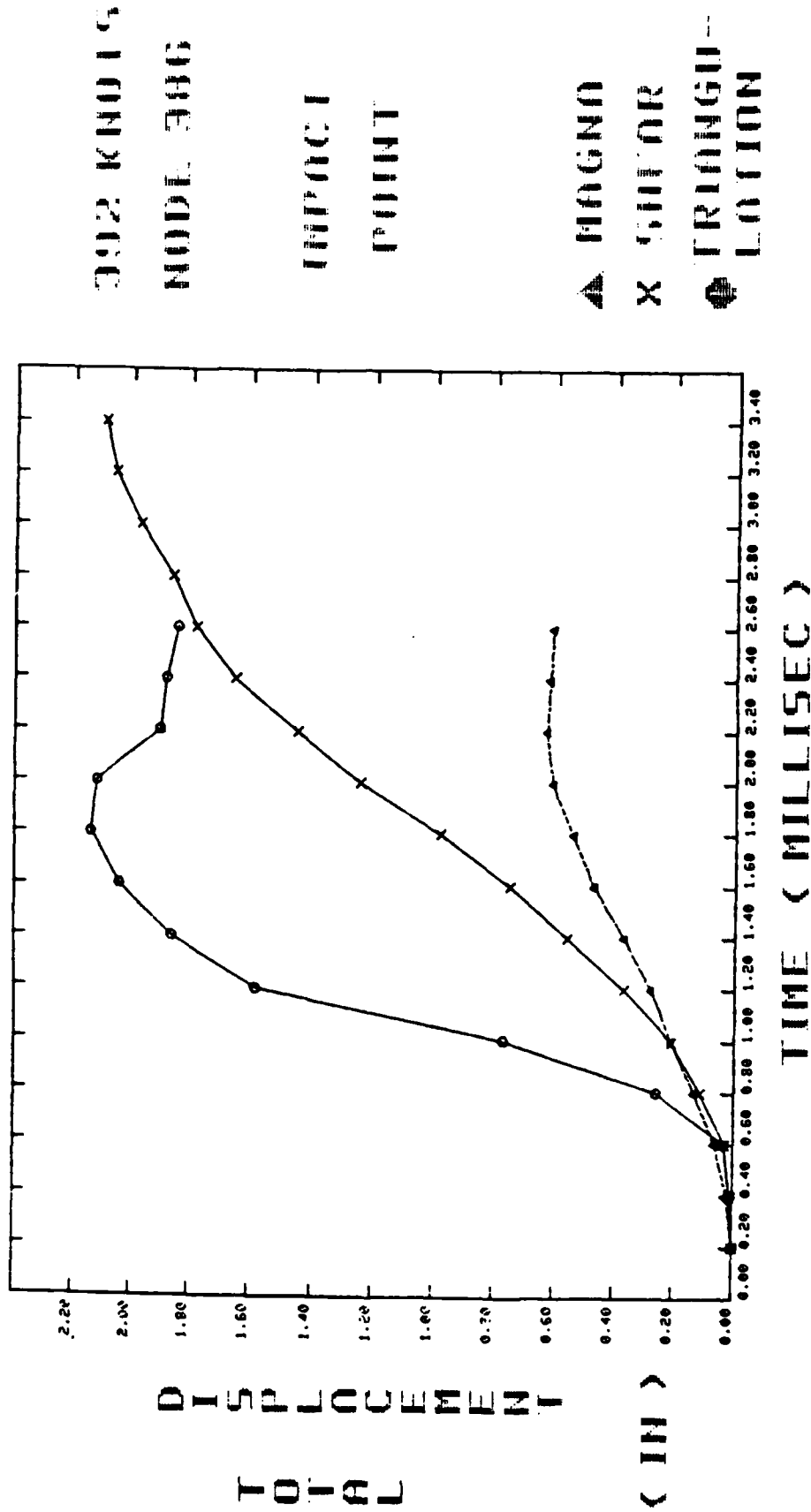


Figure 6. F-4 One Piece Windshield Deflection Results for the Impact Point

# F-4 WINDSHIELD DEFLECTIONS

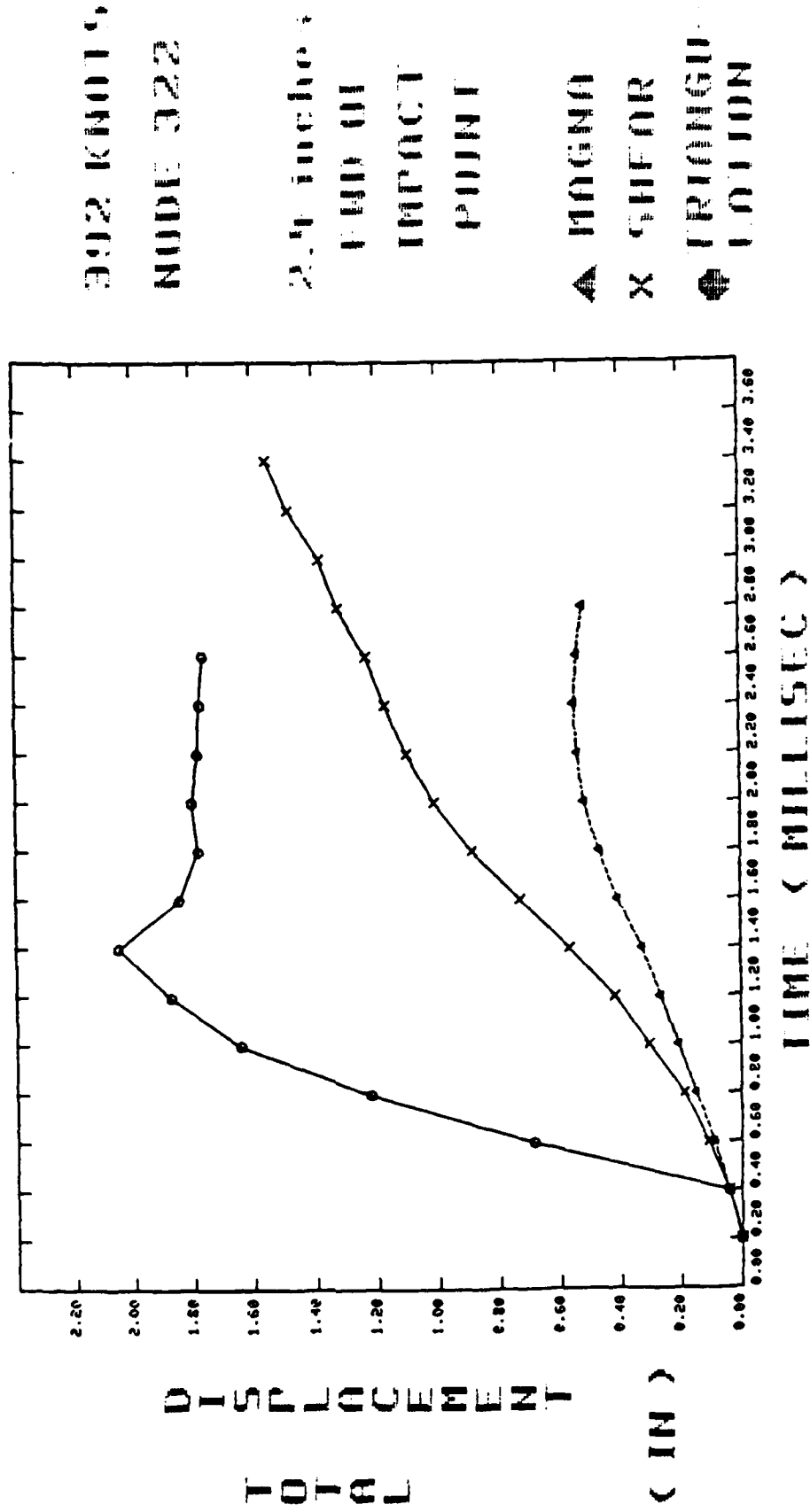


Figure 7. F-4 One Piece Windshield Deflection Results for a Point Forward of the Impact

# F-4 WINDSHIELD DEFLECTIONS

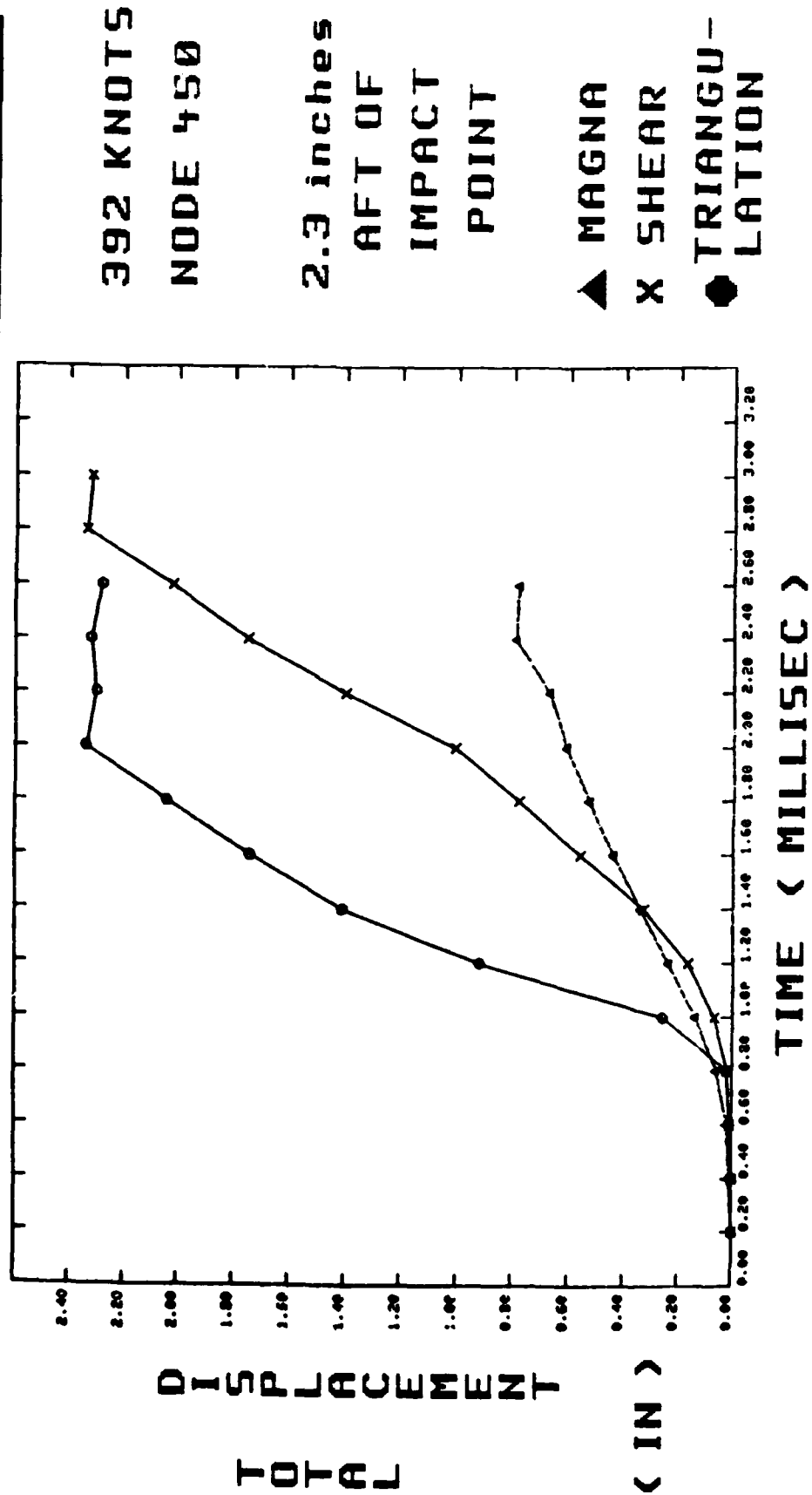
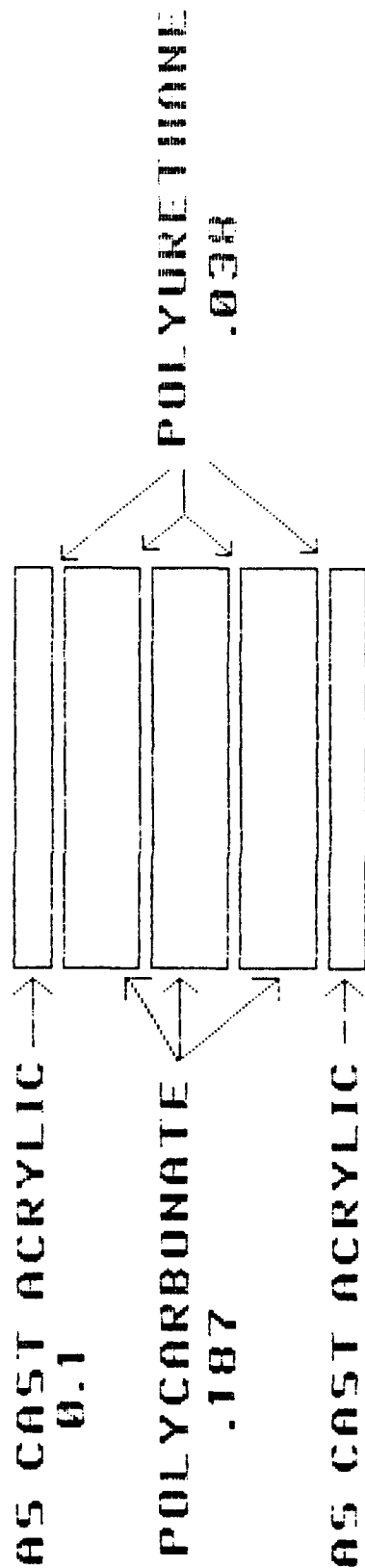


Figure 8. F-4 One Piece Windshield Deflection Results for a Point Aft of the Impact

# F-4 SINGLE PIECE WINDSHIELD

## CROSS SECTION



TOTAL THICKNESS = 0.915 inches

Figure 9. F-4 One Piece Windshield Cross Section

The transparency panel was modeled by the University of Dayton Research Institute. The model consists of 100 type 11 elements. The transparent panel model is shown in Figure 10. The type 11 element in MAGNA is an isoparametric sixteen-node layered shell element. This allows different layers to be modeled through the thickness of the shell element. The usual method is to stack sixteen-node solid elements on top of each other to represent the different layers through the thickness of the transparency. This was not possible at this particular point in time, because of the large number of solid elements that would be required to represent this design. The computers at this time would limit a reasonable finite element nonlinear analysis to a certain number of solid elements, because of the size and computer costs. Using the layered shell element allows the panel to be modeled with only one hundred elements, instead of using nine hundred. The only problem with using this type of element was that it had not been used as extensively as the solid element and consequently little validation had been accomplished with the shell element.

The aft arch and merging elements were modeled by the Subsystems Development Group. The model consisted of the transparency that merged into the arch channel, along with the arch itself and the bonding sealant. The aft arch portion of the model is shown in Figure 11. The first task was to determine the shape of the arch that would best represent the actual design. A computer program was run by UDRI to calculate different parameters for various cross sections and compare those results to the actual design. Some of the parameters calculated where; moments of inertia with respect to different axes, centroids, area of the cross section, lengths and angles. These calculations determined the best model representation of the aft arch. These calculations and the cross sections that where analyzed are shown in Figures 12A,B. Since the failure of the system occurred at the aft arch, this was an important task to match the parameters of the actual design as much as possible in order to get reasonable results from the analysis. In order to model the complex shape of the aft arch, a computer program was written to generate the model after the case 5 cross section design had been selected. The computer program also modeled the sealant that would bond the windshield to the aft arch, and the merging transparency elements in the channel. The arch and bond where modeled with solid isoparametric sixteen-node elements. In MAGNA the type 8 element represents the isoparametric sixteen-node element. This same element has been proven effective in earlier studies which have been conducted with MAGNA.[3-8] There was a problem with merging some of the bonding elements to the transparency elements. The problem involved the middle elements of the bonding elements in the cross section and are shown in Figure 13. The middle bonding element had to become variable node isoparametric elements. In MAGNA this is the type 7 solid element. The transparency elements where still type 11 shell elements with a different cross section than the cross section

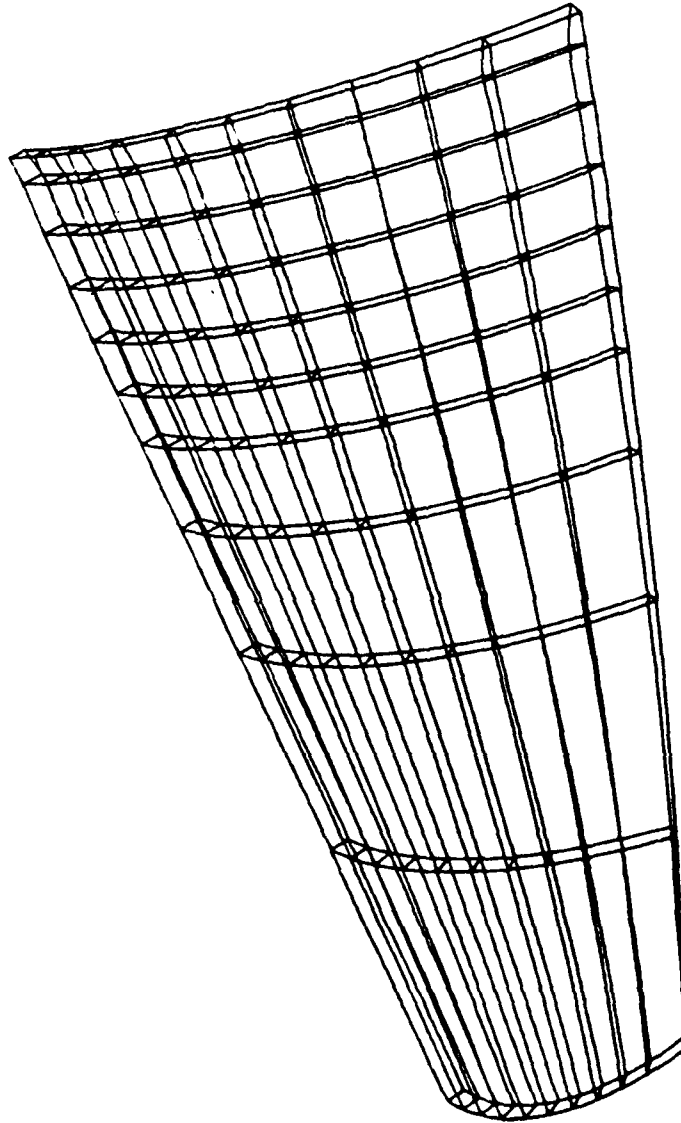


Figure 10. F-4 One Piece Windshield Transparent Panel Model

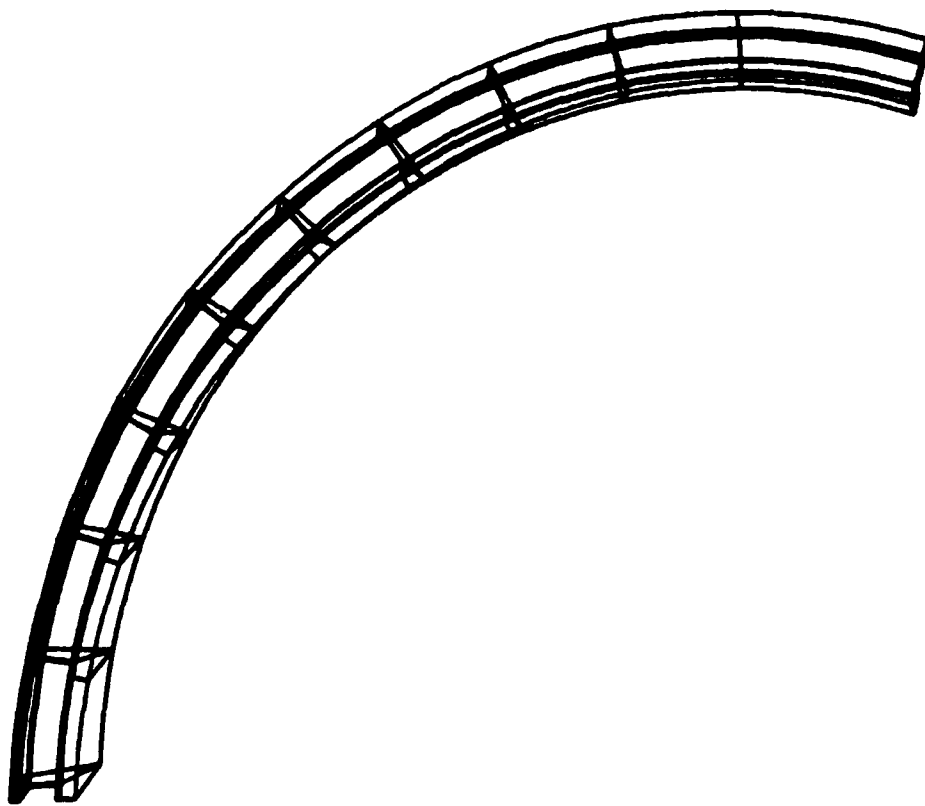
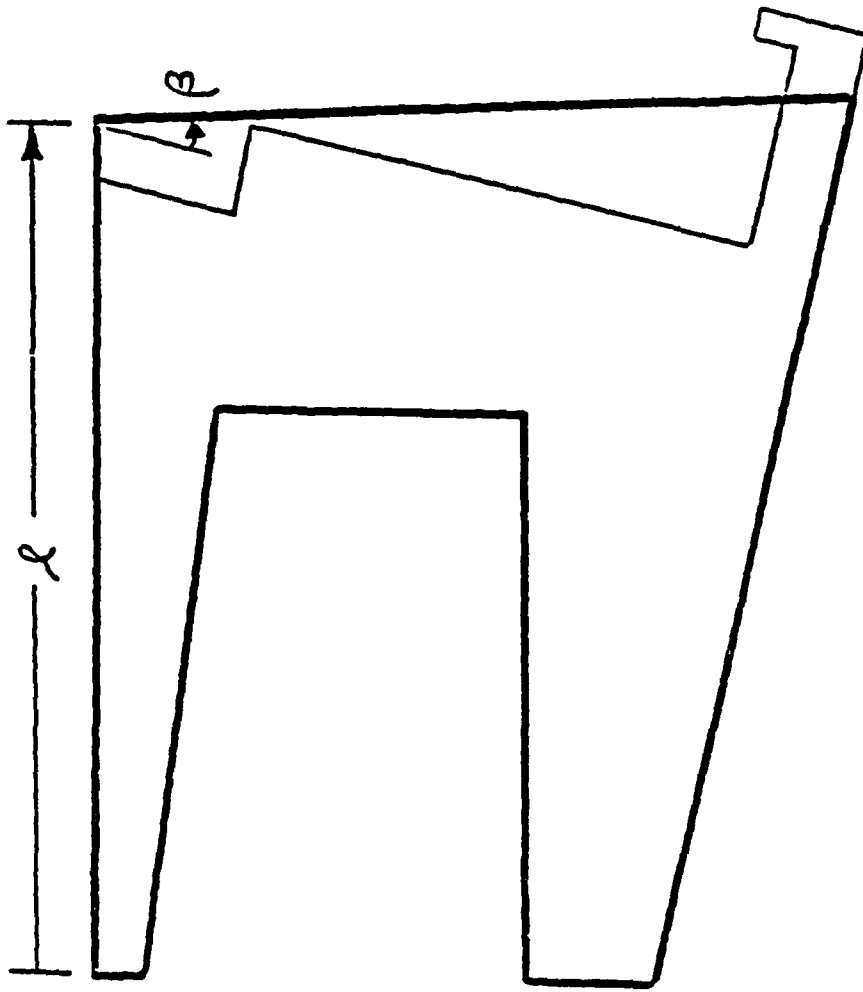


Figure 11. F-4 One Piece Windshield Aft Arch Model

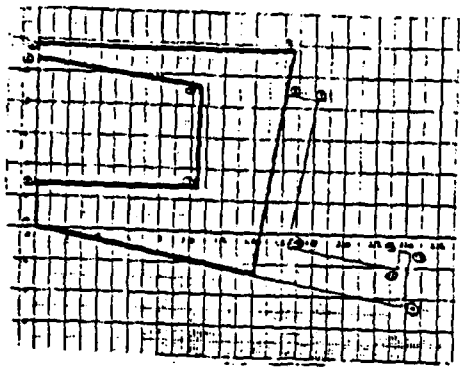




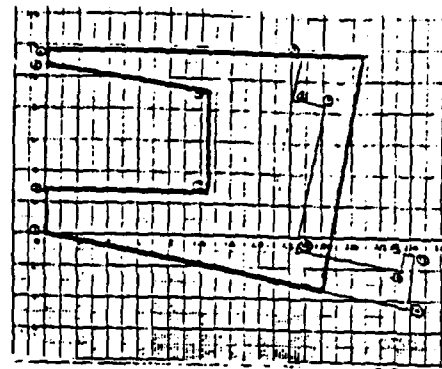
$l$  = length (in.)

$\beta$  = angle (deg.)

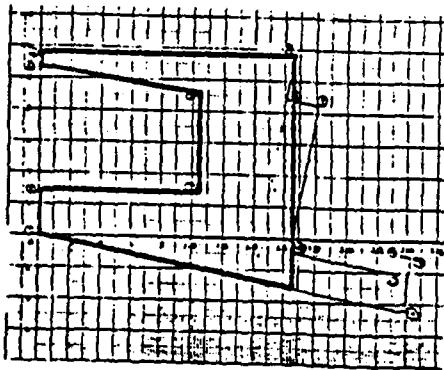
Figure 12A F-4 One Piece Windshield Aft Arch Modified Cross Section



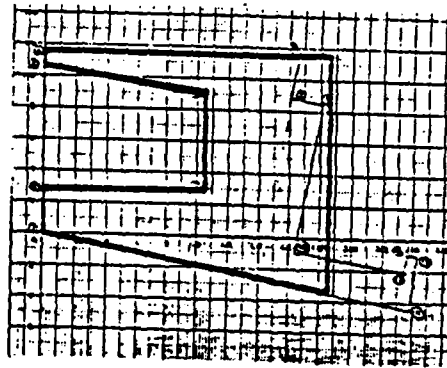
CASE 1  
 $\rho = 1.666, \beta = 0^\circ$



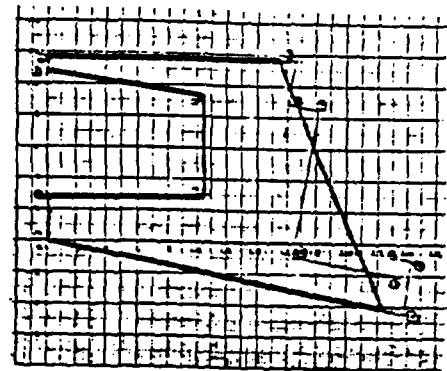
CASE 2  
 $\rho = 2.074, \beta = 0^\circ$



CASE 3  
 $\rho = 1.666, \beta = 10.5^\circ$



CASE 4  
 $\rho = 1.870, \beta = 10.5^\circ$



CASE 5  
 $\rho = 1.550, \beta = 35^\circ$

CASE	$\rho$	$\beta(^{\circ})$	$\bar{x}$	$\bar{y}$	A	$I_{xx}$	$I_{yy}$	$I_{xy}$	$I_{max}$	$I_{min}$	$\theta(^{\circ})$	$K_c$	$K_R$
ACTUAL	-	-	1.180	.358	1.676	.347	.478	-.087	.521	.304	-26.6	.08	.16
1	1.666	0	.969	.461	1.250	.235	.228	.092	.273	.190	42.4		
2	2.074	0	1.217	.452	1.845	.341	.477	.051	.494	.324	18.6		
3	1.666	10.5	1.051	.426	1.444	.269	.291	.017	.300	.260	28.6		
4	1.870	10.5	1.176	.424	1.748	.326	.421	.015	.423	.324	8.6		
5	1.550	35.0	1.214	.346	1.797	.334	.491	-.085	.528	.297	-23.6	.22	.25

$\bar{x}$  = centroid (in.)

$\theta$  = angle (deg.)

$\bar{y}$  = centroid (in.)

$K_c$  = Torsion Constant by channel  
 (Roark #20) very approximate

A = area (in<sup>2</sup>)

$K_R$  = Torsion Constant by rectangle  
 (Roark #4) very approximate

I = moment of inertia

Figure 12B F-4 One Piece Windshield Aft Arch Cross Section Calculations

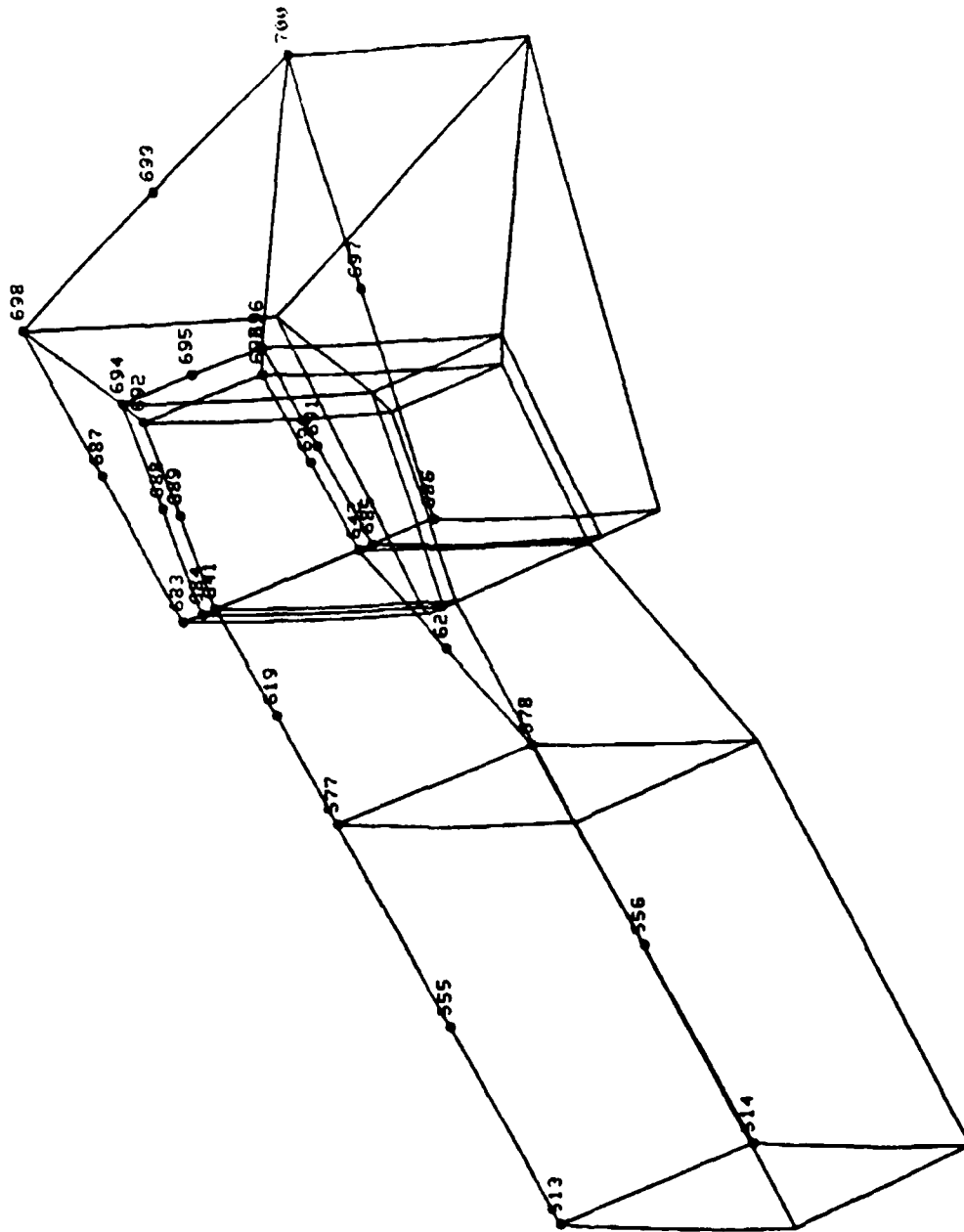


Figure 13. The Bonding and Aft Arch Elements Merged with the Transparent Panel Elements

of the rest of the transparency elements. This transition took place on the last two rows of layered shell elements for the transparency panel. The cross sections, as well as the geometry, were changed for these last two rows in order to merge the elements to the aft arch. The as cast acrylic face plies are cut off before the transparency goes into the arch. This is represented in the model by having no acrylic in the last two rows of layered shell elements. The cross sections are easily changed to accommodate the different material thicknesses with the layered shell element.

The two separate models were then merged into one using the MAGNA preprocessor utilities. This work was accomplished by the Subsystems Group. The merged model is shown in Figure 14. These utilities allow the user to merge the two models and renumber the entire model in a few minutes. This is a very important feature of the MAGNA package, because to accomplish this task by hand would be a long and tedious process. The computer then changes the connectivity tables. The next step was to determine the boundary conditions of the merged model. The boundary conditions were critical for the correct representation of the actual part. The forward and sill free edges of the transparent panel were clamped. The centerline elements, for the transparent panel, bonding elements and aft arch, were constrained in the lateral (x) direction for symmetry. The aft arch was allowed to move in any direction and was only clamped at the sill. The entire model had a total of 170 elements. The 110 transparency elements were all type 11 layered shell elements. The aft arch and bonding elements had a total of 60 solid elements. The type 7 isoparametric variable node solid was used on 10 elements, while the type 8 isoparametric sixteen-node solid element was used on the other 50 elements. A total of 980 nodes were defined for the complete model. The total number of unconstrained degrees of freedom resulting from the boundary conditions employed was 2595, representing a medium size problem for nonlinear dynamic finite element analysis. Maximum half-bandwidth of the model was 846, and the average half-bandwidth was 205.

### Material Properties

The material properties were then added to the complete model. The transparent plastics used in the windshield panel were characterized as nonlinear elastic-plastic materials using tensile data obtained at room temperature and very low ("static") strain rates. The face ply, both inner and outer, material properties were in accordance with MIL-P-5425 as cast acrylic. The metallic aft arch was titanium and was treated as being nonlinear elastic-plastic. The titanium was annealed Ti-6Al-4V and the stress strain curves used were at room temperature. The specification for the titanium was MIL-T-9047. The windshield interlayer and the bonding sealant materials were represented as being linear elastic. The interlayer material was polyurethane, while the sealant for bonding was PR 1725. The linear material properties for the

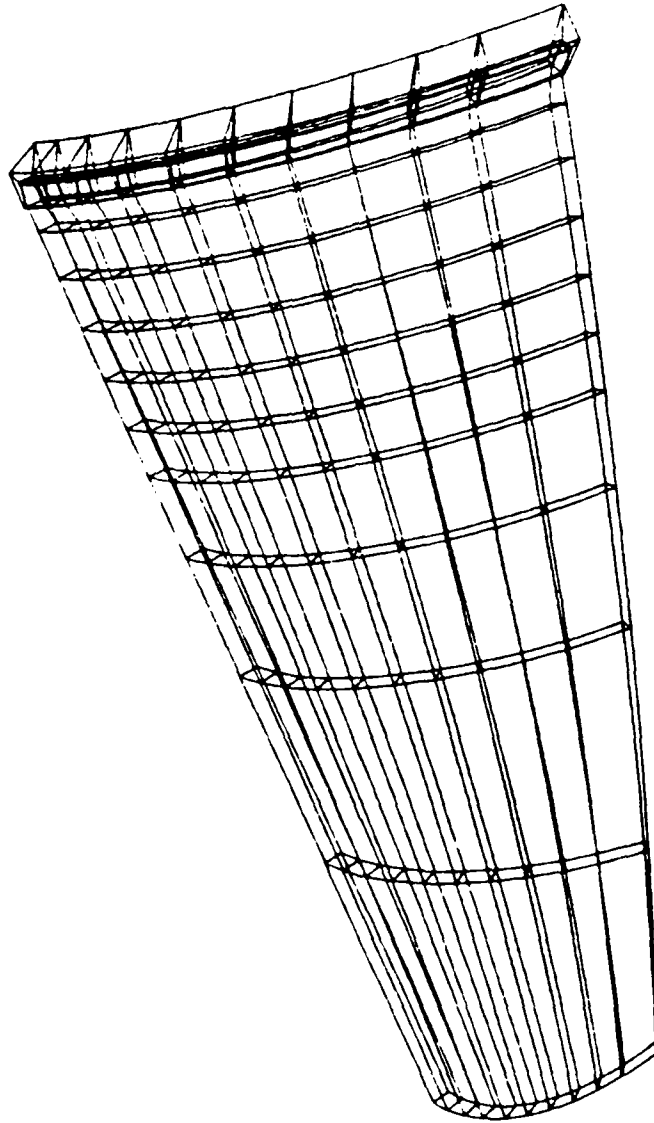


Figure 14. F-4 One Piece Model

five materials are shown in Table 1. The initial analysis with no shear correction used isotropic material description for the type 11 shell element. In MAGNA this allows a nonlinear description of the material. But for the shear correction part of the analysis, the material must be described as orthotropic and this does not allow for any nonlinearities. MAGNA permits the user to provide a table of stress-strain data to describe the behavior of the material beyond the point represented by the value of the yield stress. These plastic strain and stress values are shown in Table 2 for titanium. Only the elastic properties may be used for the type 11 shell element. The model was now complete and only the loading had to be determined before the analysis could begin.

## Bird Impact Loading

### Theory

The definition of the bird impact loads is one of the most important procedures in the analysis. A procedure for the mathematical definition of bird impact loads has been developed by WRDC/FIVR for the use with MAGNA finite element simulations of aircraft transparency bird impact dynamic response.[5] This procedure is based firmly on an extensive experimental data base accumulated over a period of several years.[18-22] The data base is valid for the case of a rigid, flat, inclined target and comprises pressure data recorded at the surface of the target during bird impact. Application of this data base for the case of a compliant transparency is possible using a procedure discussed later.

The loads definition procedure is simple and straightforward to use. The essential points of the theory upon which the loads definition procedure is based are as follows:

1. The bird behaves as a fluid during impact.
2. The impulse delivered to the structure is equal to the component of the bird's linear momentum which is normal to the target surface.
3. The bird may be represented as a right circular cylinder having length to diameter ratio of 2.0.
4. The pressure resulting from a bird impact is relatively constant at any point on the surface of the target (quasi-steady fluid flow).

The following section briefly describes the procedure used to define bird impact loads.

### Procedure for Bird Impact Loads Definition

The first step in the definition of bird impact loading was the calculation of the magnitude of the impulse

Table 1

## Linear Material Properties Used

<u>Material</u>	<u>Young's Modulus (psi)</u>	<u>Poisson's Ratio</u>	<u>Yield Stress (psi)</u>	<u>Density (lb sec<sup>2</sup>) (in<sup>4</sup>)</u>
Polycarbonate MIL-P-83310	324,000.	0.38	9392.	0.111x10 <sup>-3</sup>
Interlayer Swedlow SS6710	1,305.	0.45	-	0.104x10 <sup>-3</sup>
Cast Acrylic MIL-P-5425	450,000.	0.35	9808.	0.111x10 <sup>-3</sup>
Titanium MIL-T-9047	16,000,000.	0.31	132,000.	0.414x10 <sup>-3</sup>
PR 1725	300.	0.49	-	0.149x10 <sup>-3</sup>

## Table 2

### Data Points for the Behavior of the Material Beyond Yield Stress

Titanium Stress vs Strain	
Stress (psi)	Plastic Strain (in./in.)
130900.	0.0
138431.	0.0113
139423.	0.0318
139811.	0.0546
140740.	0.0773
141727.	0.0959



delivered to the windshield from Equation 1.

$$I = M V \sin \theta \quad (1)$$

I = impulse (lb sec)

M = mass (sl)

V = velocity (ft/sec)

$\theta$  = complement of angle between bird trajectory and inward surface normal vector (deg)

Next, both the period of the bird impact and the locus of the bird impact pressure footprint on the surface of the transparency were estimated from high speed (5000 fps) film footage of a 392 knot full scale test. The full scale bird impact test was conducted at AEDC using this prototype one piece windshield design. The period was taken to be 0.0032 sec, and the footprint was laid out on the surface of the finite element model.

When the boundary of the pressure footprint had been located on the surface of the finite element model, a group of finite elements were selected which most closely approximated the area and location of the footprint. These became the elements to which bird impact pressure was applied during the finite element solution.

After the elements representing the impact pressure footprint were identified, a table was assembled of the times at which load rise and unloading occurred for each element. A rectangular pressure versus time history was assumed for each element.

When the intervals of time had been defined during which each element in the footprint was to be loaded, a sum of products was calculated. A computer program that calculates these products and determines the pressure for the loaded elements was developed by the Subsystems Development Group. Each of the products were the surface area of an individual element multiplied by the time interval for its loading. The sum of these products was divided into half of the impulse defined by Equation 1 to determine the value of the constant (and spatially uniform) pressure to be applied to each element in the footprint area. The value obtained for the pressure,  $P_u$ , was 157.6 psi in this specific analysis.

Since the windshield system is not actually rigid, Equation 1 represents only a lower bound for the value of the impulse delivered to the structure by the bird impact. Another limiting case which establishes the upper bound for the value of the impulse is the very flexible target which forms a pocket upon impact, completely arresting all bird material. In this case the impulse delivered is equal to 100 percent of the linear momentum of the bird before impact, or  $M V$ . For a target of intermediate flexibility or compliance, the impulse delivered to the structure lies somewhere between  $M V \sin \theta$  and  $M V$ . The actual value depends on the history of the dynamic response of the target.

To account for this increase in the impulse delivered to the structure as a result of windshield flexibility, the next step was to write two standard user subroutines which are compatible with MAGNA. These subroutines are ULOAD and UPRESS.[13] The subroutines are written in FORTRAN 77 and attached to the end of the MAGNA input job stream. Because the actual pressure,  $P_c(t)$ , is directly proportional to  $\text{Sin } \theta(t)$ , the user subroutines were used to scale  $P_u$  with the Sine of the instantaneous bird impact angle,  $\theta(t)$ , as shown by Equation 2. As local bending develops in the transparency and the slope or inclination of the surface beneath the bird material increases, so does the local instantaneous bird impact pressure,  $P_c(t)$ .

$$P_c(t) = P_u \text{Sin } \theta(t) / \text{Sin } \theta(0) \quad (2)$$

$\theta(0)$  = Complement of angle between bird trajectory and inward surface normal vector at the beginning of the bird impact event (deg).

$\theta(t)$  = Complement of angle between bird trajectory and instantaneous inward surface normal vector at time  $t$  (deg).

$P_u$  = Rigid target value of bird impact pressure (psi).

$P_c(t)$  = Flexible target value of bird impact pressure calculated by user subroutines at time  $t$  (psi).

Such an increase in the instantaneous pressure results in a corresponding increase in the impulse delivered to the structure. In this way, the user subroutines ULOAD and UPRESS use the instantaneous deformation of the windshield, calculated by MAGNA, to modify the current value of the impact pressure. The subroutine ULOAD calculates the deformations of certain nodes in the model. These nodes are the midside nodes of the elements being loaded. A ratio of the calculated to original impact angles is determined to scale the pressures in UPRESS accordingly. The subroutine UPRESS also allows the engineer the opportunity to load and unload different elements at different times.

This procedure for the definition of bird impact loading is simplistic. It presumes a regular geometry for the bird, ignores spikes of shock pressure which occur early in the impact event, and assumes a spatially uniform distribution of pressure at all times. Even with these assumptions, the bird impact simulation results obtained with this procedure have been found to be useful and realistic.[5] The entire model was now ready for submittal to the computer to start the finite element analysis.

## NO SHEAR CORRECTION ANALYSIS

MAGNA analysis was begun on the F-4 one-piece windshield using no shear correction in this analysis. This was the regular nonlinear analysis and the objective in the beginning was trying to understand the behavior of the layered shell element. The deflections were a concern from previous experience with the shell element. In previous cases the shell element was stiffer than the actual design. For this reason only the deflections at the nodes, and both stresses and strains at the integration points were calculated. This file is called the MPOST file in the MAGNA package. The STRAVG computer program, which uses stress averaging to calculate the stresses and strains at the nodes, was not employed in these first runs. The results were compared to the actual full scale results from AEDC. This was the reason that 392 knots was chosen as the speed for the impact. It also was the reason that the impact point was 8 inches forward of the aft arch on the centerline. The high speed film for this shot from AEDC was the best for reducing the deflection data.

Free vibration analysis was used to determine the lowest frequency modes of the model and to make sure there were no errors in the model. MAGNA utilizes a vector iteration method for the free vibration analysis. For the F-4 one-piece windshield analysis, ten trial vectors were used to determine the three lowest frequency modes. The maximum number of iterations for convergence of this analysis was 15. The lumped mass option was selected to keep the computer cost down. This has been employed on other analyses, which gave realistic results. [2,6,12] All materials were assumed to exhibit linearly elastic behavior. A 14 point rule available with MAGNA was used for integration within the 60 solid elements in the model. This rule does not constitute reduced integration for the sixteen-node isoparametric solid element.[13] The type 11 layered shell element used the two point Gaussian rule, corresponding to 36 integration points per layered shell element, four for each of nine sublayers. The first mode of the free vibration analysis converged in four iterations, and the frequency obtained was 200.4 Hz. This frequency was then used to determine the time step in the nonlinear dynamic analysis. The deflection results of this first mode are plotted in Figure 15.

The nonlinear dynamic analysis simulated the four pound bird impact of the full scale test at AEDC. The speed of the impact was chosen to be 392 knots because of the quality of the data from this test. If the simulation seemed reasonable with the layered shell element, then a 500 knot simulation would be run in order to determine the reason for the failure experienced by this system on another full scale test at 500 knots. The failure of the system was that the transparency pulled out of the aft arch on the 500 knot shot. The impact point was the most critical point on the transparency and was 8 inches forward of the arch on the centerline. This analysis included the effects of both material and geometric nonlinearities. The footprint was determined on the model and

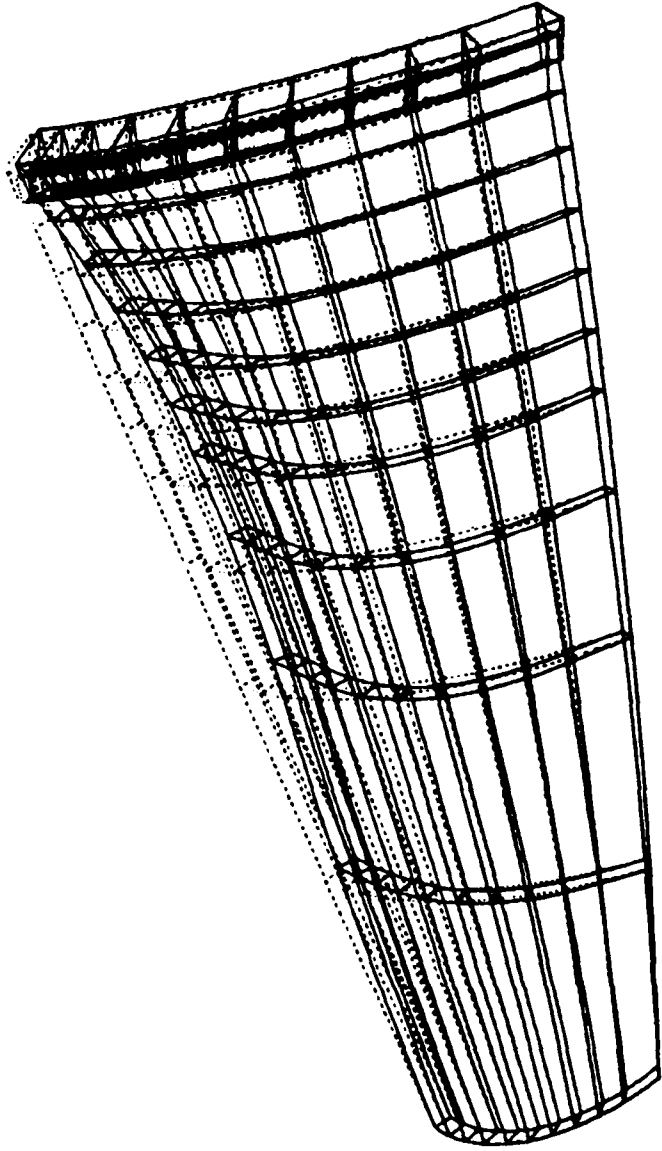


Figure 15. F-4 One Piece Windshield Eigenvalue Solution  
for the First Mode With No Shear Correction

17 elements were loaded during the simulation. The footprint was determined from the high speed films taken during the full scale test at AEDC. The size of the time increment chosen for the dynamic analysis was 0.00005 sec, which was slightly more than 1/100 of the period of the lowest free vibration mode. This mode was presumed to be principally excited by the impact event. This rule of thumb in selecting a time increment size for nonlinear dynamic analysis has been demonstrated previously to represent an effective balance between analysis costs and accuracy.[2,13] The analysis was completed with a non-iterative solution and the same integration rules that were employed as in the free vibration analysis. The non-iterative solution was chosen over the different iteration solutions for computer cost reasons. Two important variables were calculated after each increment in the solution and were monitored throughout the solution to make sure that the non-iterative solution would give reasonable results. If these variables became too large then the accuracy of the solution would suffer. The full nonlinear stiffness formulation was used for every solid element in the model. This particular analysis was completed on a Cyber 845 machine. The CDC limits the size of the problem and only 5 increments were run at a time. Another feature of MAGNA is restarting the dynamic analysis problem. This was employed and the total number of increments that were run was 100. The deflection data were the only results compared with the full scale test.

The deflection results for this simulation were very disappointing. The layered shell element performed much stiffer than anticipated. The maximum normal deflection that was predicted by the simulation was 0.79 inches at .0024 sec. This maximum deflection occurred at the same point as the actual test, 2.3 inches aft of the impact point. This prediction was only 34 % of the actual maximum deflection from the full scale test. The comparisons of the simulation results and the full scale results are shown in Figures 6-8. It was determined that more work had to be performed on the shell element before the 500 knot simulation would be performed to examine the failure mode of the transparency system. One of the solutions to these poor predicted deflections was to run a shear correction simulation.

### Shear Correction Analysis

The shear correction program was used to mathematically correct the stiffness of the layered shell element. This program was developed by the University of Dayton Research Institute (UDRI) in December of 1985. At first this program was a stand alone program, but it has been incorporated into the MAGNA package recently. The stand alone program was used for this analysis. The program is written in standard FORTRAN 77, with certain exceptions. The program consists of a few hundred lines of code. The CDC Version of the program was used for the F-4 one-piece windshield analysis. The reason for

using the shear correction program was to compare the results of the simulation with that of a regular analysis and results from a full scale test. The F-4 one-piece windshield already had all this data and was chosen for the first experiment, on a full model, with the shear correction analysis.

The purpose of the shear correction program is to perform stress recovery and related calculations for composite laminates. The laminated stress calculations included in this code are:

1. Calculation of gross stiffness characteristics (matrices A, B, and D from classical plate theory, and analogous transverse shear stiffness and flexibility matrices).
2. Calculation of the recovery coefficients for transverse shear stresses.
3. Calculation of shear correction factors for use in finite element calculations.

Material properties are defined in a material coordinate system in which direction '1' is the fiber strong direction, '2' is the inplane direction normal to '1', and '3' is the thickness direction. The material orientation for a given layer is defined by an angle theta, which is measured in degrees. The angle theta is between the material '1' direction and the x axis for the structure of the composite material. The angle has a positive sense for the counterclockwise direction with respect to the x axis.

The program computes the shear correction factors and the shear recovery coefficients for a laminate, based on cylindrical bending assumptions with no coupling of transverse shear resultants. The shear modulus and Poisson's ratio are defined by:

$$G = \frac{E}{2(1 + \nu)} \quad (3)$$

$$\nu = \frac{E}{2G} - 1 \quad (4)$$

The material properties used for the laminate in the program are:

- E1 = Longitudinal Modulus (for each material)
- E2 = Transverse Modulus
- E3 = Out-of-Plane Modulus
- ν23 = Poisson's Ratio in 2-3 Plane
- ν13 = Poisson's Ratio in 1-3 Plane
- ν12 = Poisson's Ratio in 1-2 Plane
- G23 = Shear Modulus in 2-3 Plane
- G13 = Shear Modulus in 1-3 Plane
- G12 = Shear Modulus in 1-2 Plane

The first recovery coefficient is from the following equation, applying the assumption that the transverse shear stress vanishes on the lower surface of the laminate ( $Z=-H/2$ ), where  $H$  is the total thickness of the laminate.

$$A^{(1)} = \frac{1}{2} Q_{11}^{(1)} H [A_{11} H + 4B_{11}] \quad (5)$$

Where (1) refers to the first (lowest) layer. For the remaining layers, the conditions of continuous transverse shear stress between adjacent layers gives:

$$A^{(m)} = A^{(m-1)} + [Q_{11}^{(m)} - Q_{11}^{(m-1)}] [A_{11} z^{(m)} - 2 B_{11}] z^{(m)} \quad (6)$$

In which  $Z^{(m)}$  is the  $Z$  coordinate at the lower surface of layer  $m$ , measured from the laminate midsurface. The transverse shear correction factors are obtained simultaneously from the integral:

$$k_{xz}^{-2} = A_{44} \int_{-H/2}^{H/2} G^{(m)}(z) dz \quad (7)$$

Where:

$$G^m(z) = \frac{1}{G_{xz}^m} \left[ \frac{A^{(m)}}{2D} + \frac{Q_{11}^{(m)} z (2B_{11} - A_{11} z)}{2D} \right]^2$$

$$D = A_{11} D_{11} - B_{11}^2$$

- A = Extensional Stiffness
- B = Coupling Stiffness
- D = Bending Stiffness
- G = Shear Modulus
- Q = Elasticity Matrix
- m = number of layer
- $Z^{(m)}$  =  $Z$  coordinate at lower surface of layer  $m$

The shear correction factors obtained are exact only for cylindrical bending in the  $(X,Z)$  or  $(Y,Z)$  planes, provided the corresponding transverse shears are uncoupled. The second condition is true when:

1. The two transverse shear moduli are equal.
2. The material orientation is 0 or 90 degrees with respect to the structural axes.

The shear correction factors for all the other cases are approximate.[23-26]

The shear correction factors were incorporated into the F-4 one-piece windshield analysis. The shear correction program was run on the Cyber 845 machine at Wright-Patterson. The only changes made to the F-4 one-piece model were the material properties definition. In order to incorporate the shear correction factors, the definition of all three thermoplastic materials was changed from isotropic to orthotropic. The values of the shear correction factors and the material properties are shown in Table 3 for the two F-4 one-piece windshield analyses. The analysis was then run on a CRAY XMP/12 supercomputer. The analysis was able to run 50 increments at a time before restarting, because of the CRAY's speed and capacity. The size of the finite element model and the solution parameters have always been limited by the size and speed of the computers. But with the advancing supercomputer technologies, the issue of what elements and parameters to use have decreased. Finite element analysis will be capable of using the whole supercomputer resources, but as these resources increase it also increases the options for the engineer. The main driver for this shell element was that the larger solid element problems were not capable of running on the largest computers a few years ago. This problem has not entirely gone away but improved over the past few years, with the new class of supercomputers. The results from the shear correction analysis show excellent correlation with the deflections of the full scale test. The deflection results are compared with the other simulation and the actual test in Figures 6-8. The maximum normal deflection in the shear correction analysis occurred at the same aft point as the full scale test. The point deflected 2.34 inches at a time of 0.0028 sec. The discrepancies in the times, between the full scale test and the shear correction analysis, were related to the way the elements were loaded during the simulation.

### Conclusions

The F-4 one-piece analyses provided valuable information about the layered shell element. The next step in validating this procedure is to continue the shear correction analysis and look at the outer fiber stresses. This will show how the stresses are effected by using the shear correction factors. After this has been completed, then the 500 knot simulation at the critical point should be completed, to examine the failure mode of the 500 knot full scale test. The deflections correlated excellently with the full scale results, when the shear correction factors were used in the analysis. The main advantage of using the type 11 layered shell elements are



Table 3

Shear Correction Factors and Material Properties for the Two Analyses

NO SHEAR CORRECTION			
MATERIAL	E	$\nu$	G
Polycarbonate	324000.	.38	117390.
Polyurethane	1000.	.43	350.
As Cast Acrylic	450000.	.35	166670.

SHEAR CORRECTION			
MATERIAL	$E_1 = E_2 = E_3$	$G_{12}$	$k_1^2 G_{13}$ $k_2^2 G_{23}$
Polycarbonate	324000.	117390.	1850.    1850.
Polyurethane	1000.	350.	5.5    5.5
As Cast Acrylic	450000.	166670.	2627.    2627.

$$k_1^2 = 0.01576 \qquad k_2^2 = 0.01576$$

is to increase significantly the problem size limits on any given machine. Problems that were not possible to run before can now be accomplished, using the layered shell element. Another advantage is reducing the computer cost for an analysis run. Other advantages are less time in generating the model and through the thickness changes are easily incorporated with the shell element. The advantages are significant and warrant more study and development of the layered shell element.

## F-4 FORWARD CANOPY ANALYSIS

The F/RF-4 aircraft is flying more high speed, low level missions than ever before. This places the crew in danger of severe birdstrikes. The reasons why an improved F-4 windshield system was desired, are the same reasons for an improved forward canopy. An interesting problem was proposed to the Aircrew Enclosures Group in October of 1988. The problem was to design a new F-4 forward canopy using the MAGNA finite element code. This would be the first time that MAGNA would be used to design a new system from the beginning of the design. There would be no previous full scale tests to show the loading of the canopy. There was also very little experience with this type of geometry, since it varied significantly from the previous windshield analyses. The constraints placed on the problem were to design the part so that it would fit into the existing frame. A retrofit of the entire frame assembly was not desired at this time. Texstar, Inc. would provide some guidance and fabricate two prototype parts. These parts would then be subjected to full scale birdstrike tests at AEDC. The tests were scheduled for the middle of December 1988. This would mean that only four weeks of analysis could be completed before the decision was made to build a specific design.

### Structural Modeling

#### Geometry

The F-4 forward canopy was easier to model than the F-4 one-piece windshield. The F-4 canopy model was originally developed by the University of Dayton Research Institute (UDRI). This model is shown in Figure 16. The model would be modified to show only the transparency panel, with no support structure. The model was delivered to the Air Force in 1983. The geometry of the forward canopy is very simple and was modeled originally with 104 elements. This model is shown in Figure 17. The number of elements would change with the different cross sectional designs being analyzed. A total of six different canopy designs would ultimately be analyzed, four monolithic and two laminate designs. The total thickness would vary from 0.3 inches to 0.4 inches. The existing frame was only capable of handling a part up to 0.4 inches thick. The laminated canopy and different monolithic designs were

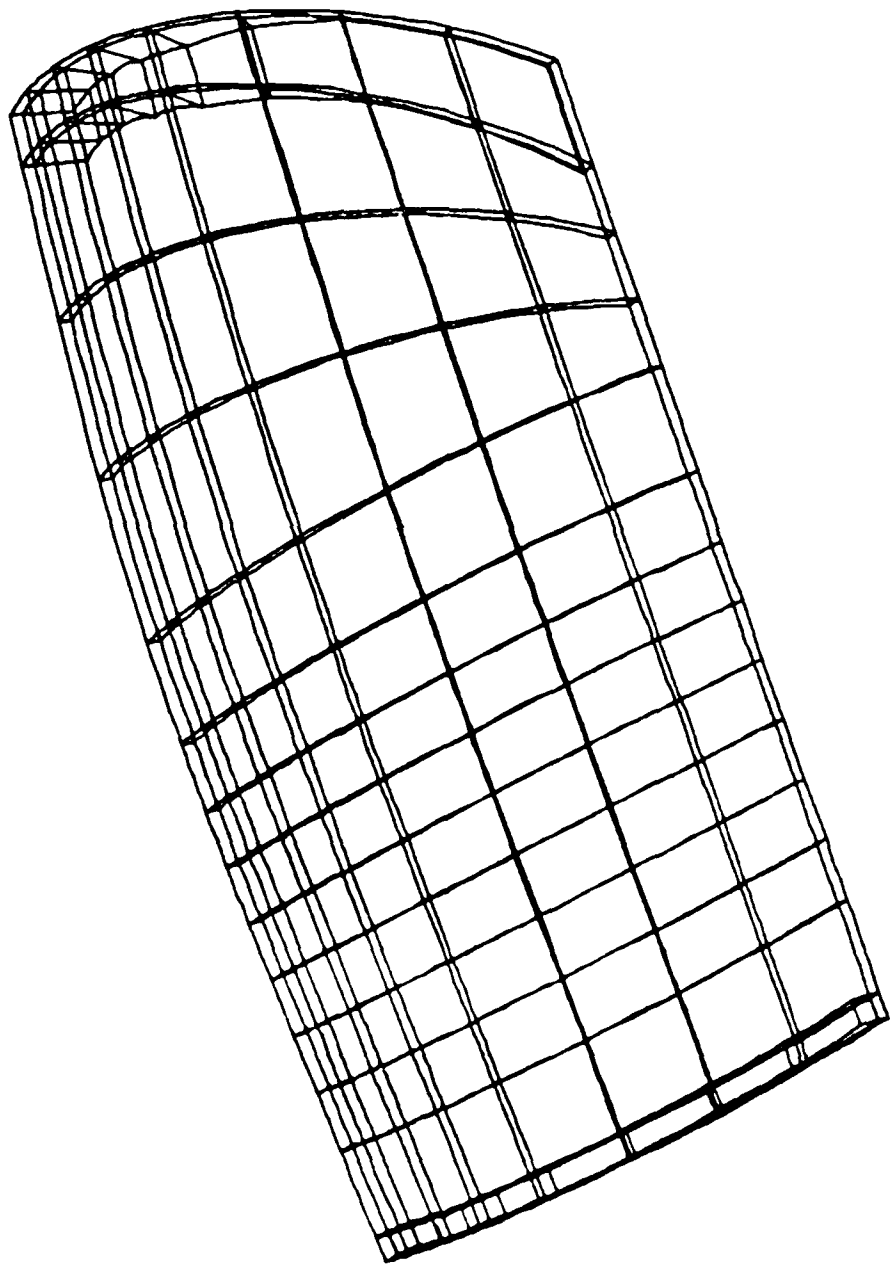


Figure 16. Original F-4 Forward Canopy Model

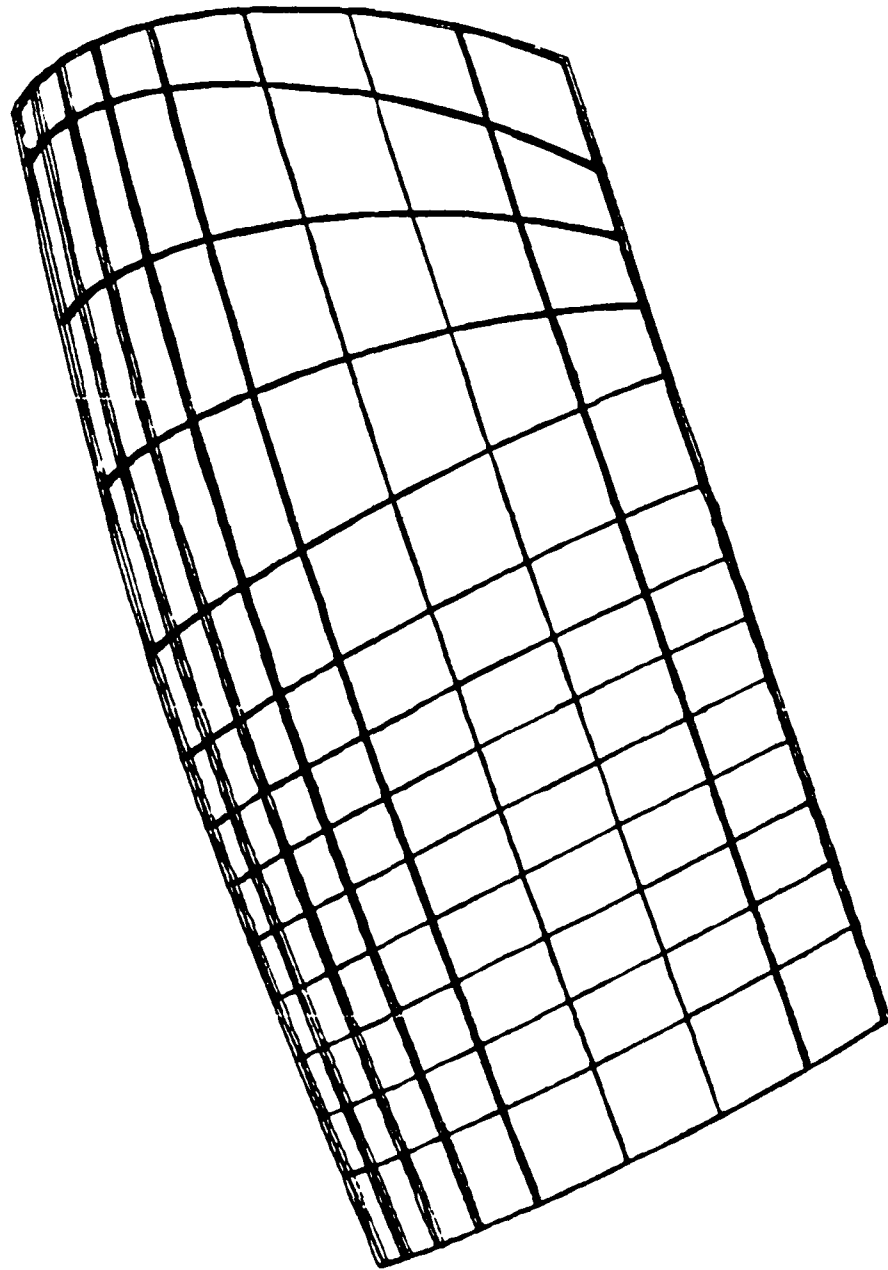


Figure 17. F-4 Forward Canopy Model

formed by using a computer program developed by UDRI. This computer program is called EXPAND and calculates thickness changes in a model using the inner surface as a reference. The MAGNA type 8, 16 node solid element was used to generate all of the forward canopy models. The forward part of the canopy was inclined at 17 degrees with respect to the longitudinal (y) axis. The vertical axis would be the z direction for this analysis. After the original forward canopy was modified, the material properties definitions were added to the input file.

### Material Properties

Three different thermoplastic materials were used in this design study. These materials were polycarbonate, polyurethane and stretched acrylic. The acrylic material was the enhanced stretched acrylic, but the mechanical properties of these two materials was essentially the same. The other two materials were the same as in the F-4 one-piece analyses. So the linear properties of all three materials are shown in Table 1 of the F-4 one-piece analysis section. The polycarbonate and stretched acrylic materials were treated as being nonlinear and isotropic. This was possible because the MAGNA type 8 element was used for modeling. A value was used for the "yield stress" which was lower than that ordinarily associated with the yield phenomenon. The value chosen was used only to represent that portion of the stress-strain curve which was most nearly linear. Significant nonlinearities are observed for values above this "yield stress". MAGNA permits the user to provide a table of stress-strain data to describe the behavior of the material beyond the point represented by the value of the "yield stress". The points used to characterize the behavior of polycarbonate and acrylic are shown in Table 4 for stress levels above "yield". The third point for polycarbonate would ordinarily be associated with the yielding phenomenon. Some strain hardening had to be assumed for the material in order to avoid numerical problems in the solution, although the material actually exhibits strain softening. This misrepresentation of actual material behavior has been used previously in similar analyses.[4] In both the cases the next to last point represents the ultimate stress of the material. This ultimate stress corresponds to the mechanical rupture or failure. The very large plastic strain which polycarbonate is capable of withstanding is the key to its ability to survive high energy bird impact loading. The MAGNA input file was now completed, except for the loading subroutines.

### ANALYSIS

MAGNA nonlinear analysis was begun on designing the best bird impact F-4 forward canopy for the thickness constraints of the existing frame. The objective of the analysis was to determine the velocity at which the forward canopy system

Table 4

Data Points for the Behavior of the Material Beyond Yield Stress

Acrylic Stress vs Strain		Polycarbonate Stress vs Strain	
<u>Stress</u> (psi)	<u>Plastic Strain</u> (in./in.)	<u>Stress</u> (psi)	<u>Plastic Strain</u> (in./in.)
3,921.	0.0000	6,353.	0.0000
5,429.	0.0031	8,061.	0.0066
6,598.	0.0055	9,392.	0.0254
7,405.	0.0089	9,700.	0.2500
8,010.	0.0127	10,043.	0.5000
8,396.	0.0169	10,728.	1.0000
8,683.	0.0215		
8,890.	0.0263		
9,029.	0.0312		
9,545.	0.0838		
10,881.	1.0000		

would fail for a four pound birdstrike. The threshold would be determined by calculating the maximum effective stress of the material during the impact. This would then be compared with the rupture stress of that material to determine if the system had failed. The impact point would be the forward most possible point on the centerline of the canopy. The center of the impact would impact at 11.4 inches aft of the windshield canopy arch, on the centerline. This point was determined to be the most critical, with a bird impact angle of 17 degrees.

The free vibration analysis was run to determine the lowest frequency mode and locate any errors in the model. The first model that was run was the 0.40 monolithic polycarbonate design. This analysis was essentially the same type of free vibration analysis run on the F-4 one-piece windshield. MAGNA utilizes a vector iteration method for the free vibration analysis. Two trial vectors were used to determine the lowest frequency mode of the model. The maximum number of iterations would be nine, but the problem converged on only four iterations. The lumped mass option was again selected. All materials were assumed to exhibit linearly elastic behavior. The 14 point integration rule was used throughout the forward canopy analyses. The frequency of the first mode of the free vibration analysis for the 0.40 monolithic polycarbonate design was 128.0 Hz. Other free vibration analyses were performed each time a new design was modeled. The parameters and options stayed the same in each analysis. The lowest frequency for a 0.389 inches thick polycarbonate laminate was 125.6 Hz. The deflection plots for the first mode of a 0.374 inches thick laminate and monolithic designs are shown in Figures 18-19. These frequencies were then employed to determine the time increment for the nonlinear analyses.

The nonlinear dynamic analyses of the different designs simulated the four pound bird impact tests that would be performed the next month. The maximum velocity of the bird not resulting in failure would be determined for each design. The ultimate stress of a material would be compared to the maximum effective stress calculated in the finite element code. In MAGNA the maximum effective stress, at the nodes, is output for the APOST file. This maximum stress is calculated for each part at all the different increments of the analysis. This APOST file is the output of the stress averaging routine. The effective stresses were calculated from the equation:

$$\sigma_e = \frac{1}{\sqrt{2}} [(\sigma_x - \sigma_y)^2 + (\sigma_y - \sigma_z)^2 + (\sigma_z - \sigma_x)^2 + 6(\tau_{xz}^2 + \tau_{yz}^2 + \tau_{zx}^2)]^{1/2} \quad (8)$$

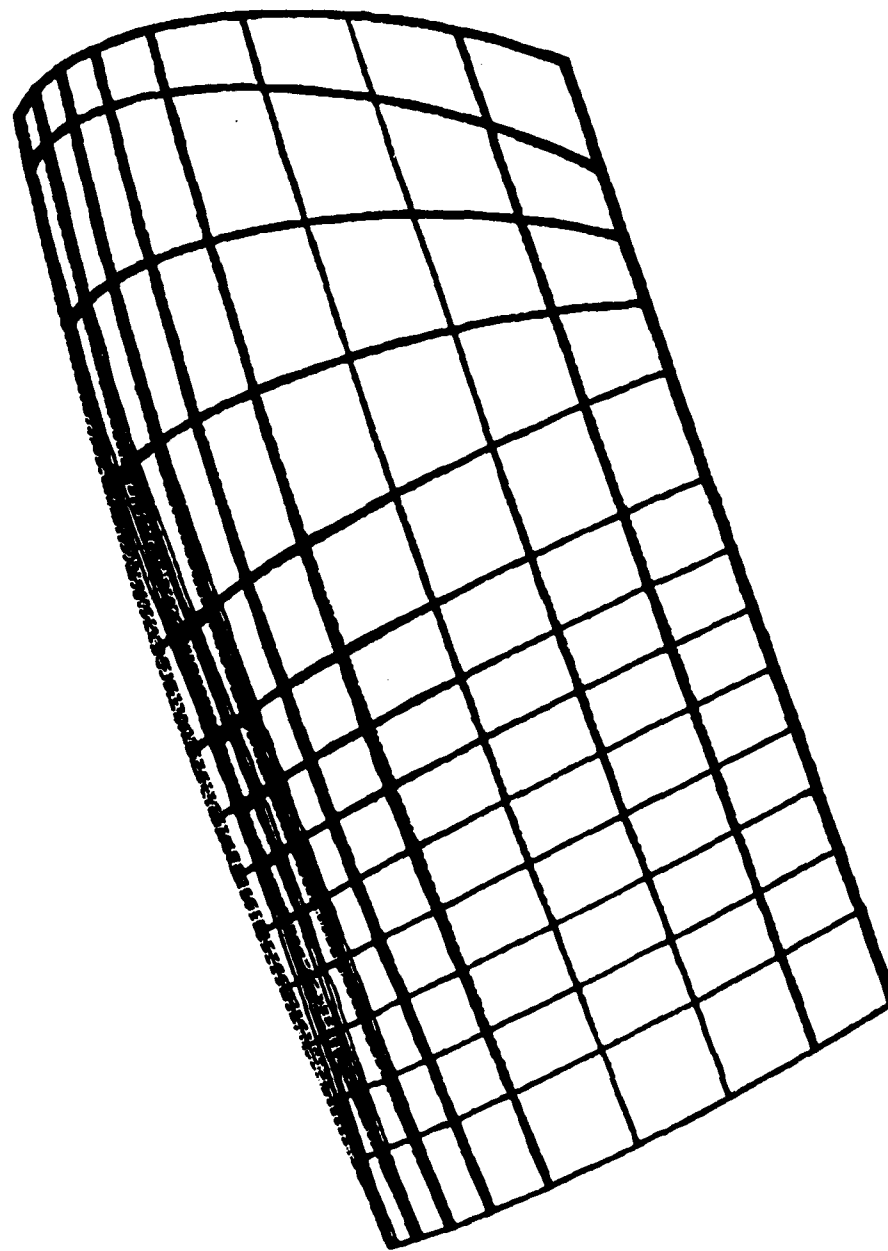


Figure 18. F-4 Forward Canopy Deflection Results for the First Mode of a .374 Inch Thick Laminate



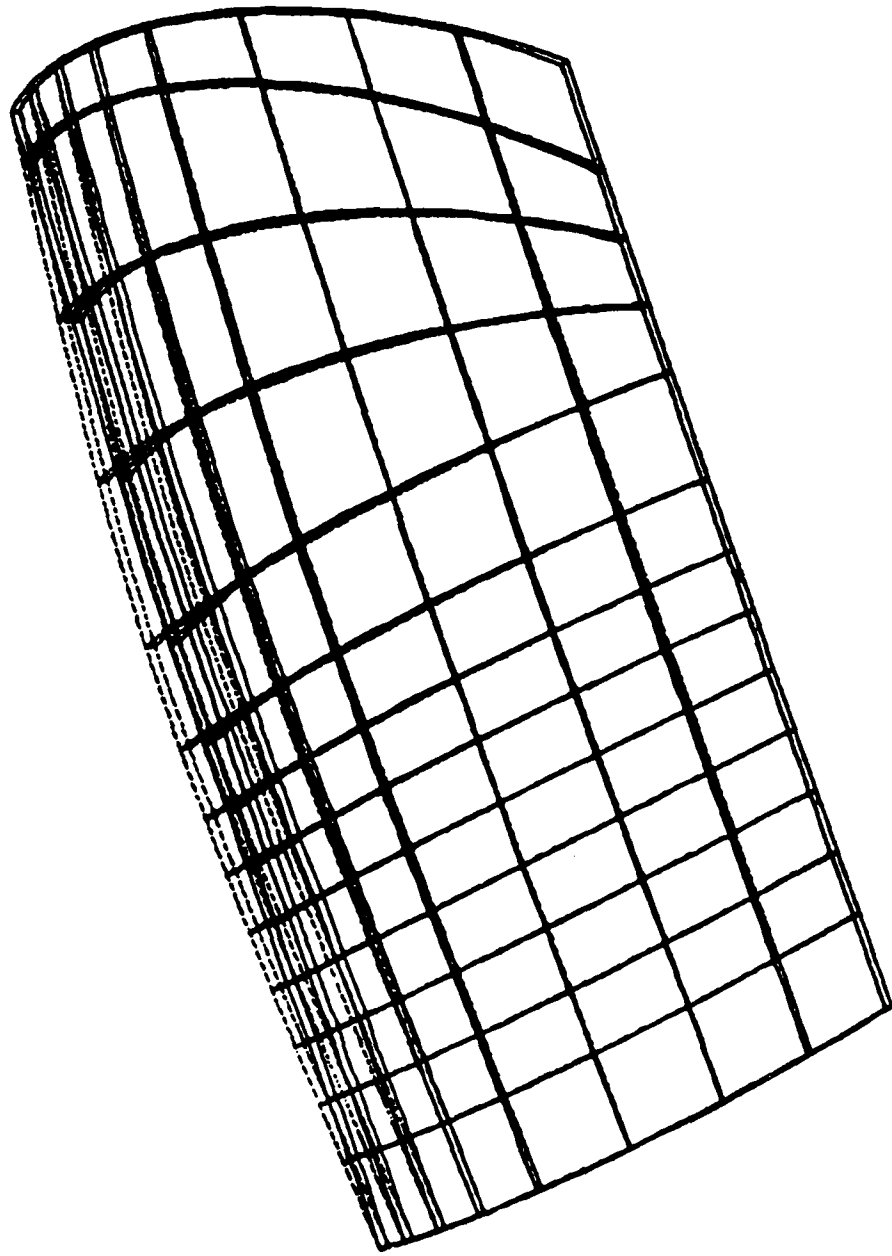


Figure 19. F-4 Forward Canopy Deflection results for the First Mode of a .374 Inch Thick Polycarbonate Monolith

The stresses and strains used in the analysis were the Green strain and Piola-Kirchhoff stress. The von Mises yield criterion is defined by:

$$\sigma_0^2 = \frac{1}{2} [(\sigma_1 - \sigma_2)^2 + (\sigma_2 - \sigma_3)^2 + (\sigma_3 - \sigma_1)^2] \quad (9)$$

When the maximum effective stress reached 9800 psi for stretched acrylic and 9400 psi for polycarbonate, failure was assumed for the transparent panels. These figures have been used in previous analyses and proven to give excellent results when compared to full scale tests. The definition of the loads was the most difficult part of the analysis. There was no high speed film of an actual full scale test to show how large the footprint area would be. There was also the problem of being unfamiliar with the type of geometry being modeled. The canopy deflections were unknown, so it was unknown how the deflection of the canopy would effect the loading pattern. The rigid target case was assumed to define the footprint of the bird impact. This assumption was made because of the small inclined angle. The normal component of the momentum would be small, compared to windshield bird impact. There was also no experience, from previous work, to predict the deflections that would influence the footprint size. The rigid target footprint was determined and used throughout the different analyses. The footprint is shown on the model in Figure 20. There were 10 elements that were loaded during the impact event. The nonlinear solution parameters, for both the 0.389 inch thick laminate design and the 0.4 inch thick monolithic polycarbonate design, are shown in Table 5. The solution parameters were similar for the two laminate designs, as were the parameters for the four monolithic designs. The boundary conditions for this model were clamping every free edge except the centerline. This meant that all nodes, through the thickness, on these three edges were fixed for the laminated designs. The lateral (x) direction was constrained on the centerline of all the models for symmetry. A plot of the boundary conditions is shown in Figure 21. The analysis was completed with a non-iterative solution. The two important variables were again monitored throughout the solutions. If these variables became too large then the accuracy of the solutions suffer. The full nonlinear stiffness formulation was used for every element in the model. Table 6 shows the different constant pressures that were applied to the loading elements at various speeds. Each of the analysis runs were made on the CRAY XMP/12 supercomputer. The CRAY allowed the problem to be run to 50 increments without being restarted. All the analysis runs were only taken out to 50 increments.

The results of the analyses of the F-4 forward canopy were very disappointing when compared to the full scale tests. The design that was picked to be built by Texstar Plastics was the 0.389 inch thick laminated design. This canopy has two 0.185 inch thick plies of polycarbonate, with a polyurethane

**F-4 FORWARD CANOPY  
ANALYSIS FOOTPRINT**

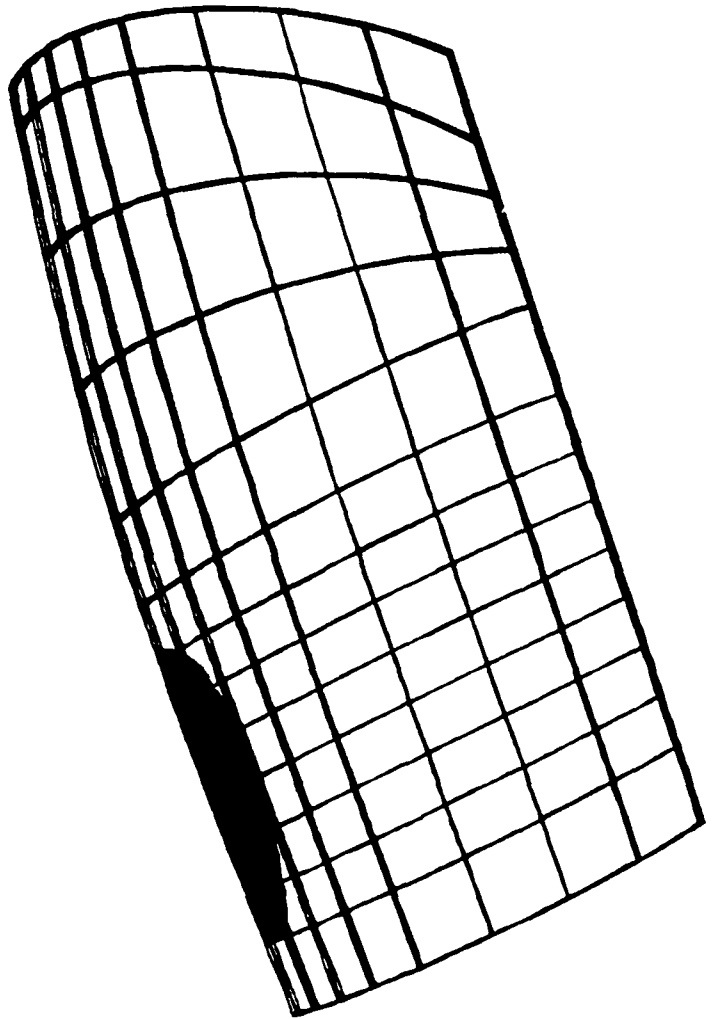


Figure 20. F-4 Forward Canopy Bird Impact Analysis Footprint

Table 5

F-4 Forward Canopy Nonlinear Solution Parameters

Parameter	Laminate Design	Monolithic Design
D.O.F.	3453	1905
Time Increment	.00008 sec	.000082 sec
Nodes	1420	710
Elements	312	104
Frequency (first mode)	125.6 (.389 ")	128.0 (.4 " poly)
Half-bandwidth	489	283
Average bandwidth	273	146

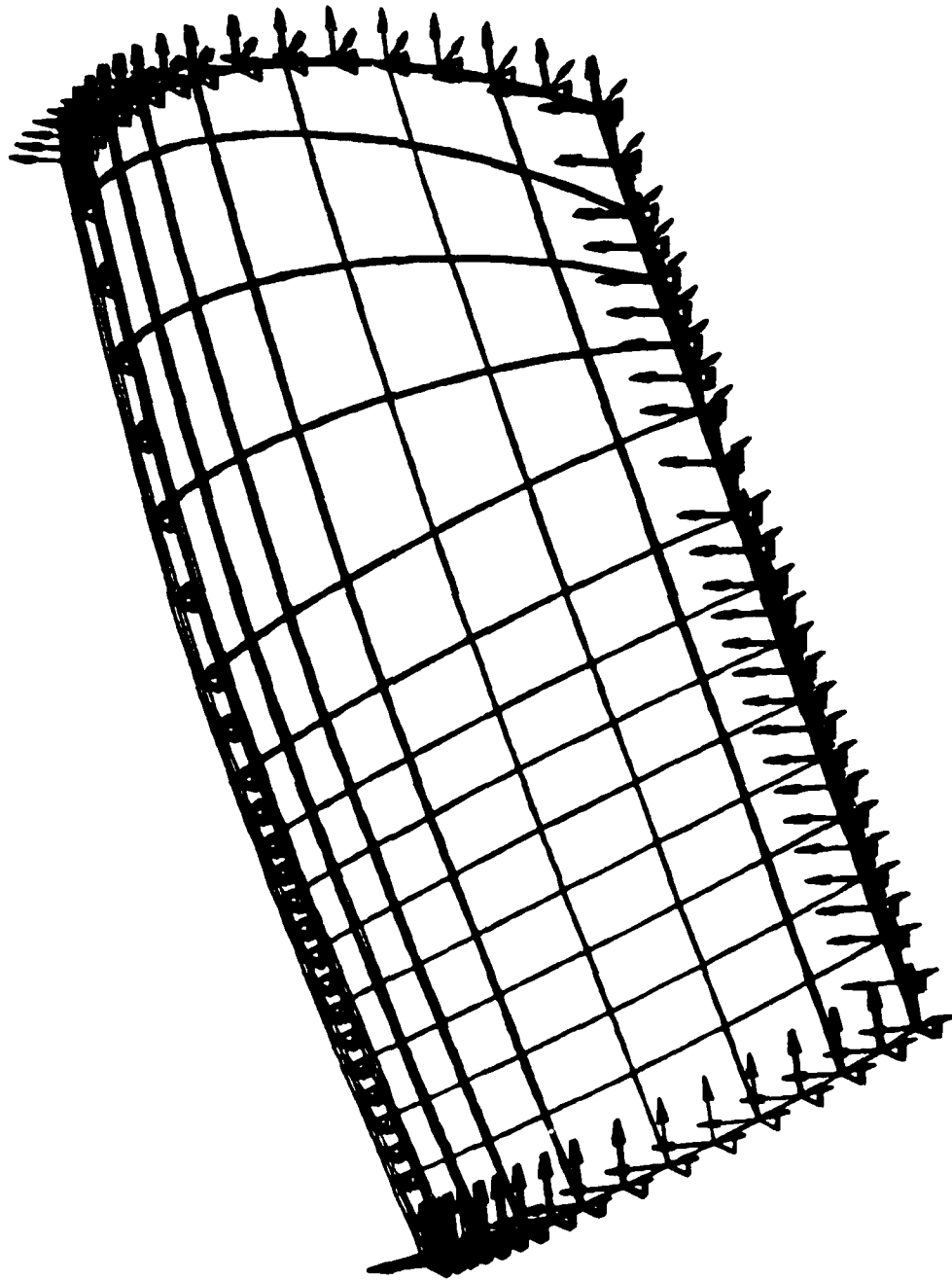


Figure 21. F-4 Forward Canopy Plot of the Boundary Conditions

Table 6

F-4 Forward Canopy Constant Pressures for Various Speeds

SPEED (KNOTS)	PRESSURE (PSI)
200	38.6
225	48.9
250	60.3
275	73.0
300	86.9

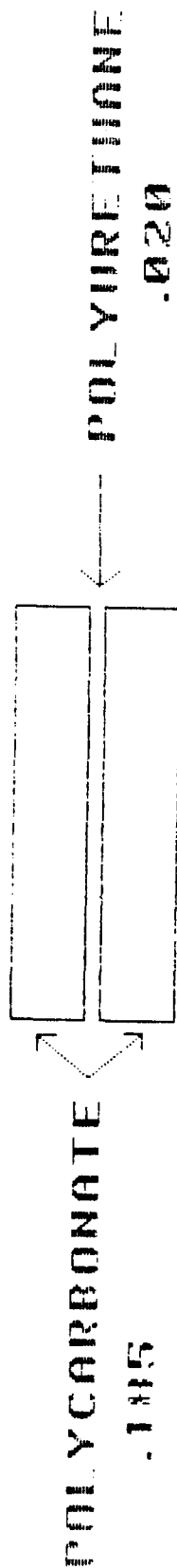
interlayer. This design is shown in Fig. 22. The predicted threshold of this design for the forward target point was 225 knots. Texstar fabricated this design and the transparencies were installed in frames. The full scale testing took place at AEDC, in December, 1988. Only the first canopy assembly arrived on time to be tested. The finite element mesh was laid out on the inner surface of the canopy to get deflection data from the triangulation method. The cameras and desired points were measured with respect to a reference point. The first shot was accomplished at 275 knots. The canopy system experienced no failure at all. The picture in Figure 23 shows the F-4 assembly after the shot. Notice the two inside cameras that are used for the triangulation method. It was decided to shoot the same part at 400 knots at the same location. This time there was some damage to the support structure, but the transparent panel passed easily. The two aft shearing pins, located between the canopy and the airframe, broke from the impact. There also was damage to the forward arch and aft arch. The forward arch experienced plastic deformation and lost some inside sheet metal. The aft arch cracked on both sides towards the sill and fasteners were broken around the centerline of the transparency. The damage to the frame was repaired as much as possible and the part was shot again, but this time at 500 knots. The same type of frame failure occurred as before, but the transparency panel passed. The frame failure was more severe than for the 400 knot case, but not severe enough to cause any concern. The high speed film was examined and the actual footprint was determined to be much larger than what was used in the analysis. This footprint is shown in Figure 24. This was the main reason why the analysis did not correlate with the tested results. Some of the graphs of maximum stress and maximum deflections are shown in Figures 25-36 for all six design cases at different velocities. A summary of all the analyses is shown in Table 7. This problem will be run again using the correct footprint on the 0.389 laminate design. Another correlation will then be made with the actual full scale tests. The deflection data will also be reduced by the triangulation method and compared to the new analysis.

### Conclusions

The F-4 forward canopy analysis was the first time that MAGNA was used to design the transparency panel from the beginning to meet the birdstrike requirement. The simulation was completed for six different designs in a few weeks. The decision was made to build the 0.389 inch polycarbonate laminate. There was no correlation between the predicted failure of the transparency panel and the actual test results. It was very difficult to predict the threshold of failure because the loading footprint used for the analysis was so much different than what actually happened. The actual

F-4 FORWARD CANOPY

CROSS SECTION



TOTAL THICKNESS = 0.389 inches

Figure 22. F-4 Forward Canopy Cross Section That Was Selected to be Built and Tested



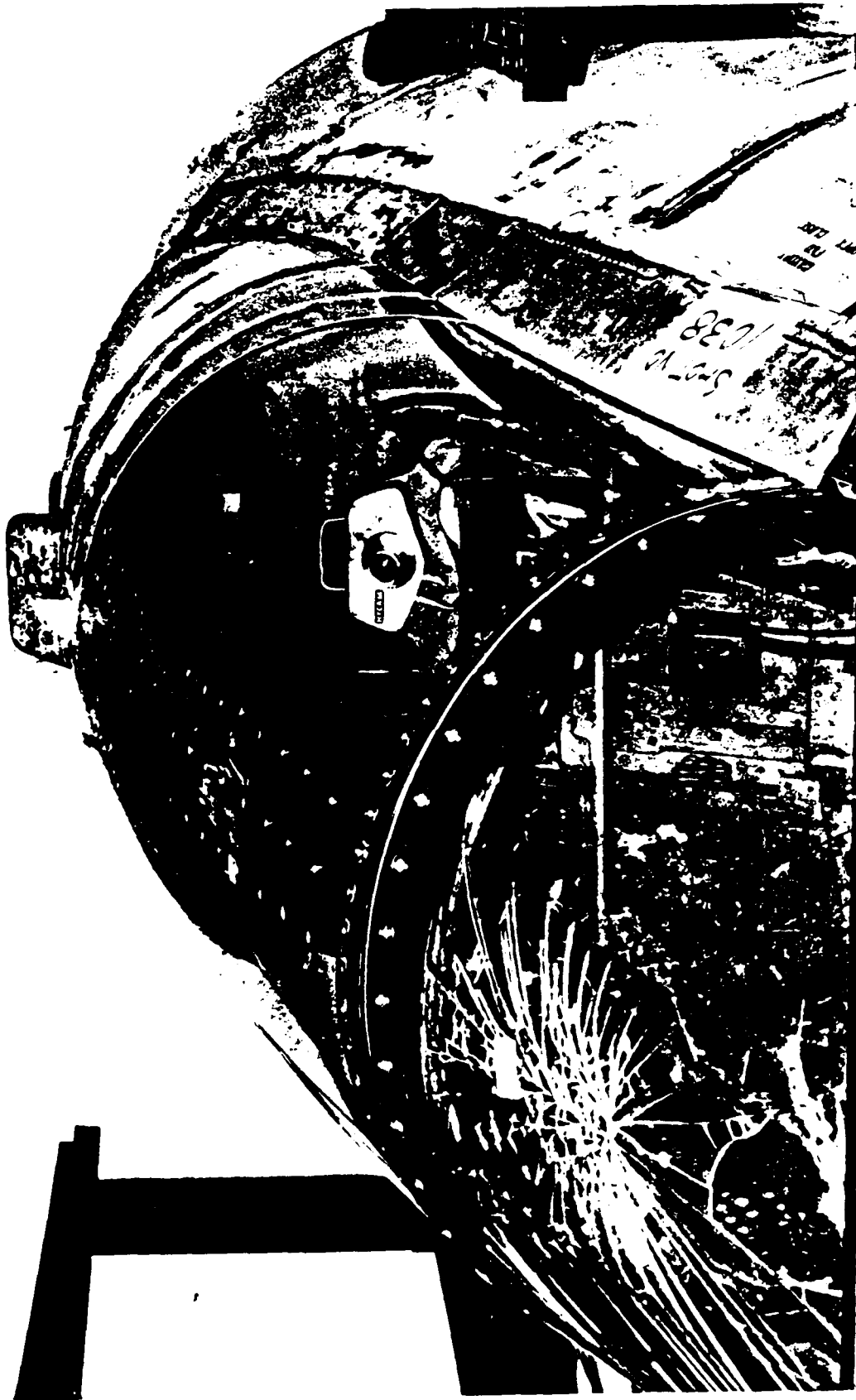


Figure 23. F-4 Forward canopy Birdstrike at 275 Knots

F-4 FORWARD CANOPY  
ACTUAL FOOTPRINT

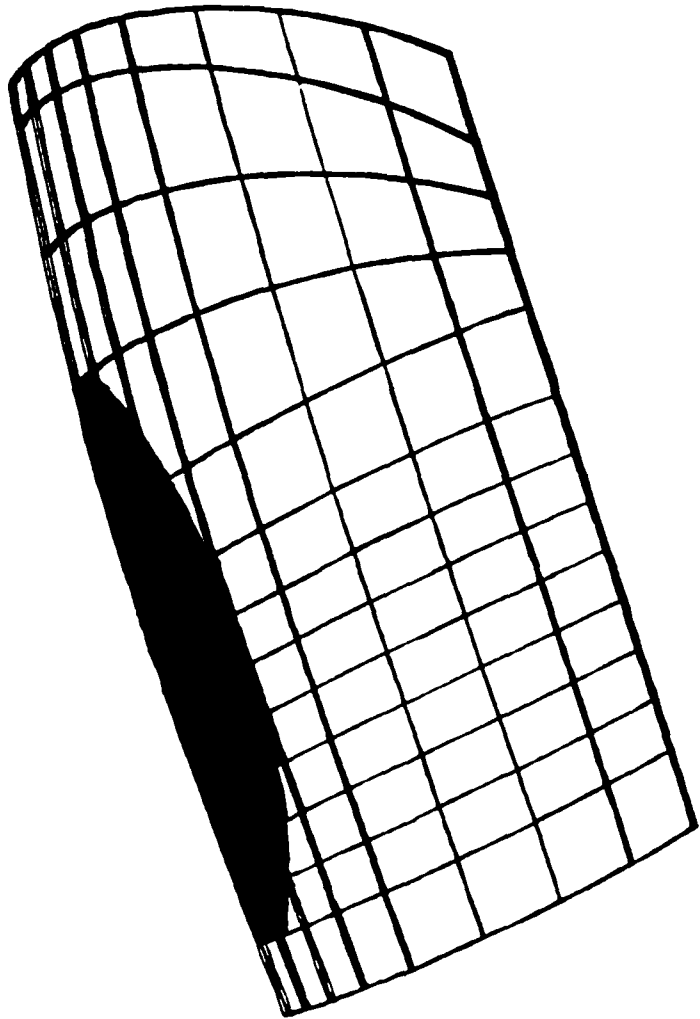


Figure 24. F-4 Forward Canopy Bird Impact Actual Footprint

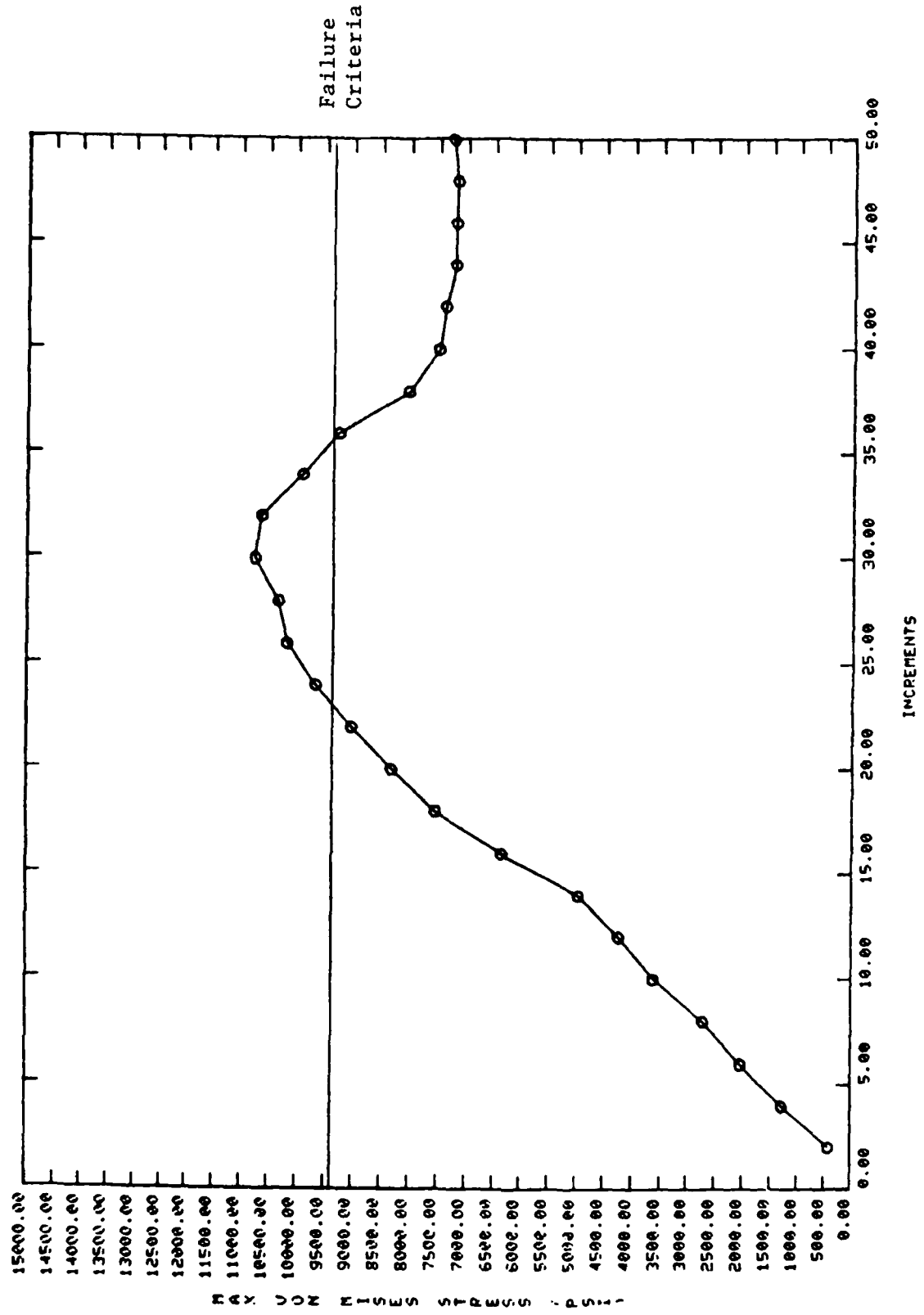


Figure 25. F-4 Canopy Stress Results for .31 Inch Monolithic Polycarbonate Design at 250 Knots

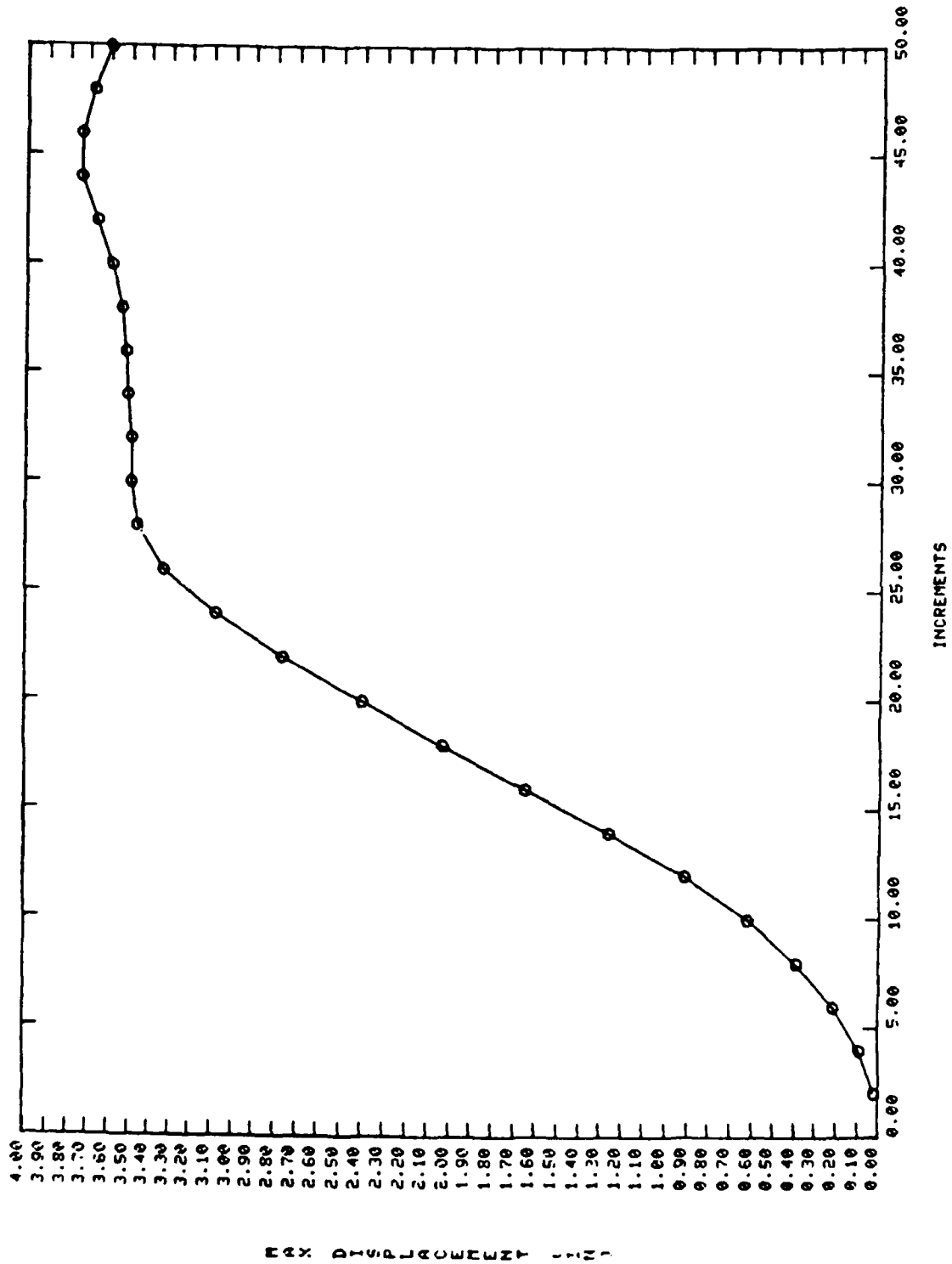


Figure 26. F-4 Canopy Displacement Results for .31 Inch Monolithic Polycarbonate Design at 250 Knots

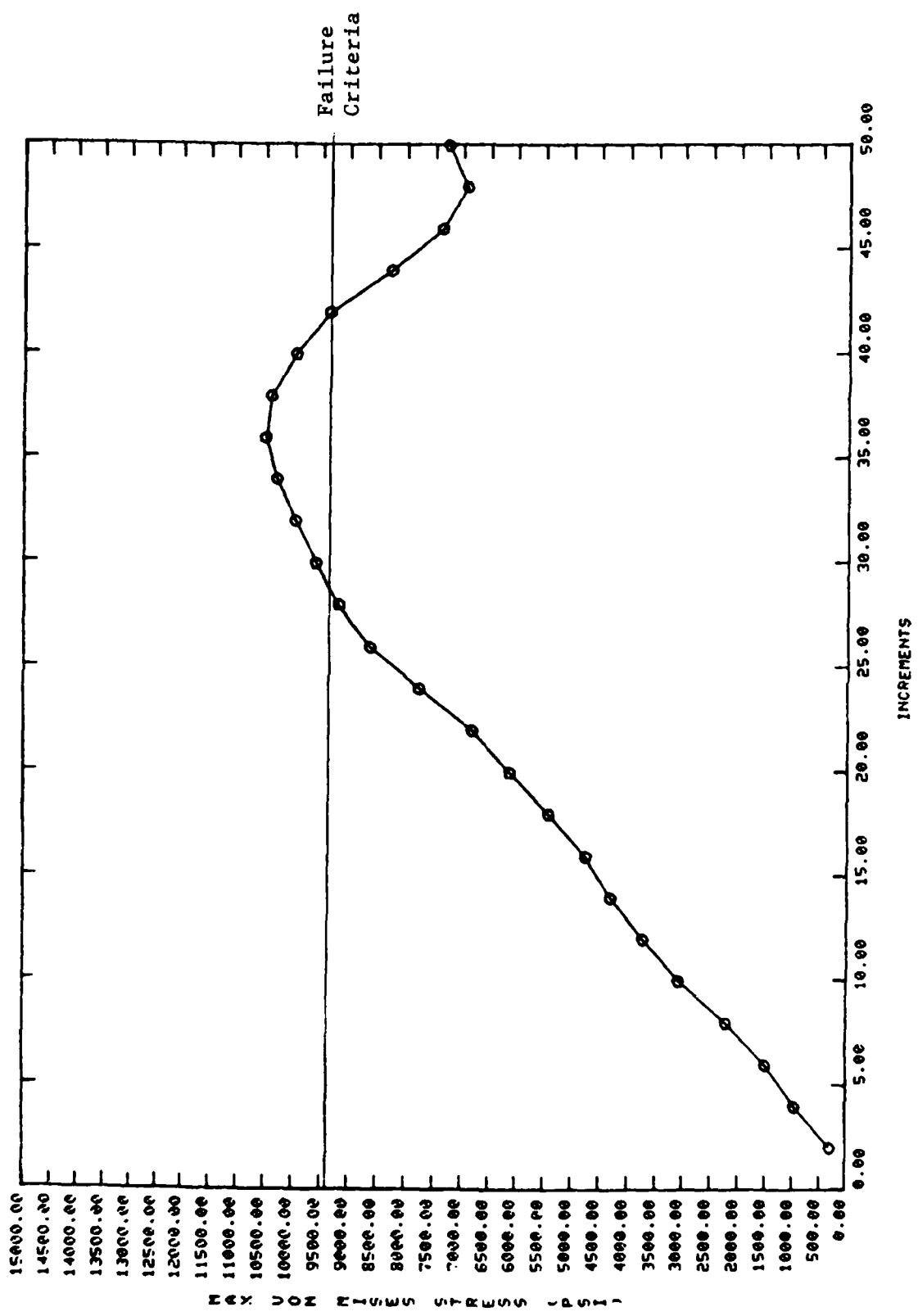


Figure 27. F-4 Canopy Stress Results for .374 Inch Monolith Polycarbonate Design at 250 Knots

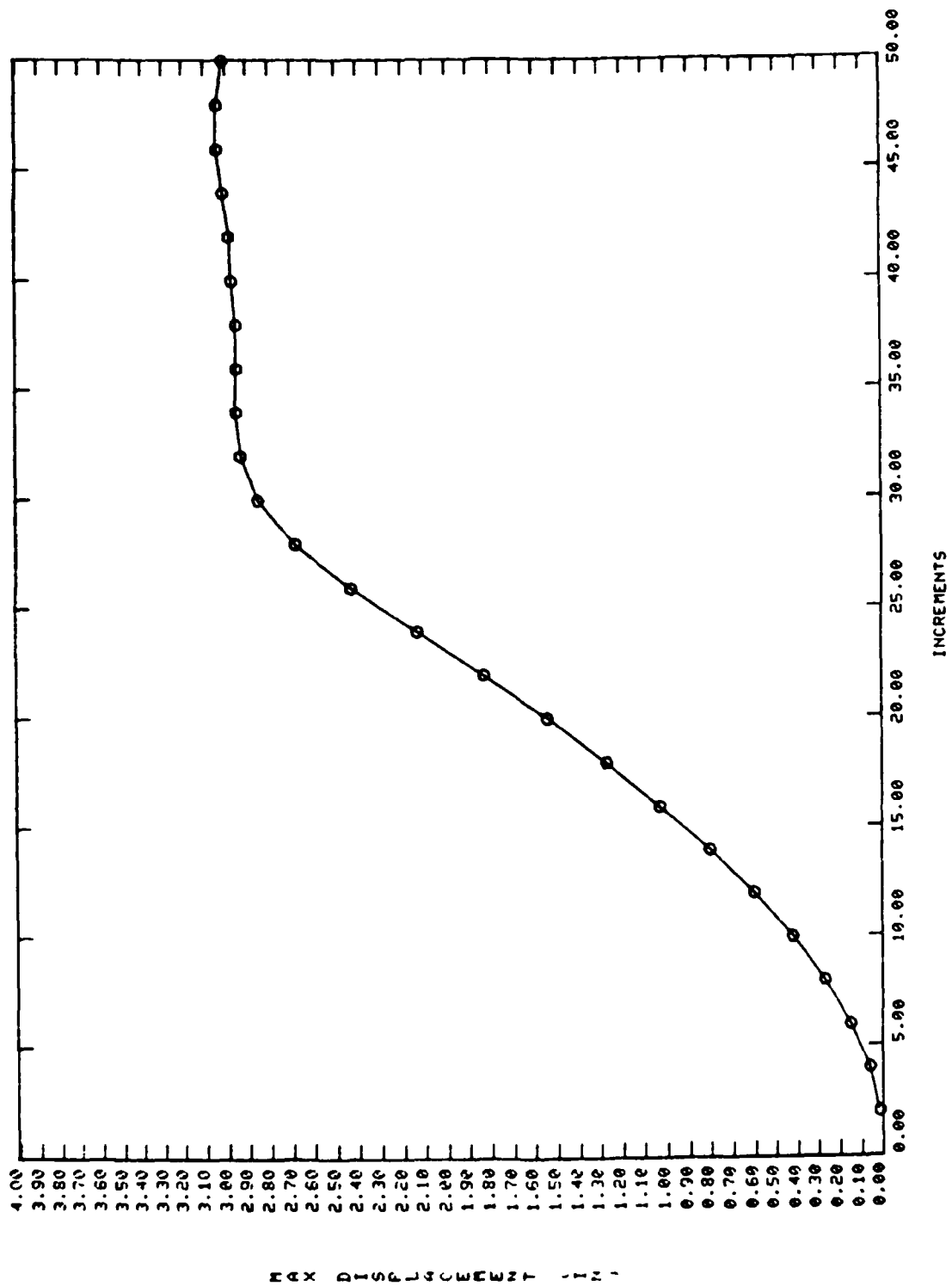


Figure 28. F-4 Canopy Displacement Results for .374 Inch Monolithic Polycarbonate Design at 250 Knots

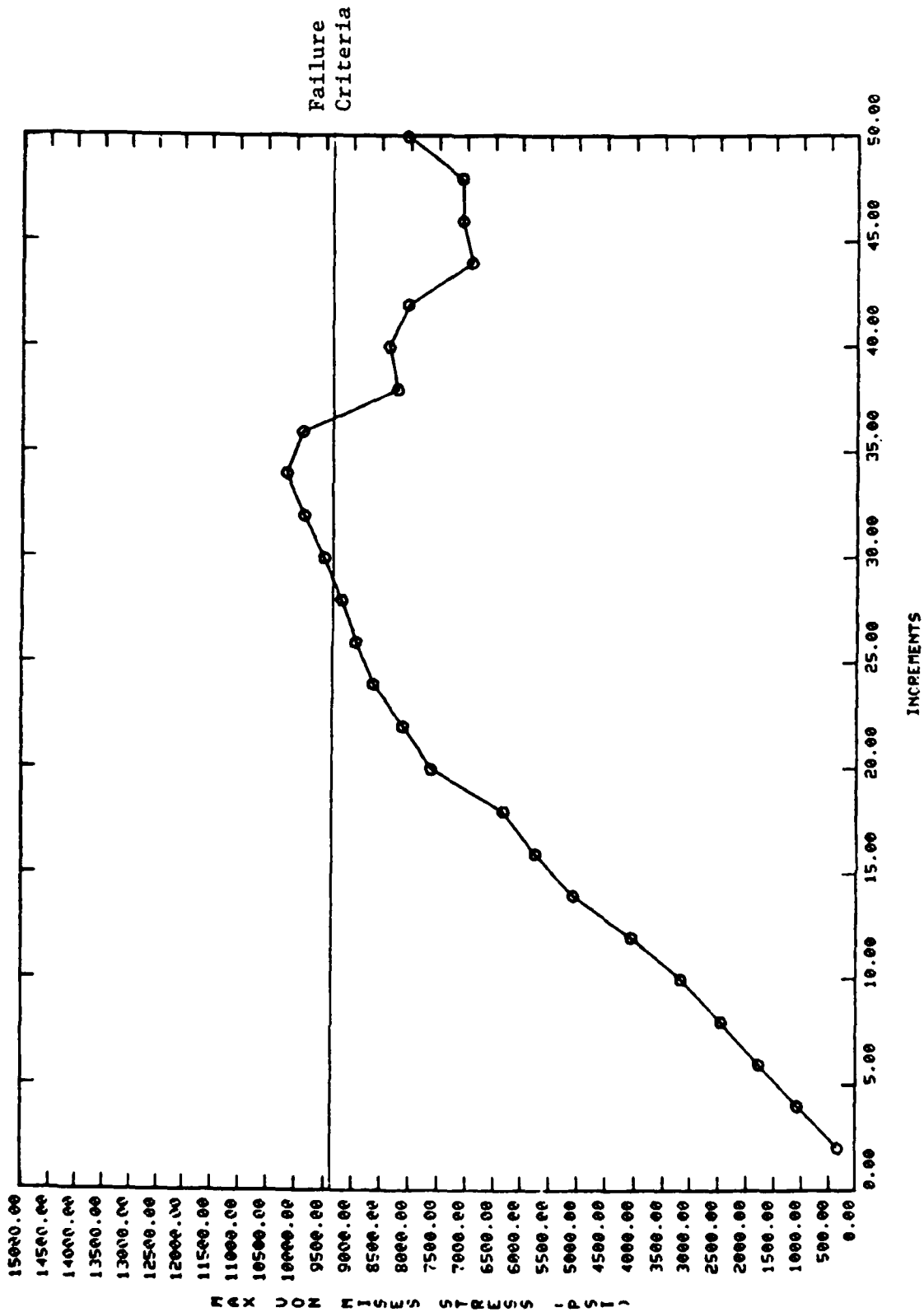


Figure 29. F-4 Canopy Stress Results for a .374 Inch Laminate Design at 250 Knots

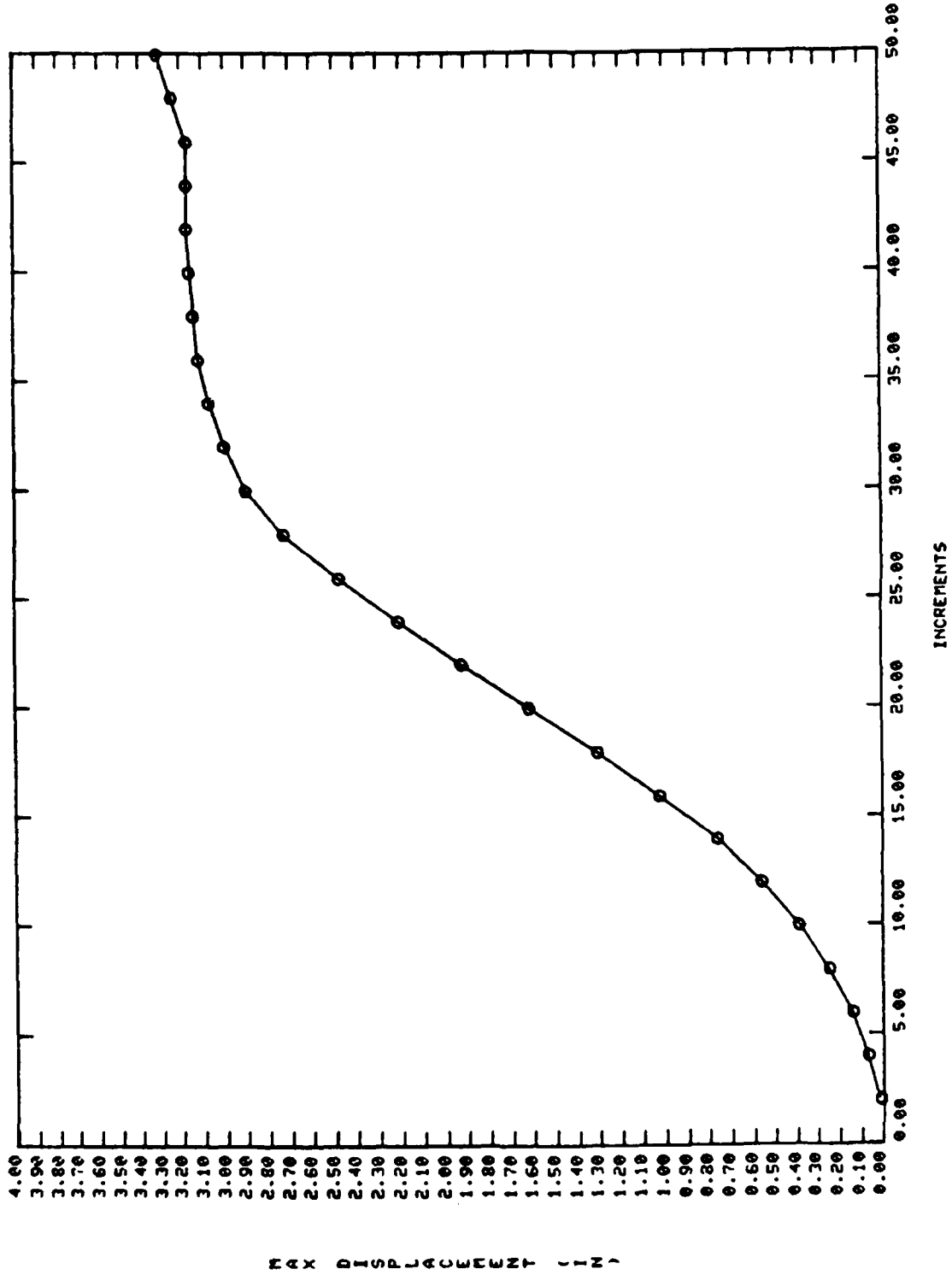


Figure 30. F-4 Canopy Displacement Results for a .374 Inch Laminate Design at 250 Knots



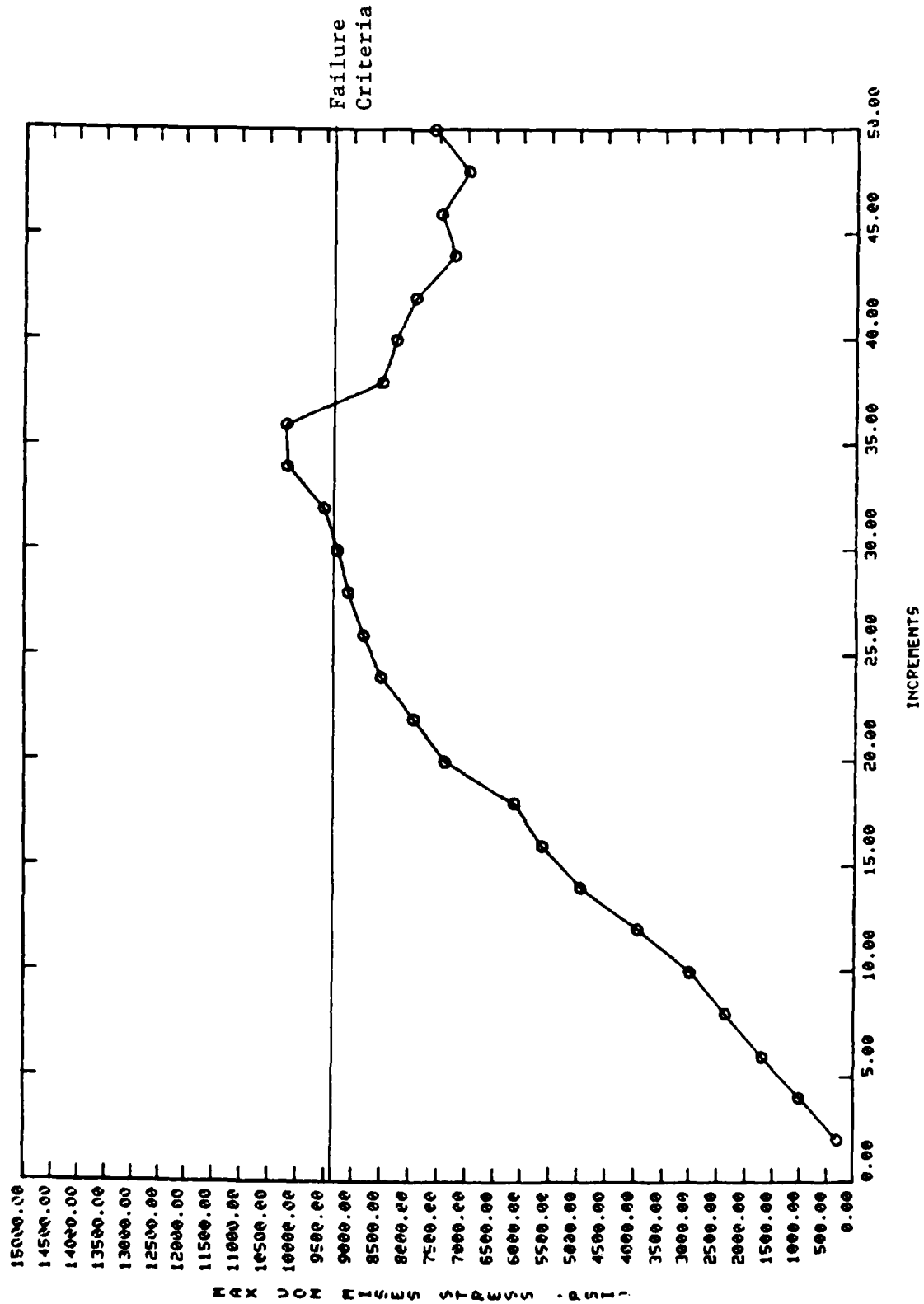


Figure 31. F-4 Canopy Stress Results for a .389 Inch Laminate Design at 250 Knots

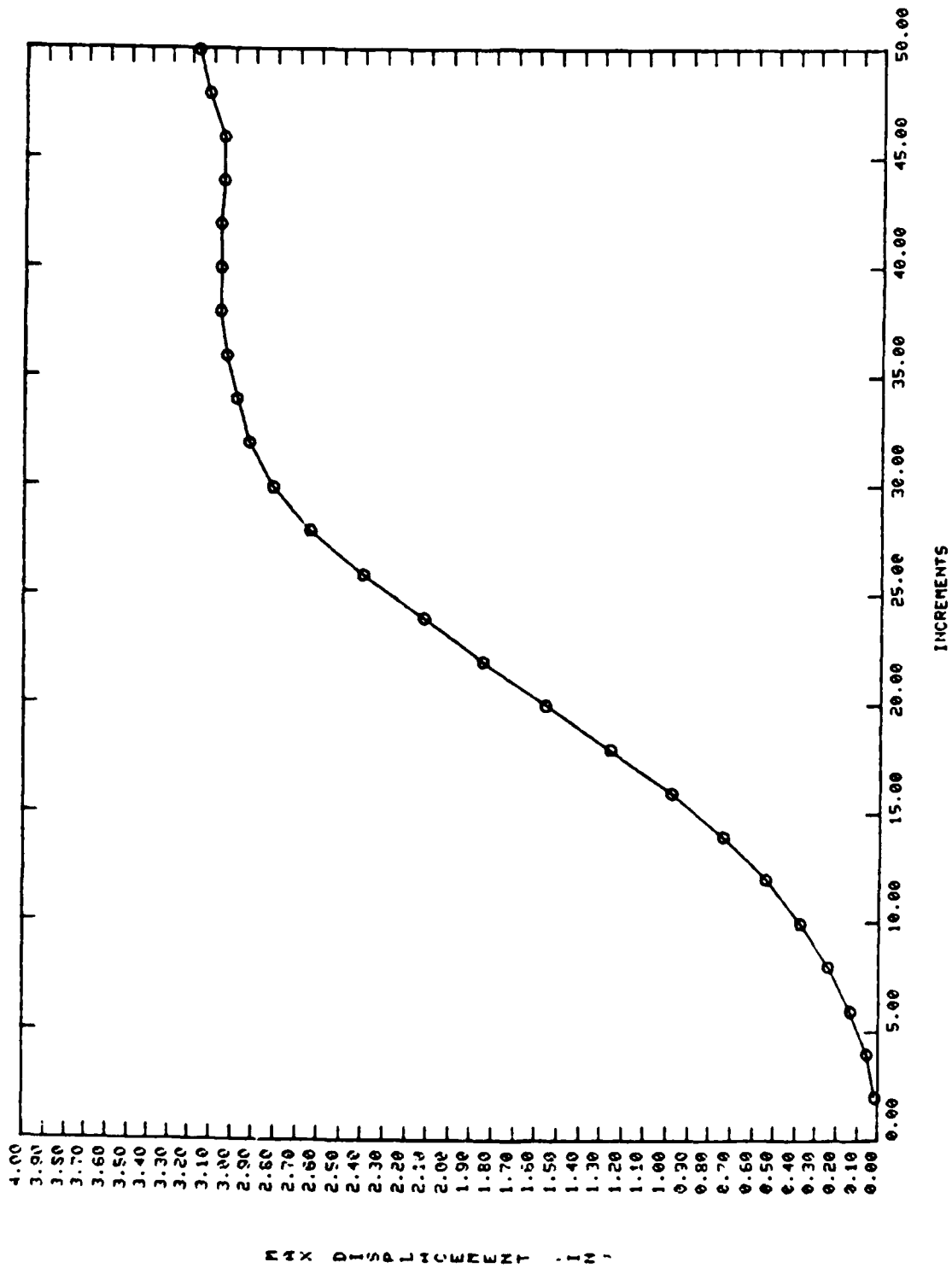


Figure 32. F-4 Canopy Displacement results for a .389 Inch Laminate Design at 250 Knots

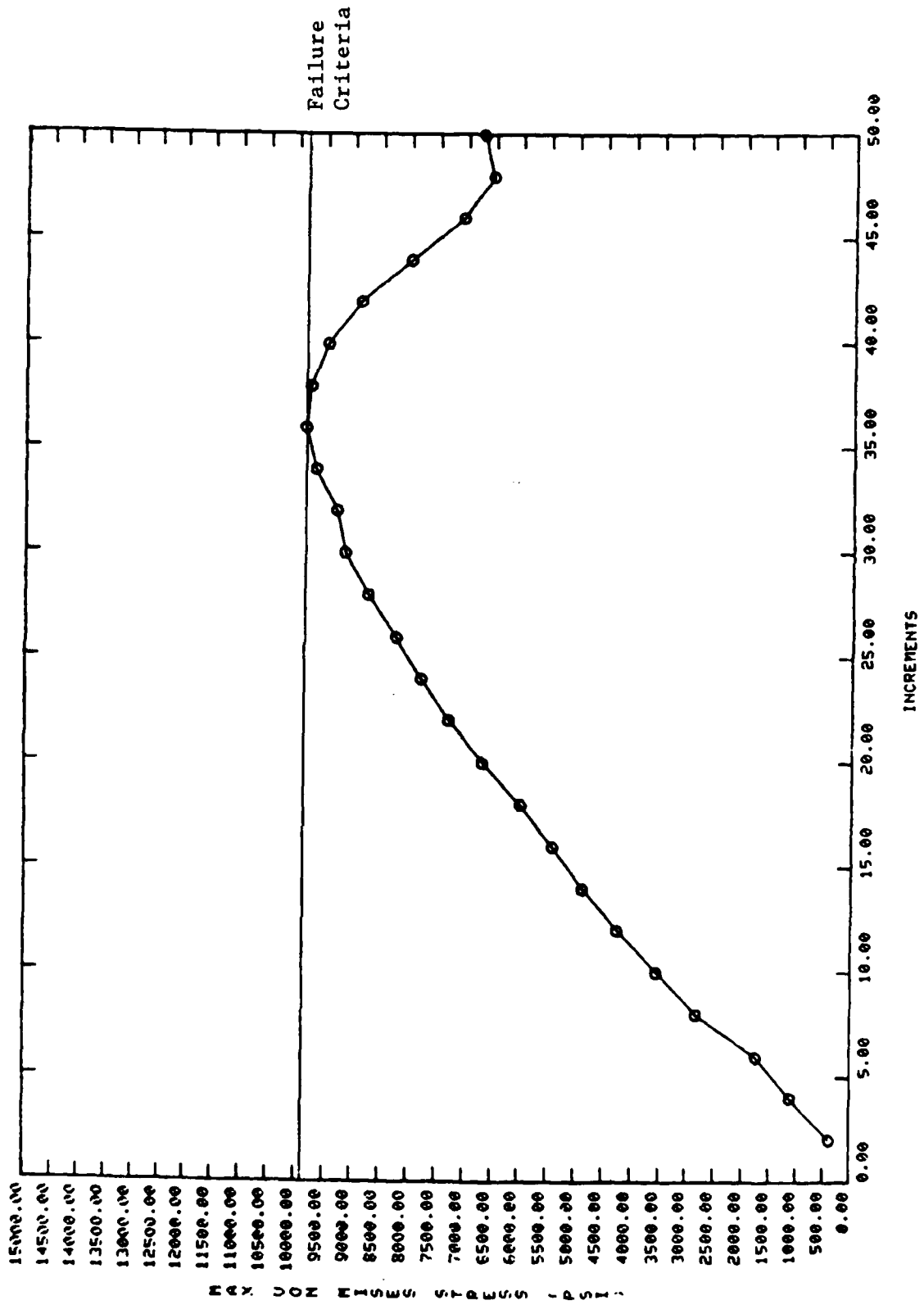


Figure 33. F-4 Canopy Stress Results for a .400 Inch Monolithic Stretched Acrylic Design at 250 Knots

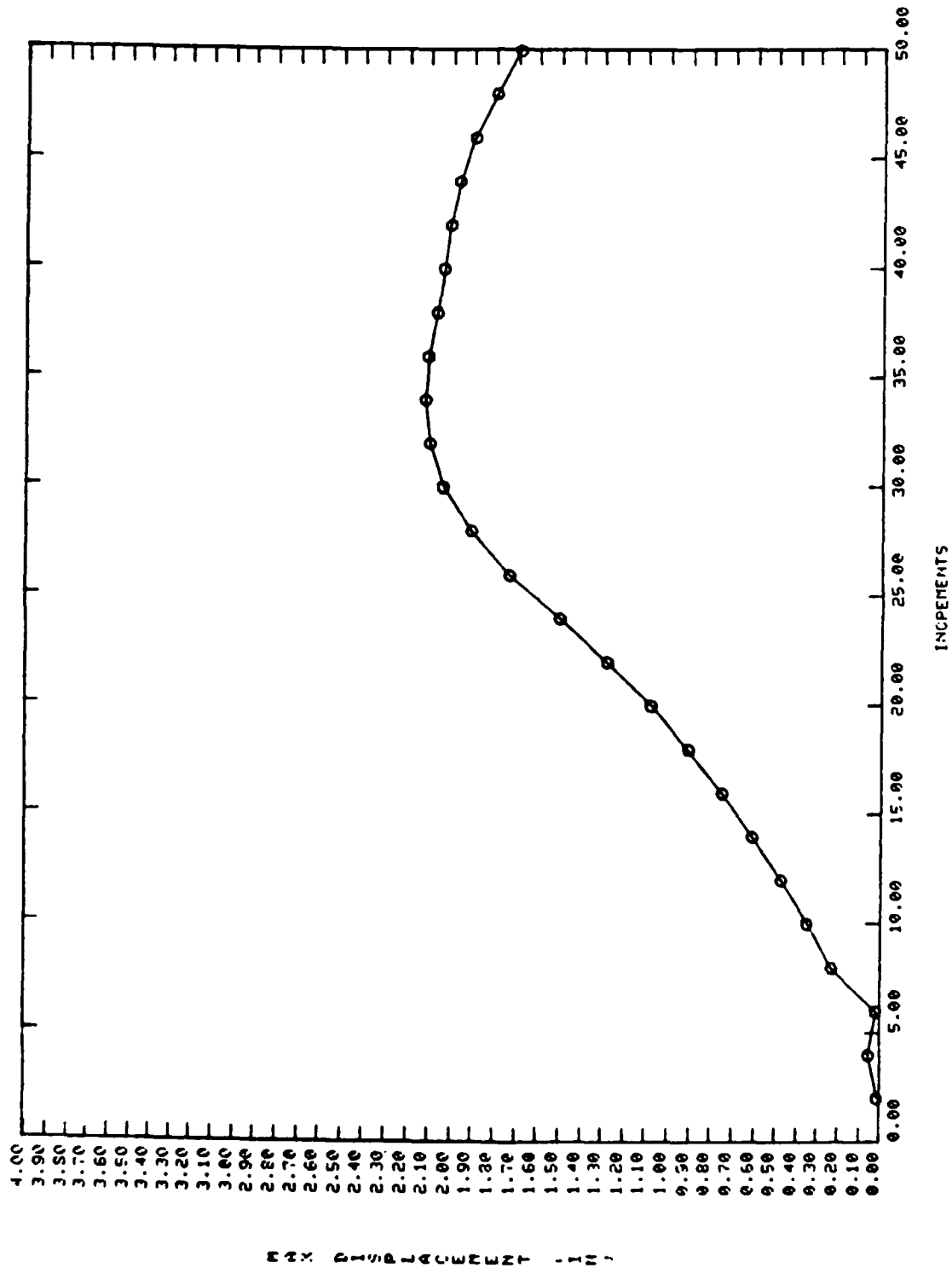


Figure 34. F-4 Canopy Displacement Results for a .40 Inch Monolithic Stretched Acrylic Design at 250 Knots

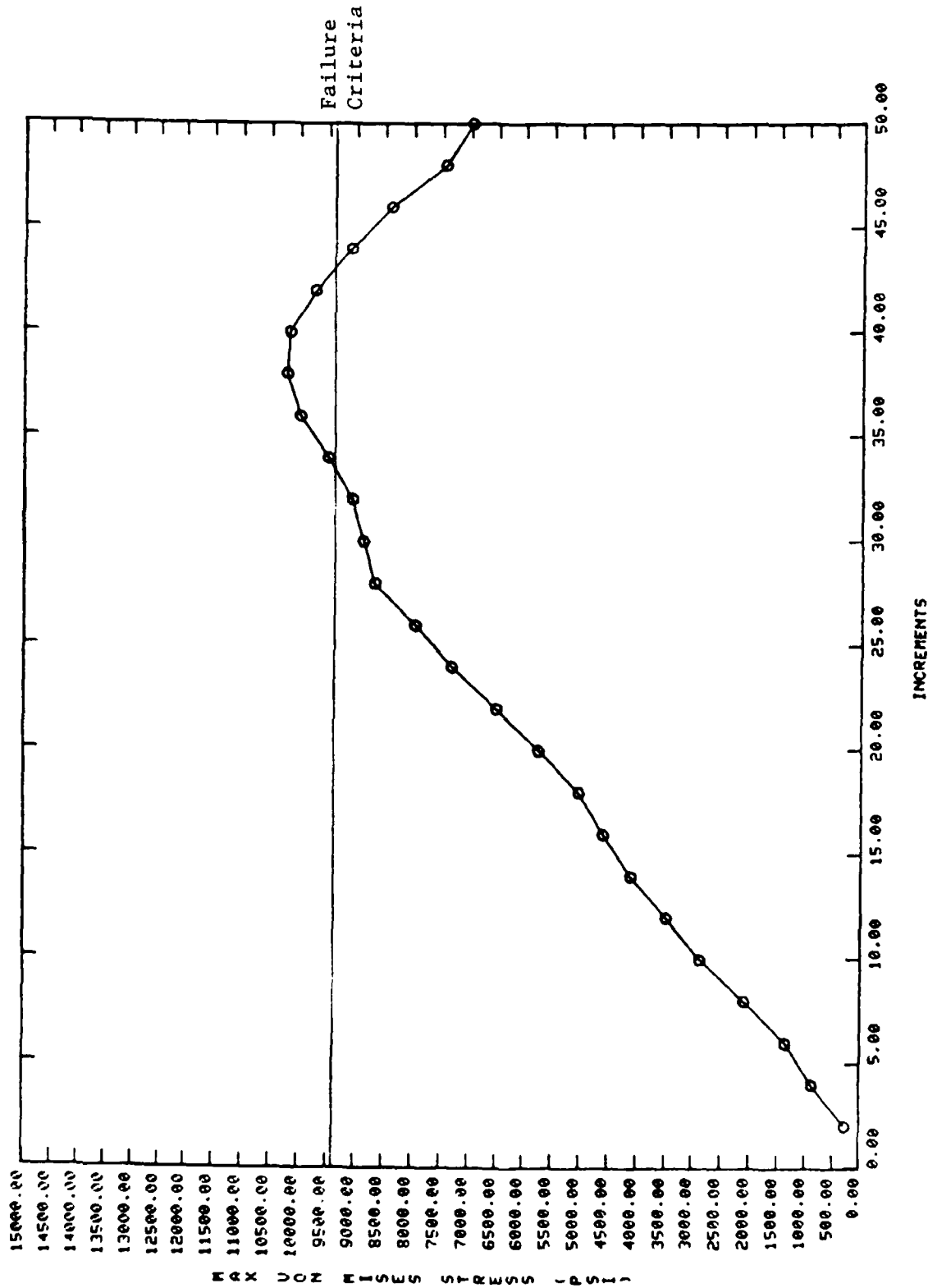


Figure 35. F-4 Canopy Stress Results for a .40 Inch Monolithic Polycarbonate Design at 250 Knots

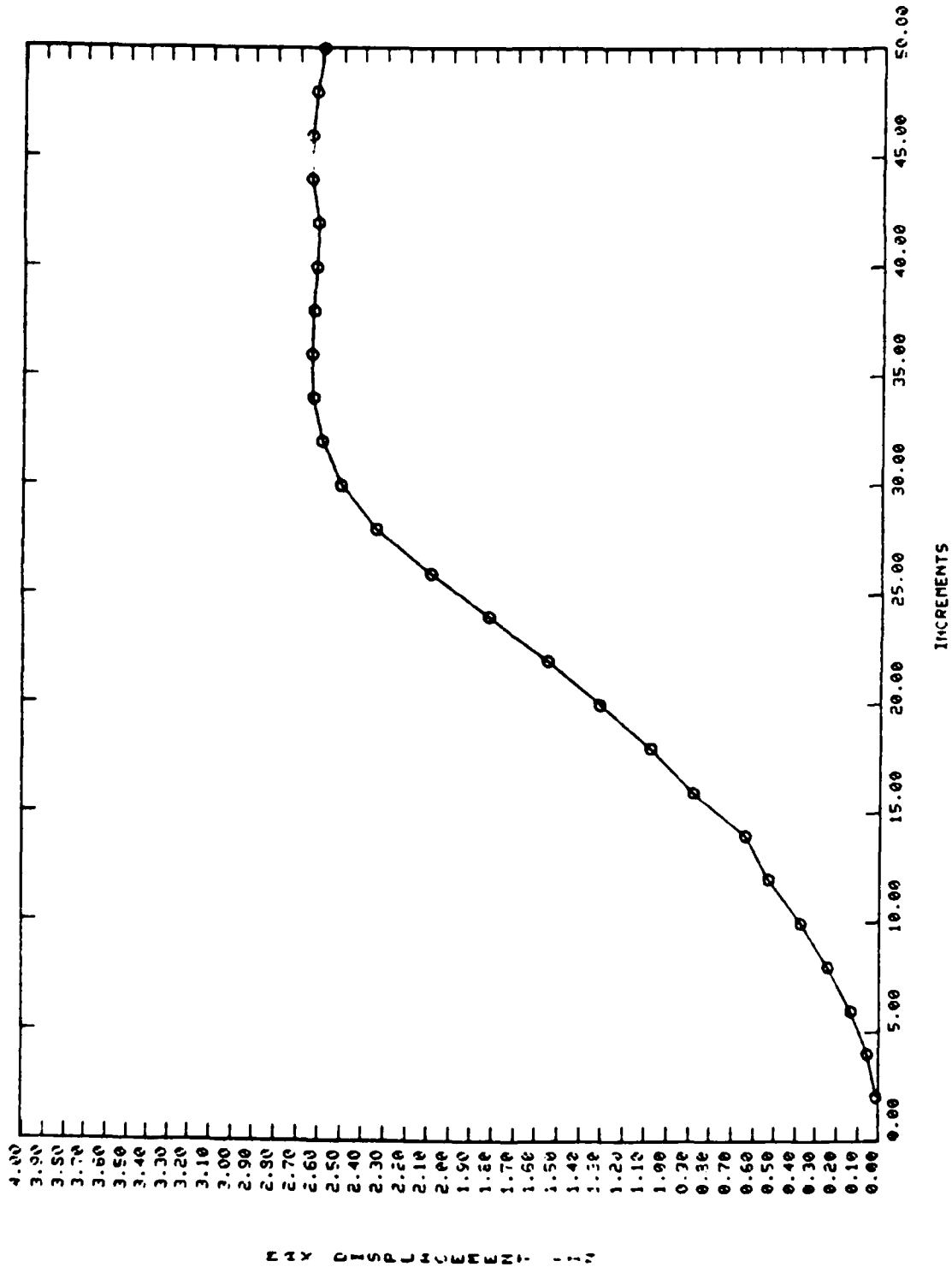


Figure 36. F-4 Canopy Displacement Results for a .40 Inch Monolithic Polycarbonate Design at 250 Knots

Table 7

## SUMMARY OF F-4 CANOPY ANALYSES RESULTS

DESIGN	SPEED (knots)	T (sec)	MAX STRESS (psi)	MAX DEFLECTION (inches)
.4 Mono Stretched Acrylic	200	.00008	6077	.967
	225	.00008	8095	1.69
	250	.00008	9850	2.12
.389 Polycarbonate Laminate	225	.000082	9337	2.78
	250	.000082	10180	3.06
.4 Mono Polycarbonate	225	.00008	8965	2.30
	250	.00008	10210	2.64
	275	.00008	10550	3.00
.374 Polycarbonate Laminate	225	.000082	9527	2.85
	250	.000082	10160	3.14
	275	.000082	10360	3.35
.374 Mono Polycarbonate	200	.000082	8503	2.19
	225	.000082	10170	2.64
	250	.000082	10480	2.97
	275	.000082	10680	3.16
.31 Mono Polycarbonate	200	.000091	9073	3.00
	250	.000091	10750	3.49

footprint was much larger than the simulated footprint. This would decrease the pressure on each element and spread the loads over a longer period of time.

This difficulty in using MAGNA to accomplish the design of very flexible aircraft transparencies was recognized as early as 1983.[6] Since then, an interim method for addressing the problem has been available which was felt to be invalid for the order of three inches or greater.[6] This interim method was employed for the F-4 forward canopy analysis, and as feared was unsuccessful. There needs to be more work done on the explicit codes now under development. These codes will model the bird directly and the loading will be handled by the computer. The hydrodynamic code and the X3D code are examples of explicit such codes.[27] These codes must be validated, but the analysis capabilities will be able to predict the threshold of any new design. Currently the threshold of impact resistance can only be predicted with the knowledge of the bird impact footprint, or for relatively stiff designs without any knowledge of the bird impact footprint.



## REFERENCES

1. McCarty, R. E., "Computer Analysis of Bird Resistant Aircraft Transparencies," Proceedings of the 17th Annual SAFE Symposium, December 1979, Las Vegas, Nevada.
2. McCarty, R. E., "Finite Element Analysis of F-16 Aircraft Canopy Dynamic Response to Bird Impact Loading," 21st AIAA/ASME/ASCE/AHS Structures, Structural Dynamics, and Materials Conference, May 1980, Seattle, Washington.
3. McCarty, R. E., "Aircraft Transparency Bird Impact Analysis Using the MAGNA Computer Program," Conference on Aerospace Transparencies Sponsored by the Society of British Aerospace Companies, September 1980, London, England.
4. McCarty, R. E., "Finite Element Analysis of a Bird-Resistant Monolithic Stretched Acrylic Canopy Design for the F-16A Aircraft," AIAA Aircraft Systems and Technology Conference, August 1981, Dayton, Ohio.
5. McCarty, R. E., and Hart, J. L., "Validation of the MAGNA Computer Program for Nonlinear Finite Element Analysis of Aircraft Transparency Bird Impact," 14th Conference on Aerospace Transparent Materials and Enclosures Sponsored by the Air Force Wright Aeronautical Laboratories, July 1983, Scottsdale, Arizona, AFWAL-TR-83-4154, December 1983.
6. McCarty, R. E., "MAGNA Computer Simulation of Bird Impact on the TF-15 Aircraft Canopy," 14th Conference on Aerospace Transparent Materials and Enclosures Sponsored by the Air Force Wright Aeronautical Laboratories, July 1983, Scottsdale, Arizona, AFWAL-TR-83-4154, December 1983.
7. McCarty, R. E., "Aircraft Transparency Bird Impact Analysis Using the MAGNA Computer Program," Conference and Training on Wildlife Hazards to Aircraft Sponsored by the FAA, March 1984, Charleston, South Carolina.
8. McCarty, R. E., Trudan, D. E., and Davis, A. D., "Three Dimensional Nonlinear Dynamic Finite Element Analysis for the Response of a Thick Laminated Shell to Impact Loads," AIAA/ASME/ASCE/AHS 26th Structures, Structural Dynamics, and Materials Conference, April 1985, Orlando, Florida.
9. McCarty, R. E., and Venkayya, V., Analysis of Bird Impact on Port Wing, Air Force Wright Aeronautical Laboratories, Wright-Patterson Air Force Base, Ohio 45433-6553, Letter Report, August 1979.
10. McCarty, R. E., and Smith, R. A., "Finite Element Analysis of Through the Canopy Emergency Crew Escape from the T-38 Aircraft," AIAA/ASME/ASCE/AHS 23rd Structures, Structural Dynamics, and Materials Conference, May 1982, New Orleans, Louisiana.

11. McCarty, R. F., and Smith, R. A., "Simulation of T-38 Aircraft Student Canopy Response to Cockpit Pressure and Thermal Loads Using MAGNA," AIAA/ASME/ASCE/AHS 24th Structures, Structural Dynamics, and Materials Conference, May 1983, Lake Tahoe, Nevada.
12. Hart, J. L., "MAGNA Analysis of the T-38 Aircraft Student Canopy Response to In-Flight Aerodynamic Pressure Loads," AIAA/AHS/ASCE Aircraft Design Systems and Operations Meeting, November 1984, San Diego, California.
13. Brockman, R. A., MAGNA (Materially and Geometrically Nonlinear Analysis) Part I - Finite Element Analysis Manual, Flight Dynamics Laboratory, Wright-Patterson Air Force Base, Ohio 45433-6553, AFWAL-TR-82-3098 Part I, December 1982.
14. Bruner, T. S., MAGNA (Materially and Geometrically Nonlinear Analysis) Part II - Preprocessor Manual, Flight Dynamics Laboratory, Wright-Patterson Air Force Base, Ohio 45433-6553, AFWAL-TR-82-3098 Part II, December 1982.
15. Brockman, R. A., MAGNA (Materially and Geometrically Nonlinear Analysis) Part III - Postprocessor Manual, Flight Dynamics Laboratory, Wright-Patterson Air Force Base, Ohio 45433-6553, AFWAL-TR-82-3098 Part III, December 1982.
16. Brockman, R. A., MAGNA (Materially and Geometrically Nonlinear Analysis) Part IV - Quick Reference Manual, Flight Dynamics Laboratory, Wright-Patterson Air Force Base, Ohio 45433-6553, AFWAL-TR-82-3098 Part IV, December 1982.
17. W. R. Pinnell and 2Lt D. A. Crocker, "A Triangulation Technique for Obtaining Deflections of Aircraft Transparencies During Bird Impact Testing," Conference on Aerospace Transparent Materials and Enclosures, AFWAL-TR-83-4154, pp. 776-791, December 1983.
18. Wilbeck, J. S., Impact Behavior of Low Strength Projectiles, Air Force Wright Aeronautical Laboratories, Wright-Patterson Air Force Base, Ohio 45433-6553, AFML-TR-77-134, July 1978.
19. Challita, A., and Barber, J. P., The Scaling of Bird Impact Loads, Air Force Flight Dynamics Laboratory, Wright-Patterson Air Force Base, Ohio 45433-6553, AFFDL-TR-79-3042, June 1979.
20. Barber, J. P., Taylor, H. R., and Wilbeck, J. S., Bird Impact Forces and Pressures on Rigid and Compliant Targets, Air Force Flight Dynamics Laboratory, Wright-Patterson Air Force Base, Ohio 45433-6553, AFFDL-TR-77-60, May 1978.
21. Barber, J. P., and Wilbeck, J. S., Characterization of Bird Impacts on Rigid Plates: Part I, Air Force Flight Dynamics Laboratory, Wright-Patterson Air Force Base, Ohio 45433-6553, AFFDL-TR-75-5, January 1975.

22. Peterson, R. L., and Barber, J. P., Bird Impact Forces in Aircraft Windshield Design, Air Force Flight Dynamics Laboratory, Wright-Patterson Air Force Base, Ohio 45433-6553, AFFDL-TR-75-150, March 1976.
23. R. M. Jones, "Mechanics of Composite Materials," Scripta Book Company, Washington, D. C., 1975.
24. R. H. MacNeal, Editor, "MSC/Nastran User's Manual, Version 64," MacNeal-Schwendler Corporation.
25. J. M. Whitney, "Shear Correction Factors for Orthotropic Laminates Under Static Load," Trans. ASME, Journal of Applied Mechanics, Vol. 40, pp. 302-4, 1973.
26. Y. C. Fung, "Foundations of Solid Mechanics," Prentice-Hall, Englewood Cliffs, NJ. 1965.
27. Brockman, R. A., Finite Element Analysis of Soft-Body Impact, Flight Dynamics Laboratory, Wright-Patterson Air Force Base, Ohio 45433-6553, AFWAL-TR-84-3035, October 1984.

SESSION VIII

COMPUTER AIDED ANALYSIS (PART B)

Chairman: C. Smith  
Flight Dynamics Laboratory  
Wright-Patterson AFB, Ohio

Co-Chairman: R. E. McCarty  
Flight Dynamics Laboratory  
Wright-Patterson AFB, Ohio

Coordinator: M. G. Gran  
Flight Dynamics Laboratory  
Wright-Patterson AFB, Ohio

ASSESSMENT OF BIRD IMPACT PROTECTION PROVIDED BY THE  
SPACE SHUTTLE ORBITER WINDSHIELD SYSTEM USING THE  
MAGNA COMPUTER PROGRAM

Robert E. McCarty  
Richard A. Smith  
Flight Dynamics Laboratory

ASSESSMENT OF BIRD IMPACT PROTECTION PROVIDED BY THE  
SPACE SHUTTLE ORBITER WINDSHIELD SYSTEM  
USING THE MAGNA COMPUTER PROGRAM

1 Robert E. McCarty  
2 Richard A. Smith

Crew Protection Branch  
Flight Dynamics Laboratory  
Air Force Wright Aeronautical Laboratories  
Wright-Patterson Air Force Base, Ohio 45433

ABSTRACT

The Structures and Mechanics Division of the NASA/Johnson Space Center requested support from the Flight Dynamics Laboratory (FDL) in assessing the level of bird impact resistance provided by the Space Shuttle orbiter windshield system design. The objective of the work planned was to predict the maximum velocity with which a 4 lb bird could strike the orbiter windows without failing them.

Results of analyses accomplished by the FDL indicated that at 355 knots true airspeed (KTAS) below 10,000 ft above ground level (AGL) during descent to landing, the forward window assembly for the orbiter offers insignificant resistance to 4 lb bird impact.

Results also indicated that the current forward window assembly design could fail at velocities lower than 175 KTAS as a result of impact with a 4 lb bird. It is recommended that the probability of orbiter forward window assembly penetrations as a result of bird impact incidents over the operational life of the Shuttle orbiter fleet be determined in future work. Completed studies which have defined the distribution of birds near orbiter landing sites should be used to support this determination. If the probability of penetrating bird impacts is determined to be unacceptable, forward window assembly designs for the orbiter vehicle which would provide improved measures of bird impact protection should be assessed. Future manned hypersonic vehicles requiring conventional forward vision through transparent panels should follow the same steps in providing adequate in-flight bird impact protection to aircrew members.

1 Supervisory Aerospace Engineer  
2 Aerospace Engineer

## INTRODUCTION

### Background

In the late 1960's, the mission profile of Air Force aircraft changed from high altitude, high speed to one of low altitude, high speed. This occurred primarily in response to the development of more effective hostile radar and surface-to-air missile systems, and gave rise to a new and significant operational hazard: bird impact on aircraft transparency systems.

Birds are rarely found at altitudes above 10,000 feet, and since military aircraft transparencies had historically not been designed to withstand bird impact loads, losses of aircraft and aircrew began to occur.

In 1972, the Air Force Flight Dynamics Laboratory (FDL) formed an Advanced Development Program Office for Improved Windshield Systems to address this bird impact problem. Since that time, the FDL has participated in the development of successful bird impact resistant windshield and canopy systems for a number of operational aircraft including the A/T-37, A-10, F-111, F-16, F-4, T-38, and A-7. In each case however, the design methods used relied heavily upon full scale bird impact testing to develop and qualify successful systems. This approach proved time consuming, and very expensive. For the F-111 transparency system development alone, approximately 50 design iterations were tested at a cost of roughly \$100,000 each, for a total development and qualification cost of \$5,000,000. Nearly five years were required to accomplish this development successfully.

To reduce the numbers of full scale bird impact tests required to develop new aircraft transparency systems, the FDL formed a new office in 1976 to develop computer analysis methods to simulate the dynamic structural response of transparency systems to bird impact loading. This new office, called the Subsystems Development Group (now the Aircrew Enclosures Group), accomplished the first delivery to the Air Force of a computer analysis system, called MAGNA (Materially and Geometrically Nonlinear Analysis) in 1979.<sup>12-15</sup>

Additional development of MAGNA was sponsored by the FDL through 1982, and its application to the aircraft transparency bird impact problem was largely validated via FDL in-house correlation studies conducted through 1985.<sup>3-10</sup> These correlation studies compared MAGNA computed results with full scale bird impact test results for a variety of Air Force aircraft transparency systems.

The Structures and Mechanics Division of the NASA/Johnson Space Center in Houston, Texas was aware of FDL's activity regarding aircraft transparency bird impact computer analysis. As a result, NASA/JSC contacted FDL to obtain analysis support. In August 1986, FDL drafted a plan to assess the level of bird impact resistance provided by the orbiter windshield system design as requested by NASA/JSC.

In November 1986, plans were laid within FDL, and coordinated with NASA/JSC, to have the Air Force Engineering and Services Center (AFESC) at Tyndall Air Force Base, Florida accomplish assessment of the orbiter vehicle bird impact hazard. Risk assessment was specific to each of the three primary landing sites: Kennedy Space Center, Edwards Air Force Base, and Vandenberg Air Force Base.

Formal request for support from NASA/JSC came to FDL on 12 January 1987. The intent was to expedite the requested support as much as possible to allow time for any specific testing which the study results might suggest, to be accomplished before the orbiter fleet resumed flight operations.

In January 1987, a data package was transmitted to FDL which included the geometry of each of the three orbiter windshield panels in their respective local coordinate systems, mathematical transforms between each of the local windshield panel coordinate systems and the vehicle global coordinate system, details of edgemember support structure design, envelopes of vehicle velocity and angle of attack versus altitude for the three primary landing sites, and an illustration of the general scheme for support of the windshield assembly in the orbiter cab structure.

#### Approach

On 2 March 1987, a kickoff meeting was held at JSC with NASA, FDL, and Rockwell International to initiate the effort. At the kickoff meeting, the direction the analysis should take was debated. Conflicting issues were whether the analysis should assume a specific velocity and find the maximum corresponding bird mass the orbiter windshield could resist, or whether it should presume a bird of a given mass and determine the orbiter velocity corresponding to the threshold of windshield system failure. It was decided that the latter approach would best meet the requirements of the NASA Safety Office. The objective of the effort was to predict the maximum velocity at which a 4 lb bird could strike the orbiter windows without failing them. Rationale for selecting the 4 lb bird is discussed later in this section.

NASA/JSC was interested only in the bird impact hazard during vehicle descent to landing. Conservative windshield bird impact analysis provides the minimum speed at which failure could occur, while unconservative analysis provides the maximum speed at which the windshield system might survive. It was agreed that FDL would conduct a conservative analysis, but use all three glass panels in the orbiter windshield system design to determine failure. Details of the orbiter windshield system design are discussed in a later section. Failure of the window system was defined as fracture of all three glass panels. For survival of the window system, the third panel is permitted to absorb as much load as possible without reaching its rupture stress. Analyzing the system for a 4 lb bird impact was agreed upon. The 4 lb weight is conservative because it represents statistically a large proportion of the birds likely to be encountered (about 92% of the birds in the continental U.S. weigh 4 lb or less). The same size bird is used as a standard by both the commercial and military flight vehicle communities.



The minimum angle of attack assumed by the orbiter vehicle at altitudes between 10,000 ft AGL and flare for landing was adopted for use in MAGNA analysis. As used here, angle of attack is defined to be the angle between the vehicle longitudinal reference axis and the relative wind, or freestream direction of airflow. Minimum angle of attack is conservative because lowering the nose of the vehicle increases the bird impact angle on the windshield surface, and correspondingly increases the impulse delivered to the windshield system during the bird impact event. As used here, bird impact angle is defined to be the complement of the angle between the bird trajectory and the windshield inward surface normal.

The assessment would encompass at least two different bird impact locations on the surface of the windshield, and subsequent analysis for that impact location for which windshield dynamic structural response was determined to be most severe.

A rigid windshield frame was assumed, rather than adding to model complexity by including the frame. Significant compliance in the actual frame would result in glass panel failure under loads lower than those required to fail the windshield with a rigid frame. The rigid frame model is therefore unconservative, but insignificantly so, because the actual edgember support for the windshield panels is massive and very stiff.

Even though the failure pattern of the glass materials used in the windshield system is relatively coarse, it was agreed that the effect of glass debris resulting from the failure of one windshield panel would not be considered upon the failure of subsequent panels. This is realistic because glass debris would impinge only the compression surface of each glass panel, and because glass does not exhibit failure in compression. Ignoring glass debris would be unconservative if glass shards from a panel failure induced premature failure of subsequent panels.

The entire remaining portion of the bird mass which had not yet reached the surface of a given windshield panel at the time of that panel's failure, would be applied to the next windshield panel in sequence. This is conservative because breaking up, or spreading out, of the bird mass makes it more likely that subsequent panels in the sequence would survive the event.

Responsibilities for each of the three participants in the study were defined. FDI would provide the stress-time history from bird impact analysis of each glass panel to NASA/JSC. NASA/JSC would work in parallel with Rockwell in determining the dynamic modulus of rupture for each glass panel based on the stress-time history provided. This modulus of rupture analysis would assume a flaw depth of 0.0018 in., and beginning of (static fatigue) life for the glass windshield panel.<sup>27</sup> FDI would use the resulting time of failure determined by NASA/JSC and Rockwell in subsequent MAGNA analysis.

## ORBITER WINDSHIELD SYSTEM

Figure 1 shows the overall configuration of all transparency assemblies on the Shuttle orbiter vehicle. Since the Space Shuttle commander and pilot sit directly behind the forward windows, and because bird impact angle is maximum for these windows, only the forward window was analyzed. The left forward window assembly was arbitrarily selected for analysis. Figure 2 shows a simplified cross-sectional view of the forward window assembly, illustrating the fact that three glass panels, separated by air gaps, are included in the design. The outermost of the two air gaps is vented to atmosphere. In general, the metallic edgember support structure around the glass window panels is massive, providing nearly rigid support for the respective panels. Aluminum and beryllium alloys, as well as a forged steel material are employed in the framing system.

The thermal panel in the forward window assembly is 0.69 in. thick. The redundant panel is 1.30 in. thick, and the pressure panel is 0.63 in. thick. Fused silica was chosen as the material for both the thermal and redundant panels in the forward window assembly, while thermally strengthened aluminosilicate glass is used for the pressure panel. Detailed discussion of the mechanical properties of both glass materials is included in a later section.

Figure 3 shows the relative spatial position of each of the three glass panels in the forward window assembly. The redundant and pressure panels are parallel each other, but the thermal panel is slightly non-parallel. Figure 3 illustrates the left forward window assembly, and also shows the origin and orientation for the local coordinate system of each of the three glass panels.

Figure 4 shows the orientation for the global coordinate system for the Shuttle orbiter vehicle. A FORTRAN computer program named TRANS was written by the FDI to facilitate coordinate transformations between each of the three local glass panel coordinate systems and the global vehicle coordinate system.

## MAGNA FINITE ELEMENT MODELS

### Geometry

As discussed above, the left forward window assembly of the orbiter vehicle was selected for MAGNA analysis. Each of the three glass panels in the assembly was modeled separately. In each case, the modeling procedure began using coordinates of the centers of each circular arc defining the rounded corners of the panel. These coordinates were in the local glass panel coordinate system.

Nodal coordinates and element connectivity were calculated for nine super elements, as shown in Figure 5 for the thermal panel case.

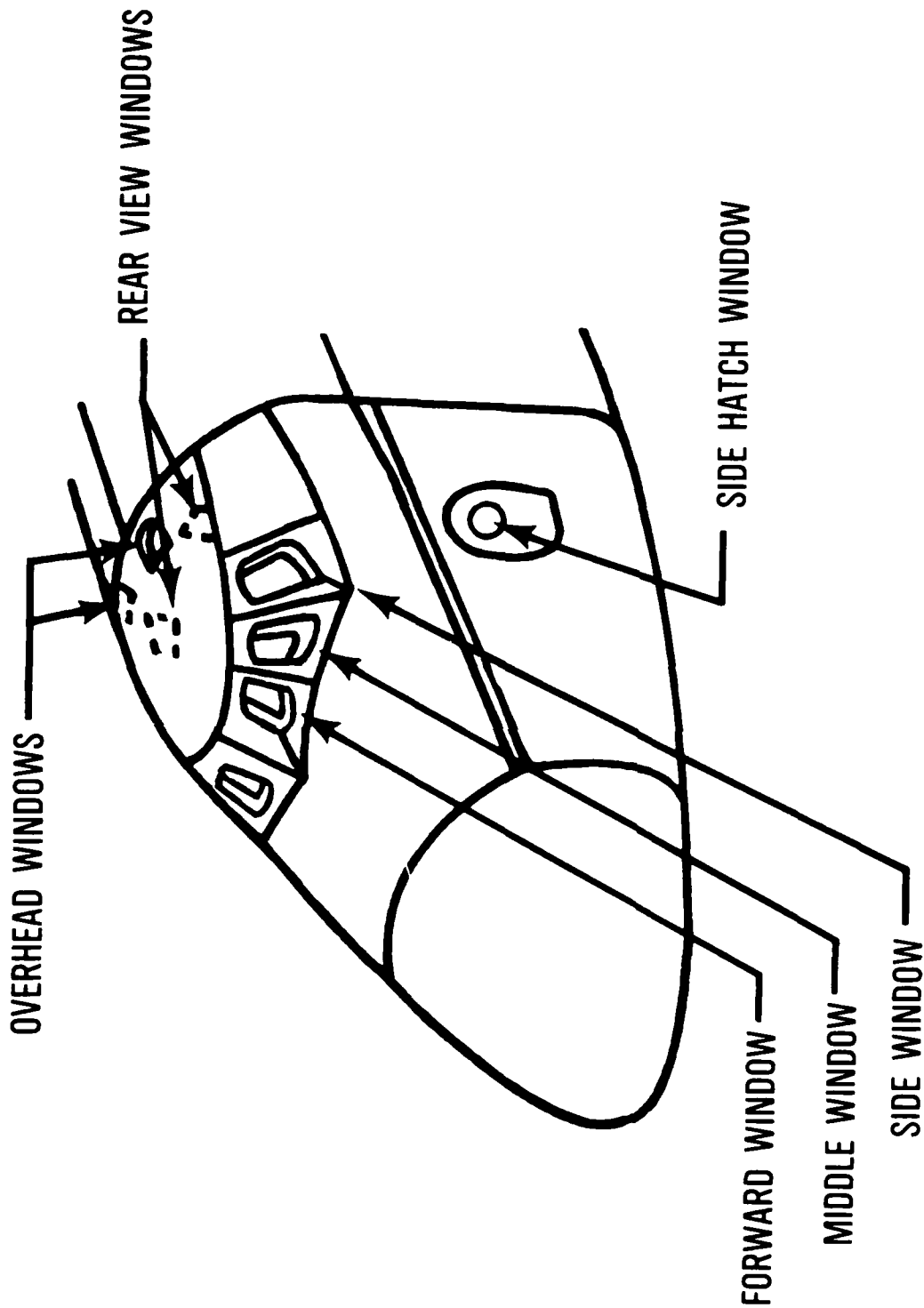


Figure 1. Shuttle Orbiter Window System

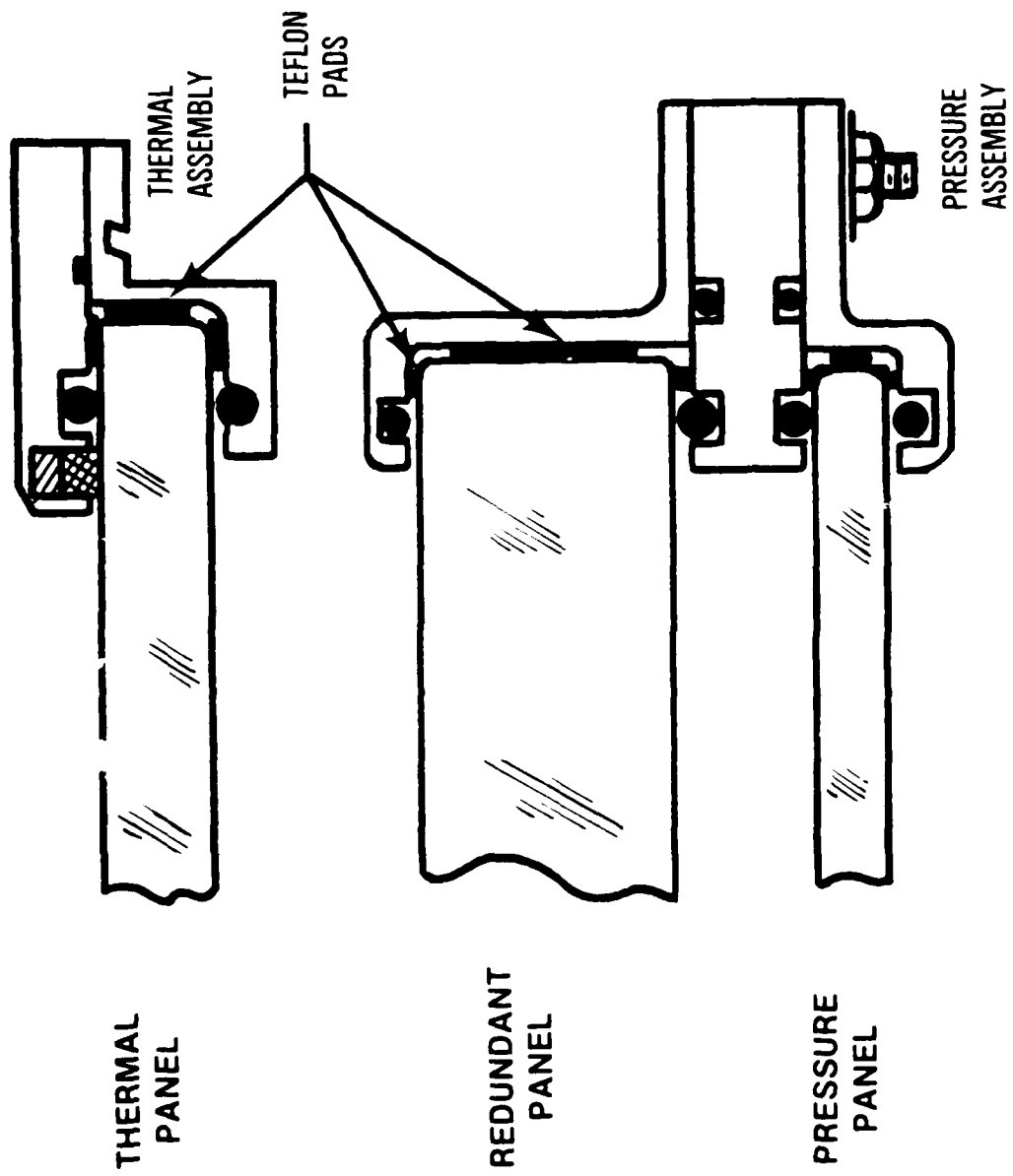


Figure 2. Forward Window System

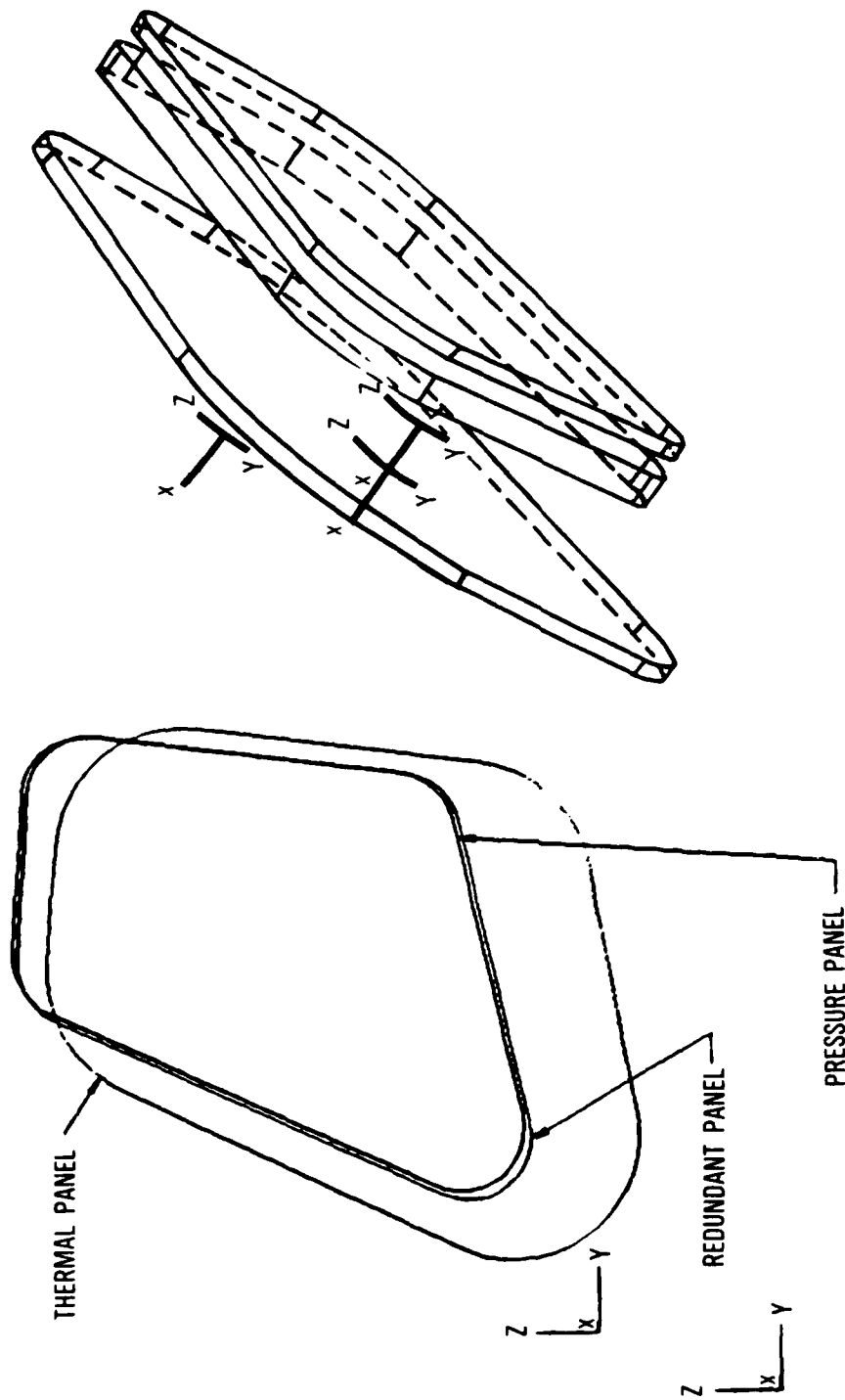


Figure 3. Relative Positions of Window Glass Panels

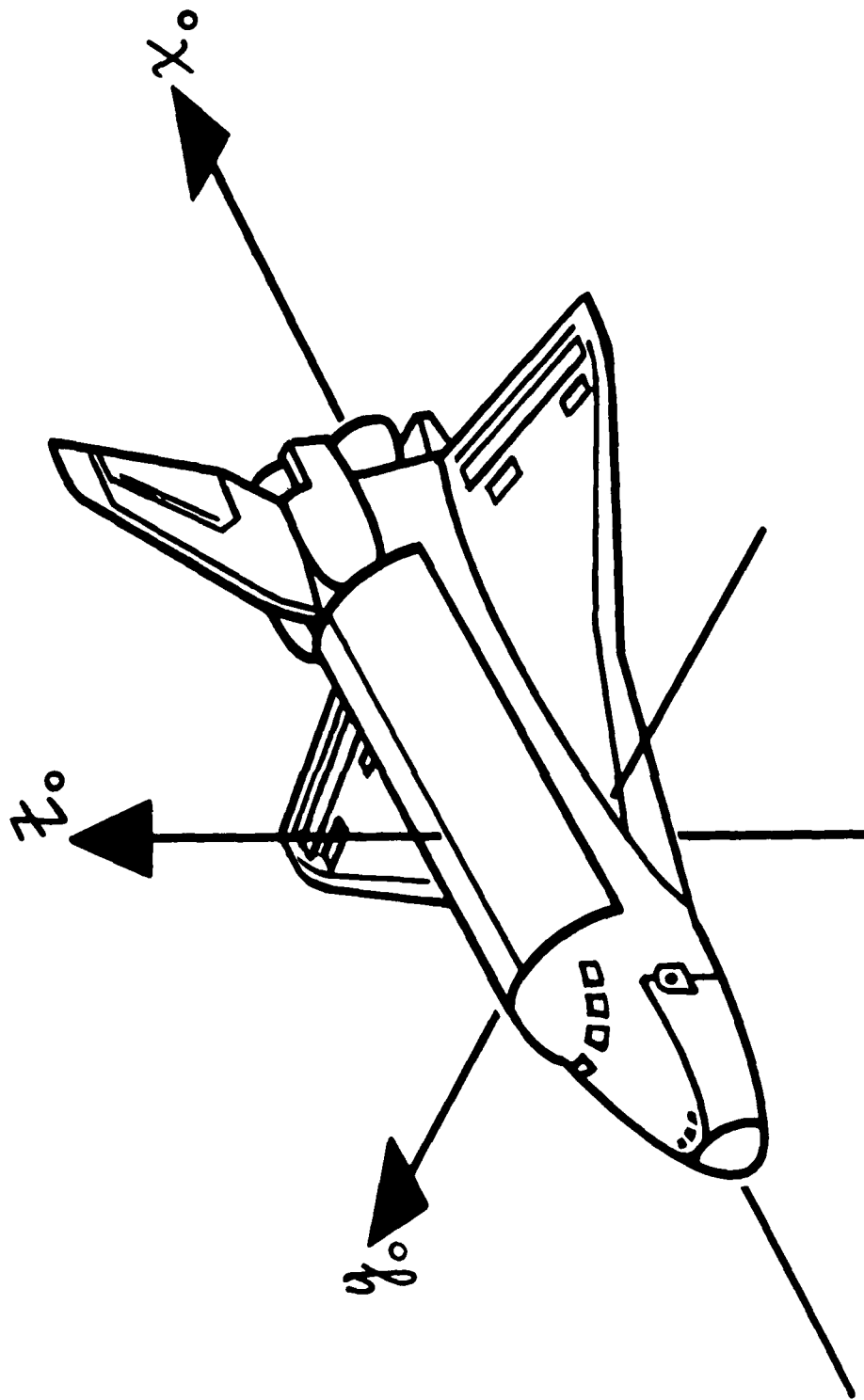


Figure 4. Orbiter Vehicle Coordinate System

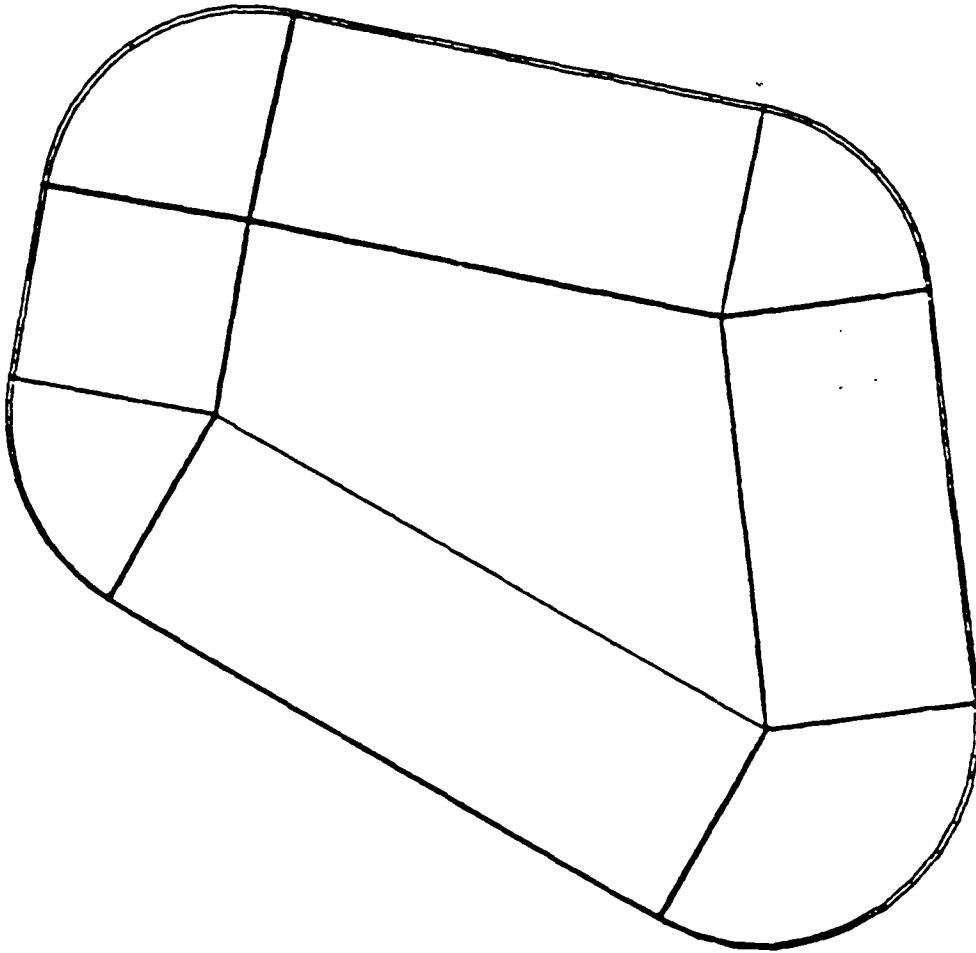


Figure 5. Thermal Panel Super Elements

The MAGNA preprocessor was used to refine the initial model as shown in Figure 6, which shows the final mesh obtained for the thermal panel. A total of 423 sixteen node solid isoparametric elements (MAGNA type 8) were included in the model. This element type was selected because the bulk of successful previous experience in using MAGNA for the transparency bird impact application was with the same element type.<sup>3-10</sup> In this previous work, a total of 100 type 8 elements in the mesh have proven sufficient to provide accurate bird impact simulation results. The MAGNA model had one element through the thickness of the panel. The total number of nodes for the model was 2672.

The same approach as that used in developing the thermal panel model was employed to develop both the redundant and pressure panel models. Figure 7 shows the final mesh obtained for the redundant panel. A total of 396 sixteen node solid isoparametric elements, MAGNA type 8, were included in the model. The total number of nodes for the model was 2514.

Figure 8 shows the final mesh for the pressure panel. A total of 396 sixteen node solid isoparametric elements, MAGNA type 8, were included in the model. The total number of nodes was 2514.

The 14 point (Iron's Rule) numerical integration scheme, available for the MAGNA type 8 element, was selected for use with every element in each of the three models. This choice was made to maximize stress resolution without resorting to the expensive 3x3x3 Gaussian integration. Previous application of MAGNA to the aircraft transparency bird impact problem has demonstrated good deflection and mechanical failure correlation with both the 2x2x2 Gaussian and 14 point integration rules.<sup>3-10</sup>

#### Boundary Conditions

Each of the glass panels in the forward window assembly of the orbiter is supported, as shown in Figure 2, by narrow Teflon pads located less than 0.25 in. from the edge of the panel. Boundary conditions for out-of-plane constraints, as shown in Figure 6-8, were applied to represent these pads at all edge nodes on one surface of the solid element models. The surface constrained was the surface opposite the surface loaded by bird material.

To prevent rigid body motion of the panels, all three translational degrees of freedom were constrained at a single node, the location of which is shown in Figure 6. To prevent rigid body rotation about a line normal to the surface of the panels, another node was selected at which to constrain one in-plane degree of freedom. The location of this node is also shown in Figure 6. For the thermal panel model, the resulting number of unconstrained degrees of freedom was 7881. The number of unconstrained degrees of freedom resulting for the pressure panel model was 7403.

The FDL was concerned about spurious modes of free vibration occurring as a result of the minimal set of constraints employed. Earlier work with a flat glass windshield system design for the British Vulcan bomber encountered such spurious modes as shown in Figure 9. The free vibration



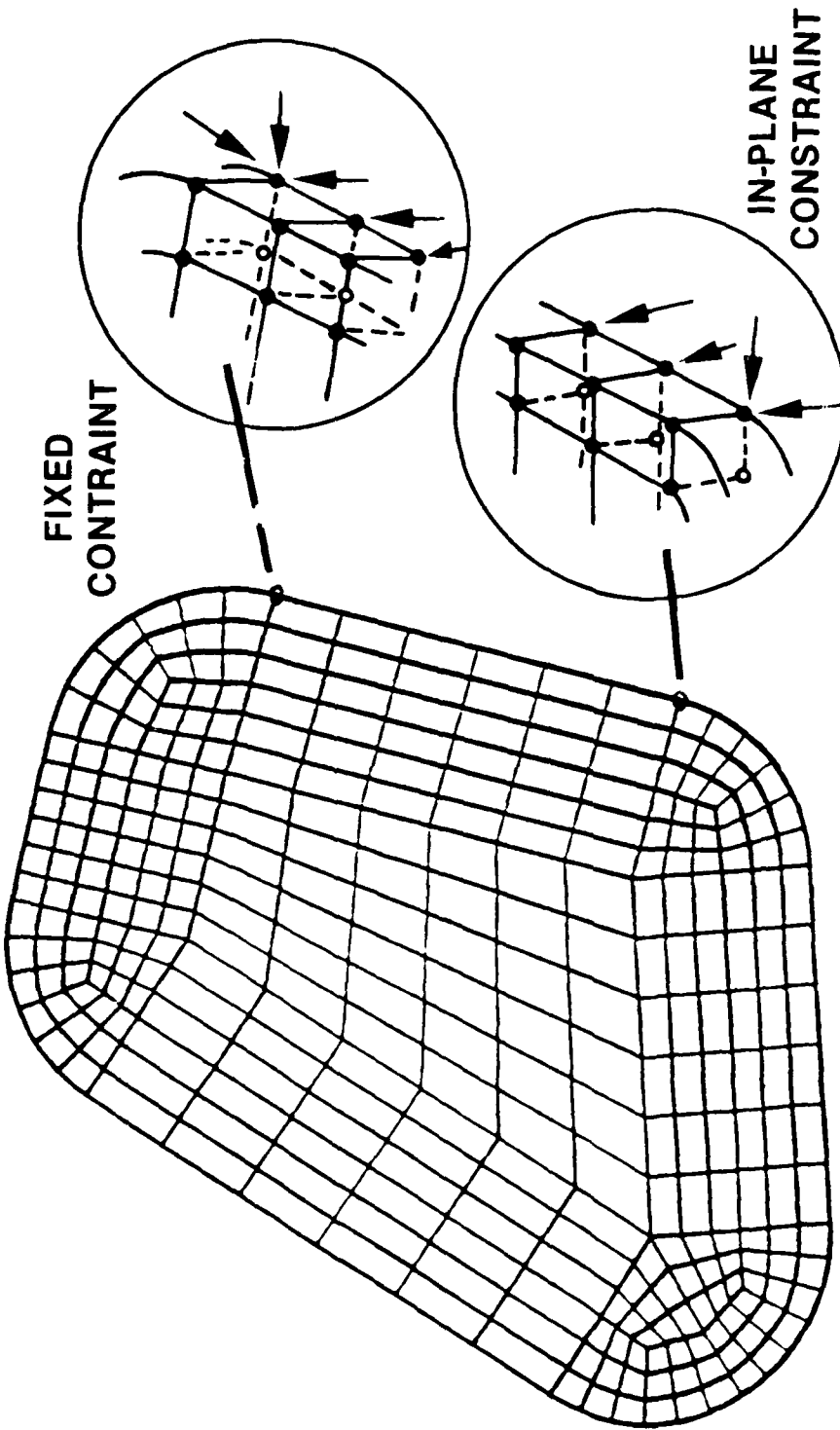


Figure 6. Thermal Panel Final Mesh

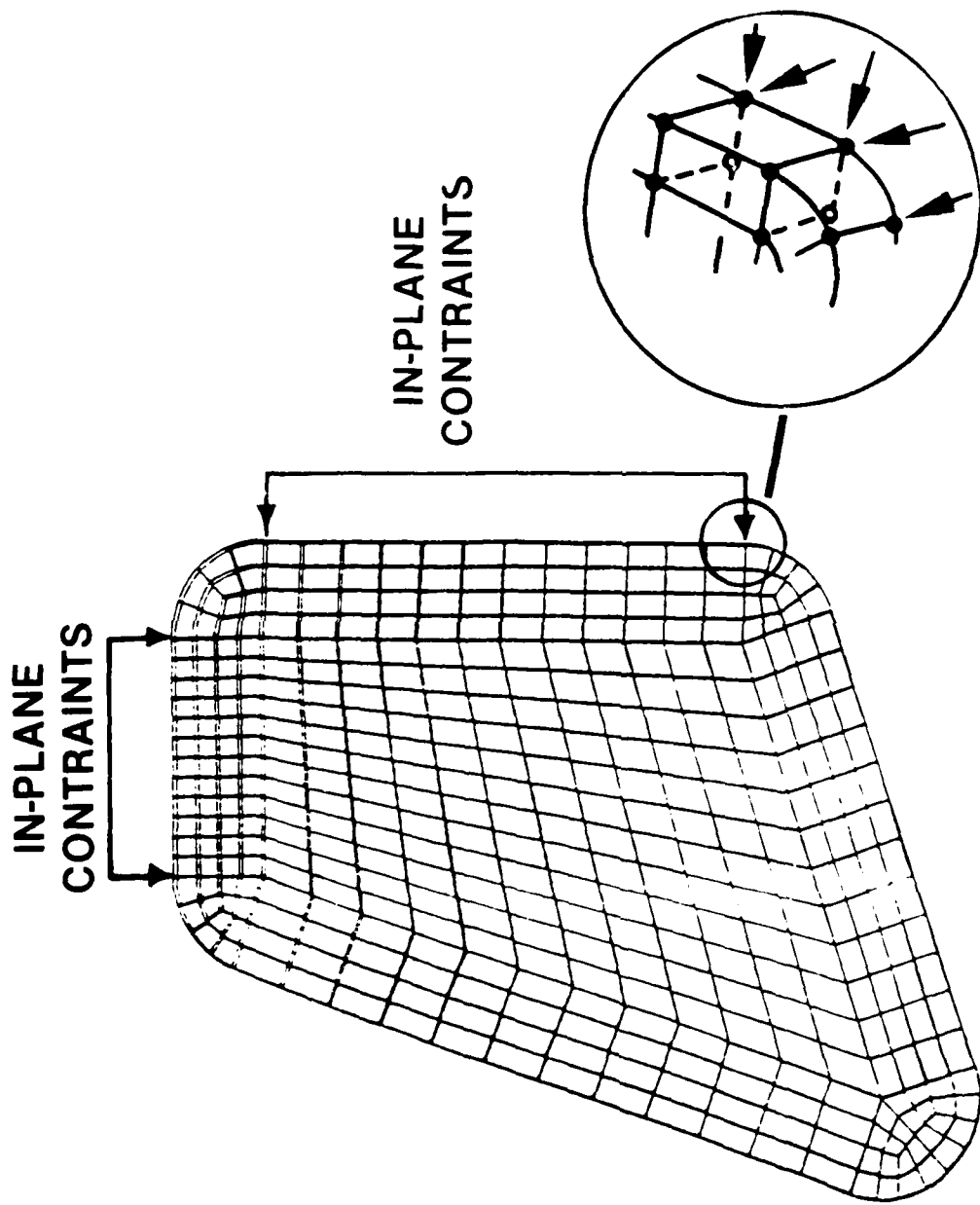


Figure 7. Redundant Panel Final Mesh

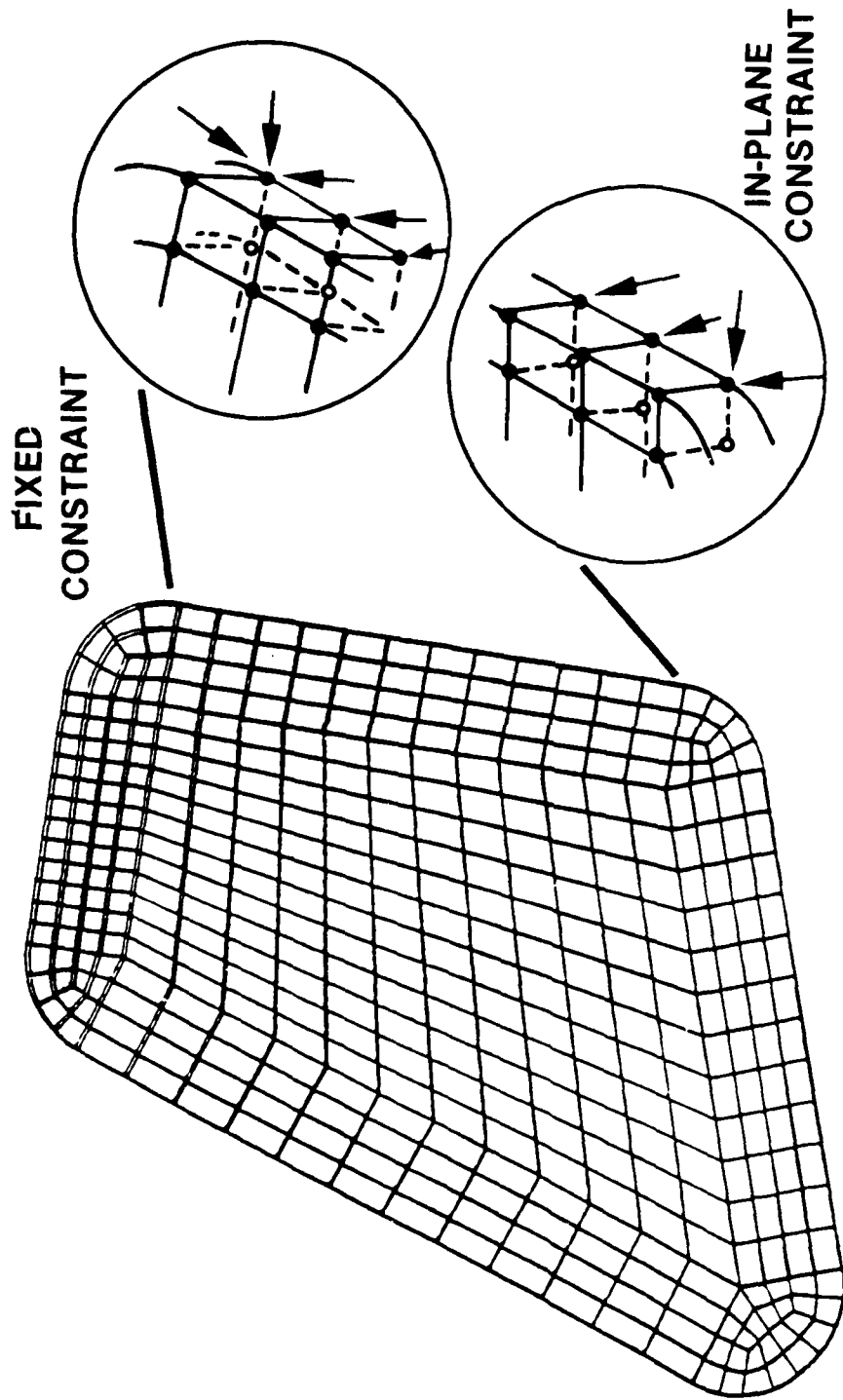
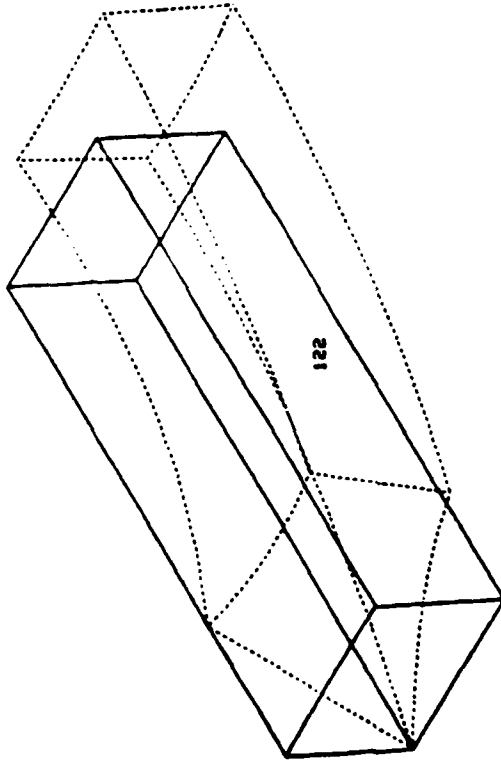


Figure 8. Pressure Panel Final Mesh

VULCAN B MK.1 CENTRE WINDSHIELD PANEL, 165 ELEMENTS TYPE 8, 14 PT INTEGRATI  
 4 LB BIRD IMPACT SIMULATION REFERENCE RAE TECH RPT 65148, JULY 1965, MCMAU  
 EIGENVECTOR ANALYSIS, LOWEST MODE



ONLY PINNED MODE IN MODEL

CONTOUR PLOT OF  
 MODEL DISPLAC.

COMPONENT - ZDIS

MAXIMUM : 1.000E+01  
 MINIMUM : 5.000E+00  
 INTERVAL : 2.000E+00  
 CORE SCALE : 0.  
 PERSPECTIVE VIEW

EYE POSITION

XEYE - 1.000E+08  
 YEYE - -1.000E+02  
 ZEYE - 1.000E+02

INCREMENT -

PLOT OPTION - UNDEF+DEF  
 DIS. SCALE - 1.000E+00

UNIVERSITY OF BAYTON  
 RESEARCH INSTITUTE

08/07/81



Figure 9. Vulcan Windshield Model Spurious Mode

displacements indicated by dotted lines in the figure are unscaled, and represent unrealistic strains around the single fixed node in the Vulcan windshield model.

Discussion of free vibration results obtained for each of the three orbiter forward window glass panels is included in later sections. Constraints like those described above were successfully used in free vibration analysis for both the thermal and pressure windshield panels, but a different set of constraints had to be employed for the redundant panel, when results similar to those illustrated in Figure 9 occurred. For the redundant panel, none of the nodes in the model were completely fixed, but in-plane constraints were applied along both the aft and outboard edges of the panel. Figure 7 shows both the location and orientation of these in-plane constraints. The number of unconstrained degrees of freedom resulting for the redundant panel model was 7356.

### Material Properties

The material for both the thermal and redundant panels was fused silica, Corning 7940. The material for the pressure panel was thermally tempered aluminosilicate, Corning 1723. Each material exhibits linearly elastic behavior, and Table 1 lists the properties used for MAGNA analysis.

Table 1 Linear Material Properties Used

Material	Young's Modulus (psi)	Poisson's Ratio	Density (lb-sec <sup>2</sup> / in.4)
Fused Silica Corning 7940	10.6E+06	0.17	2.06E-04
Thermally Tempered Aluminosilicate Corning 1723	12.5E+06	0.26	2.46E-04

### BIRD IMPACT LOADING

#### Theory

A considerable amount of work has been accomplished in studying the physics of bird impact on both rigid and compliant targets. <sup>16-25</sup> Much of this work has been sponsored by the US Air Force and has provided an extensive data base for the case of an inclined, flat, rigid target. This data base defines both the spatial and temporal distribution of bird impact pressures over the surface of the target.

A generalized description of bird impact loading has evolved from this work effort and has been validated for bird weights up to 7.9 lb, bird velocities up to 984 ft/sec, and target inclinations of 90, 45, and 25 degrees.

The procedure for mathematical definition of bird impact loading used in the MAGNA analysis support studies for the orbiter windshield system is simple and straightforward to use. The essential points of the rigid target theory upon which the loads definition procedure is based, are as follows:

1. The bird behaves as a fluid during impact.
2. The impulse delivered to the structure is equal to the component of the bird's linear momentum which is normal to the target surface.
3. The bird may be represented as a right circular cylinder having a length to diameter ratio of 2.0.
4. The pressure resulting from bird impact is relatively constant at any point on the surface of the target (quasi-steady fluid flow).

#### Mathematical Definition

The procedure for the definition of bird impact loading is quite simplistic. It presumes a regular geometry for the bird, ignores spikes of shock pressure which occur very early in the impact event, and assumes a spatially uniform distribution of pressure. Even with these approximations, bird impact simulation results obtained with this procedure have been useful and realistic. The usefulness of rigid windshield bird impact loads defined with this procedure is limited to glass transparency designs which exhibit only very small deflections before fracturing.<sup>7</sup> (Methods to represent the effects of plastic windshield compliance have also been successfully developed.)<sup>8</sup>

### MAGNA ANALYSIS RESULTS

#### Free Vibration Analysis

MAGNA free vibration analyses were conducted primarily to determine the size of the MAGNA time step to be used in subsequent linear dynamic bird impact analysis. Illustrations of eigenvectors extracted during free vibration analysis were also used to verify definition of model boundary conditions.

Each free vibration analysis was conducted using the 14 point (Iron's rule) integration rule, available for the 16 node (type 8) solid isoparametric elements used. Lumped rather than consistent mass was assumed to obtain analysis economy. Linear formulation of element stiffness was chosen in each case, and only the first mode of free vibration was extracted. The assumption inherent in extracting just first modes was that

primarily only the first mode was excited by the bird impact event being analyzed in subsequent linear dynamic analysis.

The frequency corresponding to the thermal panel eigenvector was 167 Hz. The frequency for the redundant panel eigenvector was 478 Hz, much higher than that for the thermal panel because of the greater panel thickness involved. The frequency corresponding to the pressure panel eigenvector was 261 Hz, higher than that obtained for the slightly thicker thermal panel, because of the stiffer material involved.

#### Bird Impact Analysis

After free vibration analyses were conducted to determine first mode frequencies for each windshield panel model, linear dynamic analyses were accomplished to simulate bird impact response. In each dynamic analysis, the 14 point integration rule was employed for all elements in the model. This integration rule was selected because it affords double the stress resolution provided by the 2x2x2 Gaussian rule, and because it halves the computer resources required for the 3x3x3 Gaussian rule. Furthermore, the 3x3x3 Gaussian rule tends to yield results which are too stiff for bending problems.<sup>13</sup>

Linear stiffness formulation was selected for use with all elements in each of the models, and the time step was chosen to be considerably less than 1/100th the period of any of the first modes obtained from free vibration analysis. This rule for selection of time step size has been demonstrated to represent an effective balance between solution accuracy (MAGNA employs an implicit solution technique) and cost.<sup>4</sup> The time step size was chosen to be 0.000010 sec, which is conservative because the highest first mode frequency obtained was 478 Hz.

It was agreed among the FDL, NASA/JSC, and Rockwell, that maximum principal (tensile) inner surface stress would be adopted as the parameter by which to judge glass panel failure. When maximum principal stress at the tension surface of the glass panel was equal to the dynamic modulus of rupture calculated by NASA/JSC and Rockwell, failure would be declared to have occurred.

To obtain the stress results required, contour plots of in-plane normal stresses (y and z components in windshield panel local coordinates, see Figure 3) on the tension side of the glass panel were prepared. From these contour plots, the node for each solution time increment at which the maximum value of in-plane normal stress occurred, was determined. Then for each of these nodes, maximum (tensile) principal stress versus time was extracted from the MAGNA APOST plotfile using the WRTFILA module of the postprocessor.<sup>14</sup>

The history of maximum principal stress was obtained and transmitted to NASA/JSC for flaw growth analysis. NASA/JSC calculated the dynamic modulus of rupture for the material as a function of the MAGNA stress history. The time of glass panel failure obtained determined when to stop the MAGNA

analysis for a particular glass panel, and when to begin MAGNA analysis for the subsequent panel in the three-panel orbiter windshield system.

#### Thermal Panel, Center, 355 Knots

Figures 10 and 11 show contours of in-plane normal stress on the tension (inner) surface of the thermal panel at 0.000200 sec, for 4 lb bird impact in the center at 355 KTAS. Contour plots similar to those shown in the figures were prepared for times out to 0.000300 sec, and showed that maximum in-plane normal stress always occurred at one of three nodes in the mesh.

Figure 12 shows the histories of maximum principal stress (extracted from the MAGNA APOST file) for the three nodes of interest. The fact that Figure 12 does not indicate smoothly increasing stress as a function of time, reflects the discontinuity with which bird impact pressure loading was defined. The sharp increase in slope of the data corresponds to the time when initial pressure was applied to the second row of finite elements in the bird impact footprint.

The panel failure time calculated by NASA/JSC and Rockwell from tabulated data corresponding to Figure 12 represented only about 1.2 oz of the bird having been "consumed" by the windshield thermal panel.

#### Thermal Panel, Corner, 355 Knots

Figures 13 and 14 show contours of in-plane normal stress on the tension (inner) surface of the thermal panel at 0.000250 sec, for 4 lb bird impact in the corner at 355 KTAS.

Figure 15 shows the histories of maximum principal stress for the three nodes of interest. The panel failure time was calculated by NASA/JSC and Rockwell to be 0.000220 sec.

The center location was chosen as the more critical of the two because failure occurred there at a slightly earlier time. The vector representing the bird path for thermal panel center impact was carried over to the models of the redundant and pressure panels to define corresponding bird impact loads for each.

#### Redundant Panel, Center, 355 Knots

At the outset of the study, it was agreed that the entire remaining portion of the bird mass which had not yet reached the surface of a given windshield panel at the time of that panel's failure, would be applied to the next windshield panel in sequence. Rationale for this approach is based on extensive experimental work which demonstrated that the windshield bird impact problem may be considered similar to the steady impingement of a fluid jet on the surface of a target.<sup>16-25</sup> While the target is intact, fluid is deflected to flow in directions parallel the surface of the target. But when the target is removed suddenly (fails), fluid which has not yet



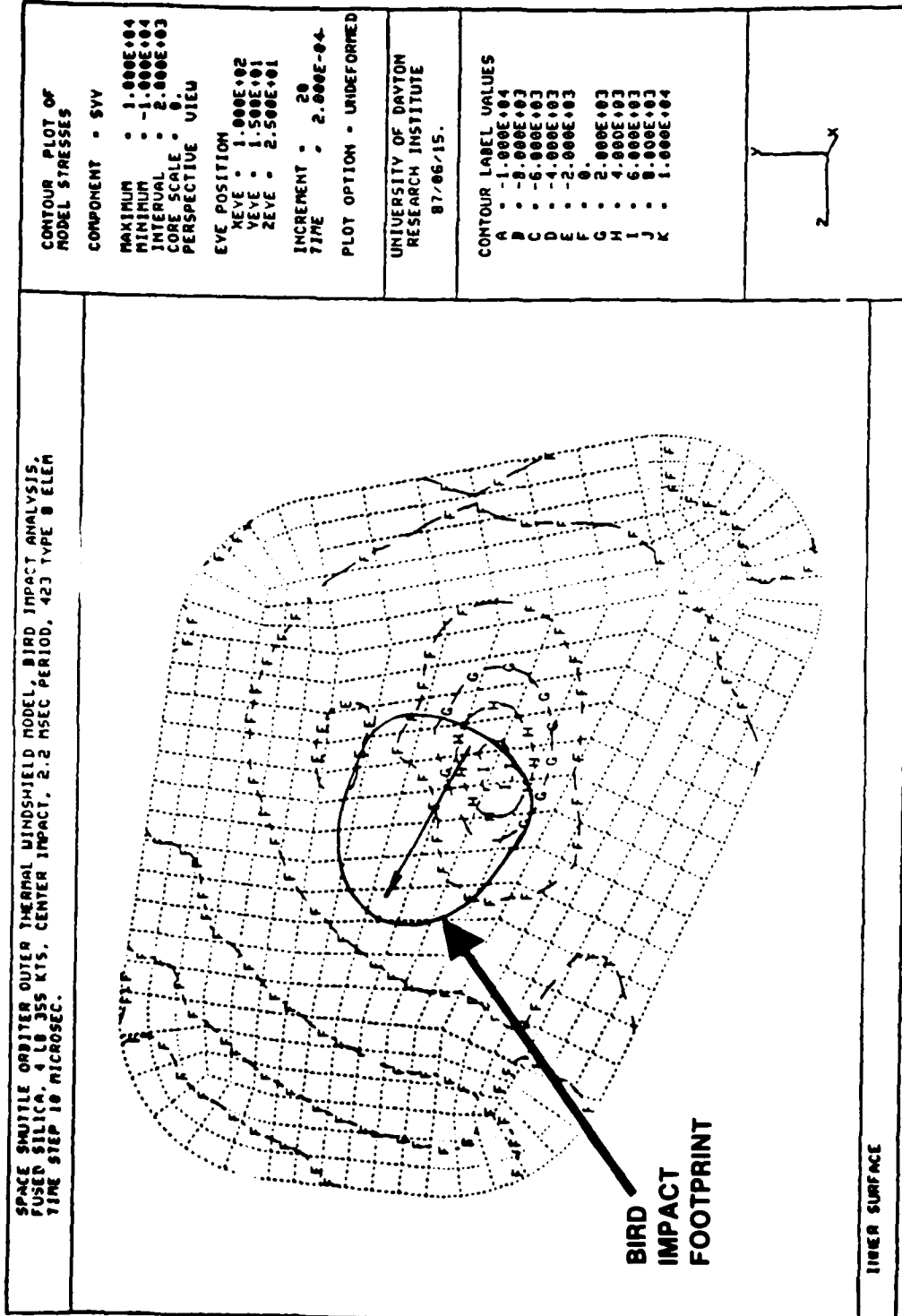


Figure 10. Thermal Panel, Y Normal Stress, Center Impact, 355 KTAS

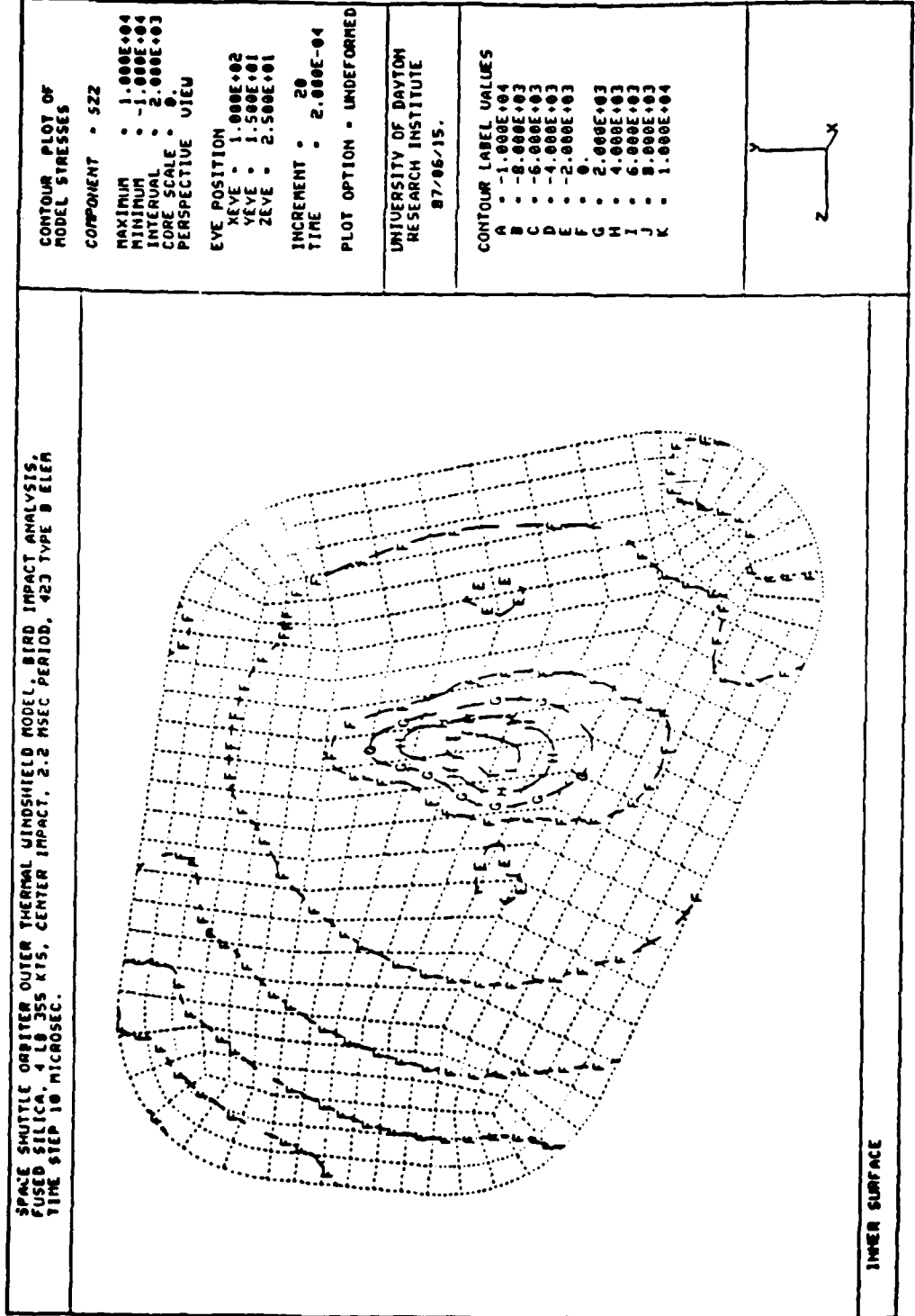


Figure 11. Thermal Panel, Z Normal Stress, Center Impact, 355 KTAS

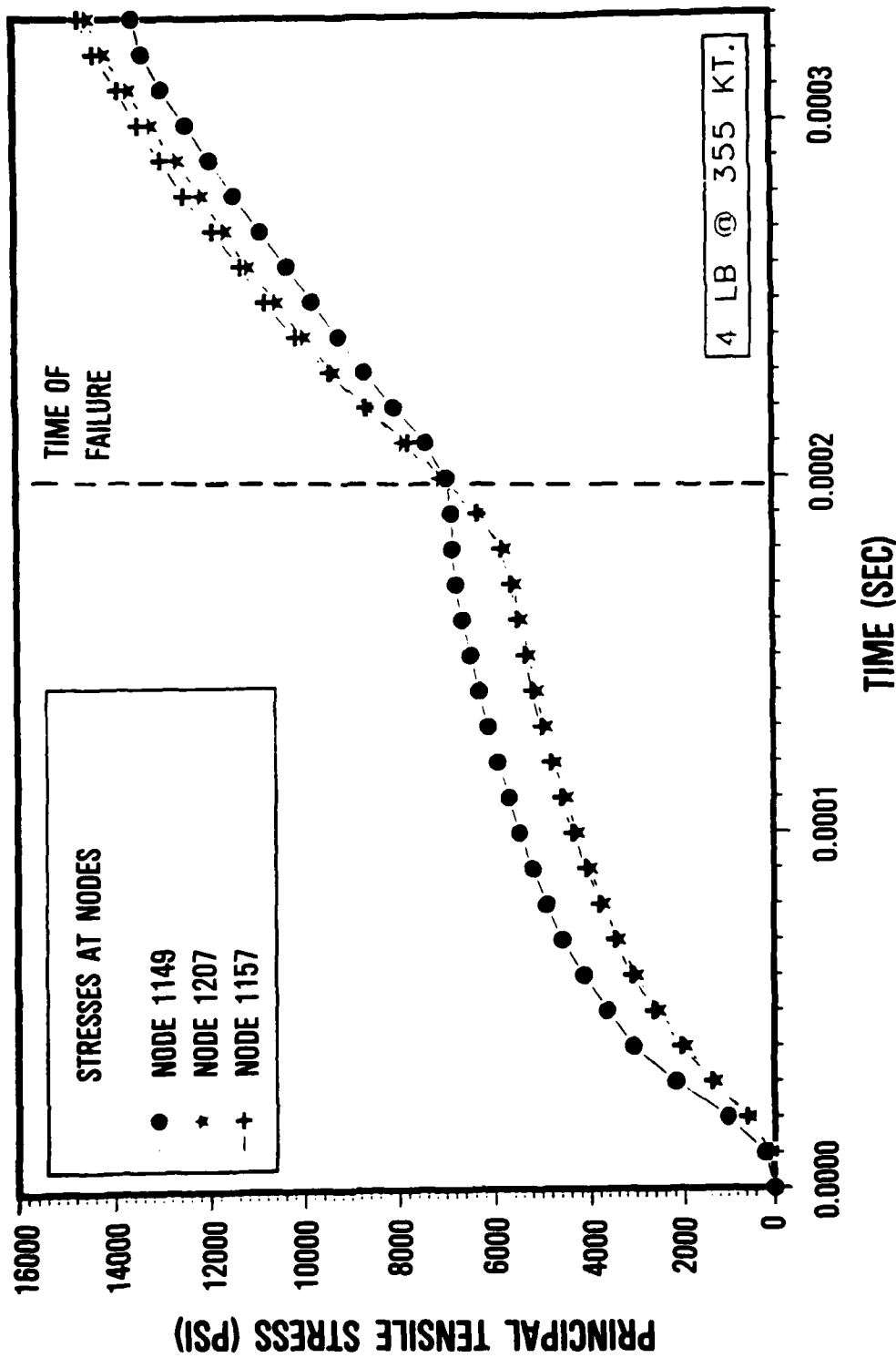


Figure 12. Thermal Panel Stress History, Center Impact, 355 KTAS

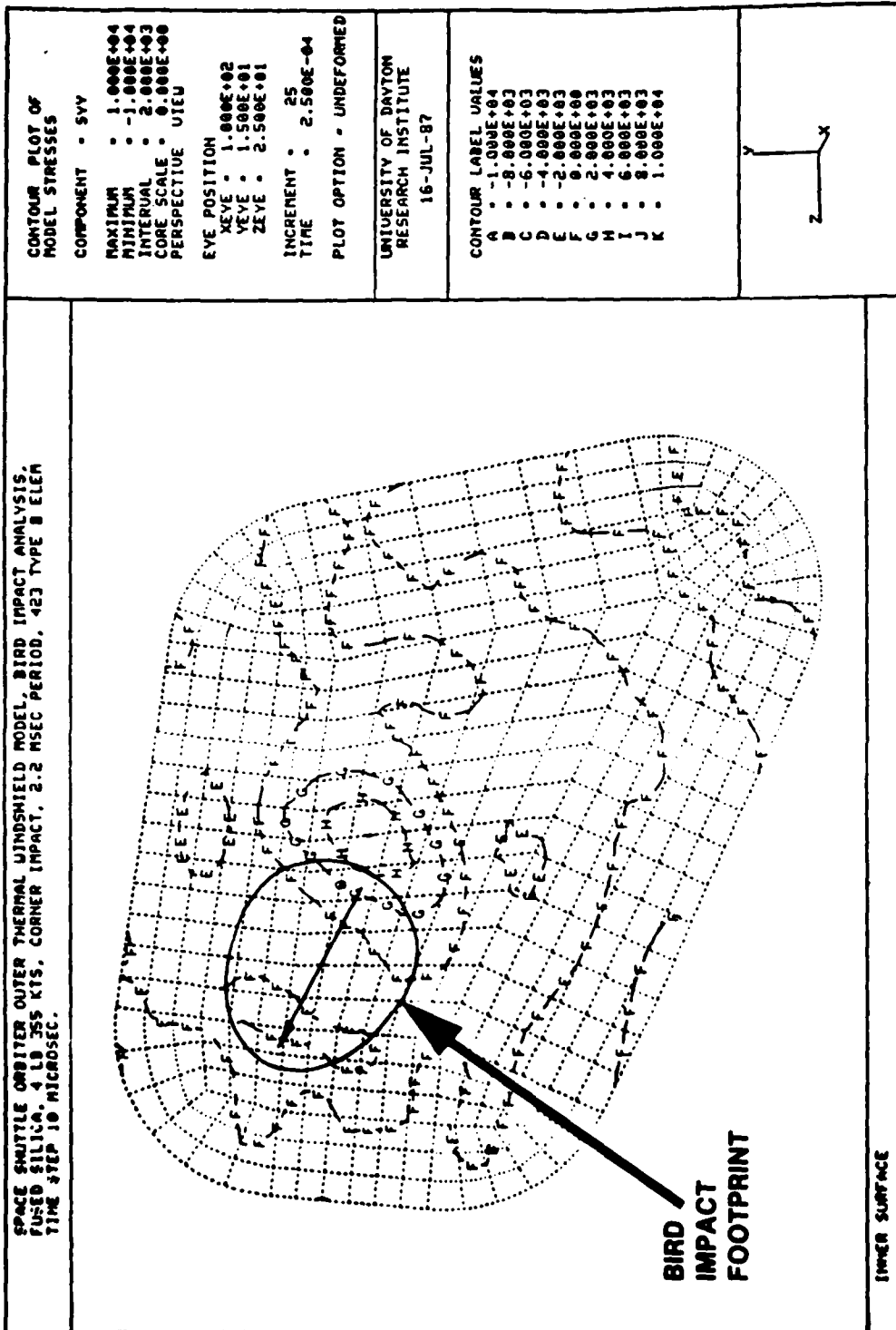
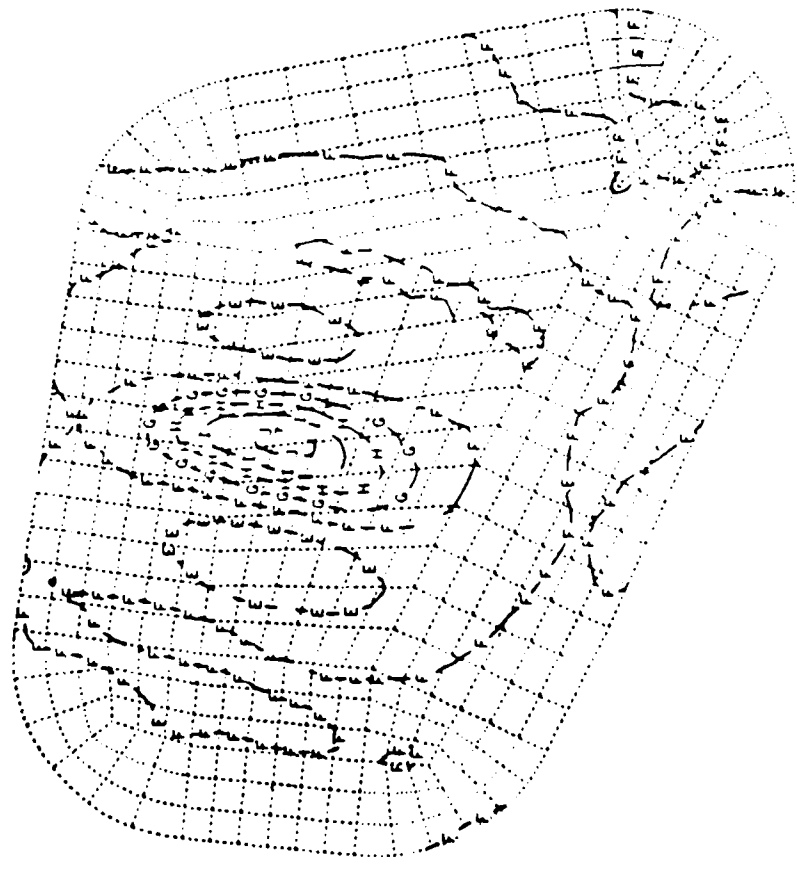


Figure 13. Thermal Panel, Y Normal Stress, Corner Impact, 355 KTAS

SPACE SHUTTLE ORBITER OUTER THERMAL WINDSHIELD MODEL, BIRD IMPACT ANALYSIS,  
 FUSED SILICA, 4 LB 355 KTS, CORNER IMPACT, 2.2 MSEC PERIOD, 423 TYPE 8 ELEM  
 TIME STEP 10 MICROSEC.



INNER SURFACE

CONTOUR PLOT OF  
 MODEL STRESSES

COMPONENT = 52Z

MAXIMUM = 1.000E+04  
 MINIMUM = -1.000E+04  
 INTERVAL = 2.000E+03  
 CORE SCALE = 0.000E+00  
 PERSPECTIVE VIEW

EYE POSITION

XEYE = 1.000E+02  
 YEYE = 1.500E+01  
 ZEYE = 2.500E+01

INCREMENT = 25  
 TIME = 2.500E-04

PLOT OPTION = UNDEFORMED

UNIVERSITY OF DAYTON  
 RESEARCH INSTITUTE  
 16-JUL-87

CONTOUR LABEL VALUES

A = -1.000E+04  
 B = -8.000E+03  
 C = -6.000E+03  
 D = -4.000E+03  
 E = -2.000E+03  
 F = 0.000E+00  
 G = 2.000E+03  
 H = 4.000E+03  
 I = 6.000E+03  
 J = 8.000E+03  
 K = 1.000E+04

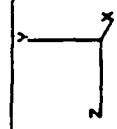


Figure 14. Thermal Panel, Z Normal Stress, Corner Impact, 355 KTAS

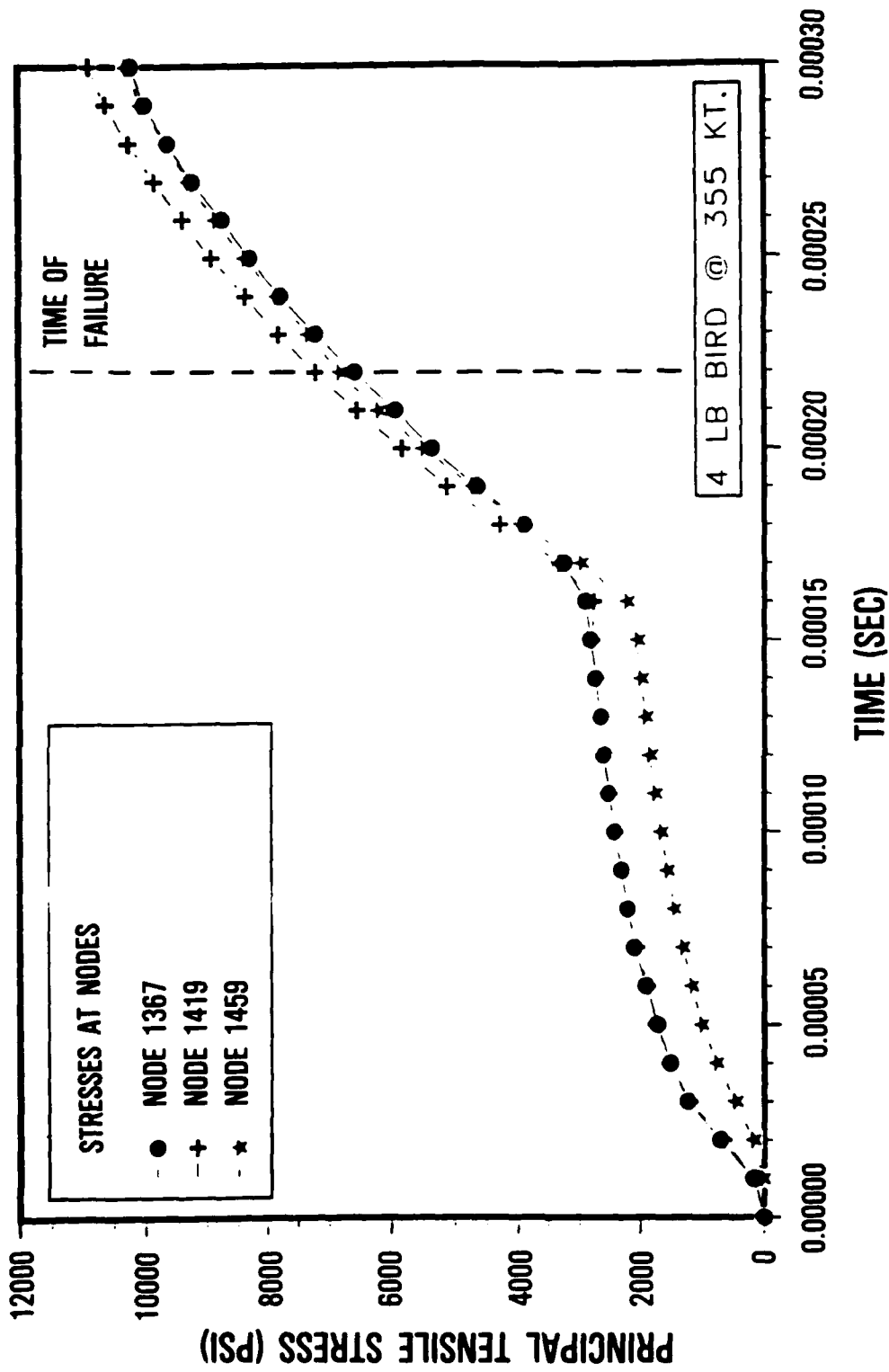


Figure 15. Thermal Panel Stress History, Corner Impact, 355 KTAS

impinged the surface continues to move in its original direction of travel (i.e. along the trajectory of the bird).

After failing the thermal panel for center impact at 355 KTAS, about 3 lb 14.8 oz of the bird had not yet reached the panel surface. This reduced mass was applied in center impact analysis for the redundant panel. To represent the effect of this reduced mass, redundant panel impact loading was defined for a 4 lb bird, but the MAGNA solution was initiated at a corresponding time later than zero (beginning of 4 lb bird impact.)

Figures 16 and 17 show contours of in-plane normal stress on the tension (inner) surface of the redundant panel at 0.000272 sec. Careful attention was paid to the distribution of stress along the two edges which had been arbitrarily constrained in-plane to avoid anomalous first mode free vibration results. No unrealistic stress concentrations were apparent along either of the constrained edges in the figures.

The panel failure time calculated by NASA/JSC and Rockwell corresponds to an additional 3.2 oz of bird having been consumed by the redundant panel, for a total of 4.4 oz having been consumed by the thermal and redundant panels together.

#### Pressure Panel, Center, 355 Knots

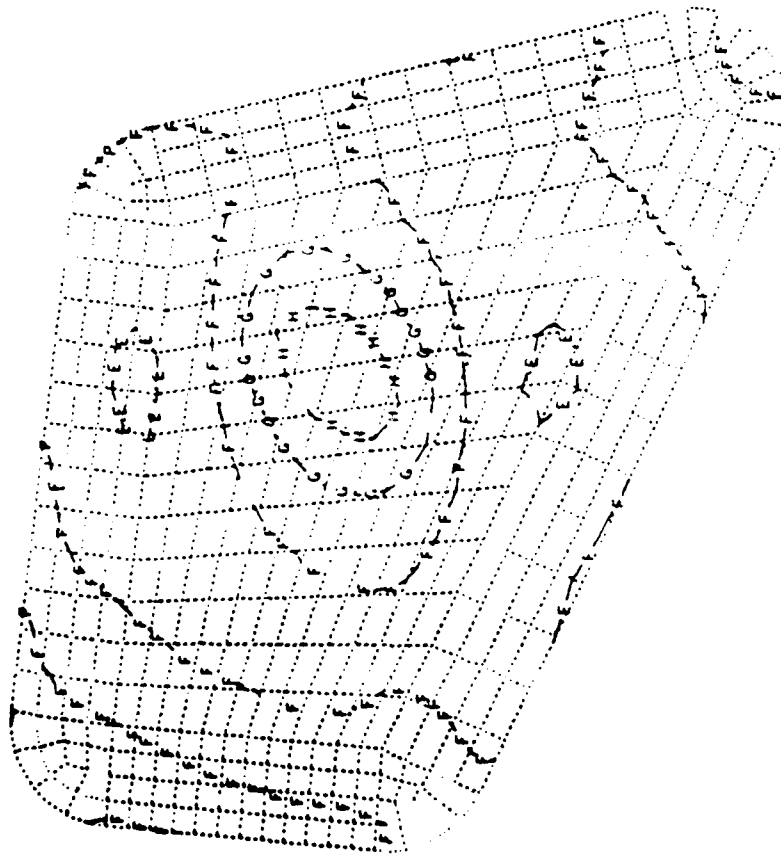
The reduced mass of 3 lb 11.6 oz was applied in center impact analysis of the pressure panel. The panel failure time calculated by NASA/JSC and Rockwell corresponds to 2.7 oz of the bird having been consumed by the pressure panel, for a 355 KTAS total of 7.1 oz for the three panels comprising the forward window assembly.

Because the analysis predicted that a velocity of 355 KTAS was well above the threshold of failure for 4 lb bird impact on the forward window assembly, steps were taken to repeat the analysis for a lower airspeed. An airspeed of 175 KTAS was chosen, based on earlier estimates made by Rockwell.

This second analysis revealed that 175 KTAS was still above the threshold velocity of failure for 4 lb bird impact on the forward window assembly. A number of additional analyses at other airspeeds were accomplished as a result.

Table 2 summarizes the results obtained from all the bird impact analyses conducted. It shows, for each of the orbiter airspeeds analyzed, that portion of the 4 lb bird required to fail each of the three respective panels mounted in the forward window assembly of the vehicle.

SPACE SHUTTLE ORBITER REDUNDANT THERMAL PAIR WINDSHIELD MODEL, BIRD  
 IMPACT ANALYSIS, FUSED SILICA, 4 TO 355 KTS., 2.0 MSEC PLIAD, 423 TYPE  
 8 ELEMENTS, TIME STEP 10 MICROSEC.



INNER SURFACE

CONTOUR PLOT OF  
 MODEL STRESSES

COMPONENT - SYV

MAXIMUM : 1.000E+04  
 MINIMUM : -1.000E+04  
 INTERVAL : 2.000E+03  
 CORE SCALE : 0.  
 PERSPECTIVE VIEW

EYE POSITION

XEYE : 1.000E+02  
 YEYE : 1.500E+01  
 ZEYE : 2.500E+01

INCREMENT : 15  
 TIME : 2.720E-04

PLOT OPTION - UNDEFORMED

UNIVERSITY OF DAYTON  
 RESEARCH INSTITUTE  
 87/08/28.

CONTOUR LABEL VALUES

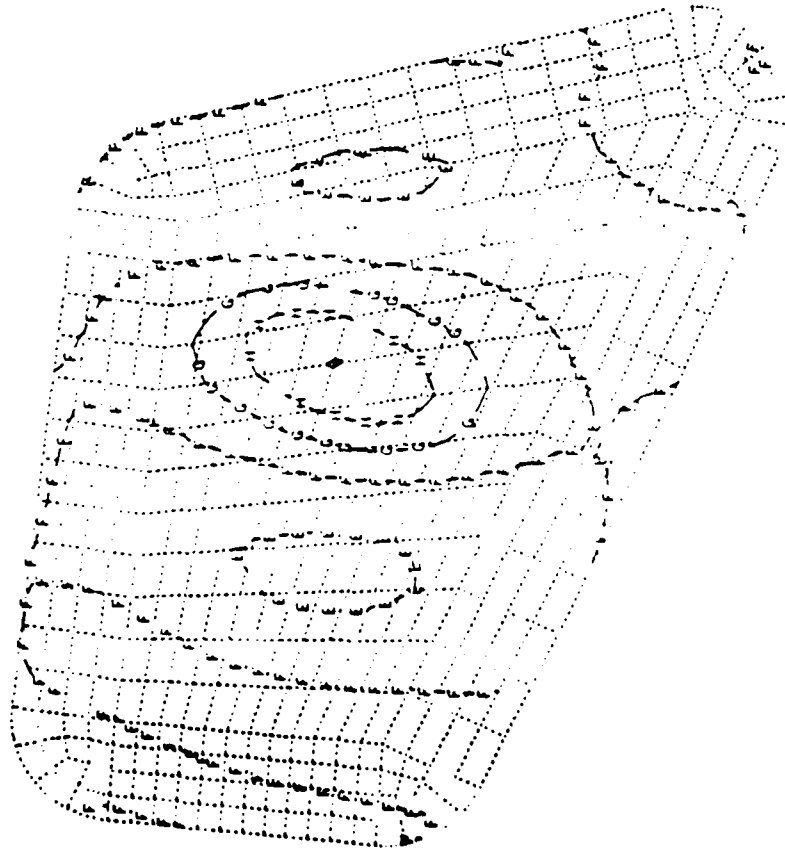
A : -1.000E+04  
 B : -8.000E+03  
 C : -6.000E+03  
 D : -4.000E+03  
 E : -2.000E+03  
 F : 0.  
 G : 2.000E+03  
 H : 4.000E+03  
 I : 6.000E+03  
 J : 8.000E+03  
 K : 1.000E+04



Figure 16. Redundant Panel, Y Normal Stress, 355 KTAS



SPACE SHUTTLE ORBITER REDUNDANT THERMAL PANEL WINDSHIELD MODEL, BIRD  
 IMPACT ANALYSIS, 1/30/88, 4 TO 355 KTAS, 2.0 MSEC PERIOD, 431 TYPE  
 8 ELEMENTS, TIME STEP 10 MICRONSEC.



INNER SURFACE

CONTOUR PLOT OF  
 MODEL STRESSES

COMPONENT = SZZ

MAXIMUM = 1.000E+04  
 MINIMUM = -1.000E+04  
 INTERVAL = 2.000E+03  
 CONT. SCALE = 0.  
 PERSPECTIVE VIEW

EYE POSITION  
 XEYE = 1.000E+02  
 YEYE = 1.500E+01  
 ZEYE = 2.500E+01

INCREMENT = 15  
 TIME = 2.720E-04

PLOT OPTION = UNDEFORMED

UNIVERSITY OF DAYTON  
 RESEARCH INSTITUTE  
 87-08/29.

CONTOUR LABEL VALUES

A = -1.000E+04  
 B = -8.000E+03  
 C = -6.000E+03  
 D = -4.000E+03  
 E = -2.000E+03  
 F = 0.  
 G = 2.000E+03  
 H = 4.000E+03  
 I = 6.000E+03  
 J = 8.000E+03  
 K = 1.000E+04



Figure 17. Redundant Panel, Z Normal Stress, 355 KTAS

Table 2 Mass Required to Fail Forward Window Assembly

Airspeed	Portion of 64 oz Bird Consumed				
	KTAS	Thermal Panel	Redundant Panel	Pressure Panel	Total
355		1.2 oz	3.2 oz	2.7 oz	7.1 oz
175		6.8 oz	15.4 oz	18.1 oz	40.3 oz
150		9.7 oz	54.3 oz	-	64.0 oz
125		14.6 oz	49.4 oz	-	64.0 oz
175 <sup>1</sup>		9.8 oz	54.2 oz	-	64.0 oz

1 For mean crack growth rate in glass panel surface  
(Other cases were for maximum crack growth rate)

#### CONCLUSIONS

At 355 KTAS below 10,000 ft AGL during descent to landing, the forward window assembly for the NASA Space Shuttle orbiter offers insignificant resistance to 4 lb bird impact.

The current forward window assembly design for the NASA Space Shuttle orbiter could fail at velocities lower than 175 KTAS as a result of impact with a 4 lb bird.

Penetration of a 4 lb bird through the forward window assembly of the vehicle could result in the death of the orbiter commander and loss of the vehicle.

#### RECOMMENDATIONS

The method of Halpin and Berens should be used to determine the probability of orbiter forward window assembly penetration as a result of bird impact incidents over the operational life of the Shuttle orbiter fleet.<sup>26</sup> Work accomplished to define the distribution of birds near orbiter landing sites should be used to support this determination.

If the probability of penetrating bird impacts is determined to be unacceptable, the MAGNA computer program should be utilized to assess forward window assembly designs for the orbiter vehicle which would provide improved measures of bird impact protection.

Future manned hypersonic vehicles requiring conventional forward vision through transparent panels should follow the steps listed above in providing adequate in-flight bird impact protection to aircrew members.

#### REFERENCES

1. Littell, H. E., Windshield and Canopy Protection Development Program, Air Force Flight Dynamics Laboratory, Wright-Patterson Air Force Base, Ohio 45433-6553, AFFDL-TR-74-75, June 1974.
2. Pretzer, F. L., Multilayer Plastic Transparencies for the F/FR-111 Aircraft, Part I - Development Test and Evaluation of Bird Impact Resistant Transparencies (BIRT), Flight Dynamics Laboratory, Wright-Patterson Air Force Base, Ohio 45433-6553, AFWAL-TR-80-3005, Part I, March 1980.
3. McCarty, R. E., "Computer Analysis of Bird Resistant Aircraft Transparencies," Proceedings of the 17th Annual SAFE Symposium, December 1979, Las Vegas, Nevada.
4. McCarty, R. E., "Finite Element Analysis of F-16 Aircraft Canopy Dynamic Response to Bird Impact Loading," 21st AIAA/ASME/ASCE/AHS Structures, Structural Dynamics, and Materials Conference, May 1980, Seattle, Washington, AIAA Paper Number 80-804.
5. McCarty, R. E., "Aircraft Transparency Bird Impact Analysis Using the MAGNA Computer Program," Conference on Aerospace Transparencies Sponsored by the Society of British Aerospace Companies, September 1980, London, England.
6. McCarty, R. E., "Finite Element Analysis of a Bird-Resistant Monolithic Stretched Acrylic Canopy Design for the F-16A Aircraft," AIAA Aircraft Systems and Technology Conference, August 1981, Dayton, Ohio, AIAA Paper Number 81-1640.
7. McCarty, R. E., and Hart, J. L., "Validation of the MAGNA Computer Program for Nonlinear Finite Element Analysis of Aircraft Transparency Bird Impact," 14th Conference on Aerospace Transparent Materials and Enclosures Sponsored by the Air Force Wright Aeronautical Laboratories, July 1983, Scottsdale, Arizona, AFWAL-TR-83-4154, December 1983.
8. McCarty, R. E., "MAGNA Computer Simulation of Bird Impact on the TF-15 Aircraft Canopy," 14th Conference on Aerospace Transparent Materials and Enclosures Sponsored by the Air Force Wright Aeronautical Laboratories, July 1983, Scottsdale, Arizona, AFWAL-TR-83-4154, December 1983.
9. McCarty, R. E., "Aircraft Transparency Bird Impact Analysis Using the MAGNA Computer Program," Conference and Training on Wildlife Hazards to Aircraft Sponsored by the FAA, March 1984, Charleston, South Carolina.

10. McCarty, R. E., Trudan, D. E., and Davis, A. D., "Three Dimensional Nonlinear Dynamic Finite Element Analysis for the Response of a Thick Laminated Shell to Impact Loads," AIAA/ASME/ASCE/AHS 26th Structures, Structural Dynamics, and Materials Conference, April 1985, Orlando, Florida, AIAA Paper Number 85-0713-CP.
11. Short, Maj Jeffrey J., USAFR, A Characterization of the Birdstrike Risk to the Space Shuttle at its Primary Landing Sites, Flight Dynamics Laboratory, Wright-Patterson Air Force Base, Ohio 45433-6553, AFWAL-TR-87-3083.
12. Bruner, T. S., MAGNA (Materially and Geometrically Nonlinear Analysis) Part II - Preprocessor Manual, Flight Dynamics Laboratory, Wright-Patterson Air Force Base, Ohio 45433-6553, AFWAL-TR-82-3098 Part II, December 1982.
13. Brockman, R. A., MAGNA (Materially and Geometrically Nonlinear Analysis) Part I - Finite Element Analysis Manual, Flight Dynamics Laboratory, Wright-Patterson Air Force Base, Ohio 45433-6553, AFWAL-TR-82-3098 Part I, December 1982.
14. Brockman, R. A., MAGNA (Materially and Geometrically Nonlinear Analysis) Part III - Postprocessor Manual, Flight Dynamics Laboratory, Wright-Patterson Air Force Base, Ohio 45433-6553, AFWAL-TR-82-3098 Part III, December 1982.
15. Brockman, R. A., MAGNA (Materially and Geometrically Nonlinear Analysis) Part IV - Quick Reference Manual, Flight Dynamics Laboratory, Wright-Patterson Air Force Base, Ohio 45433-6553, AFWAL-TR-82-3098 Part IV, December 1982.
16. Barber, J. P. and Wilbeck, J. S., Characterization of Bird Impacts on a Rigid Plate: Part I, Air Force Flight Dynamics Laboratory, Wright-Patterson Air Force Base, Ohio 45433-6553, AFFDL-TR-75-5, January 1975.
17. Peterson, R. L. and Barber, J. P., Bird Impact Forces in Aircraft Windshield Designs, Air Force Flight Dynamics Laboratory, Wright-Patterson Air Force Base, Ohio 45433-6553, AFFDL-TR-75-150, March 1976.
18. Ito, Y. M., Carpenter, G. E., and Perry, F. W., Bird Impact Loading Model for Aircraft Windshield Design, California Research and Technology, Inc, Woodland Hills, California 91364, CRT 3090-2, July 1977.
19. Barber, J. P., Wilbeck, J. S., and Taylor, H. R., Bird Impact Forces and Pressures on Rigid and Compliant Targets, Air Force Flight Dynamics Laboratory, Wright-Patterson Air Force Base, Ohio 45433-6553, AFFDL-TR-77-60, May 1978.

20. Wilbeck, J. S., *Impact Behavior of Low Strength Projectiles*, Air Force Materials Laboratory, Wright-Patterson Air Force Base, Ohio 45433-6553, AFML-TR-77-134, July 1978.
21. Challita, A., and Barber, J. P., *The Scaling of Bird Impact Loads*, Air Force Flight Dynamics Laboratory, Wright-Patterson Air Force Base, Ohio 45433-6553, AFFDL-TR-79-3042, March 1979.
22. Parker, J. Y., *Measurement of Impact Bird Pressure on a Flat Plate*, Arnold Engineering Development Center, Arnold Air Force Station, Tennessee 37389, AFDC-TR-79-14.
23. Heath, J. B. R., Gould, R. W., and Cowper, C. R., *Momentum Transfer in Bird Impacts*, National Aeronautical Establishment, National Research Council, Ottawa, Canada, LTR-ST-1257, April 1981.
24. Challita, A., and West, B. S., *Effects of Bird Orientation at Impact on Load Profile and Damage Level*, Air Force Wright Aeronautical Laboratories, Wright-Patterson Air Force Base, Ohio 45433-6553, AFWAL-TR-80-3009, June 1980.
25. Challita, A., *Validation of a Bird Substitute for Development and Qualification of Aircraft Transparencies*, Air Force Wright Aeronautical Laboratories, Wright-Patterson Air Force Base, Ohio 45433-6553, AFWAL-TR-80-3098, October 1980.
26. Kolodziejczyk, Capt. Peter, *Evaluation of the Birdstrike Threat to the F-15 Present Fleet, Rapid Deployment Force, and Dual Role Fighter Transparencies*, Aeronautical Systems Division, Wright-Patterson Air Force Base, Ohio 45433, ASD-TR-84-5026, September 1984.
27. Dote, H., and Theodore, K. T., *"Structural Analysis and Test Space Shuttle Orbiter Window System," AIAA/ASME/ASCE/AHS 21st Structures, Structural Dynamics, and Materials Conference*, May 1980, Seattle, Washington, AIAA Paper Number ARC-0810.

RESPONSE OF TRANSPARENCIES TO INTENSE THERMAL RADIATION

Robert G. Oeding  
PDA Engineering

## RESPONSE OF TRANSPARENCIES TO INTENSE THERMAL RADIATION

Robert G. Oeding  
PDA Engineering  
2975 Redhill Avenue  
Costa Mesa, CA 92626

### ABSTRACT

An analysis technique is described which predicts the one-dimensional temperature response and the spectral transmittance of multilayer composite transparencies suddenly exposed to an intense thermal radiative flux. The effects of conductive and radiative energy transfer within each layer of the transparency, as well as convective energy transfer at the exterior surfaces, are considered. The radiative energy transfer model is spectral-dependent in order to treat realistic thermal radiation sources, reflection and absorption in real materials, and reflection from surface coatings.

The technique is capable of treating temperature dependent thermal and optical properties. The internal heat generation from electrical thin-film heaters is also considered in the thermal response analysis. The transient temperature solution is computed using a finite-difference algorithm. The analytical techniques have been incorporated in a computer code which is operational on both main-frame and personal computers.

The analytical model has been used to predict the thermal response of composite transparency cross sections exposed to intense thermal radiation. Results include transient temperature distributions within the transparency as well as the spectral-dependent radiative fluxes transmitted and reflected by the transparency. The effects of key design parameters on thermal response are examined. Comparisons with experimental measurements are also included.

## INTRODUCTION

Transparencies utilized in modern aircraft and ground vehicles are designed for optimum crew visibility and impact protection. Thus, they are characterized by high optical transmittance in the visible region of the spectrum (i.e. wavelengths from 0.4 to 0.7  $\mu\text{m}$ ) and by thick composite cross sections for birdstrike and/or ballistics protection. Although solar transmittance affects the cockpit environment, the thermal response of such transparencies to solar heating is not a serious concern due to the relatively low ambient solar heat flux. Operational temperatures experienced by typical transparencies are usually well below thermal design limits.

However, if these transparencies are exposed to intense thermal radiation from an explosive fireball or other high energy source, the response of thick composite transparencies becomes an important issue. This response includes both the thermal response of the transparency as well as the intensity and spectral characteristics of the thermal flux that is transmitted to the crew station. The spectral-dependent absorption, reflection and dissipation of this thermal radiation within the transparency cross section is critical to its performance. The ability to predict the indepth temperature response of critical materials is important in designing thermally hardened transparencies and defining crew station environments.

The response of semi-transparent materials exposed to thermal radiation is characterized by simultaneous conductive and radiative energy transfer within a multilayer composite with convective transfer at the boundaries. In addition, radiative energy transfer is spectral-dependent and may also be a function of material temperature. Both absorption, which may be significant in the ultraviolet (UV) and the infrared (IR) regions, and reflectivity at interfaces (including specialized optical coatings) are highly dependent on wavelength. Average spectral properties (e.g. gray body assumptions) are not adequate in modeling these radiative transfer effects.

This paper describes the STRAW (Spectral-dependent Thermal Response of Aircraft Windscreens) analysis model developed by PDA (References 1 and 2) and designed to treat conduction, convection, and spectral-dependent radiant energy transfer in composite transparencies. The model which is operational on both mainframe and personal computers has proved to be a useful tool in designing thermally hardened transparencies.

## ANALYTICAL MODEL

The transparency consists of an absorbing multilayer solid at a specified initial temperature. It is exposed to an intense radiative heat flux on one side and to convective heat transfer on both external surfaces. Inputs include the geometry, material properties, and thermal environment of the transparency. The primary results include predictions of (1) the spectral transmittance (and reflectance) history and (2) the temperature profile histories through the transparency. The key elements of the analytical model are described below including the important assumptions, basic equations, required inputs and solution procedures.

### General Approach

The interaction of thermal radiation with the composite transparency is treated as one-dimensional with the thermal flux incidence normal to the outer surface. Although the angle of incidence may vary, the normal incidence case represents a conservative approach in view of reflectivity effects and provides a tractable mathematical model. Figure 1 illustrates the general



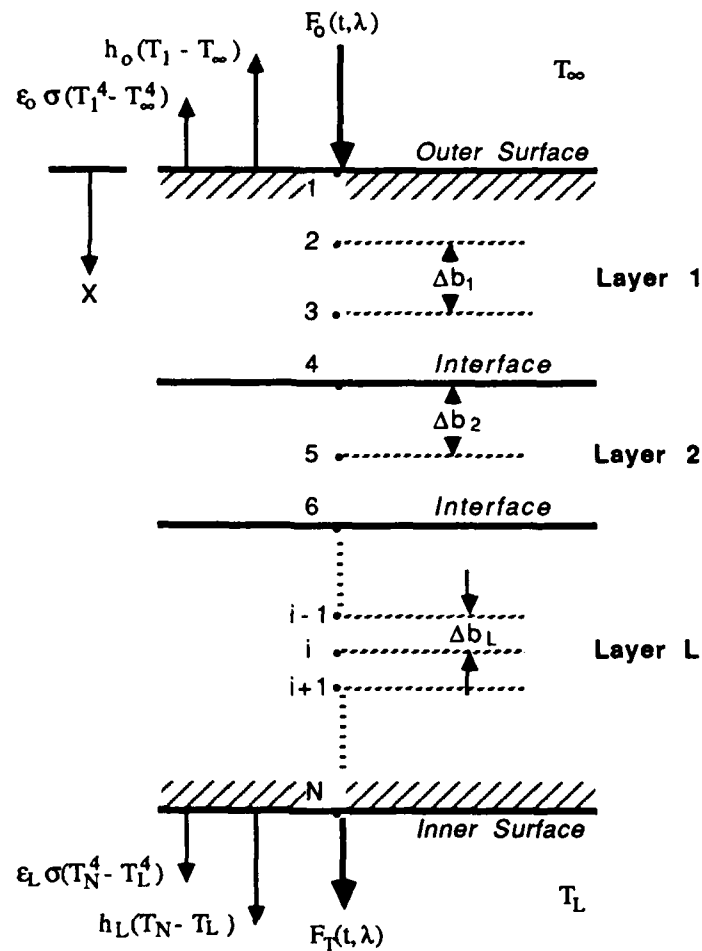


Figure 1. One-dimensional Composite Transparency Model

cross section which is composed of multiple layers having specific physical, thermal, and optical characteristics and interfaces with spectral-dependent reflectivities. Each layer is subdivided into nodes of thickness  $\Delta b_i$ . The nodes are numbered sequentially from front to back and each layer has a minimum of two nodes.

The semi-transparent multilayer solid as shown in Figure 1 is initially at a specified temperature  $T_0(x)$  and is suddenly exposed to a radiative heat flux  $F_0(t, \lambda)$ . The incident radiative flux is assumed to occur at the outer surface. However, convective heat transfer and radiant emission can be specified at both the inner and outer surfaces, and heat sources (or sinks) can be impressed on any node. Contact thermal resistance at interfaces between composite layers, if significant, may be treated as an additional layer.

The governing equation for temperature distribution  $T(x, t)$  in the composite transparency is

$$\frac{\partial T}{\partial t} = \alpha \frac{\partial^2 T}{\partial x^2} - \frac{\alpha}{k} \frac{\partial q_r}{\partial x} \quad (1)$$

where  $\alpha = k / \rho C_p$  is the thermal diffusivity,  $k$  is the thermal conductivity,  $\rho$  is the density,  $C_p$  is the specific heat, and  $q_r$  is the spectrally integrated radiant flux. The first term on the right hand side is the conduction term and the second term is a source term that represents the absorbed radiant energy. In addition to the governing equation, energy balances at the exterior surfaces, interfaces, and at internal heat sources (e.g. thin-film heater) are required. The specific equations for these boundary conditions are presented below in the nodal temperature formulations.

Since the temperature of the transparency for practical situations will be much lower than that of the thermal source, in-depth radiant emission is ignored in the thermal response equation and re-radiation of absorbed energy is considered to occur from the outer surfaces of the transparency only. This assumption has no significant effect on the internal temperature distribution but greatly simplifies the spectral-dependent radiation transfer calculations. Also, convective heating or cooling is permitted at the boundaries in order to simulate the thermal effects of an aerodynamic flow and cabin cooling. Convective heat transfer coefficients and interior/exterior air temperature are required inputs to compute convective effects.

The solution to the thermal response equations requires two basic models, (1) a radiation transfer model to provide the radiation source terms (as well as the transmitted radiant energy distribution) and (2) a numerical model for the solution of the temperature response equation presented above. For the case of constant optical properties (i.e. absorptivity and reflectivity), the radiation transfer solution is independent of the thermal response model and will only vary with the incident flux. If temperature dependent optical properties are considered, the radiation transfer and temperature response solutions must be obtained simultaneously.

### Radiation Transfer Model

The source of the radiant energy flux is assumed to be a blackbody at a specified temperature. For solar and similar high temperature thermal sources, a 6000°K blackbody spectrum is used as shown in Figure 2. The spectral blackbody emissive power distribution is normalized. The peak energy flux occurs at approximately 0.5  $\mu\text{m}$  and nearly all of the energy lies in the visible and near IR regions of the spectrum below a wavelength of 2.0  $\mu\text{m}$ . For thermal response calculations, the incident radiant energy spectrum is described by a series of discrete wavebands. Table 1 presents a 14 waveband model which approximates the 6000°K spectrum. The table includes the waveband, mean wavelength and fraction of incident energy contained within each band.

In order to solve the temperature response equation, the radiative heat flux distribution must be determined throughout the transparency at each time point. For a single layer, analytical expressions for the apparent reflectivity and apparent transmissivity (Reference 3) are as follows:

$$R = R_0 + \frac{(1 - R_0)^2 R_i \tau^2}{1 - R_0 R_i \tau^2} \quad (2)$$

$$T = \frac{(1 - R_0)(1 - R_i) \tau}{1 - R_0 R_i \tau^2} \quad (3)$$

Table 1. Waveband Model

Band No.	Waveband (microns)	Mean Wavelength (microns)	Fraction of Total Energy
1	0.130 - 0.366	0.314	0.1
2	0.366 - 0.446	0.408	0.1
3	0.446 - 0.483	0.465	0.05
4	0.483 - 0.520	0.502	0.05
5	0.520 - 0.558	0.539	0.05
6	0.558 - 0.597	0.578	0.05
7	0.597 - 0.639	0.618	0.05
8	0.639 - 0.685	0.662	0.05
9	0.685 - 0.735	0.710	0.05
10	0.735 - 0.791	0.763	0.05
11	0.791 - 0.932	0.855	0.1
12	0.932 - 1.144	1.024	0.1
13	1.144 - 1.564	1.308	0.1
14	1.564 - 9.300	2.078	0.1

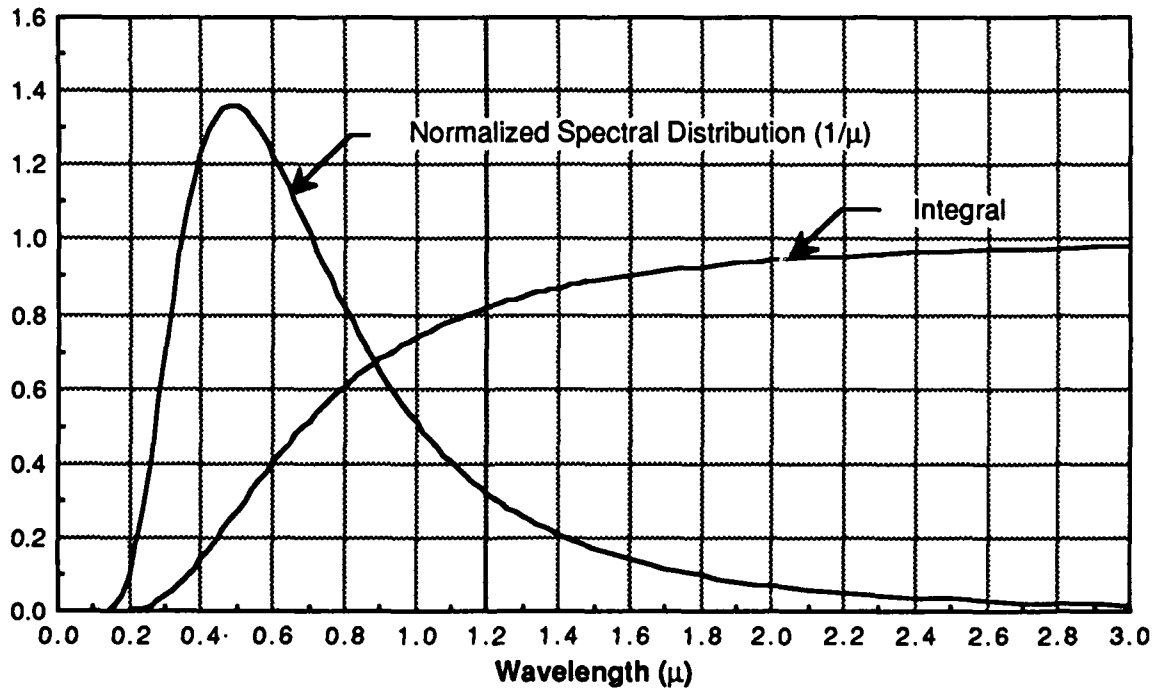


Figure 2. Spectral Blackbody Emissive Power - 6000°K Source

where  $R_0$  and  $R_1$  are the reflectivities at front and back surfaces, respectively.  $\tau$  is the internal transmissivity given by  $\tau = e^{-aL}$  where "a" is the absorptivity and L is the thickness of the layer.

For this single layer, the radiation source term appearing in equation (1) is given by the following expression (Reference 4):

$$Q(x) = \frac{\partial q_r}{\partial x} = F_0 a (1 - R_0) \left[ \frac{e^{-ax} + R_1 e^{-a(2L-x)}}{1 - R_0 R_1 e^{-2aL}} \right] \quad (4)$$

where  $F_0$  is the incident flux and "x" is the position within the layer as measured from the front surface. For spectral dependent absorptivity and reflectivity, the right hand side of equation (4) is a sum over all the discrete wavebands.

For multiple layers, the internal radiant flux is determined by an approximate method which calculates the fraction of incident radiant flux passing to each subsequent layer (forward-pass) after calculating the effects of absorption and reflectance within the layer, as noted above. After the forward-pass is completed, a reverse-pass is performed to calculate reflected energy from the back-most layer towards the forward-most layer. The radiant flux at any point within the transparency is based on the total radiant flux from the forward and reverse passes. This calculation is performed for each discrete waveband with the incident flux weighted by the plankian energy fraction (see Table 1) in the given waveband. The multilayer absorption, transmission, and reflection model is illustrated in Figure 3 for a three layer transparency.

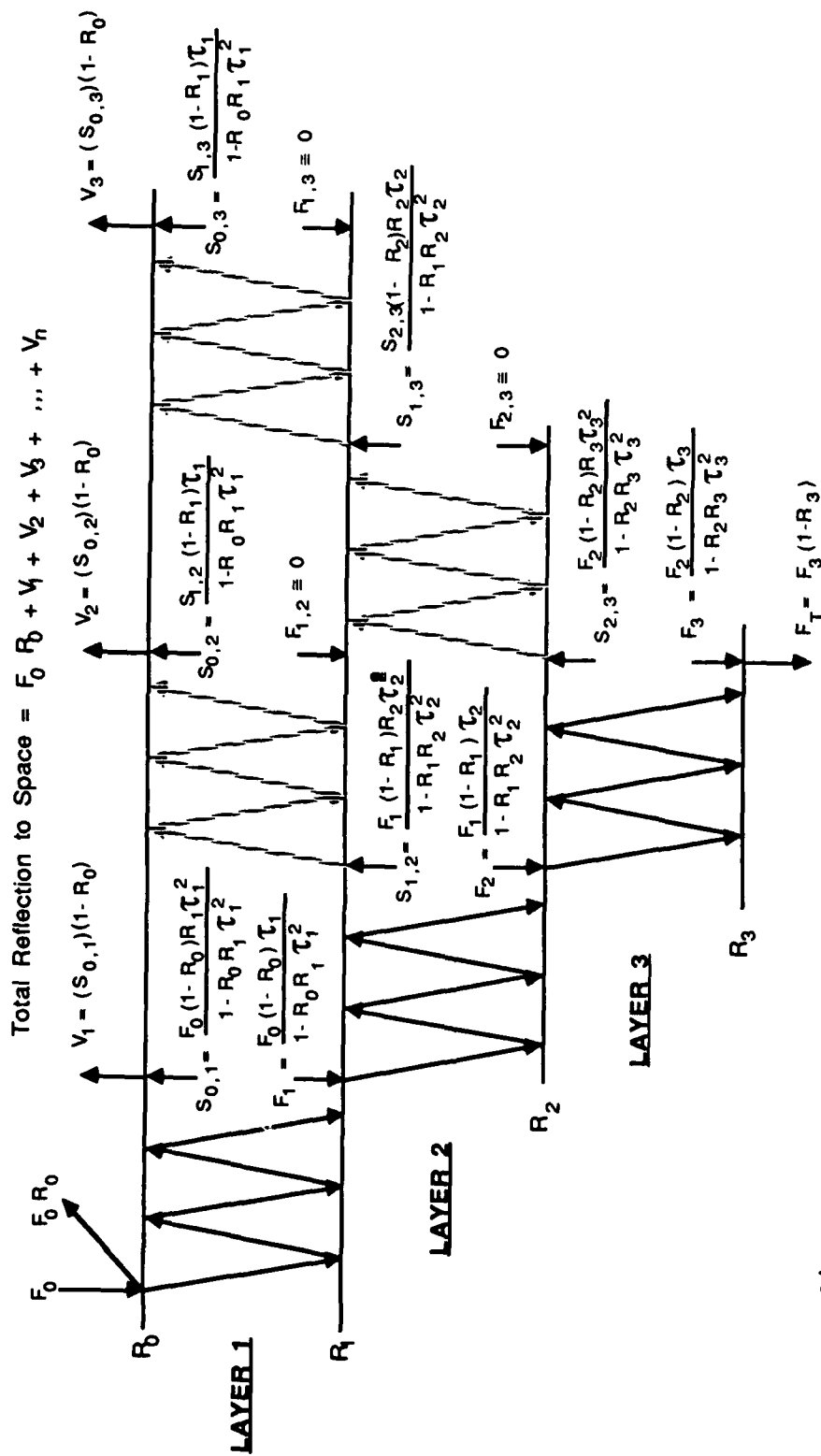
When a medium is optically thick ( $a \Delta x > 1$ ), the radiation within it can travel only a short distance before being absorbed. A numerical problem can arise in such cases with the finite difference approximation to Equation (4). If a high absorption coefficient is specified in conjunction with a wide nodal spacing such that  $a_i \Delta b_i > 1$ , the source term calculated at the node centroid is greatly diminished due to extinction in traversing the half-node thickness. This could give an erroneous value for absorbing flux, even a zero value for a nearly-opaque medium. The analytical model contains logic to identify this condition and in such cases the Equation (4) formulation for  $a \Delta b > 1$  is changed to

$$Q(x) = \frac{\partial q_r}{\partial x} = \frac{F_0 (1 - R_0)}{\Delta b} [e^{-a(x - \Delta b / 2)} - e^{-a(x + \Delta b / 2)}] \quad (4a)$$

Here, the absorbed flux at nodal location x is taken as the difference between the fluxes upstream and downstream of the node. The absorption effects due to multiple reflections at the layer interfaces are ignored since they become insignificant with high absorption coefficients. Thus, in an opaque medium ( $a \rightarrow \infty$ ) the flux will be completely absorbed within the first node.

### Temperature Response Model

The partial differential equation for heat conduction, Equation (1), may be expressed as a lumped parameter system by taking a heat balance at each node. For a 1-D system, conduction exists only between adjacent nodes. At the surface boundaries, the equations include the surface boundary conditions. The time derivatives of temperature at a specific time point are as follows:



note:  $\tau_i = e^{-a_i L_i}$  (Layer "i" internal transmissivity)  
 Solid Rays = Forward Pass  
 Dashed Rays = Reverse Pass

Figure 3. Multilayer Absorption, Transmission, Reflection Model (3-Layer Model Illustrated)

### Outer Surface Node (1)

$$\frac{dT_1}{dt} = \frac{G_1}{C_1}(T_2 - T_1) + \frac{h_0}{C_1}(T_\infty - T_1) + \frac{Q_1}{C_1} + \frac{\epsilon_0 \sigma}{C_1}(T_\infty^4 - T_1^4) \quad (5)$$

### Interior Node (i)

$$\frac{dT_i}{dt} = \frac{G_i}{C_i}(T_{i+1} - T_i) + \frac{G_{i-1}}{C_i}(T_{i-1} - T_i) + \frac{Q_i}{C_i} \quad (6)$$

### Back Surface Node (N)

$$\frac{dT_N}{dt} = \frac{G_{N-1}}{C_N}(T_{N-1} - T_N) + \frac{h_L}{C_N}(T_L - T_N) + \frac{Q_N}{C_N} + \frac{\epsilon_L \sigma}{C_N}(T_L^4 - T_N^4) \quad (7)$$

where  $G_i$  is the conduction coupling from node  $i$  to  $i+1$  ( $k/\Delta b$ ),  $C_i$  is the thermal capacitance of node  $i$  ( $\rho C_p \Delta b$ ), and  $Q_i$  is the radiation source term for the  $i^{\text{th}}$  node (i.e.  $\partial q_r/\partial x$ ) and is a sum over all of the discrete wavebands. For the interface nodes,  $Q_i$  and  $C_i$  represent the sum of contributions from the volumetric fractions of the nodes on either side of the interface. For the outer surface node,  $h_0$  is the convective heat transfer coefficient,  $T_\infty$  is the external temperature, and  $\epsilon$  and  $\sigma$  are the surface emissivity and Stefan-Boltzmann constant, respectively.

The equation for the back surface node includes re-radiation and convection terms as shown in equation (7) with a convective coefficient ( $h_L$ ), emissivity ( $\epsilon_L$ ) and internal temperature,  $T_L$ . Also, a discrete time-dependent heat source may be added to any node in order to simulate a thin film heater or other similar energy sources. The discrete energy source is not included in the above equations but is handled in the same manner as the radiation source term.

The temperature response equations (5) through (7) are solved by a forward-backward finite-difference method (Crank-Nicolson Approximation). Knowing all nodal temperature values at some time point,  $n$ , temperatures at the next time point,  $n+1$ , are obtained from

$$T_{i,n+1} = T_{i,n} + \left[ \frac{dT_i}{dt} \right]_{n,n+1} \Delta t$$

where  $i=1,2,\dots,N$  are the nodes;  $T_{i,n}$  is a known temperature at each node; and  $\Delta t$  is the time interval between  $n$  and  $n+1$ . The time derivative of temperature at each nodal point is obtained by half forward differencing and half backward differencing, and may be expressed for a 1-D problem as follows:

$$\left[ \frac{dT_i}{dt} \right]_{n,n+1} = \frac{T_{i,n+1} - T_{i,n}}{\Delta t} = \sum_{j=i-1}^{i+1} \frac{G_{i,j,n}}{2C_i} (T_{j,n+1} + T_{j,n} - T_{i,n+1} - T_{i,n}) + \frac{Q_{i,n} + Q_{i,n+1}}{2C_i}$$

The method of solution involves evaluating the time derivative of temperature for each node at time  $n$  (forward differencing) and time  $n+1$  (backward differencing) and using the average of the two. Knowing the temperatures at a current time point,  $n$ , the procedure is as follows:

(1) Compute the  $[dT/dt]$  terms at the time point,  $n$ ;

$$\frac{dT_{i,n}}{dt} = \frac{G_i}{C_i}(T_{i+1,n} - T_{i,n}) + \frac{G_{i-1}}{C_i}(T_{i-1,n} - T_{i,n}) + \frac{Q_{i,n}}{C_i} \quad (8)$$

(2) Predict a temperature at the next time point,  $n+1$ ;

$$T_{i,n+1} = T_{i,n} + \left[ \frac{dT_{i,n}}{dt} \right] \Delta t \quad (9)$$

3) Compute the  $[dT/dt]$  terms at the time point,  $n+1$ , using the predicted temperature;

$$\frac{dT_{i,n+1}}{dt} = \frac{G_i}{C_i}(T_{i+1,n+1} - T_{i,n+1}) + \frac{G_{i-1}}{C_i}(T_{i-1,n+1} - T_{i,n+1}) + \frac{Q_{i,n+1}}{C_i} \quad (10)$$

(4) Compute nodal temperatures at next time point,  $n+1$ ;

$$T_{i,n+1} = T_{i,n} + \frac{1}{2} \left[ \frac{dT_{i,n}}{dt} + \frac{dT_{i,n+1}}{dt} \right] \Delta t \quad (11)$$

where  $\Delta t$  is the stable time step for the most limiting node given by

$$\left[ \Delta t < \frac{C_i}{G_i + G_{i-1}}; \frac{C_1}{G_1 + h_0}; \text{ and } \frac{C_N}{G_{N-1} + h_L} \right]$$

The solution technique described above requires computational time steps less than the time constant for the most limiting node because the forward differencing step, Equation (8), is calculated explicitly. The explicit solution method is efficient for thermal pulse problems since the transients tend to be short duration and, for low conductivity materials, the stable time steps tend to be reasonable.

## COMPUTER CODE

The analytical model described above is incorporated into the STRAW fortran computer code which is currently operational on PDA Vax system, the Macintosh Plus PC and the IBM AT or compatible PCs. The computer code accepts input data describing the geometry, thermal/radiative properties, radiant thermal environment, the ambient boundary conditions, and the output formatting. The STRAW code is designed to predict the thermal response and spectral transmittance of composite transparencies exposed to a radiant thermal pulse. The program computes the transient temperature distribution in the composite using a combined conduction, convection, and spectral dependent radiative energy transfer analyses. The program also determines the magnitude and spectral characteristics of the transmitted and reflected energy. The computational logic and basic code capabilities are described below.

### Program Logic

The basic program logic is as follows:

- (1) Read in all properties data for each layer (e.g. geometry,  $k$ ,  $C_p$ ,  $a(\lambda)$ ,  $R(\lambda)$ ,  $h_o$ , etc.)
- (2) Calculate fraction of incident radiant flux available to subsequent layer (forward-pass) after recognizing the effects of absorption and reflection within the layer. Reverse pass to calculate reflected energy from back-most layer towards forward-most layer. Perform calculations for each discrete waveband, with incident flux weighted by the plankian energy fraction in the given waveband (e.g. see Table 1).
- (3) Calculate the radiant source term at each nodal location representing the sum of absorbed fluxes during the forward and reverse passes. Sum the contributions over all discrete wavebands to obtain the total energy source for the temperature solution.
- (4) Update the time (using stable time step or smaller input value).
- (5) Scale the source terms for flux magnitude at current time.
- (6) Solve for the thermal response (Equations 8 through 11) based on source terms, conduction, and surface boundary conditions (surface convection and emission).
- (7) If time = print time, output nodal temperatures and spectral transmittance/reflectance distributions to appropriate output files.
- (8) If time < final time, go to step (2) if layer absorption coefficient is temperature dependent. If constant radiative properties are used, go to step (4).

As currently configured, STRAW will treat temperature dependent absorption coefficients,  $a(t,\lambda)$ , and temperature dependent thermal properties,  $k(T)$  and  $C_p(T)$ . In addition, time-dependent energy sources may be added to any of the nodes as previously noted. The key computer code features are summarized below.

#### Code Features

- 1-D thermal and optical model.
- Multilayer transparencies with physical, thermal and optical properties defined in each layer.
- Interfaces and surface coatings with spectral dependent reflectivities.
- Treats media of any optical thickness ( $a*L$ ) from fully transparent to completely opaque.
- Incident radiant flux vs time profile on front surface.
- Impressed flux vs time profiles on one or more nodes.
- Convective heat transfer on front and back surfaces.
- Emission from front/back surfaces included based on user-defined emissivities.
- Each layer subdivided into user defined number of nodes.
- Temperature dependent optical properties flag to activate built-in function.
- Temperature dependent thermal properties for  $C_p$  and conductivity.
- Ambient sink temperatures on front/back surfaces for convective and radiant couplings.



## SAMPLE CALCULATIONS

Sample analyses were conducted for simplified windscreen cross sections which are initially at a uniform temperature of 80°F and are suddenly exposed to a thermal pulse. The pulse is rectangular (i.e. constant flux of 50 cal/cm<sup>2</sup>sec) with a 1 second duration. Thus, a total fluence of 50 cal/cm<sup>2</sup> is incident on the windscreen. Thermal properties are assumed to be constant and optical properties are only a function of wavelength for these calculations. The spectral distribution of the incident thermal flux is assumed to be that of a 6000 °K blackbody (Figure 2).

The windscreen geometry is presented in Figure 4 for three different cross sections. In order to reduce the number of layers and associated complexity for these sample calculations, the interlayers which would normally be present in the windscreen cross section were ignored. The simplified baseline windscreen is composed of an outer ply of soda lime (SL) glass and a polycarbonate (PC) structural ply. The other two configurations represent possible approaches to improving thermal performance of the baseline windscreen through the addition of an IR absorbing (0.07-in.) tinted soda lime (TSL) glass ply and a wide-band-hot-mirror (WBHM) coating which is a multilayer IR reflective coating. The goal of the modified cross sections is to reduce total transmittance while also reducing the energy absorbed by the windscreen. One cross section has the WBHM on the outer surface which is optimum for reflecting IR energy while the other has the WBHM on the inner surface of the TSL ply which offers better protection for the reflective coating. The analysis provides basis for evaluating thermal performance improvements and selecting the optimum cross section.

The sample analyses ignored convective heat transfer at the outer surfaces and utilized a total of 60 nodal points to describe the internal temperature distribution with 25 nodes each in the SL and PC plies and 10 nodes in the TSL ply. The initial temperature was specified as a uniform 80°F (300°K) and an initial time step of 0.006 seconds was selected for the numerical calculations. Three cases were analyzed corresponding to the three cross sections shown in Figure 4.

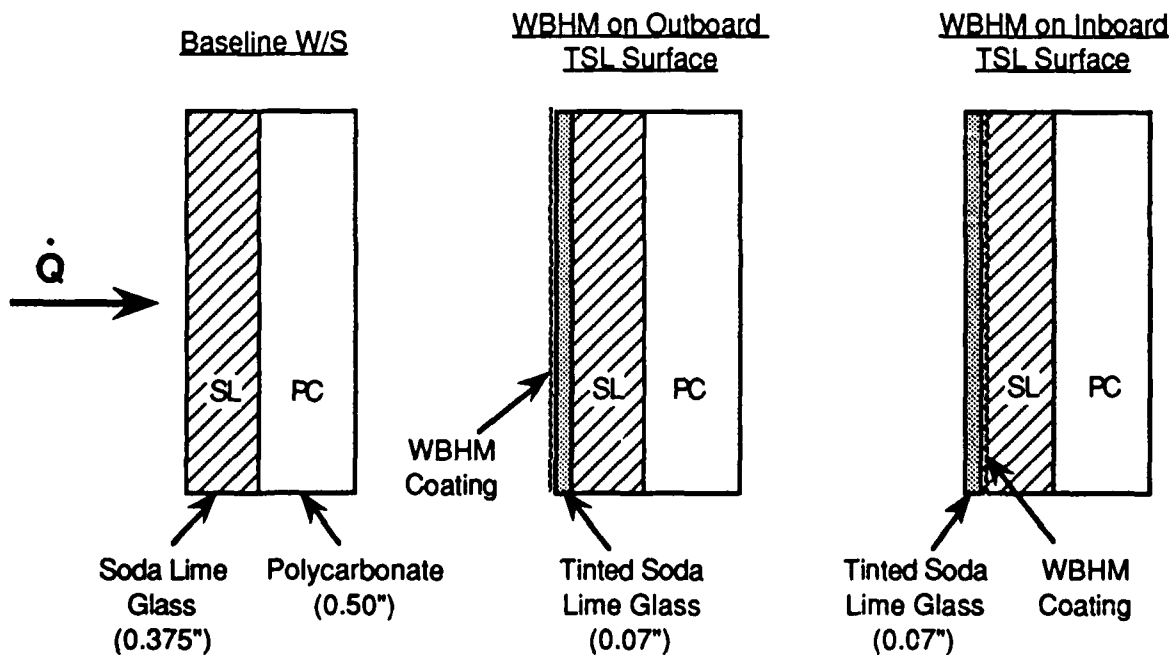


Figure 4. Windscreen Cross Sections for Sample Calculations

The results of the analyses included the temperature response of the windscreen as well as both the total (blackbody) and spectral-dependent transmittance. Figure 5 presents a comparison of predicted and measured spectral transmittance for both the baseline, Figure 5(a), and the modified cross sections, Figure 5(b). The predictions were made for each of the 14 wavebands and compared with spectrophotometer measurements. The WBHM coating greatly reduces the transmittance in the near-IR (800 to 1200 nm) as predicted without significantly affecting transmittance of the visible spectrum. The location of the WBHM on the inner versus outer TSL surface, however, had very little effect on the spectral transmittance. Thus, only one comparison is shown in Figure 5 for the modified cross sections. Within the limitations of the discrete waveband model, the predicted spectral transmittance is in good agreement with available measurements.

The predicted radiant energy balance for each cross section is presented in Table 2. Results of blackbody transmittance measurements obtained in a concentrated solar facility are also included and show good agreement with the analysis. Results show that by placing the WBHM on the outer surface of the transparency over 40% of the incident radiant thermal energy is reflected compared to 10% for the baseline cross section. This large increase in surface reflection significantly reduces internal absorption and, hence, internal temperatures. The total energy transmitted by the cross section is reduced from approximately 48% for the baseline to 28% with the best modified cross section. Placing the WBHM on the inner surface of the TSL ply is not as effective (as the outer surface) with only 30% of the total energy reflected. Also, since the TSL ply is exposed to both the incident and reflected fluxes, it absorbs more of the radiant energy than either of the inner two plies resulting in large temperature gradients.

Table 2. Radiant Energy Balance Comparison

Energy Distribution \ Cross Section	Baseline Windscreen	WBHM on Outer Surface	WBHM on Inner Surface
Total Reflected (%)	10.5	41.3	30.6
Absorbed in TSL Ply (%)	-----	5.3	13.9
Absorbed in SL Ply (%)	24.9	12.7	13.1
Absorbed in PC Ply (%)	16.7	12.8	13.2
Total Transmitted (%)	47.9	27.9	29.2
(Measured Transmittance)		(27.6)	

Typical temperature response results are illustrated in Figure 6 for the cross section having the WBHM on the inner TSL surface. Figure 6(a) shows the predicted temperature histories at the windscreen exterior surfaces and internal interfaces. Maximum temperature occurs on the front surface at 1.0 second and approaches 220°F. Figure 6(b) presents predicted temperature profiles through the windscreen at six time points and shows steep temperature gradients in the TSL glass ply.

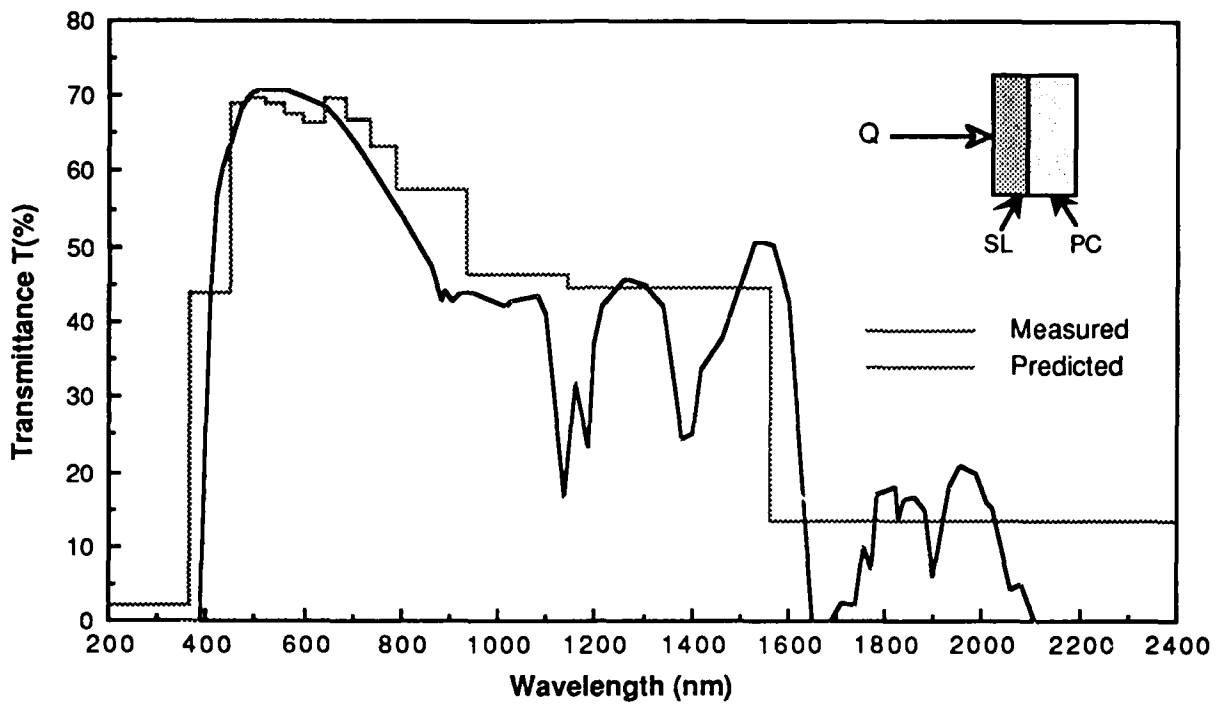
A comparison of the thermal response of the three windscreen cross sections (shown in Figure 4) is presented in Figure 7. Figure 7(a) shows the temperature profiles for each case at a time of 1.0 second from the initiation of the pulse. This corresponds to the peak temperature profile. Figure 7(b) presents temperature profiles after 10 seconds. The temperatures in SL and PC plies are generally lower with the modified cross sections since a significant fraction of the incident energy is reflected by the WBHM. As noted above, the position of the WBHM is important as seen by the large increase in the temperatures of the TSL ply when the WBHM is located inboard. The absorption of both the incident and reflected fluxes within the TSL increases the peak surface temperature by over 80°F compared to the case with the WBHM on the outer surface. With the WBHM on the outer surface, the peak temperature still occurs at the outer surface, but is less than the peak temperature in the baseline windscreen.

## SUMMARY

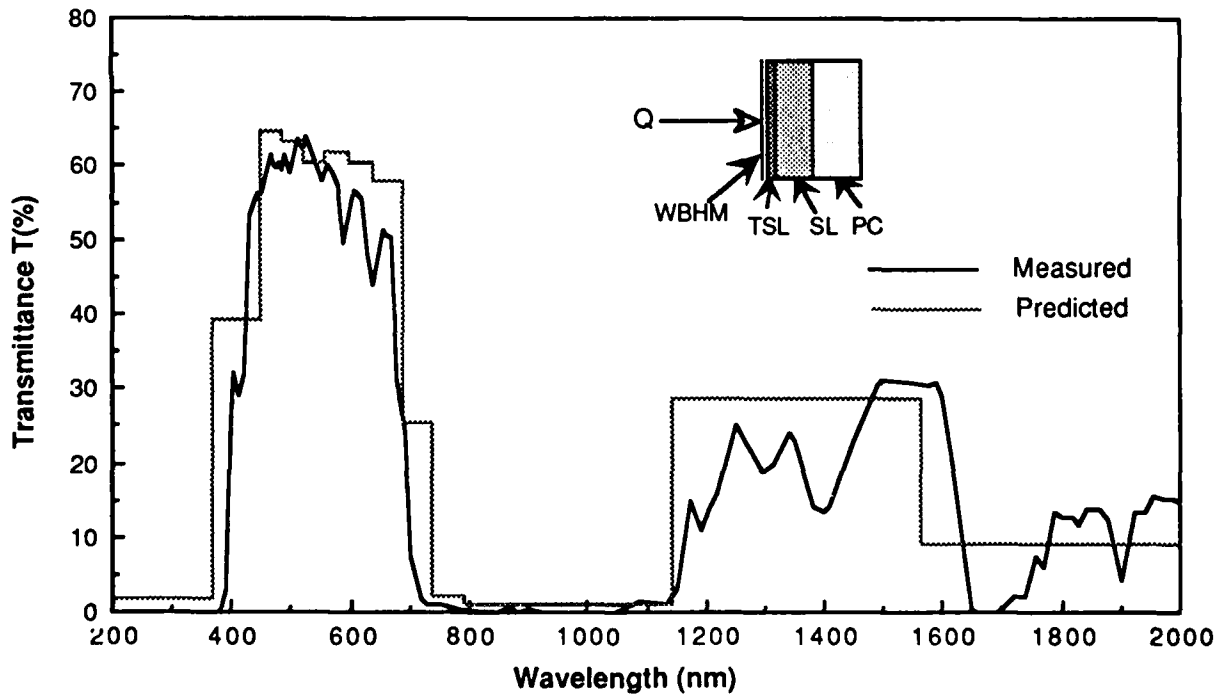
A one-dimensional analytical model has been developed to predict the temperature response and spectral transmittance of composite transparencies exposed to a radiant thermal energy flux. The model treats the simultaneous conductive and radiative energy transfer within the transparency including convective boundary conditions and internal energy sources. The model appears to adequately treat the complex and spectral-dependent interaction between transparency components. Comparisons between predicted transmittance results (both spectral and total) and experimental measurements have shown good agreement. Comparisons of predicted temperature response results with detailed experiment data are needed and are planned as part of the validation of the model.

## REFERENCES

1. Oeding, R.G., "Analytical Model for the Thermal Response of Composite Transparencies", PDA Technical Memorandum TM-4489-232, June 1987.
2. Oeding, R.G. and Diner, A.I., "Users Guide for the Spectral-dependent Thermal Response of Aircraft Windscreens (STRAW) Code", PDA Technical Memorandum TM-4870-256, June 1988.
3. Siegel, R. and Howell, J.R., Thermal Radiation Heat Transfer, McGraw-Hill Book Company, New York, 1981
4. Munson, T.R. and Spindler, R.J., "Transient Thermal Behaviour of Decomposing Materials, Part I: General Theory and Application to Convective Heating", IAS Paper No. 62-30, Presented at the Institute of the Aerospace Sciences 30th Annual Meeting, January 1962.

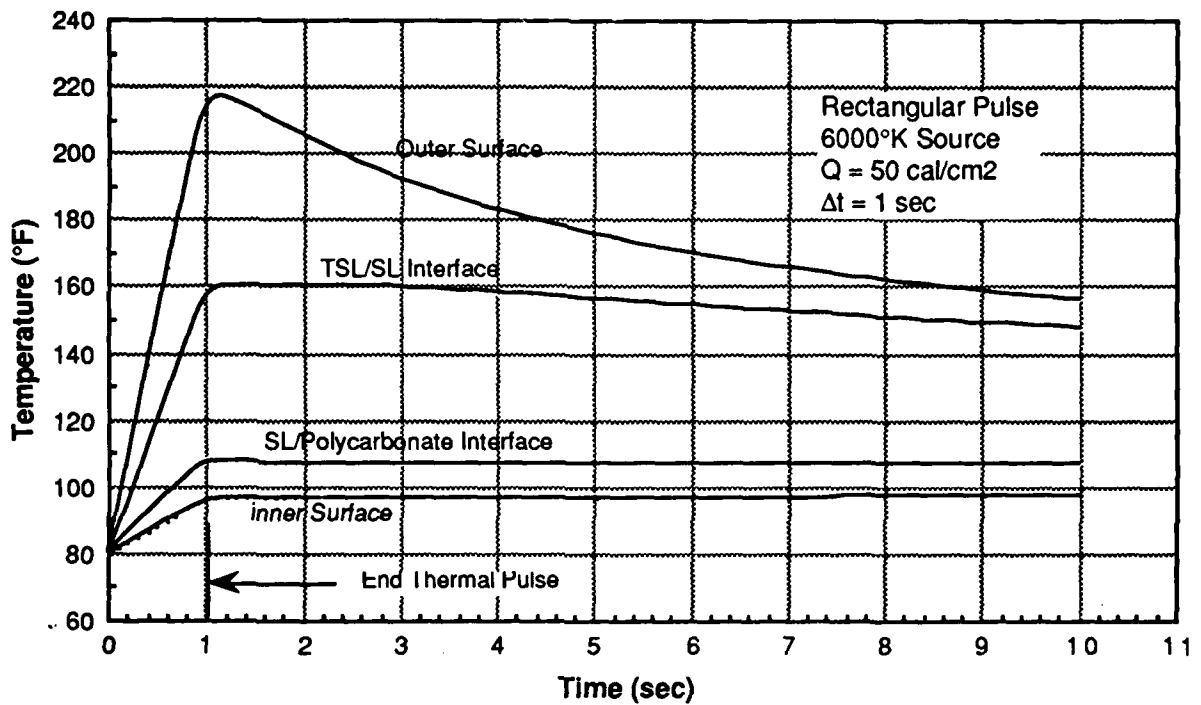


(a) Baseline Cross Section

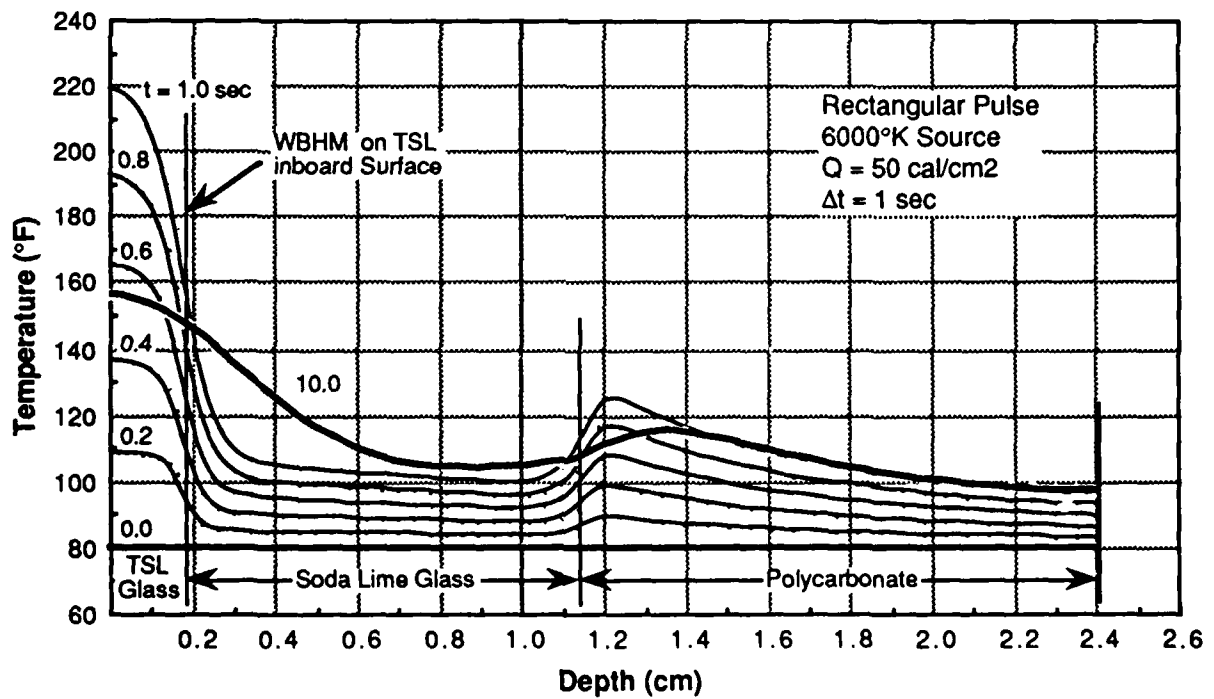


(b) Response Time = 10 seconds

Figure 5. Spectral Transmittance Comparisons

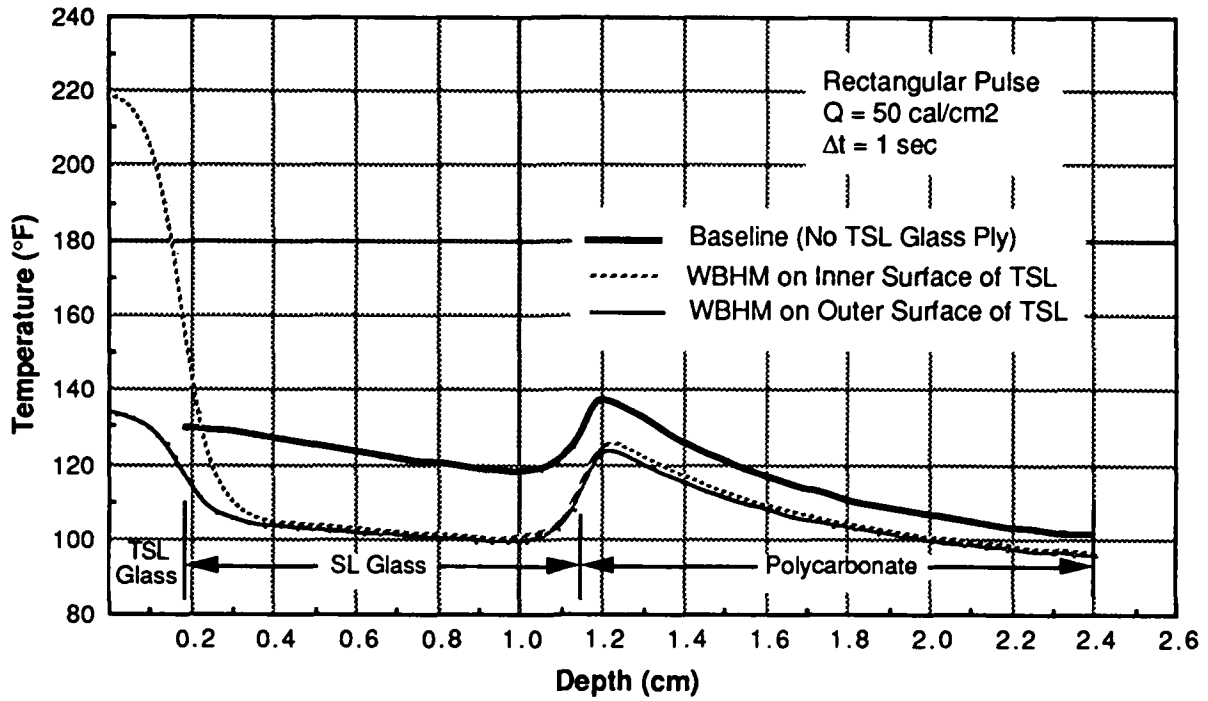


(a) Temperature Histories

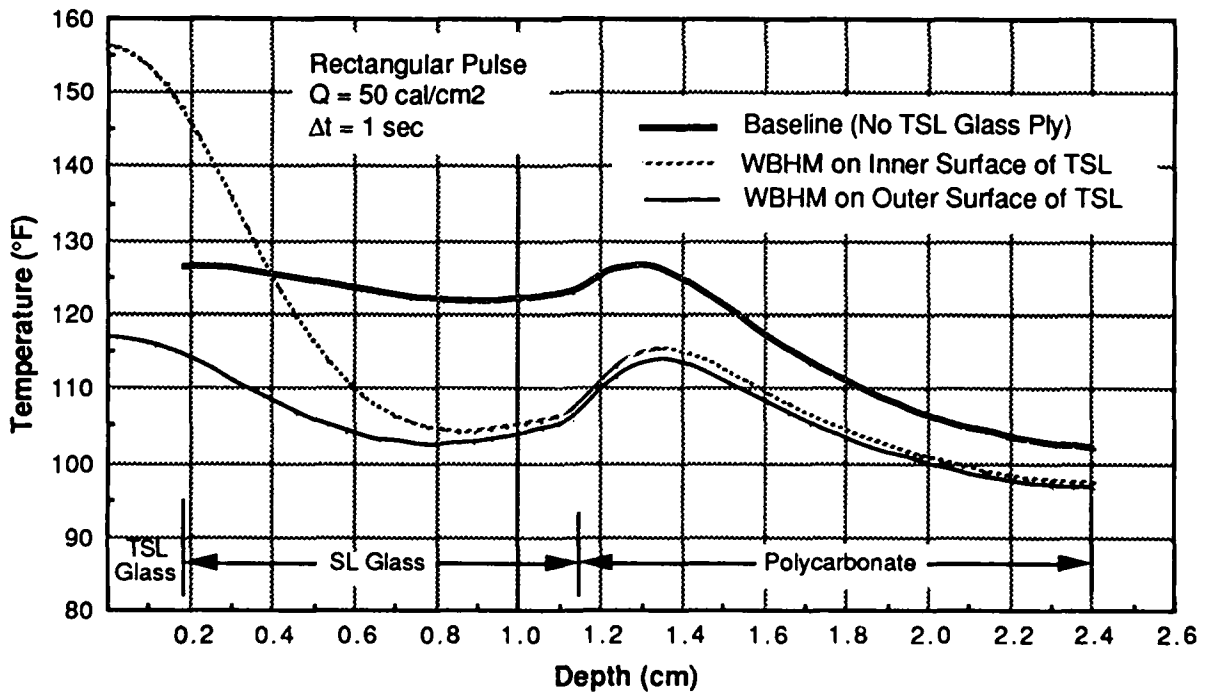


(b) Temperature Profiles

Figure 6. Windscreen Thermal Response



(a) Response Time = 1.0 second



(b) Response Time = 10 seconds

Figure 7. Temperature Profile Comparison

ANALYTIC ASSESSMENT OF BIRD IMPACT RESISTANT T-46A AIRCRAFT  
WINDSHIELD SYSTEM DESIGNS USING MAGNA  
(MATERIALLY AND GEOMETRICALLY NONLINEAR ANALYSIS)

Robert E. McCarty  
Flight Dynamics Laboratory

Paul Landry  
Lockheed Aeronautical Systems



ANALYTIC ASSESSMENT OF BIRD IMPACT RESISTANT  
T-46A AIRCRAFT WINDSHIELD SYSTEM DESIGNS USING MAGNA  
(MATERIALLY AND GEOMETRICALLY NONLINEAR ANALYSIS)

1 Robert E. McCarty

Crew Protection Branch  
Vehicle Subsystems Division  
Air Force Wright Aeronautical Laboratories  
Wright-Patterson Air Force Base, Ohio 45433

2 Paul Landry

Lockheed Aeronautical Systems Company  
Burbank, California

ABSTRACT

To reduce the level of full scale bird impact testing required in the development of aircraft transparency systems, the Flight Dynamics Laboratory (AFWAL/FD) initiated development of computer analysis methods to simulate dynamic structural response to bird impact loading. Previously, many iterations of full scale fabrication and bird impact testing were required to qualify new transparency designs. As an example, four years and \$5M were required to develop a new F-111 windshield in the early 1970's.

Development of the MAGNA computer program was sponsored by AFWAL/FD through 1982, and its application to the aircraft transparency bird impact problem was largely validated via in-house research conducted through 1985. The first significant Air Force systems application of MAGNA was for the Next Generation Trainer Aircraft, the T-46A.

In late 1985, AFWAL/FD used MAGNA to assess T-46A windshield system designs for bird impact resistance. Eighteen candidate designs were assessed using \$20,000 in supercomputer resources in only six weeks time. The nominal design chosen from all those assessed was fabricated and successfully qualified in the first round of testing conducted in the Spring of 1986, demonstrating order of magnitude savings in cost and time required to develop bird impact resistant aircraft transparency systems.

1 Supervisory Aerospace Engineer

2 Work Done While Employed at Fairchild Republic Company

## INTRODUCTION

### 1. Background

In the late 1960's, the mission profile of Air Force aircraft changed from high altitude, high speed to one of low altitude, high speed. This occurred primarily in response to the development of more effective radar and surface-to-air missile systems, and gave rise to a new and significant operational hazard: bird impact on aircraft transparency systems. Birds are found only rarely at altitudes above 10,000 feet, and since military aircraft transparencies had historically not been designed to withstand bird impact loads, losses of aircraft and aircrew began to occur.

In 1972, the Air Force Flight Dynamics Laboratory (FDL) formed an Advanced Development Program Office for Improved Windshield Systems to address this bird impact problem. Since that point in time, the FDL has participated in the development of successful bird impact resistant windshield and canopy systems for a number of operational aircraft including the A/T-37, A-10, F-111, F-16, F-4, and T-38. In each case however, the design methods used relied heavily upon full scale bird impact testing to develop and qualify successful systems. This approach proved time consuming, and very expensive. For the F-111 transparency system development alone, about 50 design iterations in all were tested at a cost of roughly \$100,000 each, for a total development and qualification cost of \$5,000,000. <sup>1-5</sup> Nearly five years were required to accomplish this development successfully.

To reduce the level of full scale bird impact testing required in the development of new aircraft transparency systems, the FDL formed a new office in 1976 to develop computer analysis methods to simulate the dynamic structural response of transparency systems to bird impact loading. This new office, called the Subsystems Development Group (now the Aircrew Enclosures Group), accomplished the first delivery to the Air Force of a computer analysis system called MAGNA (Materially and Geometrically Nonlinear Analysis) in 1979. <sup>15-18</sup> Additional development of MAGNA was sponsored by the FDL through 1982, and its application to the aircraft transparency bird impact problem was largely validated via FDL in-house research conducted through 1985. <sup>6-13</sup> The first significant Air Force systems application of MAGNA was for the Next Generation Trainer Aircraft, the T-46A shown in Figure 1, and this technical report documents that application.

#### a. System Design Requirements

The original Air Force requirement for the T-46A windshield system was that it provide protection to the aircrew against the impact of a 4 lb bird at 360 knots anywhere on the windshield. Test plans written to qualify the windshield system only required 4 lb bird impact protection for speeds up to 320 knots however. The windshield system design for the T-46A was the responsibility of the prime airframe contractor for the vehicle, Fairchild Republic Company (FRC). Swedlow Incorporated was responsible for

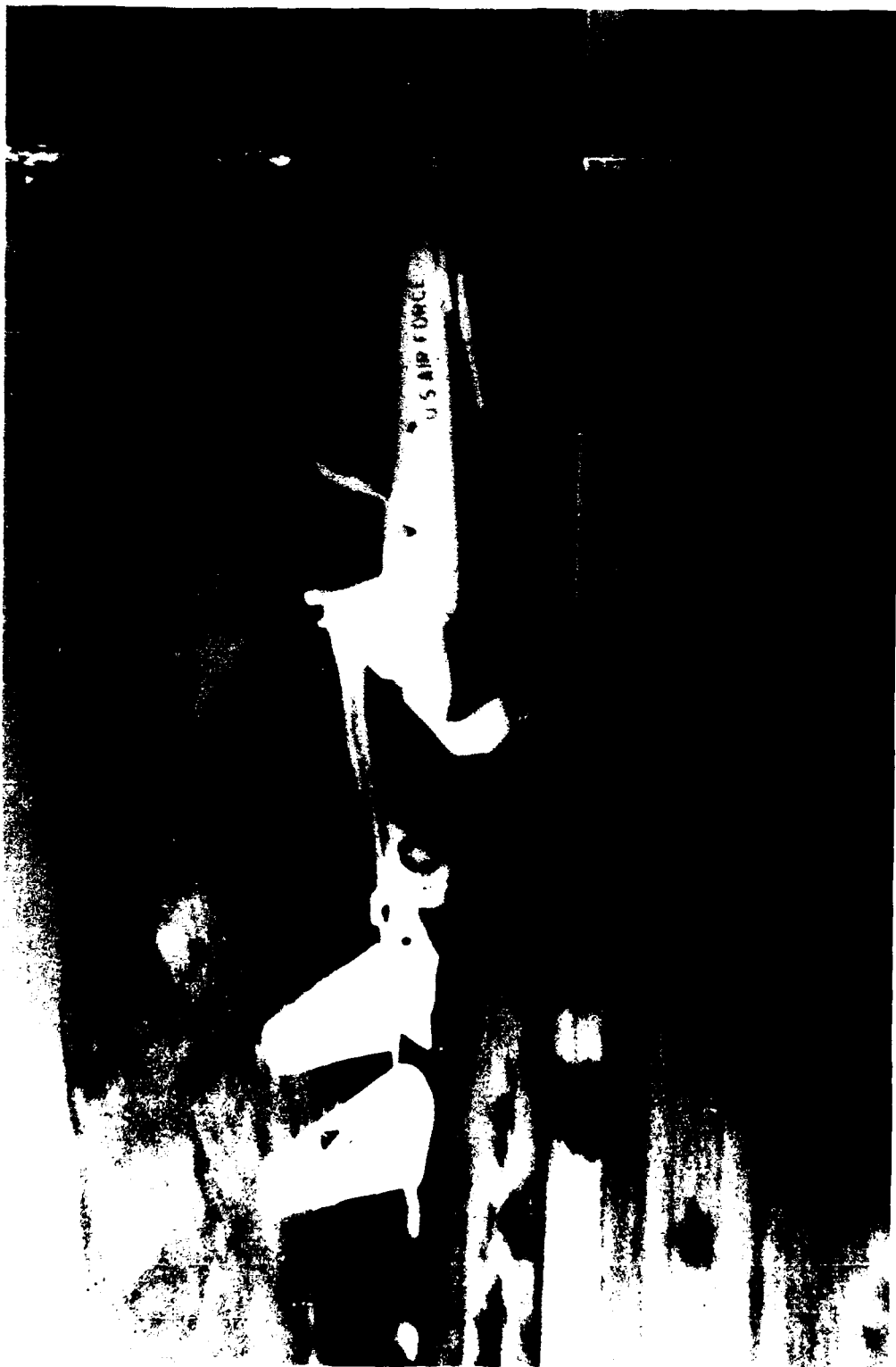


Figure 1. T-46A First Flight Test Vehicle

manufacturing the windshield transparency, but was not responsible for its design. Details of each of several windshield system designs developed by FRC are discussed later.

As a result of technical presentations, papers, and reports generated by the FDL regarding the development and validation of MAGNA, FRC became interested in the application of MAGNA to the development of T-46A windshield system designs. In August 1983, FRC proposed to the T-46A Systems Program Office (T-46A SPO) at Wright-Patterson Air Force Base (WPAFB) that FRC expend a relatively low level of effort in order to assess MAGNA for this application. The SPO authorized the FRC activity and, by July 1984, a number of trial analyses had been conducted by FRC, running MAGNA remotely at the WPAFB Aeronautical Systems Division (ASD) Computer Center from their Farmingdale, New York plant. At the time, all analyses were run on CDC Cyber 845 mainframes at WPAFB.

b. Baseline System Design

By December of 1984, the baseline design for the T-46A windshield system had been developed by FRC and manufactured with the windshield panel being supplied by Swedlow. The first full scale bird impact test, conducted on the Von Karman S-3 Range at the Arnold Engineering Development Center (AFDC) in Tennessee, resulted in failure of the windshield system design. The aluminum bow structure failed, the windshield panel separated from the bow in the region near the centerline, and some bird debris entered the cockpit space. The failure mode of the bow was severe plastic deformation from bending at the root of the windshield attachment flange.

c. Mod I System Design

From a review of the data and films, it was determined that the primary mode of this windshield system failure was bow failure as an arch, and a secondary failure was rotation of the bow where it attached to the transparency. A redesign of the windshield system by FRC, called Mod I, was accomplished by adding a steel reinforcement to cut down on arch bending. The next series of tests were conducted in March 1985, and resulted in substantially more bird matter penetrating the cockpit. Again following a review of the data, it was concluded that the failure resulted from excessive rotation of the ledge supporting the transparency, with the aluminum portion of the bow cross section bending around the steel reinforced portion.

d. Mod II System Design

In a second redesign effort called Mod II, FRC set out to reinforce the attachment point between the windshield panel and its bow support structure. The windshield bow was redesigned by adding steel gussets under the fasteners along the top of the bow. June 1985 testing of the Mod II system resulted in more failures however, with the transparent panel itself failing for the first time. It is important to note at this point that the difficulty which the FRC/T-46A SPO team had in successfully

qualifying a T-46A windshield system design for bird impact resistance was not unusual, and did not in any way indicate shortcomings in either of the two engineering staffs involved. Rather, the difficulty encountered was another in a long series of similar experiences with earlier Air Force systems, all pointing to the complex nature of the problem. Dynamic structural response to bird impact loading is a highly nonlinear, coupled, systems engineering problem which historically has been tackled with largely empirical design methods, and typically has required many expensive and time consuming iterations to solve.

It is to the credit of the FRC/T-46A SPO team that theirs was the first Air Force systems acquisition program for which a new and better approach to developing and qualifying a windshield system was attempted. In June 1985, the T-46A SPO requested support from the Air Force Wright Aeronautical Laboratories (AFWAL) in applying MAGNA to the T-46A windshield system. This request was based upon a review conducted by SPO personnel of earlier work accomplished by the FDL to validate MAGNA for the aircraft transparency bird impact application. <sup>6-13</sup>

The FDL was requested by the T-46A SPO to determine whether or not 4 lb bird impact at 250 knots could fail the Mod I design for the T-46A windshield system. The reason for this request was that the Mod I design had been selected for use on the first flight test vehicle, designated T-1, and that the first few flights for T-1 were to be limited to an airspeed of 250 knots. A number of full scale bird impact tests had already been conducted on the various T-46A windshield system designs as noted above, but the Mod I design had not yet been tested at 250 knots at the target point location believed to be most critical. Preparation for another round of full scale bird impact testing would have involved considerable expense and required a postponement of first flight for T-1, so it was hoped that a MAGNA analysis could be done to certify flight safety for windshield system bird impact in time to meet the schedule for first flight.

It was agreed among all parties involved that if the MAGNA analysis could be accomplished in time, and that if it showed that the T-46A Mod I windshield system design would protect the aircrew against 4 lb, 250 knot bird impact, then T-1 would be released for first flight without that particular windshield system design ever having been tested under those particular impact conditions. This marked a significant milestone in the history of the development and application of the MAGNA computer analysis system because it was the first time that an Air Force systems acquisition program agreed to use computed results instead of full scale qualification test results to certify the bird impact protection of an aircraft transparency system design.

The agreement included the use of AFWAL/FDER developed procedures for key aspects of the analysis such as the mathematical definition of bird impact loading, and the characterization of the transparent plastic materials used in the system design. There was some discussion at this point in time regarding the possibility of subsequent AFWAL/FDER analysis support to the T-46A SPO to assist in developing the windshield system

design in order to meet the bird impact test requirement of a 4 lb bird at 320 knots.

AFWAL/FDER work to conduct this MAGNA analysis began in June 1985. The computer hardware employed was a commercially available Cray 1/S, operated by United Information Systems in Kansas City, Missouri. A Cray class machine was required by the size inherent in the analysis problem, and the commercial machine was used because no similar machine was available at the time at the WPAFB ASD Computer Center. The analysis was accomplished successfully over a period of two months, and the final results were reviewed at FRC in September 1985. The computed results showed the Mod I windshield system design safe for 4 lb, 250 knot bird impact, and these results were accepted both by FRC and the T-46A SPO. Certification of windshield system bird impact protection was based upon the MAGNA results, and first flight of T-1 was not delayed as a result of the bird impact issue. This work has been reported in some detail elsewhere, and was a strictly theoretical study which was never verified via full scale bird impact test.

e. Production System Design

After the first flight of T-1 occurred on 15 October 1985, AFWAL/FDER undertook the additional work noted above to provide analysis support in developing the T-46A windshield system design to meet its 4 lb, 320 knot requirement. By 23 October 1985, the first MAGNA analysis was running for a theoretical fixed bow case. Throughout this next period of AFWAL/FDER MAGNA analysis support, the role of FRC was to develop new designs for the windshield system, while AFWAL/FDER assessed one design candidate after another for its ability to meet the bird impact requirement.

By 30 October 1985, FRC had laid plans for a new integral aluminum bow structure for the windshield system. The material selected for the new bow was 2024-T852 aluminum alloy, which was 50% stronger than the 6061-T6 used in the baseline design. Allowable elongation for the 2024 material was only about half that for the 6061, however.

A 20 November 1985 meeting was held at FRC with AFWAL/FDER, Swedlow Inc, and the T-46A SPO attending to assess the windshield assembly recovery program formulated by FRC which included the new configuration for the bow. A number of very significant decisions were made at this meeting. Among these decisions was that for qualification of the final T-46A windshield system design, the penetration of some bird material into the cockpit space would be acceptable. This decision was especially significant, because the interpretation up to that point in time had been that no bird material would be permitted to enter the cockpit, and this interpretation had driven FRC to very stiff designs for the windshield bow structure to severely limit deflection during the dynamic structural response to bird impact.

It was further agreed during the November 1985 meeting, that a number of windshield system design parameters would be reopened for further consideration. These design parameters included the thickness of individual

plies in the windshield panel itself, the geometry of the cross section of the bow structure as well as the material to be used in the bow, and finally the attachment scheme employed to fasten the windshield panel to its bow support. By December 1985, the new windshield system design was to be finalized with 16 December being the target date for FRC engineering drawing release.

The MAGNA analysis support was accomplished in time to permit the target dates established for the new windshield system design to be met. The new cross section for the windshield bow was a relatively thin walled open section with four flanges, or legs.

By March 1986, the new production system design had been fabricated, and in June 1986, it passed full scale qualification testing at the two target point locations addressed in the MAGNA analysis support. No penetration of bird material occurred. The production system design still included the original design for the windshield panel developed by FRC, with changes having been made only in the design of the windshield support structure. No cracking of the windshield panel polycarbonate plies occurred.

In July 1986, additional full scale bird impact tests were conducted to complete testing at all target point locations selected for both canopy and windshield systems. One target point, number 6, on the centerline of the windshield remained which had never been tested. Just prior to conducting this series of tests, the decision was made to move target point 6 a few inches forward of the metal bow, rather than have it remain on the bow itself. This was done to permit all of the impulse delivered by the bird to be transmitted to the windshield structural system, rather than to be spread over both the windshield and canopy systems.

The purpose of the July 1986 tests was to demonstrate 4 lb, 320 knot protection for the windshield system, and 4 lb, 230 knot protection for the canopy system. (The canopy was subsequently qualified for 4 lb, 294 knot bird impact). Target point 6 had not been considered during the MAGNA assessment conducted in late 1985. During the July 1986 testing, windshield system failure occurred for the relocated target point 6, first at 335 knots, and then at 323 knots. (Target point 6 on the windshield was subsequently qualified for 4 lb, 275 knot bird impact. This level of protection relative to the aircraft performance envelope was found acceptable when compared to other currently operational fighter/trainer aircraft).

As a result of these failures, the T-46A SPO again requested additional analysis support from AFWAL/FDER. First, it was requested that FDER attempt to successfully simulate the target point 6 failure which was observed, then that the level of 4 lb bird impact protection for target point 6 be predicted using MAGNA.

In October 1986, MAGNA was successfully employed to simulate the surprising test failures observed at target point 6 on the windshield

system, and succeeded further in predicting a 275 knot threshold of failure at that target point location which was verified in full scale bird impact testing conducted in October 1986.

## 2. Design Approach

As noted previously, in June 1985 FRC and the T-46A SPO agreed to use MAGNA computer analysis results to support FRC efforts to design a windshield system which successfully met bird impact resistance requirements. At the outset of this work, AFWAL/FDER used the MAGNA preprocessor to model the original windshield panel design. FRC used the IBM CAEDS Computer Aided Engineering Design System at their Farmingdale facility to model the Mod I bow structure. The MAGNA preprocessor system was used then to merge both the MAGNA windshield panel model and the CAEDS bow model to provide the first model of the complete (Mod I) windshield system. This merged model was used in the work already discussed to certify the Mod I windshield system design for bird impact resistance up to airspeeds of 250 knots.<sup>14</sup>

After certification of the Mod I system design for use up to 250 knots, FRC began windshield system design development studies to meet the 4 lb 320 knot bird impact test requirement. To support this work, MAGNA was run on the WPAFB ASD Cray XMP/12. The first MAGNA analysis step planned in this work was to simulate full scale bird impact results observed for the baseline windshield system design. This was to be accomplished by assigning essentially zero stiffness to that portion of the merged windshield model representing the steel reinforcement which had been added to the Mod I design.

After the new FRC bow design had been developed, it was planned to model it by modifying the existing model of the windshield system. An AFWAL/FDER developed FORTRAN 77 code named T46BOW would be used to accomplish this modification of the existing model.

When a design iteration was reached for which the bow survived, MAGNA stresses along the edge of the bow would be integrated to obtain in-plane loads and moments being transmitted to the bow. These edge loads would be used to design a fastener scheme for attaching the windshield to the bow. Both bolt diameter and pitch or spacing would be selected to prevent bolt or polycarbonate bearing failures.

## 3. Scope

During the FRC redesign development studies for the T-46A windshield system which were supported by MAGNA analysis, four different windshield cross section designs were considered. Three different cross section designs for the supporting bow structure were also evaluated, with two different aluminum alloys being assessed as candidate bow materials. As mentioned earlier, a theoretical fixed edge case (rigid bow) was also analyzed. Two different bird impact locations on the windshield system were also treated.



Altogether then, four windshield cross section designs, seven different bow configurations, and two bird impact target point locations were included in the work effort for a total of 56 different windshield system bird impact cases. The MAGNA analysis support, conducted by AFWAL/FDER, began in late November 1985 and ran until mid January 1986. During this period of time, 18 different windshield system bird impact cases were evaluated in depth using MAGNA, and from those 18 analyses, a nominal system design selection was made for subsequent fabrication and full scale bird impact testing.

Four additional MAGNA analyses were accomplished in October 1986.

## T-46A WINDSHIELD SYSTEM DESIGNS

### 1. Windshield Designs

The T-46A windshield transparency configuration (Figure 2) uses two layers of polycarbonate, 3/16 and 1/4 in. thick, an 0.060 acrylic face ply, and two 0.050 urethane interlayers between the polycarbonate and acrylic plies.

During the initial windshield design and subsequent redesign efforts, development studies were conducted by FRC which included increasing the polycarbonate thickness from 1/4 in. / 3/16 in. (outer/inner thickness) to 1/4 in. / 1/4 in. and 5/16 in. / 1/4 in.

### 2. Bow Designs

#### a. Geometry

##### (1) Baseline

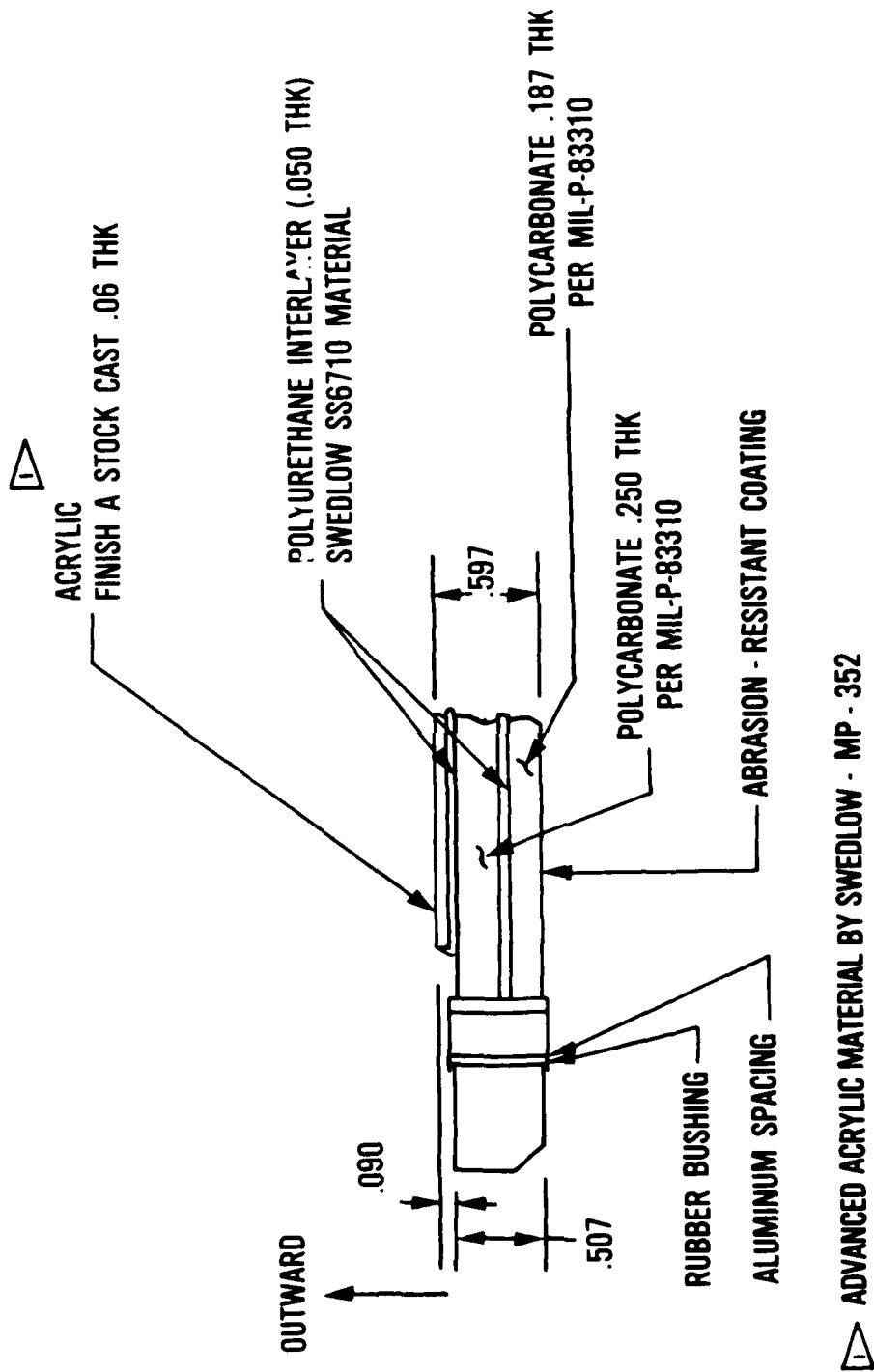
The windshield bow used in the initial phase of the T-46A bird proof tests is depicted in Figure 3. This bow was an integral one piece machining from 6061-T6 aluminum.

##### (2) Mod I

After the first bird impact test failure, a redesign of the bow was done. After reviewing the data from the first test, FRC felt that the bow had to be stiffened in order to reduce the out of plane displacements. This was accomplished by stiffening the bow along its circumference by adding a steel reinforcement angle (Figure 4). This configuration was called Mod I, and it flew on the first flight test vehicle, T-1.

##### (3) Mod II

As discussed in the Introduction, local crippling failures were observed for the Mod I bow cross section in full scale bird impact testing. To circumvent these failures, another redesign of the bow was



△ ADVANCED ACRYLIC MATERIAL BY SWEDLOW - MP - 352

Figure 2. T-46A Windshield Design

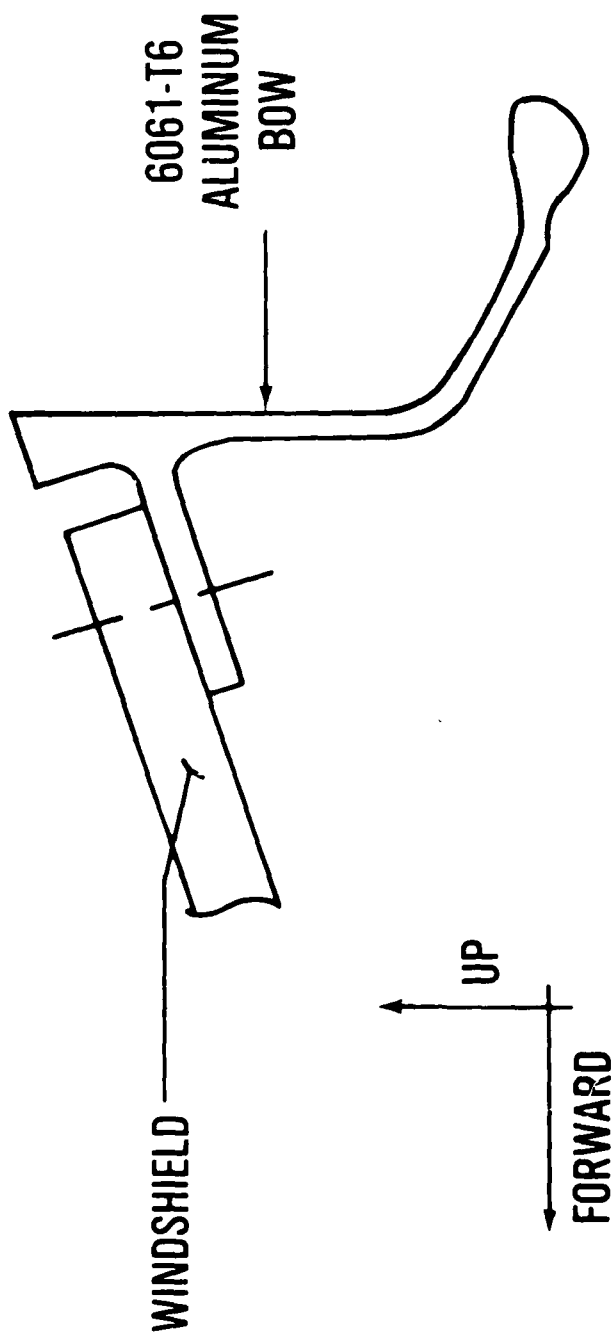


Figure 3. T-46A Windshield Bow Baseline Design

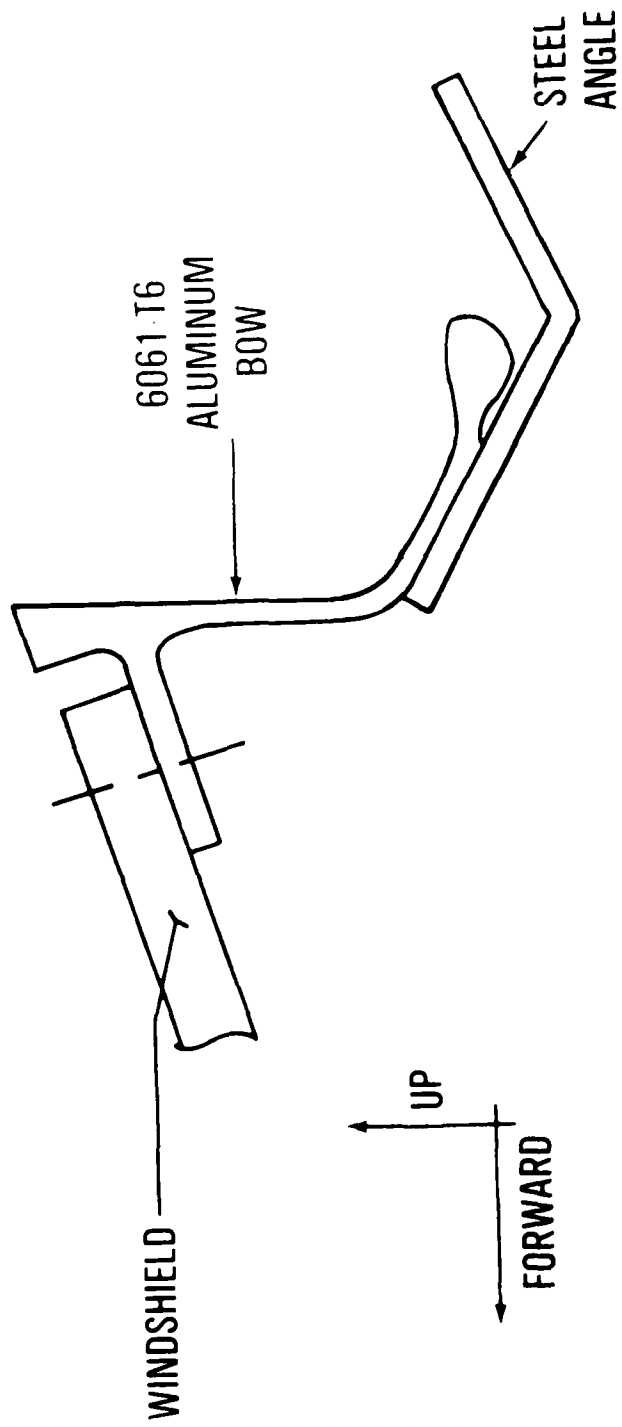


Figure 4. T-46A Windshield Bow Mod I Design

accomplished as shown in Figure 5. This version, called Mod II, included additional formed steel parts intended to tie the Mod I steel reinforcement more directly to the windshield panel portion of the system. The Mod II windshield system design flew in the second flight test vehicle, T-2.

#### (4) Production

Following the unsuccessful test of Mod II configuration, a new production configuration was developed by FRC (Figure 6). This design is lighter than Mod I or Mod II and it utilized MAGNA in the assessment of its capability. The feature of this design is the decreased torsional stiffness allowing the transparency and bow to act as a unit. Figure 7 compares cross sections for the production, and (MAGNA model of) the Mod I bow designs.

#### b. Materials

With the exception of the 4340 steel used to reinforce the bow in both the Mod I and Mod II designs, only aluminum alloys were considered for use in the T-46A windshield bow. As noted earlier, 6061-T6 was the material used in the baseline bow design, and although 2024-T851 was the material first proposed for the production bow design, at one point in the FRC design development studies, the use of 6061-T6 was again considered.

#### c. Fastener Designs

##### (1) Baseline

A number of different schemes were employed to fasten these various bow designs to the edge of the windshield panel. In the baseline bow design, 3/16 in. diameter steel bolts were spaced 2.8 in. apart to fasten the windshield panel to the bow. Metal bushings with 0.35 in. outside diameter were used, and the bolts had 2126 lb maximum shear, 2210 lb maximum tension, and 121 in. lb maximum bending allowables. The distance from bolt centerline to mounting flange edge was 0.4 in., and the distance from bolt centerline to windshield panel edge was 0.8 in. In the baseline bow design, gussets were machined into the bow with a spacing double that used for the bolts to support the windshield attachment flange. Location for these gussets began on the centerline of the design. A rubber bushing was located between the metal bushings and the laminated windshield panel.

##### (2) Production

For the production bow design, 1/4 in. diameter steel bolts were spaced 1.4 in. apart to fasten the windshield panel to the bow. Metal bushings with 0.35 in. outside diameter were used, and the bolts had 3680 lb maximum shear, 4080 lb maximum tension, and 276 in. lb maximum bending allowables. Distances from bolt centerline to mounting flange edge and windshield panel edge were the same as for the baseline design, 0.4 in. and 0.8 in. respectively. In the production bow design, gussets were machined into the bow with a spacing double that used for the bolts to support the

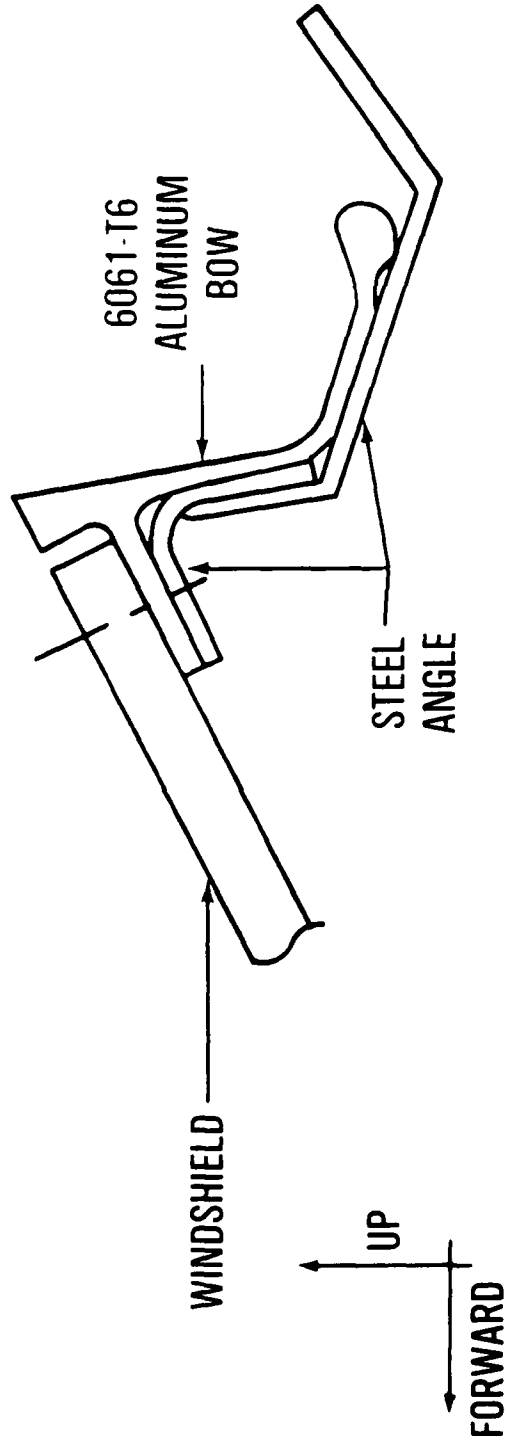


Figure 5. T-46A Windshield Bow Mod II Design

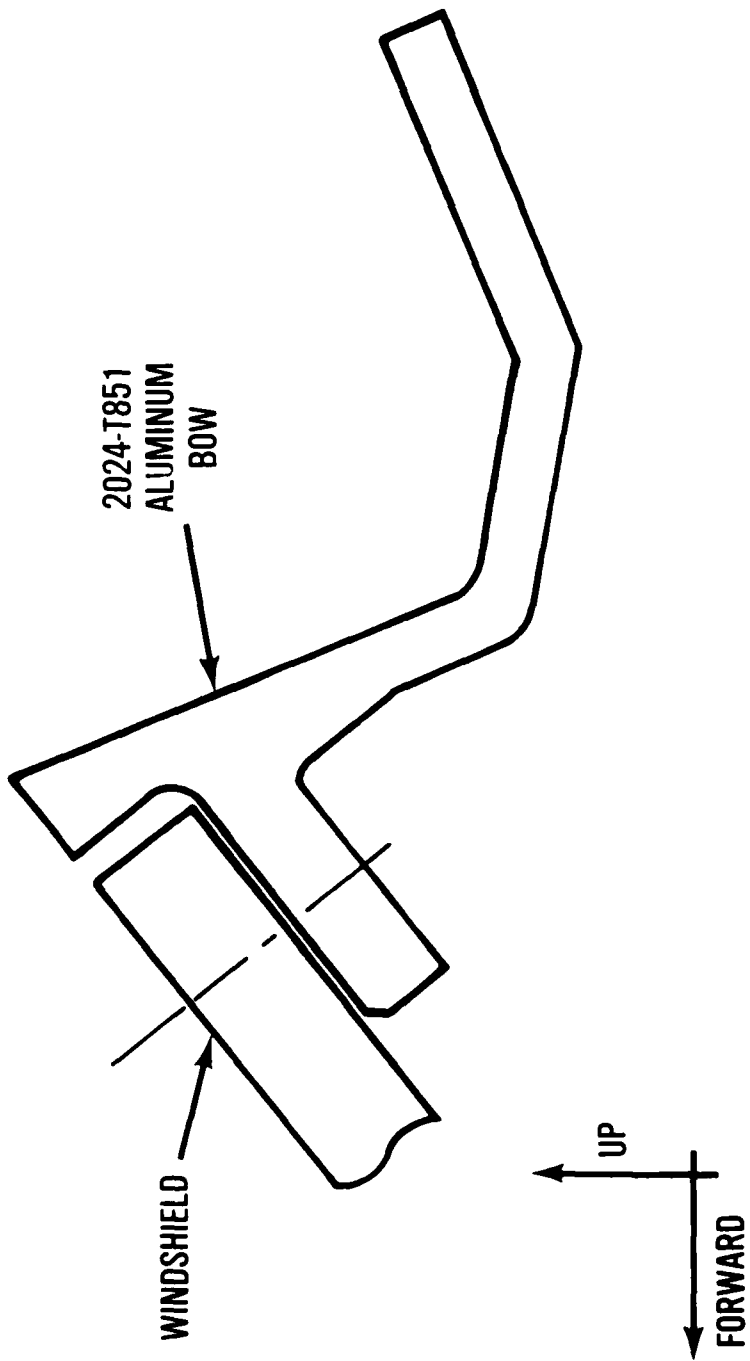


Figure 6. T-46A Windshield Bow Production Design

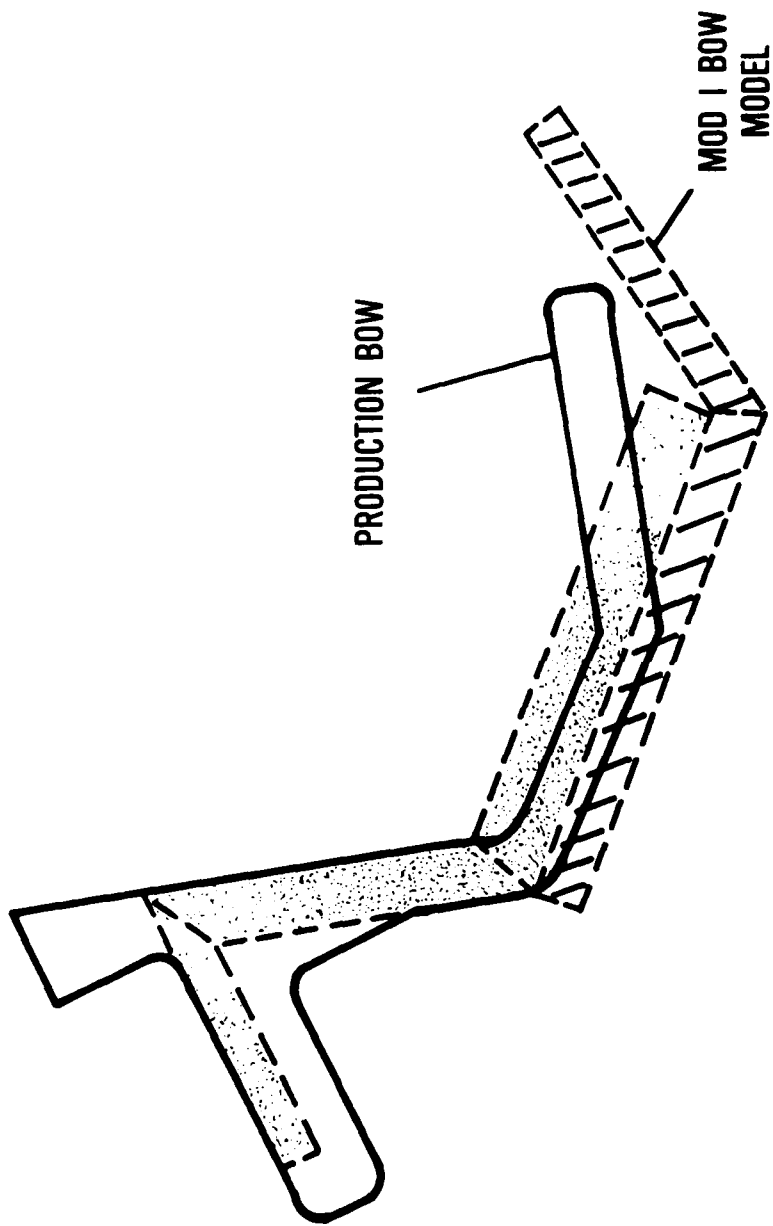


Figure 7. Production versus Mod I Bow Design



windshield attachment flange. Location for these gussets began on either side of the centerline of the design. A single bolt was located on the centerline.

## MAGNA FINITE ELEMENT MODELS

### 1. Finite Element Mesh:

#### a. Windshield

As discussed, the original windshield design for the T-46A had five plies. Starting from the outside surface, these were acrylic, urethane, polycarbonate, urethane, and polycarbonate with respective thicknesses of 0.060, 0.050, 0.250, 0.050, and 0.187 in. The preprocessing system for MAGNA was used to model this windshield panel.<sup>15</sup> Type 8 elements, which are 16 node isoparametric solids, were used. This element type was selected because the bulk of successful previous experience in using MAGNA for the transparency bird impact application was with element type 8.

Each ply in the windshield was modeled directly with a separate layer of type 8 elements. The starting point for the model generation was loft data of the outer surface of the windshield transparency. The aftmost edge of this surface corresponded to the aft edge of the supporting bow structure as is shown in Figure 8. Because bird impact on the centerline of the system was being considered, the problem exhibited symmetry, and only the left half of the windshield was modeled to conserve computer resources. Since half the windshield resulted in a three-sided figure for the T-46A system, the outboard corner where the bow meets the sill was truncated slightly in the model. This permitted the mesh to be four-sided, rather than three.

While this AFWAL/FDER MAGNA preprocessor generation of the windshield panel mesh was taking place, FRC was using their IBM CAEDS system to model the bow structure for the windshield system. To reduce the number of iterations involved in each of the two meshes being generated, the windshield mesh was frozen in the configuration with 240 elements shown in Figure 9, while the bow mesh was completed. Although the figure is too small for details through the thickness to be seen clearly, it does contain five layers of solid elements.

#### b. Bow

##### (1) Mod I

As mentioned above, FRC used their IBM CAEDS system to model the Mod I bow for the T-46A windshield system. The 16 node isoparametric element was used again as for the windshield panel. FRC modeled the cross section of the bow, starting at the rear edge of the windshield mesh which had already been generated.

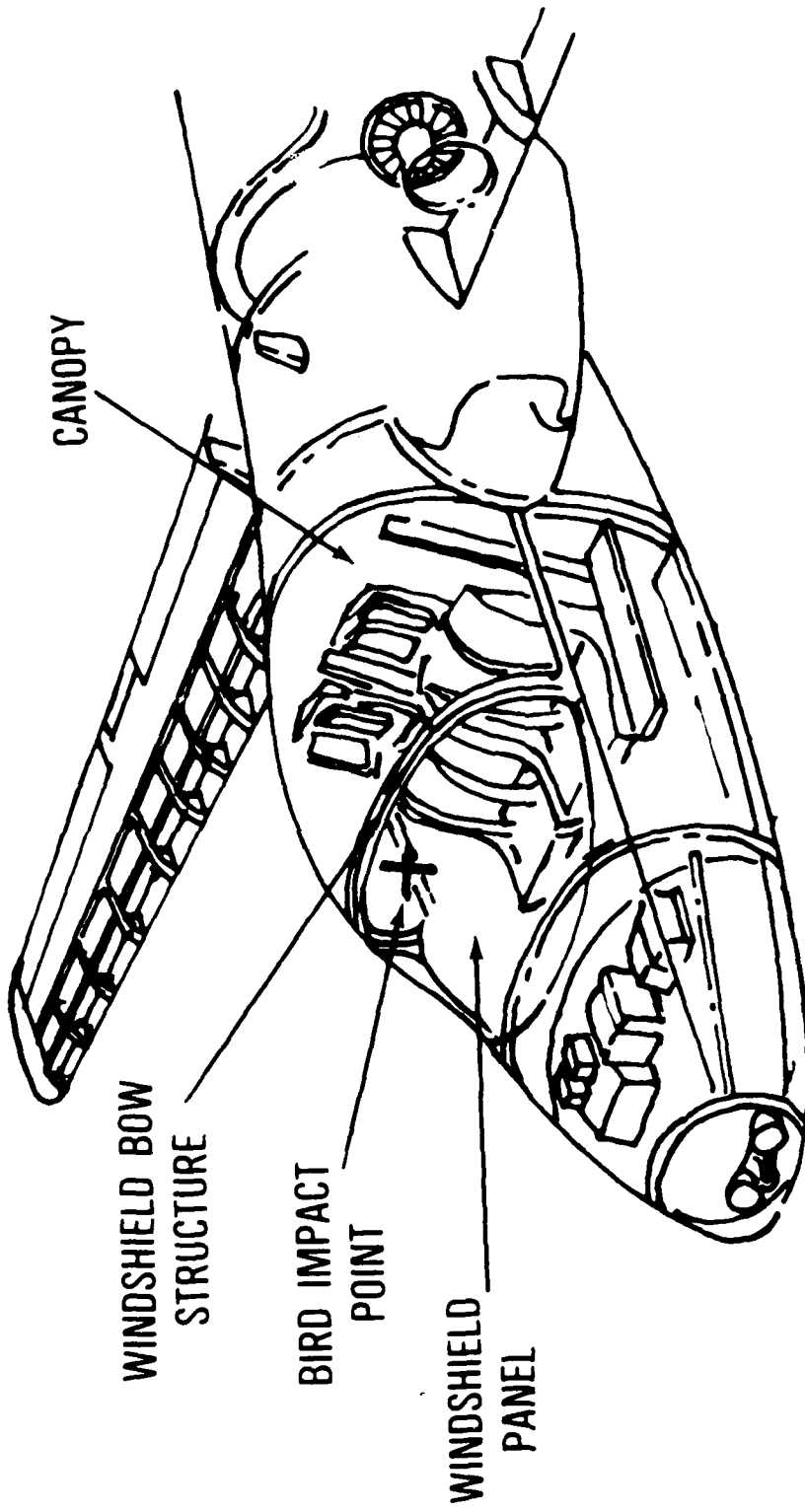


Figure 8. T-46A Transparency System

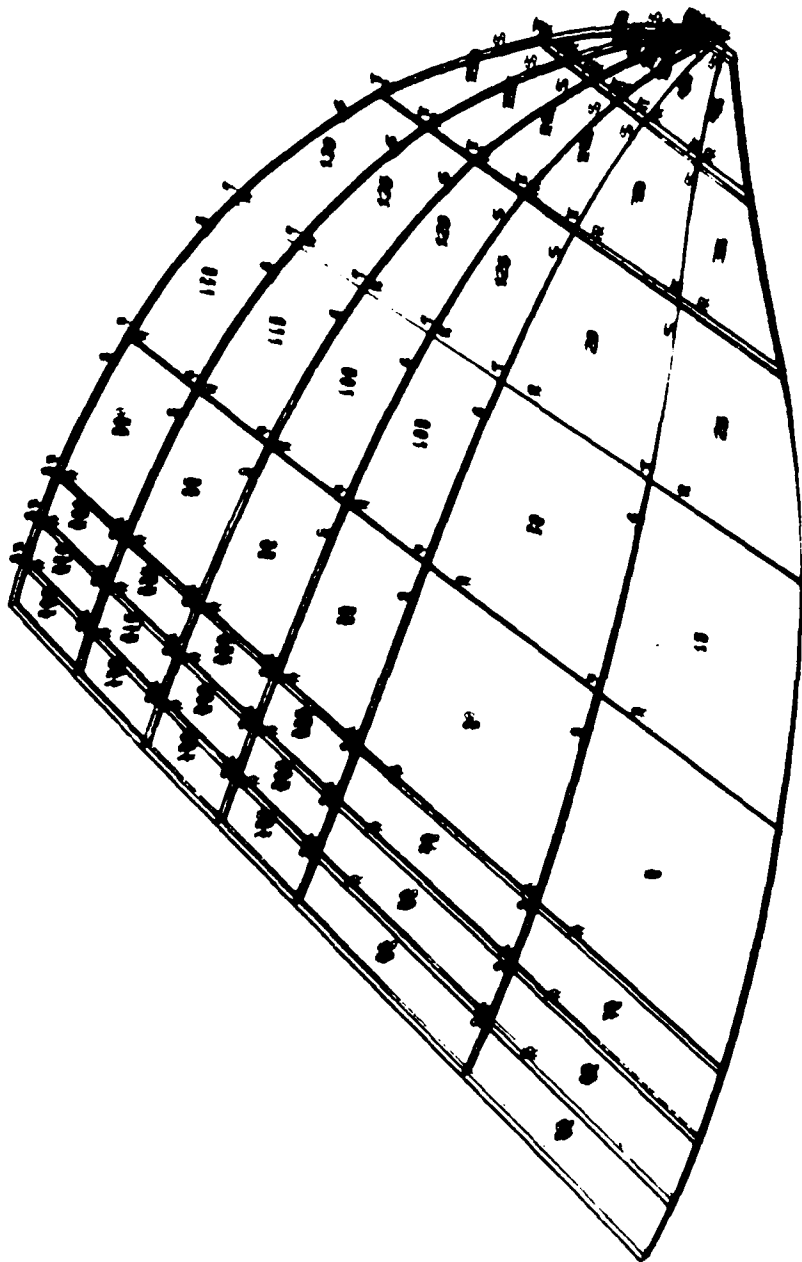


Figure 9. MAGNA Windshield Mesh

The gussets machined into the aluminum portion of the bow under the windshield attachment flange were excluded from the model primarily because they were too complex to model in the time available for this work. It was felt that excluding them would result in conservative stresses in the bow, especially as a result of bending at the root of the windshield attachment flange.

With the eight elements along the length of the bow required by the already complete windshield mesh, a total of 64 elements were required for the bow.

Because the aft edge of the windshield panel mesh actually corresponded to the aft edge of the physical bow, when the FRC IBM CAEDS bow model was merged with the AFWAL/FDER MAGNA windshield model using the MAGNA preprocessor, the aft edge of the completed model extended about 1.3 in. further aft than the aft edge for the physical system. This was done, again, for expediency because pushing the windshield bow model forward 1.3 in. would have required significant rework of the windshield mesh in the region of the slightly truncated corner. The fact that the aft edge of the completed model was not located correctly in space had insignificant effects on computed deflections and stresses in the neighborhood of the bird impact target location shown in Figure 8, because the relative location of the bird impact loading with respect to the aft edge of the structure was maintained.

With 240 elements in the windshield panel mesh, and 64 in the bow mesh, a total of 304 elements resulted for the completed model. Figure 10 illustrates the completed mesh for the Mod I system design.

The total number of nodes for the merged model was 1384. Boundary conditions representing symmetry were applied all along the centerline of the model, and pinned boundary conditions were applied along the sill of the windshield panel. These pinned boundary conditions were applied along the inner edge of the laminate to give slightly conservative results in the analysis. The pinned condition gives the model more flexibility in bending than does the actual physical attachment scheme. Greater flexibility results in greater bending deflections under the same load, with correspondingly higher local bending stress. An additional conservative effect comes into play for the bird impact problem because increased local deflections actually result in increased bird impact loads, for the same bird mass and impact velocity.

The end of the bow toward the sill was completely fixed in the model. All subsequent models prepared for other bow designs were derived from this Mod I windshield system model.

## (2) Baseline

For expediency, the MAGNA model for the baseline T-46A windshield system design was derived by assigning very low stiffness and strength to the elements representing the formed steel reinforcement in the Mod I model.

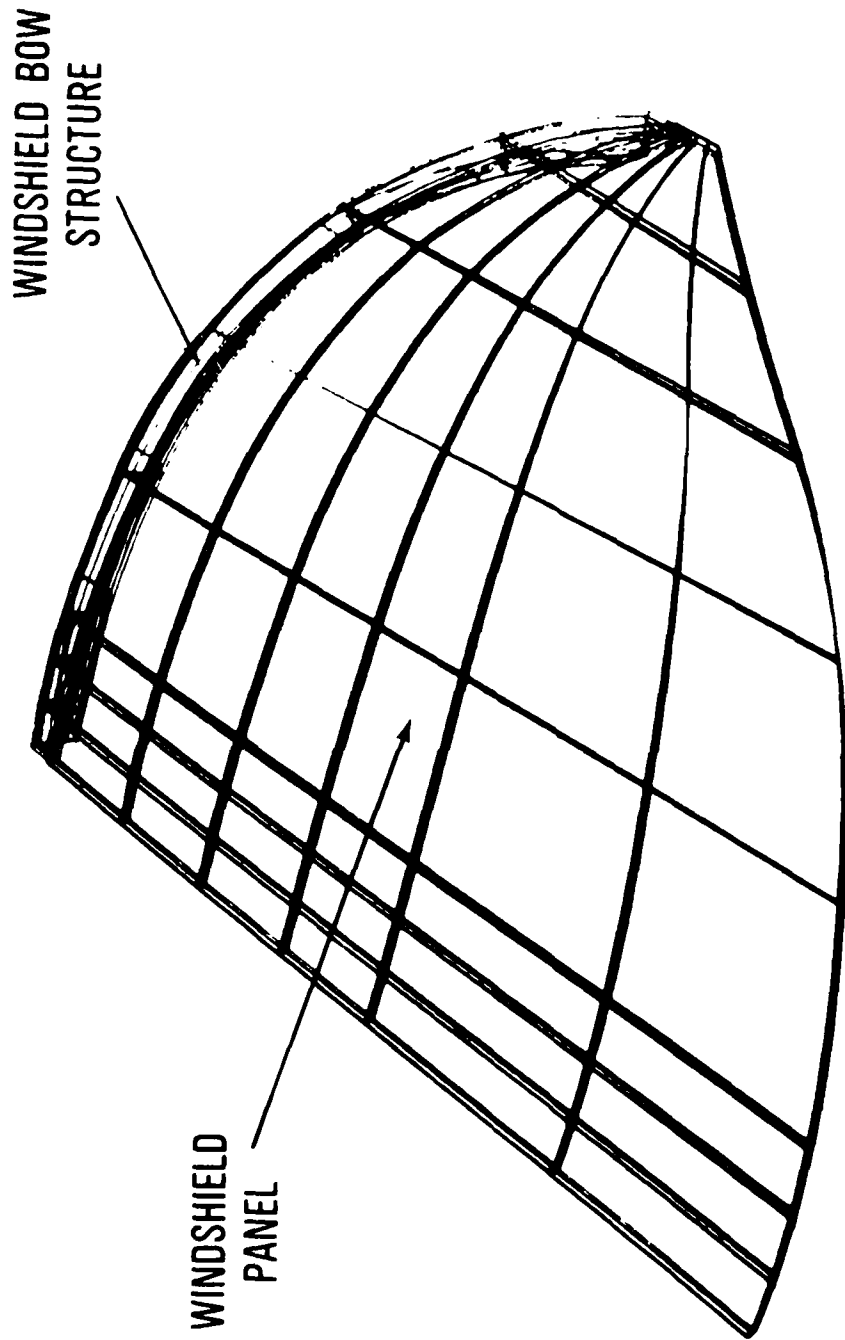


Figure 10. MAGNA Windshield System Mesh

(a) Fixed

Two versions of the MAGNA model for the baseline windshield system design were used. One involved the theoretical boundary condition of fixing the edge of the windshield panel along the bow. A cutting plane through the thickness of the windshield panel and running along the forward edge of the bow contained 68 nodes on the polycarbonate windshield plies. All 68 of these nodes were fixed in space for this fixed-edge model of the baseline system design. It was felt that this artificial boundary condition would result in maximum polycarbonate stresses during bird impact simulation. The plan was to iterate polycarbonate ply thicknesses until a conservative windshield cross section design was obtained which would meet the bird impact requirement. During the conduct of the subsequent analyses, it became apparent that this approach would yield an unconservative rather than a conservative windshield design.

(b) Free

The baseline windshield system design was modeled without the artificial fixed edge boundary condition simply by removing the 68 polycarbonate node constraints described above.

(3) Production

Just as the mesh for the baseline bow was derived from the mesh for the Mod I bow, the mesh for the production bow was also derived from the mesh for the Mod I bow. To generate the production bow mesh, however, an AFWAL/FDER FORTRAN77 code called T46BOW was used to interactively read and modify the Mod I bow mesh.

2. Material Properties

As mentioned earlier, the stretched acrylic actually used for the outer face ply of the T-46A windshield panel was an advanced Swedlow Incorporated material known as MP-352.

Table 1 lists the linear elastic properties used for MP-352 acrylic material in the MAGNA analysis, which are essentially the same as those for MIL-P-25690.

All of the materials used in the T-46A windshield system, with the exception of the Swedlow SS6710 urethane interlayer material, were treated as being nonlinear elastic-plastic using tensile data obtained at room temperature and very low ("static") strain rates. Table 1 shows material properties corresponding to the initial linear segment of the stress-strain curve used in each case. For the transparent plastic materials, a value was used for the "yield stress" which was not necessarily the same as that ordinarily associated with the physical yield phenomenon. The value chosen was used only to represent that portion of the stress-strain curve which was most nearly linear. Above the value chosen for the "yield stress," significant nonlinearity is observed. MAGNA permits the user to provide a

Table 1

## Linear Material Properties Used

Material	Young's Modulus (psi)	Poisson's Ratio	Yield Stress (psi)	Density $\frac{(\text{lb sec}^2)}{(\text{in.}^4)}$
Polycarbonate MIL-P-83310	324,000.	0.38	# 6,353.	0.111x10 <sup>-3</sup>
Interlayer Swedlow SS6710	*1,305.	*0.45	-	0.104x10 <sup>-3</sup>
Stretched Acrylic MIL-P-25690	485,000.	0.35	# 2,425.	0.111x10 <sup>-3</sup>
Aluminum 6061-T6	9,900,000.	0.33	40,197.	0.254x10 <sup>-3</sup>
Aluminum 2024-T851	10,500,000.	0.33	55,704.	0.259x10 <sup>-3</sup>

\*Reference D. Holdridge, Swedlow, 1 Aug 1986

#Does not correspond to physical yield

table of stress-strain data to describe the behavior of the material beyond the point represented by the value of the "yield stress" shown in Table 1.

During late 1985 when FRC developed the production design for the T-46A windshield system, a hand forged billet of 2024-T852 aluminum alloy was selected to fabricate the bow. When mechanical properties for 2024-T852 proved not readily accessible to AFWAL/FDER, the decision was made to use data available for 2024-T851 because virtually no difference existed between the data required by MAGNA for these two alloys.

## BIRD IMPACT LOADING DEFINITION

## 1. Theory

Over the past decade a considerable amount of work has been accomplished in studying the physics of bird impact on both rigid and compliant targets. <sup>19228</sup> Much of this work has been sponsored by the US Air Force and has provided an extensive data base for the case of an inclined, flat, rigid target. This data base defines both the spatial and temporal distribution of bird impact pressures over the surface of the target.

A generalized description of bird impact loading has evolved from this work effort and has been validated for bird weights up to 7.9 lb, bird velocities up to 984 ft/sec, and target inclinations of 90, 45, and 25 degrees. The effects of target compliance upon this generalized description of rigid target bird impact loading have been qualitatively defined.

The procedure for mathematical definition of bird impact loading used in the MAGNA analysis support studies for the T-46A windshield system is simple and straightforward to use. The essential points of the rigid target theory upon which the loads definition procedure is based are as follows:

1. The bird behaves as a fluid during impact.
2. The impulse delivered to the structure is equal to the component of the bird's linear momentum which is normal to the target surface.
3. The bird may be represented as a right circular cylinder having a length to diameter ratio of 2.0.
4. The pressure resulting from bird impact is relatively constant at any point on the surface of the target (quasi-steady fluid flow).

## 2. Mathematical Definition

A more detailed description of the procedure used for mathematical definition of bird impact loading for the T-46A windshield system has been documented elsewhere.

## 3. Target Point Locations for T-46A

Figure 11 shows the different bird impact target locations on the surface of the windshield system used in full scale testing. The installed angle along the centerline of the windshield for the T-46A was 37 degrees.

## MAGNA ANALYSIS

### 1. Free Vibration

#### a. Solution Parameters

MAGNA free vibration analyses were accomplished for a number of different T-46A windshield system configurations. These were conducted primarily to determine the size of the MAGNA time step to be used in nonlinear dynamic bird impact analyses. Illustrations of the eigenvectors extracted during free vibration analysis were also used to help verify the definition of model boundary conditions.



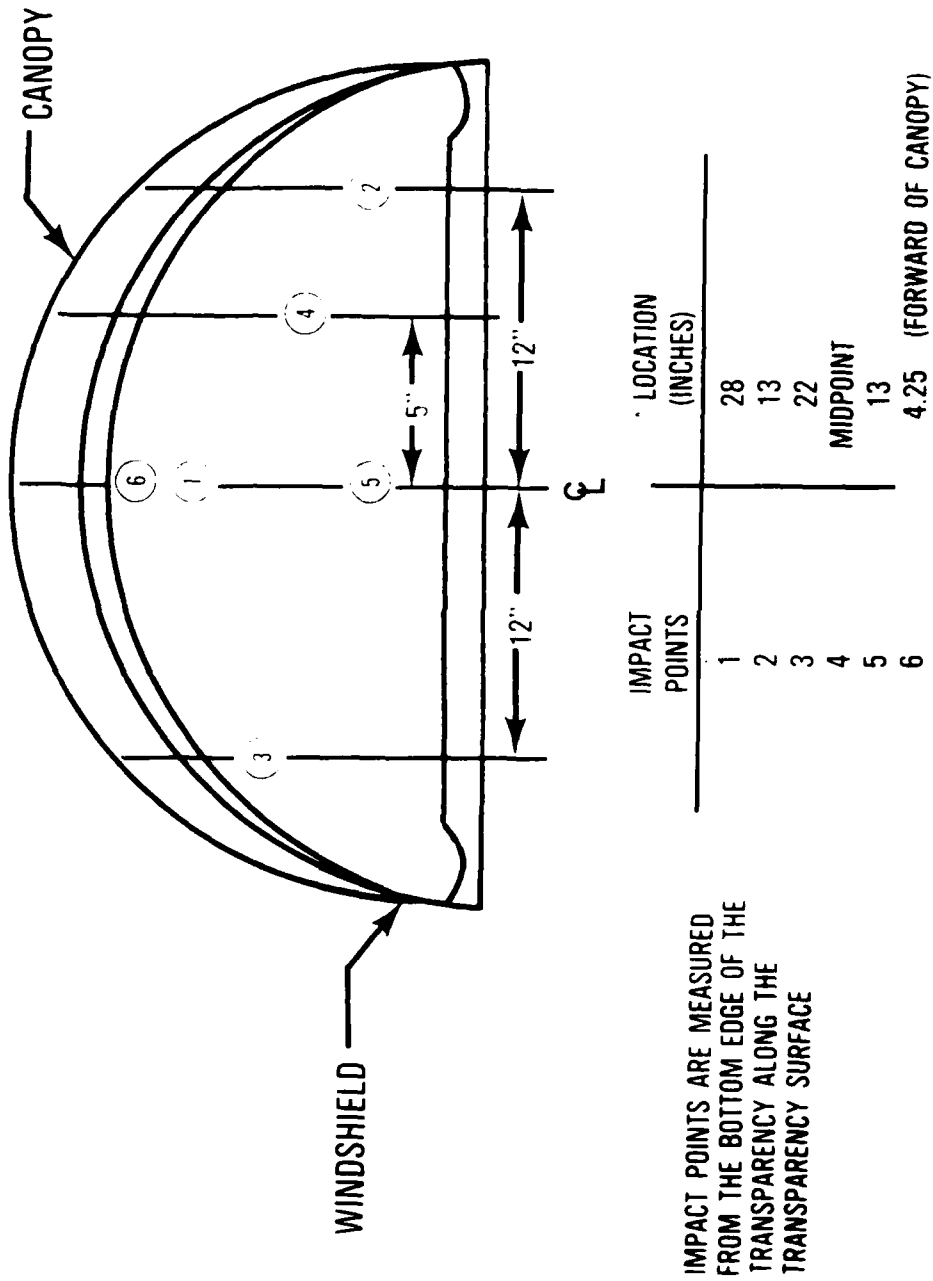


Figure 11. Windshield Bird Impact Target Points

Each free vibration analysis was conducted using the 14 point (Iron's rule) integration rule available for the 16 node (type 8) solid isoparametric elements used. The linear formulation of element stiffness was chosen in each case, and only the first mode of free vibration was extracted.

## 2. Bird Impact

### a. Solution Parameters

After free vibration analyses were conducted to determine the frequency of the first mode for a number of windshield system models, nonlinear dynamic analyses were accomplished to simulate bird impact response. In each nonlinear dynamic analysis, the 14 point integration rule was employed for all elements in the model and a non-iterative solution was chosen. Previous experience in simulating the bird impact response of plastic aircraft windshield systems has demonstrated that the extra time and expense associated with iterative solution techniques is not warranted.

The full nonlinear stiffness formulation available was chosen for use with all elements in the model, and the time step, was chosen to be less than 1/100th the period of the first mode obtained from free vibration analysis. This rule for selection of time step size has been demonstrated to represent an effective balance between solution accuracy and cost.

### b. Analysis Results

A number of different forms of MAGNA solution parameters were employed in order to illustrate the results of the bird impact simulations conducted. Each parameter used in the analyses is described briefly below.

#### (1) Bird Impact Pressure

Since the value of bird impact pressure used in the analyses was a function of the dynamic response calculated by MAGNA, plots were made for each case analyzed to show the ratio of the value of flexible windshield pressure to the value of rigid windshield pressure versus time measured in milliseconds. Figure 12 shows a sample plot of this pressure ratio versus time. For the example shown in the figure, the value of flexible windshield bird impact pressure rises almost 50% above the value of rigid windshield pressure by the time the end of the bird impact event is reached - 5.2 msec in this case.

#### (2) Deflection versus Time

For each case analyzed, plots were made of vertical displacement versus time like that shown in Figure 13. Results for two points on the outer surface of the windshield and a point on the outer surface of the bow were plotted for each case as shown in the figure.

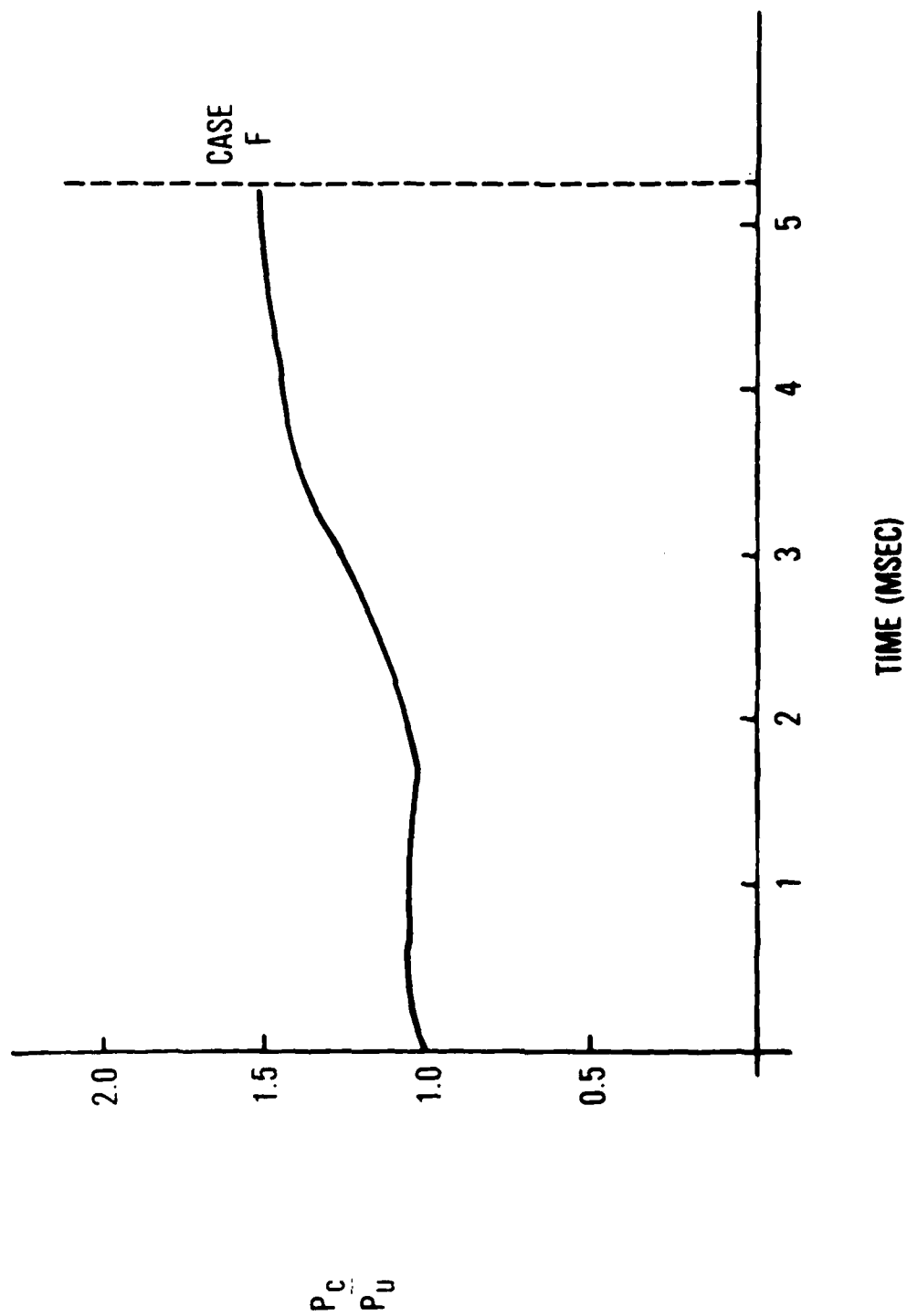


Figure 12. Bird Impact Pressure Coupling

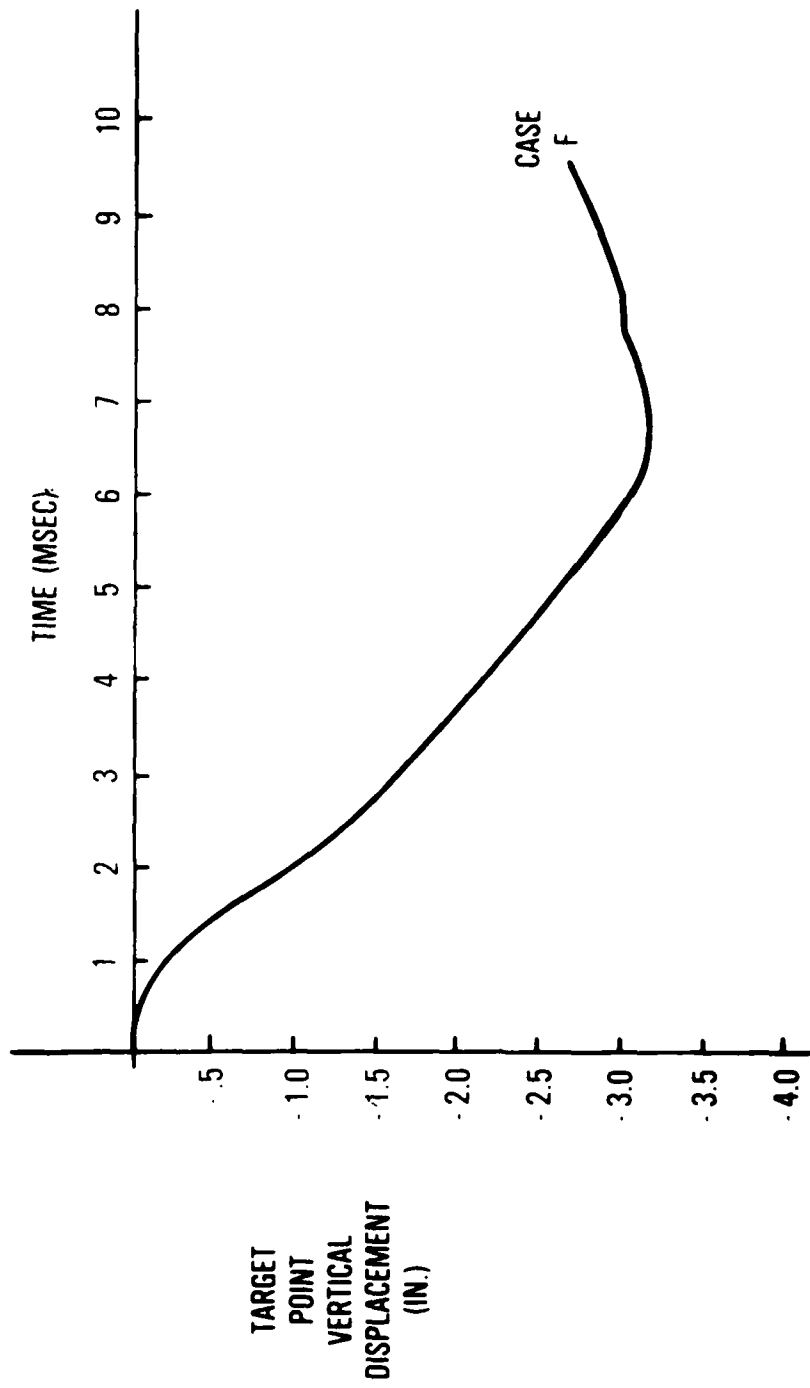


Figure 13. Deflection versus Time

### (3) Deformed versus Undeformed Shape

For some of the cases analyzed, various plots of deformed versus undeformed shape were prepared to illustrate the structural deflections calculated by MAGNA. Figure 14 shows an example of such a plot. The dotted lines in the figure represent the undeformed shape of the outer face of the acrylic face ply of the windshield, and the solid lines show the deformed shape of the same surface at 3.5 msec into the bird impact response. A bowl shaped depression can be seen lying along the centerline of the windshield panel, and some deflection out-of-plane can be seen at the location of the windshield bow structure. Similar plots were made through the cross section of the bow on the centerline of the part.

### (4) Maximum Stress versus Time

Another plot which was prepared for each case analyzed was that for maximum polycarbonate equivalent nodal stress versus time, as shown in Figure 15. This type of plot did not represent the history of polycarbonate stress at any particular point in the windshield panel, but rather represented the envelope of maximum equivalent stress occurring at different locations in the windshield.

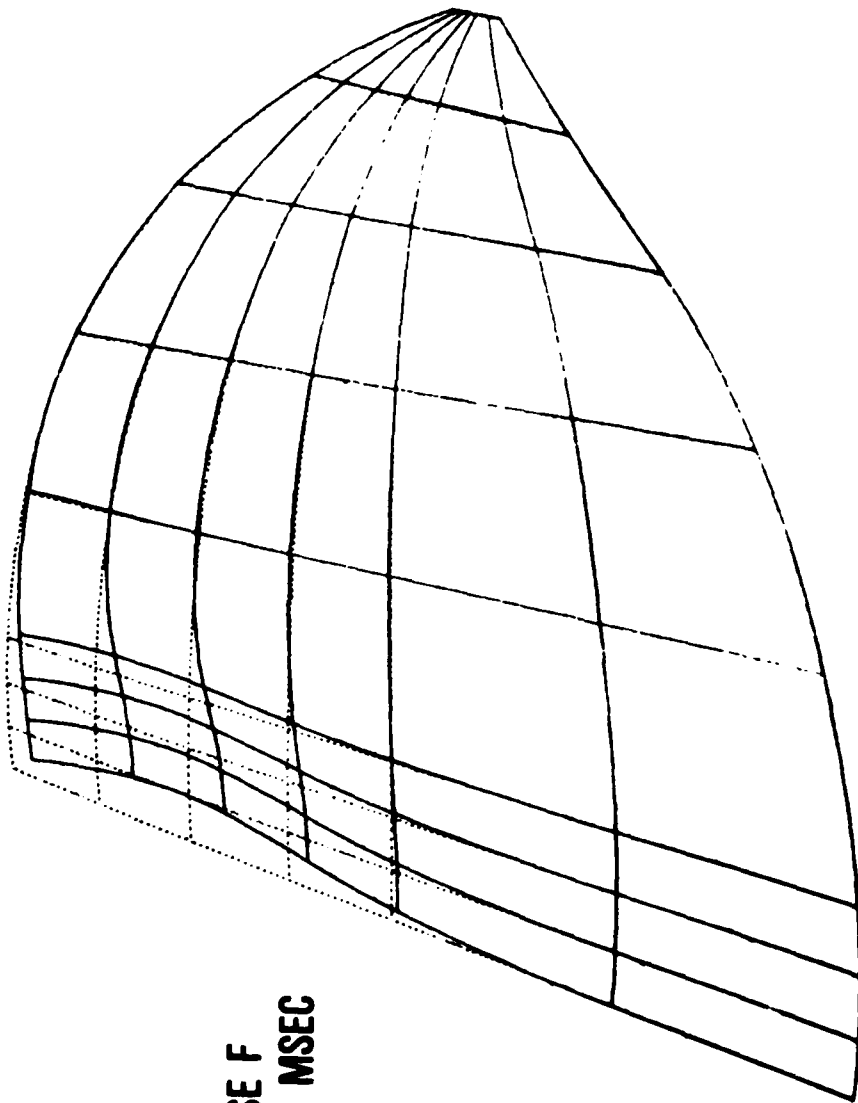
### (5) Stress Contour Maps

When predicted time histories of stress or maximum strains indicated the possibility of mechanical failure, stress contour maps were prepared to illustrate the location of the regions of critical stress involved. Figure 16 shows an example of an equivalent stress contour map drawn on the cross section of the metallic bow. Regions enclosed by the F contour represent areas where equivalent stress exceeds ultimate for the material, 6061-T6 aluminum in this case. Failure of the windshield support flange due to bending at its root is indicated. Similar maps were prepared in some cases to illustrate polycarbonate equivalent stress on the surfaces of both structural plies in the windshield panel.

### (6) Edgemember Loads

As discussed, the fasteners used between the windshield panel and the bow structure were not treated directly as part of the MAGNA analyses conducted. Instead, a FORTRAN77 code named STRSLT was used to process results of the MAGNA bird impact analyses.

For the two polycarbonate structural plies in the windshield, the STRSLT code was used to integrate nodal stresses to obtain in-plane loads in the 1 direction indicated in Figure 17. Bending moments for both polycarbonate plies in the 3 direction shown in the figure were also calculated using STRSLT. Then the in-plane loads and bending moments calculated for the polycarbonate plies along the forward edge of the bow were transferred to the fasteners in order to calculate shear and tension loading on the fasteners as well as bearing stress in both polycarbonate plies.



**CASE F  
AT 3.5 MSEC**

Figure 14. Deformed versus Undeformed Geometry

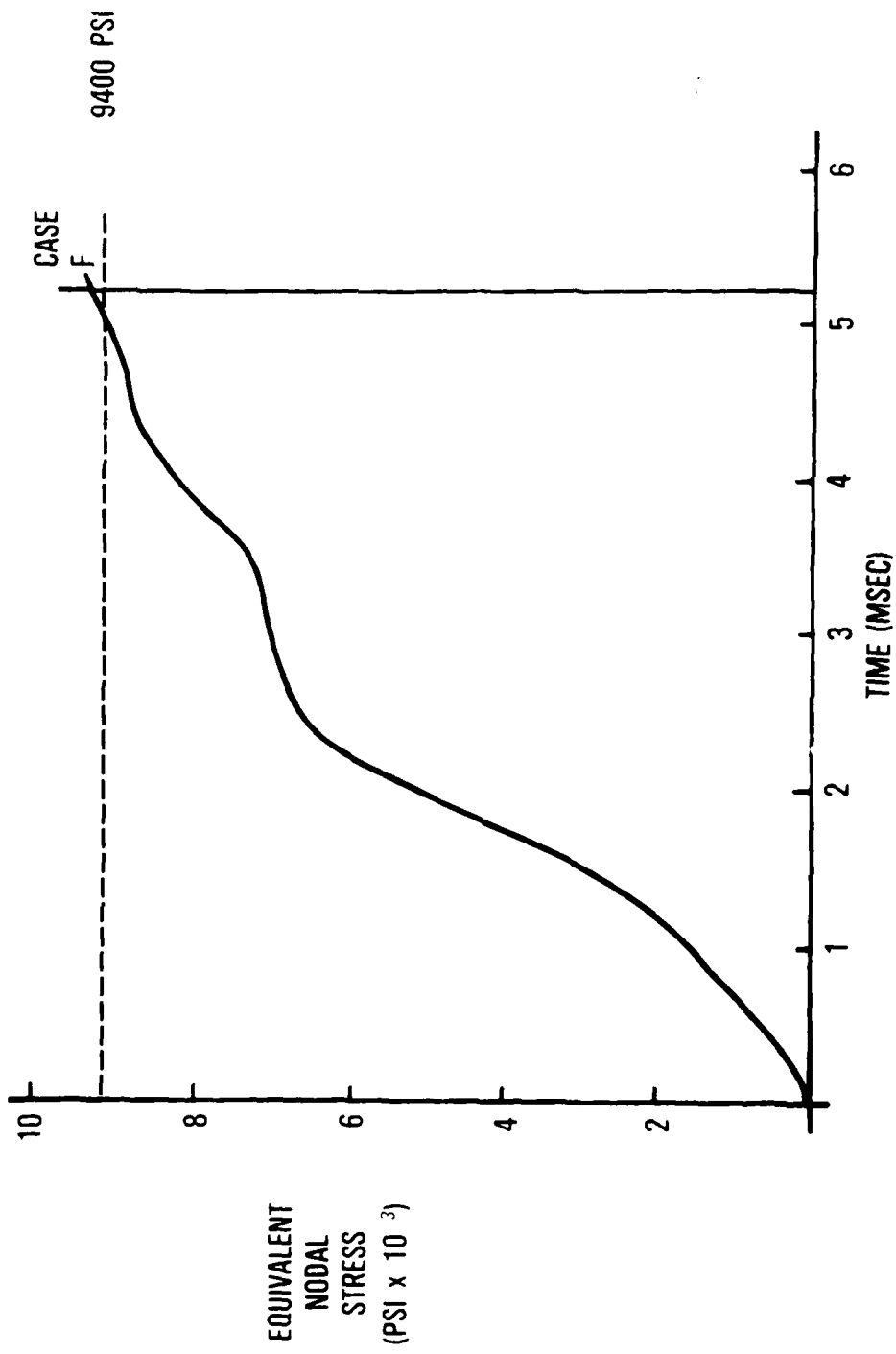


Figure 15. Maximum Polycarbonate Stress versus Time

**CASE F  
AT 5.1 MSEC**

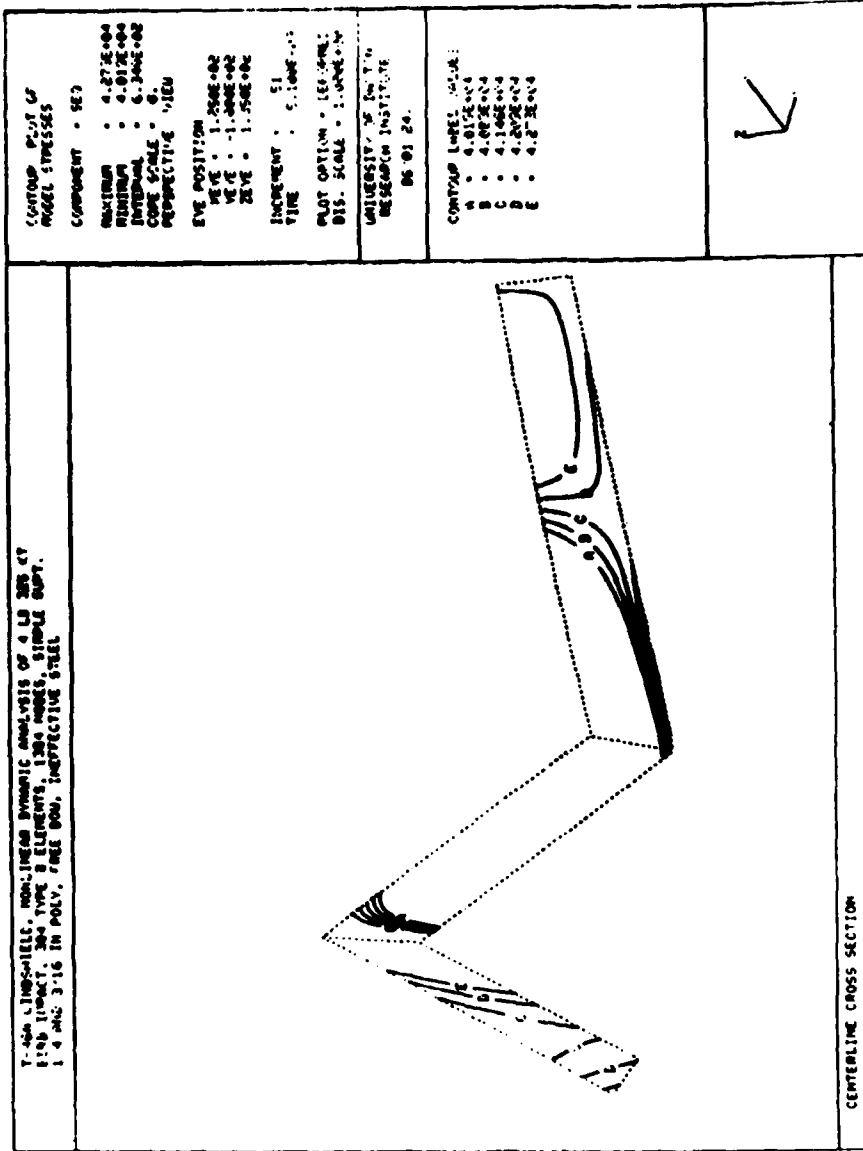


Figure 16. Stress Contour Map



- 1 - INPLANE LOAD
- 3 - BENDING MOMENT

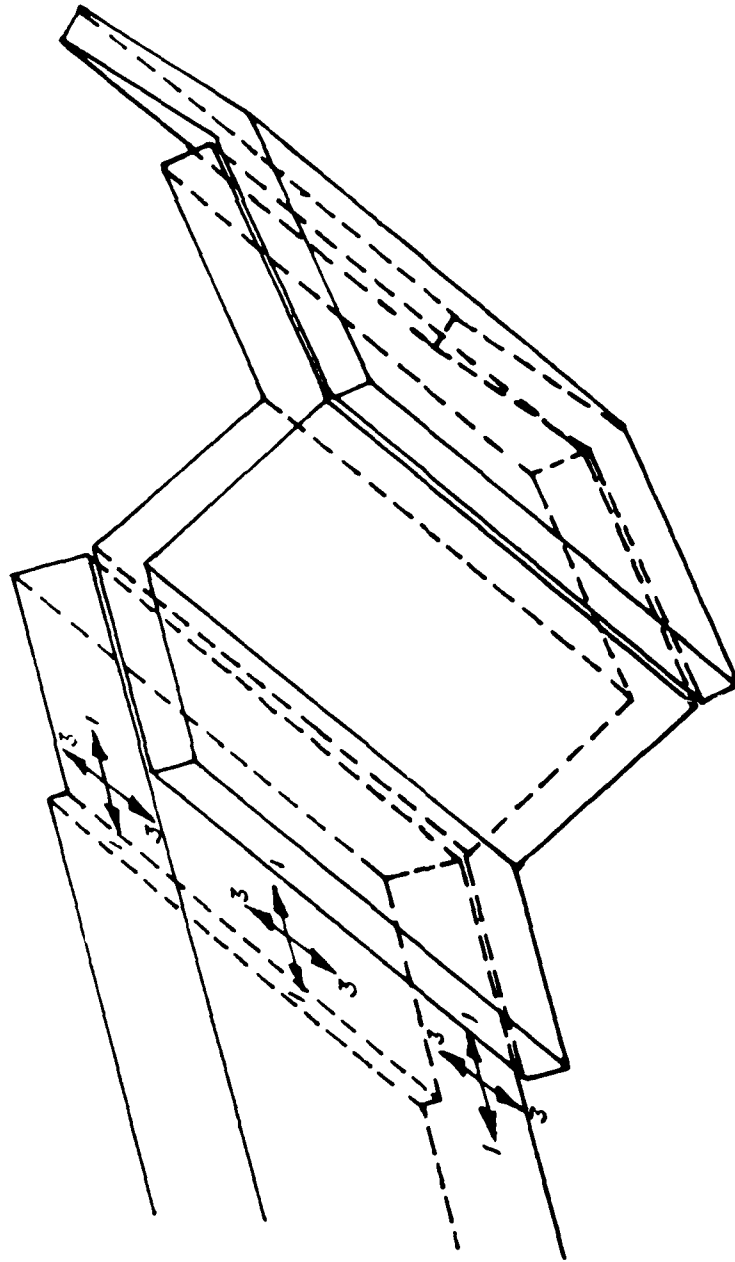


Figure 17. Edgemember Loads

### c. Analysis Cases

In all, 21 analyses were performed for various combinations of six different design parameters. Table 2 provides an index of the analyses, and can be used to follow the history of the MAGNA analysis support as it unfolded.

In the conduct of these MAGNA analysis cases, only a single windshield system design parameter was permitted to vary from one case to the next. Table 3 is a graphic representation of all the analysis cases included in Table 2. Table 3 shows, for a particular analysis case, which of the six windshield system design parameters was varied. In some instances, this single parameter variation did not involve sequential cases. For example, in the parametric sense, Case D followed Case A, and Case I followed Case G, as shown in Table 3. In another example, Case O was exactly the same as Case J, except for the Bow Material which was changed to 6061 aluminum. Adherence to this single parameter variation rule insured the ability to clearly define the effect of each individual windshield system design parameter upon analysis results.

The detailed results of each of the 21 analysis cases run have not been included here, but Table 4 graphically summarizes the results of those analyses. Up or down arrows, or horizontal dashes indicate the effect of each independent design parameter upon respective dependent parameters.

Some of the parameter sensitivities illustrated in Table 4 were anticipated beforehand. Others came as surprises and greatly complicated accomplishment of successful system design development. This points to the severely nonlinear nature of the problem.

As discussed above under Analysis Results, fasteners between the windshield panel and the bow structure were not analyzed directly using MAGNA. Instead, MAGNA stresses in the windshield were integrated for some cases of interest to obtain the in-plane loads and bending moments which had to be carried by the fastener scheme as shown in Figure 17. Polycarbonate bearing stress, as well as combined bolt shear and tension loading for various attachment schemes were calculated by hand. Results are shown in Table 5. In addition, system weight changes were determined for the various windshield panels, bow designs, and attachment schemes.

Table 6 summarizes in yet another form, the results of all windshield panel, bow, and fastener analyses accomplished. Absolute results with respect to allowables are shown in Table 6.

Case J was the nominal design selected for full scale fabrication and test, based on the results presented in Table 6. Case J, FRC Drawing Number 210D111033, exhibited much less load/response coupling, greatly reduced deflections, and much lower peak polycarbonate stress, than did Case F which represented the baseline FRC windshield system design. Indications of marginal failure or damage to the aluminum bow were observed for Case J, compared to the clear indication of failure seen for Case F.

Table 2

## MAGNA Bird Impact Analyses Conducted

MAGNA Analysis Case	Windshield Design Parameters					
	Windshield Cross Section 1	Impulse 2	Edgemember Fixity 3	Bow Material 4	Target Point 5	Bow Cross Section 6
A	1/4 & 3/16	289	Fixed	-	1	-
B	1/4 & 1/4	289	Fixed	-	1	-
C	5/16 & 1/4	289	Fixed	-	1	-
D	1/4 & 3/16	325	Fixed	-	1	-
F	1/4 & 3/16	325	Free	6061	1	Baseline
G	1/4 & 3/16	325	Free	2024	1	Baseline
H	1/4 & 3/16	325	Free	2024	3	Baseline
I	1/4 & 3/16	325	Free	2024	1	Production 7
J	1/4 & 3/16	325	Free	2024	1	Production 8
K	1/4 & 3/16	325	Free	2024	1	Mod Prod 9
L	1/4 & 1/4	325	Free	2024	1	Production 8
M	1/4 & 1/4	325	Free	6061	1	Production 8
N	3/16 & 3/16	325	Free	2024	1	Production 8
O	1/4 & 3/16	325	Free	6061	1	Production 8
P	1/4 & 1/4	325	Free	6061	1	Baseline
Q	1/4 & 1/4	325	Free	2024	1	Mod Prod 9
R	1/4 & 3/16	288	Free	2024	1	Production 7
S	1/4 & 3/16	325	Free	2024	6	Production 8
T	1/4 & 3/16	300	Free	2024	6	Production 8
U	1/4 & 3/16	275	Free	2024	6	Production 8
V	1/4 & 3/16	250	Free	2024	6	Production 8

1. Outer/inner polycarbonate ply thickness, in.
2. Speed in knots for 4 lb bird impact
3. Aft edge of windshield mesh either fixed or joined to bow mesh
4. Aluminum alloy designation
5. See Figure 11
6. See T-46A Windshield System Designs
7. Flange thicknesses fore to aft: 0.38/0.25/0.25/0.25 in.
8. Flange thicknesses fore to aft: 0.38/0.36/0.30/0.32 in.
9. Flange thicknesses fore to aft: 0.38/0.48/0.42/0.44 in.

Indication of possible failure at the root of the windshield attachment flange for the production bow design (Case J) was felt to be conservative. The basis for this opinion was the fact that the closely spaced and relatively thick webs or gussets machined into the production bow to provide additional support for the windshield attachment flange had been excluded from the MAGNA model of the system.

Table 3. Sequence of Analysis Cases

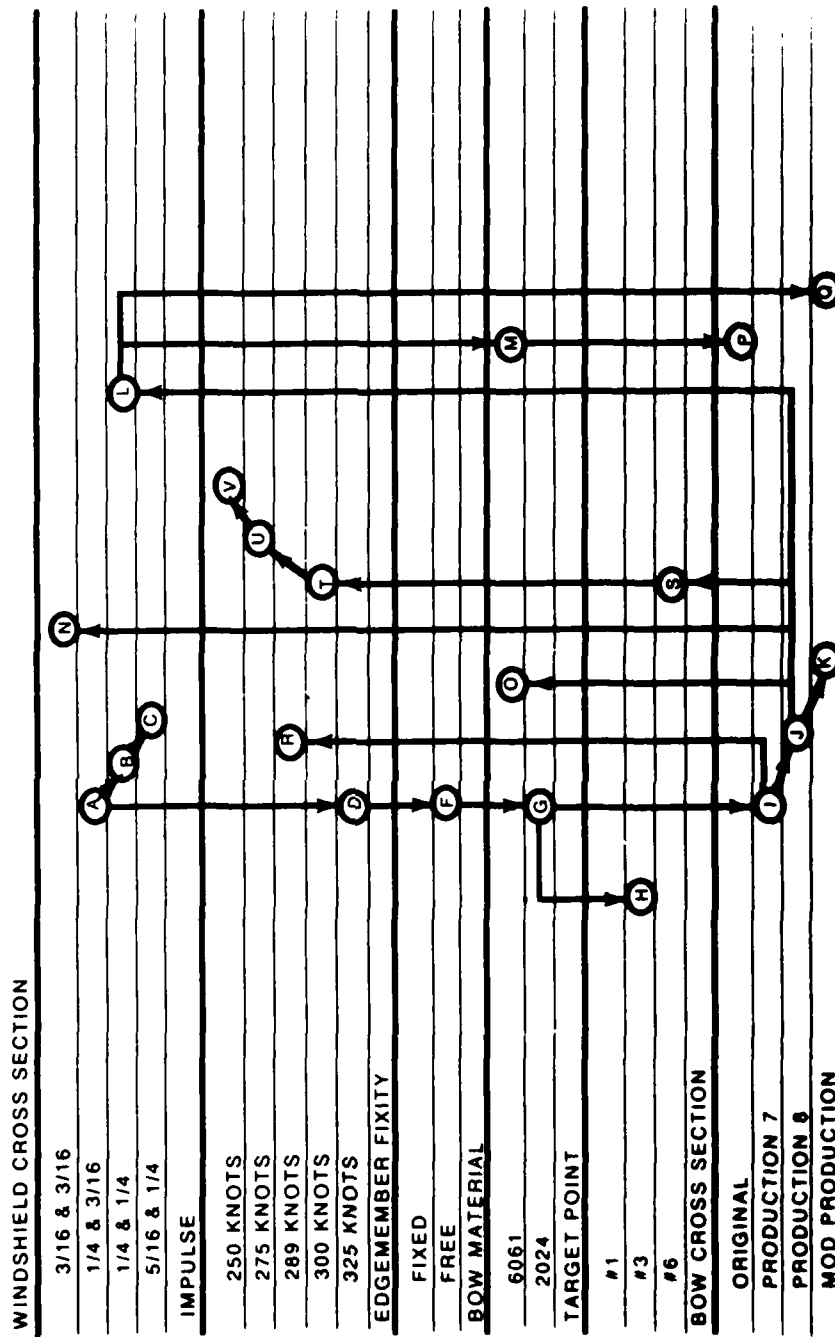


Table 4. Design Parameter Sensitivities

ANALYSIS (DEPENDENT) PARAMETERS

	IMPACT PRESSURE	NORMAL DEFLECTION	POLYCARBONATE STRESS	ALUMINUM STRESS
THICKER POLYCARBONATE PLIES	(L) ↑ (N) ↑	(L) ↑ (N) ↑	(B) ↑ (C) ↑ (L) ↑ (N) ↑	(L) ↑
INCREASED IMPULSE		(R) ↑	(D) ↑ (T) ↑ (U) ↑ (V) ↑	
INCREASED EDGE FIXITY	(F) ↑		(F) ↑	
STRONGER BOW MATL	(G) ↑ (M) ↓	(M) ↓ (O) ↓ (G) ↑	(M) ↓ (G) ↑	(M) ↓ (G) ↑ (H) ↑
TARGET PT OFF CENTER	(H) ↑		(H) ↓	
TARGET PT NEARER BOW			(S) ↓	
STIFFER BOW X SECTION	(Q) ↓ (J) ↓ (K) ↓	(P) ↓ (J) ↓ (K) ↓	(Q) ↓ (K) ↓	(I) ↓ (J) ↓ (K) ↓ (O) ↓

DESIGN (INDEPENDENT) PARAMETERS

○ CASE ↑ DEPENDENT PARAMETER INCREASED    ↓ DEPENDENT PARAMETER DECREASED  
 — DEPENDENT PARAMETER UNCHANGED

Table 5. Edgemember Analysis Results

CASE	BOLT BENDING MOMENT (IN LB)	ALLOW BOLT BENDING (IN LB)	BOLT SHEAR FORCE (LB)	ALLOW BOLT SHEAR (LB)	BOLT TENSION FORCE (LB)	ALLOW BOLT TENSION (LB)	COMB SHEAR TENSION	POLY BEARING STRESS (PSI)	ALLOW POLY BEARING (PSI)
F (P = 3 0 IN)	668	121	2859	2126	5010	2210	7 6	18671	14000
J (P = 1 6 IN)	599	276	2631	3680	3235	4080	0 99	17181	14000
K (P = 1 0 IN)	444	121	1589	2126	1110	2210	0 67	10379	14000
f (P = 2 8 IN)	624	121	2668	2126	4598	2210	6 3	17426	14000
J (P = 1 4 IN)	389	276	1707	3680	1362	4080	0 21	11145	14000
K (P = 1 4 IN)	622	276	2225	3680	2177	4080	0 51	14528	> 14000

Table 6. Windshield System Analysis Results

CASE	WINDSHIELD WEIGHT	BOW WEIGHT	BOW MATERIAL	POLYCARBONATE (STRESS)	BIRD ENTRY (DEFLECTION)	BOW (STRAIN)	BOLT	POLY (BEARING)
F	(63.0)	(8.0)	6061	PASS	PASS	MAJ DAM	FAIL	FAIL
G	0	0	2024	PASS	PASS	FAIL		
J	0	+5.9	2024	PASS	PASS	DAMAGE	PASS	PASS
K	0	+9.7	2024	PASS	PASS	POSS DAM	PASS	PASS
L	6.8	+5.9	2024	PASS	PASS	POSS DAM		
M	6.8	+5.9	6061	PASS	PASS	MAJ DAM		
N	6.8	+5.9	2024	POSS FAIL	PASS			
O		+5.9	6061					
P	6.8	0	6061					
Q	6.8	+9.7	2024	PASS	PASS	PASS		
MODII	0	+17.90	6061/2024	?	?	?	?	?

\* WEIGHT DIFFERENCE COMPARED TO INITIAL DESIGN (CASE F)

NOTE

WEIGHT DIFFERENCE BETWEEN ORIGINAL (F) AND CURRENT (J) DESIGNS WHICH CAN BE ATTRIBUTED TO STEEL BOLTS IS ONLY ABOUT 1 LB

## BIRD IMPACT TEST CORRELATION

A number of the MAGNA analysis cases accomplished, corresponded to particular full scale tests which had been conducted during T-46A windshield system development.<sup>32</sup> Good correlation was demonstrated for these cases between MAGNA computed results, and results observed in bird impact testing. This strong correlation between computed and experimental results provided the basis for selection of the Case J configuration as the nominal production design for the system.

Test number 876 corresponded to the Case F MAGNA analysis: 4 lb, 325 knot bird impact at target point 1 on the baseline windshield system design. This was the first full scale bird impact test, and it resulted in aluminum bow failure as indicated by MAGNA analysis. Predicted out-of-plane displacements approached 2.0 in. on the centerline of the bow, just at the end of the period of the bird impact event which was sufficient to open a direct path for entry of bird debris underneath the forward bow of the aircraft canopy. Some bird debris was observed to enter the cockpit area in Test Number 876.

Test number 912 corresponded to the Case J MAGNA analysis: 4 lb, 325 knot bird impact at target point 1 on the production windshield system design. This test was completely successful, with no mechanical failure of windshield panel, bow structure, or fasteners. No bird debris entered the cockpit area. As shown in Table 6, the only potential for failure indicated by MAGNA analysis in Case J was for the aluminum bow, and this computed result was regarded as being conservative. MAGNA results predicted out-of-plane displacements during the period of the bird impact event to be less than 1.0 in. on the centerline of the bow; not sufficient to permit entry of any significant amount of bird debris.

Test number 918 corresponded to the Case S MAGNA analysis: 4 lb, 325 knot bird impact at target point 6 on the production windshield system design. Tensile failure of polycarbonate plies in line with the row of bolts was observed during the test. No other failures of system components occurred. Results of MAGNA analysis Case S also clearly indicated only polycarbonate failure along the bow.

Test numbers 923, 925, and 924 were additional tests conducted with 4 lb bird impact at target point 6 on the production windshield system design. Speeds for these tests were 250, 265, and 275 knots respectively. Tests 923, and 925 were accomplished successfully, with no failures of any kind occurring. Test 924 resulted in polycarbonate failure. MAGNA analysis Cases T, U, and V simulated 4 lb bird impact at the same target point on the same system design, but at speeds of 300, 275, and 250 knots respectively. This series of three analyses were run before the actual tests were conducted, and the threshold of failure indicated was 275 knots, corresponding exactly to the full scale test results.



## CONCLUSIONS

### 1. Design Parameters

Windshield cross section design effects as determined by thicker polycarbonate structural plies had the anticipated effects for reducing peak bird impact pressure, out-of-plane displacements, and maximum polycarbonate stress. It was anticipated that thicker polycarbonate plies would also increase peak strains in the aluminum bow, but the opposite effect was observed in MAGNA analysis results.

Increased bird impact impulse delivered to the windshield had the expected effect of increasing peak polycarbonate stress.

Increased fixity at the aft edge of the windshield panel was expected to increase both the peak bird impact pressure on the windshield, and the maximum polycarbonate stress resulting from the impact. Instead both impact pressure and polycarbonate stress were very strongly decreased by increased fixity at the edge.

Both stronger bow materials and stiffer bow cross sections were believed to result in increased peak bird impact pressure, greater windshield deflections, increased maximum polycarbonate stress, and decreased strains in the bow itself. All of these preconceptions of parameter sensitivities were proven wrong by MAGNA analysis results. In fact, aluminum strains were seen to increase for stronger bow material with the baseline bow cross section design, but decrease for the production bow design.

Because the center region of the T-46A windshield was relatively flat, it was anticipated that bird impact pressure, peak polycarbonate stress, and maximum strains in the aluminum bow would all increase for target point 3, located 12 in. off the centerline of the windshield. It was felt that the local curvature near target point 3 would result in strong softening in the bending response (contrasting with membrane stiffening on the centerline), with a corresponding increase in load/response coupling, and maximum stresses and strains. MAGNA results indicated instead that both impact pressure and peak aluminum strain decreased at target point 3, while maximum polycarbonate stress remained unchanged.

Movement of the bird impact target point along the centerline and toward the bow, increased maximum polycarbonate stress, as anticipated.

Since the bird impact response of aircraft windshield systems is a highly nonlinear problem, the design parameter sensitivities determined for the T-46A system (Table 4) should not all be expected to hold in general for other windshield systems involving different dimensions, geometries, and materials.

### 2. Computer Aided Design Methods

As pointed out in the Introduction, the work reported here marks the

first significant Air Force systems acquisition application of MAGNA in bird impact resistant aircraft transparency system development. A number of years and considerable funds had been expended in unsuccessfully designing, fabricating, and testing three previous T-46A windshield system designs. Application of MAGNA was proven effective because it permitted 18 additional configurations to be assessed over the period of a few weeks time, at minimal cost. The initial nominal design selection based on these MAGNA assessment results was fabricated and qualified successfully in its first round of full scale testing.

MAGNA has been demonstrated to be a cost and time effective assessment tool, but at the same time, aircraft transparency system computer-aided design methods have been found sorely lacking. Aircraft transparency system design is still poorly understood, even for a single requirement such as bird impact resistance. The lack of straightforward convergence toward a qualified design which would result from effective design methods, if they did exist, is graphically illustrated in Table 3. Confusing and even contradictory sensitivities for system design parameters are shown in Table 4.

### 3. T-46A Windshield System

As discussed under Bird Impact Test Correlation, the T-46A windshield system design corresponding to MAGNA analysis Case J (FRC Drawing Number 210D111033) was selected for production. This design was successfully qualified for 4 lb 320 knot bird impact except for target point 6, at which it was qualified for 275 knots.

Because of concern regarding indications of possible failure for the Case J aluminum bow, consideration was given to a backup or alternate production design. Analysis Cases K and L both indicated lower bow strains, for a thicker bow and thicker windshield respectively. Since the thicker windshield option added twice as much weight as the thicker bow option, and was still not as effective in reducing bow strains, the thicker bow was selected as the backup production design. Another reason to opt for a thicker bow was that in the event of the nominal bow design being successfully qualified, the backup bow could be made into a production bow instead of having to be scrapped. In the end, the backup system design was not required.

### RECOMMENDATIONS

Application of the MAGNA analysis package on supercomputer systems should be employed by the aircraft transparency community to assess the performance of system design candidates with respect to bird impact resistance. Selection of designs for full scale fabrication and qualification testing should be based upon the results of such MAGNA analyses.

Similar application of MAGNA should also be employed to assess performance with respect to other types of mechanical loading such as cockpit pressure, aerodynamic loads, and thermal loads.

Just as MAGNA should be applied in conjunction with various requirements for mechanical loading, the STAPAT analysis package should be applied to assess the thermal performance of high temperature transparency system designs.<sup>30</sup> STAPAT application should include runway (aircraft parked) conditions, and low level transonic flight because both of these environments can result in very significant transparency system heating.<sup>31</sup>

In addition to those for mechanical (MAGNA) and thermal (STAPAT) loads, additional computer analysis tools should be developed to permit assessment of candidate transparency system designs with respect to other types of requirements. Such analysis tools should be developed or enhanced for optical performance, low observability, and advanced wartime threat protection.

Effective design methods which can take full advantage of such powerful computer assessment tools are in their infancy, and clearly need to be developed. Such design methods should utilize expert system drivers to streamline use of the numerous computer assessment tools involved, and must enable success in meeting multiple conflicting design requirements in a coordinated or systems engineering manner. The experience reported here in using MAGNA to successfully meet a single design requirement for the first time should serve as the starting point for such design method development.

#### REFERENCES

1. Littel, H. E., Windshield and Canopy Protection Development Program, Air Force Flight Dynamics Laboratory, Wright-Patterson Air Force Base, Ohio 45433-6553, AFFDL-TR-74-75, June 1974.
2. Lewis, A. L., and Cooke, K. W., F-111 Bird Resistant Windshield Support Structures, Air Force Flight Dynamics Laboratory, Wright-Patterson Air Force Base, Ohio 45433-6553, AFFDL-TR-74-40, May 1974.
3. West, B. S., Design and Testing of F-111 Bird Resistant Windshield/Support Structure; Volume 1 - Design and Verification Testing, Air Force Flight Dynamics Laboratory, Wright-Patterson Air Force Base, Ohio 45433-6553, AFFDL-TR-76-101, October 1976.
4. Olson, J. B., Design, Development and Testing of a Light-Weight Birdproof Cockpit Enclosure for the F-111, 1978 Conference on Aerospace Transparent Materials and Enclosures, Air Force Material Laboratory, Wright-Patterson Air Force Base, Ohio 45433-6553, AFFDL-TR-78-168, December 1978.

5. Pretzer, F. L., Multilayer Plastic Transparencies for the F/FB-111 Aircraft, Part I - Development Test and Evaluation of Bird Impact Resistant Transparencies (BIRT), Flight Dynamics Laboratory, Wright-Patterson Air Force Base, Ohio 45433-6553, AFWAL-TR-80-3005, Part I, March 1980.
6. McCarty, R. E., "Computer Analysis of Bird Resistant Aircraft Transparencies," Proceedings of the 17th Annual SAFE Symposium, December 1979, Las Vegas, Nevada.
7. McCarty, R. E., "Finite Element Analysis of F-16 Aircraft Canopy Dynamic Response to Bird Impact Loading," 21st AIAA/ASME/ASCE/AHS Structures, Structural Dynamics, and Materials Conference, May 1980, Seattle, Washington, AIAA Paper Number 80- 804.
8. McCarty, R. E., "Aircraft Transparency Bird Impact Analysis Using the MAGNA Computer Program," Conference on Aerospace Transparencies Sponsored by the Society of British Aerospace Companies, September 1980, London, England.
9. McCarty, R. E., "Finite Element Analysis of a Bird-Resistant Monolithic Stretched Acrylic Canopy Design for the F-16A Aircraft," AIAA Aircraft Systems and Technology Conference, August 1981, Dayton, Ohio, AIAA Paper Number 81-1640.
10. McCarty, R. E., and Hart, J. L., "Validation of the MACNA Computer Program for Nonlinear Finite Element Analysis of Aircraft Transparency Bird Impact," 14th Conference on Aerospace Transparent Materials and Enclosures Sponsored by the Air Force Wright Aeronautical Laboratories, July 1983, Scottsdale, Arizona, AFWAL-TR-83-4154, December 1983.
11. McCarty, R. E., "MAGNA Computer Simulation of Bird Impact on the TF-15 Aircraft Canopy," 14th Conference on Aerospace Transparent Materials and Enclosures Sponsored by the Air Force Wright Aeronautical Laboratories, July 1983, Scottsdale, Arizona, AFWAL-TR-83-4154, December 1983.
12. McCarty, R. E., "Aircraft Transparency Bird Impact Analysis Using the MAGNA Computer Program," Conference and Training on Wildlife Hazards to Aircraft Sponsored by the FAA, March 1984, Charleston, South Carolina.
13. McCarty, R. E., Trudan, D. E., and Davis, A. D., "Three Dimensional Nonlinear Dynamic Finite Element Analysis for the Response of a Thick Laminated Shell to Impact Loads," AIAA/ASME/ASCE/AHS 26th Structures, Structural Dynamics, and Materials Conference, April 1985, Orlando, Florida, AIAA Paper Number 85-0713-CP.
14. McCarty, R. E., and Gran, M. G., "MAGNA Nonlinear Finite Element Analysis of T-46 Aircraft Windshield Bird Impact," AIAA/AHS/ASEE Aircraft Systems, Design & Technology Meeting, October 1986, Dayton, Ohio, AIAA Paper Number 86-2732.

15. Bruner, T. S., MAGNA (Materially and Geometrically Nonlinear Analysis) Part II - Preprocessor Manual, Flight Dynamics Laboratory, Wright-Patterson Air Force Base, Ohio 45433- 6553, AFWAL-TR-82-3098 Part II, December 1982.
16. Brockman, R. A., MAGNA (Materially and Geometrically Nonlinear Analysis) Part I - Finite Element Analysis Manual, Flight Dynamics Laboratory, Wright-Patterson Air Force Base, Ohio 45433-6553, AFWAL-TR-82-3098 Part I, December 1982.
17. Brockman, R. A., MAGNA (Materially and Geometrically Nonlinear Analysis) Part III - Postprocessor Manual, Flight Dynamics Laboratory, Wright-Patterson Air Force Base, Ohio 45433-6553, AFWAL-TR-82-3098 Part III, December 1982.
18. Brockman, R. A., MAGNA (Materially and Geometrically Nonlinear Analysis) Part IV - Quick Reference Manual, Flight Dynamics Laboratory, Wright-Patterson Air Force Base, Ohio 45433-6553, AFWAL-TR-82-3098 Part IV, December 1982.
19. Barber, J. P. and Wilbeck, J. S., Characterization of Bird Impacts on a Rigid Plate: Part I, Air Force Flight Dynamics Laboratory, Wright-Patterson Air Force Base, Ohio 45433-6553, AFFDL-TR-75-5, January 1975.
20. Peterson, R. L. and Barber, J. P., Bird Impact Forces in Aircraft Windshield Designs, Air Force Flight Dynamics Laboratory, Wright-Patterson Air Force Base, Ohio 45433-6553, AFFDL-TR-75-150, March 1976.
21. Ito, Y. M., Carpenter, G. E., and Perry, F. W., Bird Impact Loading Model for Aircraft Windshield Design, California Research and Technology, Inc, Woodland Hills, California 91364, CRT 3090-2, July 1977.
22. Barber, J. P., Wilbeck, J. S., and Taylor, H. R., Bird Impact Forces and Pressures on Rigid and Compliant Targets, Air Force Flight Dynamics Laboratory, Wright-Patterson Air Force Base, Ohio 45433-6553, AFFDL-TR-77-60, May 1978.
23. Wilbeck, J. S., Impact Behavior of Low Strength Projectiles, Air Force Materials Laboratory, Wright-Patterson Air Force Base, Ohio 45433-6553, AFML-TR-77-134, July 1978.
24. Challita, A., and Barber, J. P., The Scaling of Bird Impact Loads, Air Force Flight Dynamics Laboratory, Wright-Patterson Air Force Base, Ohio 45433-6553, AFFDL-TR-79-3042, March 1979.
25. Parker, J. Y., Measurement of Bird Impact Pressure on a Flat Plate, Arnold Engineering Development Center, Arnold Air Force Station, Tennessee 37389, AEDC-TR-79-14.
26. Heath, J. B. R., Gould, R. W., and Cowper, G. R., Momentum Transfer in Bird Impacts, National Aeronautical Establishment, National Research Council, Ottawa, Canada, LTR-ST-1257, April 1981.

27. Challita, A., and West, B. S., Effects of Bird Orientation at Impact on Load Profile and Damage Level, Air Force Wright Aeronautical Laboratories, Wright-Patterson Air Force Base, Ohio 45433-6553, AFWAL-TR-80-3009, June 1980.
28. Challita, A., Validation of a Bird Substitute for Development and Qualification of Aircraft Transparencies, Air Force Wright Aeronautical Laboratories, Wright-Patterson Air Force Base, Ohio 45433-6553, AFWAL-TR-80-3098, October 1980.
29. Shaver, J. E., and Mead, K. D., T-46A Windshield Impact Test, Arnold Engineering Development Center, Arnold Air Force Station, Tennessee 37389-9998, AEDC-TSR-86-V58 and Data Package, January 1987.
30. Varner, M. O., Adams, J. C., Boylan, D. E., Gwinn, A. F. Jr., LeMaster, R. A., Martindale, W. R., and Nopravarakorn, V., Specific Thermal Analyzer Program for High-Temperature Resistant Transparencies for High-Speed Aircraft (STAPAT), Volume I Methodology, Air Force Wright Aeronautical Laboratories, Wright-Patterson Air Force Base, Ohio 45433, AFWAL-TR-84-3086, Volume I, (AD B089 497), October 1984.
31. Babish, C. A. III, and Rakolta, M. J., Effect of Forebody Shape on Temperature of Aircraft Windshields at Transonic Speeds, Air Force Wright Aeronautical Laboratories, Wright-Patterson Air Force Base, Ohio 45433, AFWAL/FDER Letter Report, September 1988.

HYPersonic THERMAL ANALYSIS FOR AIRCRAFT TRANSPARENCIES

Bret L. Boman  
McDonnell Aircraft Company

Charles A. Babish III  
Flight Dynamics Laboratory

# HYPERSONIC THERMAL ANALYSIS FOR AIRCRAFT TRANSPARENCIES

BRET L. BOMAN

Senior Engineer - Propulsion and Thermodynamics  
McDonnell Aircraft Company  
McDonnell Douglas Corporation  
St Louis, Missouri 63166

CHARLES A. BARISH III

Aerospace Engineer  
Flight Dynamics Laboratory  
Air Force Wright Aeronautical Laboratories  
Wright-Patterson Air Force Base, Ohio 45433

## ABSTRACT

The Air Force has identified the need for advancements in key technology areas applicable to hypersonic flight vehicles. Specifically, new analysis techniques are needed for transparency systems which are expected to be critical subsystem structures of future Forecast II systems such as hypersonic interceptor and hypervelocity vehicles. The state-of-the-art for aerothermodynamic analyses of transparency systems is represented by the STAPAT computer program. STAPAT is a Specific Thermal Analyzer Program for Aircraft Transparencies that was originally developed for supersonic, fighter-type aircraft.

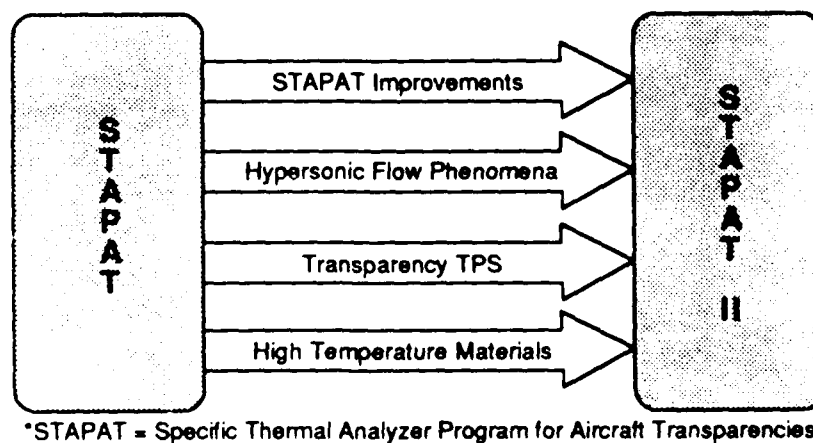
This paper documents the status of a program to develop STAPAT II, a significant enhancement of STAPAT, that will perform transient, three-dimensional thermal analyses of windshields, canopies, and windows of aerospace vehicles that operate at hypersonic speeds. STAPAT II is being developed in a manner similar to the development of STAPAT. Development emphasizes the integration of currently available aero-thermal/thermal analysis techniques. Given a finite element model of the transparency system, the shape of the forward fuselage of a hypersonic aerospace vehicle, and freestream Mach number, altitude, and attitude as functions of time, STAPAT II will calculate transparency system temperatures. It will also calculate values for all required parameters associated with inviscid aerodynamic flow through shock waves, viscous boundary layer flow for aerodynamic heating, solar radiation, radiation to the earth and sky, surface-to-surface radiation, conduction through the transparency system, convection to the cabin, and active cooling and heating of the transparency system. Pre- and post-processing of input and output information will also be provided.



## INTRODUCTION

The increasing pace of hypersonic vehicle research requires advances in a number of technical disciplines and enhancements in the available analysis tools. The thermal-structural design of transparency systems falls in this category. The current state-of-the-art for aerothermodynamic analyses of transparency systems is represented by the STAPAT\* computer code which is described in References 1 and 2. However, STAPAT was developed specifically for the analysis of supersonic, fighter-type aircraft transparency systems.

The objective of this paper is to describe the status of a new U.S. Air Force sponsored program to develop and validate a nonproprietary computer code which performs transient, three-dimensional thermal analysis of hypersonic vehicle transparency systems. This work is being performed by McDonnell Aircraft Company, Rockwell International's North American Aircraft Operations, and Dr Fred R. DeJarnette (North Carolina State University). The work began in October 1987 and is scheduled for completion in March 1990. The final product, STAPAT II, will be a significant extension of the current STAPAT code. Modifications to STAPAT (Figure 1) will include: (1) improvements to existing STAPAT capabilities; (2) improvements to model hypersonic flow phenomena; (3) improvements to model transparency thermal protection systems (TPS); and (4) additions to the material property data base to model high temperature transparency system materials. The transparency systems that STAPAT II will be able to analyze include crew station windshields/canopies/windows plus both visual and non-visual sensor windows. Once the development and validation of STAPAT II code is completed, it will allow evaluation of transparency system concepts for a wide range of configurations and trajectories.



\*STAPAT = Specific Thermal Analyzer Program for Aircraft Transparencies

GP83-0474-3-D

Figure 1. STAPAT II Development

## BACKGROUND (OVERVIEW OF STAPAT)

The original STAPAT computer software package merges state-of-the-art technology with functional and accuracy requirements, resulting in an efficient aerothermodynamic analytical technique that is specifically applicable to the study of high-temperature resistant transparencies for supersonic aircraft. STAPAT is a modular software package consisting of four discrete program modules (Figure 2). Each module has a unique function as related to a specific flight or wind tunnel-simulated mission.

The STAHET module is used for the generation of the forced, external convection environment over the transparency system surface for specific points within flight and wind tunnel mission profiles. For flight missions, the methodology utilized in the STAHET module is based on the DeJarnette streamline tracing approach to define the heat transfer variation along specified streamlines traced from a point near the configuration nose (Reference 3). The DeJarnette methodology has been modified to provide solutions for sharp-nose forebody configurations throughout the subsonic and low-to-moderate supersonic speed ranges. Pressure distributions utilized in the STAHET methodology are based on the application of the modified Newtonian theory. For wind tunnel missions, heating rates for two-dimensional, wedge-shaped configurations are computed using reference enthalpy and Van Driest II techniques.

Thermal analyses of flight and wind tunnel mission problems are performed in the thermal analyzer program module TAP. TAP is a transient, finite-element aerothermodynamic analysis tool that has been specifically configured for the analysis of aircraft transparency systems in realistic flight mission and wind tunnel environments. Solutions obtained from TAP are temperature histories as functions of time of the thermal environment within the transparency system for all previously defined finite-element nodes. Time-varying radiation, convection, heat flux, and temperature boundary conditions can be modeled. Two types of mission profiles can be executed on TAP. These consist of flight-type missions where altitude and Mach number as functions of time are required and wind tunnel-type missions to simulate a wind tunnel test environment where Mach number, total pressure, and total temperature are required as functions of time.

Generation of the finite-element grid for the thermal analyzer program is primarily performed in the STABLD module. STABLD is a pre-processor program that allows for the interactive generation of the finite element grid for a wide class of transparency system configurations. Capabilities of STABLD include surface generation, thru-thickness generation, and cursor model generation capabilities. Once a finite-element model has been generated by the STABLD module, a completed nodal and element definition is available for use in the thermal analyzer program. Data files are created for both the nodal coordinates and element connectivities of the generated finite-element model.

Post-processing data analysis is accomplished through the post-processor module STAPLT. This module is a totally user-interactive program that allows for visual display of the forebody geometry, the finite-element model, and the STAHET and TAP solution results. Capabilities exist to display: (1) normalized flow field parameter and heat transfer rate isolines occurring on the forebody surface, (2) isotherm lines projected onto finite-element surfaces, (3) linear plots of atmospheric conditions as functions of time, (4) linear plots of heat transfer rates and temperatures as functions of time for selected node points within the finite-element model, and (5) linear plots of temperature as a function of distance through the thickness of the finite-element model.

Output from the STAHET module consists of tabular output and a formatted data file. The tabular output format contains the heating distribution over the body for all conditions specified in the input data file at two specified wall temperature conditions. The data file generated by the STAHET module contains the heat transfer distribution over the forebody surface for all input conditions that are compatible with the thermal analyzer program input requirements.

Output from the TAP module consists of both tabular and post-processing data formats. The tabular output identifies all input jobstream data and the resulting detailed boundary condition information, as well as the temperature-time histories of all node points as a solution evolves in time. The post-processing data file contains the finite-element grid definition, mission definition, heat transfer, and thermal environment as functions of time.

Data files required for the implementation of the STAHET module are the input data stream defining the control parameters for the STAHET module and the forebody and transparency system geometry coordinates. Both flight and wind tunnel model calculations may be performed with the STAHET module. Flight-type calculations require the input of Mach number, altitude, and atmospheric type. Wind tunnel-type mission inputs of Mach number, wedge angle and stagnation pressure and temperature are required as functions of time. TAP uses a free-format, machine-independent command interpreter to provide a flexible mechanism for inputting material and geometric data and communicating with the program. STAPAT incorporates embedded data files including the 1976 standard atmosphere, high and low temperature military specification atmospheres, material thermophysical properties values as functions of temperature, and sky and earth radiation temperatures and solar radiation as functions of altitude.

The pre- and post-processing modules, STABLD and STAPLT, have been developed for execution on the Digital Equipment Corporation, VAX 11/780 computer and the Tektronix 4014 interactive computer terminal employing PLOT 10 Software (the 4010A01 Terminal Control System (TCS) and the 4010A01 Advanced Graphing II package). The use of TAP on 32 and 36-bit word machines requires the double-precision version of the code; the single-precision version is required for 60 or 64-bit word machines.

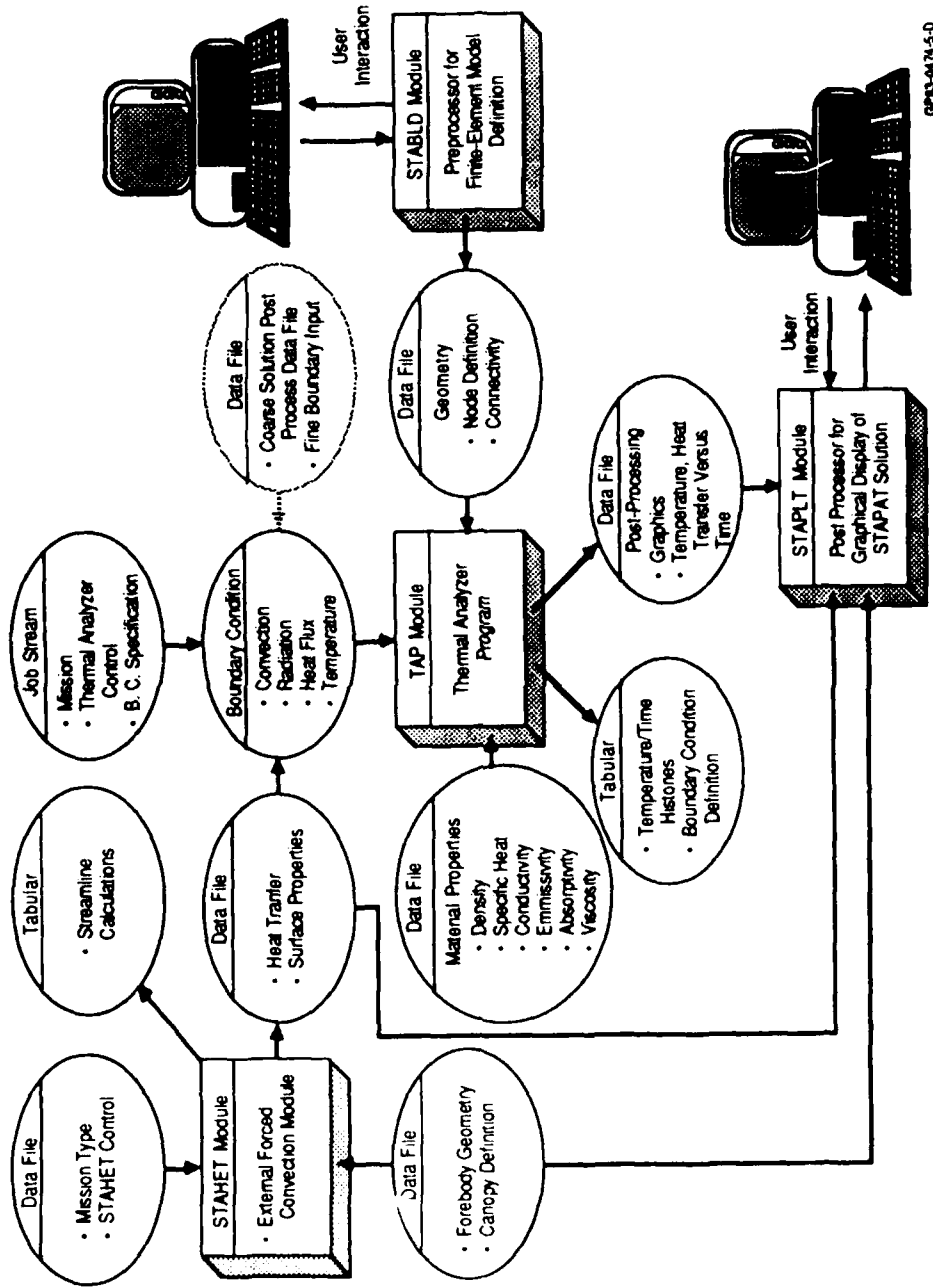


Figure 2. STAPAT Modular Software Description

## STAPAT MODIFICATIONS

STAPAT is being modified to produce additional and enhanced capabilities as shown in Figure 1 to create STAPAT II. These capabilities are being established by: (1) identifying desired capabilities; (2) analyzing the desired capabilities' importance in predicting transparency temperatures; (3) selecting capabilities based on a cost/benefit approach; and finally, (4) defining the selected capability's methodology for incorporation into STAPAT II. In addition, STAPAT modifications are required to: (1) be user friendly and non-proprietary; (2) provide reasonably accurate transparency temperatures without requiring excessive computing resources; (3) use existing methodologies to predict heating rates and resulting temperatures; and (4) not degrade current STAPAT capabilities.

Potential capabilities for STAPAT II were identified by reviewing the current features of the existing STAPAT code and determining which capabilities required improvement for both supersonic and hypersonic analyses. Since the aerodynamic heating portion of STAPAT is based on the DeJarnette heating code (References 3, 4, and 5), improvements made to this code under other efforts were reviewed (References 6, 7, 8, 9, 10, and 11).

### STAPAT CAPABILITY IMPROVEMENTS

Improvements to the existing STAPAT code, regardless of the vehicle speed regime, were desired for the modeling techniques described in the following subsections.

#### Forebody Geometry Definition/Fitting

Vehicle forebody surface geometry is currently input to STAPAT as a set of surface coordinates specified at constant axial locations from the nose tip aft to the end of the forebody. At each cross-section, the axial distance is specified along with the radial and angular positions from the top centerline to the bottom centerline. Because most supersonic fighter aircraft have relatively sharp noses, a sharp cone is added to the user input geometry. This cone extends from the nose to an axial distance equal to 10 percent of the distance to the first cross-section. The end of the cone becomes the starting point of the DeJarnette heating code calculations. The vehicle geometry is then fitted using parametric cubic spline equations. While this technique provides a reasonable fit it can produce wiggles in the surface geometry and tends to round off discontinuities. An additional important drawback of the current technique is that it does not allow the user to review or alter the fitted geometry.

Two promising techniques which overcome shortcomings of the existing method are the ASTUD (Reference 12) and QUICK (Reference 13) geometry modelers. Both methods involve an interactive fitting of cross-section data points. The resulting geometry can be reviewed and altered as

desired. These new techniques have been incorporated in STAPAT II as a supplement to the current geometry input/fitting technique. Choice of the geometry fitting method to be employed (i.e., current, ASTUD, or QUICK) will depend on vehicle complexity, geometry model development time, required accuracy, computing resources required/allotted, and user familiarity with the geometry modeler.

### Forebody Nose Geometry

While boundary layer solutions are obtained from equations which are strictly valid only in the vicinity of the vehicle top or bottom centerline, the heating code method provides acceptable results up to about 30 to 40 degrees from the centerline. All vehicle noses have some degree of bluntness, though many hypersonic vehicles are blunter than supersonic aircraft. In addition, transparencies on hypersonic vehicles may be located anywhere on the forebody not just in the vicinity of the vehicle top centerline. STAPAT II will therefore be modified to provide the capability of modeling varying degrees on nose bluntness and calculating aerodynamic heating over the entire forebody.

### Forebody Geometry Data Base

STAPAT II will also incorporate a built-in, forebody geometry data base file which will contain supersonic fighter aircraft forebodies and hypersonic aerospacecraft forebodies, as shown in Figures 3 and 4, and simple shapes such as sphere/cones, sphere/ogives, sphere/cylinders, ogive cylinders, hyperboloids and spherically blunted, bent biconics.

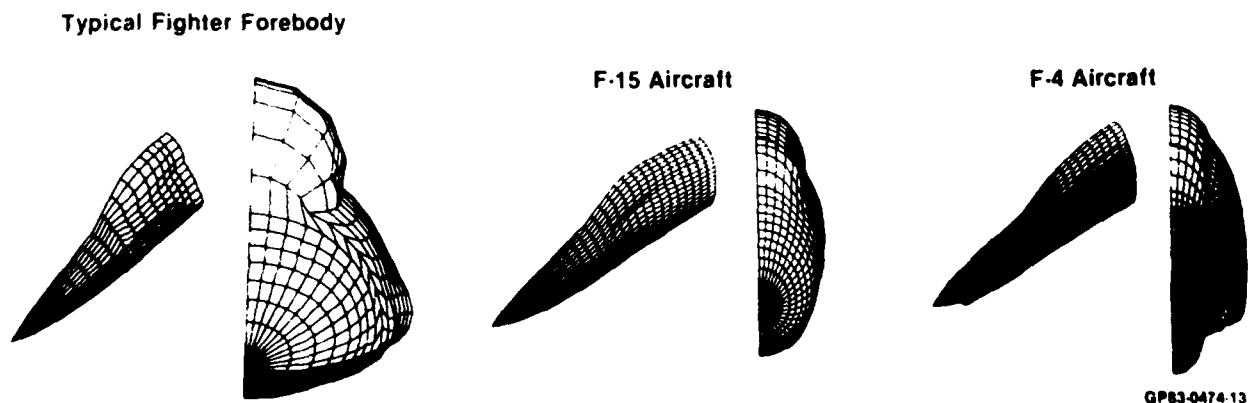
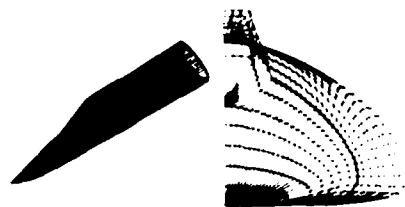
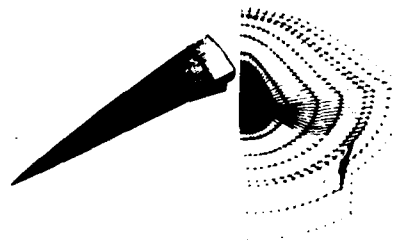


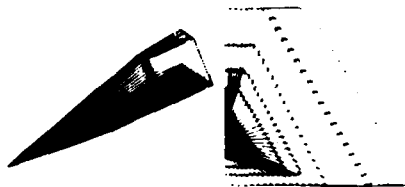
Figure 3. Supersonic Forebody Geometry Data Base



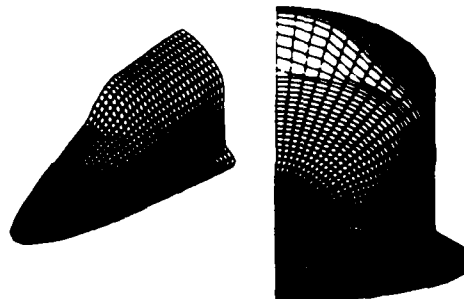
**Advanced Manned Interceptor**



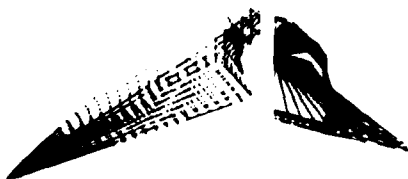
**Hypersonic Cruise Vehicle**



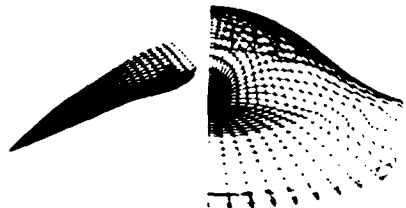
**Transatmospheric Vehicle**



**Space Shuttle**



**NASP Option Caret**



**NASP Option Blended Wing Body**

GP83-0474 12

**Figure 4. Hypersonic Forebody Geometry Data Base**

### Surface Pressure (Shadow Region/Separated Flow)

Surface pressure values are currently calculated in STAHET using the modified Newtonian method. The boundary layer edge pressure is then set equal to the surface pressure to evaluate local properties. While this method is generally adequate, one area where improvement of surface pressure prediction is needed is in shadow regions, such as the canopy backside shown in Figure 5. In this situation, the local body angle relative to the free-stream velocity is negative. STAFAT currently sets the pressure coefficient to zero in this area thus resulting in the local pressure equal to the free-stream pressure. In reality, flow expands around the canopy and the pressure coefficient would be negative.

As the local inclination angle becomes more negative relative to the free-stream velocity, separated flow may occur. To determine when separated flow occurs and provide an approximate method for predicting the surface pressure in separated flow, an effective flow turning angle has been defined as a function of local Mach number. If the local inclination angle is greater than the effective turning angle, separated flow is predicted.

Four methods for calculating shadow region pressure coefficients, Babish (Reference 14), Prandtl-Meyer (Reference 15), Dahlem-Buck mirror (Reference 16) and ACM empirical (Reference 17), will be made available as user options in STAFAT II. Each option will incorporate the effective turning angle method for predicting and approximating separated flow.

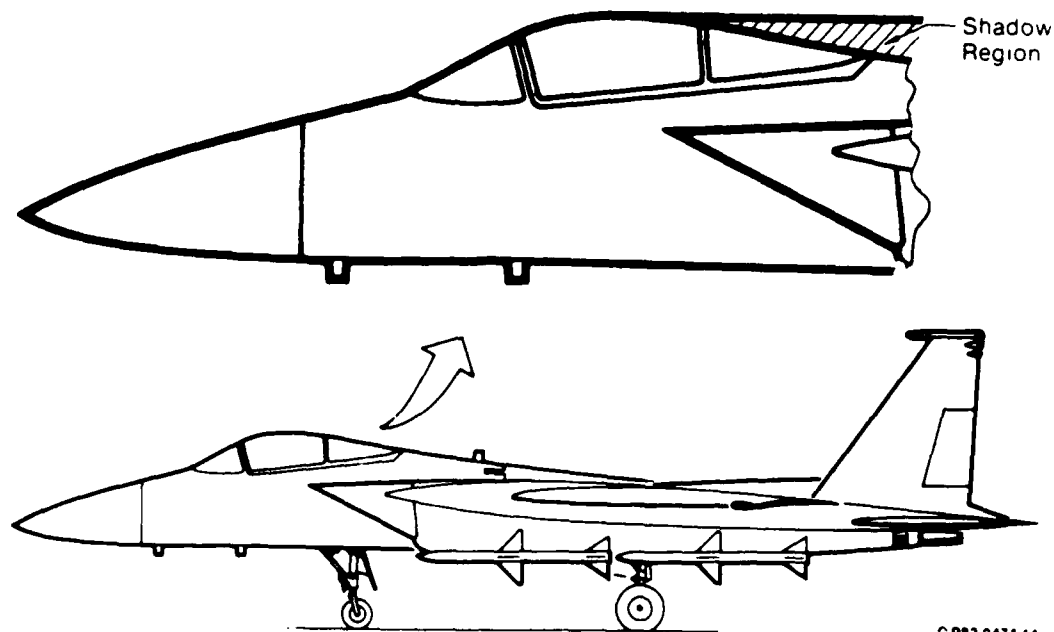


Figure 5. Canopy Shadow Region



### Convection Modeling

TAP convective heat transfer modeling includes: (1) user specified heat transfer coefficient and driving temperature; (2) aeroheating results from STAHET; (3) flat plate heating; (4) cabin cooling; (5) defog (with cabin cooling); (6) hot air gap, and (7) deice (air). Since defog flow over the windshield can occur without the presence of cabin cooling, the current TAP methodology will be modified in STAPAT II to allow for defog without cabin cooling. To provide a more realistic and flexible air gap modeling capability, the current heat transfer correlation (based on the cabin correlation) will be dropped in favor of a generalized channel flow correlation. In addition, properties for gap fluid candidates will be added to the material data base in order to make use of this correlation. To provide a more realistic air deice modeling capability the current correlation will be dropped in favor of a film heating correlation.

### Pre- and -Post Processing Capability Improvements

Both the STABLD pre-processor and the STAPLT post-processor of STAPAT use Tektronix PLOT 10 Advanced Graphics Language as their graphics software base. This graphics package requires a software license and is not compatible with all graphics hardware devices. STAPAT II will include an additional graphics software base using the American National Standard's Graphics Kernel System (GKS) to allow easy graphics program transport between hardware installations. STAPAT will also be modified to provide STAPAT II with: (1) a digitizing capability for inputting forebody geometry from drawings; and (2) a color/shaded display capability for forebody geometry and temperature results verification. A sample of the proposed shaded display capability is shown in Figure 6.



GP33-047-16

**Figure 6. Proposed Shaded Display Capability**

## HYPERSONIC FLOW PHENOMENA MODELING ADDITIONS

A wide variety of hypersonic vehicle configurations, transparency system design concepts, and mission trajectories were examined to determine the additional STAPAT II capabilities needed to model hypersonic flow phenomena. Areas examined included: (1) speed/flow regimes; (2) vehicle configuration/transparency shape; (3) vehicle attitude; and (4) special flow fields. The existing STAPAT code was developed for supersonic aircraft and is therefore applicable to speeds below Mach 3.5 and altitudes less than 100,000 ft. In this flight regime air can be modeled as a calorically perfect gas and its density is large enough to model as a continuum. Typical flight domains of hypersonic vehicles are shown in Figure 7. At these higher speeds and altitudes, the validity of these models become invalid and methods are required to model: high temperature air, viscous interaction, rarified flow, and wall temperature effects. In addition, the altitude dependent values of free-stream atmospheric conditions, sky and earth radiation temperatures, and solar radiation will be extended from 100,000 ft to 1,000,000 m in STAPAT II.

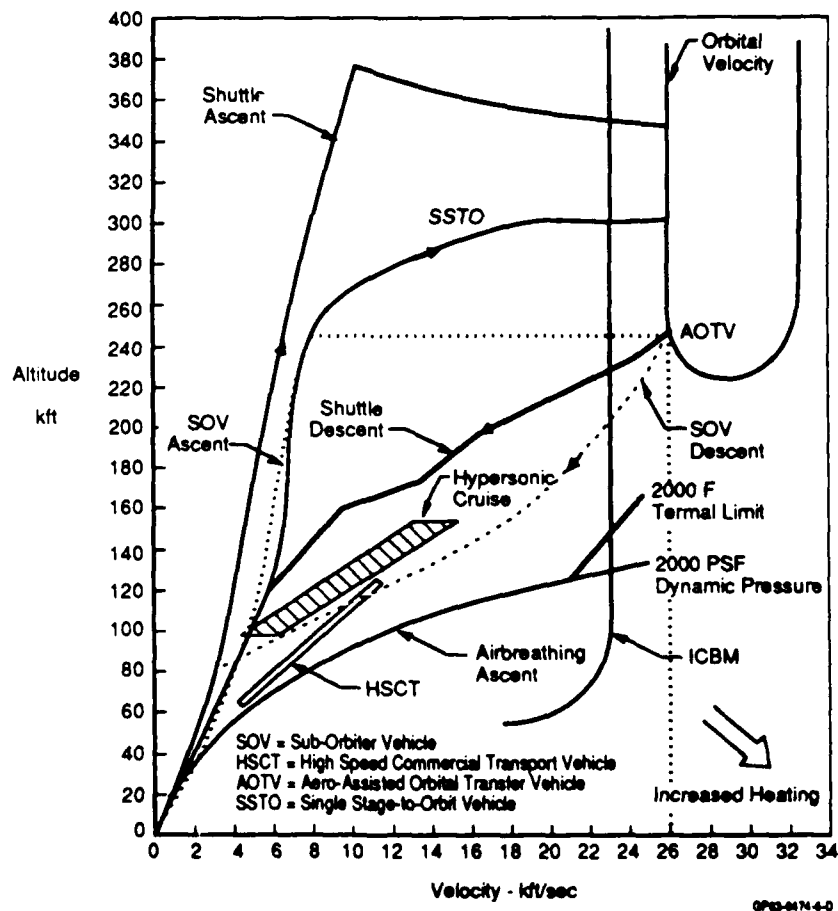


Figure 7. Flight Domain of Hypersonic Vehicles

## High Temperature Air Effects

At supersonic speeds and below, the air can be treated as calorically perfect (i.e., constant specific heat). As the air molecules slow down across the shock or in the boundary layer, their kinetic energy is converted to potential energy and manifests itself as a temperature rise. This is how STAHET currently models the air behavior. As speed increases, not all of the energy conversion results in temperature rise. Some of the energy conversion causes vibrational excitation of the air molecules. As speed increases further, the energy conversion results in first dissociation of oxygen molecules and then, at higher speeds, dissociation of nitrogen molecules. Recombination of these dissociated air molecules occurs as the flow expands around the vehicle and at the cooler vehicle surface. Still further increases in speed result in ionization of the air molecules.

If the air is sufficiently dense such that these gas reactions (dissociation, ionization) occur very fast, the flow is in chemical equilibrium. There are many chemical equilibrium air models and resulting approximations available to evaluate thermodynamic properties of excited, dissociated, and ionized flows. Two of the more efficient and accepted equilibrium air model approximations, RGAS (Reference 18) and TGAS (Reference 19), will be incorporated in STAPAT II for user selection at hypersonic speeds.

## Viscous Interaction Effects

In STAHET's flowfield solution the inviscid flowfield is solved first, then the inviscid properties are used as edge conditions for the boundary layer solution. At high speeds, especially for slender vehicles, the accuracy of this method decreases. This is because the boundary layer can grow so thick (boundary layer thickness increases with velocity) that it interacts with the inviscid flow field. This is the so-called "viscous interaction phenomena." It results in higher surface pressures and consequently higher heating rates than predicted using STAHET's two layer flowfield solution. These effects are more pronounced in the nose region. A viscous interaction parameter can be used to show where these effects are important.

A user option will be included in STAPAT II to approximate viscous-shock layer interactions. When implemented, this option will provide for: (1) calculation of a viscous shock layer interaction parameter; and (2) calculation of heating rates based on vehicle surface geometry modified to include the boundary layer displacement when the interaction parameter exceeds a value of three at the first streamline calculation point.

### Rarified Flow Effects

STAHET currently models the air flow as a continuum (e.g., because the mean free path between molecular interactions is small compared to the smallest flow field characteristic length, individual molecules can be ignored and the air consists of a continuous matter). As altitude increases such that the continuum assumption is no longer valid, the flow becomes rarified. Heating rates assuming rarified flow are lower than those predicted assuming continuum flow. Thus, the continuum flow assumption provides conservative results.

Since some hypersonic vehicles will operate in these rarified flow regions, STAPAT II will incorporate a user option to approximate reductions in heating due to rarified flow effects. When employed, this option will calculate a rarified-continuum Stanton number ratio and will multiply this ratio by the continuum based Stanton number currently calculated in STAHET. The resulting rarified based Stanton number will then be used in the thermal analyzer program (TAP) to calculate the heat transfer coefficient.

### Wall Temperature Effects

The effect of wall temperature on heat transfer was investigated during the original STAPAT development for speeds up to Mach 3.5. Development of STAPAT II includes investigation of wall temperature effects on heat transfer at higher speeds. Aerodynamic heating to the vehicle surface is given by:

$$q = h ( TAW - TW ) \quad (1)$$

where

q = aerodynamic heat transfer rate

h = heat transfer coefficient

TAW = adiabatic wall temperature

TW = wall temperature

The heat transfer coefficient is weakly dependent on the wall temperature. However, the wall temperature is a function of heat storage and the heat transfer boundary conditions. Thus, the most accurate temperature solution requires an iterative procedure in which the wall temperature is assumed, the heat transfer coefficient is calculated, and then the wall temperature is calculated and compared with the assumed wall temperature. If the difference between wall temperatures (assumed vs calculated) is small, an acceptable solution has been attained. If the difference is not small, the calculated temperature would be iterated until convergence occurs. This method of coupling the heat transfer coefficient calculation with the wall temperature calculation within STAPAT is computationally difficult because streamline calculation point locations do not inherently coincide with the transparency finite element node

locations. This prevents direct feedback of the TAP calculated wall node temperature into the STAHET streamline calculations.

The original STAPAT work concluded that the free-stream based Stanton number (non-dimensionalized heat transfer coefficient, ST) for heating and cooling was relatively insensitive to wall temperature. This was shown for speeds up to Mach 3.5. As a result, STAHET currently requires the user to input two wall-to-total temperature ratios: TW/T0 less than TAW/T0 for aerodynamic heating, and TW/T0 greater than TAW/T0 for aerodynamic cooling. (Where T0 is the total temperature.) STAHET calculates free-stream based Stanton numbers for both wall temperature ratio values and passes this information to TAP. Then based on the previously calculated wall-to-adiabatic wall temperature ratio, TW/TAW, it uses the appropriate Stanton number to calculate the heat transfer coefficient.

At higher speeds, reradiative heat transfer becomes very important, stagnation temperatures become very large, and because of the potential for film or active cooling, the range of wall temperatures encountered can be very large. Therefore, the effect of wall temperature on heat transfer at hypersonic speeds was investigated. STAHET calculations showed that ST decreases with TW at all flight speeds. It was concluded that a parabolic curve fit to Stanton numbers based on wall-to-total temperature ratios of 0.1 and 1.2 provides an accurate and economical method of accounting for the wall temperature effect on convective heat transfer.

The STAPAT II approach to modeling the wall temperature effect will be to: (1) calculate ST for TW/T0 ratios of 0.1 and 1.2 within STAHET, and (2) calculate ST within TAP for a given time step from the following:

$$ST = ST_{0.1} + (ST_{1.2} - ST_{0.1}) (TW/T0)^2 (1.2)^{-2} \quad (2)$$

where

(Tw/To) = wall-to-total temperature ratio at the previous time step

Subscripts 0.1 and 1.2 = based on TW/T0 ratios of 0.2 and 1.2

### Vehicle Attitude

Since peak heating on supersonic aircraft transparencies occurs when operating at little or no angle-of-attack, the existing STAPAT code does not model angle-of-attack. Hypersonic vehicles however, will operate a sustained angle-of-attack. Airbreathing cruise and aerospace vehicles will operate at low to moderate values (less than 10 degrees) while shuttle and re-entry vehicles will operate at high values (greater than 20 degrees). Therefore, prediction of aerodynamic heating for vehicle operation at angle-of-attack will become a STAPAT II capability. Operation of hypersonic vehicles with sustained sideslip is not expected and will not be modeled in STAPAT II.

## THERMAL PROTECTION SYSTEMS MODELING IMPROVEMENTS

Thermal protection measures are often required on hypersonic vehicles to protect the transparency materials from severe heating environments. These include: active cooling, multiple pane arrangements with and without cooling, recessed transparencies, film cooling, and movable covers which protect the transparency for some portion of the flight. STAPAT II will be capable of modeling these thermal protection concepts.

STAPAT can currently model active cooling of transparencies using the user specified convection option in TAP. With the current surface-to-surface radiation capability and the more generalized between-pane cooling technique that will be added, STAPAT II will be able to model multipane arrangements with and without cooling. Methods will also be needed to predict heating over recessed transparencies, in film cooling regions, and over movable covers.

Reductions in aerodynamic heating over transparencies can be achieved by removing, or shielding, the transparency from the main flowfield. Two alternatives for shielding the transparency are shown in Figure 8. Modeling the controlled expansion technique is similar to modeling that portion of a fighter aircraft canopy located in the shadow region. The STAPAT II methods for predicting the reduction of pressure coefficients in shadow regions, then, will also be applicable to hypersonic transparency systems.

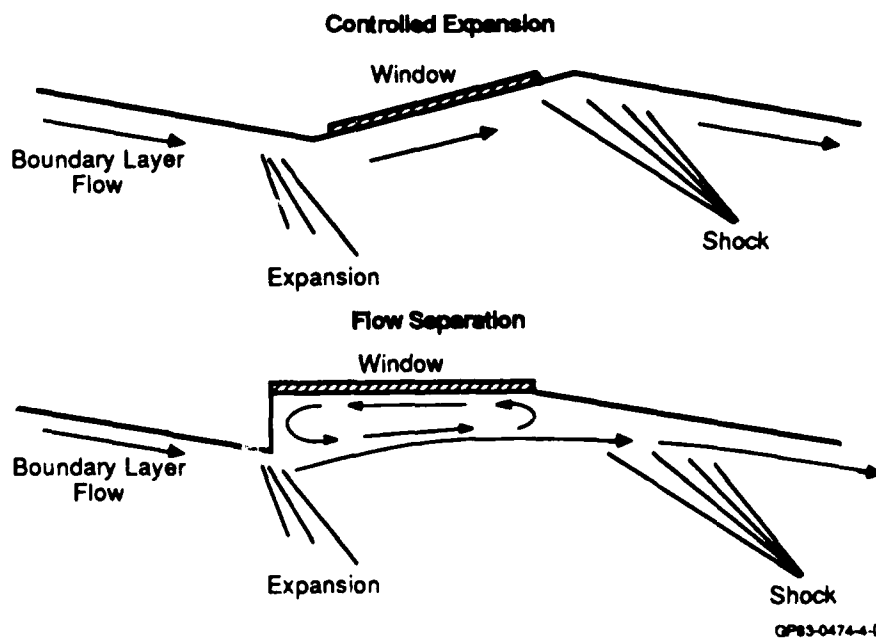


Figure 8. Transparency Shielding Techniques

Modeling the flow separation shielding technique, requires using correlations developed from experimental data. Correlations based on laminar flow upstream of a cavity showed lower heating (approximately 25 percent of local heating upstream of the cavity) over the first 60 percent of the cavity followed by a significant rise as the flow reattached at the rear of the cavity. Correlations based on turbulent flow upstream of a cavity showed similar trends. In addition, cavity temperatures were significantly lower than upstream surface temperatures.

Since the correlations are specific to particular geometries and conditions, care must be taken in applying them as general correlations. Therefore, STAPAT II will incorporate two options for predicting cavity heat transfer: (1) a user-input heat flux multiplier vs cavity length option; and (2) laminar and turbulent heating correlations based on the geometry particular conditions.

Film cooling can reduce recessed transparency temperatures even further. A correlation developed for modeling film cooling over missile sensor windows computes the heat transfer rate as follows:

$$q = h ( T_{EFF} - T_W ) \quad (3)$$

where

q = heat transfer rate to the surface

h = heat transfer coefficient based on no cooling

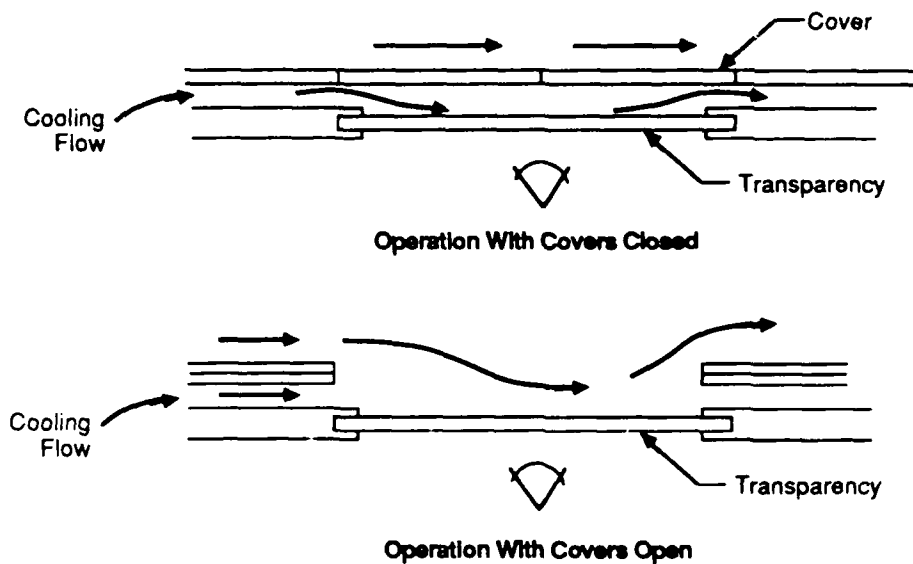
T<sub>EFF</sub> = effective adiabatic wall temperature

T<sub>W</sub> = wall temperature

T<sub>EFF</sub> is a function of the coolant total temperature, the main stream adiabatic wall temperature, and a film cooling effectiveness coefficient. This coefficient is a function of slot geometry and coolant properties.

Again, this correlation was developed for particular geometries and conditions. Therefore, in addition to providing this correlation as an option, STAPAT II will incorporate an option for the user to customize for his particular application. In this case the user can specify the effectiveness coefficient as a function of distance from the slot (coolant exit).

Movable covers may be employed to cover and protect a transparency during portions of the flight. One concept for this type of protection is shown in Figure 9. In this case, STAPAT II would use between-pane cooling modeling while the covers are closed and external film cooling modeling while the covers are opened. In addition, the cover structure and radiation from the covers to the transparency would be modeled while the covers are closed but would not be modeled when the covers are open.



GP83-0474-7-D

Figure 9. Use of Transparency Covers

#### HIGH TEMPERATURE MATERIALS DATA BASE ADDITIONS

STAPAT currently provides a material property data base for transparent, structural and coating materials used on supersonic aircraft transparency systems. The data was extracted from Reference 20 and is stored in terms of density, thermal conductivity, specific heat, viscosity (for fluids), total emissivity and solar absorptivity as segmented-linear functions of material temperature. For STAPAT II, the material property file will be revised to extend the upper limit from 1000 F to 2000 F and to add new materials applicable to hypersonic aerospacecraft transparencies. Figure 10 shows a list of materials that will be included.

In addition to the modifications discussed in this paper, STAPAT II will also include improvements to STAPAT in the areas of streamline tracing, boundary layer transition location, three-dimensional wind tunnel modeling, heat flux modeling, radiation modeling, high-temperature (non-equilibrium air and catalytic wall) effects, and air transport properties.



<b>Transparent Structural Materials</b>		
<b>Acrylics</b>	<b>Polycarbonates</b>	<b>Glasses</b>
As-Cast MIL-P-5425 As-Cast MIL-P-8184 Stretched MIL-P-25690 Cast LP 391 Cast Selectron 400 Plexiglass Lucite	Lexan MIL-P-83310 Swedlow Processed Sheet Makrolon Merlon Unspecified	Fused Silica; Victor 96% Silica; Quartz Soda Lime; Fused Quartz Borosilicate Aluminosilicate Chemically Strengthened Chemically Tempered Annealed and Semi-Tempered Soda Lime Silicon Dioxide (Opal) Unspecified
<b>Transparent Interlayer Materials</b>		
<b>Silicones</b>	<b>Polyurethanes</b>	<b>Polyvinyl Butyrals (PVB)</b>
Swedlow SS 5272Y (HT) Sierracin CIP 97 Cast-In-Place Swedlow Sierracin Unspecified	PPG CIP 97-1 PPG-112 Sierracin S-120 Unspecified	MIL-G-25871 (3GH) MIL-P-25374 (DBS) Unspecified
<b>Metallic Edge Attachment Materials</b>		
<b>Aluminum Alloys</b>	<b>Titanium Alloys</b>	<b>Stainless Steels</b>
6000, 7000, 7075 Series 6061; 7075-T6 75 ST; 24 ST 53S0, 61S0 Unspecified	Ti-6Al-4V Ti-6Al-6V-2Sn Ti-6Al-2Sn-4Zr-2Mo Ti-8Al-1Mo-1V Ti-13V-11Cr-3Al	AM-350, 355 Custom 455 (H950) PH13-8MO 17-4PH; 17-7PH AISI-301, 302, 316, 347
<b>Nickel Base Alloys</b>	75 A; C-110M	18-8; 321, 310
Hastelloy X, B Waspalloy Rene 41	A11OAT Unspecified	350, 440 PH15-7MO Unspecified
Inconel B, X, 600, 625	<b>Beryllium, BE</b> <b>Columbium, CB</b>	<b>Molybdenum, MO</b>

OPES-0474-1-T

Figure 10. STAPAT II Data Base Materials

<b>Nonmetallic Edge Attachment Materials</b>		
<b>Composite Reinforcements</b>	<b>Insulations</b>	<b>Rubber Sealants</b>
Fiberglass-Polyester	MIN-K-503	Silicone
Fiberglass-Epoxy	MIN-K-1301	Neoprene
Fabric-Phenolic	Cres Cloth No. 304	Butyl
Fabric-Teflon	<b>Carbon-Carbon, C</b>	Unspecified
Fiberglass-Polyimide	<b>Silicon, Si</b>	
Unspecified		
<b>Sensor Window Materials</b>		
Sapphire (Corundum) (Alumina), AL2-03		; Magnesium Aluminate (Spinal) MG-AL-04
Magnesium Oxide (Magnesia) (IRTRAN 5) MG-0		; Strontium Titanate, SR-TR-03
Titanium Dioxide (Titanium Oxide) (Titania) (Rutile), TI-02		
Yttrium Oxide (Ytria), Y2-03		; Zinc Selenide (IRTRAN 4), AN-SE
Titanium Aluminide		; Aluminum Oxynitride
Gallium Arsenide, GA-AS		; Strontium Fluoride SR-F2
Magnesium Fluoride (IRTRAN 1), MG-F		; Germanium, GE
Zinc Sulfide (Wurtzite) (IRTRAN 2), ZN-S		
Calcium Fluoride (Fluorite) (IRTRAN 3), CA-F2		
<b>Electrical Conductive Coating Materials</b>		
Pure Gold, AU		Tin Oxide, SN-0
Tin Oxide, SN-02		Indium Oxide, IN-0
Indium Oxide, IN2-0		Indium Oxide, IN2-03
Zinc Oxide, ZN-0		Zinc Oxide, ZN-02
<b>Thermal Control Fluids</b>		
Air		Nitrogen
Helium		Hydrogen
Water		

GP93-0474-2-T

**Figure 10. (Continued) STAPAT II Data Base Materials**

## SUMMARY

Status of a new transparency thermal analysis tool, STAPAT II is presented. STAPAT II will predict transient, three-dimensional transparency system temperatures on supersonic and hypersonic vehicles. STAPAT II will represent a significant enhancement of the original STAPAT code used for supersonic fighter aircraft transparency thermal analysis. Additions to the original code will include improvements/corrections for existing capabilities, modeling of hypersonic flow phenomena, modeling of transparency system thermal protection measures, and modeling of high temperature transparency system materials.

## REFERENCES

1. M. O. Varner and C. A. Babish III, "Status of a New Aerothermodynamic Analysis Tool for High-Temperature Resistant Transparencies," a paper published in AFWAL-TR-83-4154, "Conference on Aerospace Transparent Materials and Enclosures," edited by S. A. Marolo, December 1983.
2. M. O. Varner, et al, Specific Thermal Analyzer Program for High-Temperature Resistant Transparencies for High-Speed Aircraft (STAPAT), Volume I - Methodology, Volume II - Users Manual, Main Text and Volume III - Appendices of Sample Problems," AFWAL-TR-84-3086, October 1984.
3. DeJarnette, F. R., "Calculation of Inviscid Surface Streamlines and Heat Transfer on Shuttle Type Configurations, Part I - Description of Basic Method," NASA CR-111921, August 1971.
4. DeJarnette, F. R., and Jones, M. H., "Calculation of Inviscid Surface Streamlines and Heat Transfer and Shuttle Type Configurations, Part II - Description of Computer Program," NASA CR-111911, August 1971.
5. DeJarnette, F. R., "Calculation of Heat Transfer in Shuttle-Type Configurations Including the Effects of Variable Edge Entropy at Boundary Layer Edge," NASA CR-112180, October 1971.
6. DeJarnette, F. R., "Aerodynamic Heating on Complex Configurations," AIAA Paper No. 79-0891, 1979.
7. DeJarnette, F. R., Kania, L. A., and Chitty, A., "Aerodynamic Heating and Surface Temperatures on Vehicles for Computer-Aided Design Studies," AIAA Paper 83-0411, January 1983.

REFERENCES (Continued)

8. Fivel, H. J., "Numerical Flow Field Program for Aerodynamic Heating Analysis, Volume I, Equations and Results," AFFDL-TR-79-3128, Volume I, December 1979.
9. Fivel, H. J., "Numerical Flow Field Program for Aerodynamic Heating Analysis, Volume II, User's Manual," AFFDL-TR-79-3128, Volume II, December 1979.
10. Fivel, H. J., "Numerical Flow Field Program for Aerodynamic Heating Analysis, Volume I, Equations and Results," AFWAL-TR-85-3054, to be published.
11. Fivel, H. J., "Numerical Flow Field Program for Aerodynamic Heating Analysis, Volume II, User's Manual," AFWAL-TR-85-3054, August 1985.
12. Cheatwood, F. M., DeJarnette, F. R., and Hamilton, H. E., "An Interactive Approach to Surface Fitting complex Geometries for Flowfield Applications," AIAA-87-1476.
13. Bapu, P. T., Orr, C. E., and Stump, W. J., "Interactive Geometry Input Processors for a Parabolized Navier-Stokes Program, Vol I-III," AFWAL-TR-87-3113, February 1988.
14. Babish, C. A. III, and Hayes, J. R., "Heat Transfer Rates on an Analytic Forebody in the AFWAL Mach 3 High Reynolds Number Wind Tunnel," AFWAL-TR-87-3091, April 1988.
15. "Equations, Tables, and Charts for Compressible Flow," NACA Report 1135, 1953.
16. Dahlem, V., and Buck, M. L., "Experimental and Analytical Investigation of Vehicle Design for High Lift-Drag Ratios in Hypersonic Flight," AFFDL-TR-67-138, June 1967.
17. Gregoire, J. E., and Krieger, J. R., "Aerodynamic Prediction Rationale for Advanced Arbitrary Shaped Missile Concepts," AIAA-80-0256, January 1980.
18. Eaton, R. R., and Larson, D. E., "Improved Real Gas Routines for Sandia's NASA Ames Flow Field Program," SAND75-0493, February 1976.
19. Tannehill, J. C., et al, "Simplified Curve Fits for the Thermodynamic Properties of Equilibrium Air," ISU-ERI-AMES-86401, June 1986.
20. Babish, C. A. III, "Material Thermophysical Property Values Recommended for Use in Thermal Analyses of Aircraft Transparent Enclosures," AFWAL-TM-83-210-FIER, November 1983, (Revised September 1988).

NONLINEAR DYNAMIC FINITE ELEMENT ANALYSIS FOR THE BIRD IMPACT  
RESPONSE OF A PREPROTOTYPE T-38 AIRCRAFT WINDSHIELD SYSTEM

R. E. McCarty  
D. E. Trudan  
Lt A. D. Davis

Flight Dynamics Laboratory

NONLINEAR DYNAMIC FINITE ELEMENT ANALYSIS FOR THE BIRD IMPACT  
RESPONSE OF A PREPROTOTYPE T-38 AIRCRAFT WINDSHIELD SYSTEM

\* R. E. McCarty  
§ D. E. Trudan  
# Lt. A. D. Davis

Aircrew Protection Branch  
Flight Dynamics Laboratory  
Air Force Wright Aeronautical Laboratories  
Wright-Patterson Air Force Base, Ohio

Abstract

The response of the T-38 aircraft student windshield structural assembly to bird impact loading is simulated using the MAGNA (Materially and Geometrically Nonlinear Analysis) three-dimensional nonlinear finite element analysis system. User subroutines are used to couple the mathematical definition of the bird impact pressures to the computed response of the aircraft windshield assembly. These pressures are applied to the faces of finite elements lying within the bird impact footprint on the surface of the windshield. The analysis problem is characterized by severe material and geometric nonlinearities as well as significant fluid/solid interaction (load/response coupling). All analyses were conducted on a 2 million word core Cray-1/S computer. The purpose of the analysis was to demonstrate the capability to simulate accurately the results of a full scale bird impact test on an actual T-38 aircraft windshield assembly. The availability of such an analysis tool would permit significant savings in the time and cost associated with full scale bird impact testing of new aircraft transparency systems. Stress versus time, stress contour, and deflection versus time plots are used to illustrate the results of the MAGNA analysis. The computed results successfully predict the mechanical failure of a piece of metallic edgemember support structure, indicating the same location of the failure and the same deflection at failure which were observed during the test. Also the computed results successfully predict the location and extent of a region of significant plasticity which occurred on another metallic edgemember article. Finally, the MAGNA results predict very accurately the maximum displacement of a number of points on the transparency panel in the region of the bird impact, and indicate the same location of rupture in the panel which was observed in tests with slightly lighter weight versions of the same windshield design. It is demonstrated that the combination of efficient state-of-the-art nonlinear finite element analysis methods and current supercomputer systems provides a powerful design and analysis tool which can be used to reduce significantly the time and cost required to develop new bird impact resistant aircraft transparency structures.

---

\* Supervisory Aerospace Engineer  
§ Engineering Technician  
# Aerospace Engineer

## Introduction

### Background

Typical missions flown by U S Air Force aircraft changed dramatically in the late 1960's and early 1970's. This resulted primarily from the development of a new generation of radars which necessitated low altitude, high speed operations. Since the density of birds in the atmosphere is greatest at low altitudes, Air Force aircraft began to encounter a very significant bird impact hazard. Since transparent crew enclosures, or transparencies, had not been designed before this period of time to provide protection against bird impact damage, unacceptable losses of aircraft and crewmembers occurred, and still continue to occur today.

In 1972 the then Air Force Flight Dynamics Laboratory (AFFDL) formed an Advanced Development Program Office (ADPO) to develop bird impact resistant transparency systems for aircraft, utilizing whatever technology was available at the time to do so. In 1976 the AFFDL formed an exploratory development office, the Subsystems Development Group (AFWAL/FIER), to develop new technologies which could then be utilized by the ADPO in future system designs. Over the years the Flight Dynamics Laboratory (FDL) participated in the development of many successful bird impact resistant aircraft transparency systems including those for the A-37, F-111, A-10, and F-16.<sup>1-2</sup> In each case, however, empirical cut and try methods played a principal role in the system development, and as a result the cost and time required to qualify these systems for flight were great.

In 1975 the FDL became interested in developing analysis tools which would permit the reduction of full scale bird impact testing required for transparency system design and qualification. The analysis problem of simulating the bird impact response of aircraft transparency system structures is, however, in general very demanding. The problem is typically a very large three-dimensional one involving dynamic response with the solution being accomplished for as many as 100 time increments. The structures of interest are often laminated thick shells comprised of structural plies fabricated from plastic materials and interlayer plies made from very soft elastomeric materials. Differences in shear moduli between structural and interlayer plies as great as 4 orders of magnitude are not uncommon. For the bird impact problem, the structural plies act primarily in bending and the interlayer plies act almost completely in shear, making familiar shell formulations for the finite element method impracticable. In other words, transverse shear in the interlayer plies has a first order effect on the dynamic response of the laminated shell. Using a separate layer of solid finite elements to represent each ply in the structure in order to account for the strong shear in the interlayers more realistically, drives the size of the problem up dramatically.

The transparency bird impact problem exhibits severe geometric nonlinearity, with deflections often an order of magnitude greater than the thickness of the shell. Severe material nonlinearity can be present too, in

particular for polycarbonate structural plies which can survive very large plastic deformations without rupturing.

The loads on the transparency structure resulting from bird impact are very difficult to define explicitly. It is known that the bird material acts as a fluid during the impact event, and extensive experimental work has been accomplished to characterize the spatial and temporal distribution of these fluid pressures on flat rigid targets.<sup>4-5</sup> The impact event involves the quasi-steady impingement of a three-dimensional fluid jet onto the surface of the solid, and compliance in the structure aggravates the problem because the impact loads then become coupled to the dynamic response of the structure.<sup>6</sup> In other words, the bird impact fluid pressures are very sensitive to the shape and rate of deformation of the transparency surface; in general the impact loads are very strongly coupled to the structural response.

One way to address the load/response coupling aspect of this problem directly is to accomplish a hydrodynamic analysis for the bird material in parallel with the structural analysis for the transparency. Deformations from the structural solution are used then to define the solid boundary for the hydrodynamic solution, and the fluid pressures from the hydrodynamic solution are used to define the loads for the structural solution. This capability is only now being developed. Until it becomes available, the coupling aspect of the loading can only be handled in a more empirical manner.

By 1979 AFWAL/FIER had taken delivery of a three-dimensional nonlinear finite element code called MAGNA to tackle the aircraft transparency bird impact problem.<sup>3</sup> It was designed to provide the capabilities required to meet each of the difficult aspects of the problem discussed above.

#### MAGNA Computer Program

The MAGNA nonlinear finite element analysis system was developed by the University of Dayton Research Institute, Dayton, Ohio and first became operational during the summer of 1978. The first edition of MAGNA for use in US Air Force aircraft transparency applications was delivered in late 1979. MAGNA was designed from the ground up for the analysis of large scale problems involving three-dimensional structures. It can account for the effects of both geometric nonlinearity (large displacements and rotations) and material nonlinearity (elastic-plastic behavior). The static, dynamic, or free vibration response of a structure can be analyzed using MAGNA. Special features such as contact analysis (e.g. bird/canopy contact, or canopy/heads-up-display contact), full restart capabilities, and convenient interactive graphics make it a powerful analysis tool which is easy to use. The interactive graphics are provided in two packages: the first, a preprocessor, enables rapid finite element modelling of transparency structures; the second, a postprocessor, permits quick visualization of the results of an analysis including structural deformation, stress, and strain.<sup>19-22</sup> The capabilities of MAGNA are documented in more detail elsewhere.



A Control Data Corporation (CDC) Cyber 175-845 version of MAGNA is operational at Wright-Patterson Air Force Base (WPAFB), Ohio. This installation includes the complete MAGNA package and permits free access for all US Government offices and contractors doing work for the US Government. A Cray-1/S version of MAGNA is offered by United Information Services (UIS) through their commercial time sharing network. The Cray installation includes only the analysis portion of the MAGNA system, with the interactive graphics portions of the system being installed on UIS CDC equipment. Other operational versions of MAGNA including PRIME, VAX 11/780, and IBM editions are available. A fully maintained operational installation of MAGNA is planned at WPAFB well into the future.

### Approach

Since the initial development and delivery of MAGNA, an intensive in-house work effort has been mounted to validate MAGNA for aircraft transparency bird impact analysis.<sup>8-14</sup> These studies typically compare computed and experimental deflection or strain data for full scale bird impact tests to demonstrate validity. It is felt that for a highly nonlinear problem such as this, accurate results for one case do not necessarily guarantee the same for others. For this reason, a number of cases are being investigated to validate MAGNA in an overall sense. The parameters for these cases include geometry (flat versus curved), construction (monolithic versus laminated), and stiffness. As good results are demonstrated<sup>15-18</sup> for some cases, applications are accomplished for other similar cases.

The study reported here is the most recent of all the attempts to validate MAGNA. This was the first case to involve a laminated plastic transparency for which the edgemember support structure had been modelled directly. In previous studies, only simple boundary conditions had been employed at the edge of the transparent panel. The transparency involved was that for the student windshield of the T-38 aircraft. Figure 1 illustrates the complete transparency system for the T-38. The FDL is currently sponsoring a program to develop improved bird impact resistant transparencies for the T-38.

### Scope

The work reported here involves MAGNA simulation of a single full scale bird impact test conducted with a prototype T-38 aircraft student windshield in February 1984. The cross section of the student windshield panel through its aft edge or arch support is shown in Figure 2. The windshield panel has three plies, an outer 3/8 in. and an inner 3/16 in. thick polycarbonate structural ply plus an 0.060 in. thick urethane type interlayer. The arch structure for the windshield was a cast magnesium frame used in the current production windshield assembly as well as a rectangular seamless steel tube reinforcement used to increase the impact resistance of the frame. The steel tube was 1.0 by 1.5 in. in outside dimensions with a wall thickness of 0.120 in.

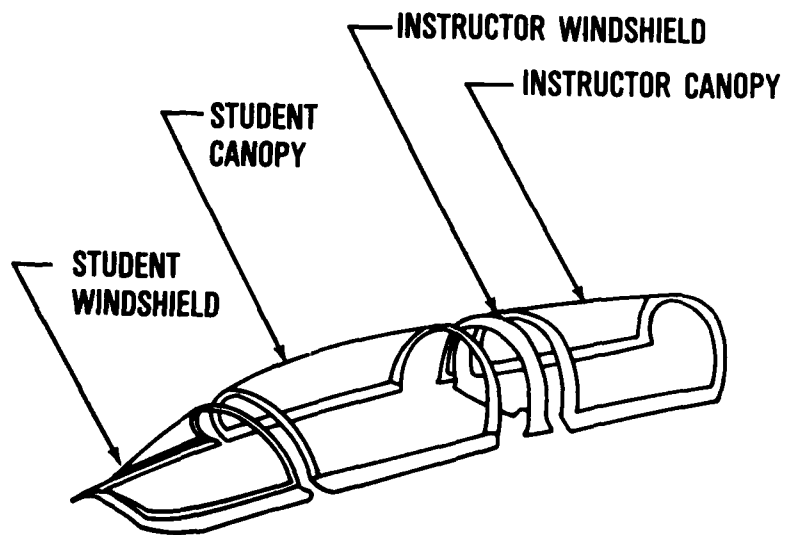


Figure 1. T-38 Aircraft Transparency System

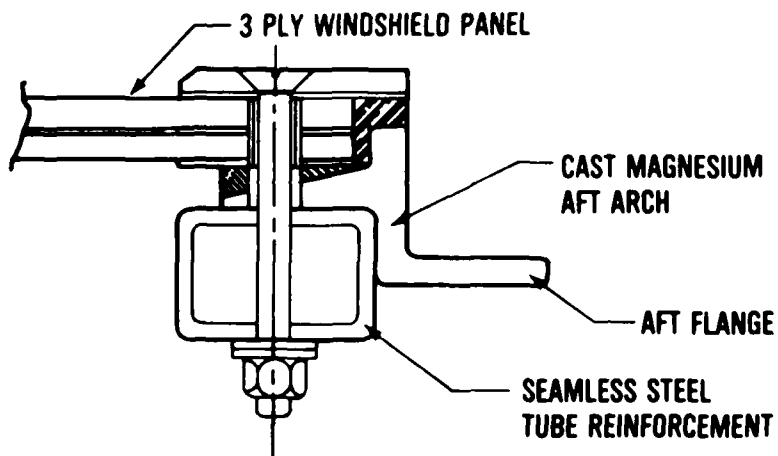


Figure 2. Cross Section of Student Windshield Aft Edge

The windshield assembly was mounted on a frame simulating the T-38 forward fuselage section and impacted with a 4 lb bird at 400 kt. The target point for the test was on the centerline of the windshield panel, about 9.0 in. forward of the aft edge of the windshield, measured along the centerline. A method utilizing high speed cameras was used to acquire data for the deflection history of points lying on the inner surface of the windshield panel.<sup>23</sup> Figure 3 shows 6 points on the windshield and 1 on the steel tube reinforcement for which deflection data were obtained. (The finite element model actually employs curved element boundaries, but this hidden line illustration shows them as being straight.)

MAGNA analyses of two types were conducted. First, a free vibration analysis was accomplished to aid in debugging the finite element model, and to determine a time increment size for use in subsequent dynamic analyses. Second, a single nonlinear dynamic analysis was conducted. It was not intended to do parametric studies in search of the "best" solution possible. Rather, it was planned to follow previously established guidelines for conducting such analyses in order to define the correlation obtained between computed and experimental results.<sup>8-14</sup>

All analyses were run on the Cray-1/S supercomputer operated by United Information Services (UIS) Company, Kansas City, Missouri.

### Structural Modelling

#### Geometry

The prototype T-38 student windshield assembly tested involved a single-piece wrap-around transparent panel as shown in Figure 1. The transparency itself involved a three ply design as shown in Figure 2 - each ply being uniformly thick. The transparent panel was bolted on all edges into a brittle, single-piece cast magnesium frame. The impact resistance offered by the aft arch region of this frame is much less than that required to withstand the loads resulting from a 4 lb 400 kt bird impact event near the edge of the windshield panel. For that reason, a seamless 4130 steel tube reinforcement was added as shown in Figure 2 to provide both the strength and ductility required to survive bird impact loading. The cross section of both the cast magnesium aft arch and steel tube reinforcement do not remain uniform all along the length of the aft arch from one corner of the windshield panel to the other; the cross section of both, however, is uniform over the center region of the arch from the centerline out about halfway on either side.

As part of earlier work, the University of Dayton Research Institute used drawings obtained from the principal airframe manufacturer for the T-38, Northrop Corporation, to write a FORTRAN code to generate nodal coordinates and element connectivity for a MAGNA finite element model of the current production T-38 student windshield.<sup>24</sup> The production T-38 windshield assembly includes a monolithic windshield panel only 0.60 in. thick and the cast magnesium arch frame without the steel tube reinforcement. A MAGNA model with total thickness of 0.6225 in. was

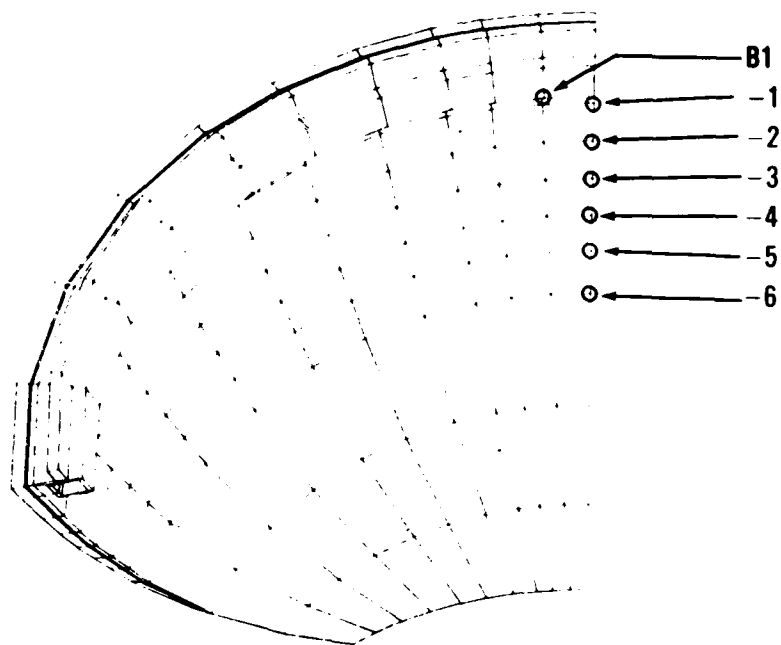


Figure 3. Aft View of Computer Model from Underneath Showing Deflection Data Points

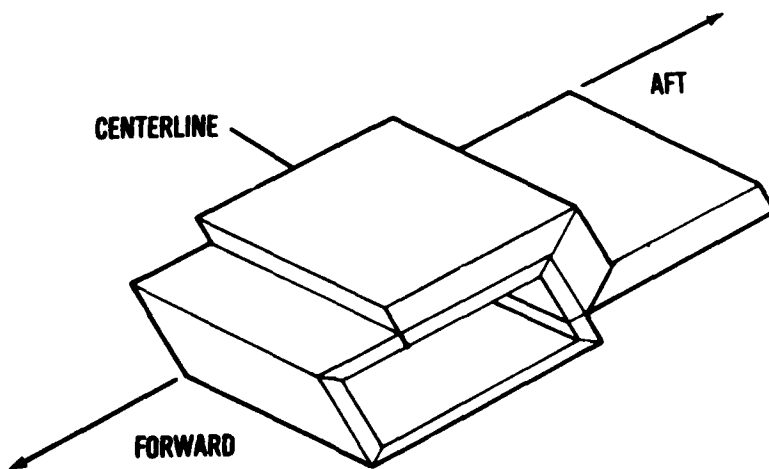


Figure 4. Solid Elements Used for the Magnesium Aft Arch and Steel Tube Reinforcement

generated using this FORTRAN code, and used as the starting point for modelling of the prototype windshield structure illustrated in Figure 2. Some differences between the actual and modelled cross sections of the magnesium arch exist, but torsional and bending stiffnesses of the arch were matched closely.

### Discretization

Since both the structure and the loads involved exhibited symmetry, it was possible to model only half the transparency system to reduce the computer resources required. A module of the MAGNA preprocessor named TRNSFR was used to translate the coded model of the production windshield assembly generated by the FORTRAN code into one with the internal binary format required for preprocessing.

Next, the main module of the MAGNA preprocessor, named PREP, was used to refine the single solid element through the thickness of the initial model into 3 solid elements having thicknesses corresponding to the individual ply thicknesses shown in Figure 2. Element type 8 in the MAGNA library, which is a 16 node solid isoparametric brick, was chosen for use in modelling the windshield panel. This same element type has been proven effective in earlier studies which have been conducted with MAGNA. Since the original monolithic windshield panel model had 100 solid elements, the refined 3 ply windshield model had a total of 300 - already very large for nonlinear dynamic analysis of a three dimensional model. In the past, as few as 50 solid elements per ply have been shown sufficient to provide acceptable deflection results, and as few as 100 per ply have been shown to provide acceptable stress results.

At this point the binary version of the model included the (300 element) 3 ply windshield panel and a 30 element representation of the cast magnesium arch - also using the Type 8 (16 node) solid element. The only thing needed to complete the model was a discretization for the seamless steel tube reinforcement. Starting with the coordinate data for the nodes lying on the inner surface of the cast magnesium arch against which the steel tube was fitted, another FORTRAN code was written by AFWAL/FIER to represent the steel tube using 6 solid elements around the cross section. Again the Type 8 bricks were employed as shown in Figure 4.

Having generated a coded model for the steel tube and translated it into binary format through the TRNSFR module of the MAGNA preprocessor, the MERGE command in the PREP module was used to join the windshield and tube models, deleting all (85) redundant nodes in the process. Since the model had 10 elements in the lateral direction of the grid, the steel tube itself required 60 solid elements for an overall model total of 390 - a large solid model for nonlinear dynamic analysis. The limit for nonlinear dynamic analysis using MAGNA had been determined previously to be about 235 solid elements for a CDC Cyber 175-750 used at WPAFB. The size of the T-38 windshield model made it necessary to accomplish the solution on a Cray-1/S class machine.

Figure 5 illustrates the final finite element model - the details of the 3 individual windshield plies and the aft arch support structure are not apparent in the illustration. A total of 1844 nodes were defined. All nodes on the forward and outboard edges of the model were fixed representing a clamped boundary condition, and lateral motion was constrained all along the centerline to represent the condition of symmetry existing there. Other than at outboard and centerline ends, no constraints were applied along the length of either the cast magnesium aft arch or the steel tube portions of the model.

In the actual T-38 transparency system (Figure 1), the student canopy closes over the aft flange of the cast magnesium windshield aft arch shown in Figure 2. Figure 6 shows schematically how during the bird impact event on the windshield centerline, the top portion of the windshield arch moves inward away from the student canopy arch while the outboard portions tend to move outward and apply load to the forward arch structure of the student canopy. Boundary conditions employed for this analysis don't represent this latter reaction between the respective arch structures for the student windshield and student canopy, but are realistic in the region near the centerline where the greatest out-of-plane deformations are observed to occur. The total number of unconstrained degrees of freedom (UDOF) resulting from the boundary conditions used was 4840, again a large problem for long, nonlinear dynamic analysis.

#### Material Properties

During the course of previous MAGNA validation studies for the aircraft transparency bird impact dynamic response problem, simplistic characterization of the mechanical properties of transparent plastic materials has been demonstrated to be sufficient to obtain realistic results.<sup>9-14</sup> In general the mechanical properties of transparent thermoplastic and elastomeric materials used in fabricating aircraft transparency systems are highly variable and are strongly dependent upon a number of parameters including strain rate, temperature, thermal history encountered during forming processes, age, environmental exposure including ultraviolet radiation, abrasion, and cleaning chemicals. Because the complete characterization of the transparent materials in use today has not been accomplished with respect to all the parameters noted above, and because to do so would require a very broad scale research project, a simplistic approach has been taken in representing their mechanical properties for studies such as this one. Emphasis has been placed upon using simple material models and learning how to interpret the computed results obtained, instead of on conducting a large scale research program beforehand to improve the characterization of transparent plastic materials.

In general for the work leading up to that reported here, transparent plastics have been characterized as nonlinear plastic materials using tensile data obtained at room temperatures and very low ("static") strain rates. This approach appears to be justified by the outcome of earlier work efforts, and is demonstrated to be sufficient once again in this work.

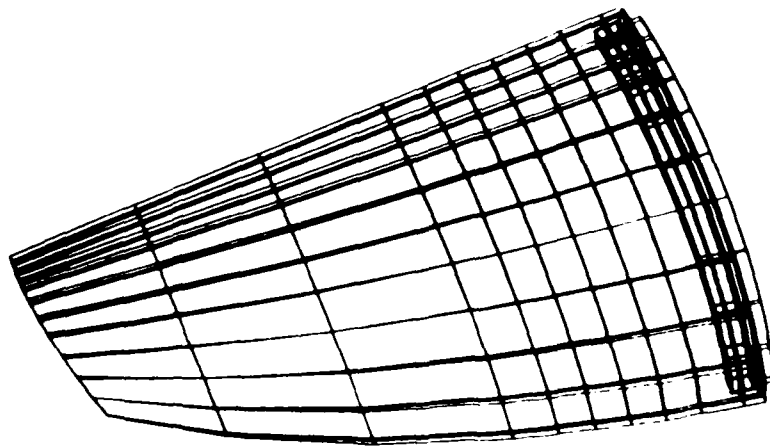


Figure 5. Completed MAGNA Finite Element Model

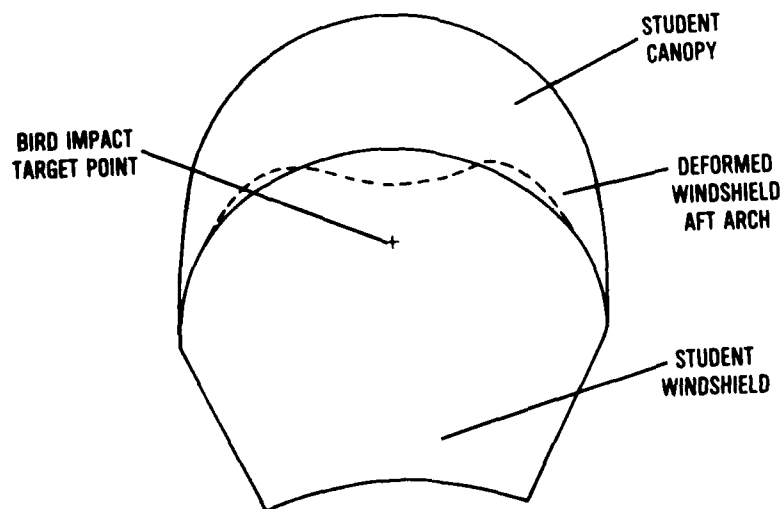


Figure 6. Frontal View of T-38 Aircraft Transparency System

For the prototype T-38 windshield model, the windshield interlayer material was represented as a linear material having 3 independent material properties: Young's Modulus, Shear Modulus, and Poisson's Ratio. Laboratory testing has demonstrated that values observed for these three interlayer properties often do not satisfy the expression given in Equation 1, for elastic isotropic materials, which implies that only two independent material properties exist.<sup>23</sup> Values which were used for these properties are shown in Table 1. The polycarbonate material used in the two structural

$$E = 2 G ( 1 + V) \quad (1)$$

E - Young's Modulus

G - Shear Modulus

V - Poisson's Ratio

plies was represented as being nonlinear plastic. Table 1 shows material properties corresponding to the initial linear segment of the stress-strain curve which was used for polycarbonate. A value was used for the "yield stress" which was lower than that ordinarily associated with the yield phenomenon. The value chosen was used only to represent that portion of the stress-strain curve which was most nearly linear. Above the value chosen for the "yield stress", significant nonlinearity is observed. MAGNA permits the user to provide a table of stress-strain data to describe the behavior of the material beyond the point represented by the value of the "yield stress" shown in Table 1. Table 2 shows the points used to characterize the behavior of polycarbonate at stress levels above "yield". The third point from Table 2 is that which would ordinarily be associated with the yield phenomenon. Some strain hardening was assumed for the material to avoid numerical problems in the solution, although the material actually exhibits strain softening.

Both the cast magnesium used in the arch and the steel used in the arch reinforcement were characterized in a way similar to that used for the polycarbonate - as a nonlinear plastic material. The values used for both are shown in Tables 1, 3, and 4. Even though the steel typically behaves as a perfectly plastic material, some strain hardening was assumed, again as for the polycarbonate to avoid numerical instabilities in the solution. In each case for Tables 2, 3, and 4 the next to the last point shown on the table represents ultimate stress, corresponding to mechanical rupture or failure. The very large plastic strain which polycarbonate is capable of withstanding is the key to its ability to survive high energy bird impact loading.



Table 1

Material Properties Used

<u>Material</u>	<u>*Young's Modulus (psi)</u>	<u>*Shear Modulus (psi)</u>	<u>Poisson's Ratio</u>	<u>*Yield Stress (psi)</u>	<u>Density (lb sec<sup>2</sup>) (in<sup>4</sup>)</u>	<u>Reference Number</u>
PPG-112 Interlayer	10000	525	0.43	--	0.104x10 <sup>-3</sup>	26
Polycarbonate MIL-P-83310	324000	--	0.38	6353	0.111x10 <sup>-3</sup>	--
Magnesium AZ91C-T6	6500000	--	0.35	9980	0.168x10 <sup>-3</sup>	27
Steel 4130	29000000	--	0.32	74800	0.733x10 <sup>-3</sup>	27

\* Engineering Values

Table 2  
Polycarbonate Stress vs Strain

<u>Stress 1</u> (psi)	<u>Plastic 2*</u> <u>Strain</u> (in./in.)
6353.	0.0000
8061.	0.0066
9392.	0.0254
9700.	0.2500
10043.	0.5000
10728.	1.0000

\*Zero plastic strain corresponds to "yield stress" in Table 1  
 1 Piola-Kirchoff Stress  
 2 Green St. Venant Strain

Table 3  
Magnesium Stress vs Strain

<u>Stress</u> (psi)	<u>Plastic</u> <u>Strain</u> (in./in.)
9980.	0.0000
13000.	0.0002
16900.	0.0008
20400.	0.0017
21900.	0.0023
23800.	0.0032
33700.	0.0356
35417.	0.5000

Table 4  
Steel Stress vs Strain

<u>Stress</u> (psi)	<u>Plastic</u> <u>Strain</u> (in./in.)
74800.	0.0000
84800.	0.1240
115000.	0.5000

## Bird Impact Loading

### Theory

A procedure for the mathematical definition of bird impact loads has been developed by AFWAL/FIER for use with MAGNA finite element simulations of aircraft transparency bird impact dynamic response.<sup>12</sup> This procedure is based firmly on an extensive experimental data base accumulated over a period of several years.<sup>4-6,28,29</sup> The data base is valid for the case of a rigid, flat, inclined target and comprises pressure data recorded at the surface of the target during bird impact.

The loads definition procedure is simple and straightforward to use. The essential points of the theory upon which the loads definition procedure is based are as follows:

1. The bird behaves as a fluid during impact.
2. The impulse delivered to the structure is equal to the component of the bird's linear momentum which is normal to the target surface.
3. The bird may be represented as a right circular cylinder having a length to diameter ratio of 2.0.
4. The pressure resulting from bird impact is relatively constant at any point on the surface of the target (quasi-steady fluid flow).

The following section briefly sketches the procedure used to define uncoupled bird impact loads. The loads are referred to here as being uncoupled because the theory upon which their definition is based assumes that the target involved is rigid, i.e. that the impact loads are uncoupled or independent from the resulting dynamic response of the target.

### Procedure for Uncoupled Bird Impact Loads Definition

An in-depth discussion of this loads definition procedure will be documented elsewhere as time permits.<sup>30</sup> Only the key points will be noted here.

The first step in the uncoupled definition of bird impact loading was the calculation of the impulse delivered to the target from Equation 2.

$$I = M V \sin \theta \quad (2)$$

I - impulse (lb sec)

M - mass (sl)

V - velocity (ft/sec)

$\theta$  - complement of angle between bird trajectory and inward surface normal vector (deg)

Next, both the period of the bird impact event and the locus of the bird impact pressure footprint on the surface of the transparency were estimated from high-speed (5000 fps) film footage of the actual test. The period was taken to be 0.003410 sec, and the footprint was laid out on the surface of the finite element model as illustrated in Figure 7. A tape grid, which is shown schematically in Figure 8 and which corresponded to the MAGNA finite element model grid, was applied to the inside surface of the transparency to make these tasks easier.

When the boundary of the pressure footprint had been located on the surface of the finite element model, a group of finite elements was selected which most closely approximated the area and location of the footprint. These became the elements then to which bird impact pressure was applied during the finite element solution. Figure 7 shows the set of elements which were selected to be loaded.

After the elements representing the impact pressure footprint were identified, a table was assembled of the times at which load rise and unloading occurred for each element. Times were based on the assumption that bird material moves over the surface of the transparency at a uniform rate throughout the period of the bird impact event. A rectangular pressure versus time history was assumed for each element. The details of this process are too tedious to cover here.

When the intervals of time had been defined during which each element in the footprint was to be loaded, a sum of products was calculated. Each product was the surface area of an individual element multiplied by the time interval for its loading. The sum of these products is divided into the impulse defined by Equation 2 to determine the value of the constant (and spatially uniform) pressure to be applied to each element in the footprint area. The value obtained was 207 psi in this case.

This step completed the definition of uncoupled bird impact loading. The (single) value of the pressure obtained plus the table of load rise and unloading times for each element in the footprint were sufficient to define the applied loads for MAGNA analysis.

This procedure for the definition of bird impact loading is quite simplistic. It presumes a regular geometry for the bird, ignores spikes of shock pressure which occur very early in the impact event, and assumes a spatially uniform distribution of pressure. Even with these features, bird impact simulation results obtained with this procedure have been found to be useful and realistic.<sup>12</sup> The usefulness of uncoupled bird impact loads defined with this procedure is apparently limited, however, to glass transparency designs.<sup>12</sup>

#### Procedure for Coupled Bird Impact Loads Definition

When the target, or aircraft transparency in this case, is not actually rigid, Equation 2 represents only a lower bound for the value of the impulse delivered to the structure by the bird impact. Another limiting case which

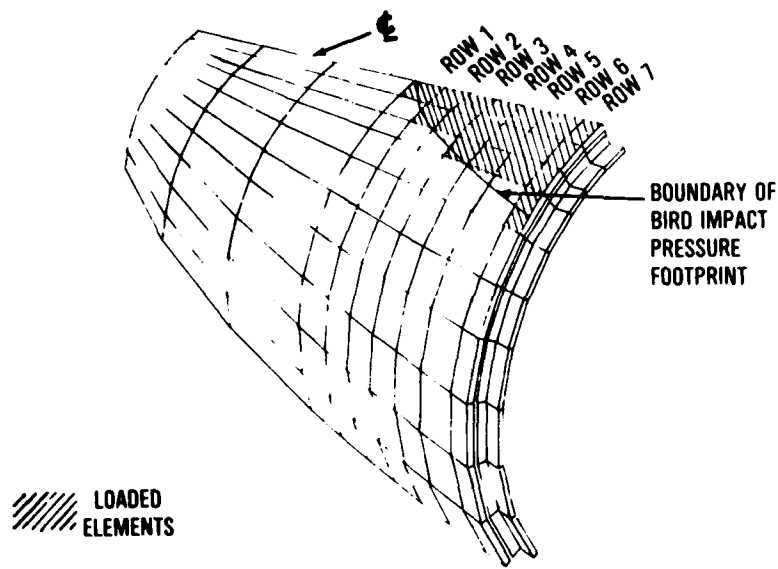


Figure 7. Location of Bird Impact Pressure Footprint

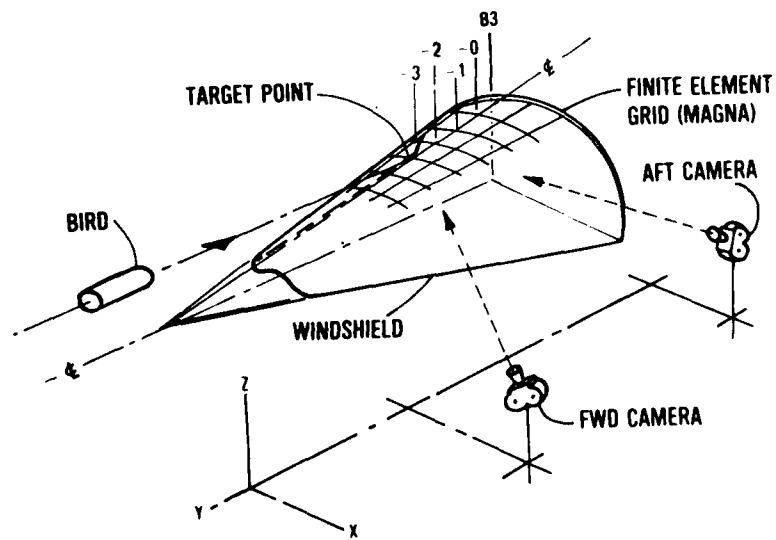


Figure 8. Schematic for Deflection Data Acquisition System

establishes the upper bound for the value of the impulse is the very flexible target which forms a pocket upon impact, completely arresting all bird material. In this case the impulse delivered is equal to 100 percent of the linear momentum of the bird before impact, or  $M V$ . For a target of intermediate flexibility or compliance, the impulse delivered to the structure lies somewhere between  $M V \sin \theta$  and  $M V$ , the actual value depending upon the history of the dynamic response of the target.

The procedure for the definition of coupled bird impact loads is intended to represent this dependence of the impulse upon the resulting dynamic response of the structure. Instead of being completely defined a priori in an explicit manner, the bird impact loads are implicitly defined and as a result are continually updated or modified during the progress of the MAGNA numerical solution itself. The key points in the procedure for coupled loads definition are noted here.

The first part of the procedure is identical to that for the uncoupled definition of loads discussed above. The end results of these steps are the (constant) value of the uncoupled pressure,  $P_u$ , and the load rise and unloading times for each finite element included in the impact pressure footprint.

The next step, having determined  $P_u$  and the element timing, is to write two standard user-subroutines which are compatible with MAGNA. These subroutines are ULOAD and UPRESS. Because the procedure for uncoupled loads definition makes the pressure,  $P_u$ , directly proportional to  $\sin \theta$ , the user-subroutines are used to scale  $P_u$  with the instantaneous bird impact angle,  $\theta(t)$ , as shown by Equation 3. Figure 9 shows that as local bending develops in the transparency and the slope or inclination of the surface

$$P_c(t) = P_u \sin \theta(t) / \sin \theta(0) \quad (3)$$

$\theta(0)$  - complement of angle between bird trajectory and inward surface normal vector at the beginning of the bird impact event (deg)

$\theta(t)$  - complement of angle between bird trajectory and inward surface normal vector at time  $t$  (deg)

$P_u$  - uncoupled (constant) value of bird impact pressure (psi)

$P_c(t)$  - coupled (variable) value of bird impact pressure calculated by user subroutines at time  $t$  (psi)

beneath the bird material increases, so does the local instantaneous bird impact pressure. Such an increase in the instantaneous pressure results in a corresponding increase in the impulse delivered to the structure. The user-subroutines ULOAD and UPRESS use the instantaneous deformation calculated by MAGNA to modify the current value of the impact pressure.

The task of developing the user-subroutines was minimal - only 150 executable lines of FORTRAN were required. The effect upon the computed

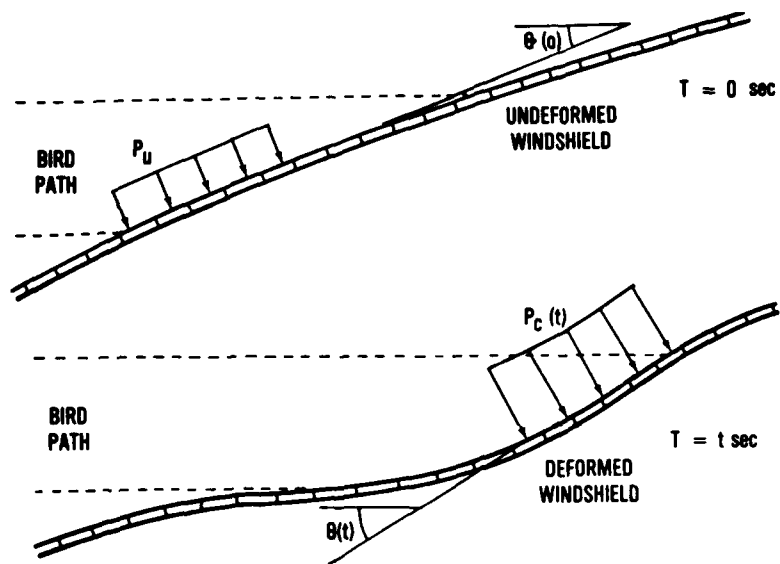


Figure 9. Bird Impact Pressure Dependence Upon Windshield Deformation

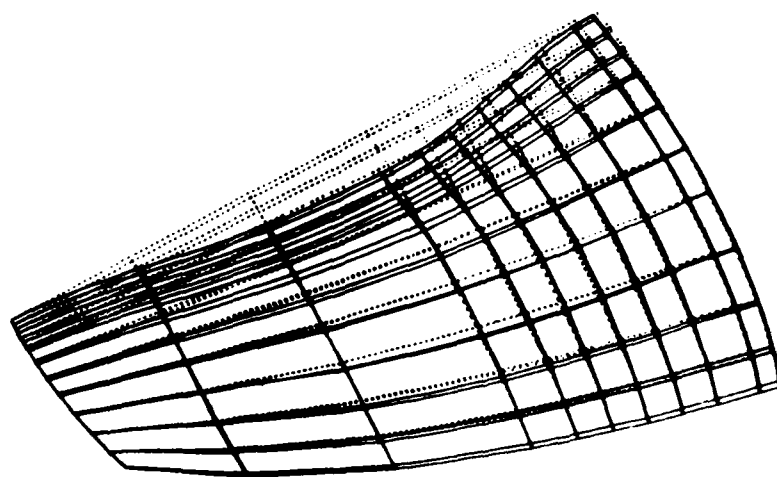


Figure 10. First Mode of Free Vibration

results, however, for analysis with the user-subroutines was very significant. This will be discussed in more detail in later sections.

### Analysis

As mentioned earlier in the Scope Section, two types of analysis were conducted as part of this study. The first was a free vibration analysis intended to aid in debugging the finite element model, and to determine the time increment size to be used in subsequent nonlinear dynamic analysis. The second was a single nonlinear dynamic analysis. No parametric studies were planned in order to obtain the best possible result. Both of these analyses were run on the United Information Services (UIS) Cray-1/S, 2 million word core machine mentioned earlier in the MAGNA Computer Program Section. Table 5 shows the analysis parameters used for both the free vibration and nonlinear dynamic jobs.

#### Free Vibration Analysis

MAGNA utilizes a vector iteration method for free vibration analysis, and for the T-38 windshield problem, 4 trial vectors were employed to extract the 2 lowest frequency modes. Lumped mass was assumed to lower the cost of the analysis. All materials were assumed to exhibit linearly elastic behavior. A 14 point rule available with MAGNA was used for integration within the solid elements in the model. This rule does not constitute reduced integration for the 16 node isoparametric solid element involved; i.e. integration within the elements was complete.

Because MAGNA utilizes a bandwidth solution technique, the size of the numerical problem depends upon the order of node numbering in the model. For this model as numbered by the MAGNA preprocessor, the maximum half-bandwidth of the problem was 1465, and the average half-bandwidth was 392.

The free vibration analysis converged in 5 iterations, and frequencies obtained were 186 Hz for the first mode and 303 Hz for the second mode. The normal listed output for MAGNA showed that for both modes 1 and 2, the proportion of the total normalized strain energy stored in the urethane interlayer material was roughly 10%, much more than that stored in either the magnesium arch or the steel tube reinforcement. This implies that the dynamic bird impact response of the overall assembly would be quite sensitive to the shear stiffness of the interlayer material itself, even for such a soft material (See Table 1).

Figures 10 and 11 show both the deformed and undeformed geometry computed for modes 1 and 2 respectively. The normalized displacements have been scaled up so that the maximum displacement is equal to 3 in. to make the mode shapes easier to visualize. The forward and outboard edges of the assembly can be seen to be fixed in both figures, slight movement of the arch is apparent, and displacements along the centerline are only in the out-of-plane direction as a result of the symmetry boundary conditions employed there.



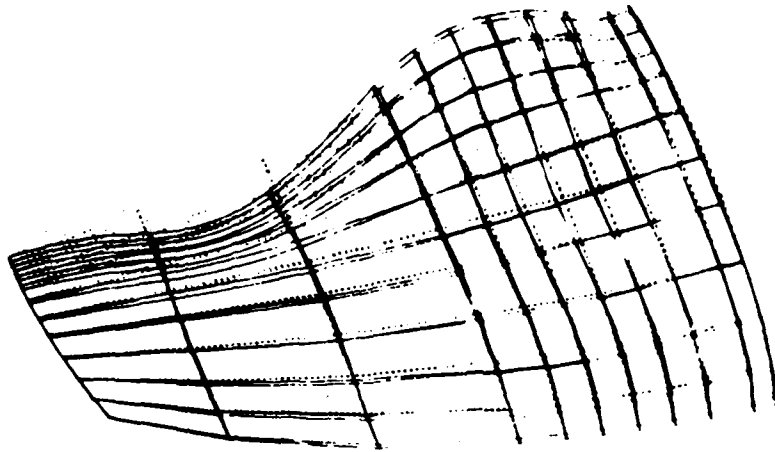


Figure 11. Second Mode of Free Vibration

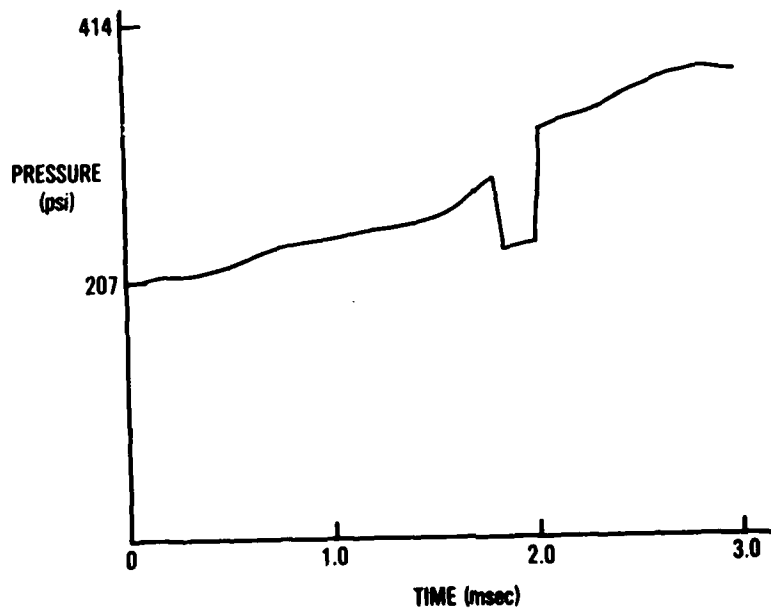


Figure 12. Bird Impact Pressure versus Time

Table 5  
MAGNA Analysis Parameters

<u>Analysis</u>	<u>Date</u>	<u>Steps/ Modes</u>	<u>Central Memory</u>	<u>CP Seconds</u>	<u>Cost</u>
Free Vibration	3Aug84	1,2	677100	99	\$192
Nonlinear Dynamic	8Aug84	1,2	708600	235	\$370
Nonlinear Dynamic	11Aug84	3-10	711100	934	\$1014
Nonlinear Dynamic	13Aug84	11-20	711500	1159	\$1950
Nonlinear Dynamic	14Aug84	21-30	711500	1160	\$1952
Nonlinear Dynamic	15Aug84	31-40	711500	1163	\$1956
Nonlinear Dynamic	23Aug84	41-45	710400	596	\$989
Nonlinear Dynamic	25Aug84	46-60	712400	1808	\$1983

No errors were uncovered in the specification of boundary conditions as a result of the free vibration analysis, and the period of the first (lowest) mode was determined to be 0.0054 sec.

#### Nonlinear Dynamic Analysis

This analysis, intended to simulate the full scale bird impact test, included the effects of both material and geometric nonlinearities. The size of the time increment chosen for dynamic analysis was 0.000050 sec, slightly less than 1/100 the period of the free vibration mode presumed to be principally excited by the impact event. This rule of thumb in selecting time increment size for nonlinear dynamic analysis has been demonstrated previously<sup>9,19</sup> to represent an effective balance between analysis cost and accuracy.

MAGNA permits the user to select one of several types of iteration to be used during nonlinear dynamic analysis including no iteration at all; for this study, a non-iterative solution was chosen in order to reduce to a minimum the cost and time required. This approach invokes a pseudo-force technique to represent nonlinear effects in the solution; a correction is made on the right hand side of the equation in the form of an artificial

force at the end of the time increment. The technique has proven effective in earlier work.<sup>10-14</sup>

The RESTART feature of MAGNA was used to start and stop the solution in order to be able to examine its progress, and to alter solution parameters accordingly if need be. As an example, if the pseudo-force corrections being made by the non-iterative solution grew too large, it might have been desirable to restart the solution as an iterative one.

The bandwidth and integration rule used for the nonlinear dynamic analysis were the same as those for the free vibration analysis. A total of 7 separate jobs were run, an initial one plus 6 restarts, with a number of time increments being accomplished for each. Job parameters for individual jobs are shown in Table 5, covering a total of 60 time increments. The differing dollar rates shown on Table 5 for CP time reflect the fact that the jobs were run at various times of day: daytime, nighttime, and weekend.

Listed output from these 7 jobs included three-dimensional stresses and strains at element integration points for the 3 magnesium arch elements lying against the windshield centerline, as well as for the 6 steel tube elements adjoining the windshield centerline. For time increments 41-60, integration point stresses and strains for 8 polycarbonate elements were also listed. These 8 elements were those adjoining the windshield centerline, beginning at the aft edge of the windshield and continuing forward 4 rows, for both the inner and outer structural plies.

Sensitivity of bird impact pressure to windshield deformation computed during the solution is illustrated in Figure 12. The scheme described in the Section on the Procedure for Coupled Bird Impact Loads Definition nearly doubled the initial value of the pressure near the end of the solution. The dip seen in the figure for increments 37-40 is the result of a previously undetected coding error in the user subroutines being used to define the impact pressure loads. The effect of this error upon the overall impulse delivered to the structure is felt to have been negligible; however the effect upon the deflection history of nodes being loaded at the time may not have been negligible as discussed later in the Results Section.

## Results

### Experimental

During the actual bird impact test, the transparent panel remained attached to the arch edgemember support structure. No failure of the polycarbonate plies occurred. Total deflection of the steel tube reinforcement exceeded 3 in., with permanent plastic deformation reaching about 1.25 in. The region of plastic deformation extended from the centerline out to about 3 in. on either side. The magnesium arch failed near the centerline of the assembly, cracking completely through its cross section. The arch also exhibited some cracking part way through its cross section in the two regions about halfway between the centerline of the part and either corner of the windshield.

Tests at the same impact energy, but with transparent panels having thinner polycarbonate plies exhibited a "smile" shaped tear in the windshield just forward of and parallel to the arch, centered on the panel. This tear or opening in the windshield permitted bird debris to enter the cockpit during the test. Again, for tests at the same bird impact energy but with slightly less total thickness of polycarbonate (0.50 in. versus 0.5625 in.), cracking of the magnesium arch occurred at about 0.002200 sec. At this time (0.002200 sec), the total deflection of point B1 on the steel tube reinforcement (see Figure 3) was observed to be about 0.80 in.

#### Computed

Figure 13 shows the maximum equivalent nodal stress versus time predicted for the magnesium arch. Various nodes on the arch are represented by this curve, each involving the instantaneous maximum stress at a particular point in time. The figure shows that at times near 0.003000 sec, the maximum equivalent nodal stress exceeds the ultimate strength for the material, 33,700 psi. Figure 14 shows that at 0.003000 sec, on the centerline of the part, a small region of the aft flange of the magnesium arch has exceeded the ultimate strength of the material. The A and D contours represent the yield and ultimate strengths respectively for the material, while the B and C contours represent uniform intervals in between. This was the region of highest computed outer fiber stress on the arch. The numerical solution was not carried beyond this point because MAGNA cannot be made to represent the "failure" of specific elements in the model. In the actual structure, the magnesium arch was broken completely through at one point, and cracked significantly in two more regions, one on either side of the centerline. If the MAGNA simulation had been continued past the 0.003000 sec point in time, the magnesium arch would have been represented as continuing to carry higher and higher loads, even though internal stresses had exceeded the ultimate stress for the material - the computed response would have been stiffer than the actual response of the structure for this reason.

Figure 15 shows the maximum equivalent stress at any integration point for the 6 steel tube elements adjoining the centerline of the assembly. The figure shows that plasticity is predicted to occur, beginning at 0.002000 sec at a stress level of 74,800 psi. When the solution was interrupted at 0.003000 sec, the steel tube could have survived still greater plastic strains because the figure shows that the maximum equivalent stress at any integration point was well below the ultimate strength for the material, 84,800 psi. These 6 steel tube elements at the centerline of the assembly exhibited higher equivalent stress than any other elements along the length of the steel tube.

Figure 16 shows the region of the steel tube which exhibited significant plasticity at 0.003000 sec. The B and C contours represent 50% and 100% respectively of the yield stress for the 4130 steel material. The area inside the largest C contour extends from the centerline of the assembly outboard about 3.25 in. along the steel tube.

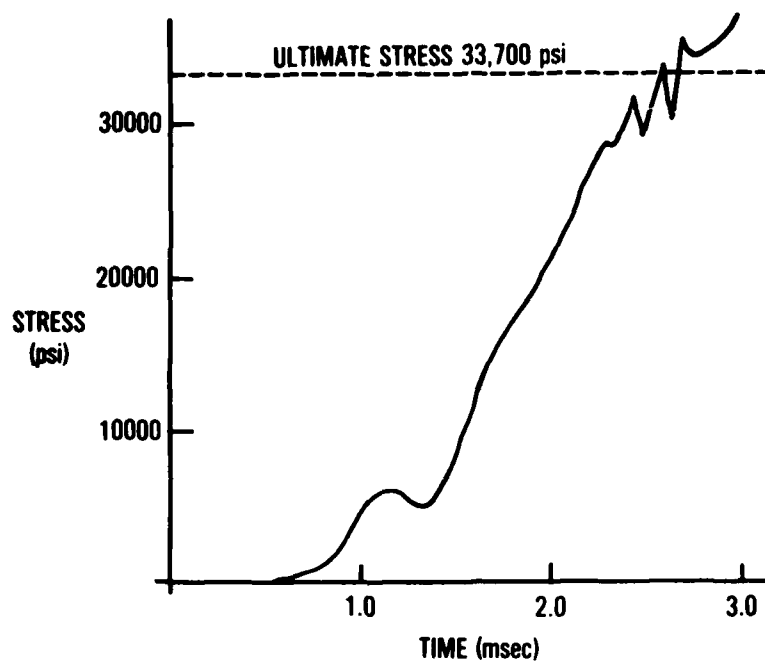


Figure 13. Maximum Equivalent Nodal Stress Versus Time for Magnesium Aft Arch

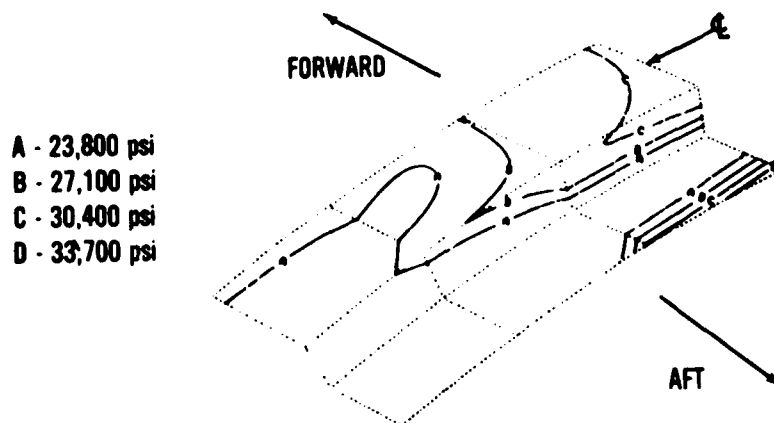


Figure 14. Equivalent Stress Contours on Magnesium Arch at 0.003000 Sec

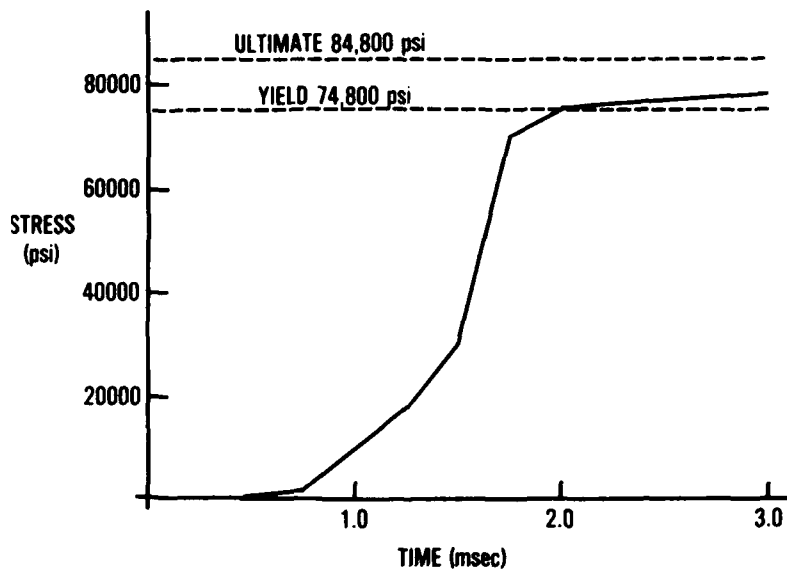


Figure 15. Maximum Equivalent Integration Point Stress versus Time for Steel Tube

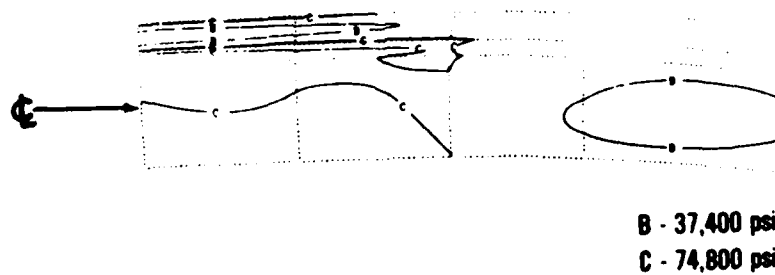


Figure 16. Equivalent Stress Contours on Steel Tube at 0.003000 Sec, Aft Walls of Tube, Viewed from Front

Figure 17 shows the total deflection versus time for point B1 on the steel tube, the location of which is shown in Figure 3. The solid line represents the computed results, and the dotted line the results observed during the test. The computed results are shown out to 0.003000 sec because that is the time corresponding to the predicted failure of the magnesium arch. The experimental data is only shown out to 0.002200 sec because that was the best estimate of the time at which the magnesium arch actually broke into two pieces during the test. In this way, the end of both curves signifies the same event: rupture of the magnesium arch.

An explanation was sought for the fact that the total deflection at rupture for the magnesium arch agreed very well between computed and experimental results, while the time at which rupture occurred did not. The pressure versus time schedules used to load the elements within the bird impact pressure footprint were suspected as the most likely cause for the time disagreement shown in Figure 17. The procedure used to mathematically define bird impact pressure loading assumed that the speed at which bird material moved over the surface of the transparency was uniform throughout the period of the impact event. This uniform rate was used to determine the "arrival time" of bird material on the windshield surface for row after row of elements within the pressure footprint. But when high speed films of the test were reviewed, it was observed that the actual "arrival time" of bird material at any given finite element within the footprint was earlier than that used in the MAGNA simulation. The overall period of the impact event observed in the films was the same as that used in the computer simulation, but the rate at which bird material "arrived" at succeeding finite element rows had been assumed to be uniform in the mathematical definition of the loading, while it was observed to be quite nonuniform in test films.

Figure 18 shows the calculated pressure schedules for the seven rows of elements in the bird impact pressure footprint. The bars in the figure indicate the periods of time during which the respective 7 rows of elements were loaded in the MAGNA analysis, while the cross-hatched areas indicate how much earlier the bird material was observed to "arrive" in high speed test films. The observed "arrival times" average about 77% of those used in the computer simulation.

The factor 0.77 was used to estimate the computed deflection versus time response had more realistic timing for the pressure loads been used in the MAGNA analysis. Figure 19 shows the same data as that presented in Figure 17 except that the time for the computed results has been multiplied by 0.77. The solution was not actually repeated with altered timing for the bird impact pressure loads. To reiterate, the actual results obtained are shown in Figure 17; the total deflections corresponding to rupture of the magnesium arch were nearly identical in both computed and experimental results, but the times corresponding to rupture were significantly different.

Turning finally to the computed results for the two polycarbonate windshield plies, Figures 20-25 show total deflection versus time correlation between computed and experimental results for 6 points on the

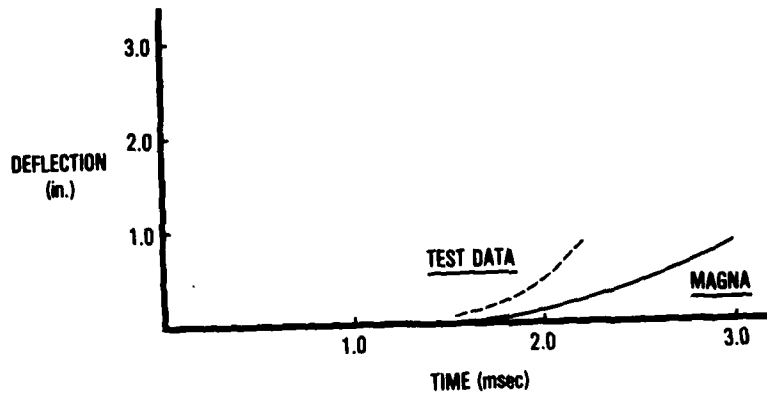


Figure 17. Total Deflection versus Time Correlation for Point B1

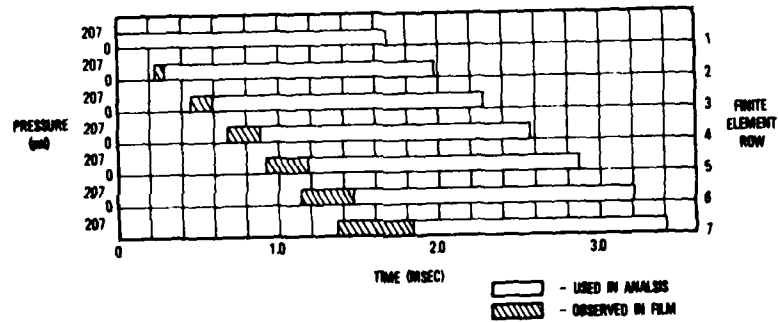


Figure 18. Bird Impact Pressure versus Time Schedules



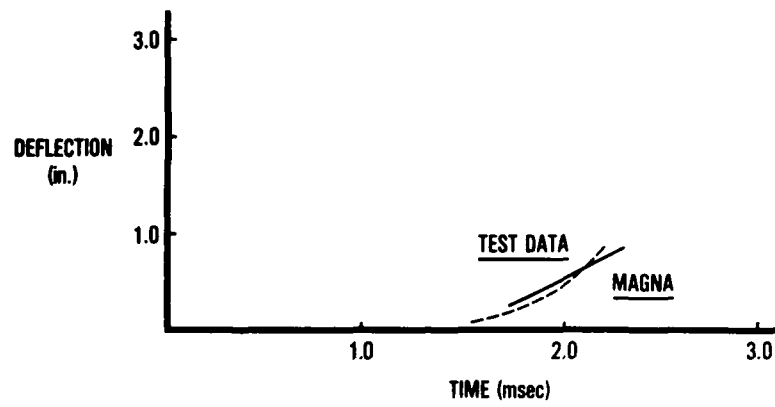


Figure 19. Estimated Total Deflection versus Time Correlation for Point B1

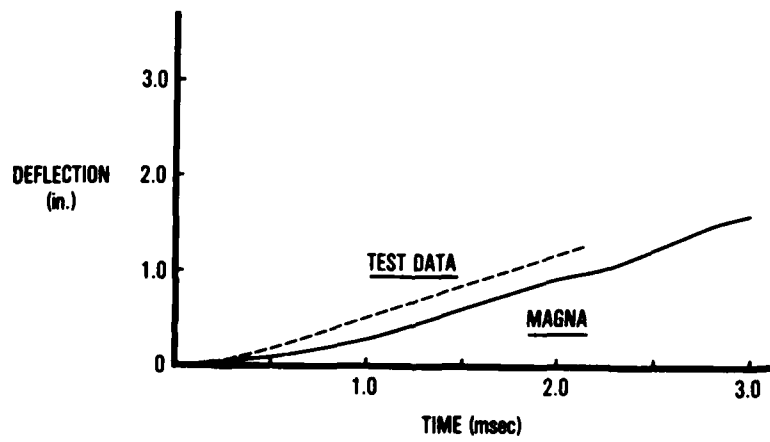


Figure 20. Total Deflection versus Time Correlation for Point -6

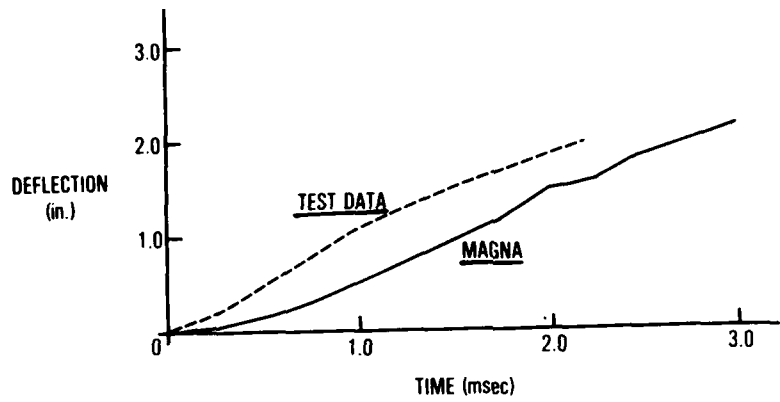


Figure 21. Total Deflection versus Time Correlation for Point -5

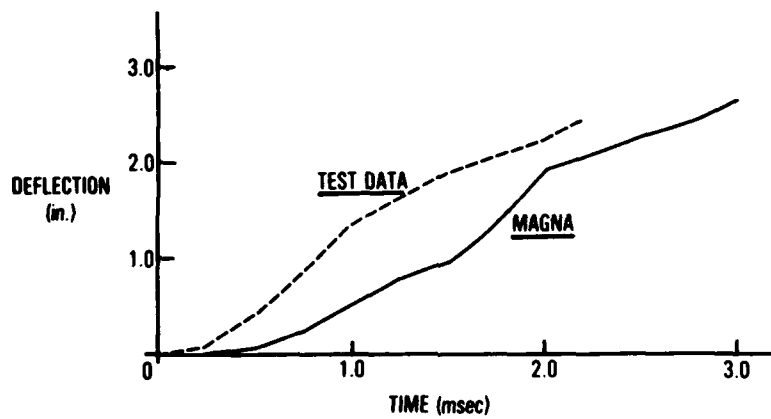


Figure 22. Total Deflection versus Time Correlation for Point -4

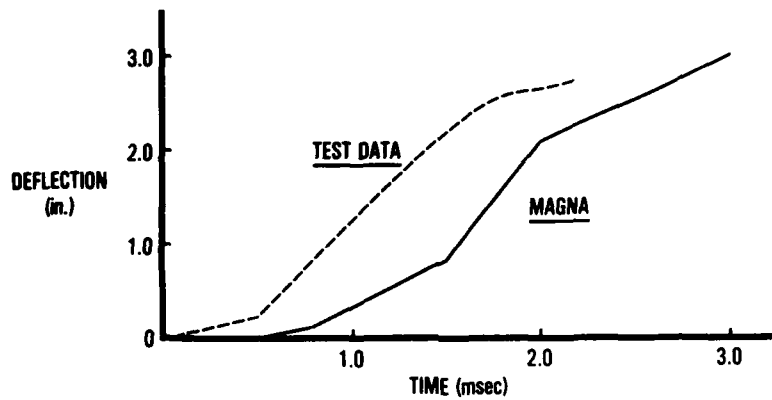


Figure 23. Total Deflection versus Time Correlation for Point -3

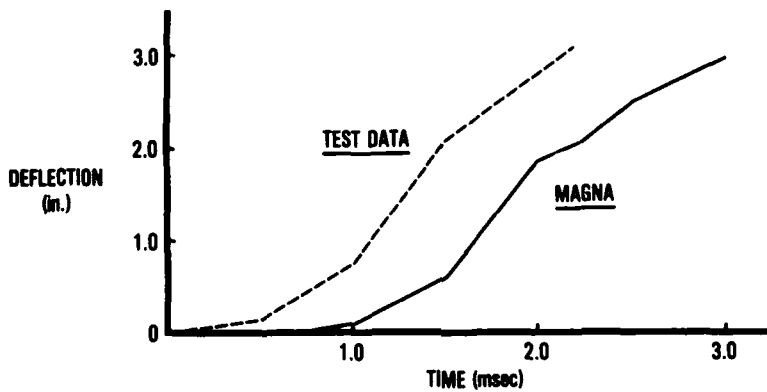


Figure 24. Total Deflection versus Time Correlation for Point -2

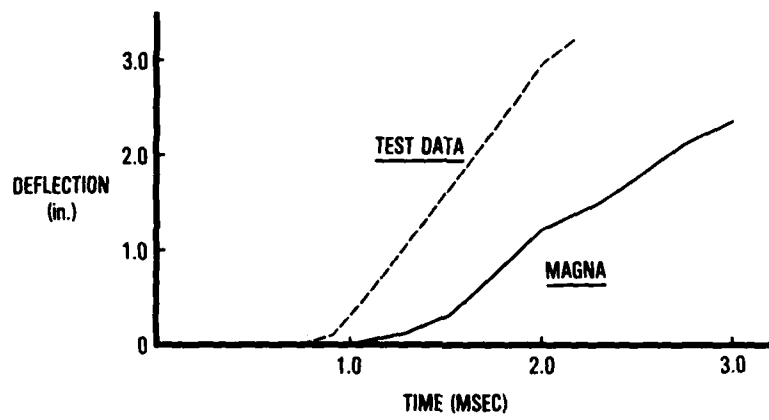


Figure 25. Total Deflection versus Time Correlation for Point -1



Figure 26. Equivalent Stress Contours on Outer Surface of Outer Polycarbonate Ply at 0.002050 Sec

inner surface of the windshield panel. The location of each point is illustrated in Figure 3. In each of the figures, data is shown out to the points in time corresponding to rupture of the magnesium arch: 0.002200 sec for the experimental data and 0.003000 sec for the computed data. Comparison of computed and experimental data past these respective points in time is invalid because the MAGNA simulation cannot be made to represent mechanical failure in any region of the structure.

As for point B1 on the steel tube shown in Figure 17, points -6 to -1 on the windshield show excellent correlation between computed and experimental results for maximum total deflection, but significant differences between the times at which given deflections occur. It is felt that the schedule of times used in the definition of bird impact pressure loads is primarily responsible for the significant differences seen in the history of deflection of points on the structure.

The greatest difference between computed and experimental maximum deflections on the windshield is seen in Figure 25 for point -1 which is located immediately forward of the arch region of the assembly as shown in Figure 3. It was felt that three factors contributed to this disagreement. First, the finite element mesh for the steel tube was quite coarse for the purpose of realistically tracking the progression of plasticity through the material (see Figure 16). Figure 25 shows at the time when plasticity is first predicted to occur on the steel tube (see 0.002000 sec in Figure 15), the rate of increase of deflection for point -1 (nearest the steel tube on the windshield) drops noticeably. Had the rate of deflection for point -1 computed between 0.001500 and 0.002000 sec continued unchanged out to 0.003000 sec, the maximum computed deflection for the point would have agreed almost exactly with experimental results. In other words, it is felt that a more refined mesh for the steel tube in the region near the centerline would have resulted in a less stiff computed response, or higher computed deflections for points like -1 near the arch.

The second reason for lower than expected computed deflections at point -1 was felt to be that initial cracking of the magnesium arch probably occurred before the point in time when cracks were first discerned in high speed test film. This again would be expected to make the actual response less stiff than the computed response since no mechanical failure was represented in the MAGNA simulation.

The third reason for lower than expected computed deflections at point -1 was felt to be the lower than planned magnitude of bird impact pressure applied to the windshield between 0.001850 sec and 0.002000 sec as shown in Figure 12. This came at a time when loads were only just beginning to be applied in the region of the windshield near point -1 (see Figure 18). Although the total impulse delivered to the structure should not have been affected significantly by this loading error, the local effect upon the histories of deflection of nearby points such as -1 might have been, in fact, quite significant.

In summary, the computed deflections for points on the windshield surface in the region of the bird impact agreed very well with respect to magnitude, but not as well with respect to time at which a given deflection occurred.

Figure 26 shows a contour map of equivalent stress on the outer surface of the outermost polycarbonate ply for the windshield panel. The contours are drawn on the deformed shape of the surface at the time indicated (0.002050 sec). A large depression or bowl in the windshield surface can be seen along the centerline of the assembly just forward of the arch. The narrow row of elements at the top of the figure are those elements fixed to the arch structure itself (see Figure 2); these elements have not rotated nearly as much as those more forward of the arch due to the torsional stiffness of the arch structure. The A, B, C, D, and E contours represent four equal intervals between 0 and 9392 psi, the yield strength assumed for the polycarbonate material. The only E contour shown in the figure is the one lying on and running parallel to the forward edge of the arch where the most severe bending in the polycarbonate ply occurs. The location and orientation of this high stress region corresponds precisely to the region where windshield failure actually was initiated in tests with slightly thinner polycarbonate plies. MAGNA, it appears, accurately predicted the region of highest stress in the polycarbonate windshield plies.

It is also interesting to note that Figure 26 indicates the point in time at which maximum stress in the polycarbonate windshield plies was predicted by MAGNA to occur. This time, about 0.002000 sec, also corresponds to the initiation of significant plasticity in the steel tube arch reinforcement (see Figure 15). A mechanism for generating the maximum stress in the polycarbonate material is suggested by these results: as long as the metallic arch structure is able to accept and bear higher and higher loads, stresses in the polycarbonate continue to grow greater as windshield deflections increase. But when the steel tube yields, load relief occurs in the plastic windshield panel and stresses begin to grow smaller in the polycarbonate structural plies. If this is an accurate assessment of the true response, a useful approach for transparency system design is indicated: design the edgemember support structure to deform plastically at a load level corresponding to high but safe levels of stress in the polycarbonate. In this way, before rupture of the windshield panel takes place, plasticity in the edgemember can occur to absorb additional bird impact energy.

### Conclusions

The MAGNA nonlinear finite element analysis system has been shown in previous studies and again in this work to be an efficient and effective tool for use in the design and analysis of aircraft transparency structural systems. A wide variety of thermal and mechanical loads on the transparency have been involved in these studies. The use of analysis procedures developed in earlier work leads to realistic and useful results. The time and cost required for full scale testing can be reduced significantly through the use of MAGNA.

In this study, it has been demonstrated that MAGNA can realistically predict deflection, plasticity, and rupture or mechanical failure in windshield arch edgemember support structure. The location at which the cast magnesium arch ruptured, and the deflection corresponding to rupture which were computed by MAGNA agree well with experimentally observed results. The location of the region of significant plasticity on the steel tube arch reinforcement computed by MAGNA also agrees well with experimental results. As for other cases analyzed in earlier studies, the deflection of points on the windshield panel itself, and the location on the windshield of impending failure were both predicted realistically by MAGNA.<sup>10-13</sup>

As a result of the correlation obtained between computed and experimental results, relatively high confidence can be placed on the stresses predicted by MAGNA to occur in the two polycarbonate windshield plies. It can be concluded, because yield is indicated in both polycarbonate plies for 4 lb 400 kt bird impact, that failure of the windshield panel itself would occur for 4 lb bird impact at the same location on this transparency system at speeds only slightly in excess of 400 kt. In other words, the 4 lb bird impact protection offered by this transparency system design is felt to exceed 400 kt only slightly.

It has been shown that the dynamic response of aircraft transparency structural systems can be very strongly coupled to bird impact pressure loading. The magnitude of the impact pressure is very sensitive to the deformed shape of the transparency surface. Although procedures devised in earlier studies can account for some of the more significant aspects of this coupling, a fluid/solid interaction analysis capability is needed to treat the problem directly.

The simple characterization of transparent plastic materials used in this study has been demonstrated to be sufficient for obtaining a realistic simulation of the dynamic structural response to bird impact loading. It is felt that this is the case, not so much because material sensitivities to parameters such as strain rate and temperature are not truly significant, but primarily because the dynamic response of the structure is overwhelmingly sensitive to the impact pressure loads, i. e. more so than to material properties.

It has been demonstrated that the analysis of practical aircraft transparency structural engineering problems, such as the one described here, with tools like MAGNA requires Cray-1/S class computer systems. The size of numerical problems like this one preclude the use of common scientific mainframe computers such as the CDC Cyber 170-750 or 170-845 machines. The Cray-1/S and even more powerful computer systems permit many practical problems previously too large for cost-effective analysis to be accomplished with ease and with costs which grow continually smaller.

One development need which became apparent as a result of this study is the capability to represent the mechanical failure of an element or elements within the finite element model during the progress of the computer solution. Currently, MAGNA does not provide the user this feature, and if

it had been available at the time this study was conducted, the computer solution could have been carried further to predict the response of the structure after the point in time at which the cast magnesium arch failed by cracking in two. In general, it is agreed that aircraft transparency structural systems have performed satisfactorily under bird impact loading even when several components of the structure fail, as long as bird debris or fractured pieces of structure don't enter the cockpit in such a way as to injure or kill the crewmembers. As a result of this thinking, MAGNA should be provided the capability to represent fracture in order for it to serve as a more general analysis and design tool.

#### References

1. Littel, H. E., Windshield and Canopy Protection Development Program, Air Force Flight Dynamics Laboratory, Wright-Patterson Air Force Base, Ohio 45433-6553, AFFDL-TR-74-75, June 1974.
2. Olsen, J. B., and Hinds, B. G., Manufacturing Methods for Large Laminated One-Piece Canopy, Air Force Wright Aeronautical Laboratories, Wright-Patterson Air Force Base, Ohio 45433-6553, AFWAL-TR-81-4018, April 1981.
3. Brockman, R. A., MAGNA: A Finite Element Program for the Materially and Geometrically Nonlinear Analysis of Three Dimensional Structures Subjected to Static and Transient Loading, University of Dayton Research Institute, Dayton, Ohio 45469-0001, UDR-TR-79-45, November 1979.
4. Wilbeck, J. S., Impact Behavior of Low Strength Projectiles, Air Force Wright Aeronautical Laboratories, Wright-Patterson Air Force Base, Ohio 45433-6553, AFML-TR-77-134, July 1978.
5. Challita, A., and Barber, J. P., The Scaling of Bird Impact Loads, Air Force Flight Dynamics Laboratory, Wright-Patterson Air Force Base, Ohio 45433-6553, AFFDL-TR-79-3042, June 1979.
6. Barber, J. P., Taylor, H. R., and Wilbeck, J. S., Bird Impact Forces and Pressures on Rigid and Compliant Targets, Air Force Flight Dynamics Laboratory, Wright-Patterson Air Force Base, Ohio 45433-6553, AFFDL-TR-77-60, May 1978.
7. Brockman, R. A., Finite Element Analysis of Soft-Body Impact, Flight Dynamics Laboratory, Wright-Patterson Air Force Base, Ohio 45433-6553, AFWAL-TR-84-3035, October 1984.
8. McCarty, R. E., "Computer Analysis of Bird Resistant Aircraft Transparencies," Proceedings of the 17th Annual SAFE Symposium, December 1979, Las Vegas, Nevada.



9. McCarty, R. E., "Finite Element Analysis of F-16 Aircraft Canopy Dynamic Response to Bird Impact Loading," 21st AIAA/ASME/ASCE/AHS Structures, Structural Dynamics, and Materials Conference, May 1980, Seattle, Washington.
10. McCarty, R. E., "Aircraft Transparency Bird Impact Analysis Using the MAGNA Computer Program," Conference on Aerospace Transparencies Sponsored by the Society of British Aerospace Companies, September 1980, London, England.
11. McCarty, R. E., "Finite Element Analysis of a Bird-Resistant Monolithic Stretched Acrylic Canopy Design for the F-16A Aircraft," AIAA Aircraft Systems and Technology Conference, August 1981, Dayton, Ohio.
12. McCarty, R. E., and Hart, J. L., "Validation of the MAGNA Computer Program for Nonlinear Finite Element Analysis of Aircraft Transparency Bird Impact," 14th Conference on Aerospace Transparent Materials and Enclosures Sponsored by the Air Force Wright Aeronautical Laboratories, July 1983, Scottsdale, Arizona, AFWAL-TR-83-4154, December 1983.
13. McCarty, R. E., "MAGNA Computer Simulation of Bird Impact on the TF-15 Aircraft Canopy," 14th Conference on Aerospace Transparent Materials and Enclosures Sponsored by the Air Force Wright Aeronautical Laboratories, July 1983, Scottsdale, Arizona, AFWAL-TR-83-4154, December 1983.
14. McCarty, R. E., "Aircraft Transparency Bird Impact Analysis Using the MAGNA Computer Program," Conference and Training on Wildlife Hazards to Aircraft Sponsored by the FAA, March 1984, Charleston, South Carolina.
15. McCarty, R. E., and Venkayya, V., Analysis of Bird Impact on Port Wing, Air Force Wright Aeronautical Laboratories, Wright-Patterson Air Force Base, Ohio 45433-6553, Letter Report, August 1979.
16. McCarty, R. E., and Smith, R. A., "Finite Element Analysis of Through the Canopy Emergency Crew Escape from the T-38 Aircraft," AIAA/ASME/ASCE/AHS 23rd Structures, Structural Dynamics, and Materials Conference, May 1982, New Orleans, Louisiana.
17. McCarty, R. E., and Smith, R. A., "Simulation of T-38 Aircraft Student Canopy Response to Cockpit Pressure and Thermal Loads Using MAGNA," AIAA/ASME/ASCE/AHS 24th Structures, Structural Dynamics, and Materials Conference, May 1983, Lake Tahoe, Nevada.
18. Hart, J. L., "MAGNA Analysis of the T-38 Aircraft Student Canopy Response to In-Flight Aerodynamic Pressure Loads," AIAA/ARS/ASEE Aircraft Design Systems and Operations Meeting, November 1984, San Diego, California.

19. Brockman, R. A., MAGNA (Materially and Geometrically Nonlinear Analysis) Part I - Finite Element Analysis Manual, Flight Dynamics Laboratory, Wright-Patterson Air Force Base, Ohio 45433-6553, AFWAL-TR-82-3098 Part I, December 1982.
20. Bruner, T. S., MAGNA (Materially and Geometrically Nonlinear Analysis) Part II - Preprocessor Manual, Flight Dynamics Laboratory, Wright-Patterson Air Force Base, Ohio 45433-6553, AFWAL-TR-82-3098 Part II, December 1982.
21. Brockman, R. A., MAGNA (Materially and Geometrically Nonlinear Analysis) Part III - Postprocessor Manual, Flight Dynamics Laboratory, Wright-Patterson Air Force Base, Ohio 45433-6553, AFWAL-TR-82-3098 Part III, December 1982.
22. Brockman, R. A., MAGNA (Materially and Geometrically Nonlinear Analysis) Part IV - Quick Reference Manual, Flight Dynamics Laboratory, Wright-Patterson Air Force Base, Ohio 45433-6553, AFWAL-TR-82-3098 Part IV, December 1982.
23. Pinnell, W. R., "A Triangulation Technique for Obtaining Deflections of Aircraft Transparencies During Bird Impact Testing," 14th Conference on Aerospace Transparent Materials and Enclosures Sponsored by the Air Force Wright Aeronautical Laboratories, July 1983, Scottsdale, Arizona, AFWAL-TR-83-4154, December 1983.
24. Nash, R. A., and West, B. S., Alternate T-38 Transparency Development, Part IV, Parametric Studies, Flight Dynamics Laboratory, Wright-Patterson Air Force Base, Ohio 45433-6553, AFWAL-TR-80-3132 Part IV, June 1983.
25. Clayton, K. I., and West, B. S., Aircraft Transparency Testing Methodology and Evaluation Criteria, Flight Dynamics Laboratory, Wright-Patterson Air Force Base, Ohio 45433-6553, AFWAL-TR-83-3045, April 1983.
26. Rhodes, G. F., Damping, Static, Dynamic, and Impact Characteristics of Laminated Beams Typical of Windshield Construction, Air Force Flight Dynamics Laboratory, Wright-Patterson Air Force Base, Ohio 45433-6553, AFFDL-TR-76-156, December 1977.
27. Military Standardization Handbook - Metallic Materials and Elements of Aerospace Vehicle Structures, Volumes 1 and 2, MIL-HDBK-5C, 15 September 1976.
28. Barber, J. P., and Wilbeck, J. S., Characterization of Bird Impacts on Rigid Plates: Part I, Air Force Flight Dynamics Laboratory, Wright-Patterson Air Force Base, Ohio 45433-6553, AFFDL-TR-75-5, January 1975.

29. Peterson, R. L., and Barber, J. P., Bird Impact Forces in Aircraft Windshield Design, Air Force Flight Dynamics Laboratory, Wright-Patterson Air Force Base, Ohio 45433-6553, AFFDL-TR-75-150, March 1976.
30. McCarty, R. E., Hart, J. L., and Smith, R. A., Nonlinear Finite Element Analysis of Aircraft Transparency Bird Impact Using the MAGNA Computer Program, Flight Dynamics Laboratory, Wright-Patterson Air Force Base, Ohio 45433-6553, AFWAL-TR- , pending technical report.

AUTHOR INDEX

<u>Name</u>	<u>Affiliation</u>	<u>Page</u>
Abdi, F. F.	Rockwell International	1159
Andrechak, Janet	Swedlow, Inc.	212
Anselmo, Capt John	AFWAL/FDST	678
Babish, Charles A. III	Flight Dynamics Laboratory	1425
Baile, Madhu "Dolly"	Dow Corning Corporation	936
Bales, Stephen E.	Dow Chemical Company	621
Berry, Capt Paul	OO-ALC/MMBRE	998
Bimanand, Alexander Z.	Sierracin/Sylmar Corp.	555
Boman, Bret L.	McDonnell Aircraft Co.	1425
Bouchard, M. P.	University of Dayton	122, 702, 1195
Bowman, D. R.	University of Dayton	122, 387
Braisted, William R.	University of Dayton	1195
Brockman, R. A.	University of Dayton	1173
Brown, Jennie H.	U.S. Army Materials Technology	360
Brown, John A.	John Brown Associates	1136
Bruce, R. S.	Triplex Aircraft & Spec. Prod.	57
Burchill, Peter	National Research Laboratory	248, 370, 1033
Chapin, Don	Sierracin/Sylmar Corp.	742
Cieslak, S. J.	Alcoa Technical Center	227
Clark, G.	Rockwell International	1159
Clayton, K. I.	University of Dayton	727, 737
Coble, David G.	Dow Corning Corporation	936
Corney, N. S.	Royal Aircraft Establishment	345
Davidson, R. G.	Materials Research Laboratory	370
Davis, Lt A. D.	Flight Dynamics Laboratory	1447
DeCamp, H.	Sierracin/Sylmar Corp.	898
DeFusco, Capt Russell P.	Bird Aircraft Strike Hazard Team	834
Dogan, Capt Robert L.	Bird Aircraft Strike Hazard Team	834
Dorey, R.	EMI-MEC Ltd	104
Dversdall, D.	AFWAL/FDER	821
Ewald, Klaus	Lufthansa German Airlines	434
Fielman, John W.	University of Dayton	1105
Freeman, Glenn E.	PPG Industries	87
Fuller, D. B.	Loral Defense Systems-Arizona	522
Gallagher, Vincent P.	Boeing Helicopters	2
Graham, Charles R.	PPG Industries	240
Gran, Michael	AF Wright Aeronautical Lab	875, 976, 1256
Greenberg, Charles B.	PPG Industries, Inc.	1124
Griffith, J. R.	Naval Research Laboratory	605
Gurev, Harold	Swedlow, Inc.	312
Hargis, S.	AFWAL/FDER	821
Held, T. W.	University of Dayton	1173
Hewitt, F. J.	CYRO Industries	331
Hinds, B. G.	Sierracin/Sylmar Corp.	898, 1013
Hoffman, J. B.	Northrop Corporation	762
Hsieh, Alex J.	U.S. Army Materials Technology	360
Juengst, Cliff	Swedlow, Inc.	290
Kama, William N.	Human Engineering Division, AAMRL	1072
Kelley, Malcolm	AFWAL/FDER	727, 943, 952

Kivlighn, H. D. Jr.	Grumman Corporation	1135
Kochanowski, J. E.	G. E. Plastics	193
Kolbow, Capt Steve	AFWAL/FDER	998
Kolodziejski, Paul J.	AFWAL/FDER	702
Kovensky, D.	Mcdonnell Aircraft Co.	191
Landry, Paul	Lockheed Aeronautical Systems	1378
Larson, Kent R.	Dow Corning Corporation	936
Lee, Paul S.	North Carolina A & T Univ.	875
LeMasters, Don	Swedlow, Inc.	290
Lewis, William	Swedlow, Inc.	212
Loh, I. H.	Spire Corporation	497
Loomis, John S.	University of Dayton	1105
Lu, P. H.	Spire Corporation	497
Mason, Neal E.	Boeing Helicopters	2
Mathys, G.	Materials Research Laboratory	370
Mayer, Arnold H.	AF Wright Aeronautical Lab	875, 1231
McCarty, Robert E.	Flight Dynamics Laboratory	1327, 1378, 1447
Merkel, Capt Harold S.	AAMRL/HEF	1094
Merritt, Maj Ronald L.	Bird Aircraft Strike Hazard Team	834
Michalsky, Douglas L.	Southwest Research Institute	153
Miller, J. E.	Sherwin Williams Co.	193
Minter, E. M.	Royal Aircraft Establishment	345
Moniz, W. B.	Naval Research Laboratory	248
Moody, R. A.	Spire Corporation	497
Mountford, E.	EMI-MEC Ltd.	104
Myers, James W.	PPG Industries, Inc.	917
Nisar, Mohammad	Swedlow, Inc.	312
Nkonge, Japheth	North Carolina A & T Univ.	875
Oeding, Robert G.	PDA Engineering	1360
Pinnell, W. R.	AFWAL/FDER	164, 507
Raffo, J. A.	Sierracin/Sylmar Corp.	555, 1013
Reinhart, T. J.	AFWAL/MLSE	497
Renieri, G.	Mcdonnell Aircraft Co.	191
Robbins, Gerald L.	Mobay Corporation	264
Ross, Halver V.	OO-ALC/MANEP	153
Sandlin, S.	Swedlow, Inc.	582
Savoni, G. L.	Rockwell International	1159
Schreyer, G. G.	Rohm GmbH	331
Schumacher, Paul E.	Sierracin/A.P.G.	639
Shaikh, Nisar	University of Nebraska-Lincoln	875
Short, Maj Jeffry J.	AFWAL/FDER	763
Sioshansi, P.	Spire Corporation	497
Sjostrom, Lars	Saab Aircraft Division	797
Skubic, Raymond J.	Mcdonnell Aircraft Co.	476
Smith, F. N.	Alcoa Technical Center	227
Smith, Richard A.	AFWAL/FDER	660, 1159, 1231
Soulen, R. L.	Naval Research Laboratory	605
Speelman, Scott A.	Texstar, Inc.	206
Stacewicz, R. H.	Materials Research Laboratory	370, 1033
Stedman, M.	National Physical Laboratory	104
Stenger, G. J.	University of Dayton	122, 164, 821, 845
Stevens, John I.	U.S. Army Chemical RD&E	360
Stewart, Sherman D.	PPG Industries	2

Stone, G. C.	General Dynamics Fort Worth	28
Task, H. Lee	Human Engineering Division, AAMRL	1046
Tattershall, P.	Royal Aircraft Establishment	345
Terry, J. L.	Flight Dynamics Laboratory	845
Teten, Lance	Texstar, Inc.	714
Thornton, William A.	John Brown Associates	1136
Thorpe, John	UK Civil Aviation Authority	775
Trudan, D. E.	Flight Dynamics Laboratory	1447
Uram, J., Jr.	Loral Defense Systems	582
Urzi, Russ	AFWAL/FDER	678
Vanselow, Janice J.	U.S. Army Materials Technology	360
Wang, Hai-Tao	Swedlow, Inc.	290
Wegmann, Rolph	Saab Aircraft Division	797
West, Blaine S.	University of Dayton	387, 660
Wielonski, Roy F.	Battelle	1144
Wright, R. W.	Triplex Aircraft & Spec. Prod.	57